IMPERIAL COLLEGE LONDON

Lanthanum Nickel Oxide Based Double Perovskites and their Exsolution Phenomena

Jia GUO

Supervised by Prof. Stephen J SKINNER

A thesis submitted in (partial) fulfilment of the requirements
for the award of the degree

Doctor of Philosophy

from the

Imperial College London

Faculty of Engineering, Department of Materials
2023

Declaration of Originality

I, Jia Guo, declare the work included within this thesis is wholly my own except where reference is made to that of others. The contents of this work form solely as part fulfilment of doctoral requirements of Imperial College London, and do not contribute towards any other degree course at another institution.

Jia Guo
October 2023

The copyright of this thesis rests with the author. Unless otherwise indicated, its contents are licensed under a Creative Commons Attribution-Non Commercial 4.0 International Licence (CC BY-NC). Under this licence, you may copy and redistribute the material in any medium or format. You may also create and distribute modified versions of the work. This is on the condition that: you credit the author and do not use it, or any derivative works, for a commercial purpose. When reusing or sharing this work, ensure you make the licence terms clear to others by naming the licence and linking to the licence text. Where a work has been adapted, you should indicate that the work has been changed and describe those changes. Please seek permission from the copyright holder for uses of this work that are not included in this licence or permitted under UK Copyright Law.

To my beloved family

This thesis is dedicated to my family, especially my parents, whose unwavering support, love, and encouragement have been my guiding light throughout this journey.

Abstract

The increasing energy demand and the need to reduce greenhouse gas emissions are driving a transition to renewable energy sources. Solid-oxide cells (SOCs) offer promise for integrating intermittent renewables into the grid, yet current fuel electrode materials, exemplified by Ni cermet, face limitations including degradation and poisoning. A novel approach called 'exsolution,' involving the creation of metal nanoparticle-decorated oxides, is gaining traction for its potential to improve SOCs by producing stable and efficient electrode materials.

This thesis investigates double perovskite materials as potential fuel electrodes due to their favourable electrochemical properties and unique exsolution behaviour. Specifically, lanthanum nickel ruthenates (La_xNiRuO_{6-y}, x = 2, 1.9,1.85) and ruthenium-doped lanthanum nickel titanates ($La_xNiTi_{0.9}Ru_{0.1}O_{6-\delta}$, x = 2, 1.85) were studied. A-site deficiency was found to facilitate exsolution. Notably, A-site deficient lanthanum nickel ruthenate ($La_{1.85}NiRuO_{6-y}$) exhibited exsolution of Ni and Ru cations at relatively low temperatures, with particle size increasing at higher temperatures. In this study, $La_{1.85}NiRuO_{6-y}$ underwent exsolution of Ni and Ru cations at 450°C, with separate B-site cation exsolution initiating at lower temperatures (300~360°C). *In-situ* microscopy and electrochemical analysis confirmed rapid exsolution at 450°C, resulting in enhanced electrochemical performance in single cells test due to the exsolution of Ni-Ru bimetallic nanoparticles.

A-site deficient ruthenium-doped lanthanum nickel titanates ($La_{1.85}NiTi_{0.9}Ru_{0.1}O_{6-\delta}$) displayed exsolution of Ni nanoparticles over a wide temperature range, contrasting with Ru cations, which required extremely high temperatures for exsolution. The thesis proposes a critical temperature range (400-450°C) influencing exsolution behaviour. Additionally, attempts to replace exsolved cations with infiltrated iron cations showed enhanced exsolution of Ni-Ru alloy nanoparticles.

In summary, this thesis extensively examines double perovskite materials as fuel electrodes for SOCs, emphasizing their exsolution behaviours. It illuminates exsolution in B-site ordered double perovskites with varied cation properties and proposes metal nanoparticle-decorated lanthanum nickel ruthenates and titanates as promising SOC fuel electrode candidates.

Acknowledgement

I am deeply grateful to my supervisor, Prof. Stephen Skinner, for his unwavering support, invaluable guidance, and expert mentorship throughout this research. His patience, encouragement, and constructive feedback have been instrumental in shaping the direction of this work. The opportunities I've had, from conducting research in top-notch laboratories to attending summer schools, conferences, collaborations, and presenting and publishing results, would not have been possible without Prof. Stephen's enduring support and dedication over the past five years. Thank you for your unwavering effort and guidance.

My heartfelt appreciation goes to my parents, who have been the cornerstone of my journey. Their unwavering support, understanding, and patience have sustained me during my time in London while they were five thousand miles away in China. My PhD journey and life would have been inconceivable without their support.

I would also like to extend my sincere gratitude to the collaborators who made this PhD study possible. Their valuable insights, critical evaluations, and thoughtful suggestions were indispensable. I extend my appreciation to the following individuals: Dr. Ronsheng Cai and Prof. Sarah Haigh from the University of Manchester, Prof. Simone Mascotto from the University of Koblenz, Dr. Xiao Sun from DESY, and Miss Princess Inangha from the University of Hamburg, also thanks to Dr. George Wilson, Dr. Eleonora Cali, Dr. Inyoung Jang, and Dr. Arim Seong from Imperial College London, who not only provided support but also became cherished friends.

I want to acknowledge the departmental facility managers for their guidance and training: Dr. Catriona McGilvery, Dr. Mahmoud Ardakani, and Dr. Ecaterina Ware for electron microscopy, Dr. Gwilherm Kerherve for X-ray photoelectron spectroscopy and analysis, and Mr. Richard Sweeney and Dr. Andrey Berenov for X-ray diffractometry and thermal analysis.

My thanks extend to my colleagues, peers, and all members of the Fuel Cell and Electro-ceramics group who generously shared their knowledge, experiences, and academic camaraderie, enriching my academic journey. Gratitude also goes to my friends outside the group for their companionship and occasional distractions over the past five years.

Last but not least, I would like to thank my boyfriend, Dr. Jiamin Xu, for his unwavering support and belief in me.

Table of Contents

Abstract 4
Acknowledgement 5
List of figures 9
List of tables 22
List of acronyms 24
Chapter 1 Introduction 27
1.1 Background 27
1.2 Fundamentals of SOCs 29
1.3 Motivation 32
1.4 Thesis outline 33
Chapter 2 Literature Review 36
2.1 Introduction 36
2.2 Double perovskite oxides 36
2.2.1 Ru-based $A_2BB'O_6$ double perovskite oxides 38
2.2.2 Ti-based $A_2BB'O_6$ double perovskite oxides 40
2.3 Exsolution method 44
2.3.1 Concept and system 44
2.3.2 Mechanisms and steps 48
2.3.3 Driving forces 52
2.3.4 Multi-component exsolution 63
2.4 Summary 66
Chapter 3 Experimental Methods 67
3.1 Introduction 67
3.2 Materials synthesis 67
3.2.1 Solid-state reaction 67
3.2.2 Sol-gel synthesis 67
3.2.3 Exsolution thermal treatment 69
3.2.4 Test-cell fabrication 69
3.3 Materials characterisation 71
3.3.1 X-ray characterizations 71
3.3.2 Thermal analysis (TA) 79
3.3.3 Electron microscopy (EM) 80
3.3.4 Inductively coupled plasma-optical emission spectroscopy (ICP-OES) 84
3.3.5 Electrochemical performance characterizations 85
Chapter 4 Synthesis and intrinsic properties of lanthanum nickel ruthenate double perovskite 90

4.1. Introduction 90
4.2. Synthesis of L2NR 90
4.3. Crystal structure of L2NR 92
4.4. A-site deficient lanthanum nickel ruthenate 95
4.5. Chemical composition 96
4.6. Thermal behaviour 102
4.7. Summary and future work 104
Chapter 5 Exsolution of A-site deficient lanthanum nickel ruthenate double perovskite 106
5.1. Introduction 106
5.2. Structural stability in 5%H_2/Ar 106
5.3. Exsolution of nanoparticles 108
5.3.1. Morphology 108
5.3.2. Ni-Ru bimetallic nanoparticles 114
5.4. Dry reduction 119
5.5. Temperature-dependent exsolution 122
5.6. Summary and Future Work 126
Chapter 6 *In-situ* investigation of L1.85NR exsolution behaviour and its electrochemical performance 128
6.1 Introduction 128
6.2 Thermogravimetric analysis 128
6.3 *In-situ* electrochemical impedance spectroscopy (EIS) and full cell test 130
6.3.1 In-situ EIS observation 130
6.3.2 Fuel cell test 136
6.4 *In-situ* TEM investigation 142
6.4.1 Fast nucleation at 450°C 142
6.4.2 Temperature dependent exsolution of Ni and Ru 145
6.5 Synchrotron X-ray scattering analysis 151
6.6 Summary and future work 155
Chapter 7 *In-situ* investigation of ruthenium doped lanthanum nickel titanium double perovskite exsolution 157
7.1 Introduction 157
7.2 Synthesis of lanthanum nickel titanates 157
7.2 Exsolution of nickel nanoparticles 162
7.3 Temperature-dependent exsolution 166
7.3.1 Temperature dependent nanoparticles 166
7.3.2 *In-situ observation of the exsolution process* 169
7.4 Impedance investigation of lanthanum nickel titanates and exsolution process 177
7.5 Topotactic exchange enhanced Ru-exsolution 182

7.6 Summary 186
7.7 Future work 186
Chapter 8 Conclusion and future work 188
8.1 Conclusion 188
8.2 Future work 190
8.2.1 Studies on the A-site deficiency concentrations and its effect of exsolution 190
8.2.2 Studies on the facet-dependency of the exsolution 190
8.2.3 Studies on hydrogen partial pressure and its effect on the exsolution 191
8.2.4 Studies on the electron-beam induced exsolution 191
8.2.5 Studies on the re-oxidation and reversibility of the exsolved nanoparticles 191
8.2.6 Studies of cations diffusion in topotactic exchange 191
8.2.7 Studies on optimizing symmetric cell and single cell structure 192
References 193
Appendix 209
5.1 ASAXS analysis 209
5.2 Copyright 213

List of figures

Figure 1.1 Stack columns chart of the UK investment in the energy industry from 2005 to 2022 [1]. Reused under the Open Government Licence v3.0. 27
Figure 1.2 schematic illustration of the working principles of (a) SOFC and (b) SOEC with oxygen transportation electrolyte. 30
Figure 1.3 theoretically illustration of the cell voltage vs. current density curve. Reproduced under permission from reference [9]. Copyright 2007, Elsevier....31
Figure 1.4 Artificially coloured SEM micrograph of cross-section of a manufactured SOC from Technical University of Denmark (DTU). Reused under permission from reference [4]. Copyright 2020, Elsevier. 33
Figure 2.1 Schematic diagram of ideal ABO_3 perovskite structure. The red spheres represent oxygen anions; the blue spheres represent A-site cations; and the green sphere represent B-site cation. 36
Figure 2.2 Cation ordering schemes in double perovskite. Rock-salt ordering is A-site (first row) or B-site (second row) cations alternate along three dimensions; columnar ordering is two cations alternate along x and y axis; layered ordering is two cations only alternates along z axis. Reproduced under the terms and condition of CCC. [23] Copyright 2010, Royal Society of Chemistry. 37
Figure 2.3 Schematic of the intelligent catalyst self-regeneration and conventional catalysts enlargement. Reused under permission from reference [80]. Copyright 2006, Elsevier. 45
Figure 2.4 Schematic of the exsolution process of perovskite unit cells with built-in A-site vacancy. Reproduced under the permission from reference [82]. Copyright 2013, Springer Nature. 45
Figure 2.5 (a) TEM micrograph (dark field) of a Ni particle exsolved on (110) native surface facet showing the partially submerge of the nanoparticle, scale bar 10 nm; (b) schematic illustration of the exsolved nanoparticle-bulk interface and the deposited nanoparticle-substrate interface; SEM images of the exsolved Ni nanoparticle on the surface of $La_{0.52}Sr_{0.28}Ni_{0.06}Ti_{0.94}O_3$ before (c) and after (d) aging for 70 hours, scale . Comparison of the carbon growth of (e) Ni nanoparticles prepared by vapor deposition (scale bar 500nm) and (f) exsolved Ni nanoparticles on lanthanum strontium titanates (scale bar 100nm). Reproduced under the terms of the CC-BY license. [70] Copyright 2015, the authors. Published by Springer Nature. 46
Figure 2.6 Illustration of the process. (a) The exsolution method and (b) key processes fundamental to exsolution. Reuse under the terms of CC-BY license [174]. Copy right 2021, the authors. Published by John Wiley and Sons. 49
Figure 2.7 (a) Illustration of the exsolution process. (b) The average particle size and the fitting curves with strain-limited model (solid line), reactant-limited model (dashed line), and diffusion-

limit model (dotted line). Reproduced under the permissions from reference [177]. Copyright 2016, Elsevier Ltd. 50
Figure 2.8 (a) In-situ TEM images of the exsolution of a Ni metal particle at the surface of a $La_{0.43}Ca_{0.37}Ti_{0.94}Ni_{0.06}O_3$ powder at different times during an in-situ E-TEM reduction carried out under vacuum at 900 °C. (b) Schematic illustration of particle−socket genesis during exsolution. Reused with permission from reference [179]. Copyright 2019 American Chemical Society. 51
Figure 2.9 (a) 3D model of a catalyst particle with nanoparticles dispersed on its surface and within its bulk. (b) SEM image of the overview of the surface of the perovskite after exsolution. (c) SEM image of cross-section view after exsolution revealing surface and bulk particles. (d) Detail of the particles exsolved in the bulk Reuse permission from reference [181]. Copyright 2019, John Wiley and Sons. 52
Figure 2.10 Inverse fast Fourier transform High-angle annular dark-field imaging (HAADF)-Scanning transmission electron microscopy (STEM) images of a [−3 1 2] zone axis of Ir-doped $SrTiO_3$ grain at 700 °C (a,b), 640 °C (c,d,e), and644 °C (f) during in situ monitoring during heating in vacuum. The yellow and circle in (a) and (b) indicated the movement of the Ir atom. (c-f) showed a trapping and nucleation process of Ir atoms. Reproduced under terms and conditions of CC-BY license. [180] Copyright 2023, the authors. Published by Springer Nature. 53
Figure 2.11 Gibbs free energy of reduction of oxides to metals or certain oxides, at 900 °C in H_2. Reused under the permission from reference [82]. Copyright 2013, Springer Nature. 54
Figure 2.12 (a) Schematic illustration of the model used for the calculations of co-segregation energy. (b) Comparison of the co-segregation energy with the dopant (M) materials. Reused under terms of CC-BY license [183]. Copyright 2017 The Authors. Published by Springer Nature. 55
Figure 2.13 (a) Proposed phase diagram of $Pr_{0.5}Ba_{0.5-x}Sr_xFeO_{3-\delta}$ material (x = 0, 0.1, 0.2, 0.25, 0.3, 0.4, and 0.5) in H_2 environment as functions of reduction temperature and Sr^{2+} concentration from in-situ XRD measurements, and (b) the corresponding schematic illustration of the phase transition. Reproduced under terms of CC-BY license [187]. Copyright 2021, the Authors. 56
Figure 2.14 SEM images of the reduced (pure H_2, 550 °C, 80 h) $La_{0.2}Sr_{0.7}Ni_{0.1}Ti_{0.9}O_{3-\delta}$ films on (a) $(LaAlO_3)_{0.3}$– $(SrAl_{0.5}Ta_{0.5}O_3)_{0.7}$ (LSAT), (b) $SrTiO_3$ (STO), (c) $DyScO_3$ (DSO), and (d) $GdScO_3$ (GSO) substrates, respectively; Scale bars, 100 nm. (e) Effects of the substrate on three important physical parameters related to the exsolved thin films. (f) Ex-situ cross-sectional STEM-HAADF image and (g) corresponding Ni EDS map of the reduced film on LSAT substrate; Scale bars, 10 nm. Reuse under the terms of CC-BY license [189]. Copyright 2019, the authors. 57

Figure 2.15 (a) SEM image of the native surface of a porous $La_{0.4}Sr_{0.4}Ni_{0.03}Ti_{0.97}O_{3-d}$ sample after reduction (5% H_2/Ar, 930 °C, 20 h); scale bar, 1 mm. (b) 3D AFM reconstruction of a native surface highlighting the calculated orientations of the facets. Reuse under the terms of CC-BY license [70]. Copyright 2015, the authors. (c) AFM and SEM top-view images of as-reduced $La_{0.2}Sr_{0.7}Ti_{0.9}Ni_{0.1}O_{3-\delta}$ films of (001), (110) and (111) orientation, and corresponding schematics. Scale bars in SEM images are 1 μm and 200 nm in the insets. Adapted with permission from [191]. Copyright 2019, American Chemical Society. (d) SEM-EBSD analysis reveals differences in the surface morphology of $SrTi_{0.9}Nb_{0.05}Ni_{0.05}O_{3-\delta}$ perovskite facets with different orientations. (e) EBSD orientation mapping and AFM analysis of $SrTi_{0.9}Nb_{0.05}Ni_{0.05}O_{3-\delta}$ reduced at 600°C in 4%H_2/Ar for 1 hour. Reuse under the terms of CC-BY license [192]. Copyright 2022, the authors 58

Figure 2.16 (a) Schematics of conditions used to trigger exsolution in a SOC at the fuel electrode (shaded in blue or orange); SEM micrographs of $La_{0.43}Ca_{0.37}Ni_{0.06}Ti_{0.94}O_{3-\gamma}$ electrodes produced by (b) reduction in hydrogen at 900 °C for 20 hours and (c) electrochemical switching, under 50% H_2O/N_2 at 900 °C for 150 seconds. (d) Various characteristics results of the samples shown in (b-c). Reuse under permission from reference [197].Copyright 2016, Springer Nature. 59

Figure 2.17 (a) Schematic of exsolution process with and without topotactic ion exchange. (b) Schematic of topotactic ion exchange energetics for the mechanism of particle exsolution via Fe infiltration on the $Pr_{0.5}Ba_{0.5}Mn_{0.85}Co_{0.15}O_{3-\delta}$ surface. (c) HAADF scanning TEM image of Fe infiltrated the $Pr_{0.5}Ba_{0.5}Mn_{0.85}Co_{0.15}O_{3-\delta}$; and EDS elemental map of Pr, Ba, Mn, Co, and Fe; scale bar 20 nm. Reuse under the terms of CC-BY license [199]. Copyright 2019, the authors. Published by Springer Nature. 61

Figure 2.18 (a) Schematic of the reactor employed for plasma- triggered exsolution. SEM and TEM images of the Ni nanoparticles grown on the $La_{0.43}Ca_{0.37}Ni_{0.06}Ti_{0.94}O_{3-d}$ perovskite surface after (b, c) conventional H_2 gas reduction for 2 h and (f, g) N_2 plasma for 1 h at 650 °C. Schematics of Ni exsolution during e) hydrogen gas reduction and h) nitrogen plasma exposure. Reused under the permissions from reference [204]. Copyright 2021, John Wiley and Sons. ..62

Figure 2.19 (a,b) SEM images of $La_{0.43}Ca_{0.37}Ni_{0.06}Ti_{0.94}O_{3-d}$ after argon plasma treatment (15 min); sketches of (c) ion bombardment on perovskite surface with “plasma sheath” region, supporting an electric field and (d) process of plasma driven exsolution. . Reuse under the terms of CC-BY license [203]. Copyright 2022, the authors. Published by John Wiley and Sons. 63

Figure 2.20 Schematic illustrations and energetics of (a) bulk alloy formation and (b) surface alloy formation for the exsolution of alloy nanoparticles. Reused under permission from reference [207]. Copyright 2018, Royal Society of Chemistry. 64

Figure 2.21 (a) Schematic representation of the crystallization mechanism for Pd core exsolution and asymmetric Ni shell growth. (b-d) STEM-EDX images showing TEM particles in the last three stages of the proposed mechanism in (a); Scale bar 5 nm. Reused under permission from reference [195]. Copyright @ 2019, Royal Society of Chemistry. (e) TEM and STEM-EDX elemental mappings of Fe25, Fe50, and Fe75 reduced at 800 ℃ for 12 h in a dry H_2 atmosphere. Reuse under permission from reference [196]. Copyright @ 2022, Elsevier. ...65
Figure 3.1 (a) schematic of solid-sate reactions particle diffusion. Reused under permissions from reference [197]. Copyright 2016, Elsevier. (b) schematic of sol-gel method with citric acid as chelating agent[201]. Reused under terms and conditions of CC-BY license. Copyright 2016, authors. Published by Royal society of chemistry. 68
Figure 3.2 Schematic illustration of Bragg's law.....72
Figure 3.3 Schematic illustration of the fundamental principles of XPS: the Photoelectric effect. 76
Figure 3.4 Schematic view of the photoelectron spectrometer with a hemispherical electron energy analyser. Reused under terms and conditions of CC-BY license [240].. Copyright 2020, authors. Published by Elsevier.....77
Figure 3.5 Energy level diagrams of sample and spectrometer with (a) good electric contact and (b) poor or no electric contact[225].Φ_{SA} represent the work function of sample, while Φ_{SP} represent the work function of spectrometer; E_B^F represent the binding energy respect to energy position of E_F of Femi lever (FL); E_{kin}^{SA} represent the kinetics energy of photoelectron after leaving the sample, while E_{kin}^{SP} represents the kinetic energy measured at the spectrometer; V_C represents the contact potential difference of sample and spectrometer; E_{VAC}^{SA} and E_{VAC}^{SP} represent the vacuum level energy of sample and spectrometer respectively. Reused under terms and conditions of CC-BY license [240].. Copyright 2020, authors. Published by Elsevier.....78
Figure 3.6 Schematics of the X-ray induced photoelectronic effect and resulted Auger effect. Reused under permission from reference [241]. Copyright 2020, AIP publishing. 78
Figure 3.7 A schematic view of the TG-DSC stage of Netzsch 449c F5 system.....79
Figure 3.8 A Schematic diagram of a dilatometer.....80
Figure 3.9 schematic view of primary electron beam interacting with sample. 81
Figure 3.10 The mechanism of mass and thickness creating image contrast in a bright-field TEM image. Reused under permission from reference [245]. Copyright 2012, Springer Science. 82
Figure 3.11 schematic view of the bright-filed and HAADF signal collection of STEM mode. Reused under permission from reference [246]. Copyright 2021 Elsevier.....83
Figure 3.12 Schematic illustration of (a) Nyquist plot with impedance vector; (b,c) Bode plots of |Z| and phase ϕ as function of frequency. 86

Figure 3.13 current-voltage (I-V) curve showing pseudo linearity. Adapted from reference[254]. 87
Figure 3.14 Schematic illustration and picture of sample assembly of the lab-customized symmetric cell test stand. 87
Figure 3.15 Symbols of equivalent circuit with (a) resistor and capacitor (R/C); and (b) resistor and constant phase element (R/CPE). 88
Figure 4.1 Comparison of XRD patterns for synthesized L2NR in powder form with 10mol%, 5mol% and 0mol% RuO_2 excess. The green stick below indicates the Bragg position of L2NR double perovskite. The rhombus symbol indicates the impurity of La_2O_3. The inserted diagrams are a zoomed-in view of plots from 28° to 30°. The 10%Ru excess sample and 5%Ru excess sample are characterized in as-synthesized pellet form, then ground into powder form for powder X-ray diffraction. 91
Figure 4.2 Polyhedral sketch of L2NR unit cell of two different model (a) ICSD202277 [257]: Monoclinic structural model with ordered Ni^{2+}/Ru^{4+} ions. (b) ICSD202431 [258]: Orthorhombic structural model with discorded Ni^{2+}/Ru^{4+} ion on octahedral sites. The green balls indicate the La cations; the red balls indicate the O anions; the grey balls indicate the Ni cations; the beige balls indicate the Ru cations. 93
Figure 4.3 XRD pattern and Rietveld refinement refined plots L2NR. The red dots indicate the XRD pattern, and the black line plots the calculated plots from the model P $2_1/n$. The blue line plots the difference curve of the observed intensity and calculated intensity. The green sticks indicate the calculated Bragg position. The agreement indices are 'the goodness of fitting' χ^2 =6.83, R_p =3.42, R_{wp} =4.68 and R_{exp} =1.79. The reflection peak labelled with '*' indicate the reflection of (0kl) planes, suggesting the monoclinic structure P $2_1/n$. 94
Figure 4.4 XRD patterns of as-prepared L2NR, L1.9NR, L1.85NR, L1.8NR, L1.75NR and peak positions of the referenced pattern (ICSD96120)[261]. The inset are higher magnification regions to highlight the presence of secondary phases of NiO (ICSD9866)[266] and RuO_2 (ICSD15071)[267]. Reused from published work [268] under terms and conditions of CC BY 4.0. Copyright 2022, Authors. 96
Figure 4.5 (a) Le Bail refinement results of lattice parameters and calculated lattice volume of L2NR, L1.9NR and L1.85NR. The fitting agreement indices of L2NR are R_p= 5.36%, R_{wp}= 6.94%, R_{exp}= 5.20% and χ^2 = 1.78. The fitting agreement indices of L1.9NR are R_p= 5.50%, R_{wp}= 7.46%, R_{exp}= 4.38% and χ^2 = 2.89. The fitting agreement indices of L1.9NR are R_p= 6.30%, R_{wp}= 9.73%, R_{exp}= 4.62% and χ^2 = 4.44. Reused from published work [268] under terms and conditions of CC BY 4.0. Copyright 2022, Authors. (b) Vegard plot with linear fitting of pseudo cubic lattice parameters calculated from Le Bail refined lattice volume vs concentration of A-site deficiency. 96

Figure 4.6 (a) Combined spectrum of Ni2p and La3d XPS scanning measured of L2NR sample; (b) fitting plots of La3d spectrum of La_2O_3 adapted from reference [272] under terms and conditions provided by Elsevier and Copyright Clearance Center. Copyright © 2011 Elsevier B.V. 97
Figure 4.7 Ni2p spectrum measured of NiO fitted with Ni(II) multiplet structure. Adapted from literature [271] under terms and conditions provided by Elsevier and Copyright Clearance Centre. Copyright © 2006 Elsevier B.V. 98
Figure 4.8 XPS spectrum of O 1s orbitals of L2NR (black circles), fitted envelop plots (red line), and the fitting components (coloured peaks). Reused from published work [268] under terms and conditions of CC BY 4.0. Copyright 2022, Authors. 99
Figure 4.9 XPS spectrum of Ru 3d orbitals of L2NR (black circles), fitted envelop plots (red line), and the fitting components (colored peaks). Reused from published work [268] under terms and conditions of CC BY 4.0. Copyright 2022, Authors. 100
Figure 4.10 (a) XPS spectrum of Ni LMM Auger signals in kinetic energy (KE) measured of L2NR sample; (b) Ni LMM auger spectra of NiO, Ni(OH)2 and γ-NiOOH adapted from reference [284] under terms and conditions of Copyright Clearance Centre. Copyright 2012, Royal Society of Chemistry. 101
Figure 4.11 Plots of temperature change (black line), dimensional change (red line) and the derivative of expansion/shrinkage (blue line) of L2NR sample characterized by dilatometer. 103
Figure 4.12 TGA plot of weight change (%) versus temperature. The first drop of 0.05% weight loss from room temperature to 300 °C is attributed to the loss of moisture and carbonates. 104
Figure 5.1 XRD patterns of L2NR reduced in 5%H_2/Ar at temperatures ranging from 450°C to 600°C for 3 hours. The double perovskites start to decompose when the reducing temperature exceeds 500°C, forming La_2O_3, NiO, RuO_2 and metallic phases. Adapted from the published work [268] under terms and conditions of CC BY 4.0 license. Copyright 2022, Guo et al.....107
Figure 5.2 XRD patterns of L1.85NR after reduction in 5%H_2/Ar at temperatures ranging from 500°C to 700°C, illustrating the significant decomposition observed when the reduction temperature exceeded 600°C.The reduction treatment were kept as 3 hours. 108
Figure 5.3 SEM images (a-d) of L2NR sample reduced at 450°C in wet 5%H_2/Ar for 3hours, showing overall view of samples in the four presented areas. Adapted from published work [268] under terms and conditions of CC BY 4.0. Copyright 2022, authors. 109
Figure 5.4 SEM images of L1.9NR samples reduced at 450°C in wet 5%H_2/Ar for 3 hours, showing four areas (a-d) selected of the L1.9NR sample. The inserted images highlighted the presence and morphology of the exsolved nanoparticles with adjusted brightness and contrast

of area in dash box. The scale bar of the inserted images referred to the dash box area of the original images. 110
Figure 5.5 SEM images of L1.85NR samples reduced at 450°C in wet 5%H_2/Ar for 3 hours in form of powder (a-c) and pellet (d). Due to the resolution limitation of the instrument, smaller nanoparticles on certain planes/surfaces were not obvious under SEM. The inserted images in (a) and (b) are zoomed in display with adjusted brightness and contrast of the selected area marked by dash box. The scale bar of the inserted images in (a) and (b) referred to the dash box area of the original images. The green and orange dash boxes in figure (d) selected two adjacent grains which were detailed in Figure 5.6. 111
Figure 5.6 SEM images of adjusted brightness and contrast of the selected area in Figure 5.5 (d)..... 111
Figure 5.7 TEM bright field images of L1.9NR samples reduced at 450°C in wet 5%H_2/Ar for 3 hours. These images highlight the presence and morphology of the exsolved nanoparticles. Both socketed and 'subsurface' particles were observed in L1.9NR sample after reduction. 112
Figure 5.8 TEM bright field images of L1.85NR samples reduced at 450°C in wet 5%H_2/Ar for 3 hours. Figure (d) showed the zoomed-in image of selected area in figure (c). 113
Figure 5.9 Comparison of XPS signals of Ru 3d and C 1s spectra between the as-prepared L1.85NR sample (black) and the reduced L1.85NR sample (red). Adapted from the published work under terms and conditions of CC BY 4.0 license. Copyright, 2022, authors. 115
Figure 5.10 (a) Comparison of Ni LMM spectra of L1.85NR before and after reduction. Adapted from published work [254] under terms and conditions of CC BY 4.0 license. Copyright 2022, authors. (b) Ni LMM spectra of Ni^0 phases. Reused under permission from reference [284]. Copyright 2012, Royal Society of Chemistry. 116
Figure 5.11 HAADF STEM images and corresponding EDX analysis maps of the L1.85NR sample reduced at 450°C in wet 5%H_2/Ar for 3 hours. The white arrows indicate the observation of the socketed structure, with a clearer display provided in Figure 5.12(d). The magenta arrow highlights the same particle analysed in Figure 5.13. Adapted from published work [268] under terms and conditions of CC BY 4.0 license. Copyright, 2022, authors. 117
Figure 5.12 HAADF STEM images of L1.85NR sample reduced at 450°C in wet 5%H2/Ar for 3 hours, displaying details of the particle shape and particle-bulk interface. 117
Figure 5.13 (a) HAADF STEM image of exsolved nanoparticles on the surface of L1.85NR bulk. The inset image shows the FFT pattern derived from the area marked by the red dashed square. (b) Combined patterns of two sets of diffraction fringes (Fringes1 and Fringes2) of the exsolved particles (from region marked by the red dash square). Inverse FFT of the two FFT spots marked by red dots in (a) were used to generate the pattern. Adapted from published work under terms and conditions of CC BY 4.0 license. Copyright 2022, authors. (c, d) Plots of

contrast vs. spacing for Fringe 1 and Fringe 2, respectively, revealing the values of lattice spacings. 118
Figure 5.14 XRD pattern of L1.85NR sample reduced at 450°C in wet 5%H_2/Ar for 3 hours. The insert plots showed zoomed-in display of 2θ range 41-49°, showing the details of secondary phase diffractions. Adapted from published work [268] under terms and conditions of CC BY 4.0 license. Copyright, 2022, authors. 119
Figure 5.15 XRD pattern of L1.85NR sample reduced at 450°C in dry 5%H_2/Ar for 3 hours. The inset plots show a zoomed-in display of 2θ range 43-47°, showing the details of secondary phase diffraction. 121
Figure 5.16 SEM images of L1.85NR sample reduced at 450°C in dry 5%H_2/Ar for 3 hours, providing a general view of four areas (a-d).The inserted images detail the presence of exsolved nanoparticles on surface of grain by sharpened display with varied brightness and contrast of the area selected by the dash box. The scale bar of the inserted images referred to the dash box area of the original images. 121
Figure 5.17 Comparison of XPS spectra of Ru 3d and C 1s spectra between the as-prepared L1.85NR sample (black) and the dry reduced L1.85NR sample (red). 122
Figure 5.18 TEM images of L1.85NR sample reduced at 350°C in dry 5%H_2/Ar for 3 hours. (a) 250k; (b) 400k at the same area of (a); (c-d) 120k. 124
Figure 5.19 TEM images of L1.85NR sample reduced at 400°C in dry 5%H_2/Ar for 3 hours at different magnifications: (a) 300k; (b) 400k at the same area of (a); (c) 150k; (d) 300k. 124
Figure 5.20 TEM images of L1.85NR sample reduced at 450°C in dry 5%H_2/Ar for 3 hours at different magnifications: (a-b) 300k; (c) 250k; (d) 120k. 125
Figure 5.21 (a) Particle size evolution with increasing temperature from 350 to 450 °C. The particle sizes are average values measured by ImageJ software from a total of 250 manually selected exsolved particles (more than 70 for each temperature condition). Error bars represent the standard error of the average particle size. e) Particle size distribution of nanoparticles exsolved under different temperatures. Adapted from published work under terms and conditions of CC BY 4.0 license. Copyright 2022, authors. 125
Figure 5.22 XRD patterns of the L1.85NR samples reduced in wet 5%H2/Ar at 450°C, 400°C and 350°C for 3 hours. The green droplines indicated Bragg position of double perovskite (ICSD 96120 [261]). The inset plots show the subtle peaks of the $Ni0_{.32}Ru_{1.68}$ metallic phase (ICSD 646325 [292]). Adapted from published work under terms and conditions of CC BY 4.0 license. Copyright 2022, authors. 126
Figure 5.23 HAADF electron image of the L1.85NR sample reduced at 350°C in wet 5%H2/Ar (a) and corresponding STEM EDX maps of La, Ru, Ni and O elements in the area of the electron image (b). Adapted from published work under terms and conditions of CC BY 4.0 license. Copyright 2022, authors. 126

Figure 6.1 TG and DTG curves as well as corresponding temperature profiles as a function of time, encompassing both the heating and dwelling stages. 130
Figure 6.2 (a) Nyquist plot and the fitted result of symmetric cell in static air. The inset sketch is the equivalent circuit for fitting the second arc. (b) Bode plot (phase-shift vs log frequency) and the fitted result of symmetric cell measured in static air. The fitted result plot (red line) showed the estimated spectrum of the equivalent circuit in a wide frequency range (10^{-5} to 10^{7} Hz). 131
Figure 6.3 In-situ impedance spectra of the symmetric cell measured in air and humidified 5% H_2/Ar for different dwell times: 0, 11, 25, and 40 min.....132
Figure 6.4 Residual plot (%) of the impedance spectrum of the symmetric cell measured in humidified 5% H_2/Ar after 25 mins of reduction.....132
Figure 6.5 (a) Nyquist plot and the fitted result of symmetric cell reduced in wet 5%H_2/Ar for 25mins. The inset sketch is the equivalent circuit for fitting the second arch. (b) Bode plot (phase-shift vs log frequency) and the fitted result of symmetric cell reduced in wet 5%H_2/Ar for 25mins. The fitted result plot (red line) showed the estimated spectrum of the equivalent circuit in a wide frequency range (10^{-5} to 10^{7} Hz). Adapted from the published work [268] under terms and conditions of CC BY 4.0 license. Copyright 2022, authors. 134
Figure 6.6 In-situ impedance spectra of the symmetric cell measured in wet 5% H_2/Ar for different dwell times from 25 mins to 12 hours. Adapted from the published work [268] under terms and conditions of CC BY 4.0 license. Copyright 2022, authors. 135
Figure 6.7 SEM images of the microstructure of L1.85NR/LSGM/L1.85NR symmetric cell before (a) and after (b) EIS measurements. 135
Figure 6.8 XRD pattern of the symmetric cell after EIS test in wet 5%H_2/Ar.....136
Figure 6.9 Schematic illustration of testing rig set-up for the single cell test.....137
Figure 6.10 SEM images depict the microstructure of both the cross-sectional view and top view of the fabricated single cell before electrochemical test, with the current collector omitted.(a) cross-section of the single cell; (b-c) cross-section view highlighting the microstructure of L1.85NR electrode; (d) top view of the L1.85NR electrode; (e-f) cross-section view highlighting the microstructure of LSCF electrode. 138
Figure 6.11 In-situ EIS spectra measured at 450°C in wet 5%H_2 of the single cell with (a) L1.85NR and (b) L2NR as fuel electrode. 139
Figure 6.12 I-V curves and power density measured at 450°C and 600°C in commonly working atmosphere of SOFC with the single cells employing (a) L1.85NR and (b) L2NR as fuel electrode. 140
Figure 6.13 SEM images of the cross-section view of L1.85NR electrode after full cell test. 141

Figure 6.14 XRD pattern of the L1.85NR electrode after full cell test and its correspondence with the reference peaks from La_2NiRuO_6 [261], Ni0.32 Ru1.68 [286], silver current collector [306] and LSGM electrolyte [307]. 142
Figure 6.15 In-situ BF TEM observations of L1.85NR sample in high vacuum at 450°C after different reduction time: (a) initial images at room-temperature; (b) after 20s reduction at 450°C; (c) after 2mins reduction at 450°C; (d) after 6mins reduction at 450°C; (e) after 23mins reduction at 450°C. A fast response of exsolution and nucleation process was observed within 23mins of exposure in high vacuum at 450°C. 144
Figure 6.16 In-situ TEM image of the L1.85NR sample reduced at 450°C in high vacuum for 42 mins, highlighting a higher number of nanoparticles compared to Figure 6.15 and a board distribution of nanoparticles. 145
Figure 6.17 Schematic illustration of the thermal cycle and the characterization applied to the sample. 146
Figure 6.18 (a) STEM-ABF, (b) STEM-ADF combined with EDX maps, (c) STEM-HAADF, (d) STEM-MAADF images and (e-h) EDX maps of the L1.85NR pristine. 146
Figure 6.19 (a) STEM-ABF, (b) STEM-ADF, (c) STEM-HAADF, (d) STEM-MAADF images and (e-h) EDX maps of the L1.85NR quenched after reduction at 300°C. 147
Figure 6.20 in-situ STEM images of the same L1.85NR grain observed in Figure 6.18-19, showing the evolution of morphology and surface particle at 350°C with the reduction time progressing: (a) 18s; (b) 35s; (c) 1min 30s. 147
Figure 6.21 (a) STEM-ABF, (b) STEM-MAADF, (c) STEM-ADF, (d) STEM-HAADF images and (e-i) EDX maps of the L1.85NR quenched after reduction at 450°C 149
Figure 6.22 BF TEM images of same L1.85NR grain before (a) and after (b) the temperature-dependent in-situ TEM/STEM probing session. 150
Figure 6.23 photos of the in-situ measurement instrument set-up for the ASAXS and WAXS characterization. 151
Figure 6.24 WAXS data converted AXRD patterns of L1.85NR measured at room temperature in compressed gas air. 152
Figure 6.25 contour graph (a) and waterfall plots (b,c) of WAXS data of L1.85NR reduced at 450°C under 5% H_2/N_2. measured with 21,831 keV X-ray beam 153
Figure 6.26 contour graph (a) and waterfall plots (b,c) of WAXS data measured with 21.831 keV X-ray beam of L1.85NR underwent the reduction treatment at 550°C. 153
Figure 6.27 WAXS data converted AXRD patterns of in-situ observations: L1.85NR pristine in air, L1.85NR reduced at 450°C for 6 hours and L1.85NR re-oxidized for 1 hour. 154
Figure 6.28 WAXS data converted AXRD patterns of in-situ observations: L1.85NR pristine in air, L1.85NR reduced at 550°C for 4 hours and L1.85NR re-oxidized for 1 hour. 155

Figure 7.1 (a) XRD patterns of stoichiometric lanthanum nickel titanate L2NT and Ru-doped lanthanum nickel titanate L2NTR; (b) Le Bail refinement profiles of L2NT with R_p = 6.87, R_{wp} = 10.30, R_{exp} = 6.24 and χ^2= 2.71; (c) Le Bail refinement profiles of L2NT with R_p = 7.00, R_{wp} = 11.30, R_{exp} = 6.27 and χ^2= 3.23. 159
Figure 7.2 XRD pattern and the Rietveld refinement profiles of L1.85NTR. The factors of agreement are R_p = 4.95, R_{wp} = 6.41, R_{exp} = 4.11 and χ^2 = 2.43. Two inset plots are the zoomed pattens of resolved peaks. The green arrows mark the Cu K_β reflections. 161
Figure 7.3 (a) XRD patterns of A-site deficient L1.85NTR as prepared and reduced at 450°C, 800°C, 900°C and 1000°C. (b) zoomed-in XRD profiles at 20°-50° range. The droplines indicate the Bragg position of La_2O_3 phase (ICSD28555[285]) and nickel metal phase (ICSD64989[315]).....164
Figure 7.4 XRD pattern and Rietveld refinement profiles of L1.85NR reduced at 800°C. The factors of agreement are R_p = 5.59, R_{wp} = 7.08, R_{exp} = 4.12 and χ^2 = 2.95. Lattice parameters of nickel metal phase were refined based on reference structure ICSD64989 [315]. Lattice parameters of lanthanum oxide phase were refined based on reference structure ICSD28555 [285]. 164
Figure 7.5 SEM images of (a) as prepared and (b) reduced L1.85NTR sample at 800°C for 3hours. The inserted image is the enlarged display of the reduced sample. 166
Figure 7.6 TEM bright field (BF) images and STEM annular bright field (ABF), annular dark field (ADF), medium angle annular dark field (MAADF) and high angle annular dark field (HAADF) images of region (a) and (b) of L1.85NTR sample reduced at 800°C in wet 5%H_2/Ar for 3 hours. The corresponding elemental distribution maps of La, Ni, Ru and Ti are listed at the left of the STEM images. 166
Figure 7.7 (a) SEM images (b) STEM-ABF and ADF images and (c) BF-TEM images, STEM-ABF and ADF images and corresponding EDX maps of the sample L1.85NTR reduced in wet 5%H_2/Ar at 450°C for 3 hours. 167
Figure 7.8 SEM images of L1.85NTR sample reduced at 800°C for the particle analysis. ..168
Figure 7.9 SEM images of L1.85NTR sample reduced at 450°C for the particle analysis. ..169
Figure 7.10 Size distribution diagrams of exsolved nanoparticles of L1.85NTR reduced in wet 5%H2/Ar at 800°C(a) and 450°C(b) for 3 hours. 169
Figure 7.11 (a) TG curves and corresponding temperature profiles as a function of time, encompassing both the heating and dwelling phases; (b) TG and DTG curves as a function of increasing temperature, ranging from room temperature (RT) to 1000°C. 172
Figure 7.12 Schematic illustration of the thermal cycle applied to the sample. 173
Figure 7.13 In-situ STEM-ADF images of (a) initial and reduced L1.85NTR sample at 350°C (b), 450°C (c) and 800°C (d). 175
Figure 7.14 In-situ STEM-ADF image of the L1.85NTR sample at 950°C in high vacuum. .176

Figure 7.15 (a) STEM-ABF, (b) STEM-ADF, (c) STEM-MAADF, (d) STEM-HAADF images and (e) EDX maps of the quenched L1.85NTR after reduction at 350°C. Same area with the in-situ observation in Figure 7.13. 176
Figure 7.16 (a) STEM-ABF, (b) STEM-ADF, (c) STEM-MAADF, (d) STEM-HAADF images and (e) EDX maps of the quenched L1.85NTR after reduction at 500°C. 177
Figure 7.17 (a) STEM-ABF, (b) STEM-ADF, (c) STEM-MAADF, (d) STEM-HAADF images and (e) EDX maps of the quenched L1.85NTR after reduction at 800°C. 177
Figure 7.18 SEM images of the microstrucutre of the L1.85NTR/LSGM/L1.85NTR symmetric cell.....178
Figure 7.19 EIS spectra of L1.85NTR/LSGM/L1.85NTR symmetric cell measured in flowing wet 5%H_2/Ar at different temperatures. The spectra of each temperature were measured continuous with the reduction progressing. Each spectrum was scanned for 30mins. 181
Figure 7.20 EIS spectrum of L1.85NTR/LSGM/L1.85NTR symmetric cell measured after reduction in flowing wet 5%H_2/Ar for 4.5 hours at 343°C, and the fitted plots. The inserted sketches illustrate the equivalent circuits. 182
Figure 7.21 EIS spectrum of L1.85NTR/LSGM/L1.85NTR symmetric cell measured after reduction in flowing wet 5%H_2/Ar for 4.5 hours at 800°C, and the fitted plots. The inserted sketches illustrate the equivalent circuits. 182
Figure 7.22 STEM images and EDX maps of two distinct regions (a) and (b) of the L1.85NTR sample reduced at 1000°C in a wet 5%H_2/Ar for 3 hours. 183
Figure 7.23 SEM images of (a) L1.85NTR sample and (b) Fe_2O_3 infiltrated L1.85NTR sample reduced at 800°C in wet 5% H_2/Ar for 3 hours. The dashed circles mark some of the sintered-like particles present on the surface of L1.85NR which was considered as unexchanged iron oxide. 184
Figure 7.24 TEM images of Fe-L1.85NTR sample reduced in wet 5%H_2/Ar at 800°C for 3 hours. 185
Figure 7.25 STEM images and EDX maps Fe- L1.85NTR sample reduced in wet 5%H_2/Ar at 800°C for 3 hours. 186
Figure A.26 ASAXS curves of the L1.85NR sample during the reduction in 5%H_2/N_2 at 450°C at 22.121 KeV energy: the intensity of high-q range increased with the reduction progressing. 209
Figure A.27 ASAXS curves of the L1.85NR sample during the reduction in 5%H_2/N_2 at 450°C at 22.106 KeV energy. A similar trend with higher energy that with the reduction progressing, the high-q range showed elevated intensity. 210
Figure A.28 ASAXS curves of the L1.85NR sample during the reduction in 5%H_2/N_2 at 450°C at 22.106 KeV energy. 210

Figure A.29 ASAXS curves of the L1.85NR sample during the reduction in 5%H_2/N_2 at 450°C at 22.057 KeV energy. A.....211
Figure A.30 ASAXS curves of the L1.85NR sample during the reduction in 5%H_2/N_2 at 450°C at 221.981 KeV energy. 211
Figure A.31 ASAXS curves of the L1.85NR sample during the reduction in 5%H_2/N_2 at 450°C at 21.831 KeV energy. Similar with the discussion in section 6.5 on WAXS, the initial scanning at the beginning of experiments showed distinguished lower intensity and background which might attributed to the setting of measurement. 212
Figure A.32 Respective size distribution of the exsolved nanoparticles contained Ru. The legend of the plots indicates the number of scans collected. The scanning rate was 1 scan/min. 213

List of tables

Table 1.1 UK Electricity generated by fuel type from 1990 to 2022 [1]. Reused under the Open Government Licence v3.0.....28
Table 2.1 Synthesis, lattice structure of reported Ru-based double perovskites.....40
Table 2.2 Synthesis, lattice structure of reported Ti-based double perovskites 43
Table 2.3(a) Applications of exsolution method, corresponding exsolved elements and host lattices: SOCs, water splitting and hydrocarbon reforming.....47
Table 2.3(b) Applications of exsolution method, corresponding exsolved elements and host lattices: ammonia reaction catalysis and carbon dioxide reduction. 47
Table 3.1 Capacitance values and their possible interpretation. Adapted under permissions from reference [245]. Copyright 1990, John Wiley and Sons. 89
Table 4.1 Rietveld Refinement calculated lattice parameters and atomic parameters. B-factors for cations at same location was contraned to same value, and oxygen anions were fixed during reifnement. 94
Table 4.2 Fitting results of the Ru3d, O1s, C1s spectra of asprepared L2NR sample. Due to the limitation of energy reoslution of spctrometer, the error of measured and fitted binding energy poisiotns was approximately 0.2-0.5eV. 101
Table 4.3 1 ICP results of stoichiometric double perovskite L2NR and A-site deficient samples L1.9NR and L1.85NR. B-site positions were assumed fully occupied by Ruthenium and Nickel cations during the calculation of concentration ratio. Reused from published work [257] under terms and conditions of CC BY 4.0. Copyright 2022, Authors. 102
Table 6.1 Fitting results of the impedance spectrum measured after different reduction times. R_s denote ohmic resistance read through the intercept of the impedance arcs. R_H denote the resistance of the high-frequency part of the spectrum. R_{L-1}/CPE1 and R_{L-2}/CPE2 are resistances, and constant phase elements contribute to the low-frequency part of the spectrum. Adapted from the published work [257] under terms and conditions of CC BY 4.0 license. Copyright 2022, authors. 135
Table 7.1 Rietveld refined lattice parameters and atomic parameters of L1.85NTR. 161
Table 7.2 ICP results of stoichiometric sample L2NT and L2NTR and A-site deficient sample L1.85NTR. B-site positions were assumed fully occupied by nickel, titanium and ruthenium cations. Oxygen concentration is calculated based on experimental results of metal cations. 162
Table 7.3 Rietveld refined lattice parameter and atomic parameters of double perovskite phase in the reduced L1.85NR sample based on reference structure ICSD186433 [294]. The occupancy of the oxygen was fixed as 0.962 according to the nominal composition $La_{1.85}NiTi_{0.9}Ru_{0.1}O_{5.775.}$ 165

Table 7.4 Fitted parameters of the components in the equivalent circuits at 343°C, 437°C and 800°C. 182

List of acronyms

SOFCs - Solid Oxide Fuel Cells

SOECs - Solid Oxide Electrolysis Cells

SOCs - Solid Oxide Cells

CHP - Combined Heat and Power

ORR - Oxygen Reduction Reaction

OER - Oxygen Evolution Reaction

HOR - Hydrogen Oxidation Reaction

HER - Hydrogen Evolution Reaction

HHV - Higher Heating Value

OCV - Open-Circuit Voltage

ASR - Area-Specific Resistance

YSZ - Yttria-Stabilized Zirconia

LSCF - Strontium-Doped Lanthanum Cobalt Ferrite

MIECs - Mixed Ionic and Electronic Conductors

SFM - Sr0.99Fe0.75Mo0.25O3-d

CGO - Gd-Doped Ceria

XAS - X-ray Absorption Spectroscopy

DFT - Density Functional Theory

XANES - X-ray Absorption Near-Edge Structure

PEMWEs - Proton Exchange Membrane Water Electrolysers

AFM - Atomic Force Microscopy

E-TEM - Environmental Transmission Electron Microscopy

EIS - Electrochemical Impedance Spectroscopy

LHV - Lower Heating Value

LSGM - Lanthanum Strontium Gallium Magnesium

RP phase - Ruddlesden-Popper phase

PLD - Pulsed Laser Deposition

EBSD - Electron Backscatter Diffraction

TPR - Temperature Programmed Reduction

BPR - Ball-to-Powder Ratio

LSCF - Lanthanum Strontium Cobalt Ferrite

XRD - X-ray Diffraction

XPS - X-ray Photoelectron Spectroscopy

ICSD - Inorganic Crystal Structure Database

Ekin - Kinetic energy of photoelectron

TA - Thermal Analysis

TG - Thermogravimetry

DTA - Differential Thermal Analysis

DSC - Differential Scanning Calorimetry

DTG - Differential Thermogravimetric Analysis

TMA - Thermomechanical Analysis

TGA – Thermogravimetry Analysis

EM - Electron Microscopy

TEM - Transmission Electron Microscopy

SEM - Scanning Electron Microscopy

STEM - Scanning Transmission Electron Microscopy

FEG - Field Emission Gun

CCD - Charge-Coupled Device

BF - Bright-Field

ADF - Annular Dark Field

ABF - Annular Bright Field

HAADF - High-Angle Annular Dark Field

MAADF - Medium-Angle Annular Dark Field

EDX - Energy-Dispersive X-ray Spectroscopy

FEGSEM - Field Emission Gun Scanning Electron Microscopy

ICP-OES - Inductively Coupled Plasma-Optical Emission Spectroscopy

K-K Test - Kramers-Kronig Test

I-V - Current-Voltage

LSGF8282 - Lanthanum Strontium Gadolinium Ferrite $La_{0.8}Sr_{0.2}Co_{0.8}Fe_{0.2}O_{3-\delta}$

sccm - Standard Cubic Centimeters per Minute

FWHM - Full Width at Half Maximum

R/CPE - Resistor and Constant Phase Element

FCC - Face-Centered Cubic

HCP - Hexagonal Close-Packed

TPB - Triple Phase Boundary

ASAXS - Anomalous Small-Angle X-ray Scattering

WAXS - Wide-Angle X-ray Scattering

DESY - Deutsches Elektronen-Synchrotron Centre

Chapter 1 Introduction

1.1 Background

With the continuous evolution of modern society, the demand for energy has seen an inevitable surge, leading to a heightened focus on the energy industry. For instance, investments in the United Kingdom's energy sector reached £16.7 billion in 2022, nearly doubling compared to the figures from 2005[1]. Notably, the investment in the electricity sector has exhibited remarkable growth, as indicated by the UK Energy in Brief 2023 report (Figure 1.1) [1]. Electricity generation relies on various sources, including fossil fuels, nuclear energy, renewable energy, tidal energy, and geothermal energy. Among these, fossil fuels have historically dominated the electricity generation landscape. However, the use of fossil fuels for power generation exacerbates greenhouse gas emissions, contributing to climate change. In response, the United Kingdom has established a legally binding target to achieve "net zero" greenhouse gas emissions by 2050 [2,3]. Consequently, renewable energy sources such as solar power, wind power, and hydropower have emerged as the most viable and dependable sources of electricity.

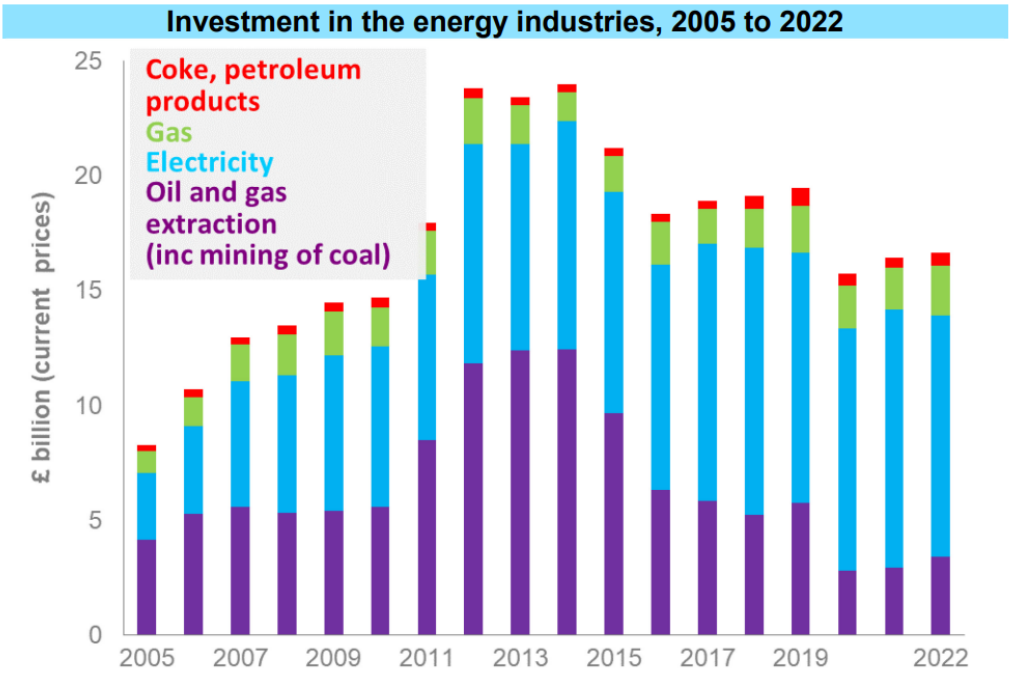


Figure 1.1 Stack columns chart of the UK investment in the energy industry from 2005 to 2022 [1]. Reused under the Open Government Licence v3.0.

Starting from 1990, the share of electricity generated from renewable sources has risen substantially, reaching 41.5% of the total electricity generation by 2022 (Table 1.1) [1]. While wind and solar energy are abundant sources of renewable energy, a limitation lies in their intermittent nature. To address this intermittency challenge, an energy storage and conversion strategy is imperative. Solid oxide cells, encompassing solid oxide fuel cells (SOFCs) and solid oxide electrolysis cells (SOECs), hold immense promise in stabilizing power generation,

managing energy demand, and facilitating the production of chemicals and fuels. In the case of solid oxide fuel cells (SOFCs), electrochemical reactions occur when a fuel (typically hydrogen, natural gas, or other hydrocarbons) is supplied to the anode and oxygen is supplied to the cathode. Electrons flow through an external circuit, generating an electric current. Conversely, solid oxide electrolysis cells (SOECs) can reverse this process. When an electric current is applied to the cell, it can split water into oxygen ions at the anode and hydrogen gas at the cathode, making SOECs valuable for hydrogen production and energy storage during periods of excess electricity availability[4].

One notable advantage of solid oxide cells (SOCs) lies in their high efficiency, as they directly convert the chemical energy in fuels into electricity or vice versa. Compared to other fuel cell or electrolyser technologies, for example, proton exchange membrane fuel cells (PEMFC) and electrolyser cells (PEMEC), the high operating temperature of SOFCs and SOECs allows for enhanced kinetics and compatibility with a broader range of fuels, including hydrogen, natural gas, and biomass-derived gases. Additionally, their solid oxide materials confer durability and longevity, making them suitable for extended operation in various applications. However, the high temperature necessitates intricate thermal management and manufacturing processes, which can contribute to complexity and cost. In contrast, PEMFCs and PEMECs operate at lower temperatures, facilitating rapid start-up and simpler system integration, albeit with limitations on fuel choice and durability imposed by the proton exchange membrane. On the other hand, the benefits gained from high-temperature operation in SOEC mode led to reduced electricity consumption [5]. Furthermore, the operating temperatures and high efficiency of SOFCs render them suitable for combined heat and power (CHP) stationary units [6]. In light of the imperatives of mitigating greenhouse gas emissions and achieving a harmonious balance between energy demand and power generation, SOCs stand as an ideal candidate.

Table 1.1 UK Electricity generated by fuel type from 1990 to 2022 [1]. Reused under the Open Government Licence v3.0.

						TWh
	1990	**2000**	**2010**	**2020**	**2021**	**2022**
Coal	229.9	120.0	107.6	5.5	6.5	5.6
Oil & other fuels*	20.7	13.6	10.5	12.0	11.2	12.0
Gas	0.4	148.1	175.7	112.7	123.1	125.0
Nuclear	63.2	85.1	62.1	50.3	45.9	47.7
Hydro	5.6	5.1	3.6	6.9	5.4	5.6
Wind & Solar	-	0.9	10.3	87.9	76.7	93.6
Other renewables	-	4.3	12.3	39.5	40.0	35.8
Total electricity generated	**319.7**	**377.1**	**382.0**	**314.6**	**308.9**	**325.3**

*Includes generation from pumped storage.

Inspired by the potential of SOCs, extensive efforts have been dedicated to the discovery and development of high-efficiency and durable SOC components. To realize the operational principles of SOCs, perovskite oxides have emerged as promising candidates. ~~This project centres on the investigation and modification of double perovskites as potential fuel electrodes for SOCs.~~

1.2 Fundamentals of SOCs

A solid oxide cell (SOC) primarily consists of three essential components: the fuel electrode, the air (oxygen) electrode, and the ionic-conducting electrolyte, as illustrated in Figure 1.2. The SOFC and SOEC modes of SOCs operate in opposite directions in terms of the overall chemical reactions. For instance, considering the reaction involving hydrogen fuel:

$$H_{2(g)} + \frac{1}{2}O_{2(g)} \leftrightarrow H_2O(g) \qquad 1-1$$

It's important to note that the oxide materials do not actively participate in the chemical reaction; instead, they serve as catalytically active sites and conductors of charge to facilitate the half-reactions and the flow of electrons through external electrical circuits. As demonstrated in Figure 1.2(a), in the SOFC mode, oxygen gas reaches the active sites on the oxygen electrode (cathode) and undergoes the oxygen reduction reaction (ORR), resulting in the production of oxygen anions as shown in Equation 1-2:

$$\frac{1}{2}O_{2(g)} + 2e^- \rightarrow O^{2-} \qquad 1-2$$

The most commonly used electrolytes in SOCs are oxygen-conducting membranes, which transport the generated O^{2-} ions toward the fuel electrode side, where they combine with H^+ produced by the complementary half-reaction (Equation 1-3) to complete the overall chemical reaction:

$$H_{2(g)} + O^{2-} \rightarrow H_2O + 2e^- \qquad 1-3$$

In the SOEC mode of SOCs, taking steam and an oxygen-conducting electrolyte as an example, on the hydrogen electrode side, water molecules accept electrons and split into hydrogen and oxygen anions, which then pass through the oxygen-conducting membrane, undergoing the oxygen evolution reaction (OER) and forming oxygen molecules:

$$H_2O_{(g)} + 2e^- \rightarrow H_{2(g)} + O^{2-} \qquad 1-4$$

$$O^{2-} \rightarrow \frac{1}{2}O_{2(g)} + 2e^- \qquad 1-5$$

As previously mentioned, SOCs are capable of directly converting energy between chemical energy and electricity in theory. Taking hydrogen fuel as an example, the overall reaction (Equation 1-1) spontaneously occurs in the SOFC mode. The Gibbs free energy (ΔG) is calculated as -237.3 kJ/mol (higher heating value, HHV), *i.e.*, producing liquid water) and -228.6 kJ/mol (lower heating value, LHV, *i.e.*, producing gaseous water) under standard conditions (298K, 1 bar)[7]:

$$\Delta G = \Delta H - T\Delta S \qquad 1-6$$

where ΔH is the total change in enthalpy at the end of a chemical reaction, ΔS is the change of entropy and T is absolute temperature in Kelvin. The energy requirement for the SOEC mode is reversed.

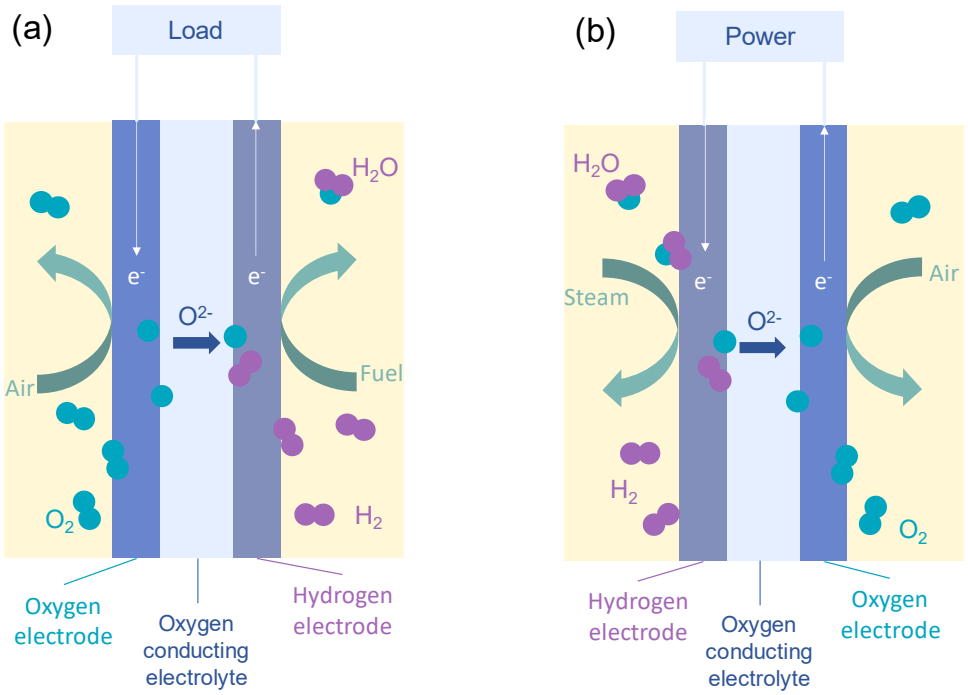


Figure 1.2 schematic illustration of the working principles of (a) SOFC and (b) SOEC with oxygen transportation electrolyte.

Given the charge transfer of the reaction of hydrogen combustion is 2, the theoretical cell voltage E^0 at standard condition can be calculated as 1.23V according to:

$$E = \frac{|\Delta G|}{nF} = \frac{237.3 \times 1000\ J/mol}{2 \times 96485\ C/mol} = 1.23V \qquad 1-7$$

Where F is Faraday's constant (96485 C/mol). The cell voltage under non-standard conditions can be determined using the Nernst Equation:

$$E = E^0 - \frac{RT}{nF} ln \frac{a_{H2O}}{a_{O_2}^{\frac{1}{2}} a_{H_2}} = E^0 - \frac{RT}{nF} ln \frac{1}{p_{H_2} p_{O_2}^{\frac{1}{2}}} \qquad 1-8$$

where E^0 is the theoretical cell voltage at standard conditions, which is also the open-circuit

voltage (OCV) at standard conditions; $a_{H2O,}$ a_{H2} and a_{O2} are activities of the species in the reaction; p_{H2} and p_{O2} are partial pressure of hydrogen and oxygen respectively. However, the actual cell voltage is lower than the theoretical value due to unavoidable energy losses. Figure 1.3 illustrates the real cell voltage versus current density for the SOFC mode, where the cell voltage drop occurs in three stages: reaction activation loss, ohmic resistance loss, and gas transportation loss (Equation 1-9). This phenomenon is similar in the SOEC mode but requires additional energy input, which can be in the form of heat and electricity [8]. The slope of the real cell voltage versus current density curves indicates the area-specific resistance (ASR) of the cell.

$$V_{cell} = E - (V_{activation} + V_{onmic} + V_{concentration})$$

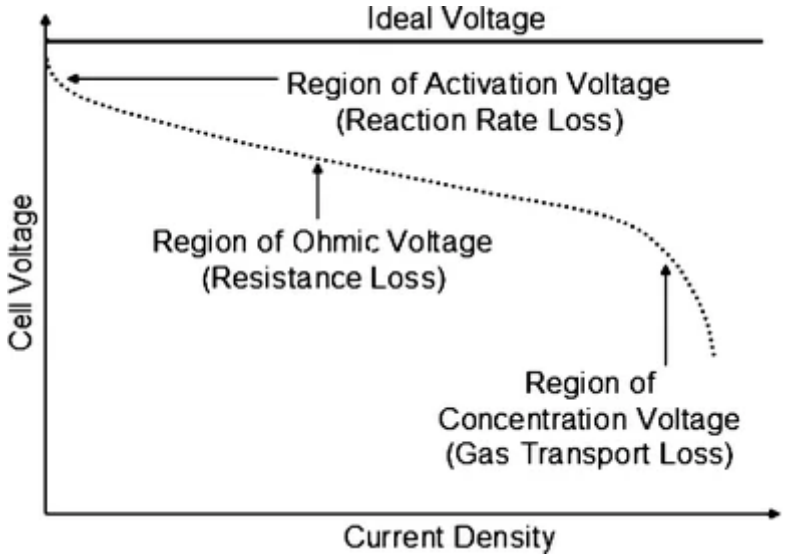


Figure 1.3 theoretically illustration of the cell voltage vs. current density curve. Reproduced under permission from reference [9]. Copyright 2007, Elsevier.

Therefore, the operating principles necessitate specific properties for each component in SOCs. For electrolyte materials, these materials must possess the following characteristics: (i) ionic conductivity (greater than 0.01Scm^{-1} at operating condition) while insulating electronically[10,11], (ii) sufficient density to prevent gas crossover, (iii) stability under reducing and oxidizing atmospheres, and (iv) thermal and mechanical compatibility with adjacent electrodes. Typically, there are two types of electrolytes: oxygen transport electrolytes and proton-conducting electrolytes. Currently, much of the research on SOCs focuses on oxygen anion-conducting electrolytes, such as yttria-stabilized zirconia (YSZ)[12], doped ceria[13,14], and doped lanthanum gallate[14,15], among others [4].

As for air electrode materials, the aforementioned working principles necessitate the following properties: (i) high electronic conductivity for facilitating electron transport (greater than 100 Scm^{-1} under operating conditions (*e.g.* at 700°C) in air[11,16], (ii) high ionic conductivity for oxygen ion transport (similar to electrolyte), (iii) electrocatalytic activity to lower the activation barrier

and promote ORR or OER reactions, (iv) porosity to allow for oxygen gas diffusion to and from active sites, (v) thermal and mechanical compatibility with the adjacent electrolyte, and (vi) a high tolerance for potential impurities originating from interconnects, such as chromium. Mixed ionic and electronic conductors (MIECs) represent a promising category of air electrode materials that have undergone intensive investigation and application, including materials like strontium-doped lanthanum cobalt ferrite (LSCF) and strontium-doped lanthanum cobaltite (LSC)[4,17].

Regarding the fuel electrode, as it operates in reducing conditions and may come into contact with impurities supplied with the fuel or the inherently carbon-containing nature of the fuel itself, it necessitates the following properties: (i) high electronic and ionic conductivity. The minimum required electric conductivity is 1 Scm^{-1} [18]; (ii) catalytic activity for fuel oxidation or evolution reactions, (iii) porosity to facilitate oxygen gas diffusion to and from active sites, (iv) thermal and mechanical compatibility with the adjacent electrolyte, and most importantly, (v) a high tolerance for impurity poisoning, such as sulfur poisoning in SOFC anodes, as well as (vi) resistance to coking during operation with carbon-containing fuels in SOFCs or during carbon dioxide electrolysis in SOECs. In addition, SOFCs and SOECs share many similarities in terms of their materials and operating principles, there are some differences in their catalytic requirements for the fuel electrode. The catalytic requirements for the fuel electrode in SOFC mode mainly involve promoting the dissociation of fuel molecules and facilitating the transport of ions (e.g., H^+ ions) through the electrode-electrolyte interface, while the catalytic requirements for the fuel electrode in SOEC mode involve promoting adsorption and dissociation of water molecules.

1.3 Motivation

Conventional materials for SOCs primarily consist of Ni cermet, a type of composite material that combines nickel metal (Ni) with ceramic materials, due to their favourable electrochemical properties and cost-effectiveness, as depicted in Figure 1.4. However, several issues have emerged with these materials, including redox instability, carbon deposition, and impurity poisoning. The Ni-ceramic-gas triple-phase boundary becomes easily poisoned by common impurities such as sulfur and phosphorous compounds in natural gas and biogas and by SiO_2 in the raw materials[19,20]. Therefore, alternative materials have undergone intensive study to address the challenges associated with Ni cermets. One such attempt involves combining highly conductive perovskite materials such as $Sr_{0.99}Fe_{0.75}Mo_{0.25}O_{3-d}$ (SFM) with Gd-doped ceria (CGO), which has shown promising electrochemical performance and excellent resistance to coking. However, in this approach, SFM was infiltrated onto the CGO electrode, necessitating additional fabrication steps. Additionally, the polarization resistance of the cells increased after redox cycling, indicating that the infiltrated material may be less electro-

catalytically active, leading to a potential loss of reaction sites on the CGO surface during operation [21].

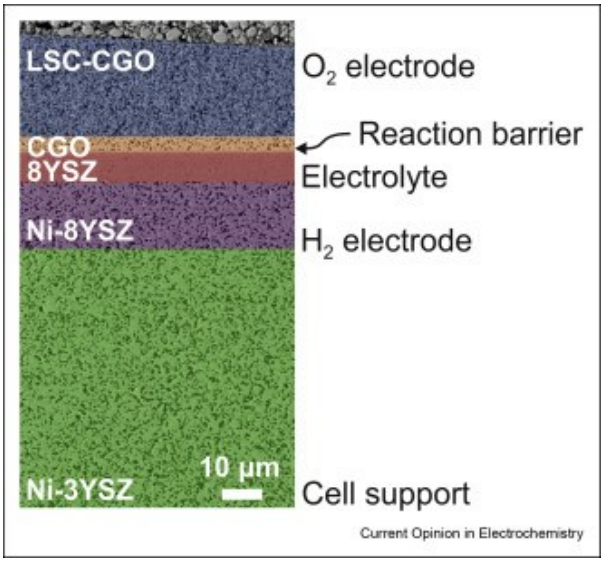


Figure 1.4 Artificially coloured SEM micrograph of cross-section of a manufactured SOC from Technical University of Denmark (DTU). Reused under permission from reference [4]. Copyright 2020, Elsevier.

Furthermore, Ni-cermet electrodes often degrade rapidly in SOEC mode at high current densities 1 A cm^2 at 800 °C, likely due to Ni migration and loss of contact between Ni and YSZ [22,23]. Thus, developing impurity-resistant, electro-catalytically active, and easy-to-fabricate fuel electrodes for SOCs, while meeting conductivity, robustness, and chemical stability requirements, is crucial. Another approach to mitigate impurity and carbon poisoning for enhanced stability and performance is 'redox exsolution.' For instance, Ni nanoparticle-decorated $La_{0.43}Ca_{0.37}Ni_{0.06}Ti_{0.94}O_{3-d}$ has shown excellent performance in both SOFC and SOEC modes, retaining its effectiveness even after 150 hours of testing [24].

Motivated by the application and advancement of electrodes, particularly fuel electrodes, for SOCs, this research project aims to develop and investigate double perovskite materials as potential electrode materials. These materials offer higher electronic conductivity, improved stability at high temperatures, and tunability for various applications and fuel types, as detailed in chapter 2. Specifically, this study explores the exsolution phenomena associated with these materials, focusing on performance enhancement and the underlying exsolution mechanisms.

1.4 Thesis outline

In chapter 2, literature on the double perovskite materials, especially ruthenates and titanates, is reviewed in terms of their intrinsic lattice structure, synthesis methods and applications in SOCs. Exsolution method is thoroughly reviewed and discussed in this chapter in terms of its discovery, applications, and mechanisms. This chapter highlights the promising perspective of

combining the ruthenates/titanates double perovskite and the *in-situ* exsolution of metal nanoparticles.

Chapter 3 introduces the synthesis and characterization methodology employed in this project. Fundamentals of the characterization including X-ray characterization, thermal analysis, electron microscopy, inductively coupled plasma-optical emission spectroscopy, electrochemical performance test has been discussed.

Chapter 4 presents the experimental results and analysis of the initial synthesis of lanthanum nickel ruthenate double perovskites. The crystal structure, solubility of A-site deficiency, intrinsic chemical information and thermal behaviour has been studied, giving the starting point of following development and exsolution investigations in chapter 5 and 6.

Following the discussion in chapter 4, stoichiometric and A-site deficient lanthanum nickel ruthenates were subjected to the exsolution treatment. The stability of this double perovskite phase was initially attempted, supporting the following exsolution treatment and temperature determine. The effect of A-site deficiency was emphasized in this chapter, by comparing the morphology after reduction treatment of stoichiometric sample and A-site deficient sample. In the end, the dry reduction results and temperature dependency has been discussed, giving clues for the mechanism investigation.

Therefore, based on the studies in chapter 4 and 5, chapter 6 discussed the *in-situ* observations of evolution of the A-site deficient lanthanum nickel ruthenate double perovskite and its electrochemical performance. The thermal analysis of A-site deficient lanthanum nickel ruthenate ($La_{1.85}NiRuO_{6-\delta}$, L1.85NR) in reducing atmosphere revealed onset of exsolution at a relatively lower temperature than the reduction temperature (450°C) adopted in chapter 5. The electrochemical performance of the L1.85NR applied as electrode of symmetric cells and the single cells has been evaluated and observed *in-situ*. The fast reducing of impedance of symmetric cells indicated the kinetics of exsolution and the increasing of peak powder density indicated the enhancement of electrochemical performance during exsolution. In the end, *in-situ* observation under high vacuum employing microscopy has been conducted on: (i) isothermal exsolution at 450°C; and (ii) step-wise increased temperature from 300°C to 450°C, showing the consistent fast exsolution response and separated exsolution of Ni and Ru cations.

The last result and discussion chapter focus on the A-site deficient lanthanum nickel titanates sample with Ru-dopant. Taking into account of the cost of Ru element, the content of Ru has been reduced to 5 at%. At the same time, the reduction of Ru was replaced by titanium, which in theory stabilize the structure and non-ex-solvable. Sythensis, temperature-dependent exsolution and the characterization of the exsolved nanoparticles has been analysed and discussed in this chapter. The exsolution of Nickel nanoparticles was observed in a broad

range of temperatures, while no Ru exsolution was shown until extreme reduction temperature (1000°C), indicating the vital role of the ex-solvable cation's concentration. In the end of this chapter, to further facilitate the exsolution of Ru, topotactic exchange with exotic iron source was attempted and discussed.

Chapter 2 Literature Review

2.1 Introduction

This chapter primarily conducts a brief introduction to double perovskite materials, with an explicit focus on those incorporating transition metals such as ruthenium or titanium at the B-site position potentially to be utilized in Solid Oxide Cells (SOCs). Subsequently, the narrative will review the phenomenon of exsolution within the realm of energy conversion. This review includes a brief survey of the reported exsolution phenomena, a discussion on the proposed mechanisms, and an examination of the exsolution of bi-metallic/tri-metallic nanoparticles.

2.2 Double perovskite oxides

Perovskite oxides, characterized by the general formula ABO_3, were initially identified by the Prussian mineralogist Gustav Rose and Russian mineral collector August Kammerer in 1839, and were subsequently named in honor of Count Lev A. Perovskiy [25]. Since their discovery, ABO_3 perovskites have seen extensive applications in various sectors, serving as ferroelectrics, piezoelectrics, and catalysts [26]. As illustrated in Figure 2.1, the archetypal cubic perovskite structure consists of a large, twelve-coordinate cation at the A site and a comparatively smaller, octahedrally-coordinate cation at the B site. The ABO_3 perovskite structure possesses several perovskite-type derivatives, including the layered Ruddlesden-Popper phases[27], layered Dion-Jacobson phases[28], double perovskite structures[29], and others [30].

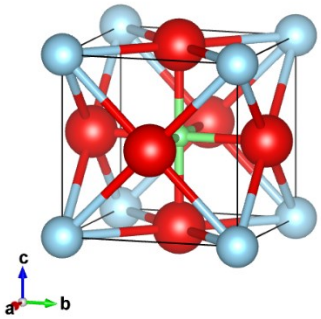


Figure 2.1 Schematic diagram of ideal ABO_3 perovskite structure. The red spheres represent oxygen anions; the blue spheres represent A-site cations; and the green sphere represent B-site cation.

Regarding the actual lattice structure, the bond lengths of A-O and B-O may not adhere perfectly to the ideal proportions observed in the cubic single-perovskite. The discrepancy between the A and B-site cations can be effectively described utilizing the Goldschmidt tolerance factor[31].

$$t = \frac{(r_O + r_A)}{\sqrt{2}(r_B + r_O)} \qquad (2-1)$$

where r_A, r_B and r_O are the ionic radii of A, B and O, respectively. For perovskites involving substitution, the radii of A or B cations typically reflect average radii. A stable ABO_3 perovskite

structure necessitates a Goldschmidt factor that fulfils the condition $0.75 < t \leq 1.05$ [32]. An ideal cubic perovskite is denoted by a unitary factor. When $t < 1$, the A-site cation radius is relatively smaller, leading to the tilting of BO_6 octahedra. Conversely, when $t > 1$, the A-site cation becomes excessively large, causing the structure to distort into a tetragonal, rhombohedral, or orthorhombic structure.

To alter the properties of ABO_3 perovskite oxides, a common approach involves partial substitution of A-site or B-site cations. If the substitution content reaches 50%, the ordering of A/B site cations might occur, giving rise to a new structural type. Double perovskite oxides, denoted by formulas $AA'BO_6$ or $ABB'O_6$, feature two types of cations occupying the A-site position or B-site position in lattices with certain ordering. This combination of two element types on the same lattice location offers high tunability of electronic and magnetic properties. In addition, the relatively 'open' structure of double perovskite can accommodate more lattice defects, such as oxygen vacancies, cation vacancies, cation interstitials, and octahedra-tilting, all of which facilitate the movement of charge carriers. For examples, the layered altering of oxygen vacancies in $LnBaCo_2O_{5+\delta}$ double perovskite[33] highly increased the oxygen diffusion rate[34] and electrical conductivity[35]. Importantly, the electrochemical properties of double perovskites can be further fine-tuned by introducing isovalent or aliovalent dopants. Substitution on A-site or B-site positions with varying metal cations can result in a more intricate structure and chemical environment within the lattice, generating desired crystal defects. Consequently, in recent years, double perovskite materials have garnered considerable interest for their potential applications in solid-state electrochemical devices.

In the case of $A_2BB'O_6$ and $AA'B_2O_6$ double perovskite, complete ordering of B-cations is rare. The ordering degree of B and B' cations (or A and A' cations) constitute a dominant parameter affecting physicochemical properties. The A/B cations of $A_2BB'O_6$ and $AA'B_2O_6$ double perovskite can ideally be arranged in three ways, as depicted in Figure 2.2:

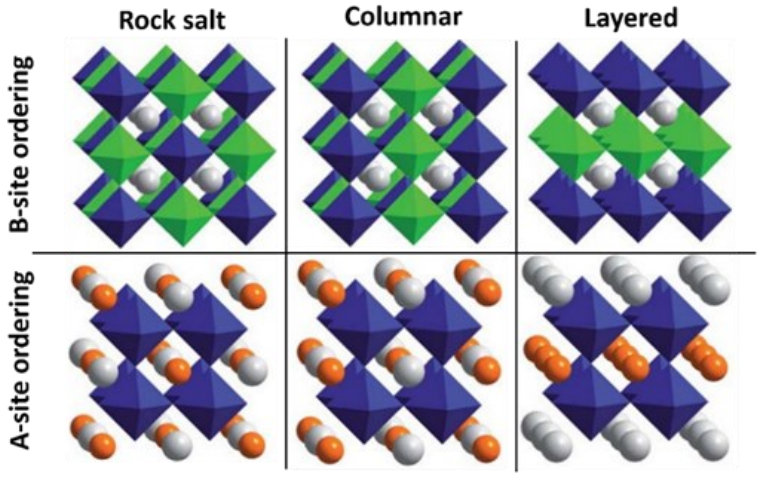


Figure 2.2 Cation ordering schemes in double perovskite. Rock-salt ordering is A-site (first row) or B-site (second row) cations alternate along three dimensions; columnar ordering is two cations alternate along x and y axis; layered

ordering is two cations only alternates along z axis. Reproduced under the terms and condition of CCC. [29] Copyright 2010, Royal Society of Chemistry.

The B-site double perovskites mostly exhibit rock-salt ordering, as shown in Figure 2.2. The degree of ordering can be assessed by a simple long-range order parameter as reported by Vasala and Karppinen [36]:

$$s = 2g_B - 1 \qquad (2-2)$$

Where g_B is the occupancy of a B-site cation at its correct site. The complete ordering corresponds to S = 1, and the completely disordered double perovskite corresponds to S = 0. The details of crystal structure and degree of ordering of La_2NiRuO_6 and La_2NiTiO_6 will be discussed in Chapter 4 and 7.

2.2.1 Ru-based $A_2BB'O_6$ double perovskite oxides

Ruthenium (Ru) is a member of the platinum group elements and is classified as a transition metal. In recent years, it has garnered considerable attention due to its distinctive characteristics and potential applications in various fields, particularly in perovskite oxide materials. The incorporation of ruthenium into perovskite oxide materials can enhance their electrical, catalytic, and electrochemical properties, thereby expanding their potential applications, especially in solid oxide cells (SOCs)[37–39].

In the case of SOCs, electrochemical reactions take place on the electrodes, involving multiple reactions such as the oxygen evolution reaction (OER), oxygen reduction reaction (ORR), hydrogen oxidation reaction (HOR) or hydrogen evolution reaction (HER). For instance, in the case of hydrogen fuel electrode, both HOR and HER involve hydrogen adsorption and desorption steps. These steps necessitate electrocatalysts or electrodes with sufficient catalytic activity to lower the kinetic barrier and accelerate the reaction rate [38,40]. B-site cations in the perovskite structure, typically d-block transition metals, are considered the catalytically active sites due to their reported ability to capture surface-absorbates bonding well through e_g-like molecular orbitals [41]. Therefore, ruthenium cations are a favourable choice as B-site cations in perovskite structures when applied in SOCs, as ruthenium possesses appropriate hydrogen binding energy (H_{ad}) and oxyphilic ability, which is neither too weak nor too strong, thereby achieving a balanced adsorption and desorption of OH_{ad} and H_{ad} [38,40]. Consequently, this project explores the potential of ruthenium-based double perovskite as a fuel electrode/electrocatalyst.

Over the past few decades, there has been significant progress in investigating and synthesizing Ru-based double perovskites, with most studies focusing on the synthesis and intrinsic properties of these double perovskites. Table 2.1 summarizes the synthesis and crystal structure details of various Ru-based double perovskites reported over the last 40 years. The majority of Ru-based double perovskites have been synthesized using the solid-state method.

For instance, Battle and Macklin [42] first synthesized the double perovskite Ca_2YRuO_6 by firing a mixture of precursors at 820°C for 6 hours, followed by calcining the stoichiometric pellet at 1100°C for 5 days with intermittent grinding. Hong et al. [43] employed a similar synthesis method for $BaLaMRuO_6$ (M= Zn, Mg) and emphasized the necessity of the initial pre-calcination stage to prevent the loss of volatile RuO_2. The synthesis of Ru-based double perovskites has also been achieved through the sol-gel method [44–46], which significantly reduces the required thermal treatment temperature and simplifies the synthesis process. The specific synthesis details investigated in this work will be discussed in Chapters 3 and 4.

As for the crystal structure, the deviation from a tolerance factor of 1 indicates a mismatch in the sizes of the A-site and B-site cations, leading to a reduction in symmetry from ideal cubic structure. Besides, the formation of superstructure and octahedral tilting also contributes to the reduction in symmetry. As anticipated, the majority of Ru-based double perovskites exhibit B-site rock-salt ordering between the ruthenium cations and other transition metals, driven by the disparities in size or charge of the two B-site cations [47]. The most common type of the Ru-based double perovskite was long-range B-site ordered monoclinic structure with space group $P2_1/n$ as Table 2.1 highlights.

In terms of the electronic structure and electrochemical properties of Ru-based double perovskites, Dani et al. [48] conducted a study on A_2SmRuO_6 compounds (where A = Ba and Sr), focusing on the evolution of the valence states of Ru cations using X-ray absorption spectroscopy (XAS) and Density Function Theory (DFT) calculations. The calculations aligned with the XAS observations, indicating that the Ru cations exhibited a valence state higher than +4. Additionally, the calculated bandgap suggested that the A_2SmRuO_6 ruthenates possessed semiconducting properties. Chen et al. [49] investigated $Sr_2YRu_{1-x}Cu_xO_6$ (x=0–0.05) through X-ray absorption near-edge structure (XANES) spectroscopy, revealing that the incorporation of copper into the Ru cation position increased the hole concentration in the material. This incorporation was accompanied by an increase in the O-Ru-O bond angle and lattice distortion. In another study, Xia et al. [46] applied the Ru-based double perovskite $SrRu_{0.5}Ir_{0.5}O_3$ in Proton Exchange Membrane Water Electrolysers (PEMWEs), demonstrating its significantly enhanced OER activity and materials stability in acidic solutions. This enhancement was attributed to the synergistic effect between Ir and Ru in the catalyst. Retuerto et al. [50] investigated the catalytic activity of $La_{1.5}Sr_{0.5}NiMn_{0.5}Ru_{0.5}O_6$, a ruthenate double perovskite, towards both the ORR and OER. The ruthenate material exhibited bifunctional catalytic activity, with an impressive index value of ~0.83V. The index is defined as the difference between the potentials required to reach an OER current density of 10 mA cm^{-2} and an ORR current density of−1mAcm^{-2} and the state-of-art bifunctional catalyst have critical value of 0.90V. This high bifunctional catalytic activity of $La_{1.5}Sr_{0.5}NiMn_{0.5}Ru_{0.5}O_6$ was attributed to the presence of active Mn sites for the ORR and Ru-active sites for the OER. Considering the focus of this work on

solid-state systems, the bifunctional catalytic activity of the ruthenate double perovskite, with active sites for both ORR and OER, could potentially enhance the efficiency and performance of SOCs by facilitating both oxygen reduction and evolution reactions.

Table 2.1 Synthesis, lattice structure of reported Ru-based double perovskites

Chemical formula	Synthesis	Lattice structure	Degree of ordering	ref
Ca_2YRuO_6	Solid-state reaction	Monoclinic structure (space group *P2₁/n*)	A-site Ca and Y disordering; B-site ordering	42
$BaLaMRuO_6$(M=Zn,Mg)	Solid-state reaction	Tetragonal structure (space group *I4/m*)	Complete ordering (S=1)	43
Sr_2RuYO_6	Solid-state reaction	Monoclinic structure (space group *P2₁/n*)	B-site ordering	51
La_2MRuO_{6+d}(M=Mg, Co, and Ni)	Sol-gel reaction (Pechini method)	Monoclinic structure (space group *P2₁/n*)	B-site ordering	44
La_2MRuO_{6+d}(M=Mn, Fe, and Zn)	Solid-state reaction	Orthorhombic structure (space group *Pbmn*)	Short-range B-site ordering	44
Ba_2HoRuO_6	Solid-state reaction	Monoclinic structure (space group *P2₁/n*)	B-site ordering	52
Ln_2CoRuO_6(Ln=La,Pr,Nd,Sm,Eu and Gd)	Solid-state reaction	Monoclinic structure (space group *P2₁/n*)	B-site ordering (S=0.8)	53
Ba_2MRuO_6(M=Sm and Dy)	Solid-state reaction	Cubic structure (space group *Fm$\bar{3}$m*)	/	54
$(Sr_{1-x}La_x)_2MRuO_6$(M=Y and Er)	Solid-state reaction	/	/	55
R_2NiRuO_6(R=Pr-Er)	Sol-gel reaction (nitrate-citrate route)	Monoclinic structure (space group *P2₁/n*)	B-site ordering (S=0.56)	45
Ca_2FeRuO_6 and $CaSrFeRuO_6$	Solid-state reaction	Orthorhombic structure (space group *Pbmn*)	Complete disordering	56
A_2CoRuO_6 (A = La, Pr, Nd and Sm)	Solid-state reaction	Monoclinic structure (space group *P2₁/n*)	B-site ordering (S=0.9~0.98)	57
$SrRu_{0.5}Ir_{0.5}O_3$	Sol-gel reaction	Orthogonal structure (space group *ibmm*)	/	46
Ba_2SmRuO_6	Solid-state reaction	Cubic structure (space group *Fm$\bar{3}$m*)	B-site ordering	48
Sr_2SmRuO_6	Solid-state reaction	Monoclinic structure (space group *P2₁/n*)	B-site ordering	48
$La_{1.5}Sr_{0.5}NiMn_{0.5}Ru_{0.5}O_6$	Solid-state reaction	Monoclinic structure (space group *P2₁/n*)	B-site ordering	50

2.2.2 Ti-based $A_2BB'O_6$ double perovskite oxides

In light of the research conducted on ruthenates, titanium was employed as a substitution for ruthenium at the B-site position in lanthanum nickel-based double perovskite oxides, taking into account the unique exsolution behaviour of titanium cations, as discussed further in Section 2.3.1.2. The synthesis method, lattice structure, and degree of ordering for several reported Ti-based $A_2BB'O_6$ double perovskite oxides have been summarized in Table 2.2.

Similar to the ruthenates, both solid-state reaction synthesis and sol-gel reaction synthesis have been documented for the titanium-based $A_2BB'O_6$ compounds. Palacin et al. [58] synthesized La_2CuTiO_6 using the conventional solid-state method, a modified solid-state method with mixed oxide precursors, and the sol-gel method, and compared the impact of these three different synthesis approaches on the resulting products. The conventional solid-state method involved 3-4 cycles of thermal treatment and regrinding. The modified solid-state method expedited the process by calcining TiO_2 and utilizing pre-prepared La_2CuO_4. Both of these solid-state synthesis methods required a higher thermal treatment temperature of over 1100°C to achieve a pure phase. On the other hand, the sol-gel reaction entailed dissolving precursors in propanol, followed by evaporation and thermal treatment at temperatures ranging from 500°C to 675°C for 3 cycles. The pure crystallized phase emerged after the thermal treatment at 675°C, which was still considerably lower than the solid-state method. Therefore, the sol-gel citric-nitrate route was employed for the synthesis of lanthanum nickel titanates in this study, as elaborated on in Chapter 3 and 7.

Regarding the lattice structure, Ti-based $A_2BB'O_6$ double perovskites exhibit higher symmetry and lower B-site ordering compared to the ruthenates. This is consistent with the tolerance factor (Equation 2-1), which indicates that the t factor of the Ti-based double perovskite is closer to 1 in comparison to the ruthenates. The smaller ion radius of Ti cations, as opposed to Ru cations, contributes to a reduced distortion in the lattice structure. In addition, the crystal structure was observed to evolve with changes in composition. Yuste et al. [59] gradually substituted La^{3+} by Sr^{2+} in La_2CoTiO_6 and investigated the phase transition as the content of Sr^{2+} increased. Initially, La_2CoTiO_6 displayed a monoclinic structure with $P2_1/n$ symmetry, along with an ordered arrangement of Co and Ti ions at the B-site. However, as the value of x in $La_{2-x}Sr_xCoTiO_6$ increased beyond 0.3, the unit cell exhibited orthorhombic symmetry, and the ordered arrangement of B-site cations began to diminish. Similarly, Shafeie et al. [60] substituted the Ti cations with Mg cations in La_2CoTiO_6, initially resulting in the same monoclinic structure with $P2_1/n$ symmetry. However, with the presence of Mg cations at the B-site, the structure transformed into an orthorhombic *Pnma* structure. As the value of x in $La_2Co_{1+z}(Mg_xTi_{1-x})_{1-z}O_6$ increased up to 0.5, the X-ray powder diffraction patterns indicated a mixture of rhombohedral and cubic phase.

The Ti-based $A_2BB'O_6$ double perovskite oxides have been proposed as promising electrode materials for solid-oxide fuel cells (SOFCs) due to their high stability, particularly under reducing atmospheres and sulfur-containing conditions [61]. Among these oxides, the La_2MTiO_6 series (M = Zn, Co, Mg, and Fe) has been suggested as fuel electrode materials for SOFCs [59–61]. Yuste et al. [59] investigated the valence states of cobalt ions in $La_{2-x}Sr_xCoTiO_6$ ($0 \leq x \leq 1.0$) through magnetic susceptibility measurements and thermogravimetric analyses. They reported a mixed oxidation state for the cobalt ions under both oxidation and reducing

atmospheres. The structure of these materials remained stable even with a significant presence of oxygen vacancies under reducing conditions, making them promising candidates for electrochemical devices.

Another highly studied series of Ti-based $A_2BB'O_6$ double perovskites for SOFC electrode applications is Sr_2MTiO_6 (M = Mo, Ni, Fe, and Sc). Niu et al. [62] used Sr_2TiMoO_6 as an anode material in SOFC single cells, with $La_{0.9}Sr_{0.1}Ga_{0.8}Mg_{0.2}O_{3-\delta}$ (LSGM) as electrolyte and $NdBaCo_{2/3}Fe_{2/3}Cu_{2/3}O_{5-d}$ (NBCFC) as cathode. The single cell demonstrated good stability, excellent resistance to coking, and tolerance to sulfur in an environment of commercial syngas containing H_2S for a testing period of 60 hours. Similarly, He et al. [63] investigated the effect of Ti-dopant in $Sr_2TiNi_{0.5}Mo_{0.5}O_6$ as an anode material for SOFCs operating with humidified H_2 and dry CH_4 fuels. They suggested that the presence of strong Ti-O bonds greatly enhanced the structural stability of the material under reducing conditions. Rath et al. [64] utilized $Sr_2ScTi_{1-x}Mo_xO_6$ (x=0.1 and 0.5) as electrodes in symmetric SOFCs. The Ti-rich double perovskite exhibited a lower activation energy for both the ORR and HOR compared to the Mo-rich double perovskite. These studies highlight the potential of Ti-based $A_2BB'O_6$ double perovskite oxides as electrode materials for SOFCs, demonstrating their stability, sulfur tolerance, structural enhancements, and improved catalytic properties for electrochemical reactions.

Table 2.2 Synthesis, lattice structure of reported Ti-based double perovskites

Chemical formula	Synthesis	Lattice structure	Degree of ordering	ref
La_2CuTiO_6	Solid-state reaction; Solid-state method with La_2CuO_4 precursor; Sol-gel reaction	Orthorhombic structure (space group *Pnma*)	B-site disordering	58
La_2MTiO_6(M=Co and Ni)	'liquid mix'' technique (similar to sol-gel method)	Monoclinic structure (space group $P2_1/n$)	Partially B-site ordering (S= 0.48 - 0.72)	65
$CaRu_{1-x}Ti_xO_{3-y}$ (x=0,0.1,0.2...0.9, 1.0)	Solid-state reaction	Orthorhombic structure (space group *Pnma*)	/	66
Sr_2TiMnO_6	Solid-state reaction	Tetragonal structure (space group *I4/m*)	/	67
$La_{2-x}Sr_xCoTiO_6$ ($0\leq x<0.3$)	Sol-gel reaction (Pechini method)	Monoclinic structure (space group $P2_1/n$)	B-site ordering	59
$La_{2-x}Sr_xCoTiO_6$ ($0.3\leq x<1.0$)	Sol-gel reaction (Pechini method)	Orthorhombic structure (space group *Pnma*)	B-site disordering with x increasing	59
La_2ZnTiO_6	Sol-gel reaction (nitrate-citrate route)	Monoclinic structure (space group $P2_1/n$)	B-site ordering	61
$La_2Co_{1+z}(Mg_xTi_{1-x})_{1-z}O_6$	Sol-gel reaction (nitrate-citrate route)	Structure changes from Monoclinic structure ($P2_1/n$) via orthorhombic structure (*Pbnm*) to rhombohedral structure ($R\bar{3}c$) and cubic structure ($Pm\bar{3}m$) with both increasing Mg content and increasing Co content.	B-site ordering of $LaCo_{0.5}Ti_{0.5}O_3$ monoclinic lattice	60
$La_2Ni(Mn_{1-x}Ti_x)O_6$ (x=0, 0.2, 0.4, 0.6, 0.8, and 1)	Solid-state reaction	Monoclinic structure (space group $P2_1/n$)	Partially B-site ordering	68
Sr_2TiIrO_6	Sol-gel reaction (nitrate-citrate route)	Orthorhombic structure (space group *Pnma*)	B-site disordering	69
Pr_2CoTiO_6	Solid-state reaction	Monoclinic structure (space group $P2_1/n$)	B-site ordering	70
$La_2MnTiO6$	Solid-state reaction	Monoclinic structure (space group $P2_1/n$)	B-site ordering	71
$Sr_2Fe_{1.4}Ti_xMo_{0.6-x}O_{6-\delta}$ (x = 0.1, 0.2 and 0.3)	Solid-state reaction	Cubic structure (space group $Fm\bar{3}m$)	/	72

2.3 Exsolution method

2.3.1 Concept and system

Based on the preceding discussion, perovskite oxides, particularly those with a double perovskite structure, have been demonstrated as effective electrodes and electrocatalysts in solid-oxide cells (SOCs). Over the past decade, a novel approach involving the decoration of oxides with uniformly grown in-situ nanoparticles has been confirmed as an efficient method for enhancing stability [73,74], resilience to impurity poisoning [75–77], electrochemical activity [78,79] and electronic conductivity [35,80] of the electrodes and catalysts. Perovskite has been identified as a suitable parent support for the exsolved nanoparticles due to its structural flexibility and ability to tolerate exotic dopants and lattice mismatch.

The process of 'exsolution' originates from geology and refers to the separation of a solid solution into different crystalline structures at various scales [81]. The early investigations of 'exsolution' were reported in the context of self-regenerated catalysts from perovskite oxides [82–85]. Shiozaki et al. [82] prepared a Ni/$BaTiO_3$ catalyst for the partial oxidation of CH_4 using the 'solid phase crystallization' method, in which surface Ni metal precipitates on the surface of $BaTiO_3$ under a reducing atmosphere. Similarly, Ni and Ru nanoclusters were observed to precipitate on the surface of a lanthanum chromite anode during the operation of SOFCs [84,85]. Nishihata and Tanaka et al. [83,86] observed Pd regenerates from the $LaFe_{0.57}Co_{0.38}Pd_{0.05}O_3$ after reduction in hydrogen/nitrogen, and its reversible re-incorporation into the perovskite structure. Similarly, Rh and Pt 'intelligent catalysts' self-regenerated and dissolved into the perovskite in a rapid fluctuation when encountering exhaust gas from a gasoline engine, preventing catalyst degradation, as demonstrated in Figure 2.3. Pavlova et al. [87] reported the enhancement of coking resistance in a catalyst for CO_2 reforming of methane by reducing $LnFeNi(Ru)O_3$ perovskites and forming Ni-Fe-(Ru) alloy particles. Along with the reduction of the perovskite, an LnO_x layer grows epitaxially between the perovskite substrate and the reduced metal particles, indicating partial destabilization of the perovskite structure under reducing atmosphere.

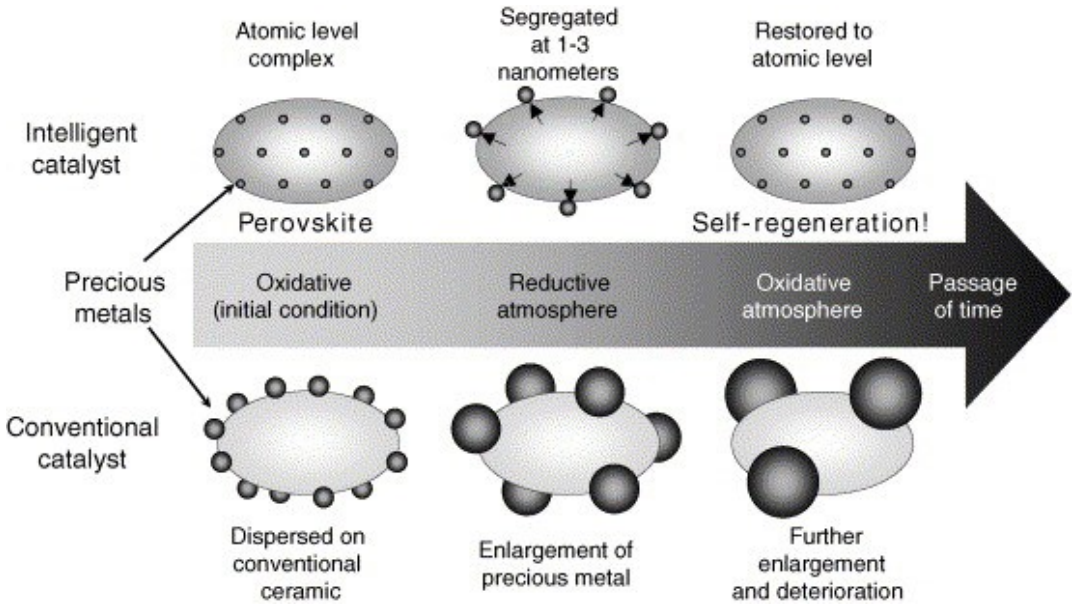


Figure 2.3 Schematic of the intelligent catalyst self-regeneration and conventional catalysts enlargement. Reused under permission from reference [86]. Copyright 2006, Elsevier.

Studies on exsolution gained momentum after Neagu et al. proposed the method of controlling and tuning exsolved nanoparticles in 2013 [88]. Non-stoichiometric lanthanum titanates with various transition metal dopants were systematically screened to investigate the in-situ growth of nanoparticles. Several factors were found to influence the surface nanoparticles, with A-site deficiency playing a predominant role in facilitating and tailoring B-site exsolution. The perovskite unit cell with built-in A-site deficiency spontaneously excludes localized B-site 'excess' to restore local stoichiometry, as illustrated in Figure 2.4. The presence of A-site deficiencies also suppresses the structural deconstruction of perovskite into oxides with extra A-site cations, as mentioned earlier.

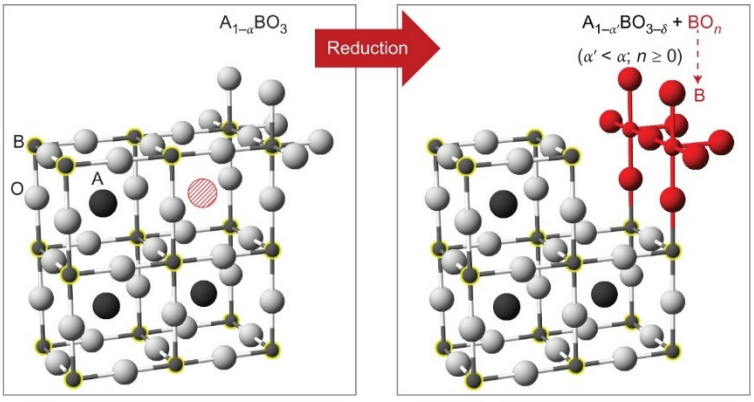


Figure 2.4 Schematic of the exsolution process of perovskite unit cells with built-in A-site vacancy. Reproduced under the permission from reference [88]. Copyright 2013, Springer Nature.

A subsequent investigation by Neagu et al. [76] into the interface between exsolved Ni nanoparticles and the lanthanum strontium titanates bulk substrate revealed a unique 'socketed' structure, with approximately 30% of the particle embedded into the parent

perovskite. The robust interaction between exsolved nanoparticles and the parent oxide contributes to high thermal stability and excellent coking resistance, as shown in the Figure 2.5, without compromising catalytic activity, thereby explaining the high performance and stability of the intelligent catalysts discovered in the early stages of research. This further explores the attractive properties of nanoparticles derived from the exsolved method, which has garnered significant attention in catalyst development and electrochemical devices.

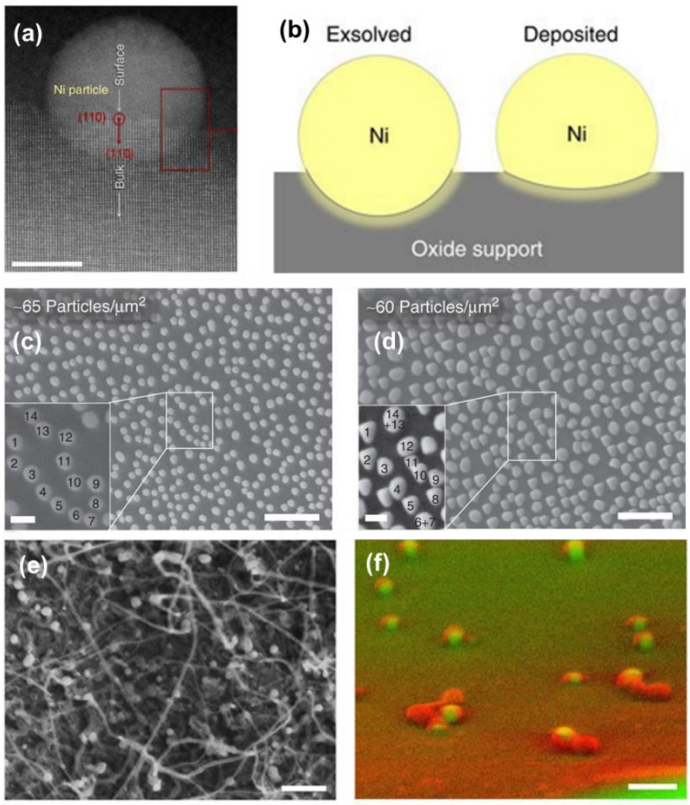


Figure 2.5 (a) TEM micrograph (dark field) of a Ni particle exsolved on (110) native surface facet showing the partially submerge of the nanoparticle, scale bar 10 nm; (b) schematic illustration of the exsolved nanoparticle-bulk interface and the deposited nanoparticle-substrate interface; SEM images of the exsolved Ni nanoparticle on the surface of $La_{0.52}Sr_{0.28}Ni_{0.06}Ti_{0.94}O_3$ before (c) and after (d) aging for 70 hours, scale . Comparison of the carbon growth of (e) Ni nanoparticles prepared by vapor deposition (scale bar 500nm) and (f) exsolved Ni nanoparticles on lanthanum strontium titanates (scale bar 100nm). Reproduced under the terms of the CC-BY license. [76] Copyright 2015, the authors. Published by Springer Nature.

In the following decade, abundance studies and effort has been put in this filed due its promising application in electrochemical devices, including SOCs [22,84,89–102], water splitting catalysis [103–115], ammonia reaction catalysis [116–123], hydrocarbon reforming [124–144] and CO_2 electrolysis [145–177], as illustrated in Table 2.3. Driving forces and multiple 'intrinsic and 'extrinsic' factors were investigated to figure out the exsolution process and mechanism.

Table 2.3(a) Applications of exsolution method, corresponding exsolved elements and host lattices: SOCs, water splitting and hydrocarbon reforming.

Application	Exsolved element	Host lattice	Ref.
SOCs	Fe	$Sr_2Fe_{1.5}Mo_{0.5}O_{6-d}$	178
	Ni	$La_{0.7}Sr_{0.3}Cr_{1-x}Ni_xO_{3-d}$; $BaZr_{0.8}Y_{0.2}O_{3-\delta}$	89,91
	Co	$Sr_2Fe_{1.3}Co_{0.2}Mo_{0.5}O_{6-\delta}$	96
	Ru	$LaSr_{0.2}Cr_{1-x}Ru_xO_{3-\delta}$	102
	Fe, Ni	$SrFe_{1-2x}Ni_xMo_xO_3$	101
	Fe, Co	$SrFeO_{3-d}$; $Sr_2Ti_{1-x}Co_xFeO_6$	95
	Fe, Co, Ni	$La_{0.6}Sr_{0.4}M_{0.2}Mn_{0.2}Fe_{0.6}O_{3-\delta}$(M= Co, Ni)	98
	Fe, Co, Ru	Sr0.95(Ti0.3Fe0.63M)O3-d (M= Ru, Ni)	100
	Ag	BaCo0.4Fe0.4Zr0.1Y0.1O3-d; $Ba_{0.95}Co_{0.8}Nb_{0.1}Ta_{0.1}O_{3-\delta}$; $Sr_{0.95}Ag_{0.05}Nb_{0.1}Co_{0.9}O_{3-\delta}$	90,92,94
Water splitting catalysis	Fe	$SrTi_{0.8}Fe_{0.2}O_{3-d}$; $La_{0.66}Ti_{0.8}Fe_{0.2}O_{3-d}$; $SrTi_{0.65}Fe_{0.35}O_3$	106,110
	Co	Sr_2FeMoO_6	113
	Pt	$LaCo_{0.94}Pt_{0.06}O_3$	104
	Cu	$LaFeO_3$	105
	Ag	$AgTaO_3$	108,111
	Ni	$La_{0.8}Sr_{0.2}Cr_{0.69}Ni_{0.31}O_{3-d}$	103
	V	$BiVO_4$	114
	Ir,CoO	$SrCoO_{3-\delta}$	107
	IrO_x	$LaFeO_3$	112
	WS_2	$SrTiO_3$	109
	Co_3O_4, $Ca(OH)_2$	Ca_3Co_4O	115
Hydrocarbon reforming	Ni	$La_{0.43}Ca_{0.37}Ni_{0.06}Ti_{0.94}O_3$; $La_{1.5}Sr_{1.5}Mn_{1.5}Ni_{0.5}O_7$; ZrO_2; CeO_2; $La_{0.7}Ca_{0.2}Ni_{0.25}Ti_{0.75}O_3$; NiAl2O4; $La_{0.4}Ca_{0.4}Ni_xTi_{1-x}O_{3-d}$; $CaTiO_3$	127,128,132,135,136,139,141,143
	Ru	$Sm_2Ru_xCe_{2-x}O_7$	142
	Rh	Al_2O_3	125
	Ni, Fe	$(La,Sr)(Cr,Fe,Ni)O_3$; $Sr_2Fe_xNi_{1-x}MoO_{6-\delta}$; $PrBaMn_{1.6}Ni_{0.3}Fe_{0.1}O_{5+\delta}$	133,137,138
	Ni, Rh	$La_{0.43}Ca_{0.37}Rh_{0.03}Ni_{0.03}Ti_{0.94}O_3$	144
	Ni, Co	$MgAl_2O_4$	126
	Ni, Cu	$LaCe_{0.1}Mn_{0.8}Ni_{0.1}Cu_{0.1}O_3$	124
	Ni, Fe, Co	$PrBaMn_{1.7}Co_{0.1}Ni_{0.2}O_{5+d}$	134
	Ni, Fe, Re	$LaFeO_3$	140
	Fe,Co	$PrBaFeCoO_{5+\delta}$	130
	IrO_x	$LaFeO_3$	131
	Ni, CeO_2	$La_{0.75}Ce_{0.05}Ca_{0.2}Cr_{0.9}Ni_{0.1}O_3$	129

Table 2.3 (b) Applications of exsolution method, corresponding exsolved elements and host lattices: ammonia reaction catalysis and carbon dioxide reduction.

Application	Exsolved element	Host lattice	Ref.
Ammonia reaction catalysis	Ru	$La_{1-x}Sr_xTiO_3$; $BaCe_{0.9}Y_{0.1}O_3$; $La_{0.33}Sr_{0.67}Cr_{0.33}Fe_{0.52}Ru_{0.15}O_{3-\delta}$; $BaCe_xO_y$	118–121,123
	Ni	$La_{0.45}Sr_{0.45}Ti_{0.9}Ni_{0.1}O_3$	116
	Ni, Co	$Sr_2CoMo_{1-x}Ni_xO_{6-\delta}$	117
	Ru, Co, Fe	$Pr_{0.6}Sr_{0.4}Co_{0.2}Fe_{0.75}Ru_{0.05}O_{3-\delta}$	122
Carbon dioxide reduction	Ni	$(La,Sr)FeO_3$; $(La,Sr)TiO_3$; $Sr_2Fe_{1.5}Mo_{0.5}O_6$	146,152,154,162
	Fe	$Sm_{0.2}Ce_{0.8}O_{2-d}$; $Sr_2Fe_{1.5}Mo_{0.5}O_6$; $(Ce, La, Sr)(Cr,Fe)O_{3-\delta}$; $La_{0.3}Sr_{0.7}Ti_{0.3}Fe_{0.7}O_{3-\delta}$	157,166,167,172,175
	Co	$Pr_{0.5}Ba_{0.5}MnO_x$; $La_{0.6}Sr_{0.4}Co_{0.7}Mn_{0.3}O_3$; $Sr_2(Fe,Co)_{1.5}(Mo,Ti)_{0.5}O_6$	151,153,170
	Cu	$(La,Sr)(Ti,Mn)O_3$; NiOOH; $Sr_xTi_{0.7}Cu_{0.2}Mo_{0.1}O_{3-\delta}$; $LaFeO_3$	145,156,168,176
	Ni, Co	$(La,Ca)TiO_3$	155,173
	Ni, Fe	$(La,Sr)(Cr,Fe)O_3$; $(La,Ca)(Cr,Fe)O_3$; $(Pr,Sr)(Fe,Nb)O_3$; $(Pr,Sr)(Fe,Mo)O_3$; $Sr_2Fe_{1.5}Mo_{0.5}O_6$; $(Pr,Ba)(Fe,Ni)O_3$; $(La,Ca)TiO_3$	147,158,160,161,164,165,171,173
	Fe, Co	$(Pr_{0.4}Sr_{0.6})_3(Fe_{0.85}Mo_{0.15})_2O_7$; $Sr_2Fe_{1.5}Mo_{0.5}O_6$; $(Pr,Sr)(Fe,Mo)O_3$	149,150,165
	Fe, Ru	$(Pr,Sr)(Fe,Mo,Ru)O_3$; $Sr_2(Fe,Mo,Ru)O_3$; $(La,Sr)FeO_3$	163,174,177
	Fe,Sn	$Sr_{1.95}Fe_{1.4}Sn_{0.1}Mo_{0.5}O_{6-\delta}$	159
	Fe, MnO_x	$(Pr,Ba)Mn_{1-x}Fe_xO_{3-\delta}$	148

2.3.2 Mechanisms and steps

Factors and driving forces of exsolution can be divided into 'intrinsic' nature, which includes built-in defects, dopants, and host elements, as well as elemental and defect concentrations, and 'extrinsic' nature, which includes temperature, voltage-bias, oxygen particle pressure, and exotic elemental exchanges [88]. This section reviews the studies on the exsolution mechanism and driving forces of exsolution.

The key process of the exsolution of metal oxides with dopant reduced under hydrogen atmosphere was demonstrated by Kuosi et al. [179] as Figure 2.6 showed. During the reduction by hydrogen, the solid solution formed a certain number of oxygen vacancies, facilitating the nucleation of metal cations. Stradi et al. [180] conducted DFT calculations and confirmed that the oxygen vacancies played a vital role in the surface segregation of precious-metal atoms from the $LaFeO_3$ perovskite. In the study on Fe exsolution on $La_{0.6}Sr_{0.4}FeO_3$ thin film, Wang et al. [181] proposed the exsolution of metal cations involves the formation of Schottky defects and the oxygen vacancies pairs served as nucleation site of iron nanoparticles exsolution based on DFT and Monte Carlo calculation.

With the accumulation of diffused and segregated-out M^{2+} cations (Figure 2.6), the surface atoms were reduced, and particles started to nucleate and grow. Gao et al. [182] investigated the Ni exsolution from $La_{0.4}Sr_{0.4}Sc_{0.9}Ni_{0.1}O_{3-\delta}$ and proposed three models of Ni particle growth: the strain-limited model, the reactant-limited model, and the diffusion-limited model. These models take into account determining factors such as reduction time, atmosphere, amount of Ni, and strains (Figure 2.7). In a subsequent in-situ investigation of Co nanoparticles growth in a $SrTi_{0.75}Co_{0.25}O_{3-\delta}$ polycrystalline thin film, Jo et al. quantitatively measured the growth of exsolved nanoparticles over time. The obtained results showed a correspondence with the reactant-limited model, while considering a modification that accounts for the vacuum reduction process used in their work.

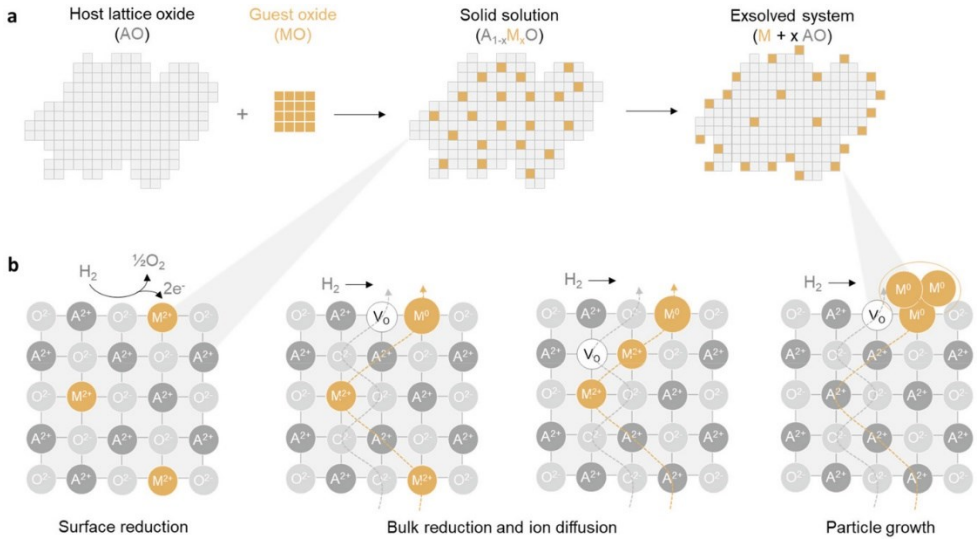


Figure 2.6 Illustration of the process. (a) The exsolution method and (b) key processes fundamental to exsolution. Reuse under the terms of CC-BY license [179]. Copy right 2021, the authors. Published by John Wiley and Sons.

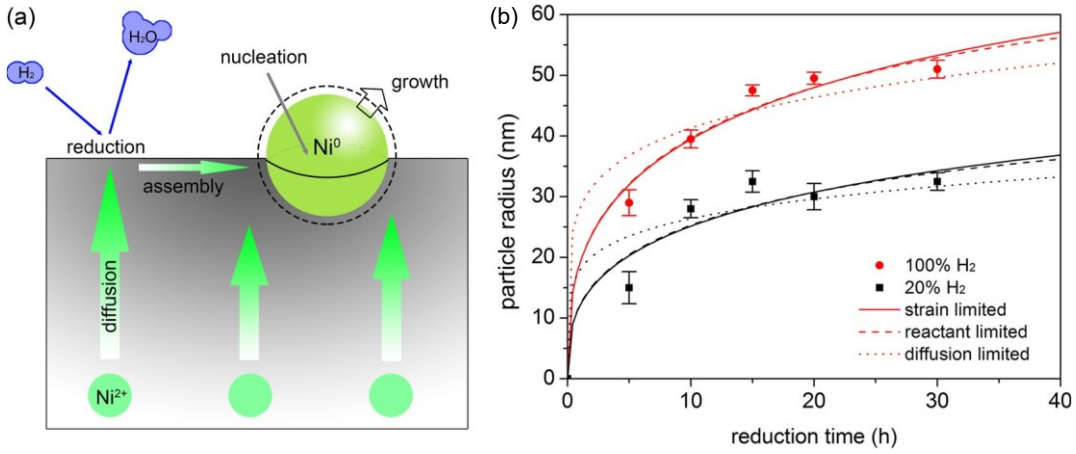


Figure 2.7 (a) Illustration of the exsolution process. (b) The average particle size and the fitting curves with strain-limited model (solid line), reactant-limited model (dashed line), and diffusion-limit model (dotted line). Reproduced under the permissions from reference [182]. Copyright 2016, Elsevier Ltd.

As mentioned earlier, the unique 'socketed structure' has raised intriguing properties and promising prospects in the application of the exsolution method. The mechanism behind the formation of this partly submerged structure of the exsolved particles was discussed by Oh et al. [183] in their observation of Ni exsolution from the perovskite $La_{0.4}Sr_{0.4}Ti_{0.97}Ni_{0.03}O_{3-\delta}$ using atomic force microscopy (AFM). They proposed the formation of subsurface nucleates and observed the movement of metal nucleates towards the surface, with a trench forming prior to it. As the metal nucleates moved out, a particle-in-pit morphology was formed, which accounted for the socketed interface. However, in a later in-situ observation of Ni exsolution by Neagu et al. [184], the kinetics of Ni exsolution from lanthanum calcium titanate were studied using high-resolution environmental transmission electron microscopy (E-TEM). A fast nucleation process was observed after 0.2 seconds under vacuum, growing to a critical size of around 1 nm within 0.4 seconds (Figure 2.8.a). The *in-situ* observation revealed the initial stage of nucleation within the subsurface of the lattice. Interestingly, in this case, the socketed interface was observed to form without the nucleates moving out but instead maintaining their initial location and growing isotropically. This resulted in the formation of a 'volcano-like' socketed structure as the parent perovskite lattice was pushed laterally, as depicted in Figure 2.8. In a more recent *in-situ* real-time observation of Ir nanoparticles from strontium titanates [185], a pyramidal base was observed for the particle socket. A new mechanism similar to the first stages of the vapour-liquid-solid mechanism was proposed for the formation of this interfacial structure. The pyramidal socket structure formed after the full formation of the particles, and due to the dilute concentration of Ir atoms, the exsolved atoms were insufficient to grow nanowires. As a result, a pyramidal base was formed between particles and host lattice. These unique socketed structures offer interesting insights into the exsolution process, and their formation mechanisms provide valuable information for understanding the behaviour of

exsolved particles at the atomic level, and tailoring materials with enhanced properties and functionalities.

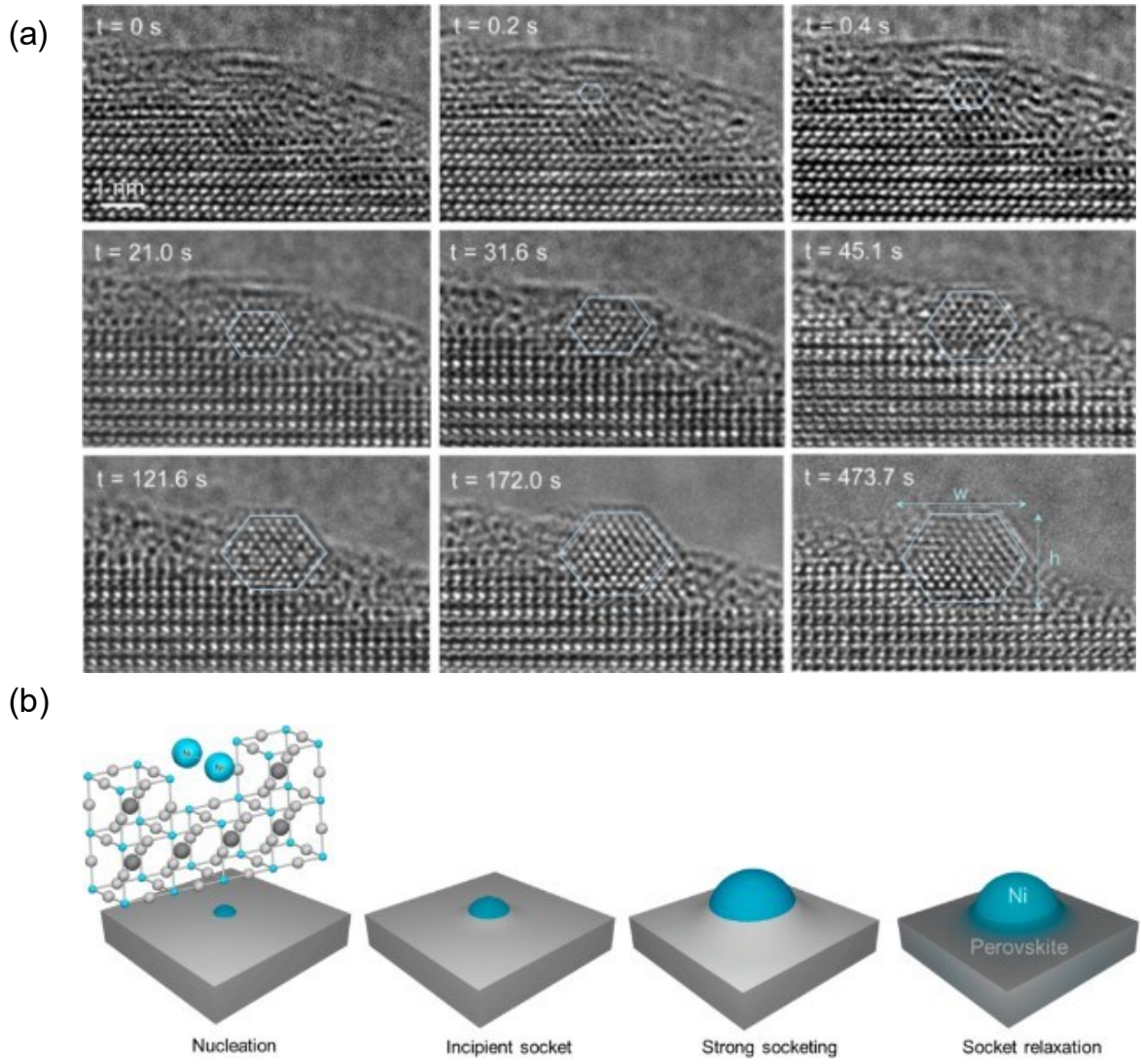


Figure 2.8 (a) In-situ TEM images of the exsolution of a Ni metal particle at the surface of a $La_{0.43}Ca_{0.37}Ti_{0.94}Ni_{0.06}O_3$ powder at different times during an in-situ E-TEM reduction carried out under vacuum at 900 °C. (b) Schematic illustration of particle−socket genesis during exsolution. Reused with permission from reference [184]. Copyright 2019 American Chemical Society.

Intriguingly, in addition to the previously reported subsurface nucleates, Kousi et al. [186]discovered metallic Ni nanoparticles dispersed throughout the bulk of the oxide hosts of $La_{0.8}Ce_{0.1}Ni_{0.4}Ti_{0.6}O_3$ when subjected to a prolonged reduction time at higher temperature (*i.e.*, 10 hours at 1000°C), as depicted in Figure 2.9. This finding highlights the ability to form endogenous particles not only on the surface but also within the bulk of the material. The tunability of these endogenous particles was found to be influenced by the reduction temperature and time. The intensive exsolution observed both at the surface and bulk of the material resulted in highly strained reduced materials, which, in turn, promoted the oxygen transportation property. This property is crucial for applications that involve oxygen storage

and migration, making these materials valuable in various fields. In their later studies, Kousi et al. [187] also discovered Ni-Co co-exsolved endogenous particles in the reduced $La_{0.7}Ce_{0.1}Co_{0.3}Ni_{0.1}Ti_{0.6}O_{3-d}$ material. These co-exsolved particles exhibited further enhanced properties of oxygen storage capacity and activity towards CH_4 conversion, showcasing the potential for tailoring and optimizing material properties through controlled exo/endogenous exsolution process.

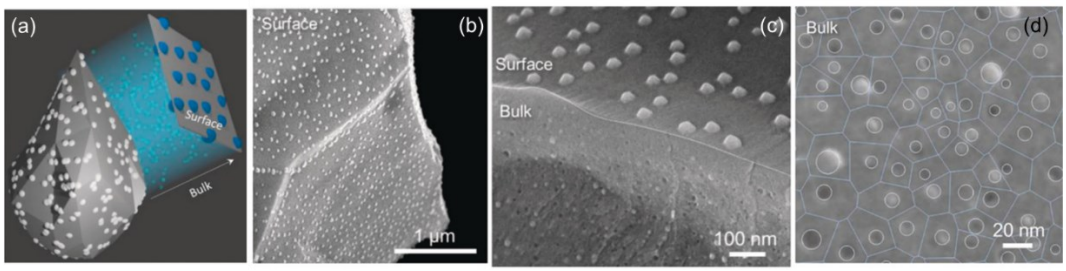


Figure 2.9 (a) 3D model of a catalyst particle with nanoparticles dispersed on its surface and within its bulk. (b) SEM image of the overview of the surface of the perovskite after exsolution. (c) SEM image of cross-section view after exsolution revealing surface and bulk particles. (d) Detail of the particles exsolved in the bulk Reuse permission from reference [186]. Copyright 2019, John Wiley and Sons.

2.3.3 Driving forces

The exsolution of a solid solution system includes multiple steps of reduction and oxygen loss, cation diffusion, nucleation, and particle growth. Various factors synergistically influence the behaviour of the exsolved particles and oxide system. As mentioned above, one intrinsic factor, built-in A-site deficiencies, has been revealed to play a vital role in promoting exsolution during reduction. For most oxides, the introduction of A-site deviations can also generate oxygen vacancies throughout the lattice, which are proposed to accompany the segregation of B-site cations [188,189]. As Equation 2-3 demonstrates, the lattice with built-in defects was considered as B-site-rich, having the tendency to exsolve 'extra' B-site cations[88]:

$$A_{1-\alpha}BO_{3-\delta} \xrightarrow{exoslution} (1-\alpha)ABO_{3-\delta'} + \alpha B \qquad (2-3)$$

Additionally, in Cali et al.'s recent work [185], local A-site Sr vacancies of Ir-doped $SrTiO_3$ have been revealed to act as active 'trapping sites' for the Ir dopant atoms. DFT calculations on surface energies of lattice surface with and without $V_{sr}^{"}$ were implemented and indicated that Ir atoms were mobile over an ideal surface without defects. However, once the Ir atoms moved to a V_{sr}'' site, forming $Ir_{Sr}^{"}$ and O-Ir-O pair, the high energy barrier made it hard for the atoms to move away from the site. The real-time atomic resolution TEM characterization evidenced the mobile Ir atoms and the 'trapping' process by a strontium vacancy, as Figure 2.8 showed.

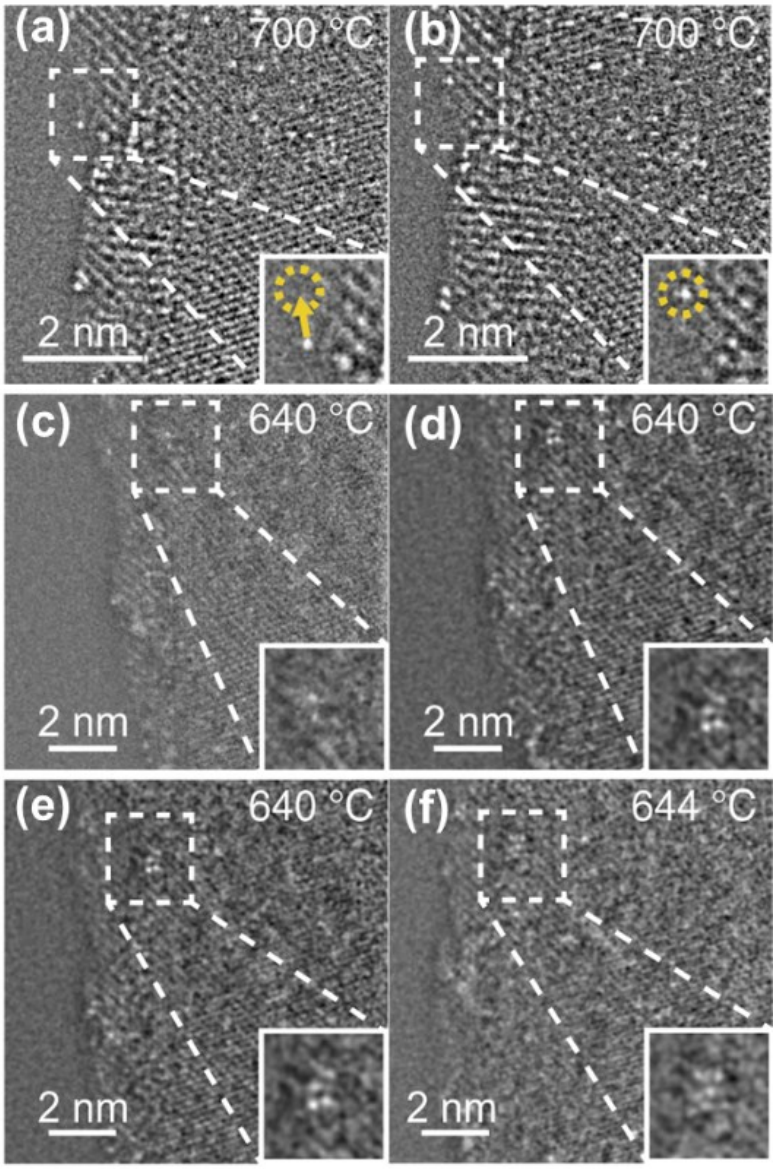


Figure 2.10 Inverse fast Fourier transform High-angle annular dark-field imaging (HAADF)- Scanning transmission electron microscopy (STEM) images of a [−3 1 2] zone axis of Ir-doped $SrTiO_3$ grain at 700 °C (a,b), 640 °C (c,d,e), and644 °C (f) during in situ monitoring during heating in vacuum. The yellow and circle in (a) and (b) indicated the movement of the Ir atom. (c-f) showed a trapping and nucleation process of Ir atoms. Reproduced under terms and conditions of CC-BY license. [185] Copyright 2023, the authors. Published by Springer Nature.

As previously mentioned, the exsolution process involves thermodynamic segregation, cation diffusion, and reduction. Therefore, the intrinsic design of the host lattice, dopant, and elements is also crucial in developing the exsolution of metallic nanoparticles. The reducibility of certain transition metal oxides, which typically exist as B-site cations in perovskites, was reviewed by Neagu et al. [88], as shown in Figure 2.11. The Gibbs free energy of the reduction reaction of these transition metals from oxides to the metal phase suggested differences in their reducibility. Ni, Co, and Fe exhibited thermodynamically spontaneous reduction by H_2, while the platinum group elements showed even lower energy requirements for reduction, which provides clues of the early-stage studies focused mostly on platinum group precious metal elements. On the other hand, certain elements like Ti and Mn proved to be challenging to

reduce to the metal phase even under an H_2 atmosphere at 900°C. This is in line with Table 2.3, which indicates that precious metal elements and nickel, iron, and cobalt tend to exsolve, whereas titanium and chromium remain in the host lattice. Manganese, however, has been reported to exsolve as MnO_x [148,190]. For example, Sengodan et al. [153] observed the exsolution of MnO during the phase transition of $Nd_{0.5}Ba_{0.5}MnO_3$ into the layered double perovskite $NdBaMn_2O_{5+\delta}$.

In another aspect, the co-segregation energies of various systems and elements had been a focal point in the simulation study of the exsolution process and its driving forces. Kown et al. [188] conducted calculations on the co-segregation energies of Co, Ni, Mn, and Fe, along with the nearby oxygen vacancy, in the $PrBaMn_{1.7}M_{0.3}O_{5+\delta}$ system. As depicted in Figure 2.12, the co-segregation energy analysis indicated that the exsolution of Co and Ni is more favoured in comparison to Mn and Fe in terms of segregation aspect. Moreover, the intrinsic nature of different dopant and transition metal cations such as oxygen-coordination bond strength and radius, not only affect reducibility and the co-segregation energy, but also the solubility of the initial preparation and the diffusivity of the nucleation and particle growth process. Therefore, it's vital to consider the exsolving metal elements in the designed structure of developing exsolution system.

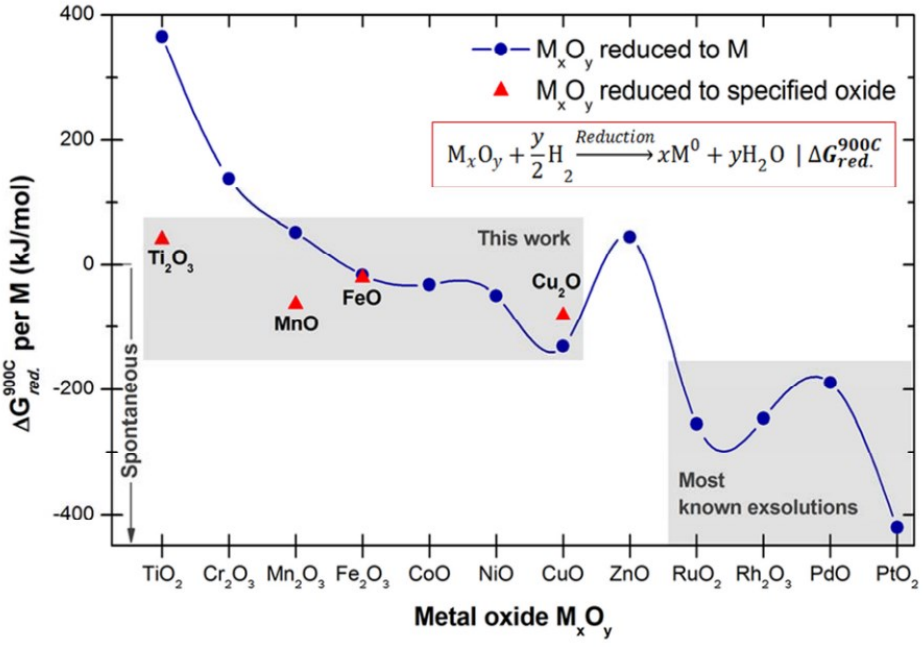


Figure 2.11 Gibbs free energy of reduction of oxides to metals or certain oxides, at 900 °C in H_2. Reused under the permission from reference [88]. Copyright 2013, Springer Nature.

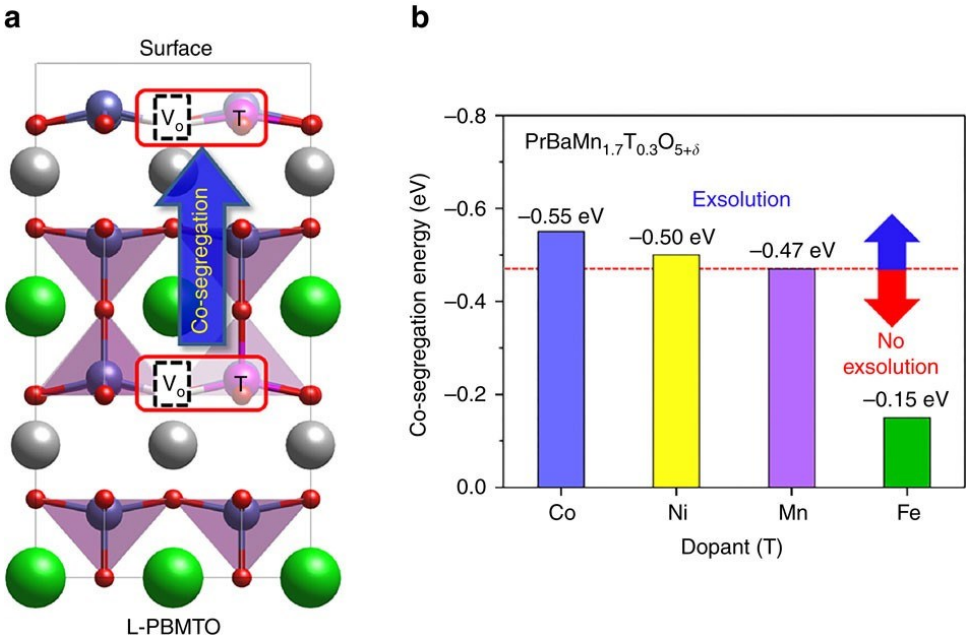


Figure 2.12 (a) Schematic illustration of the model used for the calculations of co-segregation energy. (b) Comparison of the co-segregation energy with the dopant (M) materials. Reused under terms of CC-BY license [188]. Copyright 2017 The Authors. Published by Springer Nature.

In line with the aforementioned study on $NdBaMn_2O_{5+\delta}$, it has been observed that phase transitions occurred accompanied by exsolution phenomena, and these transitions have been proposed as triggering factors for exsolution [191,192]. The layered double perovskite $AA'B_2O_6$ has gained increasing attention due to studies focusing on the preferences of oxygen vacancies in the A-site double perovskite and its fast oxygen diffusion rate [193]. Sengodan et al. [35] synthesized $PrBaMn_2O_5$ and reported its high electrical conductivity, which was achieved by reducing $Pr_{0.5}Ba_{0.5}MnO_3$ into the $PrBaMn_2O_5$ phase. In a subsequent study, Sun et al. [191] doped $Pr_{0.5}Ba_{0.5}MnO_3$ with 10 mol% Co and observed the exsolution of Co nanoparticles during the formation of the oxygen-deficient layer and double perovskite structure. DFT calculations supported the thermodynamic favourability of forming an oxygen vacancy layer together with exsolution. Another study on Fe-Ni exsolution from the B-site doubled $Sr_2FeMo_{0.65}Ni_{0.35}O_{6-\delta}$ perovskite revealed a transition from the double perovskite structure into the Ruddlesden−Popper (RP) phase $Sr_3FeMoO_{7-\delta}$ and the single perovskite $Sr(FeMo)O_{3-\delta}$. Similarly, Kim et al. [192] employed *in-situ* environmental observations to study the phase transition of $Pr_{0.5}(Ba/Sr)_{0.5}FeO_{3-\delta}$ with varying ratios of Ba/Sr, showing the transformation from a single perovskite into the RP phase. A phase diagram with three steps of phase transition was proposed, as shown in Figure 2.13, and it was observed that iron nanoparticles exsolved during the phase transition. Hence, these studies highlighted the link of intrinsic phase transition and its tendency of exsolving the 'excess' B-site cations.

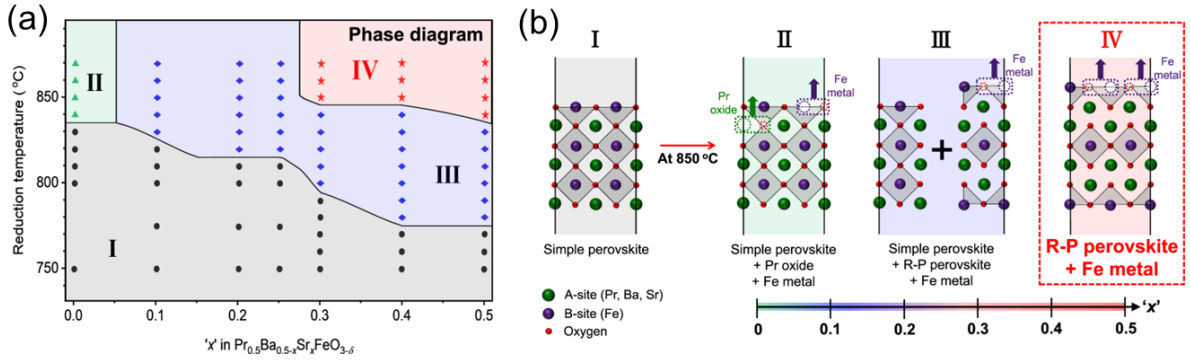


Figure 2.13 (a) Proposed phase diagram of $Pr_{0.5}Ba_{0.5-x}Sr_xFeO_{3-\delta}$ material (x = 0, 0.1, 0.2, 0.25, 0.3, 0.4, and 0.5) in H_2 environment as functions of reduction temperature and Sr^{2+} concentration from in-situ XRD measurements, and (b) the corresponding schematic illustration of the phase transition. Reproduced under terms of CC-BY license [192]. Copyright 2021, the Authors.

In addition to the intrinsic factors considered thus far, facets and strains have also been found to be highly linked to the exsolution behaviour. As previously mentioned, Gao et al. [182] proposed a particle growth model based on the strain-limits (Figure 2.7), taking into account the reduction reaction of Ni^{2+} to Ni^0, dedicated by strain energy. In the investigation of particle-in-pit morphology, the strain field modelling suggested that the interplay of surface free energy and strain energy provides the driving forces for exsolution and morphology evolution [183]. In subsequent research, Han et al. [194] investigated the exsolution of Ni nanoparticles from A-site deficient $La_{0.2}Sr_{0.7}Ni_{0.1}Ti_{0.9}O_{3-\delta}$ thin films on different substrates, resulting in different strains, as shown in Figure 2.14(a-d). Calculations based on classical nucleation theory indicated that the relaxation of the misfit strain tends to decrease the critical size of nuclei and nucleation barrier at the initial stage of exsolution. The experimental results highlighted that compressive strains enhance the exsolution of Ni particles, as depicted in Figure 2.14(e). Additionally, the particles were found to be interior to the surface of the thin film, which is consistent with previous studies on endogenous particles and the early stages of subsurface nucleation (Figure 2.14.g-f). However, Kim et al. [195] reported a conflict observation of the dependency of exsolution outcome on strain of $SrTi_{0.75}Co_{0.25}O_3$ thin film exsolution. They calculated the surface segregation energy and the cations vacancy formation energy with biaxial strain and the result proposed the exsolution of Co cations would be easier under tensile train. In the later study of Fe exsolution on $La_{0.6}Sr_{0.4}FeO_3$ thin films, Wang et al. [181] explained the confliction by comprehensively considered both cation vacancy formation and the oxygen vacancy formation prior to the onset of exsolving metal cations. They proposed two steps of the exsolution process involving the first reduction of lattice and the formation of the Schottky defects. Hence, the compressive strain was considered to enhance the formation of Fe vacancy, while the tensile strain would boost the overall exsolution phenomenon of Fe nanoparticles.

Regarding the effect of facets, initial studies of Ni-exsolution from A-site deficient lanthanum strontium titanates observed preferential growth of Ni nanoparticles on specific facets [76,88]. The

terraces with three exposed orientations were characterized by AFM, and preferential exsolution was observed at the (110) plane of the ceramic bulk compared to the (100) and (111) planes, as shown in Figure 2.13 (a). It was suggested that only the (110) plane held the key defects of A-site deficiencies, which facilitated nucleation and cation diffusion [76]. In later research, Kim et al. [196] used the pulsed laser deposition (PLD) method to deposit (001)-, (110)-, and (111)-oriented $La_{0.2}Sr_{0.7}Ti_{0.9}Ni_{0.1}O_{3-\delta}$ films on differently oriented single-crystalline $SrTiO_3$ substrates (Figure 2.13.b). In contrast to the polycrystalline ceramic exsolution studies, the (001) orientation of epitaxially grown single crystal was proposed as the favoured orientation exsolution, and the interfacial energy between the particle and the oriented perovskite lattice was considered the dominant factor in the exsolution of single crystal thin films. Similarly, Weber et al. [197] observed an enhanced exsolution response of the (001) surface of $SrTi_{0.9}Nb_{0.05}Ni_{0.05}O_{3-\delta}$. The different exsolution of different orientations associated with orientation-specific surface reconstructions of the polycrystalline thin film was characterized by SEM-electron backscatter diffraction (EBSD), showing a sluggish exsolution reaction on rough facets other than (001), as shown in Figure 2.13 (c, d).

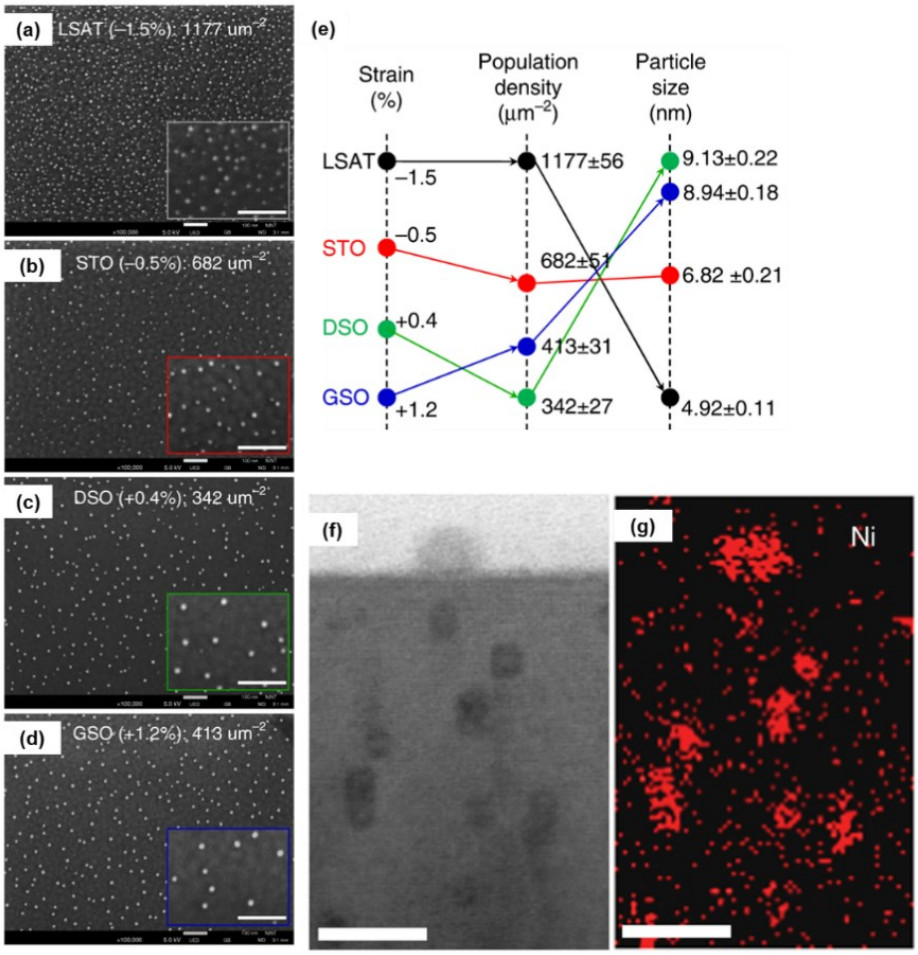


Figure 2.14 SEM images of the reduced (pure H_2, 550 °C, 80 h) $La_{0.2}Sr_{0.7}Ni_{0.1}Ti_{0.9}O_{3-\delta}$ films on (a) $(LaAlO_3)_{0.3}$–$(SrAl_{0.5}Ta_{0.5}O_3)_{0.7}$ (LSAT), (b) $SrTiO_3$ (STO), (c) $DyScO_3$ (DSO), and (d) $GdScO_3$ (GSO) substrates, respectively; Scale bars, 100 nm. (e) Effects of the substrate on three important physical parameters related to the exsolved thin

films. (f) Ex-situ cross-sectional STEM-HAADF image and (g) corresponding Ni EDS map of the reduced film on LSAT substrate; Scale bars, 10 nm. Reuse under the terms of CC-BY license [194]. Copyright 2019, the authors.

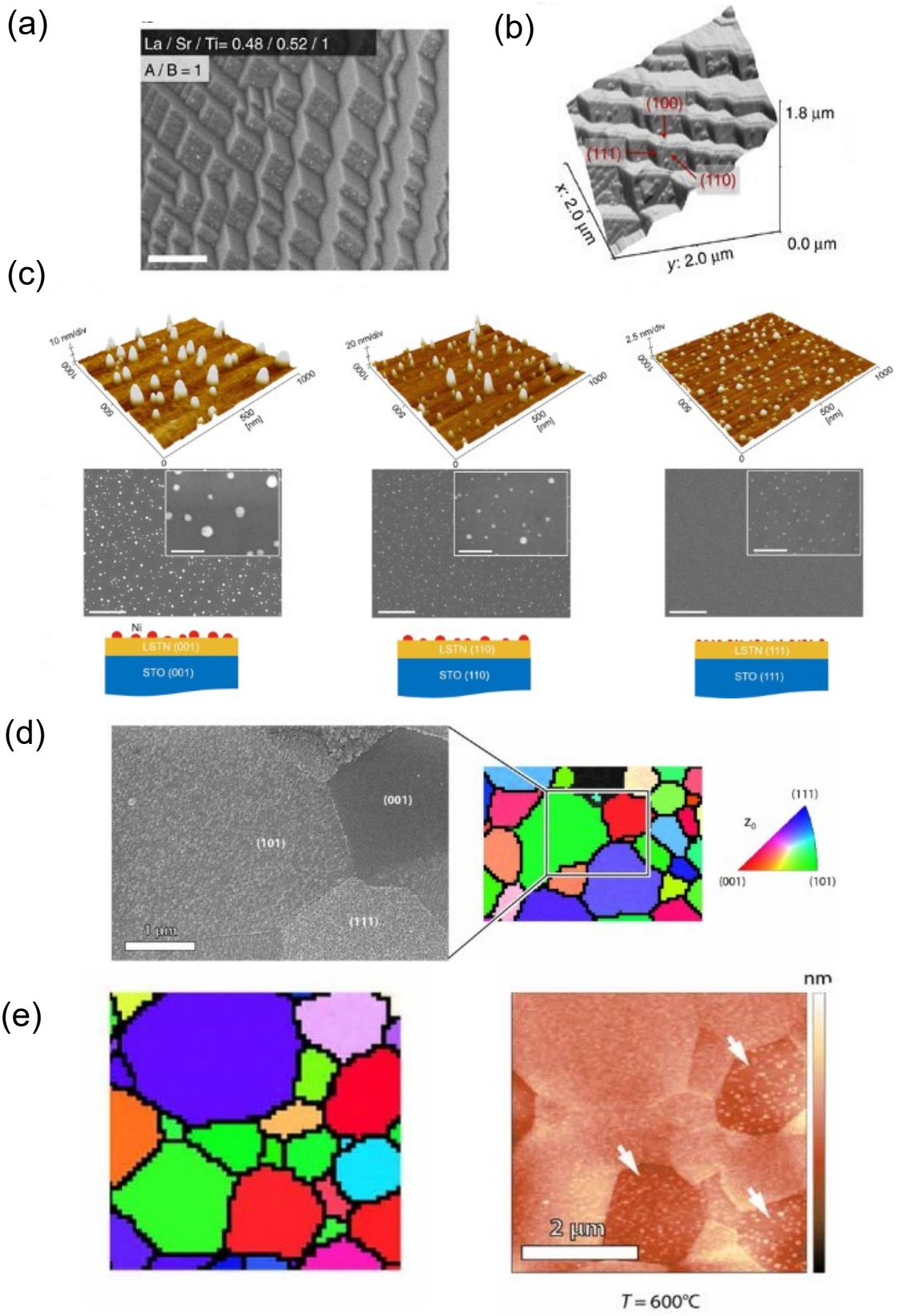


Figure 2.15 (a) SEM image of the native surface of a porous $La_{0.4}Sr_{0.4}Ni_{0.03}Ti_{0.97}O_{3-d}$ sample after reduction (5% H_2/Ar, 930 °C, 20 h); scale bar, 1 mm. (b) 3D AFM reconstruction of a native surface highlighting the calculated orientations of the facets. Reuse under the terms of CC-BY license [76]. Copyright 2015, the authors. (c) AFM and

SEM top-view images of as-reduced $La_{0.2}Sr_{0.7}Ti_{0.9}Ni_{0.1}O_{3-\delta}$ films of (001), (110) and (111) orientation, and corresponding schematics. Scale bars in SEM images are 1 μm and 200 nm in the insets. Adapted with permission from [196]. Copyright 2019, American Chemical Society. (d) SEM-EBSD analysis reveals differences in the surface morphology of $SrTi_{0.9}Nb_{0.05}Ni_{0.05}O_{3-\delta}$ perovskite facets with different orientations. (e) EBSD orientation mapping and AFM analysis of $SrTi_{0.9}Nb_{0.05}Ni_{0.05}O_{3-\delta}$ reduced at 600°C in 4%H_2/Ar for 1 hour. Reuse under the terms of CC-BY license [197]. Copyright 2022, the authors

Extrinsic factors play a crucial role in the exsolution process, involving multiple parameters such as reduction time, temperature, oxygen partial pressure (pO_2), electrical potential bias, and exotic ionic exchange. As mentioned earlier, the control of reduction conditions, including reduction time, temperature, and gas environment, determines the extent of exsolution and the morphologies of the exsolved nanoparticles [182,184–186,198]. These parameters synergistically influenced the vacancy formation, cation diffusion, nucleation, and particle growth [182,184,185,195,199–201]. Apart from controlling the reduction of materials, the application of an electrical potential has been reported to significantly promote the exsolution phenomena. For instance, Myung et al. [24] utilized the 'electrochemical switching' method by applying 2V across a solid-oxide cell with $La_{0.43}Ca_{0.37}Ni_{0.06}Ti_{0.94}O_{3-\gamma}$ as the electrode in a 50% H_2O/N_2 atmosphere at 900 °C. They observed homogeneously dispersed Ni nanoparticles, with a larger population on the surface of the parent perovskite compared to the perovskite electrode reduced in 5%H_2/N_2 at 900°C for 20 hours (Figure 2.16). This difference was explained to be related to the variations in oxygen partial pressure (pO_2) and the simulation of nucleation due to the sudden flooding of the perovskite lattice with electrons during voltage application. In a later study on Fe-Ni co-doped lanthanum calcium titanates, Fan et al. [202] investigated the influence of applied potential shocks on the exsolution phenomenon under various atmospheres. They observed both endogenous and exogenous iron and nickel nanoparticles after rapidly bringing the perovskite electrodes of a symmetric cell out of its electrochemical stability window at both anodic and cathodic shocks. However, reduction at open-circuit potential did not show significant exsolution. The formation of endogenous particles under anodic bias was proposed to be due to the incomplete oxidation leading to oxygen evolution and local charge transfer.

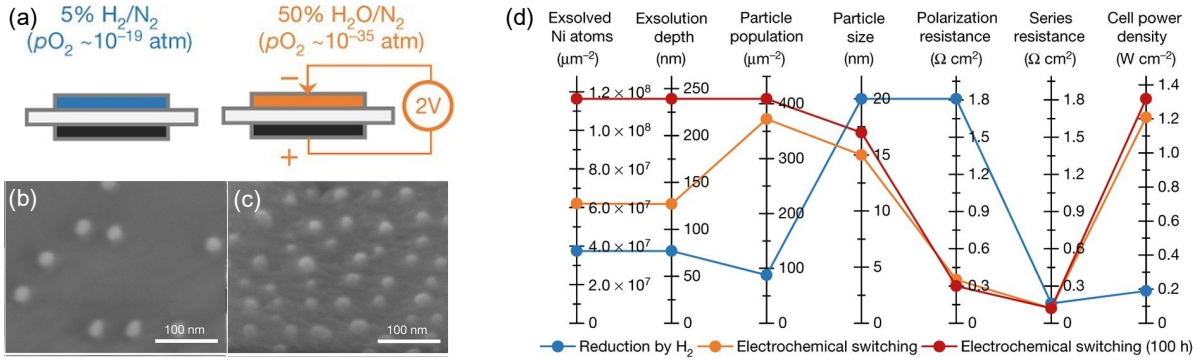


Figure 2.16 (a) Schematics of conditions used to trigger exsolution in a SOC at the fuel electrode (shaded in blue or orange); SEM micrographs of $La_{0.43}Ca_{0.37}Ni_{0.06}Ti_{0.94}O_{3-\gamma}$ electrodes produced by (b) reduction in hydrogen at 900 °C for 20 hours and (c) electrochemical switching, under 50% H_2O/N_2 at 900 °C for 150 seconds. (d) Various characteristics results of the samples shown in (b-c). Reuse under permission from reference [24].Copyright 2016, Springer Nature.

As discussed earlier, the exsolution behaviour is influenced by the difference in elemental cations. Another method of tuning and enhancing cation exsolution involves exotically inducing cations with a higher tendency to exsolve, as depicted in Figure 2.17. The cation 'swapping' or topotactic exchange method has been shown to facilitate the exsolution of the parent perovskite [203–205]. In this method, the deposition of the guest cation is achieved by infiltrating a nitrate solution of Fe on $Pr_{0.5}Ba_{0.5}Mn_{0.85}Co_{0.15}O_{3-\delta}$, followed by annealing in a humidified hydrogen environment at 850 °C [203]. During this process, Fe dissolves into the underlying perovskite lattice due to its relatively higher co-segregation energy compared to cobalt. A phase transition from the simple perovskite, $Pr_{0.5}Ba_{0.5}Mn_{0.85}Co_{0.15}O_{3-\delta}$, to layered perovskite structure $PrBaMn_{1.7}Co_{0.3-y}Fe_yO_{5+\delta}$ occurs. As a result, not only Co cations are exsolved, but the guest Fe cations also form alloy nanoparticles along with the exchanged/exsolved Co cations. DFT calculations confirmed the thermodynamically favoured incorporation of Fe into the lattice and the exchange of Fe and host Co cations. In a later study, Zhang et al. [206] demonstrated that the foreign Fe source and topotactic exchange during the exsolution process of $Sr_2Fe_{1.3}Ni_{0.2}Mo_{0.5}O_{6-\delta}$ highly enhanced the stability of the perovskite scaffold. After long-term stability testing as cathodes of SOECs in pure CO_2, the Fe-infiltrated electrode showed lower amounts of Sr segregation and secondary phases. The degradation of the cathode with exsolution was attributed to the breaking of B-O bonds and continuous diffusion of ions driven by external voltage, leading to 'structural decomposition.' This was significantly alleviated by the re-occupation of exchanged Fe cations. The cation 'swapping' or topotactic exchange method offers a promising approach for improving the stability and performance of perovskite materials through controlled exsolution processes.

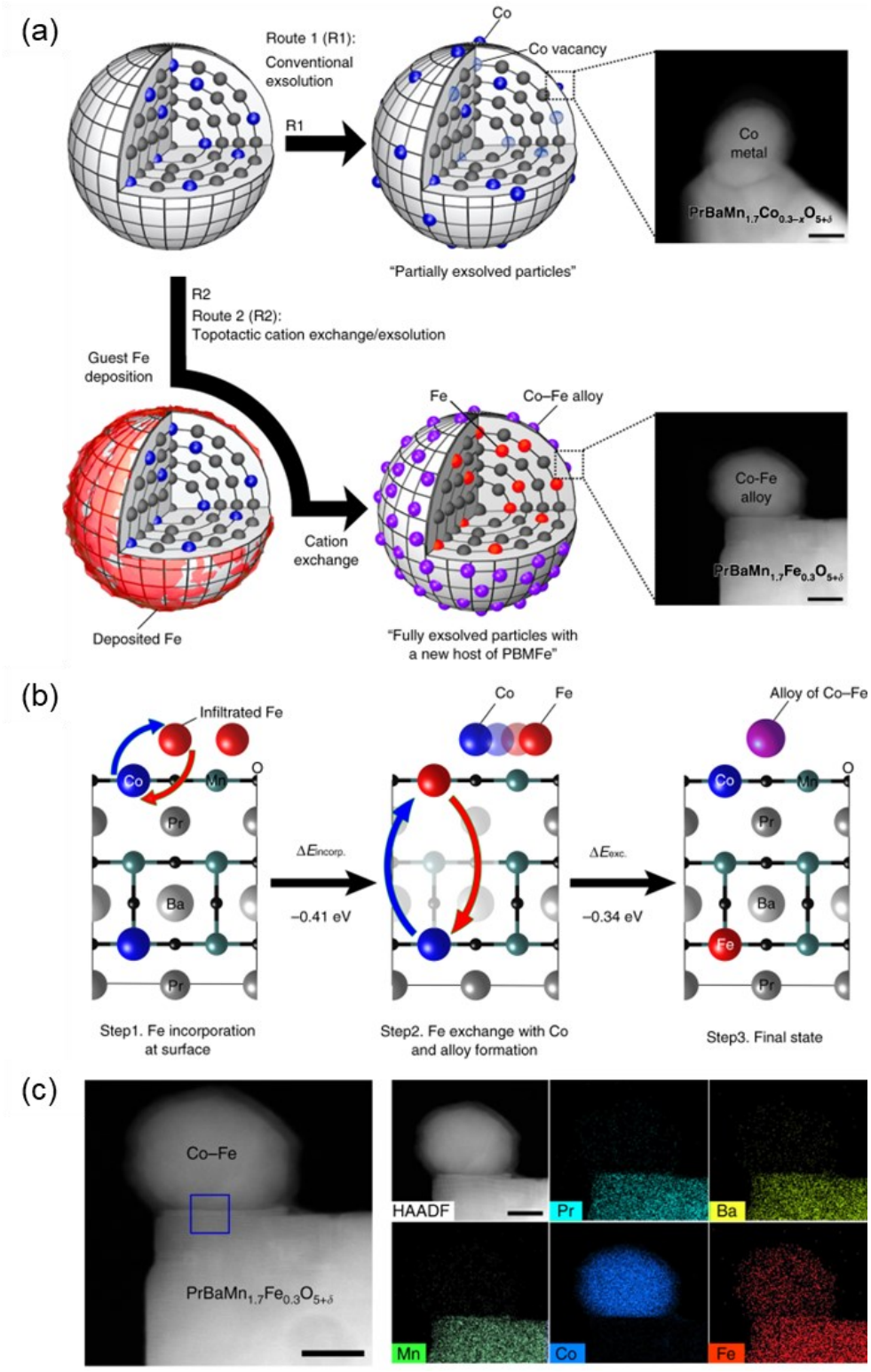


Figure 2.17 (a) Schematic of exsolution process with and without topotactic ion exchange. (b) Schematic of topotactic ion exchange energetics for the mechanism of particle exsolution via Fe infiltration on the $Pr_{0.5}Ba_{0.5}Mn_{0.85}Co_{0.15}O_{3-\delta}$ surface. (c) HAADF scanning TEM image of Fe infiltrated the $Pr_{0.5}Ba_{0.5}Mn_{0.85}Co_{0.15}O_{3-\delta}$; and EDS elemental map of Pr, Ba, Mn, Co, and Fe; scale bar 20 nm. Reuse under the terms of CC-BY license [203]. Copyright 2019, the authors. Published by Springer Nature.

Recently, another extrinsic factor influencing the exsolution process has emerged, namely plasma-induced exsolution, which has demonstrated the ability to rapidly create controlled nanoparticles on the surface of A-site deficient perovskite oxide even at room temperature

[207,208]. Kyriakou et al. [208] introduced this concept by comparing the morphology of a $La_{0.43}Ca_{0.37}Ni_{0.06}Ti_{0.94}O_{3-d}$ sample reduced using conventional hydrogen exsolution and plasma reduction, as depicted in Figure 2.18(a). Similar to the 'electrochemical switching' method, when subjected to N_2 plasma treatment for 1 hour at 650 °C, a rapid exsolution response with a high population of Ni nanoparticles was observed, compared to the thermochemical hydrogen reduction for 2 hours (Figure 2.18, b-c, f-g). The samples treated with N_2 plasma were electrically floating, leading to surface charging and the formation of an electron accumulation layer. This negatively charged layer was proposed to enhance the nucleation process (Figure 2.18, e, h). Subsequently, Khalid et al. [207] further developed the plasma enhancement method and reported the exsolution of Ni nanoparticles from a $La_{0.43}Ca_{0.37}Ni_{0.06}Ti_{0.94}O_{3-d}$ sample at extremely low temperatures within just 15 minutes, as shown in Figure 2.19 (a, b). The exsolution process under plasma treatment is illustrated in Figure 2.19(d). Aligning with Kyriakou et al.'s findings, the electric field generated by plasma treatment (Figure 2.19.c) was suggested to promote Ni nucleation on the surface. However, this work also emphasized a key factor in Ni exsolution under plasma treatment—the ion bombardment created a significant number of oxygen vacancies and defects on the perovskite's surface, greatly reducing the segregation energy and enhancing the transportation of Ni^{2+} ions. Hence, the plasma exsolution does not require thermal energy to be supplied and therefore allows for low temperature exsolution. In general, these novel insights into plasma-induced treatment offer a new method for the rapid and controlled exsolution of nanoparticles.

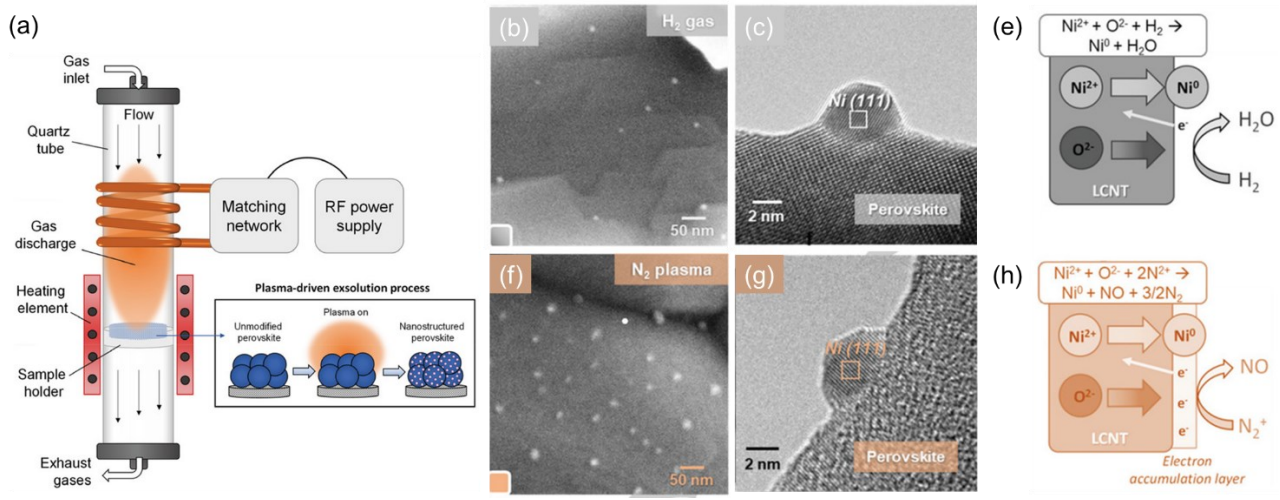


Figure 2.18 (a) Schematic of the reactor employed for plasma- triggered exsolution. SEM and TEM images of the Ni nanoparticles grown on the $La_{0.43}Ca_{0.37}Ni_{0.06}Ti_{0.94}O_{3-d}$ perovskite surface after (b, c) conventional H_2 gas reduction for 2 h and (f, g) N_2 plasma for 1 h at 650 °C. Schematics of Ni exsolution during e) hydrogen gas reduction and h) nitrogen plasma exposure. Reused under the permissions from reference [208]. Copyright 2021, John Wiley and Sons.

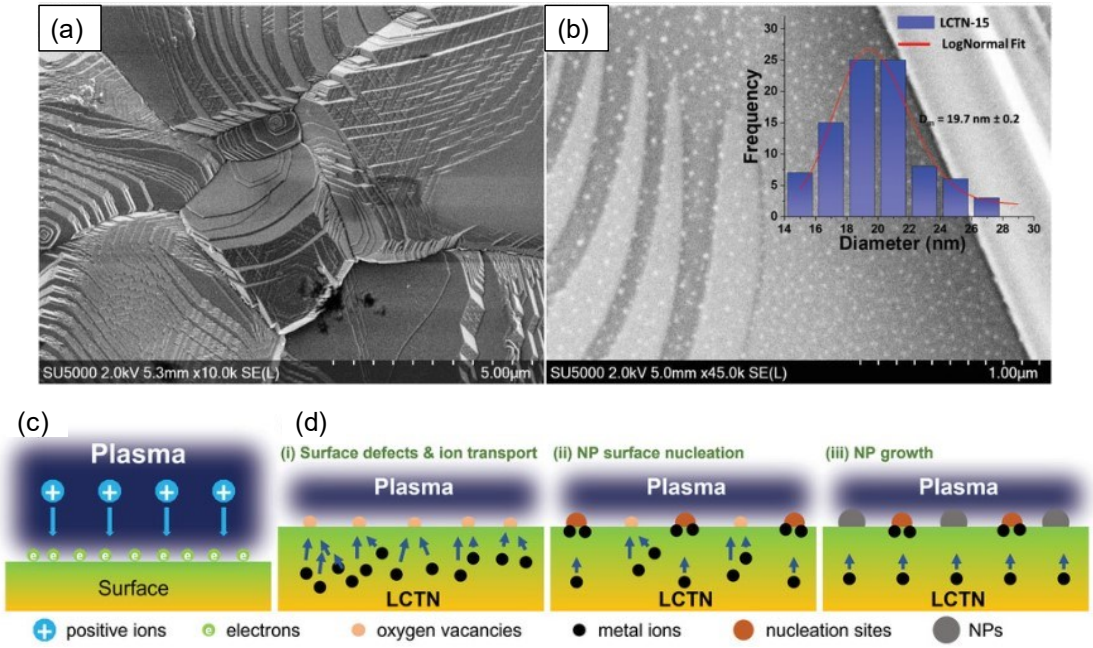


Figure 2.19 (a,b) SEM images of $La_{0.43}Ca_{0.37}Ni_{0.06}Ti_{0.94}O_{3-d}$ after argon plasma treatment (15 min); sketches of (c) ion bombardment on perovskite surface with "plasma sheath" region, supporting an electric field and (d) process of plasma driven exsolution. . Reuse under the terms of CC-BY license [207]. Copyright 2022, the authors. Published by John Wiley and Sons.

2.3.4 Multi-component exsolution

As discussed in the previous subsection and as illustrated in Table 2.3, the scope of exsolution is not limited to monometallic elements; alloy nanoparticles with multiple elements have also been reported. These alloy nanoparticles are believed to possess higher catalytic activity and stability compared to monometallic nanoparticles due to the modification of their electronic structures [209,210]. In the study of Co-Ni exsolution from $PrBaMn_{1.7}Co_{0.1}Ni_{0.2}O_{5+d}$, Kwon et al. [211] proposed two mechanisms for the exsolution of alloy nanoparticles, as depicted in Figure 2.20. The first mechanism, termed 'bulk alloy formation', involves the pairing of two metal cations with oxygen vacancies (e.g., Co–O_v–Ni) before their segregation out of the perovskite structure. The second mechanism, termed 'surface alloy formation', describes the individual segregation of two types of cations with oxygen vacancies (e.g., Co-O_v-Co and Ni-O_v-Ni), followed by the formation of a Co–O_v–Ni alloy with neighbouring atoms on the surface. DFT calculations of Gibbs energies of co-segregation indicated that both mechanisms are thermodynamically favourable, while the 'surface alloy formation' being more energy preferred for Co-Ni exsolution from $PrBaMn_{1.7}Co_{0.1}Ni_{0.2}O_{5+d}$ in terms of aggregation energy. In-situ XRD experiments conducted in a humidified H_2 atmosphere provided evidence for the individual exsolution of Ni and Co, followed by the formation of an alloy phase as the temperature increased.

In a subsequent study involving Co-doped $Sr_2Fe_{1.5}Mo_{0.5}O_{6-\delta}$[212], alloy nanoparticles of Co-Fe were observed after reduction in a 5% H_2/Ar atmosphere at 800 °C. DFT calculations indicated segregation energies of −0.64 eV and 0.91 eV for Co and Fe with oxygen vacancies,

respectively. Consequently, the exsolution of Fe cations was considered to be facilitated and promoted by the generation of cation defects and oxygen vacancies due to the prior exsolution of Co cations.

Another pathway of synthesising alloy nanoparticles with the exsolved anchorage structure is via topotactic exchange. As illustrated in Figure 2.17, the exsolved Ni cations combined with the exotic Fe cations, forming alloy phase under the reducing atmosphere [203]. Differentiated with the doping and thermal reduction method, the alloy phase exsolved through topotactic exchange is partially from exotic cation sources.

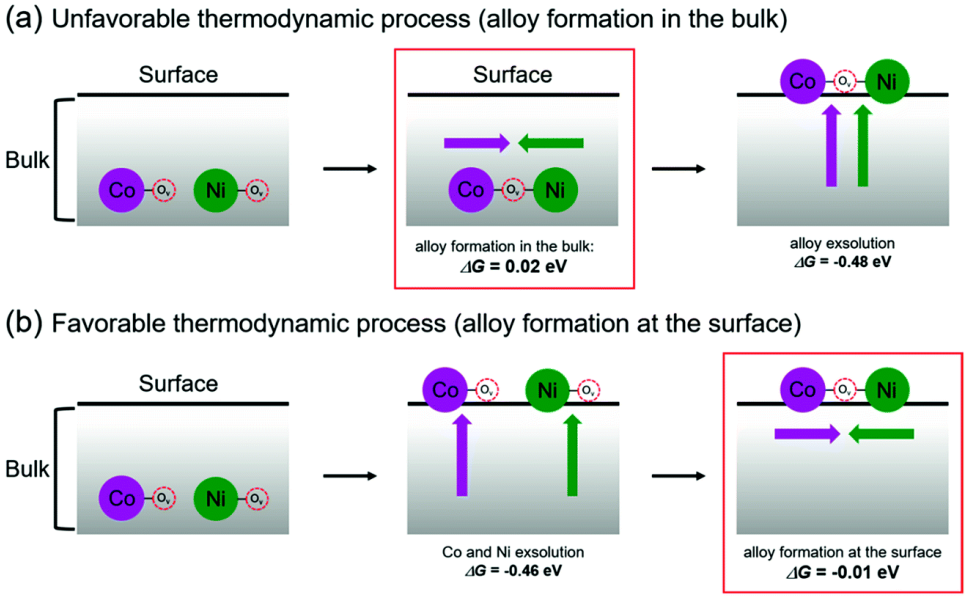


Figure 2.20 Schematic illustrations and energetics of (a) bulk alloy formation and (b) surface alloy formation for the exsolution of alloy nanoparticles. Reused under permission from reference [211]. Copyright 2018, Royal Society of Chemistry.

Beyond the exsolution of homogeneously distributed alloy nanoparticles, instances of nanoparticles with heterogeneous structures have also been observed and reported. A notable example is the core-shell structure of Pd@NiO nanoparticles resulting from the reduction of $LaFe_{0.6}Ni_{0.3}Pd_{0.1}O_{3-\delta}$ perovskite at 550 °C in a 5%H_2/N_2 environment (Figure 2.21 a-d). Temperature programmed reduction (TPR) in 5%H_2/N_2 revealed a two-step reduction process. This, combined with microscopic observations, led to the proposition of a subsequent exsolution mechanism for Pd@NiO nanoparticles (Figure 2.21 a). According to this proposed mechanism, a Pd core is initially formed within the bulk, followed by the deposition of a Ni shell, which subsequently moves out together with the Pd core. This process leaves behind slight amounts of lanthanum oxide as side products. In a more recent study, Jo et al. reported the formation of multi-heterogeneous Fe-Cu nanoparticles from $La_{0.43}Sr_{0.37}Fe_xCu_{0.12-x}Ti_{0.88}O_{3-\delta}$ perovskite compounds. The nanoparticles exhibited various structures, including hetero-structures, crescents, and Janus structures, as shown in Figure 2.21(e). The specific structure was found to be dependent on the ratio of Fe to Cu dopants. For instance, when the Fe to Cu

ratio was lower (Fe25), a hetero-structured exsolved nanoparticle with a limited amount of Fe exsolution was observed (Figure 2.21 e-i). As the Fe to Cu ratio increased to 1:1 (Fe50), the exsolved nanoparticles exhibited a crescent structure (Figure 2.21 e-ii), indicating slower exsolution of Fe in comparison to Cu. Remarkably, when the Fe to Cu ratio was 3:1 (Fe75), leading to a predominance of Fe, Janus structured nanoparticles were exsolved. These Janus structured nanoparticles demonstrated excellent catalytic activity for fuel oxidation and CO_2 reduction. In line with prior investigations into alloy exsolution, TPR analysis revealed the earlier exsolution of one component, which was copper in this case. This observation led to the proposal of a seed growth mechanism. In this mechanism, the initially exsolved Cu nanoparticles serve as heterogeneous nucleation sites that subsequently trigger the exsolution of Fe cations. The immiscibility of Fe and Cu then results in the formation of multi-heterogeneous structures. The discovery and understanding of nanoparticles with alloy composition and heterogeneous structures expand the possibilities for tailoring exsolution with enhanced functionalities for a range of applications, particularly in catalysis and energy conversion.

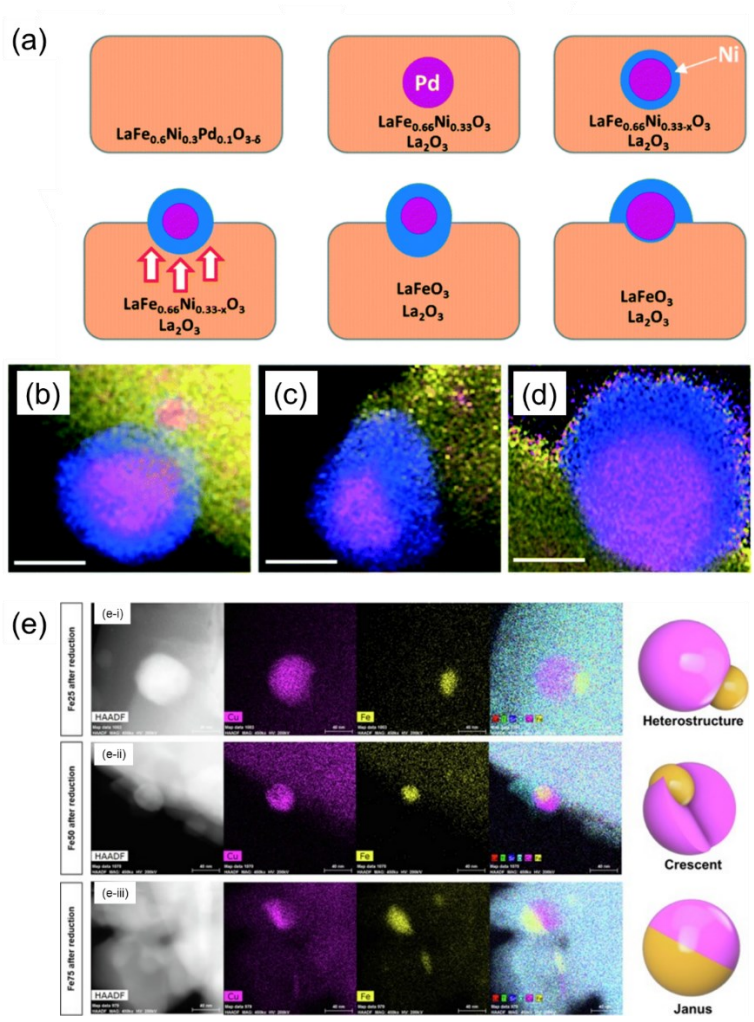


Figure 2.21 (a) Schematic representation of the crystallization mechanism for Pd core exsolution and asymmetric Ni shell growth. (b-d) STEM-EDX images showing TEM particles in the last three stages of the proposed mechanism

in (a); Scale bar 5 nm. Reused under permission from reference [195]. Copyright @ 2019, Royal Society of Chemistry. (e) TEM and STEM-EDX elemental mappings of Fe25, Fe50, and Fe75 reduced at 800 ℃ for 12 h in a dry H_2 atmosphere. Reuse under permission from reference [196]. Copyright @ 2022, Elsevier.

2.4 Summary

This chapter provided a comprehensive review of synthesis methods, crystal structures, and potential applications of ruthenium-based and titanium-based double perovskite materials, identifying them as promising candidates for SOC electrodes. The subsequent discussion delved into the exploration and advancement of the exsolution technique, focusing on key factors and mechanisms. Through exsolution, properties of parent oxides or perovskites were significantly enhanced, including catalytic activity, stability, and resistance to coking, achieved by incorporating exsolved metal nanoparticles. These distinct properties hold substantial potential for enhancing the performance of electrochemical devices. The review highlights the advantages of integrating exsolution into ruthenium-based and titanium-based double perovskite materials as potential electrodes for SOCs.

Chapter 3 Experimental Methods

3.1 Introduction

To comprehensively understand the materials and phenomena, multiple experimental methods and characterisation techniques were used and discussed in this research. This chapter discusses the experimental procedures and background of the techniques covered throughout this thesis.

3.2 Materials synthesis

Many routes can be used in the synthesis of perovskites materials, including solid-state reaction, co-precipitation, hydro-thermal, spray drying and sol-gel method *etc* [213]. Solid-state synthesis and sol-gel synthesis routes are utilized and discussed in this work.

3.2.1 Solid-state reaction

Solid-state reaction method is a well-known and conventional synthesis method for metal oxide compounds[214]. It is attractive because of the simple operation in this method, which usually includes the mechanical mixing of the precursor powders, high-temperature heat treatments and several intermediate grindings[213].

However, the solid-state reactions require elemental diffusion to form a new phase, which is usually sluggish and easily leads to incomplete reactions as Figure 3.1(a) shows. Therefore, it is common to use a high temperature and prolonged thermal treatment commonly in excess of 24h to react the entire mixture of precursors[215]. An inherent disadvantage reported of this method is that high reaction temperature can result in high vapor pressure and uncontrolled stoichiometry[214], due to the chemical loss during the heat treatment.

In this work, solid-state reaction was adopted to synthesize the lanthanum nickel ruthenate double perovskite compositions. Stoichiometric amounts of lanthanum oxides, nickel oxides and ruthenium oxides were weighed and manually mixed with a mortar and pestle. Due to the high hygroscopicity of lanthanum oxides, the lanthanum oxide precursor was dried in a muffle furnace at 1000°C for 6 hours before mixing. Product mixtures of the precursor oxides were calcined and sintered at specific temperatures with several intermediate manual grinding steps. The phases and crystallinity were checked with powder X-ray diffraction, which will be discussed later in this chapter and in Chapter 4.

3.2.2 Sol-gel synthesis

Compared to the solid-sate reaction, an advantage of the sol-gel method is the localized homogenous distribution of ions in precursors. The local stoichiometry and short diffusion paths facilitate the reaction and formation of nano-sized crystals. Besides, sol-gel method is

also energy efficient and requires lower reaction temperature and shorter heat-treatment time compared to solid-state reaction[214].

Different sol-gel routes with variable chelating agents have been reported, such as hydrolysis reactions, citric-gel process, stearic acid sol-gel method, polyvinyl alcohol assisted sol-gel method and so forth[214]. In this work, a citrate-nitrate route[216,217], as Figure 3.1(b) shows, was used for the synthesis of lanthanum nickel ruthenates and lanthanum nickel titanates. Similar to the previously reported citric-gel process by De Buysser et al.[218], citric acid was used in this work as the chelating agent. The metal cations are linked by citric acid and form a three-dimensional network of metal-citrate complexes[213,218]. The stoichiometric amount of lanthanum nitrate, nickel nitrate and ruthenium nitrosyl-nitrate were dissolved in 10 wt% citric acid. Unlike some of the reported sol-gel synthesis[217,218], precipitation was not observed in this process. Hence, ammonia solution or ethylene glycol is not required for the pH adjustment[11,217,218]. The gelation was achieved by pyrolysis of metal nitrate-citrate solution at 300°C. The gel then underwent decomposition and combustion in static air at 600°C for 6 hours, to make sure of the removal of the organic components and the formation of the first-stage amorphous oxides or nano-crystallites[217]. Then the product metal oxides were calcined at specific temperatures for the final stabilization and crystallization of the perovskite phases. For the synthesis of the titanate samples, due to the insolubility of the titanium source, titanium dioxides, the continuous stirring were implemented during the whole gelation process to make a homogenous dispersion of the titanium dioxides. The detailed parameters and discussion of the synthesis will be included in Chapter 4 and Chapter 7.

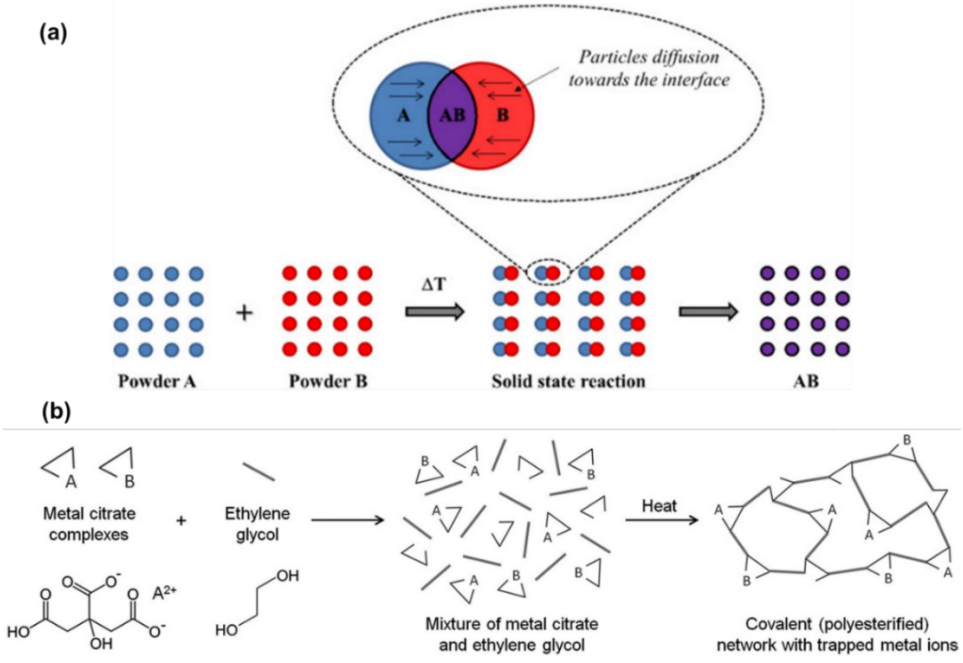


Figure 3.1 (a) schematic of solid-sate reactions particle diffusion. Reused under permissions from reference [197]. Copyright 2016, Elsevier. (b) schematic of sol-gel method with citric acid as chelating agent[201]. Reused under terms and conditions of CC-BY license. Copyright 2016, authors. Published by Royal society of chemistry.

3.2.3 Exsolution thermal treatment

To promote the exsolution of the synthesised pristine double perovskite, it has been reported that the thermal treatment of the sample is required under reducing conditions [200,203,219–222]. In this work, 5% H_2/Ar gas as balanced was used to drive the exsolution of nanoparticles from the double perovskites. Instead of pure hydrogen, incorporating 5% H_2/Ar is safer for use in lab equipment and less aggressive during the reduction treatment process. After synthesis, powder samples were pressed into green pellet bodies and heated in a tube furnace with 5% H_2/Ar gas flowing to the target temperature with 2°C/mins as heating rate, then cooled with 5°C/mins rate. The products of reduction treatment were investigated by multiple techniques as discussed in Chapter 3.3.

3.2.4 Test-cell fabrication

To investigate the electrochemical properties and performance of synthesised double perovskite materials, symmetric cell impedance spectroscopy tests and single button cell tests were utilized in this work. The details of electrochemical impedance spectroscopy (EIS) measurements and single fuel cell test measurements are discussed in Section 3.3.5. The preparation of symmetric cells and single button cells are discussed as below.

3.2.4.1 Symmetric cell preparation

The application of EIS to symmetrical cells, consisting of identical electrodes and a dense electrolyte, was firstly introduced by J. E. Bauerle [223] in 1969. Now the symmetric cell test is a commonly used test to evaluate the electrochemical performance of the solid-state cells, using the same conditions on both sides of an electrolyte. This test is useful in providing information on the intrinsic properties of the electrode materials, as it eliminates any differences in performance that might be due to differences in the anode and cathode materials[11]. The symmetric cell test can also provide a baseline measurement for comparison with asymmetric cell tests, where different materials are used for the anode and cathode.

3.2.4.1.1 Electrolyte fabrication

The symmetric cells test in this project were configured by dense lanthanum strontium gallium magnesium oxide ($La_{0.8}Sr_{0.2}Ga_{0.8}Mg_{0.2}O_{3-X}$, LSGM) electrolyte pellet and identical double perovskite electrodes. Compared to yttria-stabilized zirconia (YSZ), LSGM was selected as the appropriate electrolyte due to its outstanding ionic conductivity, particularly at temperatures below 800°C. For fabrication of dense electrolyte pellets, commercial LSGM powder was pressed into 13mm diameter green bodies by uniaxial pressure, followed by sintering in static air at 1400°C for 8 hours. To increase the contact between electrolyte and electrode materials and obtain flat electrolyte surfaces, the sintered LSGM pellets were polished to 200~500 μm thickness using SiC paper with grit size P800, 1000 and 1200 [224]. The polished electrolytes were ultrasonically cleaned by acetone and annealed in static air at 800°C for 1.5 hours to

remove the residual carbonates. Then the product electrolytes after annealing were ready for ink deposition.

3.2.4.1.2 Electrode ink preparation

Electrode inks were prepared by ball-milling, mixing and triple-roll milling. The synthesized electrode materials were milled using a planetary ball mill (XIAMEN TOB NEW ENERGY TECHNOLOGY CO., LTD. Model No.TOB-YXQM-4L) at 300 rpm for 8 hours. 3mm, 1mm, 0.5mm and 0.3mm diameter zirconia balls were combined during the milling process, as larger balls are more efficient in grinding and breaking materials whereas smaller balls were adopted for milling fine powder [225]. The product powder possesses an average grain size of 263(±60) nm in diameter within the resulting electrode layer. The ball-to-powder ratio (BPR) was kept as 10:1 [226] in the ball milling experiments. The synthesized powder was ground and milled with acetone solvents, and then acetone was removed by vacuum drying at 180°C.

Then the ball-milled electrode powder was mixed with commercial Terpineol based ink vehicle (Fuelcellmaterials, USA). The viscosity of the electrode ink, porosity and microstructure of electrode are highly dependent on the ratio of ink vehicle to powder [227]. The 2:1 powder to ink vehicle ratio was used in this project according to previous investigations [11]. Triple roll milling (EXAKT Technologies, Inc. 80E, USA) was used to homogenously disperse the sample powder in electrode ink and remove agglomerates. Three cylindrical rollers are used to shear, squeeze, and grind the ink ingredients into a homogeneous mixture in the triple roll milling machine. The product ink then was collected by a scraper and stored in a fridge before ink deposition.

3.2.4.1.3 Ink deposition

The electrode ink was deposited by lab-customized screen-printing method. A small hole was cut in a scotch tape, then used as a stencil to print electrode ink on to the dense electrolyte pellet. Viscous electrode ink was dropped into the hole area and distributed using a blade. In this method, the thickness of the printed electrode is controlled by layers of scotch tape. To make sure the functional layer is thick enough for the electrochemical performance test [228], two layers of scotch tape were used. The microstructure and thickness of the electrodes will be discussed in Chapters 5 and 6. The printed electrode was dried and sintered ~~at 950°C for 1.5 hours~~. The contact between electrolyte and electrode was tested by tape testing method by adhering scotch tape and peeling it from the electrode layer, which is also referred to as the 180° peel test [229]. The sintering temperature needs to be sufficient to form sintering necks between particles, yet it should not be too high to avoid losing the porous structure. After testing different sintering temperatures (750°C, 850°C, and 950°C), a sintering temperature of 950°C for 1.5 hours was selected as the standard procedure [230,231]. Qualified symmetric cells were printed with silver current collectors for the electrochemical impedance measurement, as discussed later in Section 3.3.5.1.

3.2.4.2 Single cell fabrication

In contrast to the symmetrical cell test, the single-button cell test in this project employs asymmetric components and a gas atmosphere on both sides of the electrolyte. This approach is utilized to assess the performance of electrode materials under conditions to those found in operational full cells. The single button cells were fabricated using a similar method to the electrolyte fabrication, electrode ink preparation and deposition with symmetric cell. The only difference is that the lanthanum strontium cobalt ferrite ($La_{0.8}Sr_{0.2}Co_{0.8}Fe_{0.2}O_{3-\delta}$, LSCF8282) materials (Praxair Ltd.) were printed on the cathode side and calcined at 850°C for 2 hours after sintering of the anode materials. The details of the single cell tests will be discussed later in this chapter.

3.3 Materials characterisation

To comprehensively understand and investigate the synthesised and reduced double perovskite materials, multiple techniques including X-ray techniques, thermal analysis, microscopy, and electrochemical tests were utilised to characterise the material and fabricated cells.

3.3.1 X-ray characterizations

Since the first discovery of X-rays by Wilhelm Röntgen in 1895, various methods for the characterization of essential information regarding metals, minerals, ceramics, biological materials, and electronic materials have been developed based on X-ray sources [225]. X-rays are conventionally generated by converting the kinetic energy of charged electrons to atom excitation and radiation of a target metal, typically copper, molybdenum, or aluminum. The possible interactions between the generated X-rays and samples include penetration, absorption, and scattering. In these interactions, the energy of the X-rays can either be elastically scattered without energy loss, or lose energy through inelastic scattering or absorption, or generate photoelectrons. Based on different interactions of the X-ray source and sample, techniques including X-ray diffraction, X-ray photoelectron spectroscopy, X-ray fluorescence, Small Angle X-ray scattering, and X-ray absorption spectroscopy have been developed to qualitatively and quantitively investigate materials. In this project, X-ray diffraction (XRD) and X-ray photoelectron spectroscopy (XPS) are utilized to obtain information regarding the crystal structure and chemical composition of the materials.

3.3.1.1 X-ray diffraction (XRD) and refinement

X-ray diffraction (XRD), as a non-destructive analytical technique, was employed to ascertain the phases and crystal structure of materials in this project. The XRD patterns obtained were analysed using Le Bail [232,233] and Rietveld refinement [234,235] methods to determine the lattice parameters, atomic ordering information, and percentage of phases present.

3.3.1.1.1 X-ray diffraction (XRD)

X-ray diffraction is based on the elastic scattering of X-rays to characterise the structure of crystalline materials, by passing a beam of X-rays through the sample surface and collecting the scattered beam with a radiation detector on the other side. The wavelength of the generated X-ray is of the same order as the spacing of the lattice planes, so that the scattered X-rays can add together and reinforce each other to yield diffraction.

In 1913, William Henry Bragg and his son William Lawrence Bragg proposed the formulation of constructive interference of the diffracted X-ray, which as known as Bragg's law [236]. This formulation delineates the relationship between the atomic spacing and the wavelength of the incident X-rays when constructive interference transpires. As Figure 3.2 illustrates, the path differences of the incident beam can be described by the atomic spacing, *d*, and the incident/scattered beam angle, *θ*. When the path difference satisfies the condition of constructive interference, that is, equal to an integral multiple of wavelength *λ*, a coherent enhanced beam can be detected by the radiation detector, as described by Equation 3-1.

$$2d_{hkl}sin\theta = n\lambda \qquad 3-1$$

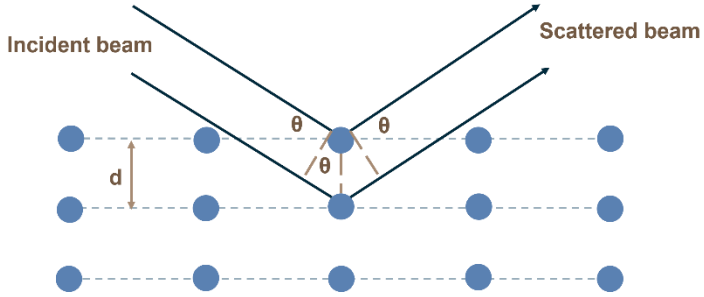


Figure 3.2 Schematic illustration of Bragg's law

Based on Bragg's law, one can calculate the atomic spacing, d_{hkl}, for a given lattice plane with a known incident beam wavelength, *λ*, and scattered beam angle, *θ*, hence the dimension of unit cell can be derived. The intensity of the diffracted X-rays for each plane is dependent on a variety of factors, including the scattering factors of the atoms, the symmetry of the crystal structure, and the experimental setup. The relative intensities of planes, which are usually described with Miller indices (*h,k,l*), are proportional to the square of the structure factor, F_{hkl}:

$$I_{hkl} \propto |F_{hkl}|^2 \qquad 3-2$$

$$F_{hkl} = \sum_{j=1}^{N} f_j e^{2\pi i(hx_j+ky_j+lz_j)} \qquad 3-3$$

Where the unit cell of the crystal is defined with *N* atoms and each atom, *j*, possesses fractional coordinates (x_j, y_j, z_j) and the scattering factor, f_j, which is related with the electron density of the atom. The calculation of the structure factor for certain planes can result in zero structure factor and hence zero diffracted beam intensity, indicating the presence of additional destructive interference of the scattered X-rays due to the symmetry of the lattice. This phenomenon is known as systematic absence. For instance, in the case of a face-cantered cubic unit cell with identical atoms, diffracted intensity is observable only when the sum of the plane indices (*h, k, l*) equals an even integer, as shown in Equation 3-4.

$$I_{hkl} \propto |F_{hkl}|^2 = f^2[1 + \cos\pi\,(h + k + l)]^2$$

$$= \begin{cases} 4f^2(h + k + l = even) \\ 0(h + k + l = odd) \end{cases} \qquad 3-4$$

Consequently, by analysing a set of the diffracted X-ray intensity and peak positions, it is possible to index the sample to a specific crystal structure. The X-ray diffractometers used in modern laboratories typically employ an X-ray tube with a tungsten filament cathode to produce accelerated electrons that are directed towards a copper target. The interaction of the accelerated electrons with the copper target excites the K orbital electrons of the copper atoms, resulting in the emission of X-rays by refilling the K-shell with electrons from higher orbitals. The characteristic lines of the Cu X-rays are denoted as K_α and K_β with wavelength 1.5406 Å and 1.3922 Å, respectively. To ensure that the incident beam is monochromatic, a nickel filter is utilized to minimize the K_β line and parts of the Bremsstrahlung radiation. In addition, it should be noted that the incident X-ray beam contains two lines, $K_{\alpha1}$ and $K_{\alpha2}$, with a 2:1 intensity ratio. As a result, the high angle diffracted peak of a same lattice plane exhibits splitting.

PANalytical X'Pert Pro MPD diffractometer was used in this project with Bragg-Brentano geometry, in which the sample is kept horizontally in the centre of the diffractometer and X-ray source and detector rotate together during the measurement. A zero-diffraction silicon plate was utilized to hold the powder sample. For the pellet sample, a rotating mode was utilized, wherein the sample plates were rotated to ensure that all lattice planes diffracted the beam. The sample was measured under an angular range from 15° to 100° with 0.016° as step size.

3.3.1.1.2 Diffraction Pattern refinement

The XRD pattern obtained from the sample crystal was referenced with databases such as the Inorganic Crystal Structure Database (ICSD)[237] to determine its general structural information. Additionally, a comprehensive analysis involving full pattern fitting was conducted to extract further information regarding the crystal structure. The refinement of XRD data is achieved through the implementation of a least-squares method, wherein the computed diffraction pattern is systematically compared to the experimental results. The crystal model is iteratively refined until the difference between the calculated and experimental patterns is minimized. In

this project the iteration was stopped when the shift of the refined parameter was ten times smaller than the estimated standard deviation.

Fullprof software [238] was employed to perform XRD pattern refinement in this project, utilizing both the Rietveld and Le Bail methods. The Rietveld method [235] simultaneously refined instrumental parameters, lattice parameters, and atomic factors by fitting the calculated and observed pattern. In contrast, the Le Bail method [239] extracted peak intensities from the observed pattern rather than calculating them from the atomic factors, ensuring the accurate refinement of the unit cell structure and lattice parameters.

Le Bail method

In this project, Le Bail refinement was used to check the phase purity and refine the lattice parameters. The result of Le Bail refinement was also adopted as a start point of further Rietveld refinement. Linear interpolation of the selected background intensity was employed to determine the background intensity. The peak shapes were refined using a Pseudo-Voigt function, which is a linear combination of Gaussian and Lorentzian functions. Additionally, instrumental factors such as systematic shifts caused by the displacement of the sample mounting were also refined. The goodness of fitting is evaluated with agreement factors: the R-factor of the profile (R_p), the weighted profile R-factor (R_{wp}), and the expected R factor (R_{exp}) [240]. The R_p value is determined as the absolute differences between the intensity values obtained from experimental observations and those calculated from theoretical models, as demonstrated by Equation 3-5 [241]. Meanwhile, the R_{wp} value is computed as the weighted sum of the squared differences between the observed and calculated intensity values, as shown in Equation 3-6. The R_{exp} value, which illustrates the optimal R_{wp} attainable for a given data set, is calculated using Equation 3-7. The R_{exp} value is considered a reflection of the quality of the data set. Thus, a statistic parameter, χ^2, is introduced as 'good-of-fit' (Equation 3-8), indicating the degree of agreement between the observed and calculated intensity values, which is also usually included to evaluate the quality of refinement [240,242].

$$R_p = \sum_i \left| Y_{obs,i} - Y_{calc,i} \right| / \sum_i Y_{obs,i} \qquad 3-5$$

Where $Y_{obs,i}$ and $Y_{calc,i}$ are the observed and calculated intensity of each data point i.

$$R_{wp} = \sqrt[2]{\sum_i w_i \left(Y_{obs,i} - Y_{calc,i} \right)^2 / \sum_i w_i {Y_{obs,i}}^2} \qquad 3-6$$

Where $Y_{obs,i}$ and $Y_{calc,i}$ are the observed and calculated intensity of each data point i, and w_i is the weighted factor.

$$R_{exp} = \sqrt[2]{(N-P)/\sum_i w_i {Y_{obs,i}}^2} \qquad 3-7$$

Where $Y_{obs,i}$ are the observed intensity of each data point *i,* w_i is the weighted factor, *N* is the number of the observed points and *P* is the number of parameters.

$$\chi^2 = R_{wp}/R_{exp} \qquad 3-8$$

Rietveld method

In order to ensure the quality of the XRD data that will be subjected to Rietveld refinement, a modified setup was utilized. This setup involved the use of narrowed slits, a small step size of 0.008°/0.004°, and a prolonged scanning time of 5 hours/16 hours [242]. Similar with the Le Bail method, the background, instrumental factors, lattice parameters and peak shapes were refined with the same functions. Three R-factors and 'good-of-fit' factor were used to estimate the quality of refinement fitting, as mentioned before. Additionally, in Rietveld method, atomic parameters and scale factors were also refined to obtain the elemental information of the sample, including occupancies, atomic positions and thermal factors. In the refinement operations, the refined parameters were refined as follow order: linear interpolation background points; instrumental factors including zero factor and displacement factor; lattice parameters; peak shape; atomic positions; thermal factors and occupancies.

To obtain the accurate refinement result, constraints were incorporated into the structure during refinement. For the double perovskite structure, the monoclinic structure with space group *P* $2_1/n$ was used as the model of Rietveld refinement in this project. The fractional positions of B-site cations in this structure were fixed according to the space group as (0, ½, 0) and (½, 0, 0) and remained unrefined. Moreover, in order to define the ordering of the B-site cations, it was assumed that the occupancy of both (0, ½, 0) and (½, 0, 0) were full and the number of cations of each element was constrained to remain the initially designed concentration in the materials. For example, for a double perovskite in which Ni and Ru occupied the B-site position, when the number of Ni cations increased at one site, the same number of Ni cations decreased on the other site. Additionally, the thermal factor of one site position was constrained to be the same, even if two or three elements occupied the same site. Details of the refined result will be discussed in Chapter 4 and 6.

3.3.1.2 X-ray photoelectron spectroscopy (XPS)

The second X-ray characterization technique applied in this project is X-ray photoelectron spectroscopy (XPS), which is a surface sensitive technique to analyse the elemental composition and the chemical information of the materials.

As mentioned before, the XPS technique is based on the inelastic interaction between the X-ray and sample. The incident X-ray beam caused excitations of the sample atoms, resulting in converting the energy of photons into the kinetic energy of photoelectrons, associated with some deexcitation phenomena. The average probing depth of XPS is 5-10 nm [243], which depend on the energy of X-ray, the kinetic energy of core-level electrons, the secondary electron escape depth from materials and the escaping angle of electrons. As Figure 3.3 below shows, the interaction involves irradiating the surface of a material with monochromatic X-rays, which causes the ejection of photoelectrons from the surface atoms. The kinetic energy and number of photoelectrons emitted are then measured to determine the binding energy and concentration of the atoms in the material. The core-level binding energy, E_B, can be calculated with the incident beam energy, hv, the kinetic energy of photoelectron, E_{kin}, and the working function of the material as Equation 3-9 shows:

$$E_B = hv - E_{kin} - \Phi \qquad 3-9$$

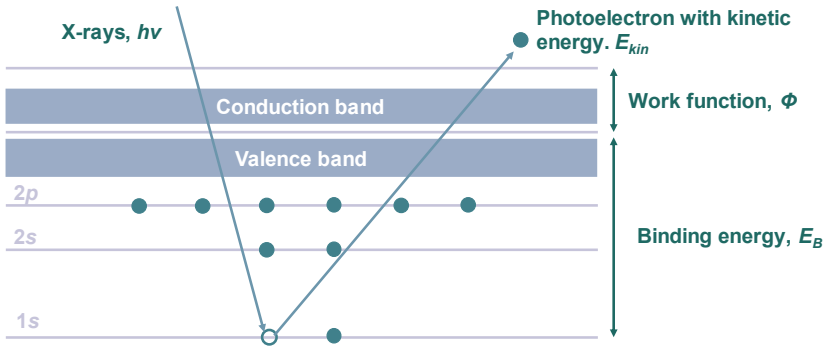


Figure 3.3 Schematic illustration of the fundamental principles of XPS: the Photoelectric effect.

The most common sources of X-rays are Al or Mg anodes, which utilize the characteristic K_α line. The primary line energy of Al anode is 1486.6 eV, which is sufficiently high to excite core level electrons from the vast majority of elements [244]. For this project, a Thermo Fisher K-Alpha+ X-ray photoelectron spectrometer was utilized, which employs a monochromatic Al K_α micro-focused X-ray source.

Thermo Fisher K-Alpha+ X-ray photoelectron spectrometer utilizes a 180° double-focusing hemispherical analyser and a 128-channel detector. A schematic view of the spectrometer with a hemispherical electron analyser is shown in Figure 3.4. The X-ray beam is focused on the sample with a spot size of 400 μm^2, generating photoelectrons near the sample's surface that exit into the vacuum and the hemispherical analyser. The hemispherical analyser measures the current of photoelectrons as a function of their kinetic energies. Voltages were applied to the entrance slit of the hemispherical analyser to make sure only the electrons with specific energy, *i.e.*the pass energy, was able to travel through the analyser. Electrons with higher or lower energy would collide with the inner or outer hemispheres[226]. Then, the photoelectrons

with specific kinetic energy can be measured. In this project, the pass energy used was 200 eV.

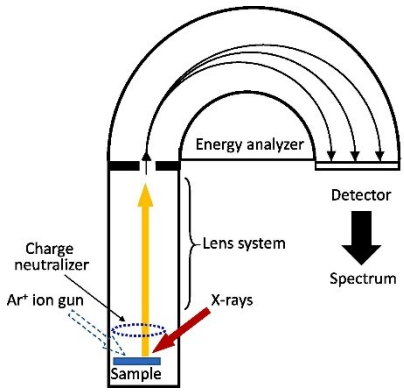


Figure 3.4 Schematic view of the photoelectron spectrometer with a hemispherical electron energy analyser. Reused under terms and conditions of CC-BY license [244].. Copyright 2020, authors. Published by Elsevier.

As mentioned before, the binding energy E_B can be determined using Equation 3-9, which requires knowledge of the incident X-ray energy, hv, the kinetic energy E_{kin}, and the workfunction Φ. However, it is not possible to directly measure the work function of the sample. Therefore, in spectroscopy, a conductive sample holder is used to align the Fermi energy of the sample with that of the spectrometer. As Figure 3.5(a) below shows, the spectrometery measures the Φ_{SP} and E_{kin}^{SP} rather than the directly measuring Φ_{SA} and E_{kin}^{SA}. However, poor conduction between the sample and the spectrometer may result in a shift of the Fermi level and false measurements, as illustrated in Figure 3.5(b). Additionally, the loss of core electrons in an insulating sample can also cause a shift in the Fermi level. To mitigate this issue, a flood gun was used during the measurement, indicated by the "charge neutralizer" on top of the sample in Figure 3.4.

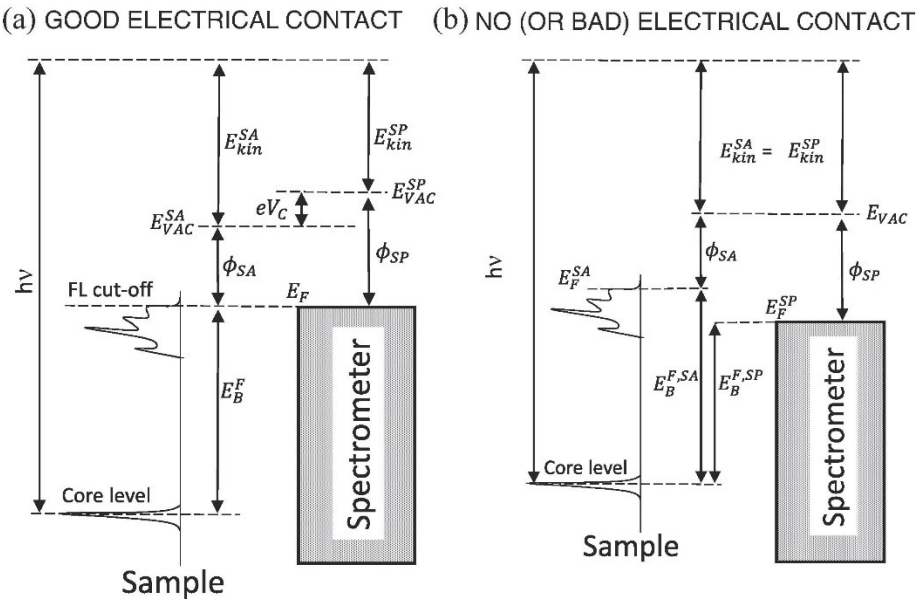


Figure 3.5 Energy level diagrams of sample and spectrometer with (a) good electric contact and (b) poor or no electric contact[225].Φ_{SA} represent the work function of sample, while Φ_{SP} represent the work function of spectrometer; E_B^F represent the binding energy respect to energy position of E_F of Femi lever (FL); E_{kin}^{SA} represent the kinetics energy of photoelectron after leaving the sample, while E_{kin}^{SP} represents the kinetic energy measured at the spectrometer; V_C represents the contact potential difference of sample and spectrometer; E_{VAC}^{SA} and E_{VAC}^{SP} represent the vacuum level energy of sample and spectrometer respectively. Reused under terms and conditions of CC-BY license [244].. Copyright 2020, authors. Published by Elsevier.

In addition to the photoelectric effect, the interaction of X-rays with the sample yields various side phenomena, including the Auger effect and X-ray fluorescence. As illustrated in Figure 3.6, unlike the photoelectric effect, Auger electrons are generated by the excess energy released during the refilling of core levels. Auger electrons were also analysed to investigate the nickel element further, particularly since the commonly studied core levels overlapped with others in the multiple element systems in this project.

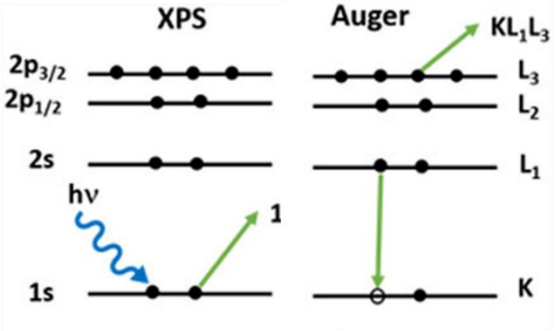


Figure 3.6 Schematics of the X-ray induced photoelectronic effect and resulted Auger effect. Reused under permission from reference [245]. Copyright 2020, AIP publishing.

In this study, survey spectra were acquired in the energy range of -5 eV to 1350 eV, with a 0.5 eV increment per energy step, for five scans, each with a 5ms dwell time. The La 3*d*, Ni 2*p*, Ru 3*d*, Ru 3*p*, O 1*s* and Ti 2*p* spectra were measured with a 0.1 eV increment per energy step, for 50 scans, each with a 50ms dwell time, in their respective energy ranges. Due to the low signal of Auger peak, Ni *LMM* Auger spectra were acquired with 150 scans and 150ms dwell

time for each scan. The analysis of XPS spectra was performed using Themo Fisher Avantage software.

3.3.2 Thermal analysis (TA)

Thermal analysis (TA) is a branch of analytical chemistry that involves measuring the physical and chemical properties of materials as they undergo controlled temperature changes. It is a widely used technique that can provide insights into various properties of materials, including their thermal stability, decomposition behaviour, melting characteristics, glass transition temperature, phase transitions, and other thermal properties. The most commonly used TA techniques include thermogravimetry (TG), differential thermal analysis (DTA), differential scanning calorimetry (DSC), thermomechanical analysis (TMA), and dilatometry [246]. In this project, both thermogravimetry and dilatometry techniques were utilized to investigate the sintering behaviour and exsolution properties of double perovskite materials under reducing atmosphere. These techniques allowed for the characterization of the materials' thermal behaviour, providing valuable insights into their properties and behaviour under various thermal conditions.

3.3.2.1 Thermogravimetry (TG)

Thermogravimetry (TG) is a thermal analysis technique that measures the mass change of a sample as a function of temperature or time. In this project, the TG curves were obtained using a Netzsch 449c F5 TA system equipped with a TG-DSC stage, using alumina powder as reference, as shown in Figure 3.7. The measurements were carried out using Pt crucibles. To ensure sufficient redox interaction between the sample and the atmosphere, the chamber was purged with compressed gas or 5% H_2/Ar at a flow rate of 60 ml/min.

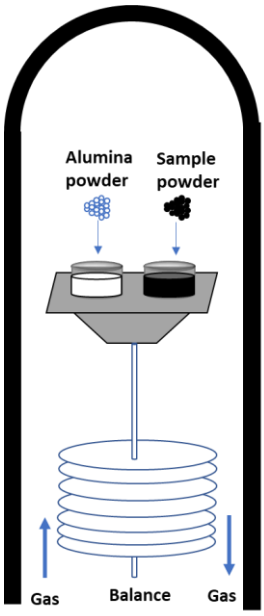


Figure 3.7 A schematic view of the TG-DSC stage of Netzsch 449c F5 system.

To ensure the accuracy of the TG measurements, correction profiles were obtained by measuring empty sample crucibles before each sample measurement. The same temperature program was applied to the correction file to measure the instrumental influence on the TG signal change. This step was taken to correct any instrumental vibration or baseline shifts, which could have affected the accuracy of the measurements.

3.3.2.2 Dilatometry

Dilatometry is a widely used method for characterizing the dimensional changes of materials as a function of temperature. This technique is often employed to investigate the thermal expansion or sintering behaviour of materials. As shown in Figure 3.8, the sample was placed on a sample holder connected to a pushing rod and displacement system, which was covered by a furnace during the measurement. The displacement system was used to measure the length changes of the sample during the heating. In this study, a dilatometer was employed to initially investigate the sintering behaviour of the lanthanum nickel ruthenate double perovskites.

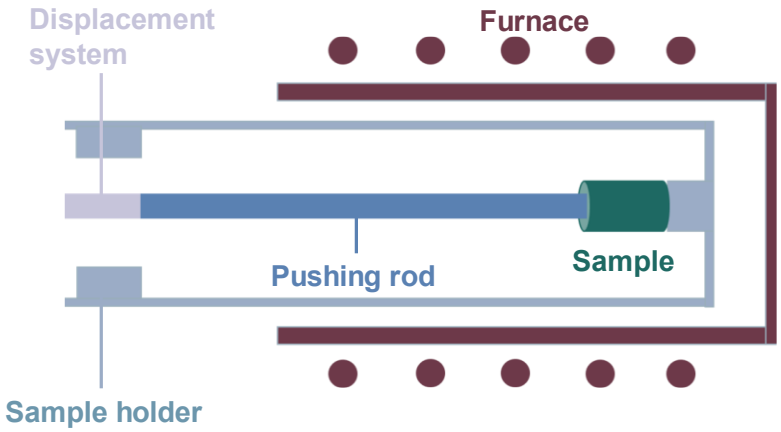


Figure 3.8 A Schematic diagram of a dilatometer.

3.3.3 Electron microscopy (EM)

In conjunction with X-ray characterization and thermal analysis techniques, electron microscopy was employed to investigate the nano- and micron-scale features of the materials. Electron microscopy is a potent imaging technique that utilizes a beam of high-energy electrons to illuminate a sample and generate a highly detailed image of its structure. According to the Rayleigh criterion (Equation 3-10 resolution is enhanced by decreasing wavelength [247]. High-energy electrons can possess wavelengths smaller than 0.01 nm, making them adept at investigating small features that are invisible to optical microscopes.

$$\Delta l = 1.22 f \frac{\lambda}{D} \qquad 3-10$$

Where f is the focal length of the objective lens, λ is the wavelength of the beam and D is the diameter of the aperture.

As shown in the Figure 3.9, if the specimen is thin enough, the primary electron beam can transmit through the specimen and be detected by the transmission electron microscopy (TEM) detector located beneath it. The elastic or inelastic scattering of the primary electron beam generated the contrast with the information of crystalline, mass, thickness, and phases [248].

Additionally, a portion of the primary electrons are elastically scattered back, referred to as 'backscattered electrons,' which is highly influenced by the atomic number of the specimen (Figure 3.9). Furthermore, the inelastic interaction between the electron beam and the specimen generates secondary electrons within a short distance of the surface. The backscattered electrons and the emitted secondary electrons are scanned by the scanning electron microscopy (SEM) detector above the specimen. In this project, SEM was used to collect secondary electron signals to investigate the microstructure and topography of the samples.

Scanning transmission electron microscopy (STEM) was also employed in this project, using a focused beam as small as a spot that was scanned across the specimen while acquiring signals. Combined with the STEM mode, X-ray detectors were positioned near the specimen to collect the generated X-ray spectra, which provides the information of elemental composition and distribution [248].

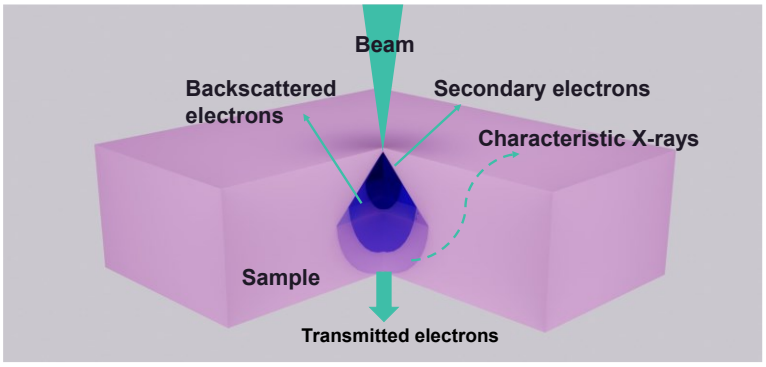


Figure 3.9 schematic view of primary electron beam interacting with sample.

3.3.3.1 3.3.3.1 Transmission electron microscopy (TEM)

As mentioned previously, high-energy electron beams can significantly enhance microscope resolution. In this project, both JOEL 2100F and TFS Talos F200i microscopes were utilized to obtain bright-field (BF) images. Both instruments are equipped with field emission guns (FEG) at an applied voltage of 200kV, serving as the source of primary electron beams. The beam current of JEOL 2100F is typically around 130 μA, while the beam current of TFS Talos F200i is typically around 59.3 μA. The specimen and instrument are operated under high vacuum conditions of approximately 10^{-7} mbar. A charge-coupled device (CCD) camera, Gatan, was used in JEOL 2100F, and a scintillator-based camera, Ceta, was used in TFS Talos F200i.

As explained earlier, when the primary beam passes through the thin specimen, both elastic and inelastic scattering occur, as shown in Figure 3.10 below. Regions of the specimen that are thicker or contain heavier atoms scatter more strongly than thinner and lighter parts. Therefore, with the same objective aperture present, thicker regions appear darker in BF images due to the contrast resulting from the elemental and thickness differences, known as mass-thickness contrast.

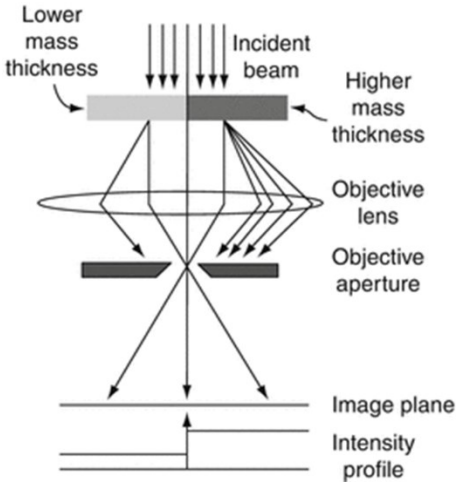


Figure 3.10 The mechanism of mass and thickness creating image contrast in a bright-field TEM image. Reused under permission from reference [249]. Copyright 2012, Springer Science.

Image contrast in electron microscopy can also be attributed to phase contrast and diffraction contrast. Diffraction contrast describes the intensity variation that occurs in electron microscope images when the diffraction condition changes across different areas of the specimen. This type of contrast is typically utilized for the identification and analysis of grain boundaries, dislocations, and defects. In contrary, phase contrast arises from differences in the phase of the scattered electron wave. The resulting interference pattern of lattice planes is known as lattice fringes, which reveal the periodicity of the lattice [248]..

3.3.3.2 3.3.3.2 Scanning transmission electron microscopy (STEM)

STEM, as mentioned before, combines the advantages of both TEM and SEM. Unlike conventional TEM, STEM does not require objective or projective lenses, which allows for a relatively large space for signal detection [229]. Typically, an annular dark field (ADF) detector is used with STEM mode to collect higher signals from more than one scattered angle compared to conventional dark field imaging, as illustrated in Figure 3.11 below. In this study, the STEM mode was used in the TFS Talos F200i microscope and the Titan G2 80-200 microscope equipped with a Cs probe corrector (CEOS), acquiring annular bright field (ABF) and ADF images. Among the signals from different scattered angles, the high-angle annular dark field (HAADF) signal is particularly well-suited to describe the "Z-contrast". This is because the collection of high angle scattered electron signals avoids the Bragg diffraction signal, and the electron signal is mostly dominated by the Rutherford scattering [248,249]. In this work, the ABF

and ADF images were collected with camera length of 98mm, the HAADF signal was collected at angle greater than 55 mrad.

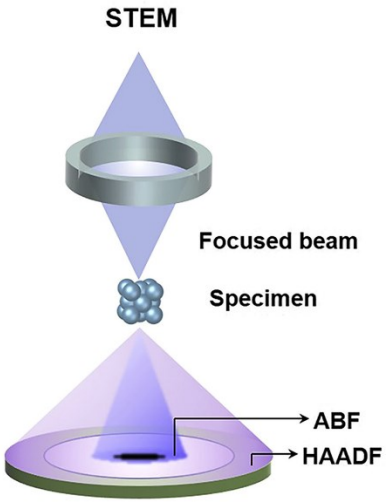


Figure 3.11 schematic view of the bright-filed and HAADF signal collection of STEM mode. Reused under permission from reference [250]. Copyright 2021 Elsevier.

The author would like to acknowledge Dr. R Cai and Prof. S Haigh from the Department of Materials at University of Manchester for their invaluable assistance with the operation of the Titan G2 80-200 microscope in the investigation of the reduced lanthanum nickel ruthenate double perovskite samples.

3.3.3.3 3.3.3.3 Energy-dispersive X-ray spectroscopy (EDX)

Characteristic X-rays are produced from a sample when it is irradiated with high-energy electron beams. This is due to the excitation of core-level electrons in the atoms of the sample, which then relax by emitting X-rays upon refilling the created hole with higher orbital electrons. The resulting X-ray emission can be utilized for qualitative and quantitative analysis of the chemical composition of the sample. Energy-dispersive X-ray spectroscopy (EDX) is a chemical analysis method that utilizes emitted X-rays. Unlike wavelength-dispersive X-ray spectrometers, which are based on single-crystal Bragg diffraction, EDX is based on the semiconducting properties of silicon or germanium. When a voltage is applied, the flux and current flow through the semiconductor is exactly proportional to the created electron-hole pairs and the energy of the X-ray. Therefore, EDX is able to collect the emitted X-rays signals as a function of energy. This makes it more convenient to integrate into modern EM equipment, as it requires less geometry alignment, although it might sacrifice some precision and resolution [248].

In this study, a Bruker X-flash EDX spectrometer was integrated onto a TFS Talos F200i microscope, while a ChemiSTEM Super-X EDX detector was integrated onto a Titan G2 80-200 microscope. EDX maps were acquired to investigate the elemental distribution of both the as prepared and reduced double perovskite samples. Specifically, the L-lines (Lα and Lβ) of

lanthanum and ruthenium, as well as the K-lines of nickel, titanium, and oxygen, were analysed. The operation of the Titan G2 80-200 microscope and ChemiSTEM Super-X EDX detector was conducted by Dr. R Cai from the Department of Materials at the University of Manchester.

3.3.3.4 3.3.3.4 In-situ TEM and STEM

In this study, both *in-situ* BF and STEM were employed to examine the temperature and time dependence of exsolution phenomena. Pristine perovskite powder samples were loaded onto Protochips Fusion Select E-chips (E-FHDC-VO) [251,252], which utilize a silicon nitride membrane for support and heat conduction, as well as an array of holey carbon films as sample holders. The powder sample was diluted, suspended in isopropanol, and a 3 µL suspension was deposited onto the chips before being left to dry in static air overnight. The sample and E-chip were subsequently mounted onto a Protochips rod connected to an external power supply. Throughout the experiment and thermal treatment, the samples were heated in vacuum conditions at a rate of 5°C/s to the desired temperature and cooled at an identical rate. Analysis of the BF and STEM images was conducted using the Protochips Axon Studio software [253].

3.3.3.5 3.3.3.5 Scanning electron microscopy (SEM)

In this study, a SEM was employed to detect secondary electron signals. As illustrated in Figure 9, the interaction volume of secondary electrons is comparatively smaller than that of backscattered electrons, resulting in superior resolution. Consequently, SEM predominantly focuses on the surface features of the sample, such as topography. An accelerating voltage of 5 keV is sufficient to generate surface signals, which is markedly lower than that required for TEM. The LEO Gemini 1525 Field Emission Gun SEM (FEGSEM) was utilized in this investigation. The electron source was generated by a field emission gun (FEG), facilitating an enhanced resolution approaching approximately 1 nm. Specimens were mounted on a sample holder using carbon tape and examined under the SEM with a working distance ranging from 6 to 7 nm.

3.3.4 Inductively coupled plasma-optical emission spectroscopy (ICP-OES)

Inductively Coupled Plasma Optical Emission Spectroscopy (ICP-OES) was employed in this study to determine the elemental concentrations present in the samples. ICP-OES operates on the principle of plasma-induced photon emission by elements within a given sample. In this project, solid samples were dissolved in a 10 wt% HCl solution to ensure that the elemental ratios remained consistent with their bulk state. During the ICP-OES analysis, the sample solution was transformed into an aerosol, which was then introduced into the plasma's central channel. With temperatures reaching approximately 1000K in the central channel, the aerosol was vaporized, producing free atoms in a gaseous state, followed by collisional excitation of these atoms and ions. The relaxation of excited elemental atoms and ions occurred through photon emission, which was subsequently detected by a spectrometer for qualitative and quantitative analysis [254]. In this study, a Thermo Scientific iCAP 6000 was employed, which

exhibits optimal accuracy in the range of 1-20 ppm. Consequently, standards with concentrations between 0 and 20 ppm were prepared utilizing commercial sources (Sigma-Aldrich; AccuStandard Inc). The concentrations of these standards were assessed by checking the concentration plots to ensure the validity of the obtained results. Additionally, the quantity of solid samples in the 10 wt% HCl solution was carefully calculated to guarantee that the elemental concentrations fell within the 0-20 ppm range. Subsequently, the obtained results were transformed into atomic ratios, based on the assumption that the B-site positions in double perovskites are entirely occupied by B-site cations.

3.3.5 Electrochemical performance characterizations

In order to assess the electrochemical performance of materials, various characterization techniques have been developed over the course of a century. These techniques include the open circuit voltage (OCV) test, electrochemical impedance spectroscopy (EIS) measurement, current-voltage (I-V) curve measurements, and long-term stability tests. For the purposes of this study, materials that were synthesized were utilized to fabricate both a symmetric cell and a single button cell, as outlined in Section 3.2.4. The symmetric cells were subjected to EIS measurements, which allowed for the evaluation of the electrical response of the electrode materials. The single button cells were subjected to both EIS measurements and I-V curves, in order to investigate both the electrode and single cell performance in the operation condition as SOFC.

3.3.5.1 Electrochemical impedance spectroscopy (EIS)

3.3.5.1.1 Basics of EIS

Electrochemical Impedance Spectroscopy (EIS) is a widely employed technique for characterizing materials and acquiring valuable insights into the electrochemical behavior of Solid Oxide Fuel Cells (SOFCs) and Solid Oxide Electrolysis Cells (SOECs). The history of impedance spectroscopy can be traced back to 1894 [255,256], when Nernst investigated the dielectric constant of aqueous electrolytes and organic fluids. In 1920, Pinkelstein employed the technique to assess the dielectric response of oxides [256,257]. By evaluating the impedance of a cell as a function of frequency, researchers can examine various electrochemical processes within devices and elucidate their performance and degradation mechanisms.

The fundamentals of EIS involve measuring the complex impedance (Z) of a cell system by applying a small-amplitude AC voltage. The complex impedance (Z) of the system is ascertained by the ratio of the applied voltage, E_t, to the resulting current, I_t. As depicted in Equation 3-11, the AC voltage possesses a constant amplitude E_0 and frequency ω. The response current exhibits the same frequency but with a phase shift ϕ. Consequently, the resulting impedance comprises both magnitude |Z| and phase components. Utilizing Euler's relationship, the resulting impedance can be represented as a complex number with magnitude, shifted phase, and imaginary unit *j*.

$$Z \equiv \frac{E_t}{I_t} = \frac{E_0\, exp(j\omega t)}{I_0\, exp(j\omega t + j\phi)} = |Z|\, exp(-j\phi) = |Z|(cos\phi - jsin\phi) \qquad 3-11$$

consequently, the impedance can be represented by its real part, *Z'*, and imaginary part, *Z''*:

$$Z = |Z|cos\phi - |Z|jsin\phi = Z' - Z'' \qquad 3-12$$

By plotting the real part of the impedance on the x-axis and the imaginary part on the y-axis at various frequencies, a 'Nyquist plot' can be obtained, as illustrated in Figure 3.12(a). In this figure, the y-axis represents -*Z''*, and data points are plotted from high to low frequency, moving from left to right. The length of the arrow of each data points signifies the magnitude of the impedance |*Z*|. In addition to the Nyquist plot, impedance data can also be presented as a Bode plot, which plots the magnitude |*Z*| and phase ϕ as functions of frequency, as shown in the Figure 3.12 (b,c).

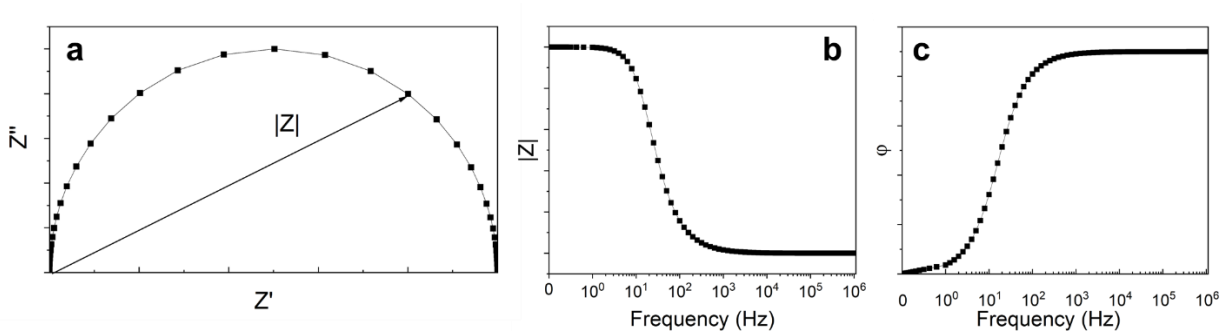


Figure 3.12 Schematic illustration of (a) Nyquist plot with impedance vector; (b,c) Bode plots of |Z| and phase ϕ as function of frequency.

The interpretation of a set of EIS data can be modelled using electronic circuits, known as 'equivalent circuits', which comprise components such as resistors and capacitors. An ideal parallel circuit consisting of a resistor and a capacitor would generate a perfect semicircle in the Nyquist plot, as depicted in Figure 3.12(a). The resistance of the equivalent circuit represents the total resistance of the tested system. The capacitances of each component are typically utilized to distinguish and identify the processes occurring during testing.

3.3.5.1.2 Experimental operation

The impedance calculation described earlier relies on the linear relationship between voltage and current. However, in practical electrochemical cell measurements, the tested system does not exhibit linearity throughout the entire potential range, particularly when considering an input AC voltage with a large amplitude E_0. Consequently, in experimental impedance measurement procedures, a small input AC voltage amplitude is typically employed, assuming a pseudo-linear system response, as illustrated in Figure 3.13. In this study, measurements were conducted using a 20mV input potential signal. EIS measurements were performed at the open-circuit voltage (OCV).

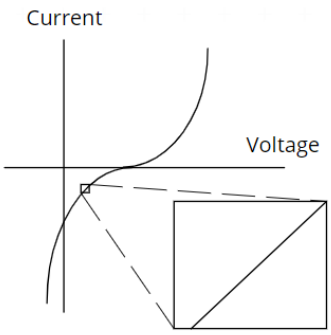


Figure 3.13 current-voltage (I-V) curve showing pseudo linearity. Adapted from reference[258].

In addition, various factors pertaining to the examined system, such as temperature, microstructure, and the unstable polarization response to frequency alterations, can impact the outcomes of EIS measurements. Consequently, in this study, to ensure the accuracy of temperature data, a delay was incorporated into the measurement process, and an internal thermocouple was employed within the chamber. Moreover, to mitigate the effects of the unstable response associated with varying frequencies, a one-second point measurement delay was introduced prior to the acquisition of each data point. The measurements were conducted over a frequency range of 1 MHz to 50 mHz, incorporating 20 data points per decade and a 3-second integration time. Solartron ModuLab XM ECS electrochemical station and 1260A frequency response analyser were used in this project to obtain the EIS spectra of tested cells. The lab-customized testing stand based on NORECES Probstat system[240] combined with vertical furnace. The illustration and picture of sample assembly method was as shown in Figure 3.14.

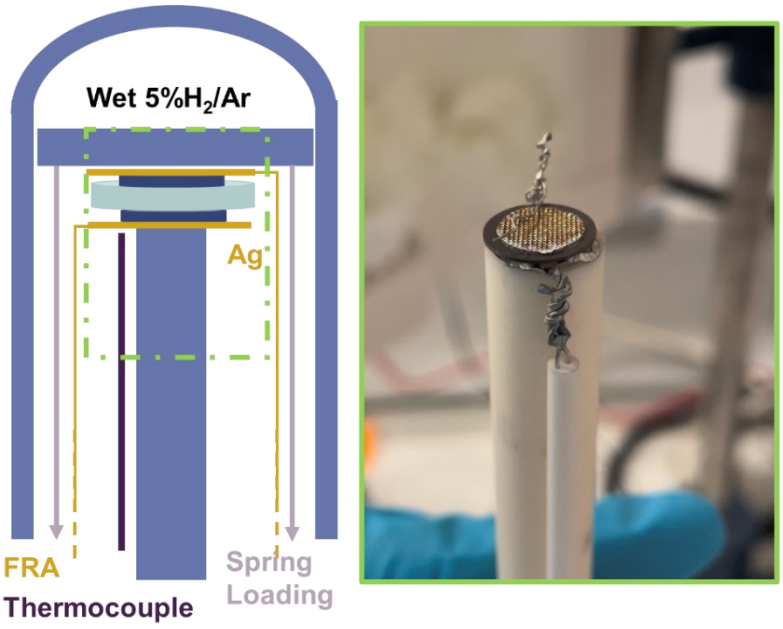


Figure 3.14 Schematic illustration and picture of sample assembly of the lab-customized symmetric cell test stand.

3.3.5.1.3 Data interpretation

The acquired EIS spectra were employed to explore the inherent electrochemical performance of the electrode materials and their time-dependent alterations related to the exsolution process. The EIS spectra were analysed using Zview software (Version 3.5 by Scribner Associates, USA) for spectrum fitting and separation of the processes occurring during the measurement.

Prior to fitting the spectra, the Kramers-Kronig (K-K) test was conducted to assess the validity of the collected data. This test ensures that the measured data adheres to the fundamental principles of causality, linearity, and stability [256]. By calculating the imaginary part from the real part and vice versa using K-K relations, the consistency of the two datasets indicates the quality of the collected data. The Lin-KK Tool MATLAB package [259] was utilized in this project to perform the K-K test.

For the datasets that passed the K-K test, the spectra were fitted with equivalent circuits. In contrast to the ideal semi-circle depicted in Figure 3.12(a), the typical behaviour of the tested system exhibits a depressed semi-circle with a phase angle between 0° and -90°. This is attributed to the non-ideal behaviour of the tested system, arising from factors such as roughness and inhomogeneity. Consequently, constant phase elements (CPEs) were employed to fit the EIS spectra (Figure 3.15. b), as different to pure capacitors shown in Figure 3.15(a). The effective capacitance of an R/CPE circuit is calculated using Equation 3-13:

$$C_{R/CPE} = \frac{(Q \times R)^{1/n}}{R} \qquad 3-13$$

Here, R represents the resistance of the resistor in the equivalent circuit, while Q and n are parameters of the CPE component. Q denotes the magnitude of the impedance of the CPE component, and n represents the frequency-dependence of the phase angle, varying between 0 and 1. When n = 0, the CPE component acts as a pure resistor, and when n = 1, it behaves as a pure capacitor.

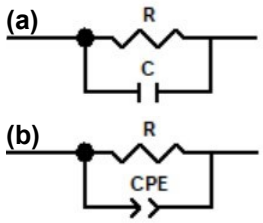


Figure 3.15 Symbols of equivalent circuit with (a) resistor and capacitor (R/C); and (b) resistor and constant phase element (R/CPE).

The most significant advantage of the EIS technique lies in its ability to separate the processes occurring in the tested cells. This is based on the varying time scales of the responses to frequency. In 1990, West, Irvine, and Sinclair noted a specific order of capacitance values for

each bulk sample property and proposed potential interpretations, as listed in Table 3.1 [260]. This gives a general clue of identifying the electrochemical process of the tested system by fitting the EIS spectra.

Table 3.1 Capacitance values and their possible interpretation. Adapted under permissions from reference [260]. Copyright 1990, John Wiley and Sons.

Capacitance (F)	Phenomenon responsible
10^{-12}	Bulk
10^{-11}	Minor, second phase
10^{-11} - 10^{-8}	Grain boundary
10^{-10} - 10^{-9}	Bulk ferroelectric
10^{-9} - 10^{-7}	Surface layer
10^{-7} - 10^{-5}	Sample-electrode interface
10^{-4}	Electrochemical reactions

3.3.5.2 Single cell test

Single button cells were fabricated using lanthanum nickel ruthenates as anode materials, $La_{0.8}Sr_{0.2}Co_{0.8}Fe_{0.2}O_{3-\delta}$ (LSCF8282) as cathode materials, and LSGM as electrolyte materials, as described in Section 3.2.4. The cells were tested for their EIS and current -voltage (I-V) curves, and prior to measuring the I-V curves, a reduction treatment using 5% H_2/Ar was performed at the anode side to induce the exsolution process at 450°C. The single cells were then operated under 100% hydrogen and air conditions, with a flow rate of 100 standard cubic centimeters per minute (sccm) at the anode side and 200 sccm at the cathode side for the current-voltage measurement. The current-voltage measurements were conducted at controlled temperatures of 450°C and 600°C using a tube furnace. Both impedance and current-voltage curves were measured using a potentiostat (PGSTAT302N). The single cell tests were conducted with the assistance of Dr. Inyoung Jang from the Department of Chemical Engineering at Imperial College London.

Chapter 4 Synthesis and intrinsic properties of lanthanum nickel ruthenate double perovskite

4.1. Introduction

Double perovskite materials, lanthanum nickel ruthenate, were synthesized and studied in this work due to their potential in the application of electrode/electrocatalyst of solid oxide cells (SOCs). This chapter presents the study of synthesis methods of stoichiometric lanthanum nickel ruthenate, La_2NiRuO_6 (denoted as L2NR), and its intrinsic properties including lattice structure, chemical composition and thermal behaviours. These properties were investigated via multiple characterization techniques including X-ray diffraction (XRD), scanning electron microscopy (SEM), transmission electron microscopy (TEM), energy-dispersive X-ray spectroscopy (EDX), dilatometry and thermogravimetric analysis (TGA). As a parent phase for the subsequent exsolution investigations (detailed in Chapters 5-6), A-site deficiency was introduced in the structure of the double perovskite to promote the exsolution process as previously reported (details in Chapter 2). The solubility of the A-site vacancies in the lanthanum nickel ruthenate system is discussed with a relatively wide range of deficiency concentration attempted.

The samples and acronyms mentioned in this chapters are: La_2NiRuO_6 (L2NR); $La_{1.9}NiRuO_{6-\delta}$ (L1.9NR), $La_{1.85}NiRuO_{6-\delta}$ (L1.85NR), $La_{1.8}NiRuO_{6-\delta}$ (L1.8NR), and $La_{1.75}NiRuO_{6-\delta}$ (L1.75NR).

4.2. Synthesis of L2NR

Solid-state synthesis method and sol-gel synthesis method were utilized to initiate the work. The solid-state synthesis of La_2NiRuO_6 (L2NR) involved the mixing of the precursor chemicals, including dried La_2O_3, NiO and RuO_2, followed by heat treatment at high temperature for mass transportation and new phase formation. Seinen et al. [261] synthesized Ln_2NiRuO_6 by firing the mixture of Ln_2O_3, NiO and RuO_2 in platinum capsules at 1400°C for 120 hours. Battle et al. [262] reported the synthesis of La_2NiRuO_6 materials by firing stoichiometric amounts of dried ruthenium dioxide and spectroscopic grade lanthanum oxide and nickel oxide as pellets in a platinum crucible at 1150°C in air for a total of eighteen days, with several intermediate grindings. However, the chemical loss and Ru-evaporation become nontrivial when the temperature was above 1200°C, which is the melting point of the RuO_2 precursor. In a TGA investigation of Ru metals in air, Liu et al. observed full oxidation of Ru metals into RuO_2 and more than 20wt% of RuO_2 lost due to the evaporation at 1300°C [263]. Hence, an excess of Ru source was considered as a solution to mitigate against Ru loss.

In the initial phase of this research, three distinct solid-state synthesis approaches were employed, involving stoichiometric amounts of RuO_2, a 5wt% excess of Ru-source, and a 10wt% excess of Ru-source, which equivalent to 5mol% and 10mol% excess of RuO_2 respectively.

The precursor materials were mixed and pressed into green bodies in the form of pellets, which were subsequently subjected to calcination at 1150°C for a duration of 12 hours in static air. To ensure the complete reaction between the precursor components and the formation of a well-crystallized double perovskite phase of L2NR, multiple cycles of additional heat treatment were deemed necessary following the initial calcination, conducted at 1200°C. Interval manual grinding using a mortar and pestle was employed, and the product phase was monitored using XRD until the desired well-crystallized product was obtained.

Figure 2.1 illustrates the XRD patterns of the three different L2NR products synthesized with varying levels of Ru-source excess. The product phase obtained with stoichiometric amounts of raw oxides exhibited additional peaks corresponding to La_2O_3 impurities. These impurities suggest a relatively low concentration of the B-site cation source due to chemical losses. In contrast, both the L2NR samples synthesized with a 10mol% and 5mol% excess of ruthenium demonstrated that the main diffraction peaks matched the double perovskite structure. However, for the 5mol% Ru-excess L2NR, an unresolved subtle peak was observed at 28.9°. Meanwhile, in the 10mol% Ru-excess sample, two impurity peaks were detected at 28.9° and 29.5°, respectively. As depicted in the inset XRD patterns (Figure 2.1), although the powder diffraction patterns showed a similar overall shape, the 10wt% Ru-excess sample displayed a slightly higher number of impurities. Consequently, the XRD plots of these three L2NR samples, synthesized via the solid-state method, highlight the need for further research to determine the optimal Ru source concentration that will minimize chemical losses during high-temperature heat treatment.

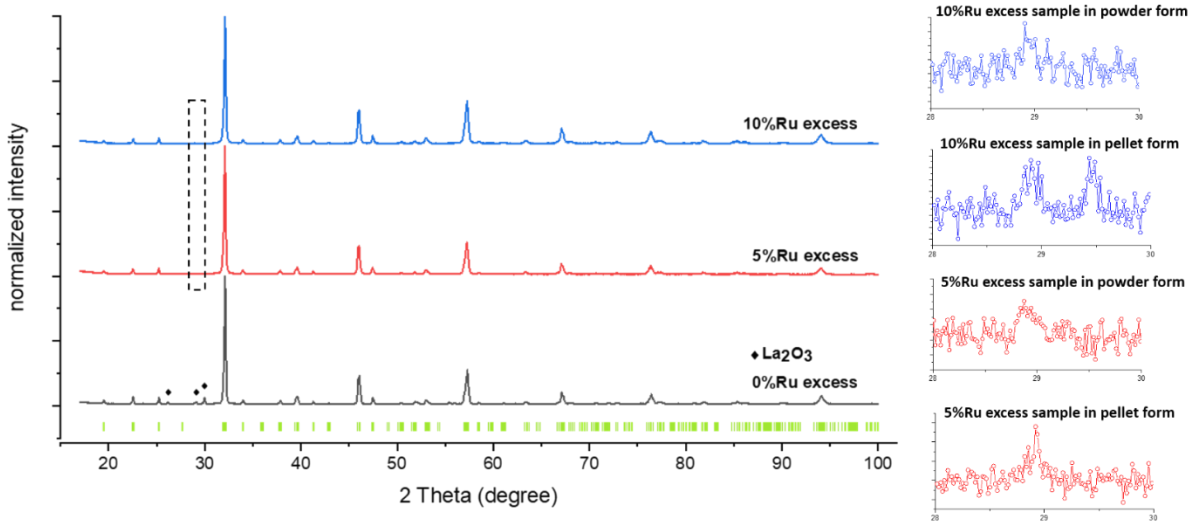


Figure 4.1 Comparison of XRD patterns for synthesized L2NR in powder form with 10mol%, 5mol% and 0mol% RuO_2 excess. The green stick below indicates the Bragg position of L2NR double perovskite. The rhombus symbol indicates the impurity of La_2O_3. The inserted diagrams are a zoomed-in view of plots from 28° to 30°. The 10%Ru excess sample and 5%Ru excess sample are characterized in as-synthesized pellet form, then ground into powder form for powder X-ray diffraction.

To further advance the synthesis process of L2NR, the sol-gel method using the citric-nitrate route [264] was also attempted. As previously discussed in Chapter 3, the sol-gel method offers distinct advantages by allowing for atomic-scale mixing of La, Ni, and Ru cations. This greatly enhances the homogeneity of the precursor mixture and reduces the required heat treatment temperature. In the experimental procedure, L2NR samples were synthesized through the citric-nitrate route. This process involved dissolving the precursors in a 10wt% citric acid solution (VWR chemicals) solution. Amounts of $La(NO_3)_3 \cdot 6H_2O$ (Sigma-Aldrich, 99.999%), $Ni(NO_3)_2 \cdot 6H_2O$ (Sigma-Aldrich, 99.999%), and $Ru(NO)(NO_3)_x(OH)_y$ solution (Johnson Matthey, 99.8%) were added into the solution and continuously stirred on a hotplate at 80°C to ensure the formation of the solution and the homogeneous distribution of cation precursors. Subsequently, the temperature was raised to 200°C to facilitate water evaporation and initiate the gelation process. After gelation, the precursor mixture was transferred to a muffle furnace for decomposition and calcination, effectively removing the organic solvent before the final heat treatment and sintering. The heat treatment of L2NR samples was carried out at 1100°C for 12 hours. Similar to the solid-state synthesis, XRD was used to validate the quality of the resulting product sample before proceeding to the next phase of investigation. In cases where a high degree of crystallinity was needed, manual intermediate regrinding and additional cycles of heat treatment at 1100°C were employed.

The sol-gel citric-nitrate route synthesis proved to be a relatively convenient and time-saving method. XRD patterns were used to verify the products of sol-gel synthesis and investigate the lattice structure of the materials as detailed in next section. Consequently, the sol-gel citric-nitrate route synthesis was adopted for the studies presented in Chapters 5 and 6.

4.3. Crystal structure of L2NR

Debates regarding the lattice structure of the La_2NiRuO_6 double perovskite have persisted since its initial discovery in 1987. Seinen et al. [261] pioneered investigations into La_2NiRuO_6, employing a trial Rietveld model based on the Nd_2MgTiO_6 structure. Their findings suggested a monoclinic structure with space group $P2_1/n$, as depicted in Figure 2.2(a). However, a subsequent study by Battle et al. [262] conducted neutron diffraction of synthesized La_2NiRuO_6 and Rietveld refinement analysis. They contended that the lattice parameter β in Seinen et al.'s work approached 90°, favouring a model based on an orthorhombic structure with space group *Pbnm*, as illustrated in Figure 2.2(b). In subsequent investigations [265–267] of the double perovskite La_2NiRuO_6, researchers consistently suggested a monoclinic crystal structure with the $P2_1/n$ incorporating B-site ordering of Ni and Ru cations.

Figure 2.2 highlights the similarity between the random B-site occupation in the *Pbnm* structure and the rock-salt B-site ordered structure $P2_1/n$, which share general reflection conditions: h0l (h + l = 2n), 0k0 (k = 2n), h00 (h = 2n), and 00l (l = 2n). Notably, the relatively higher symmetry

of *Pbnm* allows for the additional reflection of 0kl (k = 2n), implying that reflections on 0kl planes (k = 2n+1) should be systematically absent [268]. However, as shown in Figure 2.3, the X-ray diffraction patterns of sample L2NR exhibited reflections on planes with Miller indices satisfying 0kl (k = 2n+1), especially (0 1 1) plane, indicated by the label '*'. This discovery prompted further analysis based on the $P2_1/n$ model.

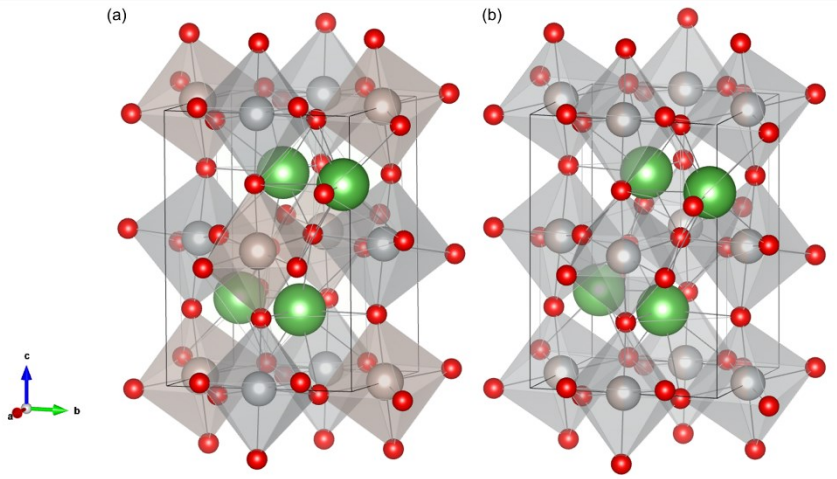


Figure 4.2 Polyhedral sketch of L2NR unit cell of two different model (a) ICSD202277 [261]: Monoclinic structural model with ordered Ni^{2+}/Ru^{4+} ions. (b) ICSD202431 [262]: Orthorhombic structural model with discorded Ni^{2+}/Ru^{4+} ion on octahedral sites. The green balls indicate the La cations; the red balls indicate the O anions; the grey balls indicate the Ni cations; the beige balls indicate the Ru cations.

The L2NR sample was thoroughly characterized through XRD and Rietveld refinement, as presented in Figure 4.3 and detailed in Table 4.1. The fitting plots and agreement indices strongly indicated an excellent fit between the observed XRD pattern and the calculated results. In line with the earlier discussion, the refinement calculations adopted the $P2_1/n$ space group. During the refinement process, oxygen anions were not adjusted due to the X-ray's limited sensitivity to light elements like oxygen, as X-ray diffraction relies on the interaction with electron clouds. Instead, more attention was given to elements such as La and transition metals, which have a greater number of electrons. In the future, neutron diffraction may prove useful in accurately determining the occupancies of oxygen anions.

Given the rarity of perfect B-site ordering in double perovskites [26], both Ni and Ru cations were considered to occupy the (1/2, 0, 0) and (1/2, 0, 1/2) positions, respectively, within the crystal lattice. These refinements were conducted using the Fullprof software suite [238]. As displayed in Table 4.1 below, the lattice parameters closely aligned with those reported in the reference (ICSD96120[265]). Regarding the ordering of Ni and Ru cations, the results indicated a preference for Ni cations to occupy the (1/2, 0, 0) site and Ru cations to occupy the (1/2, 0, 1/2) site, consistent with expectations. Therefore, the degree of ordering (S), defined by the equation:

$$S = 2g_B - 1 \qquad 4-1$$

where g_B represents the occupancy of a B-site cation at its correct site. S was found to be equal to 0.908. Partial disordering may be attributed to site defects or antiphase boundaries, but further investigation is warranted to elucidate the underlying causes.

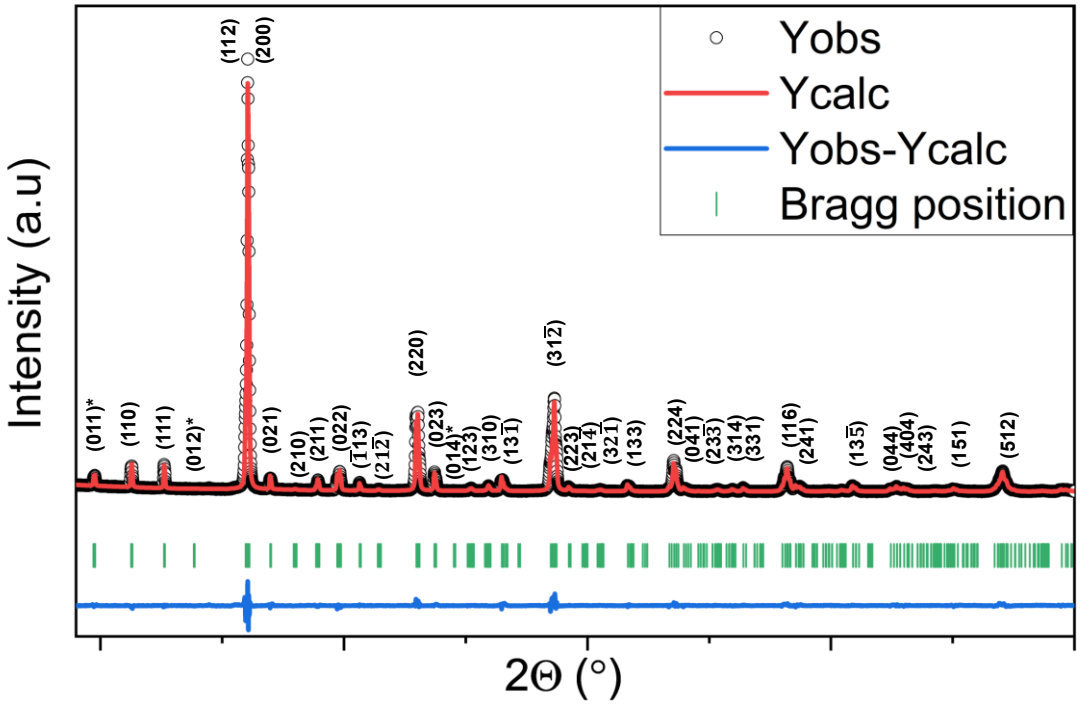


Figure 4.3 XRD pattern and Rietveld refinement refined plots L2NR. The red dots indicate the XRD pattern, and the black line plots the calculated plots from the model *P 2₁/n*. The blue line plots the difference curve of the observed intensity and calculated intensity. The green sticks indicate the calculated Bragg position. The agreement indices are 'the goodness of fitting' χ^2 =6.83, R_p =3.42, R_{wp} =4.68 and R_{exp} =1.79. The reflection peak labelled with '*' indicate the reflection of (0kl) planes, suggesting the monoclinic structure *P 2₁/n*.

Table 4.1 Rietveld Refinement calculated lattice parameters and atomic parameters. B-factors for cations at same location was contraned to same value. and oxygen anions were fixed during reifnement.

Lattice parameters and atomic parameters					
a			5.56659 (4)		
b			5.60789 (3)		
c			7.87773 (5)		
β			89.987 (2)		
	x	y	z	B	Occupancy
La1	0.0053 (4)	0.0424 (1)	0.2501 (3)	0.217(6)	1.003(0)
Ni1	0.5	0	0	0.18 (5)	0.954(1)
Ni2	0.5	0	0.5	0.34(2)	0.046(1)
Ru1	0.5	0	0.5	0.34(2)	0.954(1)
Ru2	0.5	0	0	0.18 (5)	0.046(1)
O1	0.286	0.289	0.029	0.1	1
O2	0.203	0.792	0.049	0.1	1
O3	-0.084	0.489	0.252	0.1	1

4.4. A-site deficient lanthanum nickel ruthenate

As discussed in Chapter 2, the presence of A-site deficiencies plays a crucial role in promoting the exsolution of B-site cations within the perovskite structure, in which process the perovskite lattice tends to restore the stoichiometric ratio of A/B cations by exsolving 'excess' B-site cations. Consequently, before reduction treatment for exsolution, the solubility of A-site deficiency within the double perovskite structure was investigated.

Sol-gel citric nitrate method was employed to synthesize lanthanum nickel ruthenates with varying levels of A-site deficiencies, including 5at%, 7.5at%, 10at%, and 12.5at%. These samples were denoted as L1.9NR, L1.85NR, L1.8NR, and L1.75NR, respectively. As shown in Figure 4.4, the XRD patterns of the synthesized L(2-x)NR materials exhibited a strong alignment of the main diffraction peaks with the *$P2_1/n$* reference model [265], even up to a concentration of 12.5 at% A-site deficiency. However, upon closer examination within the 26.50-33° and 42-48° 2θ positions, the appearance of diffraction signals at 28.07° and 43.27° indicated the presence of unreacted RuO_2 and NiO with a high content of A-site deficiency (L1.8NR and L1.75NR). Consequently, it was established that the lanthanum nickel ruthenate double perovskite can tolerate A-site deficiencies up to 10at%. The lattice structures of three double perovskites, L2NR, L1.9NR, and L1.85NR, each possessing different levels of A-site deficiencies, were subjected to Le Bail refinement. A comparison of lattice parameters and lattice volume is presented in Figure 4.5(a), revealing a reduction in lattice volume with increasing A-site deficiency due to the absence of large La^{3+} cations and resultant lattice distortion. The increase in lattice parameters, 'a' and 'c,' may be attributed to the increasing content of oxygen vacancies introduced by the A-site deficiencies [269]. Vegard's law was widely used for describing the relationship between lattice parameters and composition of ideal solid solution, as depicted in Equation 4-2. This law assumes that the unit cell parameter should vary linearly with composition. Figure 4.5(b) illustrates the plot of pseudo cubic lattice parameters calculated from Le Bail refined lattice volume against the concentration of A-site deficiency. Linear fitting of the plots suggests the same lattice structure of L2NR, L1.9NR and L1.85NR as Le Bail refinement suggested and the formation of a solid solution through the 'vacuum-doping' of A-site deficiency. Additionally, it indicates that the lattice structure of L2NR, L1.9NR, and L1.85NR remains consistent with the findings of Le Bail refinement.

$$a_{AB} = a_A(1 - x) + a_B(x) \qquad 4 - 2$$

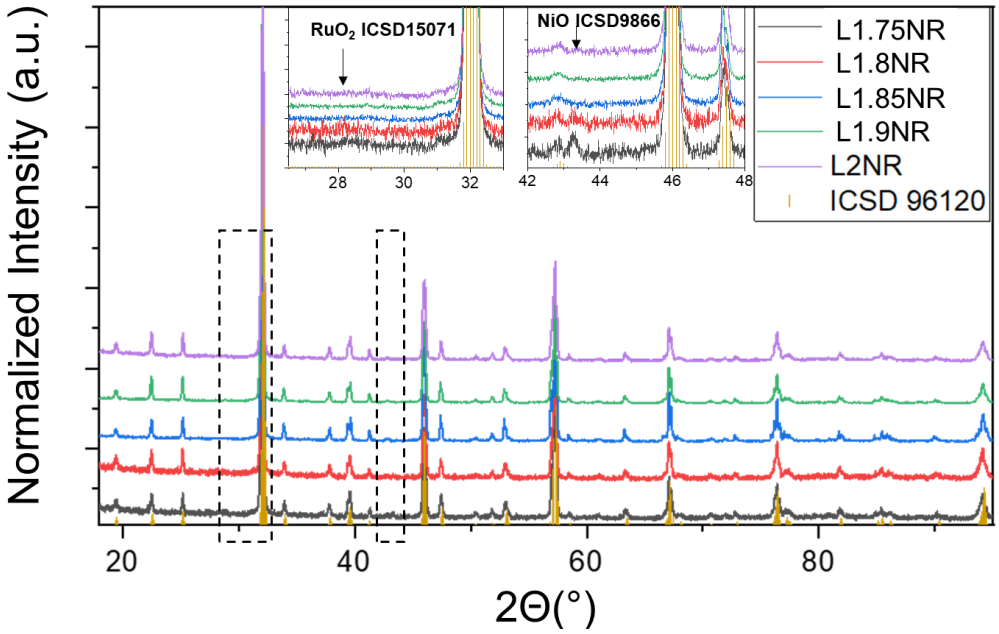


Figure 4.4 XRD patterns of as-prepared L2NR, L1.9NR, L1.85NR, L1.8NR, L1.75NR and peak positions of the referenced pattern (ICSD96120)[265]. The inset are higher magnification regions to highlight the presence of secondary phases of NiO (ICSD9866)[270] and RuO_2 (ICSD15071)[271]. Reused from published work [272] under terms and conditions of CC BY 4.0. Copyright 2022, Authors.

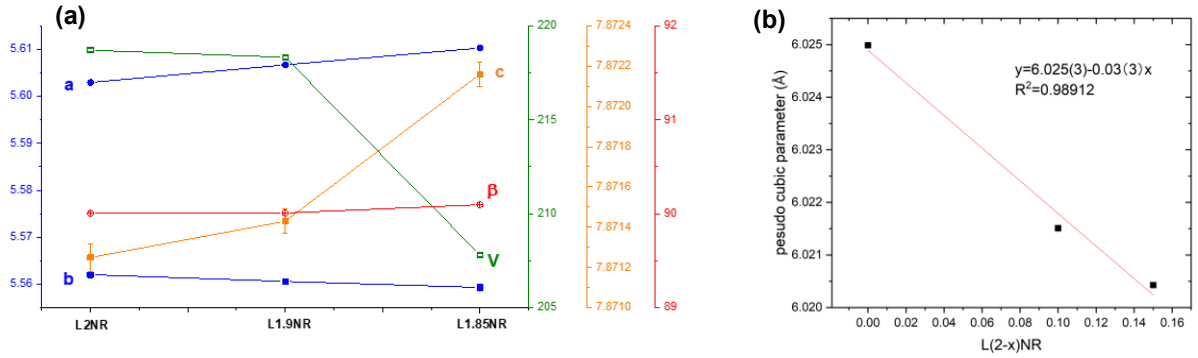


Figure 4.5 (a) Le Bail refinement results of lattice parameters and calculated lattice volume of L2NR, L1.9NR and L1.85NR. The fitting agreement indices of L2NR are R_p= 5.36%, R_{wp}= 6.94%, R_{exp}= 5.20% and χ^2 = 1.78. The fitting agreement indices of L1.9NR are R_p= 5.50%, R_{wp}= 7.46%, R_{exp}= 4.38% and χ^2 = 2.89. The fitting agreement indices of L1.9NR are R_p= 6.30%, R_{wp}= 9.73%, R_{exp}= 4.62% and χ^2 = 4.44. Reused from published work [272] under terms and conditions of CC BY 4.0. Copyright 2022, Authors. (b) Vegard plot with linear fitting of pseudo cubic lattice parameters calculated from Le Bail refined lattice volume vs concentration of A-site deficiency.

4.5. Chemical composition

The chemical information including the valence states of cations and the elemental concentration were further investigated with XPS and ICP-OES. Figure 4.6(a) presents the complex XPS spectrum that encompasses information about the La 3d orbitals, covering a binding energy (BE) range from 825 to 890 eV measured for the L2NR sample. Notably, this BE range also includes signals from the Ni 2p orbitals, which theoretically occur between 850 and 890eV [273–275]. Hence, when comparing the La 3d spectrum measured for L2NR to that of La_2O_3 (Figure 4.6b), the La $3d_{3/2}$ doublet peak displayed significantly elevated intensities. Reference La 3d spectrum of La_2O_3 (Figure 4.6b) showcases two doublet peaks corresponding

to La $3d_{3/2}$ and La $3d_{5/2}$ orbitals, each comprising bonding and antibonding components. Concerning the Ni 2p spectra, as elucidated by Grosvenor et al. [275], they involve multiplet structures with components, including main peaks, satellite peaks, and peaks attributable to the final-state effect for fitting of the Ni 2p spectrum of NiO, as depicted in Figure 4.7. Consequently, accurately fitting and distinguishing components in the overlapped signals of La 3d and Ni 2p orbitals pose challenges. However, the peak position and shape of the La $3d_{5/2}$ orbitals still provided valuable evidence regarding the chemical information of La cations. Figure 4.6(a) demonstrated that the La $3d_{5/2}$ doublet peaks centered at a binding energy position of 834.6eV, which aligns with the reported La_2O_3 (La $3d_{5/2}$ at 834.9eV of binding energy position). Therefore, the La cations in L2NR were characterized as existing in the trivalent state.

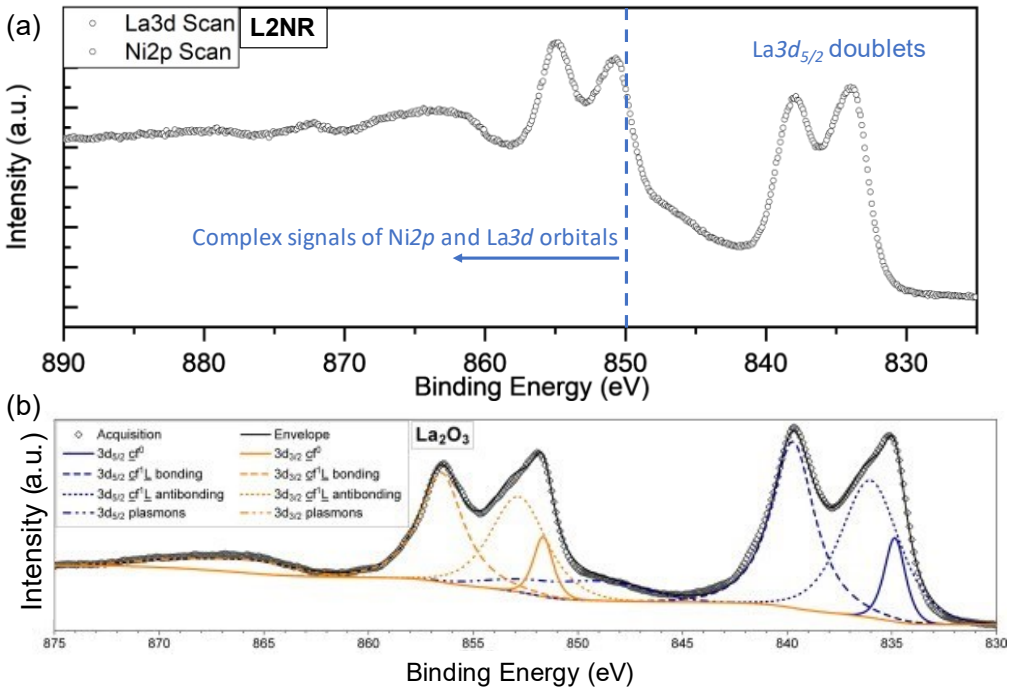


Figure 4.6 (a) Combined spectrum of Ni2p and La3d XPS scanning measured of L2NR sample; (b) fitting plots of La3d spectrum of La_2O_3 adapted from reference [276] under terms and conditions provided by Elsevier and Copyright Clearance Center. Copyright © 2011 Elsevier B.V.

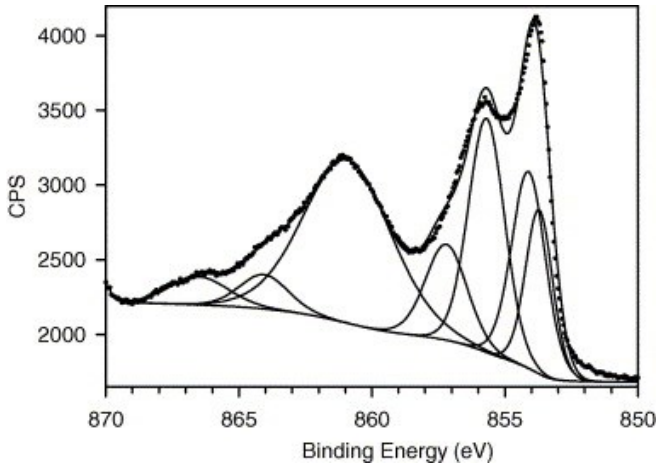


Figure 4.7 Ni2p spectrum measured of NiO fitted with Ni(II) multiplet structure. Adapted from literature [275] under terms and conditions provided by Elsevier and Copyright Clearance Centre. Copyright © 2006 Elsevier B.V.

Investigating the valence states of Ru and Ni cations, previous studies have reported the presence of various valence states, including Ni(II) [267,277], Ni(III) [278–280], Ru(III) [281], Ru(IV) [281–284] and Ru(V) [284], within perovskite and its derivatives. To explore the chemical information related to the valence states of B-site cations (Ni and Ru), XPS spectroscopy was employed. However, challenges were encountered due to overlapping signals, as discussed earlier: the overlap between Ni 2p and La 3d signals, and the overlap between C 1s and Ru 3d signals. As previously mentioned in Chapter 3, challenges such as a poor connection between the sample and spectrometer, as well as issues related to poor conductivity, can lead to unreliable chemical shifts. Calibration of binding energies is necessary under such circumstances. Typically, the widely used internal calibration standard is adventitious carbon's C 1s orbital, which typically falls within the binding energy range of 284.66 – 285.16eV [285]. However, the adventitious carbon C 1s signals occupy the same binding energy region as Ru 3d signals, ranging from 276 to 288eV. Consequently, the adventitious carbon C 1s peak position for the L2NR sample would need to be determined through spectral fitting, introducing potential inaccuracies in calibration.

Hence, an alternative calibration standard was explored for XPS analysis in this work. Similar to calibration using adventitious carbon, we employed self-referencing calibration. This approach involved calibrating the spectra using the O-M peaks of the O 1s spectrum instead of the C 1s spectrum. Figure 4.8 illustrates the O 1s orbital spectrum measured for the L2NR sample, which was fitted with two component peaks attributed to the O-M bond and surface oxygen species. The O 1s peak was calibrated to 529.2eV of binding energy with a full width half maximum (FWHM) of 1.1eV (as presented in Table 4.2). The consistent peak position and sharp peak shape of the O 1s O-M peaks provided confidence in adopting these peaks as the calibration standard in the XPS analysis of the L2NR sample and future studies.

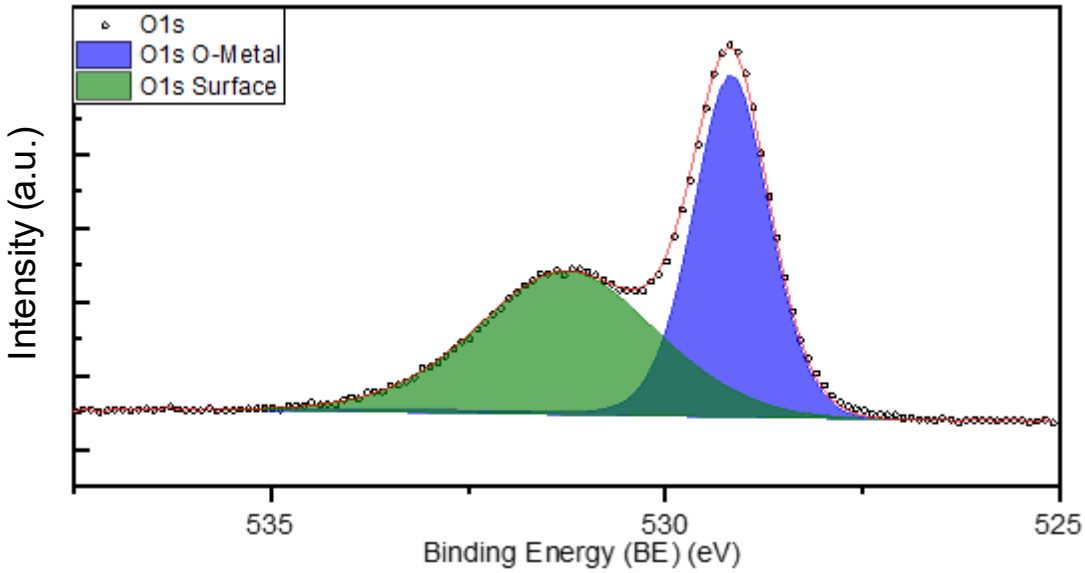


Figure 4.8 XPS spectrum of O 1s orbitals of L2NR (black circles), fitted envelop plots (red line), and the fitting components (coloured peaks). Reused from published work [272] under terms and conditions of CC BY 4.0. Copyright 2022, Authors.

The spectra of Ru 3d and C 1s orbitals were measured by XPS spectrometer from 280 to 292eV of binding energy position (Figure 4.9). The fitted parameters were as shown in Table 4.2. Morgan [286] extensively studied XPS spectra of various common ruthenium materials, where Ru compounds typically exhibit satellite components due to the screened and unscreened effects of core-level electrons. The fitting curves, depicted as the red envelope curve in Figure 4.9, suggest a good fit of the spectra with Ru 3d doublets, Ru 3d satellites, C 1s C-C peak, and C 1s C=O peak. Ru $3d_{5/2}$ peak was fitted at a binding energy position of 282.35 eV. However, this position differs from the reported Ru $3d_{5/2}$ peak position of RuO_2 [286], which may be attributed to differences in oxygen coordination numbers. Lü et al. [287] investigated Ru 3d spectra in Ruddlesden–Popper phases $LaSrNi_{0.5}Ru_{0.5}O_4$ and $LaSrCo_{0.5}Ru_{0.5}O_4$, where the Ru sites have the same 6-coordination as double perovskites. They reported a Ru $3d_{5/2}$ peak position of ~282.1–282.2 eV. Additionally, the doublet separation, as shown in Figure 4.9, was approximately 4.2 eV, in agreement with the reported value for Ru^{4+} cations [286,287]. Consequently, we characterized the Ru cations in the L2NR double perovskite system as tetravalent. Moreover, the C 1s C-C peak was fitted at 284.98eV, confirming the validity of the O 1s calibration method. In alignment with the O 1s spectrum in Figure 4.8, the presence of surface adsorbates was also indicated by the observation of C=O bond signals in Figure 4. 9.

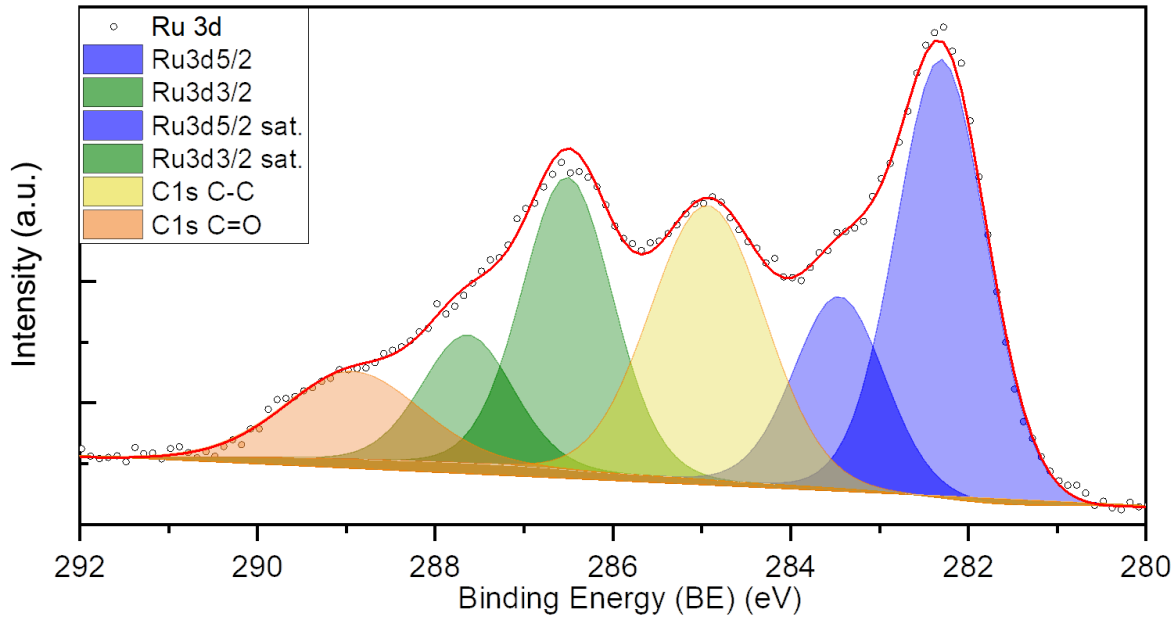


Figure 4.9 XPS spectrum of Ru 3d orbitals of L2NR (black circles), fitted envelop plots (red line), and the fitting components (colored peaks). Reused from published work [272] under terms and conditions of CC BY 4.0. Copyright 2022, Authors.

As stated above, it is a challenge to resolve the Ni 2p spectrum in the complex signal from both Ni and La cations. Biesinger et al. [288] investigated the Auger spectra of nickel alloys, halides, oxide, hydroxide and oxy-hydroxide and proposed feasibility of resolving Ni chemical information by looking at the Auger spectrum instead of Ni 2p spectrum. Hence, Ni $L_3M_{45}M_{45}$ (denoted as Ni LMM) Auger spectrum was investigate instead as shown in Figure 4.10(a). As demonstrated in Section 3.3.1.2, the binding energy values were calculated using the Equation 3-9. For Auger transitions, the kinetic energy of $L_3M_{45}M_{45}$ Auger electrons is associated with the internal electron transition process not directly from the incident beam, so it is ambiguous to use binding energy (BE) to investigate LMM Auger peaks. Hence, the spectrum was converted to the plots depending on kinetic energy, as Figure 4.10 shows. The Ni LMM spectra of Ni cations in different compounds were as shown in Figure 4.10(b). The Ni LMM spectrum of compound γ-NiOOH with trivalent Ni cations displayed a unique characteristic peak at lower kinetic energy position of 832.8 eV, while the spectra of NiO and $Ni(OH)_2$ containing Ni^{2+} presented broadened peaks. The Ni LMM auger spectrum of L2NR sample shown in Figure 4.10 (a) displayed a similar peak shape with the spectra of NiO and $Ni(OH)_2$ without obvious signals at 832.8eV, indicating the most of Ni cations in L2NR present as divalent.

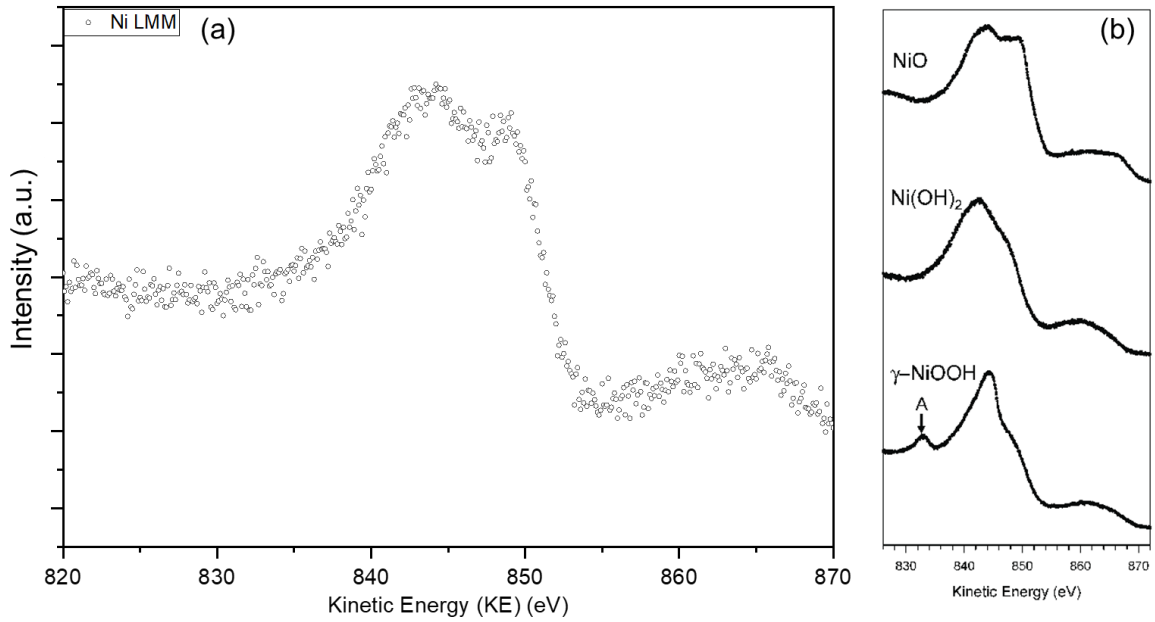


Figure 4.10 (a) XPS spectrum of Ni LMM Auger signals in kinetic energy (KE) measured of L2NR sample; (b) Ni LMM auger spectra of NiO, Ni(OH)2 and γ-NiOOH adapted from reference [288] under terms and conditions of Copyright Clearance Centre. Copyright 2012, Royal Society of Chemistry.

Table 4.2 Fitting results of the Ru3d, O1s, C1s spectra of asprepared L2NR sample. Due to the limitation of energy reoslution of spctrometer, the error of measured and fitted binding energy poisiotns was approximately 0.2-0.5eV.

Peaks	BE(eV)	FWHM eV
O1s O-Metal	529.2	1.1
O1s Surface	531.3	2.6
Ru3d5/2	282.4	1.2
Ru3d3/2	286.6	1.2
Ru3d5/2 sat.	283.5	1.2
Ru3d3/2 sat.	287.7	1.2
C1s C-C	284.9	1.5
C1s C=O	289.0	1.8

To validate the chemical composition of the synthesized double perovskite samples (stoichiometric L2NR, 5at% A-site deficient L1.9NR, and 7.5at% A-site deficient L1.85NR) inductively coupled plasma optical emission spectroscopy (ICP-OES) was used to investigate the elemental concentrations in these samples. The results are presented in Table 4.3. The intended nominal formulae for these compositions were La_2NiRuO_6, $La_{1.9}NiRuO_{5.85}$, and $La_{1.85}NiRuO_{5.775}$ respectively. The calculated concentrations were based on the assumption that the B-site positions were fully occupied by Ni and Ru cations, and the oxygen stoichiometries were determined under the assumptions of valence states for La, Ni, and Ru cations being 3+, 2+, and 4+, respectively. Observations revealed a decrease in A-site cation

concentration in the experimental composition as the designed A-site deficiency increased. The Ni to Ru cation ratios remained approximately 1:1, consistent with expectations. However, the actual composition of the A-site deficient samples, L1.9NR and L1.85NR, showed slightly higher La-occupancy compared to the nominal composition. This indicated A-site deficiencies of 3.3at% and 5.35at%, respectively. The actual composition of the samples depends on the chemical reactions during the synthesis and the defect chemistry. Therefore, the precise atomic ratio and controlling of the compositions as well as the oxygen stoichiometry need further exploration including thermal analysis combined with oxygen sensor at the exhaust, high-energy synchrotron XRD and refinement and so forth.

Table 4.3 1 ICP results of stoichiometric double perovskite L2NR and A-site deficient samples L1.9NR and L1.85NR. B-site positions were assumed fully occupied by Ruthenium and Nickel cations during the calculation of concentration ratio. Reused from published work [272] under terms and conditions of CC BY 4.0. Copyright 2022, Authors.

L(2-x)NR	Nominal composition	Concentration ratio		Experimental composition
		A-site/ B-site	Ni/Ru	
L2NR	La_2NiRuO_6	0.992(8)	1.034(2)	$La_{1.98(2)}Ni_{1.017(2)}Ru_{0.982(4)}O_{5.951}$
L1.9NR	$La_{1.9}NiRuO_{5.85}$	0.967(3)	1.053(3)	$La_{1.934(7)}Ni_{1.025(3)}Ru_{0.974(7)}O_{5.874}$
L1.85NR	$La_{1.85}NiRuO_{5.775}$	0.947(1)	1.085(3)	$La_{1.893(2)}Ni_{1.041(3)}Ru_{0.959(9)}O_{5.7985}$

4.6. Thermal behaviour

In addition to investigating the crystal structure and chemical composition of the L2NR double perovskite, the thermal behaviour of the L2NR sample was examined using a dilatometer and thermogravimetric analyser. Figure 4.11 illustrates the sintering behaviour of the L2NR sample as measured by the dilatometer. In the graph, dL represents the absolute dimensional changes of the L2NR bar sample, while L_0 denotes the original dimension. The dilatometry experiments involved a first stage of heating at a rate of 10°C/min, reaching up to 1400°C, followed by a dwell period at 1400°C for 160 minutes for sintering and densification. The dL/L_0 curve displayed a slight increase in the L2NR sample's dimension as it was heated to 400°C, indicating thermal expansion with increasing temperature. As the temperature approached 1400°C, the bar sample exhibited signs of shrinkage, signifying the onset of sintering. The derivative of length changes plotted against time, d(dL)/dt, showed an increasing rate of shrinkage until reaching the 1400°C dwell point. Therefore, the fast-sintering point as 1400°C was determined. Furthermore, the sample continued to shrink during the subsequent dwell time, indicating that the densification process of sintering was still ongoing until the experiment concluded. However, it's important to note that the dilatometry measurement is limited to

temperatures up to 1400°C and a dwell time of 160 minutes. Based on these instrumental limitations, extending the measurement to higher temperatures and longer isothermal dwells would provide a more comprehensive understanding of the sintering behaviour. The initial dimension of bar sample remained constant, and the abrupt changes of d(dL)/dt at around 400°C may be attributed to the detection limitations of the dilatometer during the initial stages of thermal expansion. Moreover, the dilatometry measurement offers evidence of the sintering temperature of the electrode discussed in Chapter 3. Considering the requirement of a porous structure for both symmetric cells and SOC single cells, it's imperative that the sintering temperature remains below the fast-sintering threshold of 1400°C.

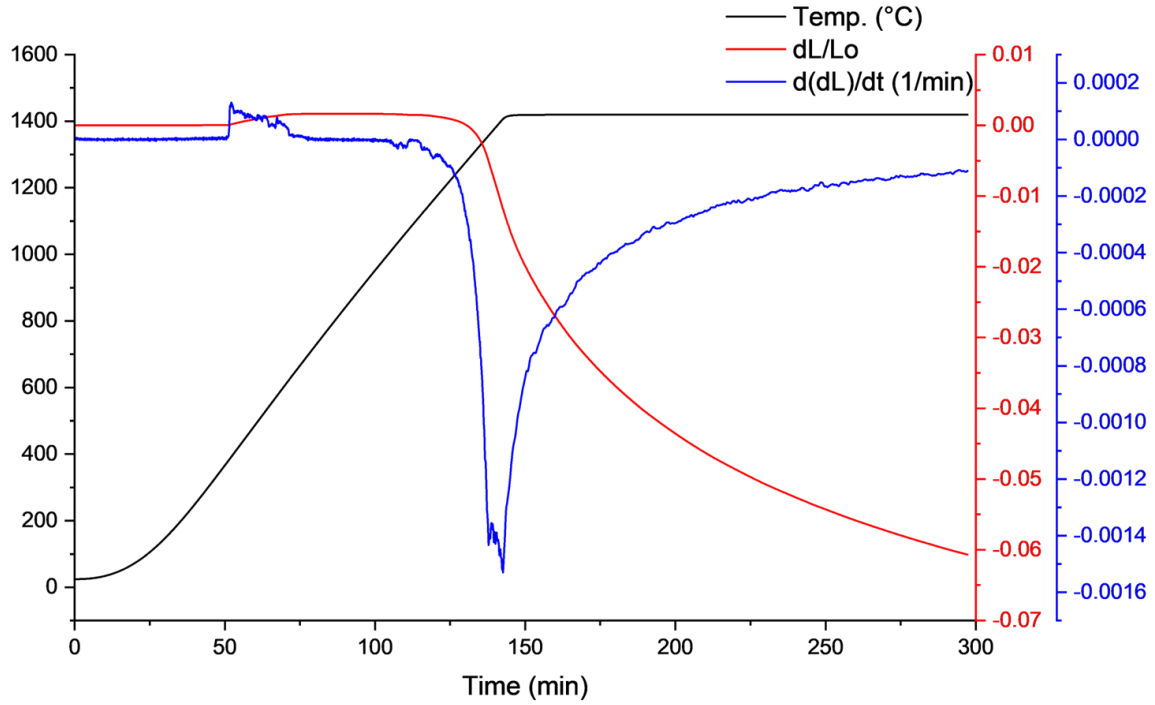


Figure 4.11 Plots of temperature change (black line), dimensional change (red line) and the derivative of expansion/shrinkage (blue line) of L2NR sample characterized by dilatometer.

Figure 4.12 present the TGA plots of the L2NR sample, measured in air up to 1200°C. The initial mass loss of approximately 0.05wt% occurred when the temperature reached 200-300°C. This loss was attributed to the evaporation of moisture and adsorbed carbonate content during heating. Subsequently, a plateau in the TG curves was observed as the temperature increased up to 800-900°C, indicating the stability of the L2NR sample in air without any redox reactions below 800°C. A slight mass loss of approximately 0.02-0.03wt% was observed as the temperature increased above 800°C and up to 1200°C. This mass loss was considered to be related to the reduction of Ru^{4+} cations and loss of oxygen due to the high temperature annealing. The loss of oxygen can be calculated as 0.0067-0.01 mol O per mol of L2NTR.

From both the dilatometry and TG investigations, we deduced that L2NR remains stable in air within the temperature range from room temperature up to 800°C. Achieving rapid sintering and dense ceramic structures for L2NR samples required temperatures as high as 1400°C, while the high temperature will cause reduction in a minor fraction of the Ru^{4+} cations during the sintering process.

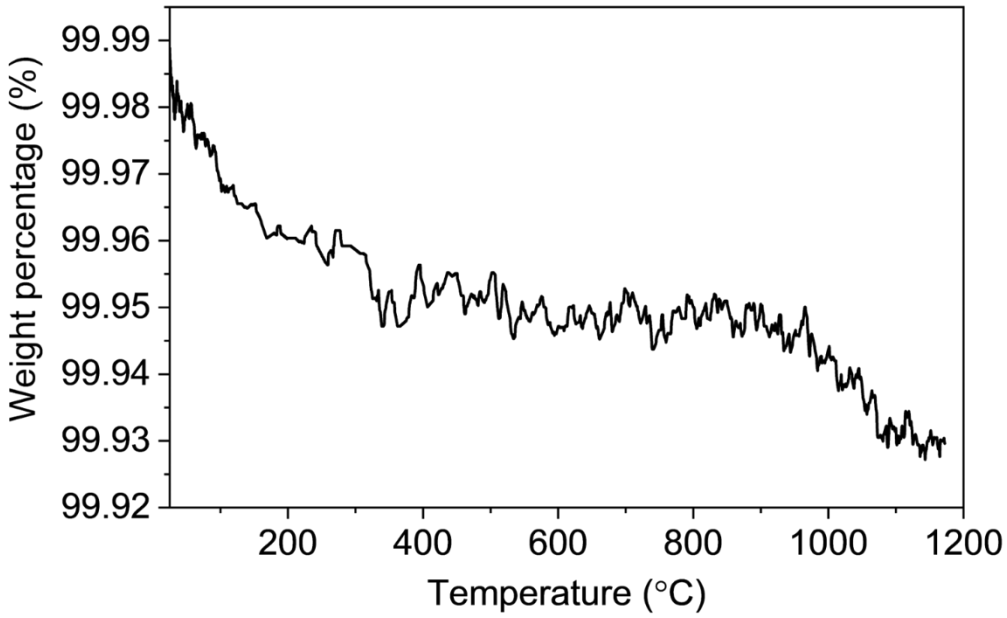


Figure 4.12 TGA plot of weight change (%) versus temperature. The first drop of 0.05% weight loss from room temperature to 300 °C is attributed to the loss of moisture and carbonates.

4.7. Summary and future work

This chapter delves into the synthesis and intrinsic properties of lanthanum nickel ruthenate double perovskite. The conventional solid-state synthesis method necessitated high-temperature heat treatments, resulting in significant losses of ruthenium and requiring an excess amount of ruthenium source. In contrast, the sol-gel method offered advantages such as atomic-level cation mixing, enabling lower heat treatment temperatures and simplified synthesis procedures. As a result, samples synthesized via the sol-gel method were chosen for the investigation of intrinsic properties and subsequent research in later chapters.

Characterization of the lattice structure of the stoichiometric sample L2NR revealed a monoclinic structure with space group $P2_1/n$. Rietveld refinement allowed for the analysis of cation occupancies, revealing a B-site rock-salt ordering of nickel and ruthenium cations with limited disorder. Chemical composition analysis confirmed the presence of La^{3+}, Ni^{2+}, and Ru^{4+}, consistent with the expected 2:1:1 ratio for the stoichiometric sample L2NR. Furthermore, A-site deficiencies were introduced into the structure, revealing that the solubility of the A-site deficiency remained within acceptable limits, typically below 10at%. However, ICP results revealed a slightly higher La occupancy for the nominal A-site deficient samples, suggesting a

topic worthy of further investigation in the future. Additionally, the thermal behaviour was investigated, including sintering temperature and thermogravimetric properties, finding that temperatures as high as 1400°C were necessary for rapid sintering and dense ceramic formation in the L2NR sample.

Overall, this chapter provides a comprehensive examination of the intrinsic physicochemical properties of lanthanum nickel ruthenates double perovskites, laying the groundwork for further investigations including reduction treatment and exsolution.

Chapter 5 Exsolution of A-site deficient lanthanum nickel ruthenate double perovskite

5.1. Introduction

Following the investigation in Chapter 4, the synthesized lanthanum nickel ruthenates were subject to reducing condition in this chapter for the initial attempts of exsolution study. The stability of this double perovskite system was firstly examined through XRD analysis, followed by a detailed morphology study employing SEM and TEM, which revealed the occurrence of low-temperature exsolution in A-site deficient samples. XPS, XRD and STEM-EDX were utilized to investigate the chemical composition of exsolved nanoparticles in the L1.85NR sample reduced at 450°C for 3 hours in wet 5%H_2/Ar, revealing the exsolution of Ni-Ru bimetallic alloy particles. Furthermore, different reduction conditions were explored, encompassing dry atmospheres and varying temperatures. SEM, TEM, XPS, and XRD were employed to investigate the different extent of exsolution under these conditions.

The samples and acronyms mentioned in this chapters are: La_2NiRuO_6 (L2NR); $La_{1.9}NiRuO_{6-\delta}$ (L1.9NR) and $La_{1.85}NiRuO_{6-\delta}$ (L1.85NR).

5.2. Structural stability in 5%H_2/Ar

Building on the discussions in Section 2.3 and Chapter 4, synthesized lanthanum nickel ruthenates (L2NR, L1.9NR and L1.85NR) via the sol-gel citric-nitrate method were subjected to a reduction treatment in preparation for the subsequent exsolution study. The XRD patterns of the L2NR samples reduced in 5% H_2/Ar are presented in Figure 5.1. It is noteworthy that the double perovskite structure remained stable until the reduction temperature exceeded 500°C. At 500°C, two subtle secondary phase peaks at 29° and 30° in the 2θ position of the L2NR sample were observed. As the reduction temperature increasing to 600°C, these peaks became more pronounced, accompanied by an additional broad peak in the XRD pattern at 43.5°-45° 2θ. The broad peak exhibited a distinctive 'hump' shape with an additional sharp signal at 44.5° 2θ, as indicated by the orange arrow in Figure 5.1. This observation suggests the presence of two types of secondary phases in the 2θ range. One phase exhibited low crystallinity and small grains, while the other was well-crystallized. The secondary phases at 29-30° and the broad peak around 44° 2θ were attributed to the decomposed phase of L2NR, which are RuO_2 [271], La_2O_3 [289] and NiO phases [270], as indicated in Figure 5.1. On the other hand, the well-crystallized phase at 44.5° 2θ was attributed to the formation of a Ni-Ru metallic phase [290,291] as a result of the reduction process.

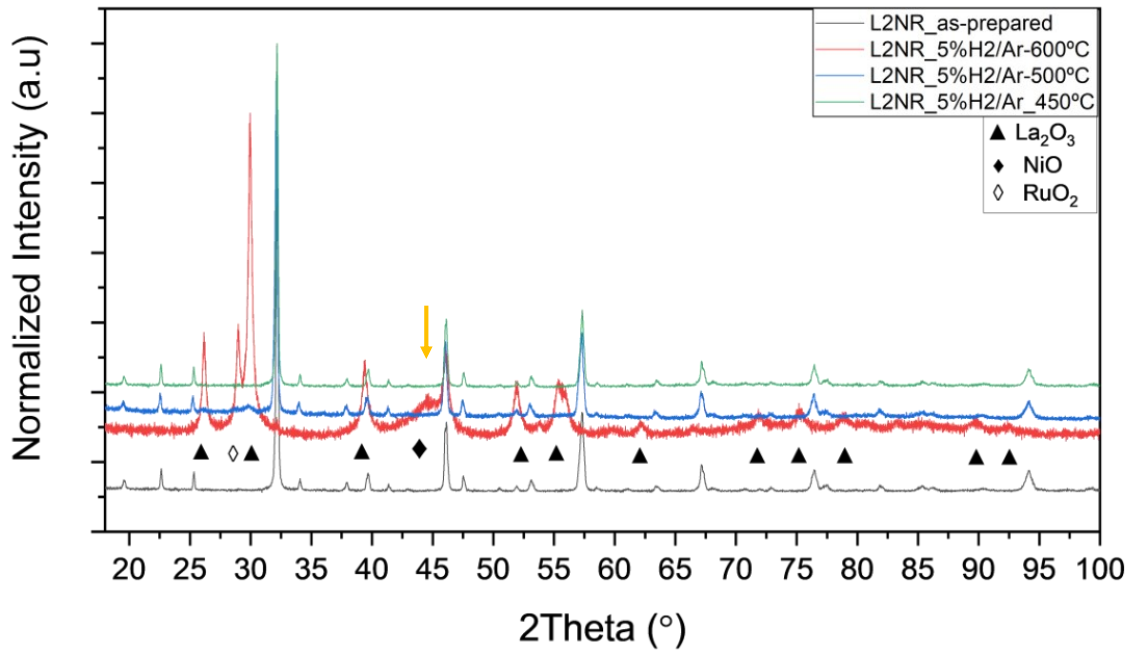


Figure 5.1 XRD patterns of L2NR reduced in 5%H_2/Ar at temperatures ranging from 450°C to 600°C for 3 hours. The double perovskites start to decompose when the reducing temperature exceeds 500°C, forming La_2O_3, NiO, RuO_2 and metallic phases. Adapted from the published work [272] under terms and conditions of CC BY 4.0 license. Copyright 2022, Guo et al.

A-site deficient samples, specifically the L1.85NR samples, were also investigated after subjecting them to reduction at various temperatures. To create a reducing atmosphere that was compatible with the intended future application in SOCs operation and to ensure that the hydrogen partial pressure was not overly aggressive to maintain the double perovskite structure, moisture was introduced into the 5%H_2/Ar atmosphere. A water bubbler was added to the reduction treatment furnace, introducing approximately 3% steam content. The presence of moisture in the reducing gas balanced the 5%H_2/Ar and the unavoidable water splitting reaction will increase the partial pressure of oxygen.

Figure 5.2 presents the XRD patterns of the L1.85NR samples following reduction at different temperatures. Similar to the stoichiometric L2NR samples, the A-site deficient L1.85NR samples exhibited a decomposition process as the reduction temperature increased beyond a certain threshold. In the case of the L1.85NR samples, they were able to maintain the double perovskite structure until the reduction temperature surpassed 600°C, in contrast to the L2NR sample reduced in dry 5%H_2/Ar (Figure 5.1). However, beyond this point, severe decomposition occurred. The decomposed phases observed were a mixture of La_2O_3, NiO, RuO_2, and reduced metallic phases. Consequently, when conducting exsolution investigations on the A-site lanthanum nickel ruthenate double perovskites, the reduction temperature should not exceed 600°C using a wet 5%H_2/Ar atmosphere.

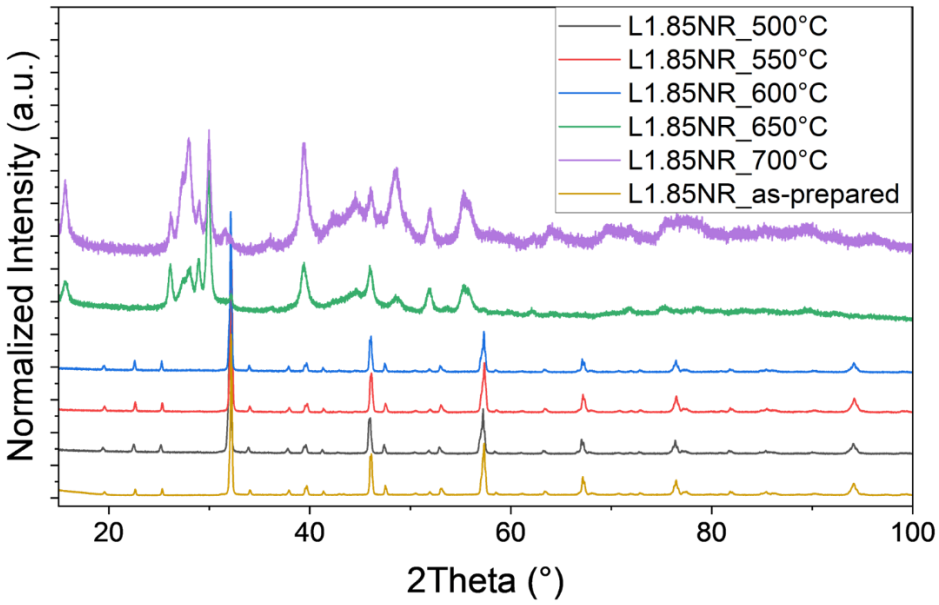


Figure 5.2 XRD patterns of L1.85NR after reduction in 5%H_2/Ar at temperatures ranging from 500°C to 700°C, illustrating the significant decomposition observed when the reduction temperature exceeded 600°C.The reduction treatment were kept as 3 hours.

5.3. Exsolution of nanoparticles

5.3.1. Morphology

Based on the discussions outlined earlier, an exsolution investigation was initiated by subjecting lanthanum nickel ruthenate double perovskites to a low-temperature treatment at 450°C in a wet 5%H_2/Ar atmosphere. Both stoichiometric and A-site deficient samples, denoted as LxNR (where x = 2, 1.9, and 1.85), underwent a 3-hour reduction process. Figure 5.3 (a-d) presents scanning electron microscopy (SEM) images of the four areas of L2NR samples after reduction, providing a general overview of the sample surface. In these images, well-crystallized ellipsoidal polyhedral grains can be clearly observed, with an average grain size of 250(±87) nm in diameter, as measured by ImageJ software (Figure 5.3). However, notably, there is no discernible exsolution of nanoparticles on the surface of the L2NR grains following reduction in wet 5%H_2/Ar at 450°C for 3 hours, especially compared to the A-site deficient sample L1.9NR and L1.85NR after reduction as shown in Figure 5.4 and Figure 5.5.

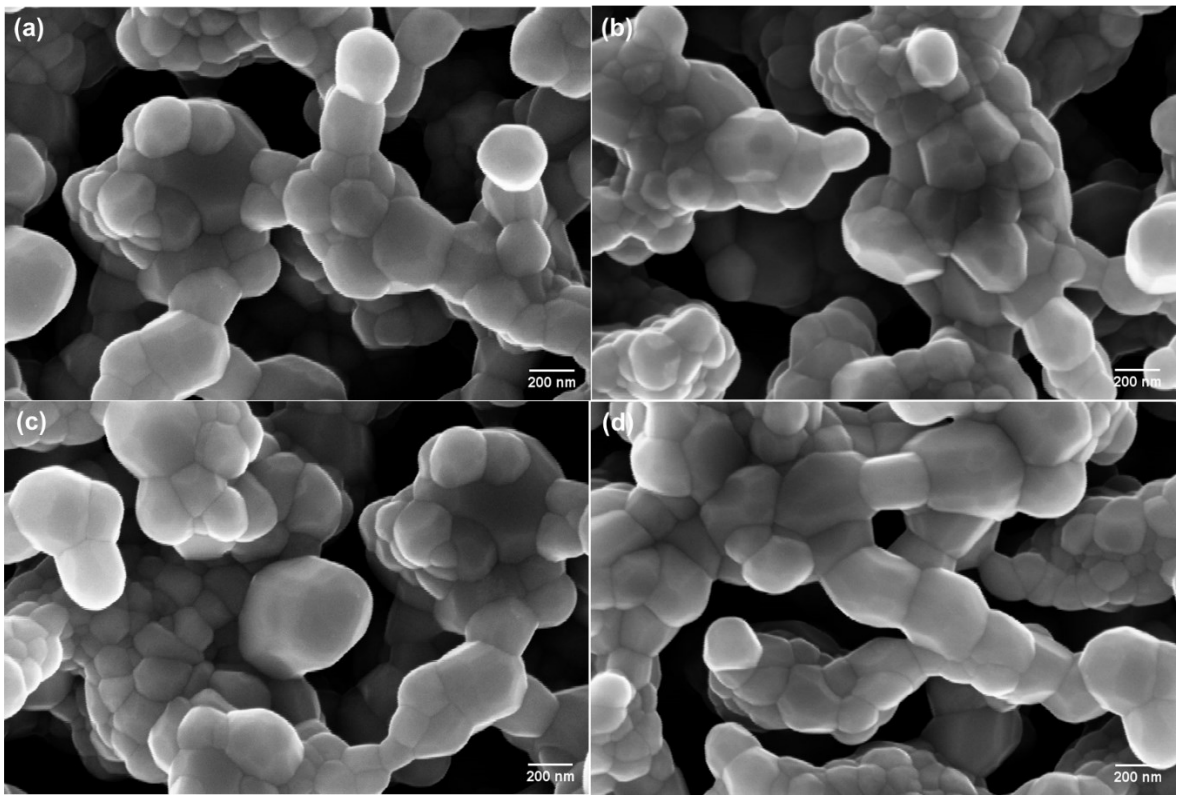


Figure 5.3 SEM images (a-d) of L2NR sample reduced at 450°C in wet 5%H_2/Ar for 3hours, showing overall view of samples in the four presented areas. Adapted from published work [272] under terms and conditions of CC BY 4.0. Copyright 2022, authors.

Figure 5.4 shows the morphologies of the A-site deficient samples L1.9NR after reduction. The sample of L1.85NR and L1.9NR were calcined at 1400°C to give a homogenously distribution of A-site deficiency and cations. Uniform nanoparticles were observed on the surface of the bulk grains, especially at the well-crystalized surface of the 'larger' grains as shown in Figure 5.4(a-c). This was because the well-crystalized large grains possessed homogeneously distributed key factor (A-site deficiency) as designed after high-temperature sintering. The preference of exsolution on certain facets and cleavage planes was also observed in the reduced L1.9NR samples, as shown in Figure 5.4 (c,d). Here, the term "cleavage plane" refers to the fracture surface of the grain exposed to the reducing atmosphere. The preference of facet-dependent exsolution can be related to locations of A-site cation vacancies and the difference of the interfacial energy barrier during the nucleation and particle growth process [76,196,197], while future research is needed to clarify the mechanisms of interaction between exsolving nanoparticles and defect chemistry and the parent double perovskite phase and the resulting facet-dependent exsolution. In addition, the preference of exsolution on the cleavage plane was also observed in agreement with the initial discovery of the Ni exsolution from lanthanum nickel titanates [88]. This was attributed to the surface composition deviation in the small grains that might hinder the exsolution of nanoparticles. Additionally, the introduction of strain effects on the cleavage plane may occur during mechanical breaking [181]. However, the

underlying mechanism during the entire exsolution process remains unclear and requires further in-depth investigation.

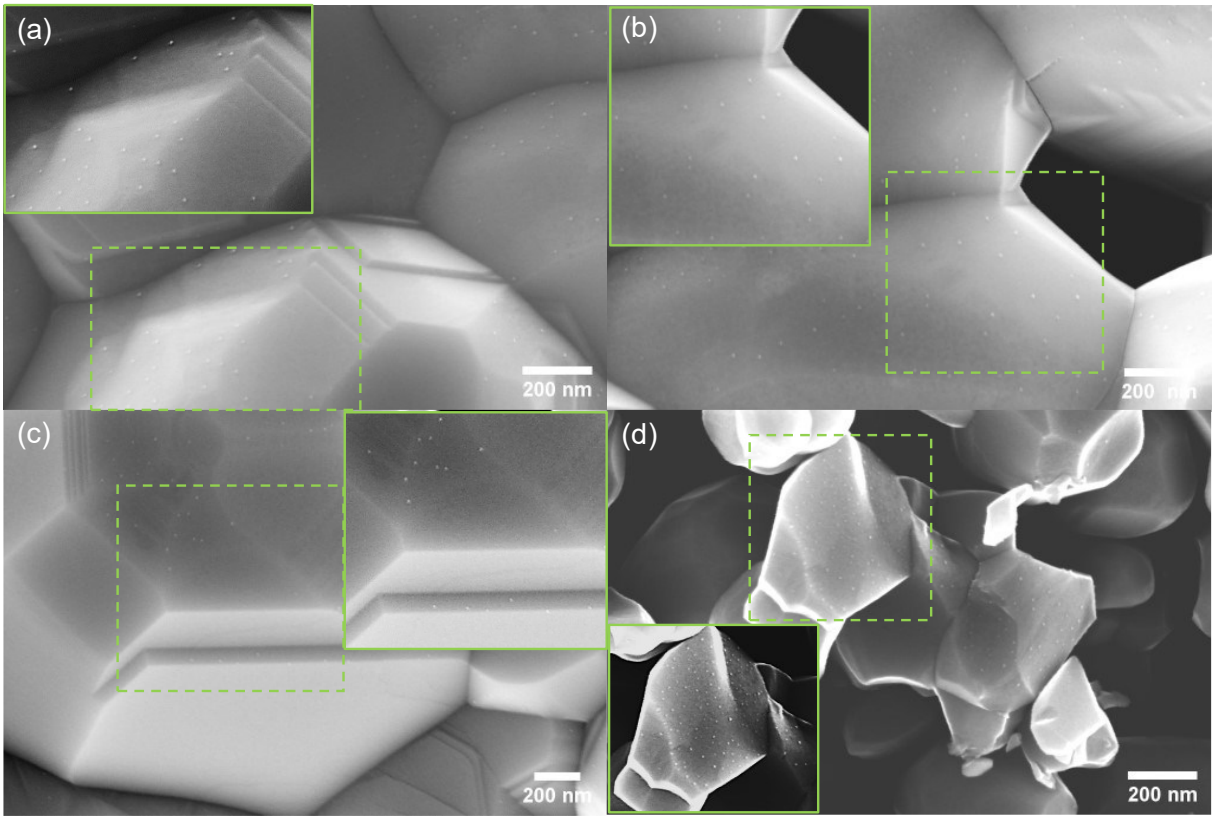


Figure 5.4 SEM images of L1.9NR samples reduced at 450°C in wet 5%H_2/Ar for 3 hours, showing four areas (a-d) selected of the L1.9NR sample. The inserted images highlighted the presence and morphology of the exsolved nanoparticles with adjusted brightness and contrast of area in dash box. The scale bar of the inserted images referred to the dash box area of the original images.

Figure 5.5 presents SEM images of L1.85NR samples following reduction at 450°C in wet 5%H_2/Ar for 3 hours, both in powder and pellet forms. In these images, numerous small nanoparticles on the surface of the bulk grain were observed. In Figure 5.5 (b), two types of nanoparticles are observed on the surface, particularly evident in the zoomed-in inset graph. One type consists of larger particles with a diameter of 23(± 3) nm, while the other type comprises smaller nanoparticles with numerous populations homogeneously distributed on the surface, measuring 5 (± 2) nm in diameter. This suggests two different exsolution behaviours of cations and emphasizes the necessity for an in-depth mechanism study, with further details provided in Chapter 6. Notably, a preference for exsolution on the cleavage plane is also evident, especially in small double perovskite grains, as illustrated in Figure 5.5(c). The extent of exsolution and particle growth at the cleavage plane is larger than other grain surfaces (Figure 5.5 a and b). The L1.85NR sample in dense pellet form was also subjected to reduction at 450°C in wet 5%H_2/Ar for 3 hours. As demonstrated in Figure 5.5(d), nanoparticles exsolved from the polycrystalline pellet. Consistent with the observations for L1.9NR, the exsolution from the dense L1.85NR pellet on different facets or orientations exhibited variations in particle

populations. Figure 5.6 displays enlarged images of two adjacent grains with adjusted brightness and contrast, clearly highlighting the favourability of one orientation of the grain over the other. Weber et al. [197] also reported differences in Ni exsolution among different orientations of polycrystalline dense pellets of $SrTi_{0.9}Nb_{0.05}Ni_{0.05}O_{3-\delta}$. However, in this work, the specific identification of each plane or orientation remains unresolved. In this regard, electron backscatter diffraction (EBSD) analysis of polycrystalline ceramics could provide valuable insights in future investigations.

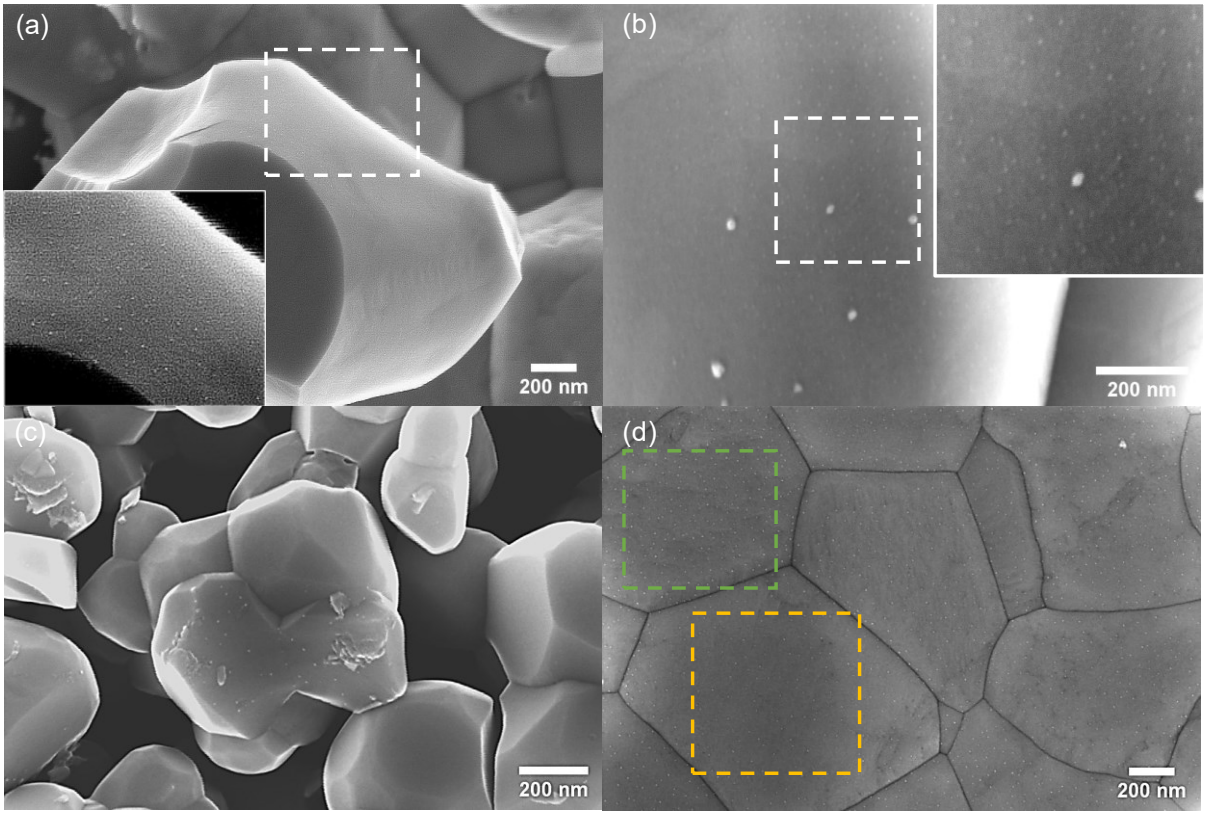


Figure 5.5 SEM images of L1.85NR samples reduced at 450°C in wet 5%H_2/Ar for 3 hours in form of powder (a-c) and pellet (d). Due to the resolution limitation of the instrument, smaller nanoparticles on certain planes/surfaces were not obvious under SEM. The inserted images in (a) and (b) are zoomed in display with adjusted brightness and contrast of the selected area marked by dash box. The scale bar of the inserted images in (a) and (b) referred to the dash box area of the original images. The green and orange dash boxes in figure (d) selected two adjacent grains which were detailed in Figure 5.6.

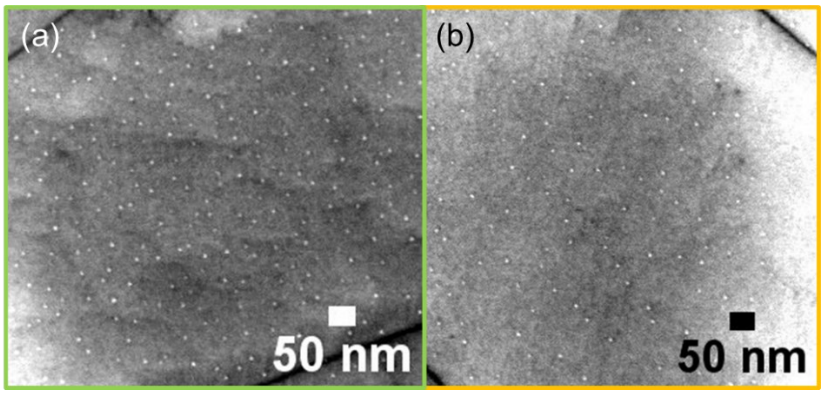


Figure 5.6 SEM images of adjusted brightness and contrast of the selected area in Figure 5.5 (d).

TEM was employed to investigate the morphology of exsolved nanoparticles in reduced A-site deficient L1.9NR and L1.85NR samples, given their small particle size. Figures 5.7 and 5.8 display TEM bright field images of L1.9NR and L1.85NR samples following reduction at 450°C in a wet 5%H_2/Ar atmosphere for a duration of 3 hours. These images reveal socketed structures, exemplified by nanoparticles indicated by yellow arrows in Figures 5.7 (a, d) and Figure 5.8 (d). These nanoparticles are partially embedded within the bulk material, suggesting a strong connection between the exsolved particles and the parent phase. Another connection was observed in Figure 5.8 (a) marked by blue arrow, which showed a structure similar to the 'pyramid-based' embedded iridium nanoparticles reported by Cali et al. [185]. Furthermore, Figure 5.7(c-d) showcases nanoparticles marked by green arrows, hinting at the presence of subsurface nanoparticles. These subsurface nanoparticles may result from subsurface nucleation or endogenous particles, as discussed in previous studies [183,186]. It is important to note that TEM has inherent limitations as it projects three-dimensional structures onto a two-dimensional image, making it challenging to precisely determine the precise location of these nanoparticles. Therefore, further investigation and validation are warranted to confirm the existence of subsurface or endogenous nanoparticles.

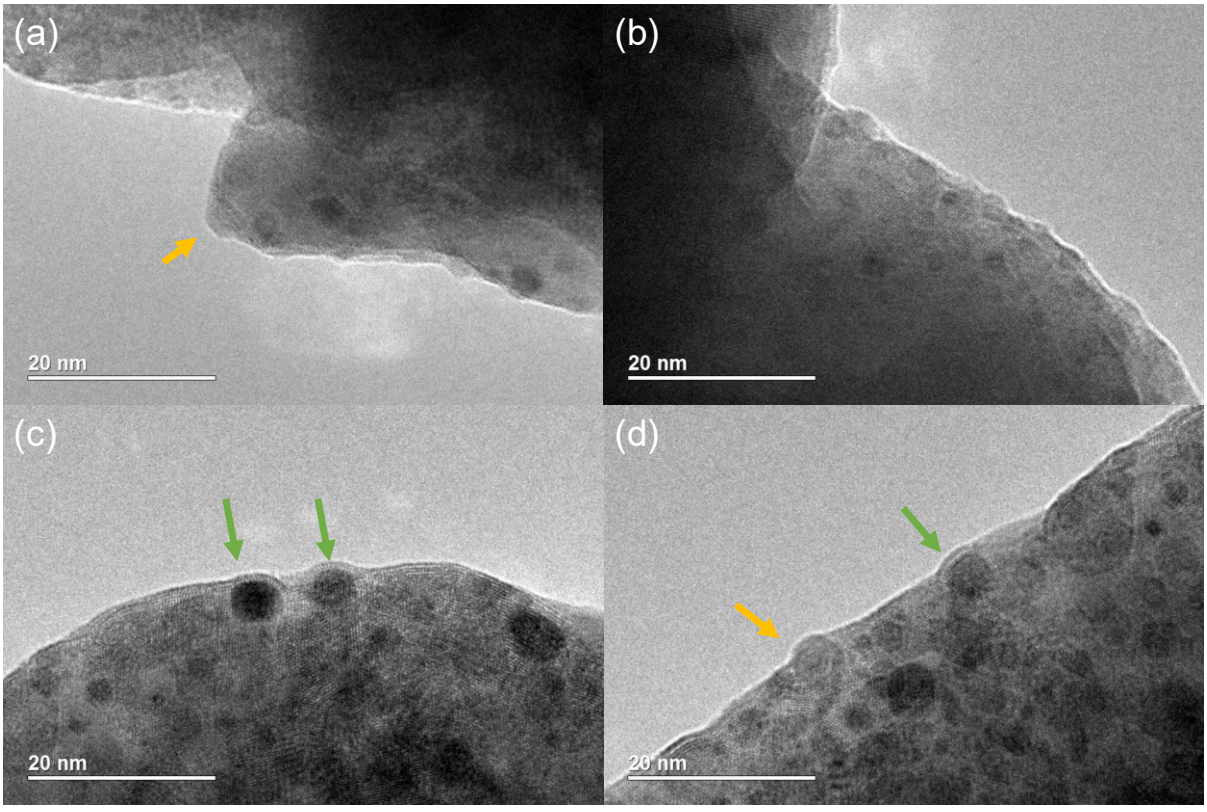


Figure 5.7 TEM bright field images of L1.9NR samples reduced at 450°C in wet 5%H_2/Ar for 3 hours. These images highlight the presence and morphology of the exsolved nanoparticles. Both socketed and 'subsurface' particles were observed in L1.9NR sample after reduction.

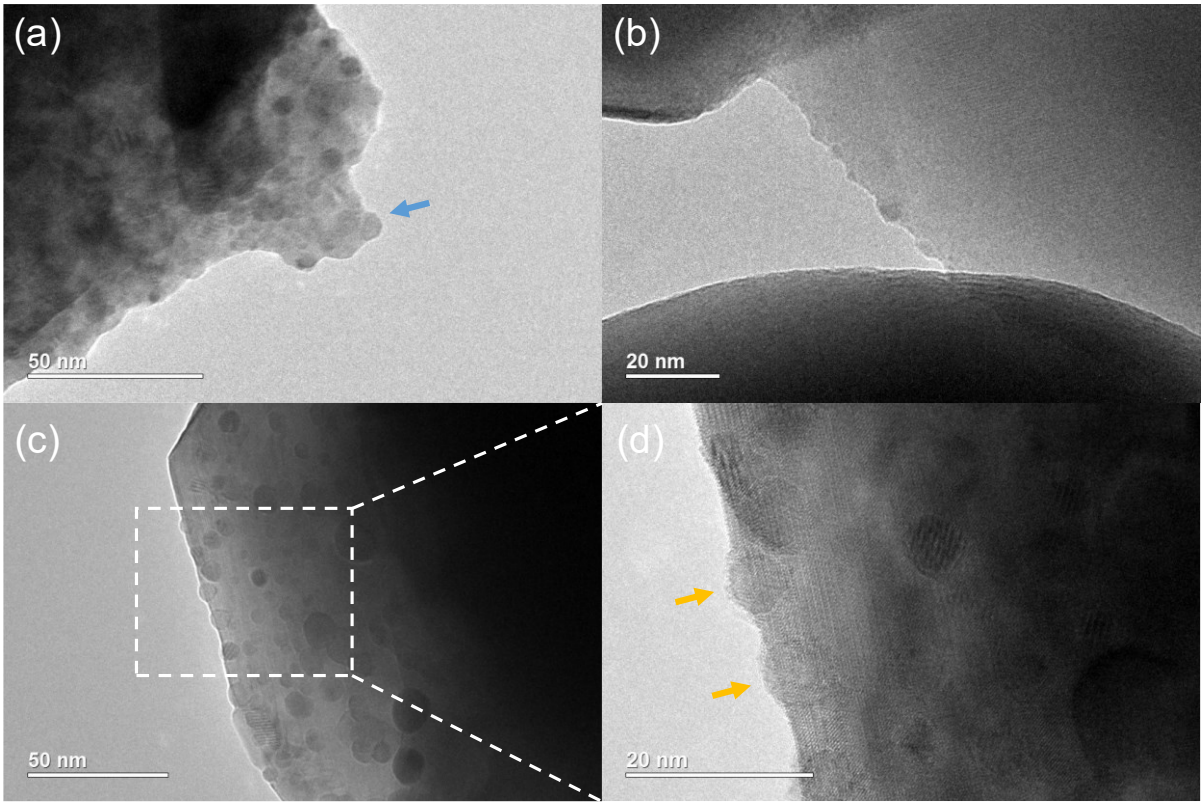


Figure 5.8 TEM bright field images of L1.85NR samples reduced at 450°C in wet 5%H_2/Ar for 3 hours. Figure (d) showed the zoomed-in image of selected area in figure (c).

From the morphology comparison of the reduced LxNR (x = 2, 1.9 and 1.85), it can be concluded that the stoichiometric sample L2NR showed rare exsolution of nanoparticles while the A-site deficient samples L1.9NR and L1.85NR showed intensive exsolution after reduction at relatively low-temperature, *i.e.,* 450°C. This indicates the A-site deficiency promoted the exsolution as expected. When the A-site deficient double perovskite phase is exposed to the reducing atmosphere, the oxygen vacancy concentration increases and the structure goes through a destabilization process, excluding the excess B-site cations:

$$La_{2-x}NiRuO_{6-\delta} \xrightarrow{\text{wet } 5\%\frac{H_2}{Ar}} \left(1-\frac{x}{2}\right) La_{2-x}NiRuO_{6-\delta} + \frac{x}{2}Ni + \frac{x}{2}Ru \qquad 5-1$$

According to the equation above, the extent of exsolution is expected to correlate with the content of A-site deficiencies. In current study, the marginal difference in A-site deficiency concentration between the L1.9NR and L1.85NR samples, which amounts to only 2.5 at%, does not readily manifest itself through observable differences in the extent of exsolution based on morphology alone. Therefore, future investigations focus on precisely identifying the effects of varying A-site deficiency content would be worthy. Additionally, it is imperative to delve into the chemical composition of the exsolved nanoparticles, given that both nickel (Ni) and ruthenium (Ru) are inclined to undergo exsolution during the reduction treatment. This

behaviour can be attributed to their high reducibility and low segregation energies, as documented in prior research studies [179,292].

5.3.2. Ni-Ru bimetallic nanoparticles

As previously mentioned, the exsolution morphology of both L1.9NR and L1.85NR samples exhibited similarities. Therefore, for the subsequent investigation, L1.85NR was adopted as a representative example. XRD, XPS and STEM-EDX were used in the study of the chemical composition of the exsolved nanoparticles.

Figure 5.9 illustrates the normalized Ru 3d and C 1s XPS spectra of the as prepared and reduced L1.85NR samples. The O 1s O-M peak was used for spectral calibration, as outlined in Section 4.5. To facilitate a meaningful comparison between the two spectra, the signals were normalized by dividing them by the Ru^{4+} $3d_{5/2}$ peak area, assuming that the Ru^{4+} content remained relatively constant within the double perovskite structure (as demonstrated in Equation 5-1). Additionally, the spectra were aligned so that the lowest points at 278 eV position remain same. From an examination of the spectral shapes, it is evident that an additional peak appeared at a lower binding energy (BE) position than Ru^{4+} $3d_{5/2}$ as reported in section 4.5, at approximately 280.5 eV. This observation is consistent with a metallic ruthenium phase, as reported by Briggs [293], signifying the exsolution of metallic Ru after reduction. Another intriguing feature is the pronounced elevation of the signal at ~289 eV BE position in the reduced L1.85NR sample compared to the as-prepared sample. This peak was attributed to the C 1s O-C=O bond, as discussed in Section 4.5. It was considered that the L1.85NR sample decorated with a substantial quantity of exsolved nanoparticles adsorbs more surface carbonate species from laboratory air compared to the as-prepared sample. This phenomenon suggests the potential enhancement of properties in applications related to catalysis and electrochemical devices.

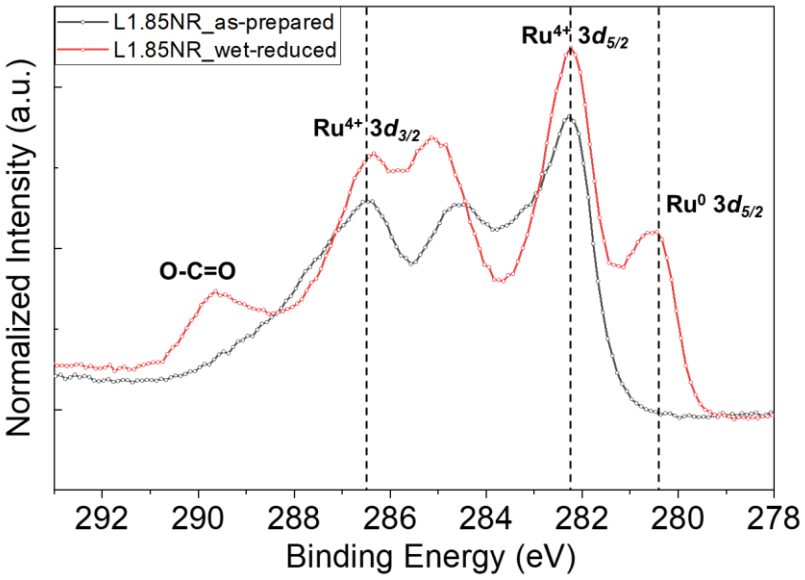


Figure 5.9 Comparison of XPS signals of Ru 3d and C 1s spectra between the as-prepared L1.85NR sample (black) and the reduced L1.85NR sample (red). Adapted from the published work under terms and conditions of CC BY 4.0 license. Copyright, 2022, authors.

Figure 5.10 presents a comparison of the Ni LMM peaks between the as prepared and the reduced L1.85NR samples. In contrast to the ruthenium spectra, there is no conspicuous evidence of a Ni metal phase observed in the Ni LMM spectrum of the reduced L1.85NR sample. In the Ni LMM Auger spectrum reported by Biesinger et al. [288], the Ni^0 LMM spectra of metal or alloy phases exhibited a distinctive peak at a kinetic energy (KE) position of 846.22 eV. However, due to the low signal to noise ratio and the limited content of exsolved nanoparticles, the evidence of exsolution is not readily discernible when examining the Ni LMM Auger spectra of these samples.

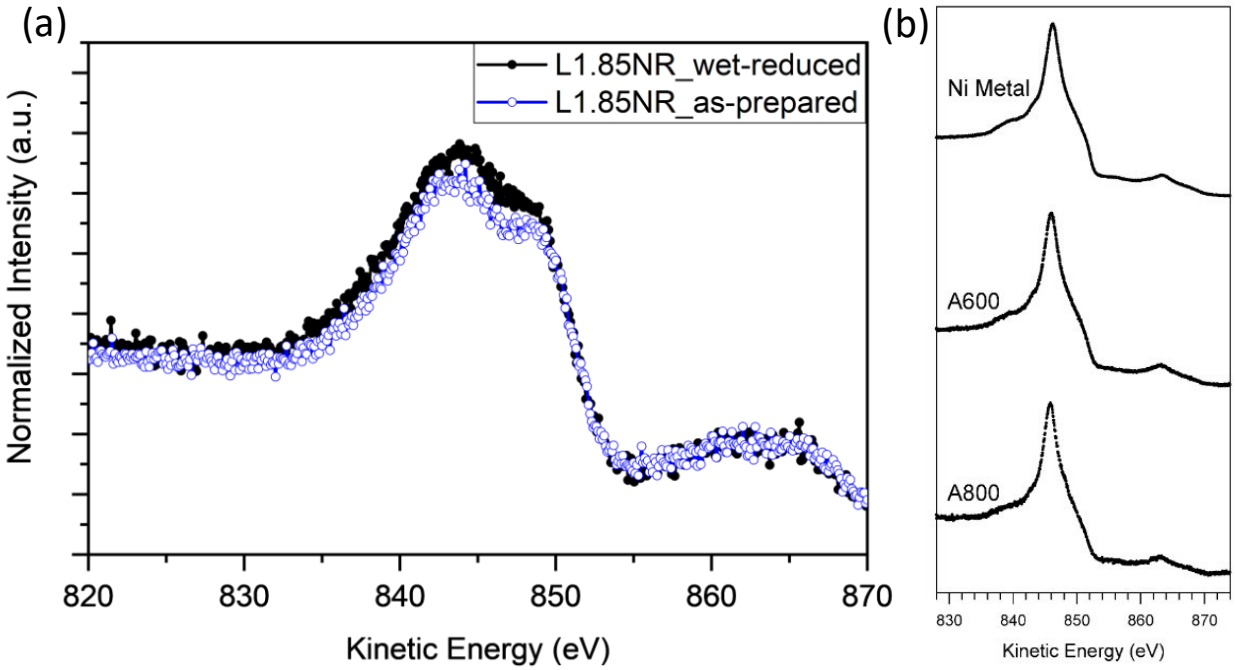


Figure 5.10 (a) Comparison of Ni LMM spectra of L1.85NR before and after reduction. Adapted from published work [254] under terms and conditions of CC BY 4.0 license. Copyright 2022, authors. (b) Ni LMM spectra of Ni^0 phases. Reused under permission from reference [288]. Copyright 2012, Royal Society of Chemistry.

Therefore, STEM and EDX was employed to investigate the elemental composition of the exsolved nanoparticles on the surface of the L1.85NR grains after reduction at 450°C in 5%H_2/Ar for 3 hours. Figure 5.11 displays the Cs probe-corrected high-angle annular dark-field (HAADF) STEM image of the reduced L1.85NR sample, clearly illustrating the socketed structure of the exsolved nanoparticles at the edge of a L1.85NR grain. The socketed structure is evident in the two particles marked by white arrows in Figure 5.11(a) and the particles shown in Figure 5.12. Consistent with the XPS analysis, the presence of ruthenium metal phase in the exsolved nanoparticles was observed. However, nickel is also present at the nanoparticle positions, while no oxygen and lanthanum enrichment were observed, indicating the presence of nickel metal phase.

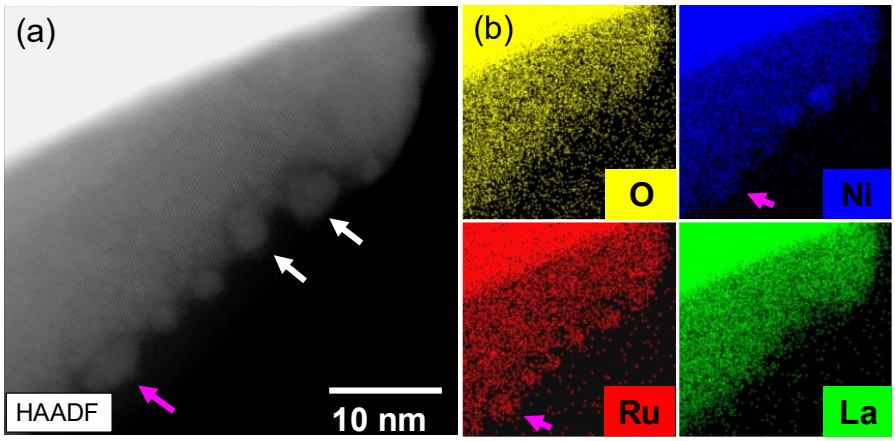


Figure 5.11 HAADF STEM images and corresponding EDX analysis maps of the L1.85NR sample reduced at 450°C in wet 5%H_2/Ar for 3 hours. The white arrows indicate the observation of the socketed structure, with a clearer display provided in Figure 5.12(d). The magenta arrow highlights the same particle analysed in Figure 5.13. Adapted from published work [272] under terms and conditions of CC BY 4.0 license. Copyright, 2022, authors.

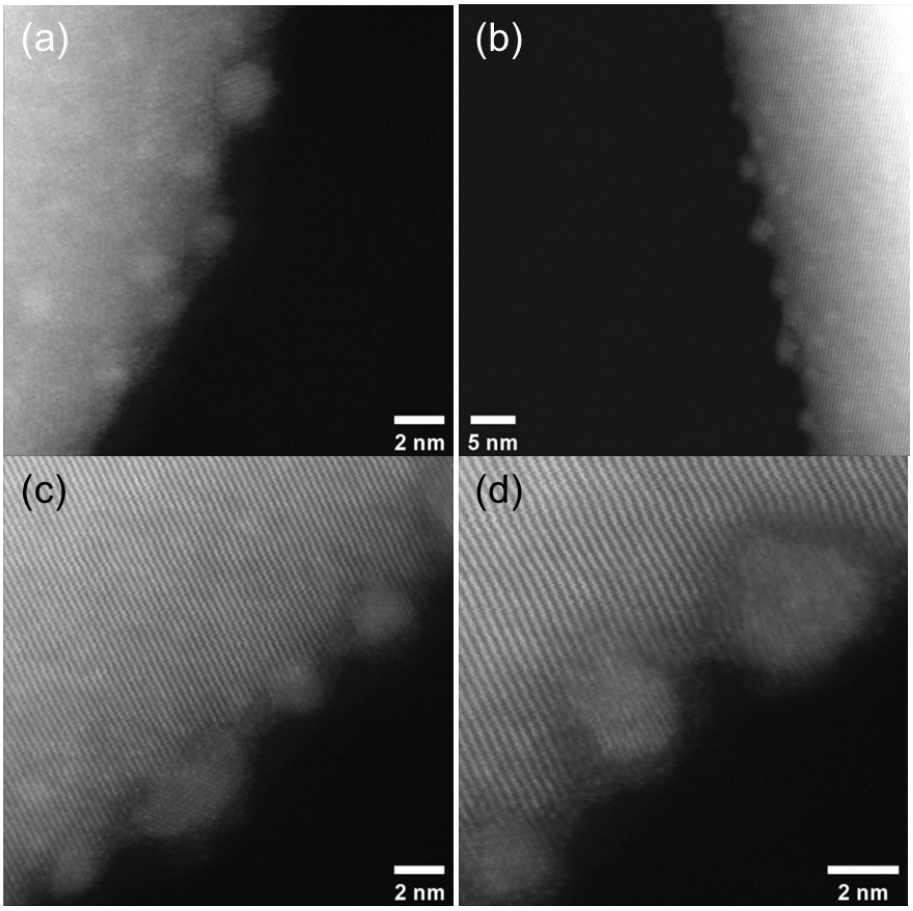


Figure 5.12 HAADF STEM images of L1.85NR sample reduced at 450°C in wet 5%H2/Ar for 3 hours, displaying details of the particle shape and particle-bulk interface.

Figure 5.13 shows the zoomed-in HAADF STEM image of the exsolved nanoparticles found on the surface of the reduced L1.85NR sample (as previously shown in Figure 5.11), along with fast Fourier transform (FFT) analysis of a selected area. The exsolved nanoparticle marked by the red dashed square in Figure 5.12(a) was chosen for detailed image analysis due to its crossed fringe pattern, which offers enhanced precision and reliability. Image analysis

was performed using Digital Micrograph [294] and ImageJ [295] software was used for the image analysis. The area within the red dashed square was converted into an FFT pattern, as displayed in the inserted image in Figure 5.12(a). The pattern was indexed to planes with [$\bar{1}$ 2 $\bar{1}$ 3] zone axis of hexagonal close-packed (hcp) structure. To provide a clearer visualization of the lattice fringes in the selected area, a filter was applied to the FFT pattern, and a corresponding reverse FFT was performed. This is presented in Figure 5.13(b). The spacing of the FFT spots corresponds to real space interplanar spacings of 2.27(1) and 1.94(1) Å, attributed to the (10$\bar{1}$0) and (0$\bar{1}$1$\bar{1}$) planes of a Ni–Ru alloy with a hexagonal lattice structure (*P 6₃/mmc*, ICSD 646325) [296]. These spacings are also evident in the measurements of 'fringes 1' and 'fringes 2' on the contrast of the reverse FFT patterns in Figure 5.13(c, d). The angle between the two sets of fringes measures 64°, further confirming the hexagonal phase of the selected nanoparticles. The monometallic phase of Ni possesses an *Fm-3m* cubic structure, while Ru exhibits a hexagonal *P6₃/mmc* structure. The hexagonal planes d-spacings of the Ru metallic phase are 1.59Å, 2.05Å, 2.14Å, and 2.39Å respectively. Upon comparison with Ru reflections, the measured d-spacings are closer to the attributed planes (2.32Å and 2.03Å). Therefore, combined with the results in Figure 5.1, the observed particles are considered to be $Ni_{0.32}Ru_{1.68}$.

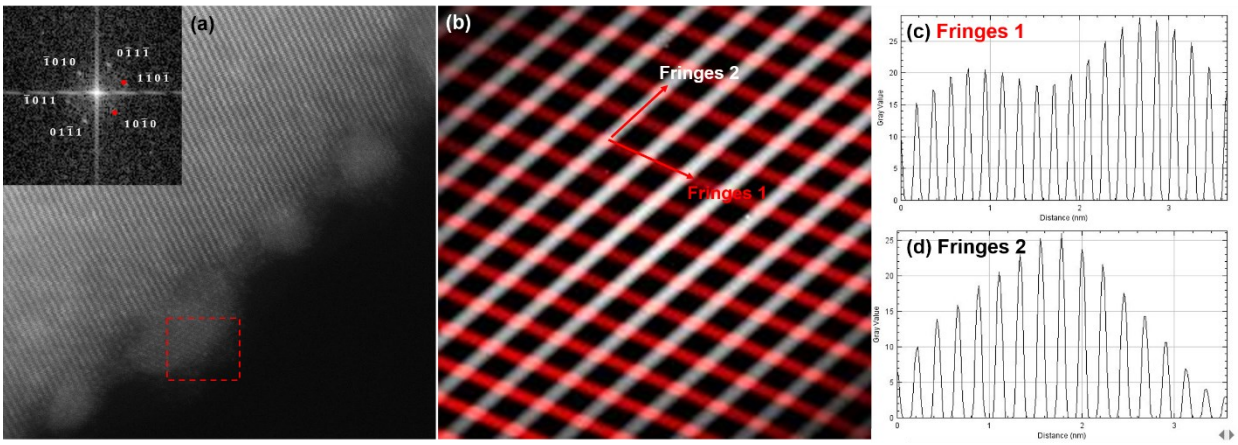


Figure 5.13 (a) HAADF STEM image of exsolved nanoparticles on the surface of L1.85NR bulk. The inset image shows the FFT pattern derived from the area marked by the red dashed square. (b) Combined patterns of two sets of diffraction fringes (Fringes1 and Fringes2) of the exsolved particles (from region marked by the red dash square). Inverse FFT of the two FFT spots marked by red dots in (a) were used to generate the pattern. Adapted from published work under terms and conditions of CC BY 4.0 license. Copyright 2022, authors. (c, d) Plots of contrast vs. spacing for Fringe 1 and Fringe 2, respectively, revealing the values of lattice spacings.

Figure 5.14 showed the XRD patterns of L1.85NR sample reduced in wet 5%H_2/Ar at 450°C for 3 hours. As expected, the XRD pattern confirms that the main double perovskite structure remains intact after reduction, with two additional features appearing at 44.1° and 44.5° in the 2θ position. These two secondary peaks are attributed to the exsolved bimetallic phase, namely, $Ni_{0.32}Ru_{1.68}$ with a hexagonal *P6₃/mmc* structure (ICSD 646325) [296] and $Ni_{0.944}Ru_{0.056}$ with a face-cantered cubic *Fm-3m* structure (ICSD 197164) [291]. This observation indicates the presence of two types of nanoparticles with varying Ni and Ru ratios in the L1.85NR sample

after reduction. The detection of the peak at 44.5° is consistent with the analysis of the STEM images (Figure 5.13). Hence, it can be concluded that the relatively low-temperature reduction in wet 5%H_2/Ar at 450°C for 3 hours leads to the exsolution of Ni and Ru cations, resulting in the formation of bimetallic nanoparticles on the surface of the L1.85NR double perovskite. As discussed in Section 2.3.2, compared to Ni, Ru possesses a lower Gibbs free energy difference for the reduction from metal oxides to metallic phase. Hence, it is suggested that Ru is easier and earlier to be exsolved. Additionally, based on the study of the exsolution of Co-doped $Sr_2Fe_{1.5}Mo_{0.5}O_{6-\delta}$[212], it has been demonstrated that the exsolution of Co facilitates Fe exsolution forming alloy nanoparticles, where Fe exhibits ΔG close to zero and is less favoured by exsolution. Therefore, it can be proposed in this work that the exsolution of Ru creates cation defects and local oxygen vacancies, further promoting the exsolution of Ni and the formation of alloy nanoparticles.

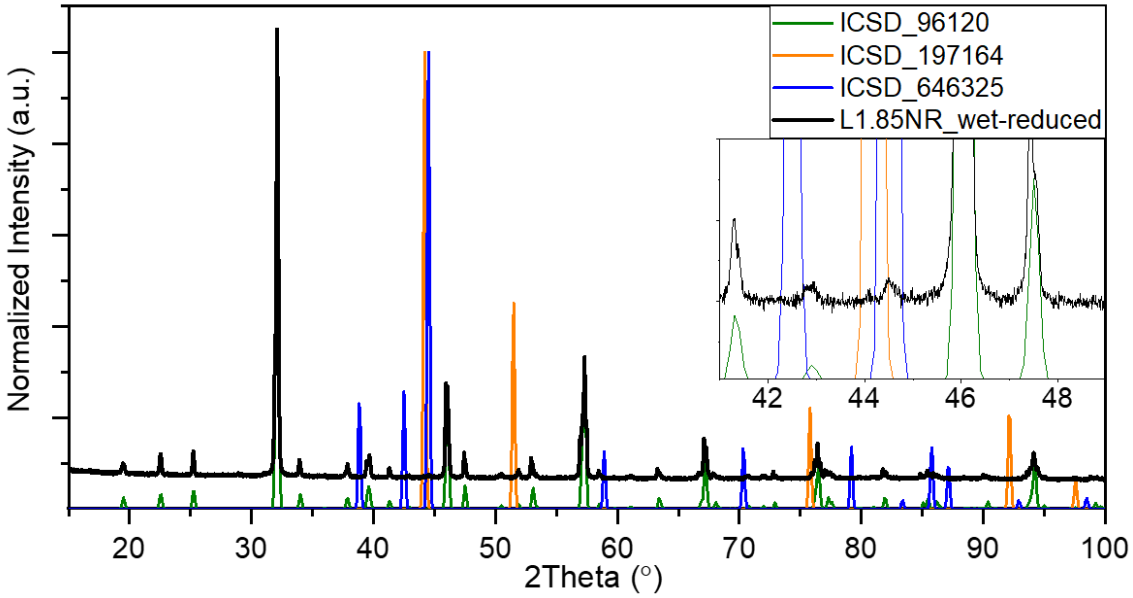


Figure 5.14 XRD pattern of L1.85NR sample reduced at 450°C in wet 5%H_2/Ar for 3 hours. The insert plots showed zoomed-in display of 2θ range 41-49°, showing the details of secondary phase diffractions. Adapted from published work [272] under terms and conditions of CC BY 4.0 license. Copyright, 2022, authors.

The HAADF STEM images and EDX maps in this subsection were obtained through collaboration with Dr R. Cai and Prof. S Haigh from University of Manchester. The author would like to acknowledge their effort and assistance in operation and collecting these data on a Thermo Fisher Titan STEM (G2 80-200) microscope equipped with a Cs probe corrector (CEOS), a ChemiSTEM Super-X EDX detector, and subsequent TEM data analysis.

5.4. Dry reduction

In addition to the investigation in wet atmosphere, the reduction in dry atmosphere has been demonstrated to be too aggressive for the stoichiometric phase L2NR in Section 5.2. While the introduction of A-site deficiency and moisture in the atmosphere has been proven effective in

preserving the double perovskite structure. However, the outcome of reducing L1.85NR at 450°C in a dry atmosphere remains uncertain. Therefore, in this section, XRD, XPS and SEM analyses were employed to explore the morphological changes in L1.85NR samples subjected to dry 5%H_2/Ar reduction.

Figure 5.15 shows the XRD pattern of the L1.85NR sample reduced in dry 5%H_2/Ar at 450°C for 3 hours. While the main diffraction peaks align with the double perovskite structure with monoclinic space group $P2_1/n$ (ICSD 96120) [265], a pronounced feature at 44.5°C is attributed to the Ni-Ru alloy phase. This observation aligns with the results obtained from wet-reduced L1.85NR samples. Further confirmation is provided by SEM images presented in Figure 5.16, which clearly depict exsolved nanoparticles on the surface of the grain. Figure 5.16 (a-d) showed the morphology of four grains of L1.85NR after dry reduction. From the inserted images, it can be observed that these nanoparticles exhibit fine sizes and a substantial population. There are also some bright species present on the surface of L1.85NR grain, as shown in Figure 5.16 (a, d), which might be due to the small fragments or contamination involved during manual griding of the parent double perovskite powder, while the actual composition of these bright species needs further study with BSE or EDX. Additionally, Figure 5.17 displays the XPS spectra of Ru 3d and C 1s orbitals for the L1.85NR ample after dry reduction. Much like the wet-reduced sample, the presence of an additional Ru^0 $3d_{5/2}$ peak at 280.76 eV is indicative of exsolved Ru metal phase.

Therefore, the results indicate that dry reduction at 450°C for 3 hours is also effective in promoting the exsolution of bimetallic nanoparticles. These findings provide important insights for subsequent investigations utilizing dry atmospheres discussed in Chapter 6.

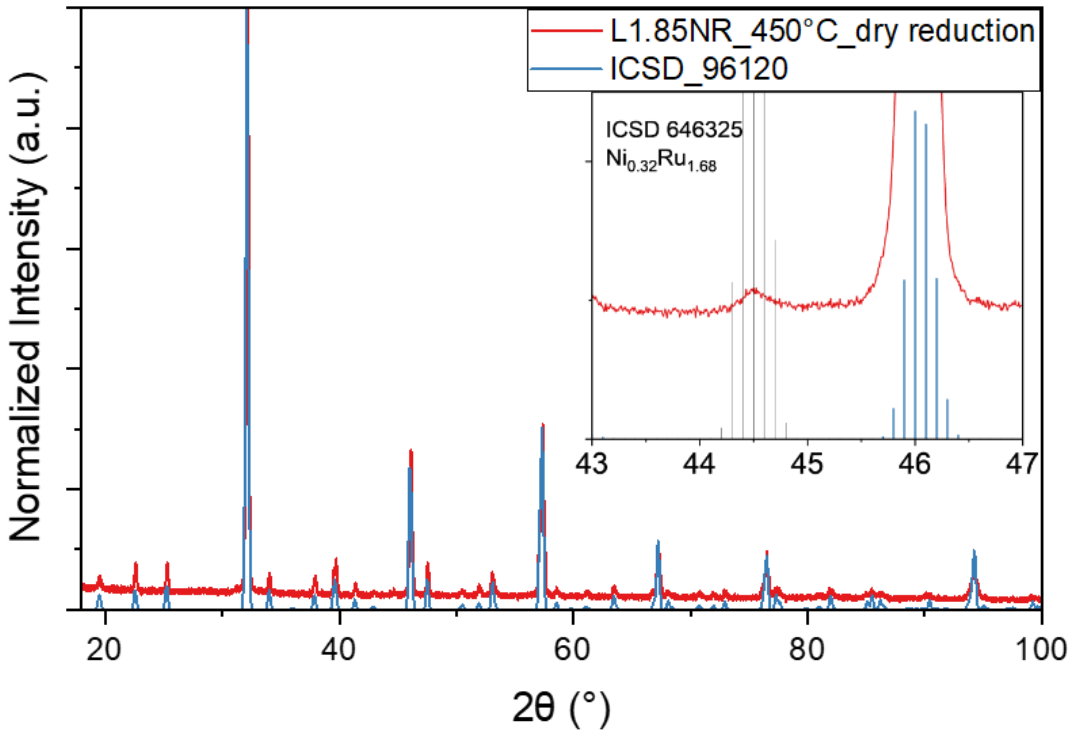


Figure 5.15 XRD pattern of L1.85NR sample reduced at 450°C in dry 5%H_2/Ar for 3 hours. The inset plots show a zoomed-in display of 2θ range 43-47°, showing the details of secondary phase diffraction.

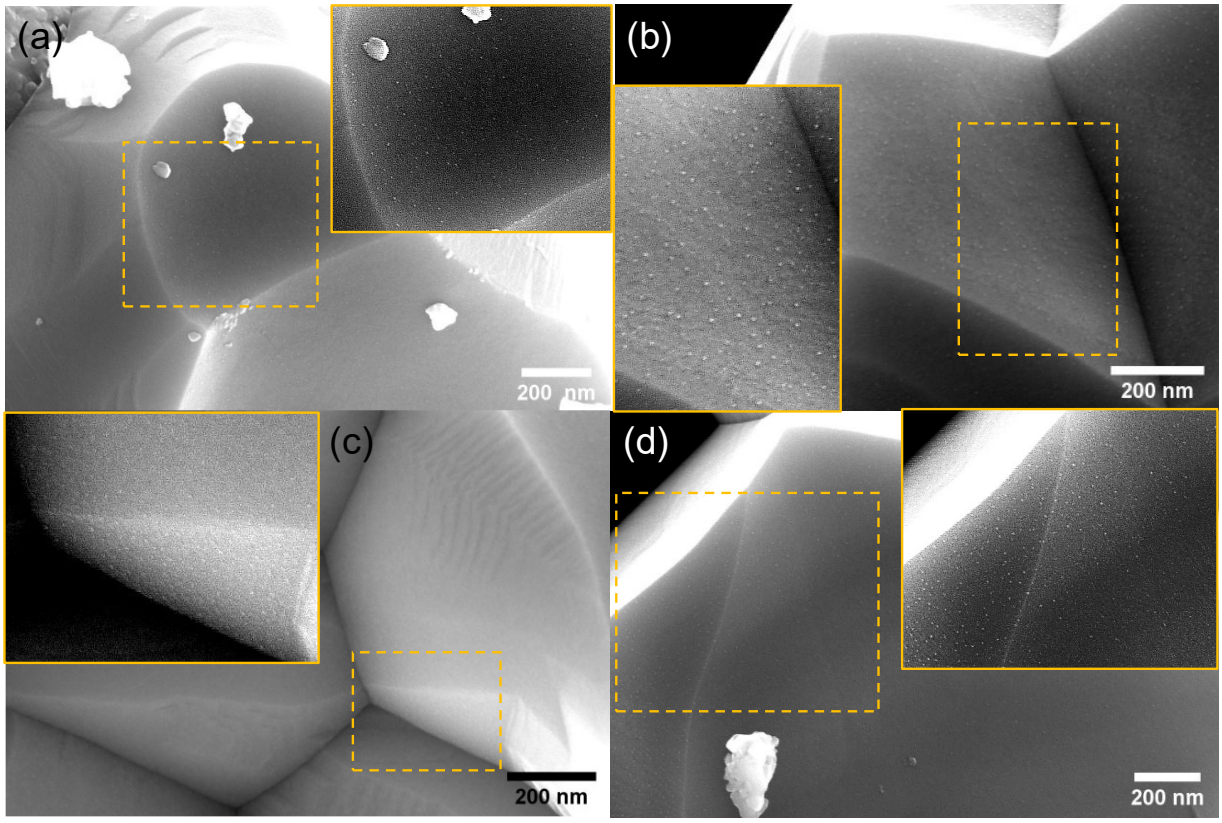


Figure 5.16 SEM images of L1.85NR sample reduced at 450°C in dry 5%H_2/Ar for 3 hours, providing a general view of four areas (a-d).The inserted images detail the presence of exsolved nanoparticles on surface of grain by sharpened display with varied brightness and contrast of the area selected by the dash box. The scale bar of the inserted images referred to the dash box area of the original images.

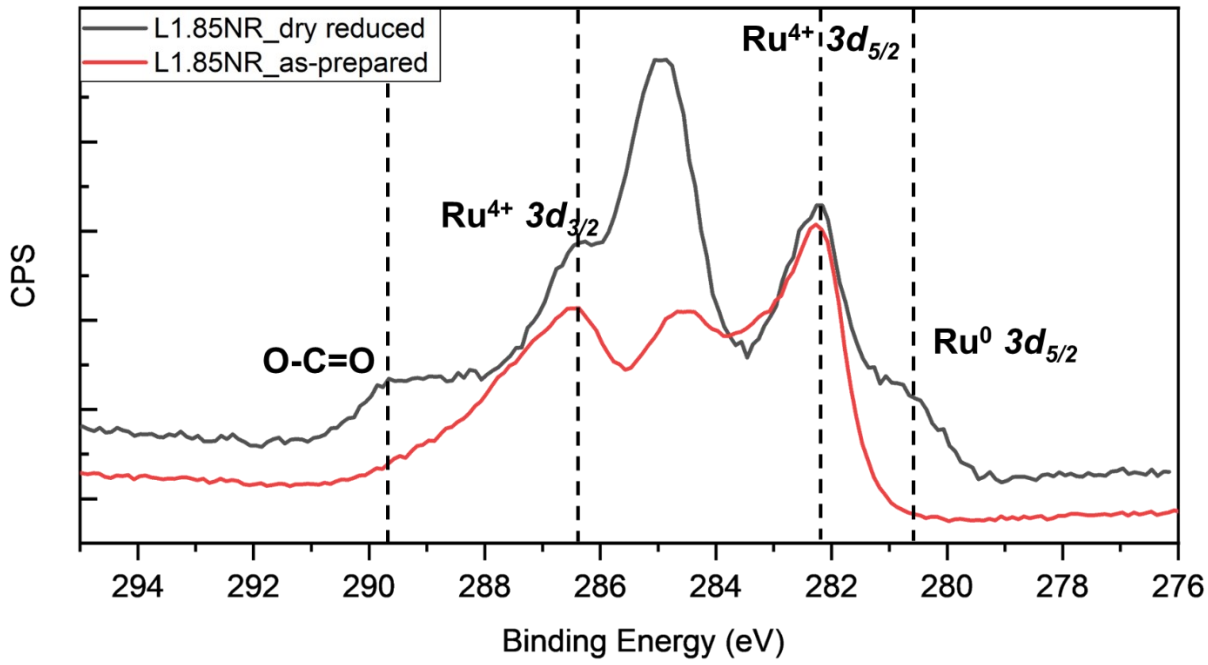


Figure 5.17 Comparison of XPS spectra of Ru 3d and C 1s spectra between the as-prepared L1.85NR sample (black) and the dry reduced L1.85NR sample (red).

5.5. Temperature-dependent exsolution

In this section, reduction experiments at temperatures below 450°C were conducted, and the morphology evolution of exsolved nanoparticles was investigated using TEM. Figures 5.18 to 5.20 present TEM images of the L1.85NR sample reduced at 350°C, 400°C, and 450°C, respectively. Intriguingly, the exsolved nanoparticles in the L1.85NR sample reduced at the lowest temperature (350°C) exhibited more uniformly distributed nanoparticles compared to samples reduced at higher temperatures (Figure 5.18). Additionally, the particle size in the higher-temperature reduced samples appeared to be larger.

As depicted in Figure 5.18 (a-d), which illustrates the morphology of the L1.85NR sample reduced at 350°C at various magnifications, an abundance of homogenous and uniformly dispersed nanoparticles was observed on the surface of the bulk grains. In contrast, the exsolved nanoparticles resulting from reduction at 400°C exhibited a wider range of sizes, as evident in different areas in Figure 5.19 (a-d). Similarly, the L1.85NR sample reduced at 450°C (Figure 5.20 a-d) demonstrated even more noticeable variations in the size of the exsolved nanoparticles. For example, this disparity can be observed in the two nanoparticles highlighted by orange arrows in Figure 5.20 (b).

Figure 5.21 summarizes the average particle size and size distribution of the exsolved nanoparticles observed in Figures 5.18 to 5.20. A total of 250 exsolved particles (over 70 for each temperature condition) were manually selected and measured using ImageJ software [295]. From 350°C to 400°C, the average size of the exsolved particles remained at approximately 2.3 nm (2.25 ± 0.05 nm at 350°C and 2.35 ± 0.07 nm at 400°C, respectively). However, when

the reduction temperature increased to 450°C, the particle size also increased to approximately 3.72 ± 0.11 nm. The size distribution showed a narrower range of particle sizes in the L1.85NR sample reduced at 350°C, while a broader distribution of particle sizes was observed in the sample reduced at 450°C. This is in agreement with previous studies that suggest exsolved particles tend to nucleate at low temperatures but favour growth at higher temperature ranges [182,200]. According to classic nucleation and growth theory, at low supersaturation levels (high temperature), crystals can grow faster than they nucleate, leading to larger crystal sizes. At low temperatures, the kinetic energy of particles in the system is relatively low. Consequently, it is more difficult for atoms or molecules to overcome energy barriers to the existed nuclei and grow larger. Therefore, higher temperatures enhance the growth rate while suppressing the nucleation rate[297].

The XRD patterns of the L1.85NR sample reduced at 350-450°C are presented in Figure 5.22. In alignment with the dry-reduced sample in Section 5.4, a diffraction peak at 44.5°, attributed to the Ni-Ru alloy phase (ICSD 64352) [296], was observed. Notably, the full width at half maximum (FWHM) of the 44.5° diffraction peak tended to be wider for the sample reduced at lower temperatures, indicating finer particle sizes. This is in agreement with the observation of TEM images (Figure 5.18-21). STEM-EDX analysis of the L1.85NR sample reduced at 350°C is depicted in Figure 5.23. Interestingly, an increase of the Ru signal is clearly observable, indicating the exsolution of Ru metal phase. However, the increase of the Ni signal in the EDX maps is only present in two nanoparticles marked by magenta dashed circles. This suggests that the exsolution of Ru and Ni may occur at different stages depending on the temperature. As discussed earlier, the different Gibbs free energy values of ruthenium and nickel oxides, as well as their reduced metal phases, indicate differing abilities of Ru and Ni to undergo exsolution. Additionally, at lower temperatures (such as 350°C), the kinetics of cation mobility are slow, hindering the formation of well-crystallized bimetallic phases. Therefore, further investigation using in-situ characterization techniques is necessary to elucidate these phenomena.

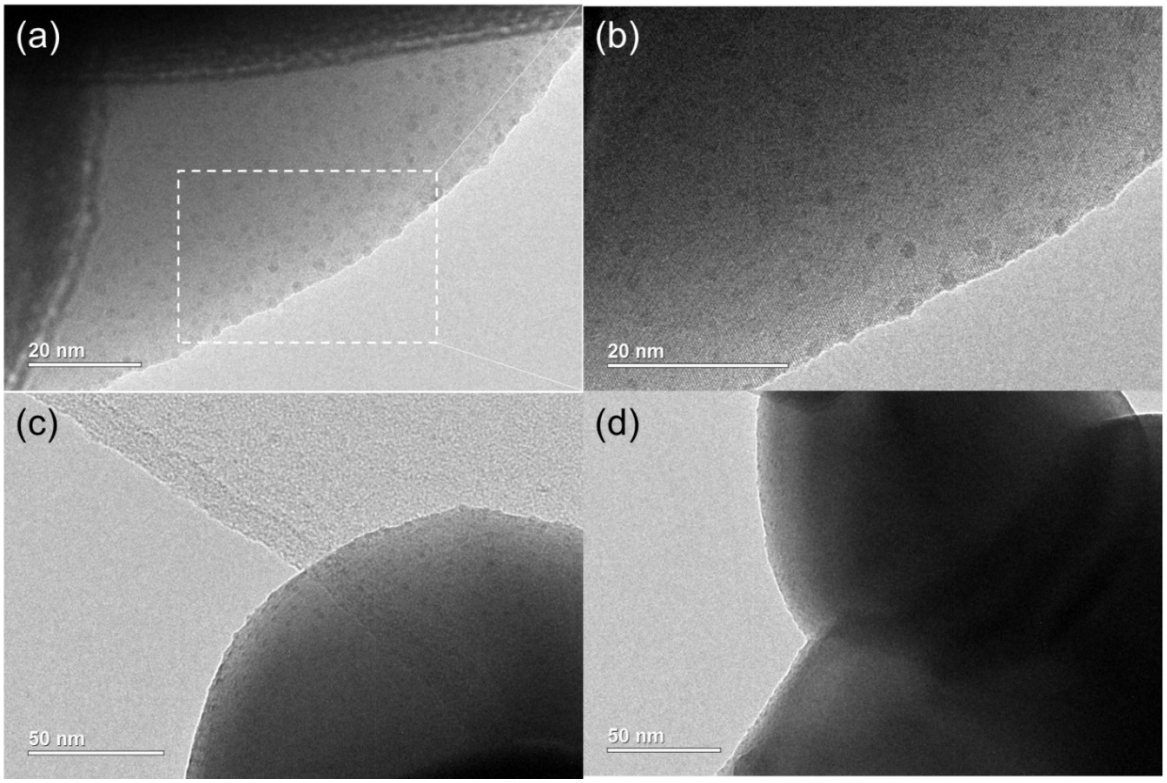


Figure 5.18 TEM images of L1.85NR sample reduced at 350°C in dry 5%H_2/Ar for 3 hours. (a) 250k; (b) 400k at the same area of (a); (c-d) 120k.

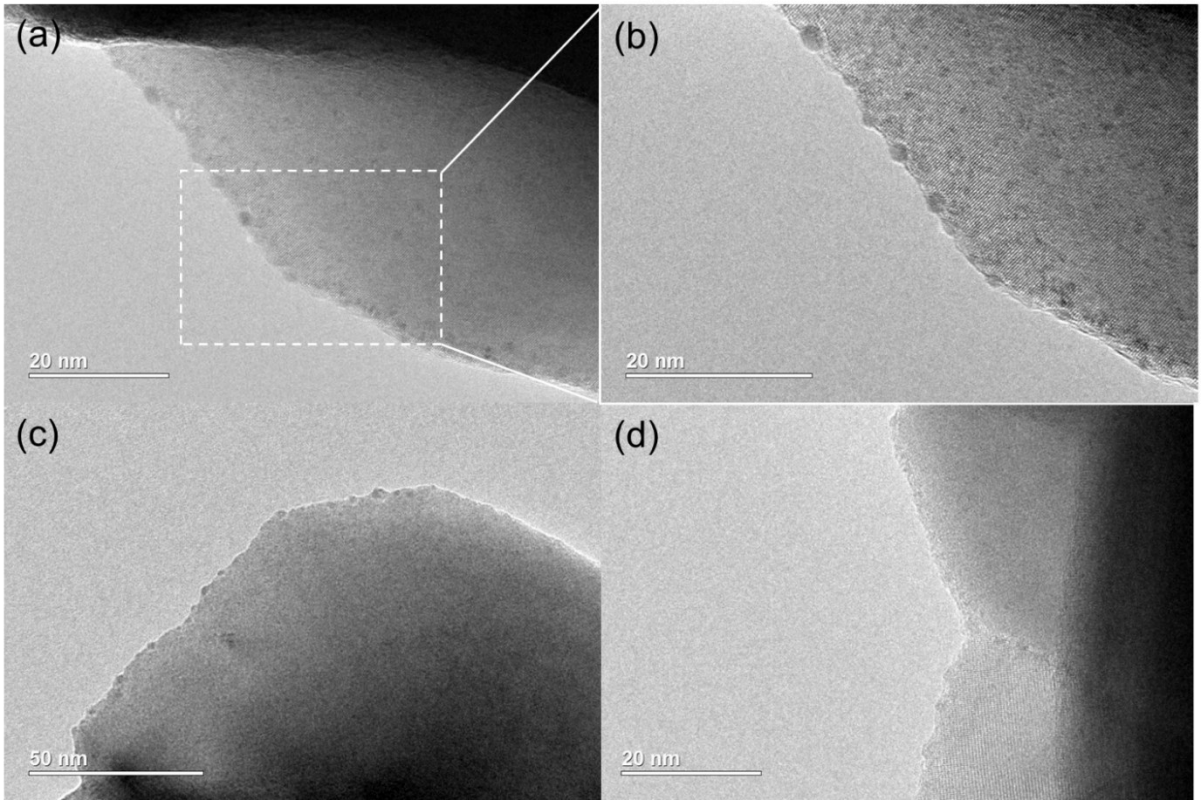


Figure 5.19 TEM images of L1.85NR sample reduced at 400°C in dry 5%H_2/Ar for 3 hours at different magnifications: (a) 300k; (b) 400k at the same area of (a); (c) 150k; (d) 300k.

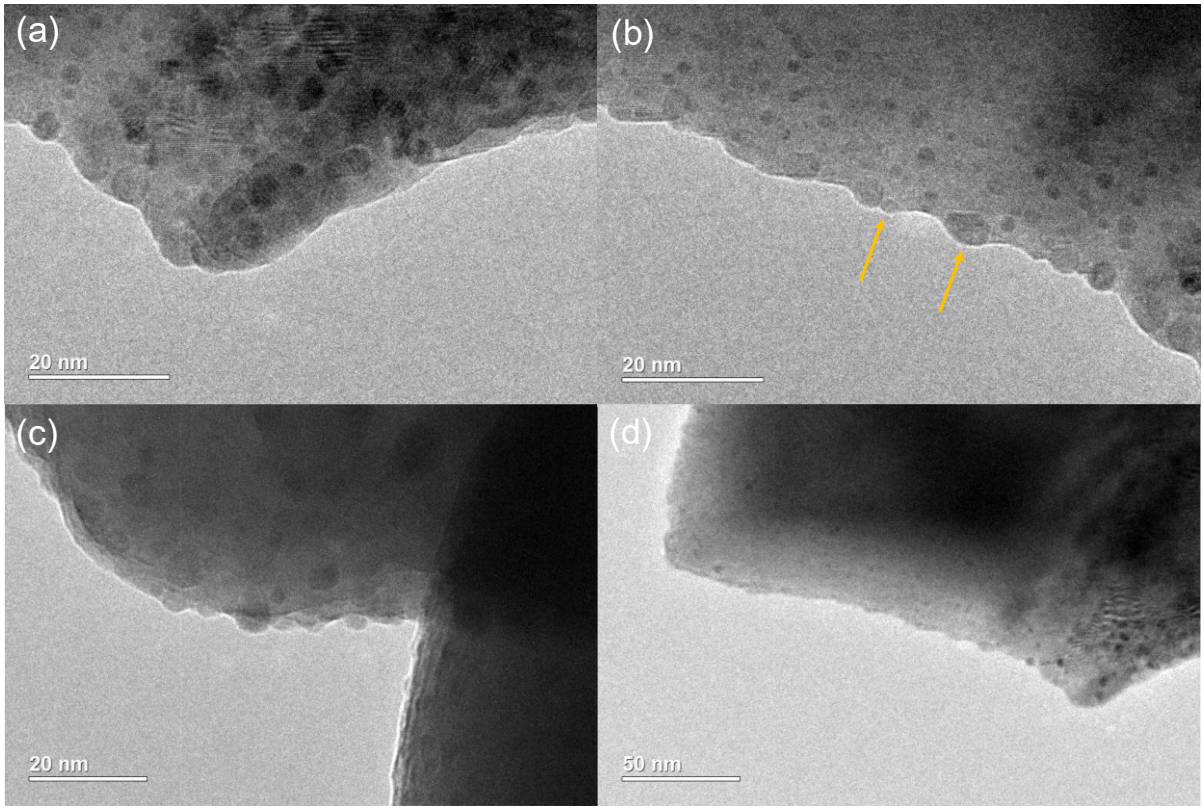


Figure 5.20 TEM images of L1.85NR sample reduced at 450°C in dry 5%H_2/Ar for 3 hours at different magnifications: (a-b) 300k; (c) 250k; (d) 120k.

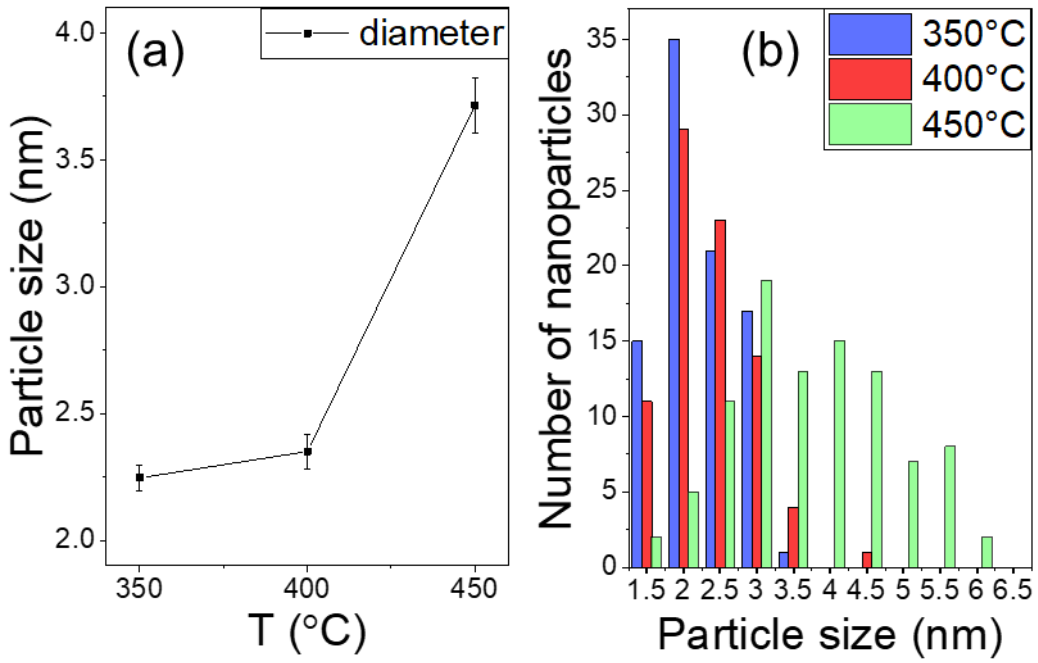


Figure 5.21 (a) Particle size evolution with increasing temperature from 350 to 450 °C. The particle sizes are average values measured by ImageJ software from a total of 250 manually selected exsolved particles (more than 70 for each temperature condition). Error bars represent the standard error of the average particle size. e) Particle size distribution of nanoparticles exsolved under different temperatures. Adapted from published work under terms and conditions of CC BY 4.0 license. Copyright 2022, authors.

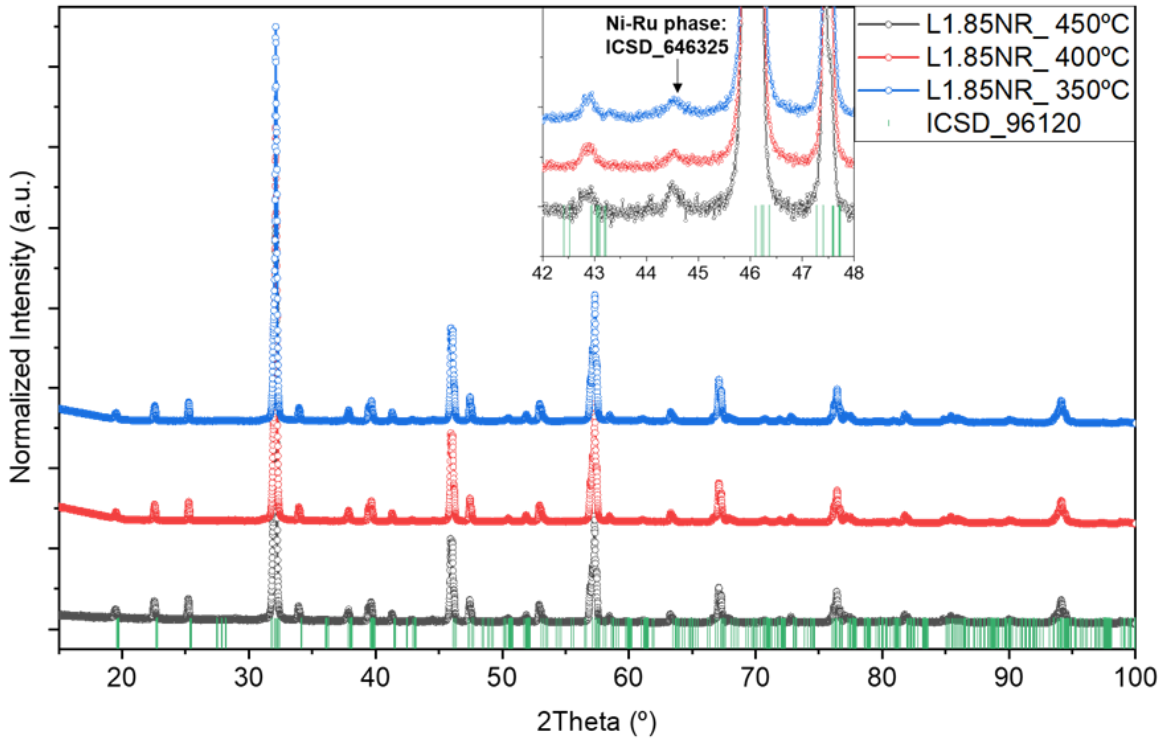


Figure 5.22 XRD patterns of the L1.85NR samples reduced in wet 5%H2/Ar at 450°C, 400°C and 350°C for 3 hours. The green droplines indicated Bragg position of double perovskite (ICSD 96120 [265]). The inset plots show the subtle peaks of the $Ni0_{.32}Ru_{1.68}$ metallic phase (ICSD 646325 [296]). Adapted from published work under terms and conditions of CC BY 4.0 license. Copyright 2022, authors.

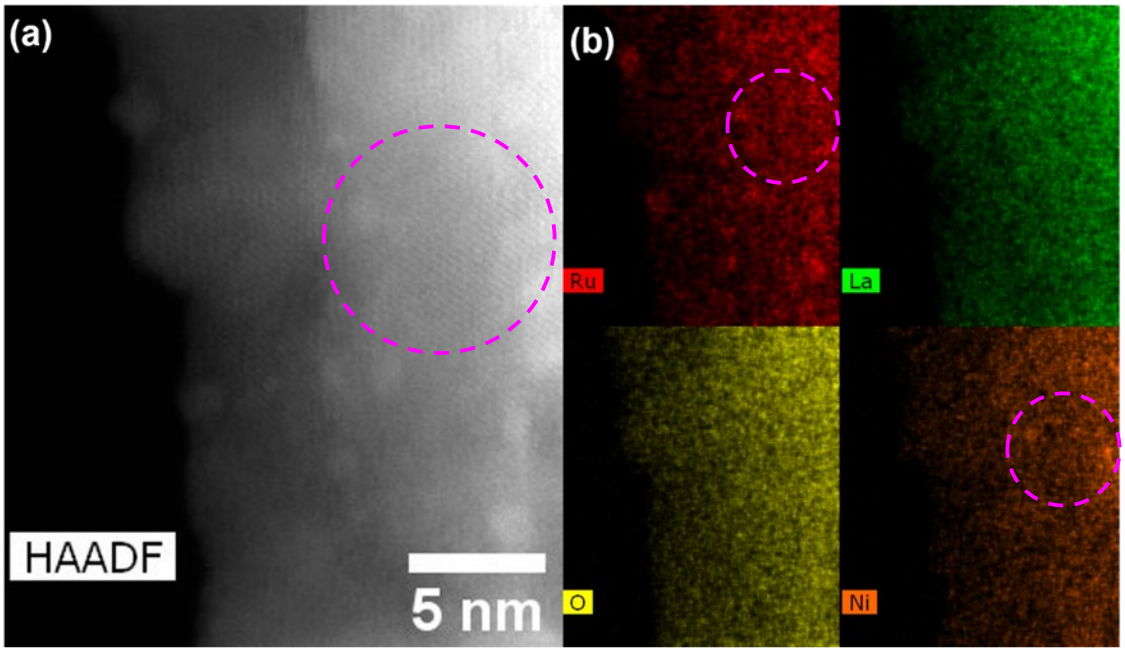


Figure 5.23 HAADF electron image of the L1.85NR sample reduced at 350°C in wet 5%H2/Ar (a) and corresponding STEM EDX maps of La, Ru, Ni and O elements in the area of the electron image (b). Adapted from published work under terms and conditions of CC BY 4.0 license. Copyright 2022, authors.

5.6. Summary and Future Work

In this chapter, the exploration was initiated by investigating the stability of both the stoichiometric double perovskite L2NR and the A-site deficient double perovskite L1.85NR

under reducing atmospheres. The decomposition as the reduction temperature increased beyond a certain threshold was observed, indicating limitations to their stability in such conditions. Subsequently, at the same reduction temperature of 450°C, the exsolution of nanoparticles in the A-site deficient samples L1.85NR and L1.9NR was observed, while the stoichiometric phase did not exhibit this behaviour, underscoring the impact of the A-site deficiency.

In a detailed study of dense L1.85NR pellets after wet reduction at 450°C for 3 hours, the variations in the populations of exsolved nanoparticles among different grains and grain orientations was characterized. Further chemical composition analysis of wet-reduced L1.85NR samples at 450°C for 3 hours revealed the presence of Ni-Ru bimetallic nanoparticles as the exsolved phase. Additionally, L1.85NR samples reduced in dry atmospheres also showed the exsolution of uniformly fine nanoparticles. However, the distinctions between dry and wet reduction in terms of particle morphology and chemical composition require additional exploration.

Finally, the evolution of exsolved nanoparticles with varying reduction temperatures in the low-temperature range was examined. Wet reduction at 350°C resulted in smaller and finer exsolved nanoparticles, with STEM-EDX analysis suggesting a higher content of exsolved Ru mono-metal phase rather than Ni-Ru alloy particles. This underscores the necessity for future investigations to discern the exsolution behaviours of Ni and Ru at varying temperatures.

Chapter 6 *In-situ* investigation of L1.85NR exsolution behaviour and its electrochemical performance

6.1 Introduction

The exsolution of Ni-Ru metal nanoparticles from the A-site deficient double perovskite has been previously demonstrated in Chapter 5. In Chapter 6, thermogravimetric analysis (TA) was employed to investigate the associated mass loss during the reduction process at 450°C. To further explore the influence of exsolution on the electrochemical performance of the A-site deficient double perovskite L1.85NR, which has potential applications as an electrode in solid-oxide cells (SOCs), this chapter utilizes *in-situ* observation of electrochemical impedance spectroscopy (EIS) and single cell testing to evaluate the exsolved nanoparticle decorated L1.85NR as a fuel electrode. In addition, *in-situ* transmission electron microscopy (TEM) and scanning transmission electron microscopy (STEM) combined with energy dispersive X-ray (EDX) analysis are employed to observe the exsolution behaviour of L1.85NR. Collaboration with Prof. Simone Mascotto from the University of Koblenz and the Deutsches Elektronen-Synchrotron (DESY) center also contributes to *in-situ* characterization, utilizing anomalous small-angle X-ray scattering (ASAXS, Appendix 1) and wide-angle X-ray scattering (WAXS) techniques.

The samples and acronyms mentioned in this chapters are: La_2NiRuO_6 (L2NR) and $La_{1.85}NiRuO_{6-\delta}$ (L1.85NR).

6.2 Thermogravimetric analysis

Thermogravimetric analysis (TA) was employed for *in-situ* observation of mass loss during thermal treatment in a reducing atmosphere. Due to instrumentation constraints, dry gas was introduced into the measurement chamber for the reduction of L1.85NR. It is noteworthy that dry reduction also promoted the exsolution of Ni-Ru nanoparticles as discussed in Section 5.4. However, given the higher hydrogen partial pressure in dry conditions compared to wet atmospheres, the mass loss behaviour should exhibit a more pronounced exsolution response.

Figure 6.1 presents the TA curves alongside the temperature program *vs*. time. During the measurement, a flow of 5%H_2/Ar gas at a rate of 60 ml/min was maintained. The L1.85NR sample was heated to 450°C at a heating rate of 5°C/min and held at this temperature for 3 hours, following the same treatment procedure discussed in Section 5.4. The TG curve (depicted in red in Figure 6.1) showed a stable mass until 300°C, where an onset of mass loss was initiated. In the thermal behaviour investigation of the stoichiometric phase L2NR in Section 4.6, a mass loss of 0.05% due to the removal of moisture and carbonates was observed in the temperature range of 200-300°C. However, in this study, no mass loss was observed in this temperature range. Instead, the initial step of mass loss measured 0.04% from

300 to 360°C, corresponding to the moisture loss observed in Section 4.6. In the subsequent treatment, the TG curve continued to decrease until reaching a stable plateau during the dwell time.

As discussed in Chapter 2, the exsolution process encompasses oxygen loss, mass diffusion, nucleation, and particle growth. Luo et al. [298] investigated Ni exsolution from stoichiometric and A-site deficient lanthanum strontium chromium oxide using TGA and reported ~2.5% total mass loss for $La_{0.6}Sr_{0.3}Cr_{0.85}Ni_{0.15}O_{3-x}$ in 5%H_2/N_2. In their subsequent work on Ni-Fe exsolution from $La_{0.6}Sr_{0.4}Fe_{0.8}Ni_{0.2}O_{3-\delta}$, they reported a mass loss of 3.48% accompanying the reduction of the materials and exsolution of Ni and Fe cations [299]. However, in this study, a much smaller mass loss was observed during the reduction of L1.85NR double perovskite.

Starting at 360°C, with increasing reduction temperature, the mass loss rate dramatically increased, reaching its maximum rate at 384°C as indicated by the peak position in the DTG curve. The total mass loss was measured as 0.37%, stabilizing after dwelling for 130 minutes. The primary cause of mass loss in the sample is the reduction of the sample and the loss of oxygen. The 0.37% mass loss suggests a loss of oxygen, l_O, at 0.11 mol per mol of the L1.85NR sample, in accordance with the equation reported by Amaya-Dueñas et al. [300]:

$$l_O = \frac{MW_{ABO_3}}{A_O} \Delta m$$

Where $\mathrm{MW_{ABO_3}}$ represents the molecular weights of the as-prepared perovskite sample; $\mathrm{A_O}$ indicates the atomic weight of oxygen and Δm is the measured mass loss.

Compared to Ni exsolution and Ni-Fe exsolution from lanthanum strontium chromates and lanthanum strontium ferrites [298–300], the oxygen loss observed in L1.85NR is smaller. This limited oxygen loss is associated with a substantial amount of exsolved nanoparticles, likely benefiting from the abundant distribution of Ni and Ru cations in the system. Moreover, the relatively small oxygen loss suggests the lattice structural stability of the double perovskites during reduction in 5%H_2/Ar at 450°C. In the isothermal stage of the reduction, the loss of oxygen reached a plateau after 130 minutes of dwelling. This plateau indicates a restricted extent of exsolution, with no further loss of mass observed, signifying no additional loss of oxygen and reduction of the double perovskite. During this stage, as no further exsolved nanoparticles were generated, the existing nanoparticles could potentially undergo agglomeration during subsequent long-term heat treatment.

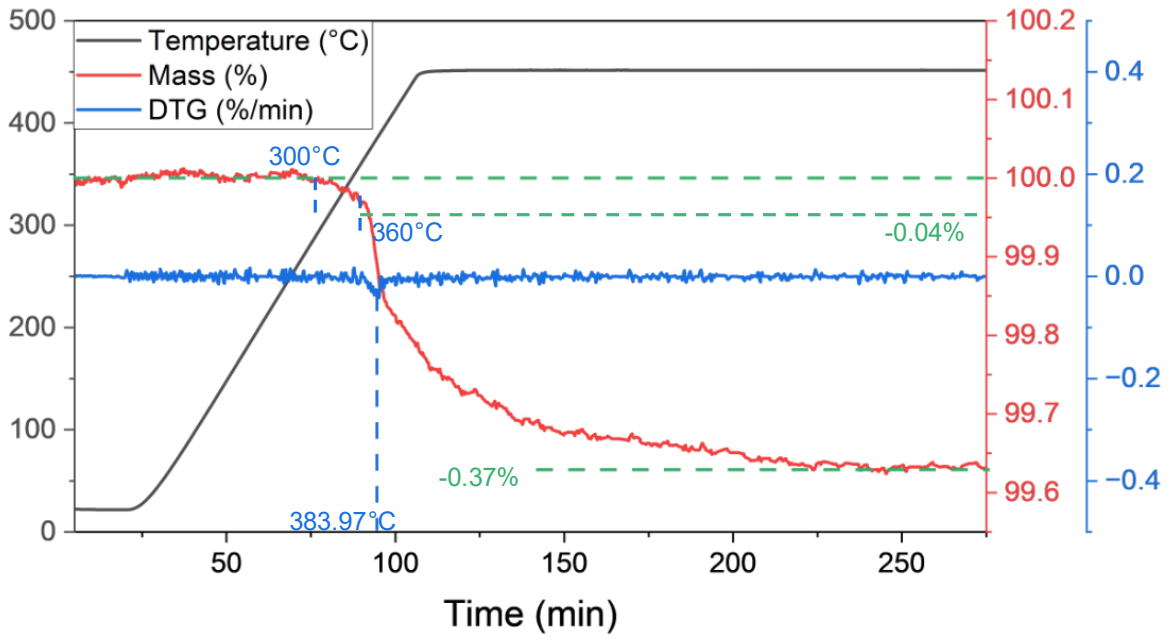


Figure 6.1 TG and DTG curves as well as corresponding temperature profiles as a function of time, encompassing both the heating and dwelling stages.

6.3 *In-situ* electrochemical impedance spectroscopy (EIS) and full cell test

To investigate the electrochemical performance of L1.85NR and the effects of Ni-Ru bimetallic nanoparticle exsolution, we conducted *in-situ* observations of electrochemical impedance responses at 450°C with wet 5%H_2/Ar supplied to the measurement condition. Additionally, single cells with lanthanum nickel ruthenates as the anode were fabricated for full-cell testing under the operating conditions of SOFCs.

6.3.1 In-situ EIS observation

Symmetric cells, specifically L1.85NR/LSGM/L1.85NR, were synthesized using the fabrication method outlined in Section 3.2.4. The testing rig employed is illustrated in Figure 3.14 in Chapter 3. The samples were heated to 450°C and allowed to equilibrate at this temperature for 40 minutes to 1 hour to ensure temperature equilibrium inside the tested cell. Impedance spectra were initially obtained in static air at open-circuit voltage (OCV), represented by black circles in Figure 6.2. In the lower-temperature range of SOC operations, the high-frequency EIS response is typically associated with electrolyte grain/grain boundaries [260]. Given the complexity of the responses from both L1.85NR electrode and LSGM electrolyte, along with the interfaces, fitting the entire spectrum with simple resistor and constant phase element (R/CPE) components posed a challenge. Since the focus of this study was primarily on the electrodes and electrode surfaces, fitting the low-frequency arc was implemented, in which the arc was fitted with a series of resistors and two R/CPE components. The fitted results are summarized in Table 6.1, with the area-specific resistance of the electrode resistance determined to be 291Ωcm^2 (R_H, R_{L-1} and R_{L-2} in Table 6.1).

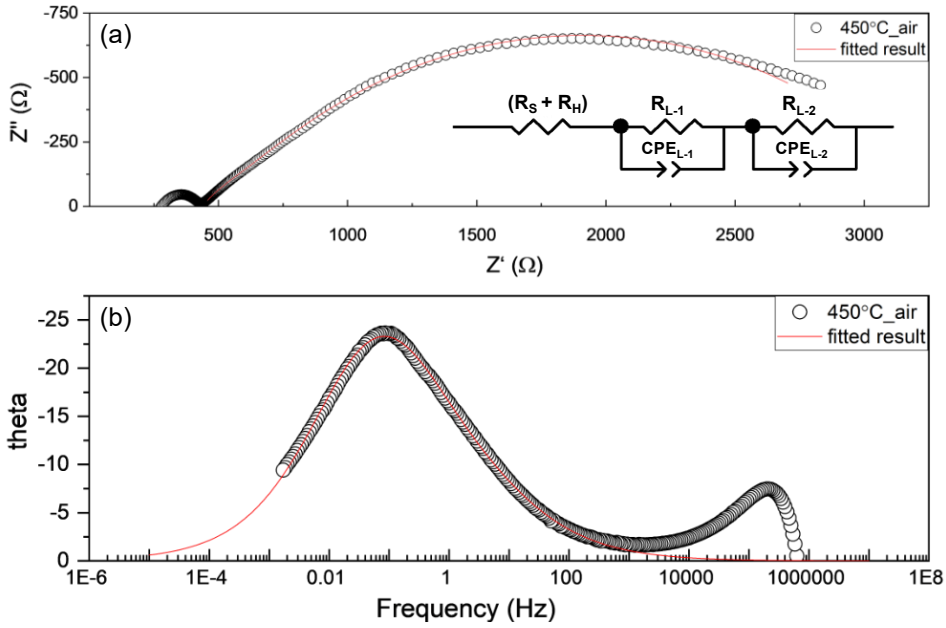


Figure 6.2 (a) Nyquist plot and the fitted result of symmetric cell in static air. The inset sketch is the equivalent circuit for fitting the second arc. (b) Bode plot (phase-shift vs log frequency) and the fitted result of symmetric cell measured in static air. The fitted result plot (red line) showed the estimated spectrum of the equivalent circuit in a wide frequency range (10^{-5} to 10^{7} Hz).

Subsequently, a wet reducing atmosphere was introduced into the testing rig for the reduction treatment, mirroring the procedures outlined in Chapter 5. A water bubbler was incorporated into the gas line, introducing approximately 3% moisture into the 5%H_2/Ar mixture. Figure 6.3 illustrates the initial EIS responses in wet 5%H_2/Ar within 40 minutes, in a comparison with the EIS spectrum obtained in air. Each spectrum, covering a frequency range from 1 MHz to 50 mHz, required 11 to 15 minutes for scanning. The starting time for each spectrum was manually recorded. It is readily noticeable that, towards the end of the first spectrum after reduction (represented by 'blue squares' in Figure 6.3), the low-frequency arc begins to bend, signifying the onset of decreasing low-frequency impedance. This bending of the low-frequency arc becomes more pronounced in the second spectrum recorded after 11 minutes of reduction (depicted as 'red triangles' in Figure 6.3). The EIS spectrum measured after 11 minutes of reduction exhibits significant reduction in the low-frequency arc during the measurement, as displayed in the inset plots of Figure 6.3. The EIS spectra acquired after 25 minutes and 40 minutes of reduction exhibit identical shapes, suggesting that the sample's response is approaching a relatively stable state. Consequently, the spectrum obtained after 25 minutes of reduction was selected for fitting with equivalent circuits.

Before proceeding with the fitting process, it is crucial to ensure that the measured sample has reached a state of equilibrium. Therefore, K-K tests, as outlined in Section 3.5.3, were employed to assess the quality of the EIS data. The relative residuals of the imaginary and real components are depicted in Figure 6.4 and are all below 1%, signifying the high quality of the EIS spectrum measured after 25 minutes of reduction. It is noteworthy that all fitted spectra in

this study successfully passed the K-K test (residual < 1%) before conducting the fitting, including the spectrum measured in static air, as shown in Figure 6.2.

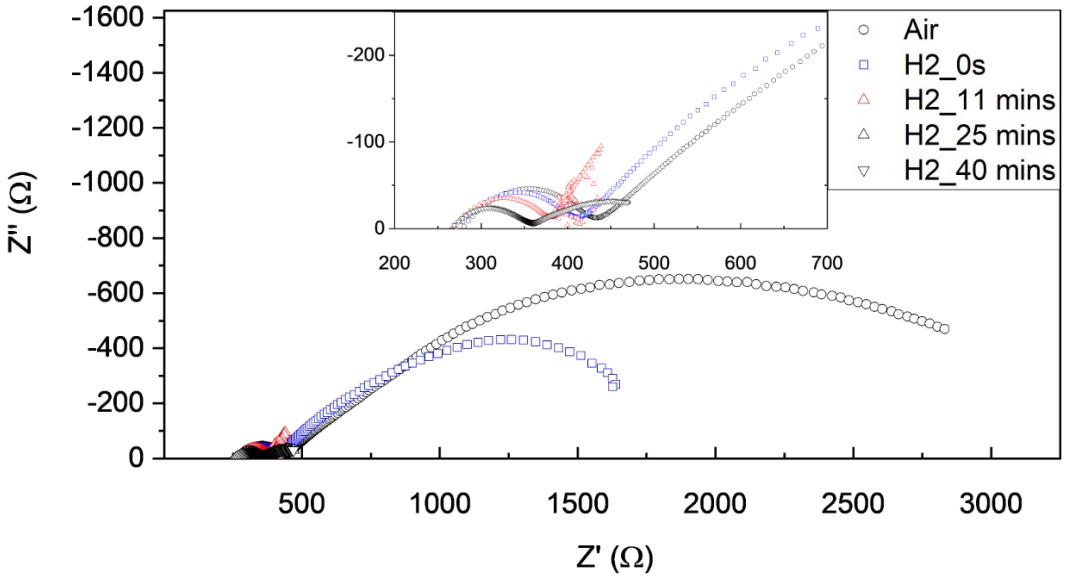


Figure 6.3 *In-situ* impedance spectra of the symmetric cell measured in air and humidified 5% H_2/Ar for different dwell times: 0, 11, 25, and 40 min.

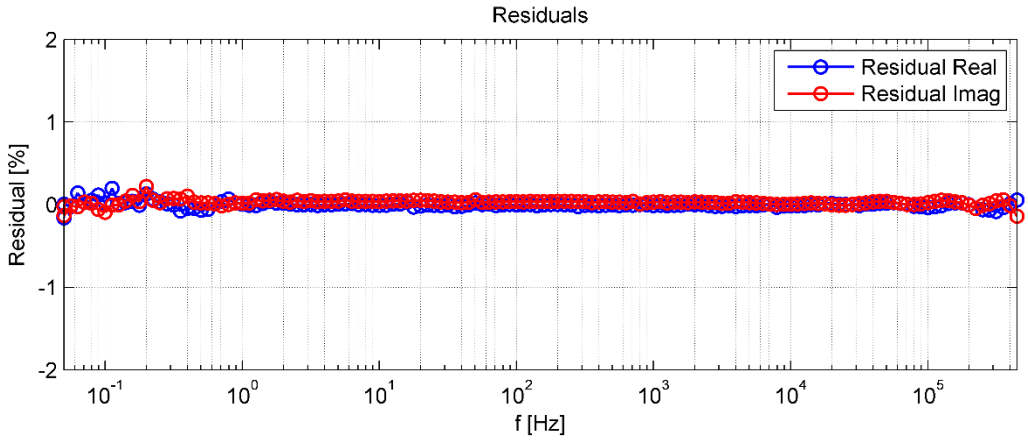


Figure 6.4 Residual plot (%) of the impedance spectrum of the symmetric cell measured in humidified 5% H_2/Ar after 25 mins of reduction.

The fitting results of the EIS spectrum of L1.85NR/LSGM/L1.85NR symmetric cells are as shown in Figure 6.5 and Table 6.1. The total area specific resistance (ASR) decreased to ~28.6 Ωcm^2. The low-frequency resistances were attributed to electrochemical reactions, while the large chemical capacitance of 10^{-2} F was reported to be related to the low oxygen stoichiometry of the electrode [301]. However, the accurate separation of each component in the EIS spectra need further systematic investigation including DRT analysis combined with varied oxygen particle pressure and temperature etc. In this work, linked with the observation of exsolved nanoparticles in Chapter 5, the decreased ASR results were considered to be a result of the reduction and exsolution. The significant decrease of the impedance indicates that the

exsolved nanoparticles on the surface of the electrode grains improve the density of triple-phase boundaries and promoted the hydrogen oxidation kinetics.

As discussed in Section 2.3, the exsolution process involves the reduction of the perovskite, leading to the formation of oxygen vacancies and cation vacancies, followed by cation diffusion, nucleation, and growth. Consequently, the electrical conductivity of the electrode is expected to alter during the exsolution process, which could be reflected in the EIS response.

Theoretically, the creation of B-site vacancies and oxygen vacancies would hinder the electronic hopping of charge carriers[302,303]. However, in the study of Ni exsolution, Yu et al.[304] found a significant increase in the conductivity of the $La_{0.2}Ba_{0.7}Sn_{0.9}Ni_{0.1}O_{3-\delta}$ support film (from 54 to ~700 $S \cdot cm^{-1}$) due to electron conduction between delocalized Sn5s orbitals in the stannate support with Ni nanoparticles. Similarly, Wang et al.[305] utilized *in-situ* XPS coupled with DC conductivity measurement to investigate Fe exsolution from $La_{0.6}Sr_{0.4}FeO_3$ films. They observed that Fe^0 exsolution profoundly modulated the bulk conductivity of the LSF film, attributing the more than 100 times higher electrical conductivity enhancement by localized enriched electronic charge carriers in the percolation channel and the formation of heterostructure interfaces.

In this work, the exsolution of Ni and Ru cations would lead to the formation of oxygen vacancies ($V_O^{\cdot\cdot}$) and cation vacancies (V_{Ni}'' and V_{Ru}'''), theoretically increasing ionic conductivity[306] but suppressing electronic conductivity. Additionally, the presence of partially reduced Ru^{4+} would produce localized electronic charge carriers. Therefore, it is necessary to investigate the physical phenomena and contributions to the decreased impedance through equivalent circuit fitting, as discussed below.

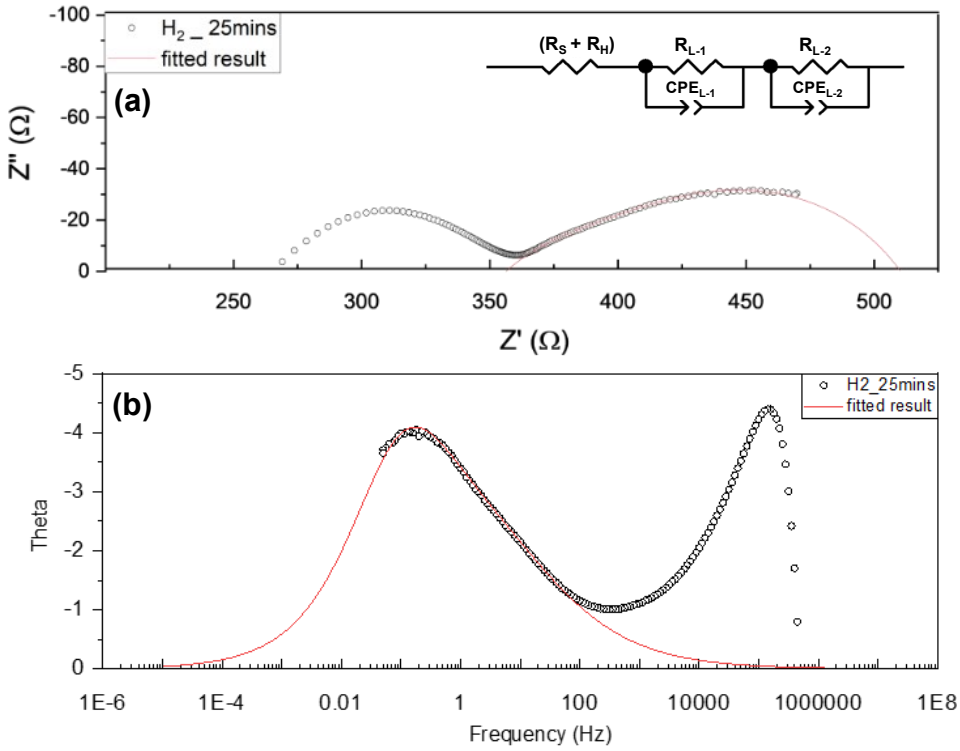


Figure 6.5 (a) Nyquist plot and the fitted result of symmetric cell reduced in wet 5%H_2/Ar for 25mins. The inset sketch is the equivalent circuit for fitting the second arch. (b) Bode plot (phase-shift vs log frequency) and the fitted result of symmetric cell reduced in wet 5%H_2/Ar for 25mins. The fitted result plot (red line) showed the estimated spectrum of the equivalent circuit in a wide frequency range (10^{-5} to 10^{7} Hz). Adapted from the published work [272] under terms and conditions of CC BY 4.0 license. Copyright 2022, authors.

Figure 6.6 depicts the impedance behaviour of the symmetric cell, showing a slight increase over the following 12 hours of reduction. During this 12-hour reduction period, the low-frequency arc gradually increased to 41.5 Ωcm² (as documented in Table 6.1). This phenomenon may be associated with factors such as a reduction in electronic conductivity, alterations in surface oxygen stoichiometry, or the loss of active surface area due to particle agglomeration as observed in the TG analysis presented in Figure 6.1. To pinpoint the exact cause and devise potential solutions, further investigations are needed to optimize cell structure, electrode microstructure and electrode composition.

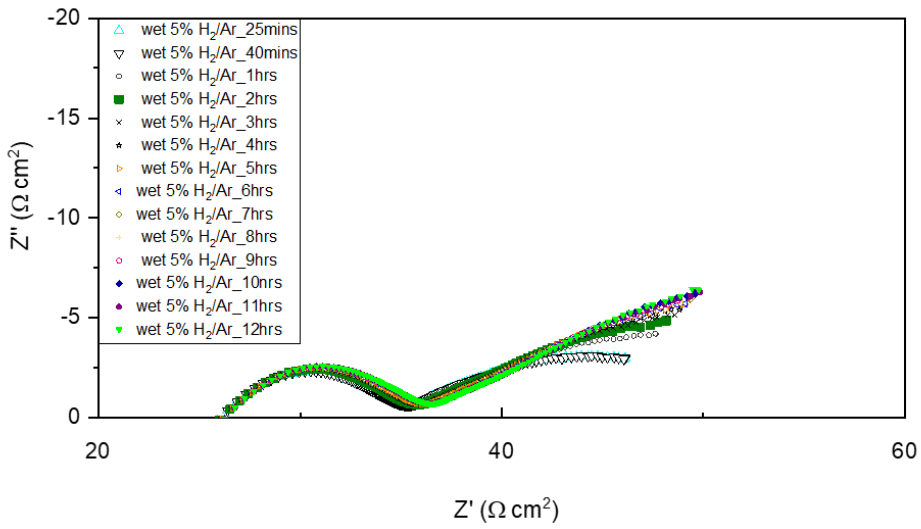


Figure 6.6 *In-situ* impedance spectra of the symmetric cell measured in wet 5% H_2/Ar for different dwell times from 25 mins to 12 hours. Adapted from the published work [272] under terms and conditions of CC BY 4.0 license. Copyright 2022, authors.

Table 6.1 Fitting results of the impedance spectrum measured after different reduction times. R_s denote ohmic resistance read through the intercept of the impedance arcs. R_H denote the resistance of the high-frequency part of the spectrum. R_{L-1}/CPE1 and R_{L-2}/CPE2 are resistances, and constant phase elements contribute to the low-frequency part of the spectrum. Adapted from the published work [272] under terms and conditions of CC BY 4.0 license. Copyright 2022, authors.

Reduction time (mins)	R_s (Ω cm^2)	R_H (Ω cm^2)	R_{L-1} (Ω cm^2)	CPE1-T (F)	CPE1-P	C_{L-1}(F)	R_{L-2} (Ω cm^2)	CPE2-T (F)	CPE2-P	C_{L-2}(F)
Air	27.5	15.8(5)	6.7(2)	0.0015(1)	0.61(2)	4.23×10^{-4}	268.8(9)	0.0014 (1)	0.567 (3)	3.78×10^{-3}
25	25.9	13.6(8)	6(1)	0.0043(3)	0.46(3)	9.1×10^{-4}	9(1)	0.0015(3)	0.63(3)	1.78×10^{-2}
720	26.2	9.4(1)	5.1(8)	0.0043(1)	0.43(3)	4.72×10^{-4}	27(2)	0.011(3)	0.55(1)	2.73×10^{-2}

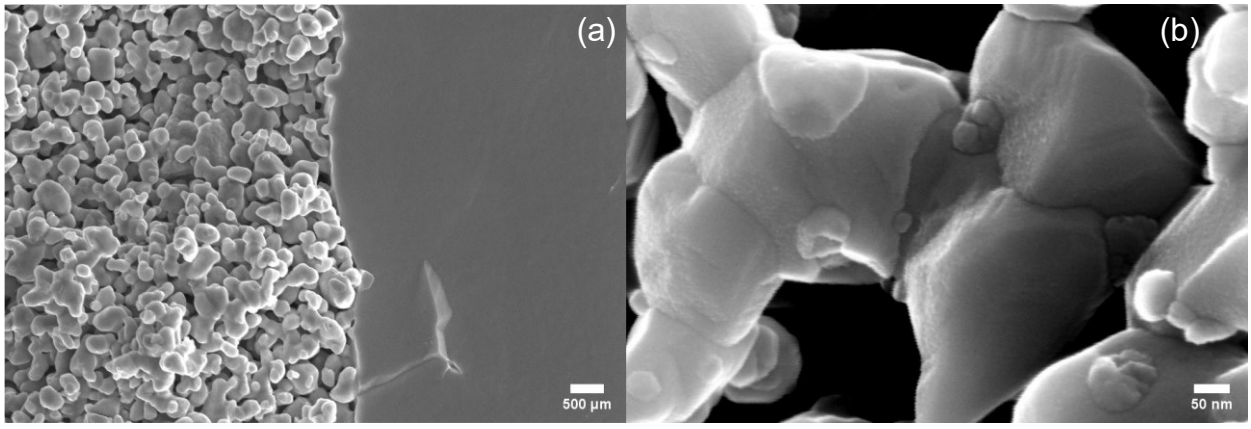


Figure 6.7 SEM images of the microstructure of L1.85NR/LSGM/L1.85NR symmetric cell before (a) and after (b) EIS measurements.

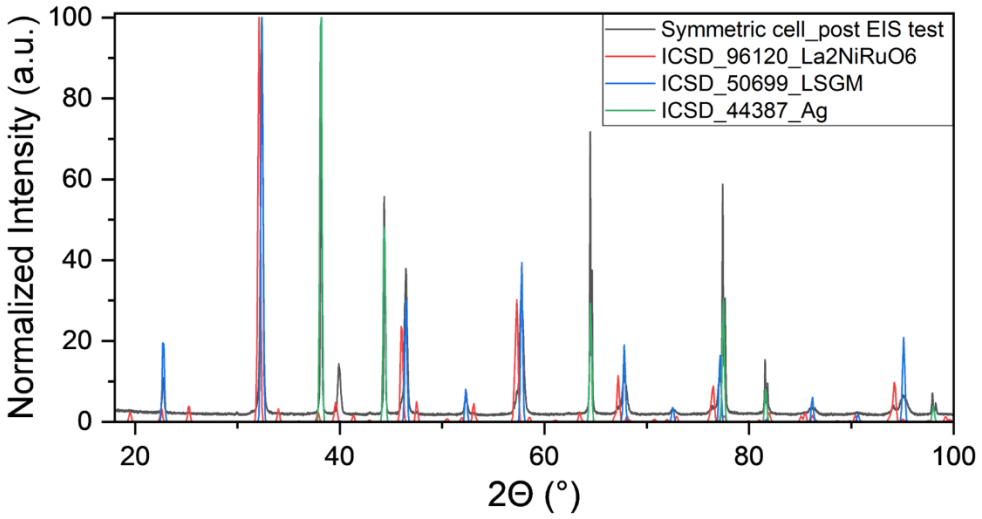


Figure 6.8 XRD pattern of the symmetric cell after EIS test in wet 5%H_2/Ar.

Figure 6.7 presents SEM images of the L1.85NR electrode surfaces before and after the EIS measurement, revealing a roughened surface after 12 hours of reduction in wet 5%H_2/Ar. This roughness can be attributed to the extensive exsolution process. The XRD pattern in Figure 6.8 confirms the chemical compatibility and stability of LSGM and Ag paste with the L1.85NR electrode during the reduction and measurement. However, the diffraction peak of the exsolved nanoparticles is not very prominent, possibly due to the low fraction of exsolved nanoparticles and limitations in the detection capabilities of the diffractometer.

Combining these observations with those from Chapter 5 and the SEM images, it can be concluded that during the reduction of L1.85NR, Ni and Ru cations exsolve. The observations in Figure 6.3 indicate fast kinetics of particle exsolution, occurring within just 11 minutes of exposure to the reducing atmosphere. Furthermore, the decrease in impedance curves demonstrates approximately a 90% enhancement in the ASR of the materials, suggesting the potential application of Ni-Ru nanoparticle-decorated L1.85NR as an electrode in SOCs.

6.3.2 Fuel cell test

In addition to the EIS observations of the symmetric cell, full cells with a configuration of LxNR(x = 2 and 1.85)/ $La_{0.8}Sr_{0.2}Co_{0.8}Fe_{0.2}O_{3-\delta}$ (LSCF8282) were also investigated under the working conditions of SOFCs. The cell fabrication methods were detailed in Chapter 3. A similar setup to the EIS measurement, as shown in Figure 6.9, was employed for the single full cell measurements. The microstructure of the fabricated cell is presented in Figure 6.10. The current collector had not been added yet to provide a clearer view of the electrode and electrolyte under SEM. The electrodes were both 30-40 μm thick (Figure 6.10 a, b). The cross-section view (Figure 6.10, c, e, and f) and top view (Figure 6.10, d) confirmed the presence of sufficient porosity for the gas to reach the triple phase boundary (TPB) and establish connections between electrode particles. However, it is observed that the population of active

sites at the triple phase boundary is limited in Figure 6.10 (c and f), suggesting the need for further optimization in the future.

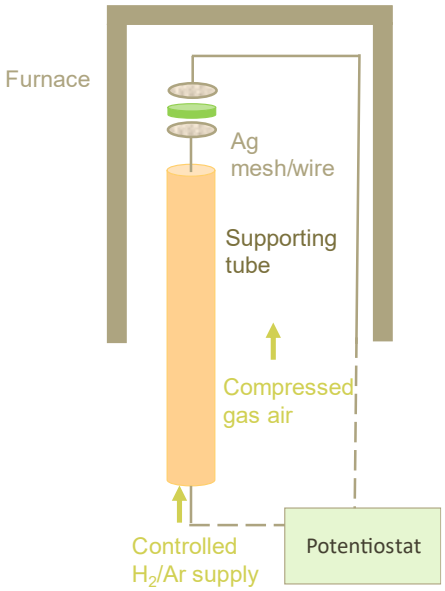


Figure 6.9 Schematic illustration of testing rig set-up for the single cell test.

Two single cells with L1.85NR and L2NR as fuel electrodes, respectively, were initially exposed to wet 5%H_2/Ar to promote the exsolution of Ni-Ru nanoparticles. *In-situ* EIS measurements, similar to the symmetric cell measurements, were also conducted as shown in Figure 6.11. The single cells were heated to 450°C, and the fuel electrode (L1.85NR) was reduced in wet 5%H_2/Ar for 130 minutes. Ceramic sealant was used for making sure the separation of the fuel gas and air to avoid leakage. Consistent with the findings from the symmetric cell study, a decrease in impedance was observed during the reduction of the fuel electrode (L1.85NR). However, for the single cell with the stoichiometric phase L2NR as the fuel electrode, no such decrease in impedance was observed during reduction. This is consistent with the observations in Section 5.3.2, where it was shown that A-site deficiency promotes the exsolution of B-site cations, while the stoichiometric phase exhibits rare exsolution. Additionally, the initial EIS spectra of the L1.85NR/LSGM/LSC82 single cell showed lower ASR compared to L2NR/LSGM/LSCF82 cell. This is due to the introduction of A-site deficiency in the double perovskite, which enhances the ionic conductivity of the material, as reported in previous studies [307,308]. However, it's worth noting that the creation of B-site deficiencies has been reported to impede electronic charge carriers [307], because electronic charge carriers typically conduct through 'B-O-B' site hopping [302,303,309]. This provides insights into the EIS observations of symmetric cells subjected to 12 hours of reduction. Additionally, the decrease in conductivity of L1.85NR during the long-term reduction suggests that L1.85NR is governed by p-type charge carriers, and the partial reduction of Ru^{4+} was insufficient to compensate for the loss of hopping electrons.

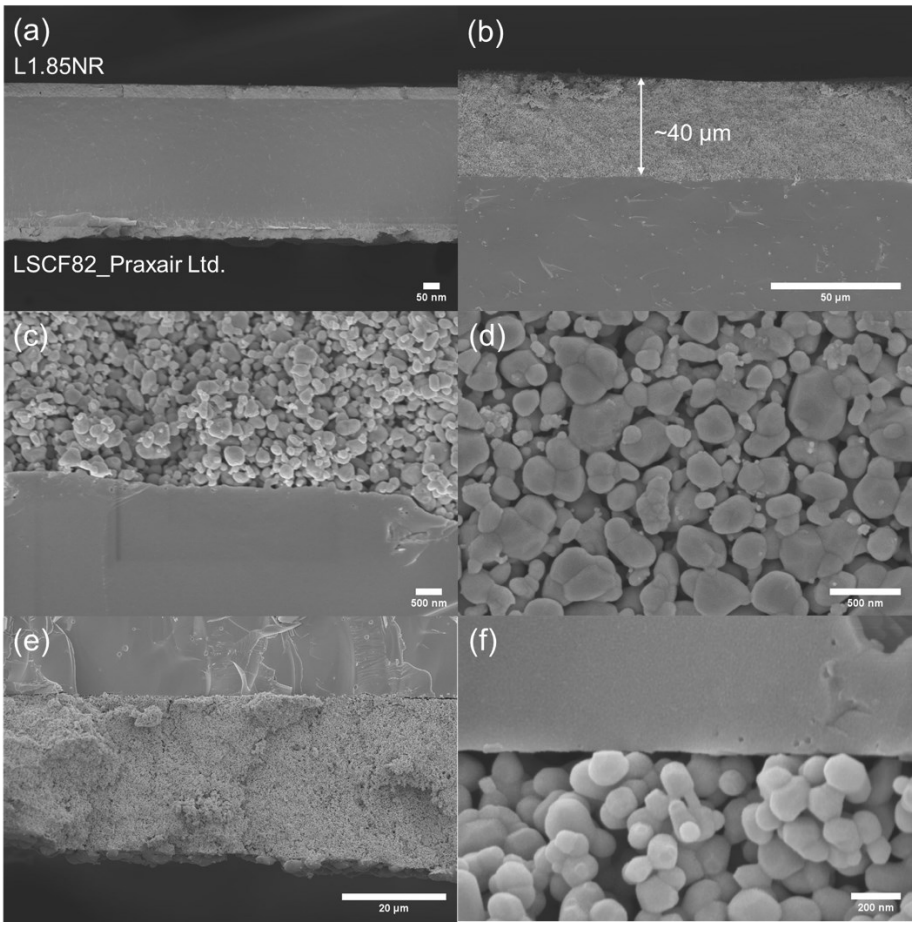


Figure 6.10 SEM images depict the microstructure of both the cross-sectional view and top view of the fabricated single cell before electrochemical test, with the current collector omitted.(a) cross-section of the single cell; (b-c) cross-section view highlighting the microstructure of L1.85NR electrode; (d) top view of the L1.85NR electrode; (e-f) cross-section view highlighting the microstructure of LSCF electrode.

The testing atmosphere was switched to wet 100% H_2 after 130 minutes of reduction for the measurement of *I-V* curves. OCV was measured before the scanning of *I-V* curve to make sure the equilibrium state of the cell measurement. OCV were stable at ~0.98V within 1mins of measurement. According to Nernst Equation (equation 1-8), based on the theoretical cell voltage E^0 (1.23V), the cell voltage at 600°C (893K) is calculated as 1.09V. As mentioned above, ceramic sealant was used in the sealing for gas tightening, however, there might be microstructural crack exist which sacrificed the cell voltage due to the gas cross-over. Therefore, the testing method could also be improved and modified in the future's study.

As discussed in section 5.2, the double perovskite structure of L1.85NR was characterized as stable and maintaining its main structure after reduction at 600°C in wet 5%H_2/Ar. Hence, the *I-V* curve measurements were attempted at 450°C and 600°C, as shown in Figure 6.12. Power densities were calculated based on the I-V measurements to evaluate the power generated per unit area, as plotted in Figure 6.12. Comparing the power density curves in Figure 6.12 (b), the peak power density measured at 450°C was 12 $mWcm^{-2}$, which was ten times higher than the cell with the stoichiometric phase L2NR as an anode. This confirms the enhancement of

electrochemical performance due to the exsolution of Ni-Ru nanoparticles. Similarly, a significant higher power output at 70 $mWcm^{-2}$ was also measured for the L1.85NR cell at 600°C. Compared to the peak power density achieved by state-of-the-art fuel cells, the L1.85NR/LSGM/LSCF82 single cell exhibits twelvefold less in performance. Nevertheless, the notable performance enhancement resulting from the exsolution of Ni-Ru nanoparticles offers promising prospects for the utilization of the exsolution method within the field of SOCs. Besides, the second repeat of the I-V curve measurement showed a slight decrease, while the L2NR cell repeated itself. This is contrary to our expectation that L1.85NR is more stable in a reducing atmosphere, which is possibly attributed to the testing condition of 100%H_2 that was too aggressive, while the reason behind this still needs further exploration in the future.

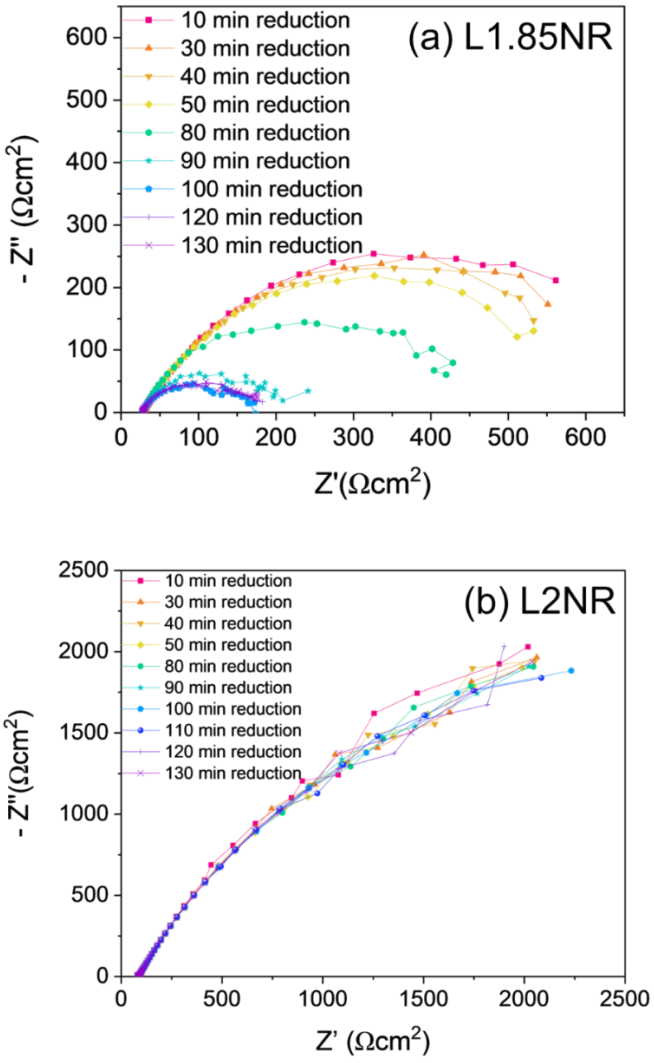


Figure 6.11 *In-situ* EIS spectra measured at 450°C in wet 5%H_2 of the single cell with (a) L1.85NR and (b) L2NR as fuel electrode.

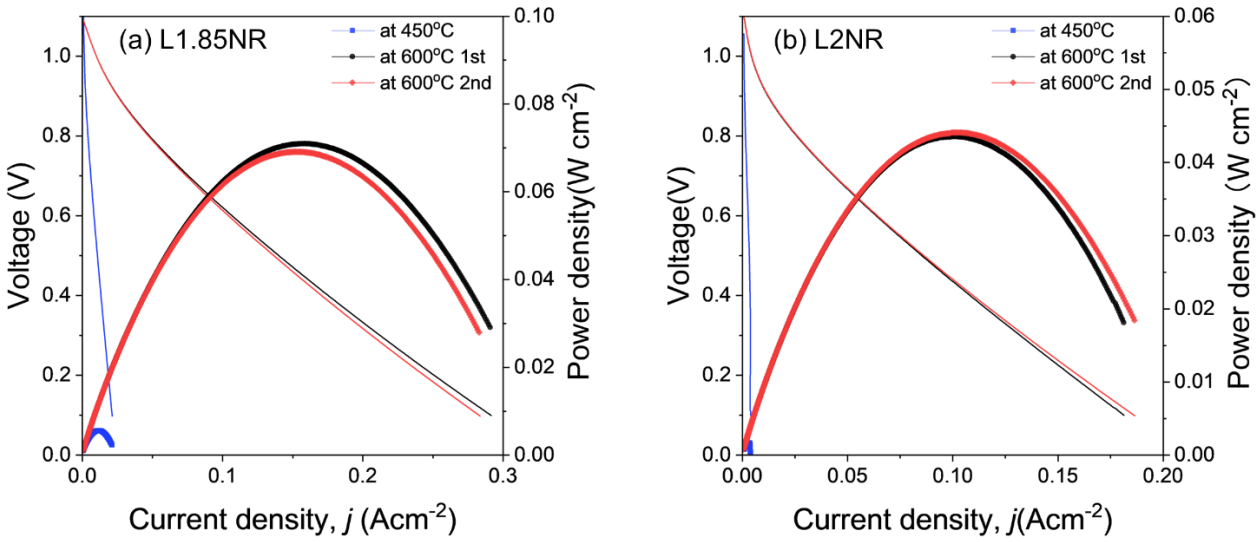


Figure 6.12 *I-V* curves and power density measured at 450°C and 600°C in commonly working atmosphere of SOFC with the single cells employing (a) L1.85NR and (b) L2NR as fuel electrode.

Post-tested cells were subjected to XRD and SEM measurements to ensure that the reduction treatment led to the exsolution of Ni-Ru nanoparticles. Figure 6.13 shows the cross-section view of the L1.85NR electrode after the fuel cell test. Exsolved nanoparticles were observed homogeneously distributed on the surface of the L1.85NR electrode. The particle size was larger than previously observed in section 5.3.1, which was attributed to the high-temperature reduction and measurement at 600°C. Figure 6.14 shows the XRD patterns of the post-test single cell with L1.85NR as the electrode. The diffraction peak of the exsolved Ni-Ru phase at 44.5° 2q was observed, in agreement with the previous observation in chapter 5 (as shown in the inserted plots of Figure 6.14). However, unresolved peaks at 28° and 30° 2q, possibly attributed to a lanthanum oxide phase, were also observed as indicated by magenta arrows. This could provide evidence of the power output degradation in Figure 6.11, as result of intensive reduction.

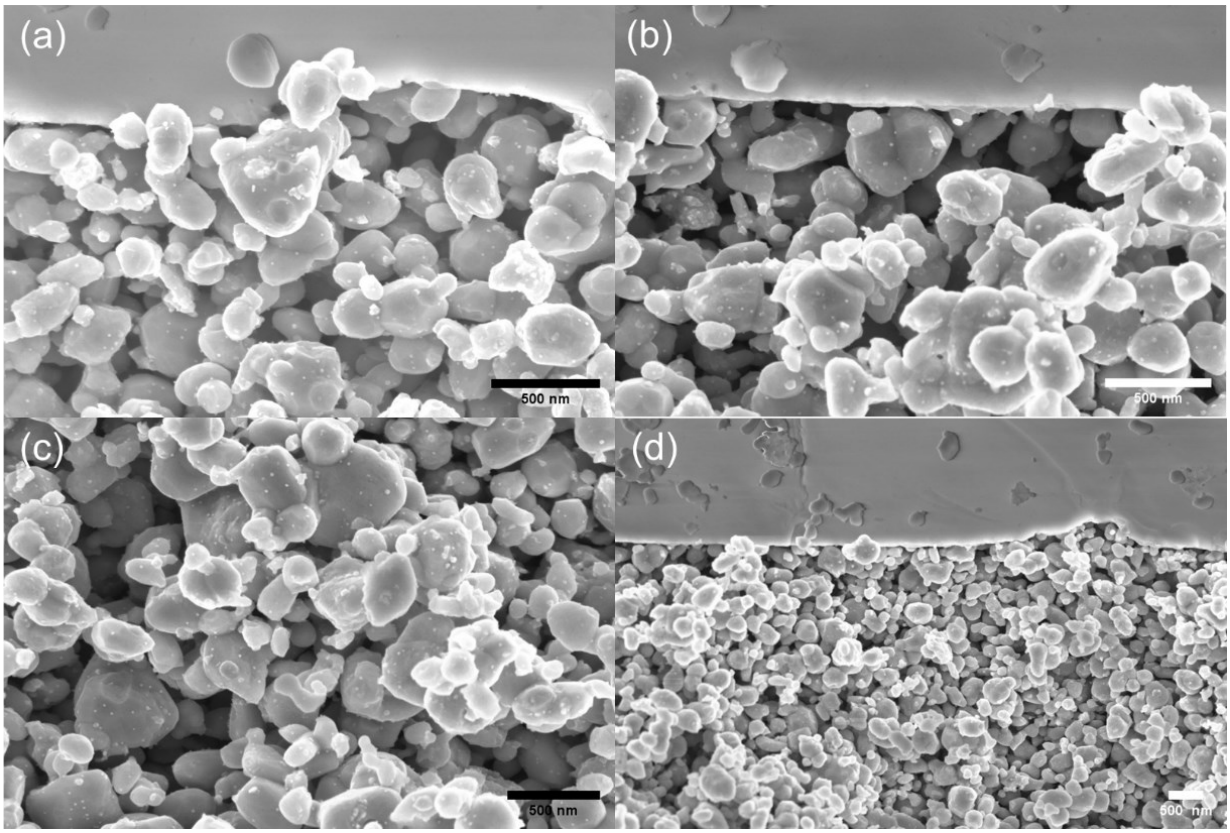


Figure 6.13 SEM images of the cross-section view of L1.85NR electrode after full cell test.

Therefore, it can be concluded that during the *in-situ* EIS measurement of symmetric cells and single full cell tests, Ni and Ru were exsolved from the A-site deficient electrode L1.85NR, which promotes the electrochemical performance of the double perovskite electrode. The enhancement of electrochemical performance can be verified by the drastic decrease in the impedance arcs during the reduction and the increased peak power density compared to the stoichiometric phase L2NR electrode. This indicates the potential of applying the exsolution method and the A-site deficient double perovskite L1.85NR in the electrodes of SOCs.

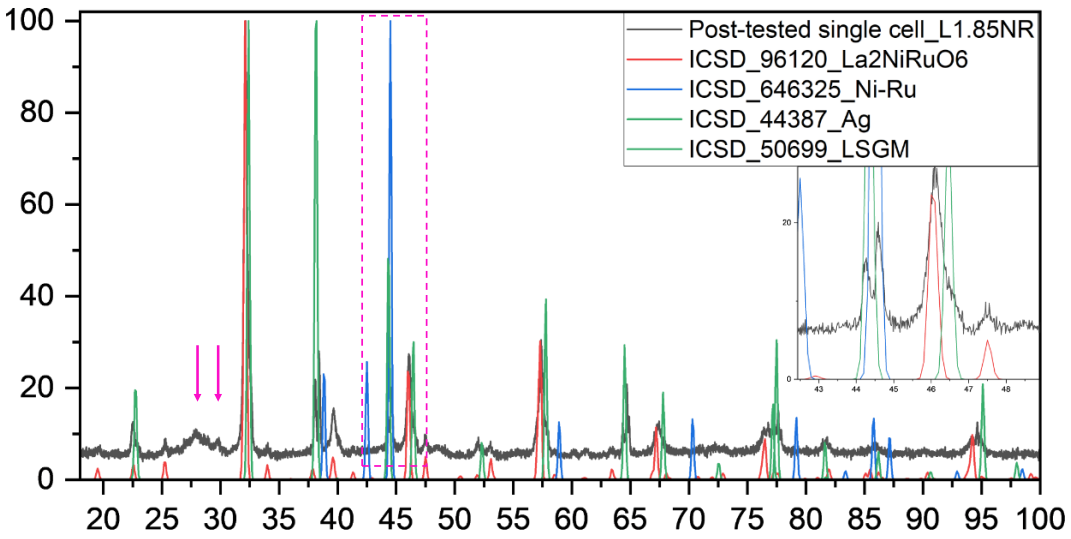


Figure 6.14 XRD pattern of the L1.85NR electrode after full cell test and its correspondence with the reference peaks from La_2NiRuO_6 [265], Ni0.32 Ru1.68 [290], silver current collector [310] and LSGM electrolyte [311].

In this subsection, the measurement of EIS and *I*-V curves of single cells were conducted with assistance from Dr Inyoung Jang from the Department of Chemical Engineering, Imperial College London. The author would like to acknowledge her contribution to the full cell measurement set-up and operations of the potentiostat.

6.4 *In-situ* TEM investigation

Following the study of *in-situ* EIS measurement in section 6.3.1 and the temperature-dependent morphology characterization in section 5.5, *in-situ* TEM coupled with STEM-EDX was employed to further probe the exsolution process and its dependence on reduction temperature. The experiments were conducted in high vacuum (~10^{-7} torr), which represents a moderate reduction condition compared to the lab reduction with wet 5%H_2/Ar. Consequently, the exsolution behaviour of the L1.85NR sample was expected to be less intensive than that observed in chapter 5.

6.4.1 Fast nucleation at 450°C

Figure 6.15 displays the *in-situ* bright-field (BF) TEM images depicting the morphological changes of L1.85NR as a function of time. The L1.85NR powder sample was loaded onto a Protochips sample holder (Fusion AX in situ heating and biasing holder, Protochips) and heated up to 450°C at a rate of 1°C/s. According to the earlier observations in *in-situ* EIS measurements, significant exsolution would not occur during the rapid heating within the initial 7 minutes. In Figure 6.15 (a), a L1.85NR grain edge was observed without any nanoparticles on its surface. However, as the temperature reached 450°C, a vague dark point appeared on the L1.85NR surface after only 20 seconds, indicating the initial nucleation of exsolved nanoparticles (Figure 6.15 b). This rapid nucleation process aligns with previous observations

of Ni exsolution from lanthanum calcium titanate by Neagu et al. [312], where instantaneous nucleation occurred within 0.2 seconds. The quick response of L1.85NR to the reduction conditions and nucleation process also supports the findings from the *in-situ* EIS observations in section 6.3.1.

During the subsequent reduction of L1.85NR at 450°C for 2-6 minutes, the exsolved particles became more pronounced, as shown in Figure 6.15 (c-d). Notably, the locations of the exsolved particles did not change, consistent with the reported Ni exsolution process [13]. The nanoparticle reduced in high vacuum was reported to be strongly facetted and aligned with parent perovskite oxides. However, it is challenging to distinguish lattice fringes or atomic arrangements in Figure 6.15 due to limited instrument resolution.

Besides the observed nanoparticle indicated by the white arrows in Figure 6.15 (b-d), another exsolved particle was seen to nucleate and grow after 2 minutes of reduction in vacuum at 450°C, marked by white dashed circles in Figure 6.15 (c-d). The growth rate of this exsolved particle appeared to be faster than that of the particles indicated by white arrows. This difference in growth rate could be related to different facets and localized mass transport variations on the two L1.85NR grains. No movement of the nuclei was observed for this exsolved nanoparticle.

Figure 6.15 (e) depicts the morphology of the exsolved nanoparticles and the L1.85NR grain after reduction in vacuum for 23 minutes. It is evident that the exsolved nanoparticle (indicated by the white arrow) appears to be socketed. The growth of the nanoparticle does not extend outward from the surface but rather pushes against the perovskite lattice and grows at the same location as the nuclei. While in section 5.3.1, a 'pyramid-based' nanoparticle was observed at the corner of a L1.85NR grain. This phenomenon is likely the result of intensive particle growth within the limited volume of perovskite, particularly when the exsolved nanoparticle exhibits a face-cantered cubic (FCC) structure, such as $Ni_{0.944}$ $Ru_{0.056}$, ICSD 197164 [291].

To reduce the stochastic nature of observing a single exsolved nanoparticle in Figure 6.15, Figure 6.16 provides an overview of several L1.85NR grains with a higher number of exsolved nanoparticles after 42 minutes of reduction in vacuum at 450°C. Several dark points indicate the presence of exsolved nanoparticles in the BF TEM image. Due to the thermal effects causing sample drift and making it challenging to maintain focus, the precise morphology and lattice fringes are not clearly discernible in this image.

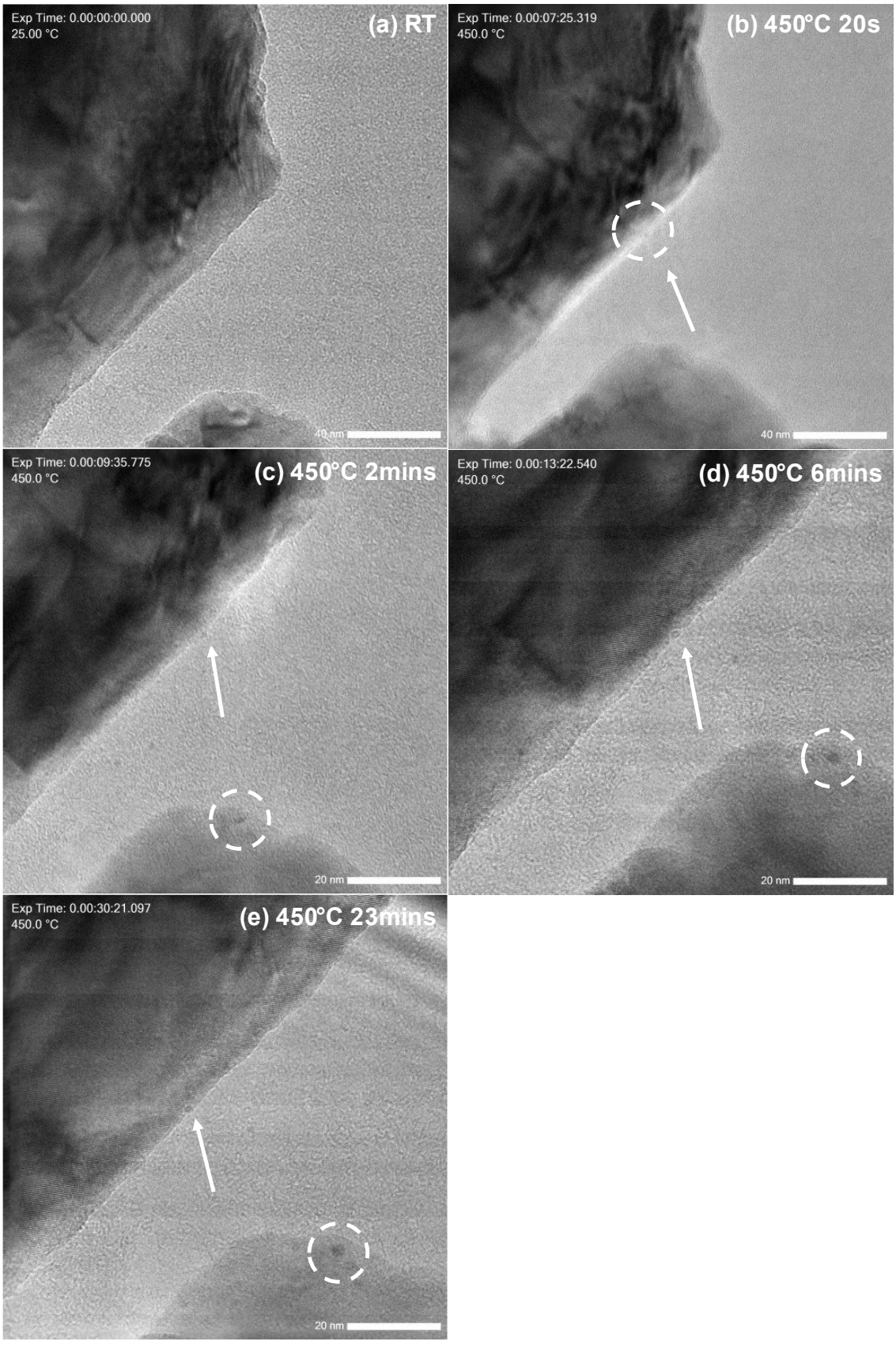


Figure 6.15 *In-situ* BF TEM observations of L1.85NR sample in high vacuum at 450°C after different reduction time: (a) initial images at room-temperature; (b) after 20s reduction at 450°C; (c) after 2mins reduction at 450°C; (d) after 6mins reduction at 450°C; (e) after 23mins reduction at 450°C. A fast response of exsolution and nucleation process was observed within 23mins of exposure in high vacuum at 450°C.

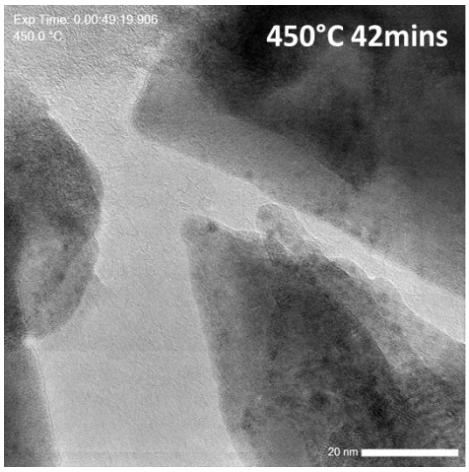


Figure 6.16 *In-situ* TEM image of the L1.85NR sample reduced at 450°C in high vacuum for 42 mins, highlighting a higher number of nanoparticles compared to Figure 6.15 and a board distribution of nanoparticles.

6.4.2 Temperature dependent exsolution of Ni and Ru

In addition to the isothermal observations at 450°C, an investigation into the temperature dependence of exsolved nanoparticles was conducted. As described in section 5.5, the exsolution of nanoparticles at temperatures lower than 450°C was also observed. Moreover, *ex-situ* STEM-EDX analysis suggested separate stages of Ni and Ru exsolution. To further understand the effect of reduction temperature, *in-situ* STEM-EDX was employed by conducting EDX mapping analysis during the interval quenching of samples reduced at different temperatures in high vacuum.

During the reduction and characterization process, the exsolution process continued. To capture a 'snapshot' of the exsolved nanoparticles, quenching was employed in this *in-situ* characterization session. The thermal treatment program and characterizations are depicted in Figure 6.17. STEM-ABF, STEM-ADF, HAADF, and MAADF signals were examined with increasing temperature. As mentioned in Chapter 3, STEM-HAADF images exhibit the 'Z-contrast' due to signal intensity being proportional to the square of the atomic number (Z^2) [250]. In contrast to STEM-HAADF imaging, STEM-ABF images exhibit less dependence on the atomic number (I_{ABF} is proportional to $Z^{1/3}$), capturing signals from both light and heavy elements. On the other hand, MAADF images collect signals at scattered angles smaller than 55 mrad, containing both coherent and incoherent scattered electrons. Therefore, MAADF images provide information on shape and defects compared to HAADF images[313]. Winckelmans et al. [313] investigated HAADF, MAADF, and low-angle annular dark field (LAADF) STEM images on Au decahedron and demonstrated superior diffraction contrast in the shape features of the MAADF and LAADF images compared to HAADF characterization. Regarding the ADF images, they include both HAADF and MAADF signals collected at the full range of scattered angles. In this study, the initial STEM images and EDX maps are displayed in Figure

6.18. Notably, there was no increase of signals from La, Ni, or Ru cations, indicating a homogeneous elemental distribution within the L1.85NR perovskite grain.

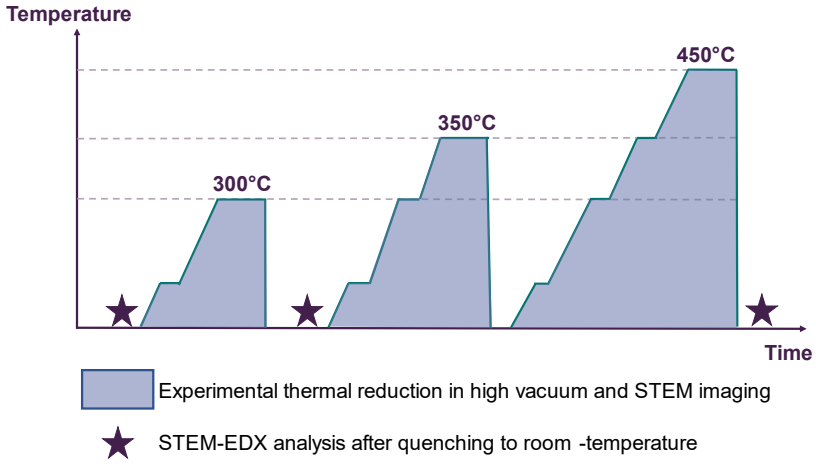


Figure 6.17 Schematic illustration of the thermal cycle and the characterization applied to the sample.

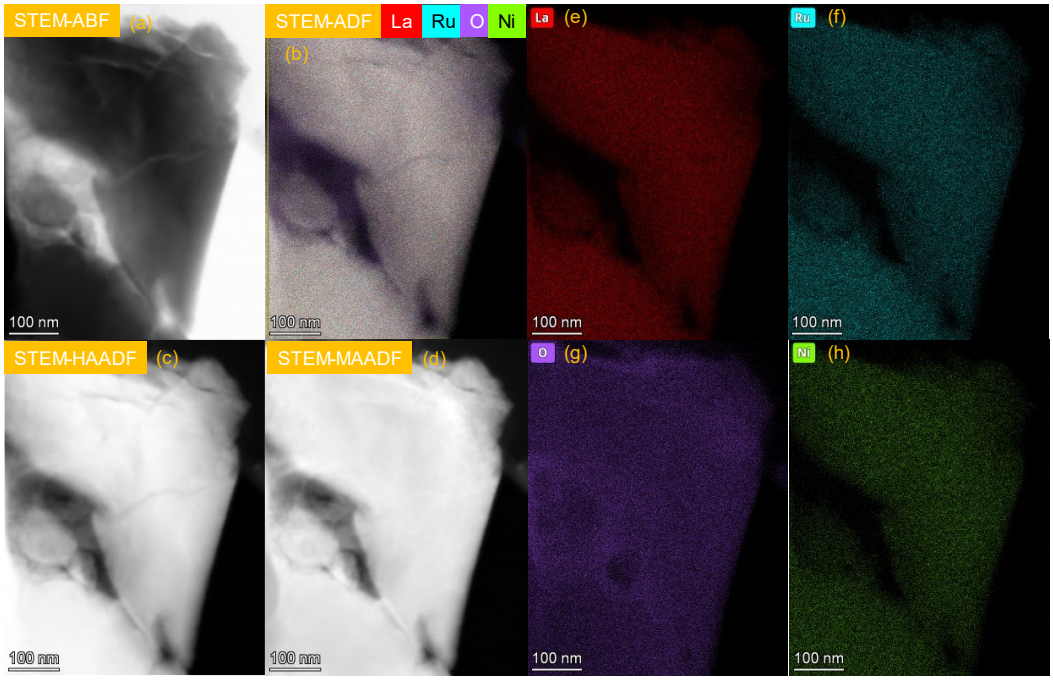


Figure 6.18 (a) STEM-ABF, (b) STEM-ADF combined with EDX maps, (c) STEM-HAADF, (d) STEM-MAADF images and (e-h) EDX maps of the L1.85NR pristine.

When the temperature increased to 300°C, the enrichment of the B-site cations was surprisingly observed as shown in Figure 6.19. Rather than exsolving as a combined bimetallic alloy, separate regions of B-site cation enrichment were observed. Large areas of Ni enrichment, each over 50 nm in size, were visible in the STEM-EDX images, along with smaller nanoparticles of Ru metal. In contrast to Ni and Ru, no increase of La and O signals was observed, indicating the exsolution of Ni and Ru metal phases.

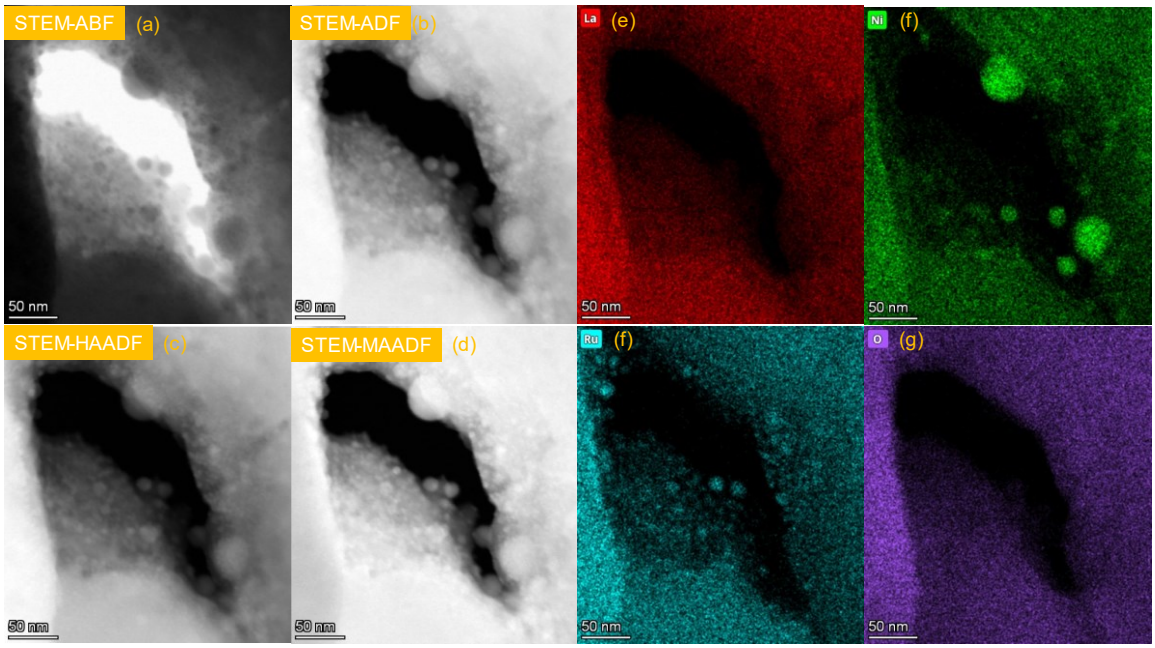


Figure 6.19 (a) STEM-ABF, (b) STEM-ADF, (c) STEM-HAADF, (d) STEM-MAADF images and (e-h) EDX maps of the L1.85NR quenched after reduction at 300°C.

As the temperature increased to 350°C, numerous smaller nanoparticles, similar to those observed in Section 5.5, appeared on the surface of L1.85NR. Intriguingly, the large enriched areas that were visible in Figure 6.19 rapidly re-dissolved into the bulk material, as indicated by the yellow arrows in Figure 6.20. After remaining at 350°C for 1 minute, all the prominent areas of Ni metal vanished, replaced by a greater quantity of smaller nanoparticles that had exsolved. It's noteworthy that under reducing conditions, particularly when the particle size is around 50nm in diameter, it is unusual for exsolved nanoparticles to dissolve back into the bulk. Similar surface restructuring and particle disappearance were also noted in subsequent investigations in Chapter 7. However, in Chapter 7, the Ni particles are suggested to be metastable nuclei with a diameter of only 3nm. Here, the gradual disappearance of the exsolved large Ni chunk is attributed to the focused electron beam effect.

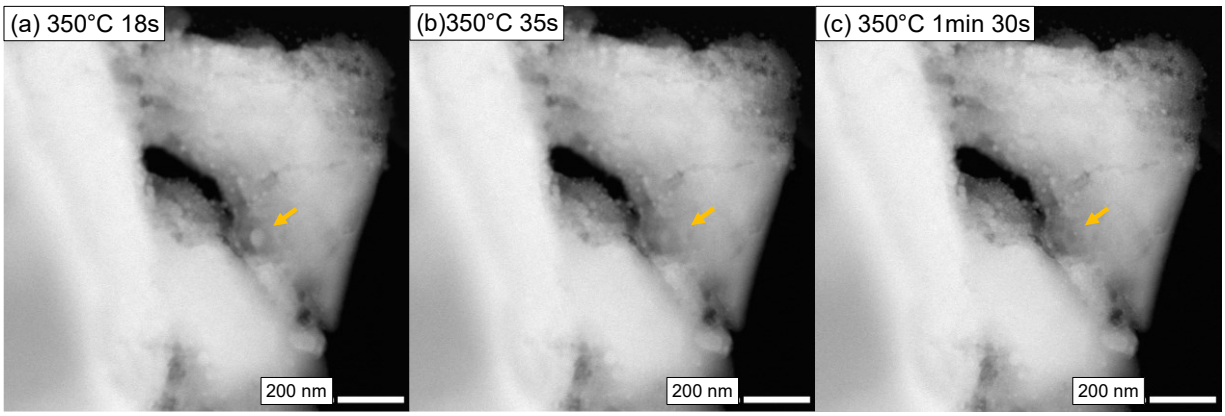


Figure 6.20 *in-situ* STEM images of the same L1.85NR grain observed in Figure 6.18-19, showing the evolution of morphology and surface particle at 350°C with the reduction time progressing: (a) 18s; (b) 35s; (c) 1min 30s.

Figure 6.21 (a-i) presents the STEM-EDX images of the same area after quenching from the reduction at 450°C. The EDX analysis confirmed the exsolution of both Ni and Ru metal phases. Additionally, the locations of the increased Ni and Ru signals started to overlap with each other. However, when examining the STEM images in Figure 6.21 (a-d), it appeared that several small clusters were sitting close to each other. Therefore, it was challenging to distinguish whether the overlapped signals represented alloyed or monometallic particles. Furthermore, when comparing Figure 6.18 (h) and Figure 6.19 (f), Ni deficiency was observed in the area near the exsolved Ni metal nanoparticles, suggesting the exsolution of Ni metal nanoparticles was a result of localized mass transportation.

Therefore, according to the observation at these different reduction temperatures, it can be concluded that the exsolution/segregation of Ni and Ru cations occurs separately. The exsolution of Ni and Ru cations initiates at temperatures lower than 450°C, in agreement with the discussion in Section 5.5 and the TG analysis in Section 6.2. It is intriguing that as the reduction progresses, the exsolution of Ni cations initially forms large metal particles that then redissolve into the bulk and form small nanoparticles.

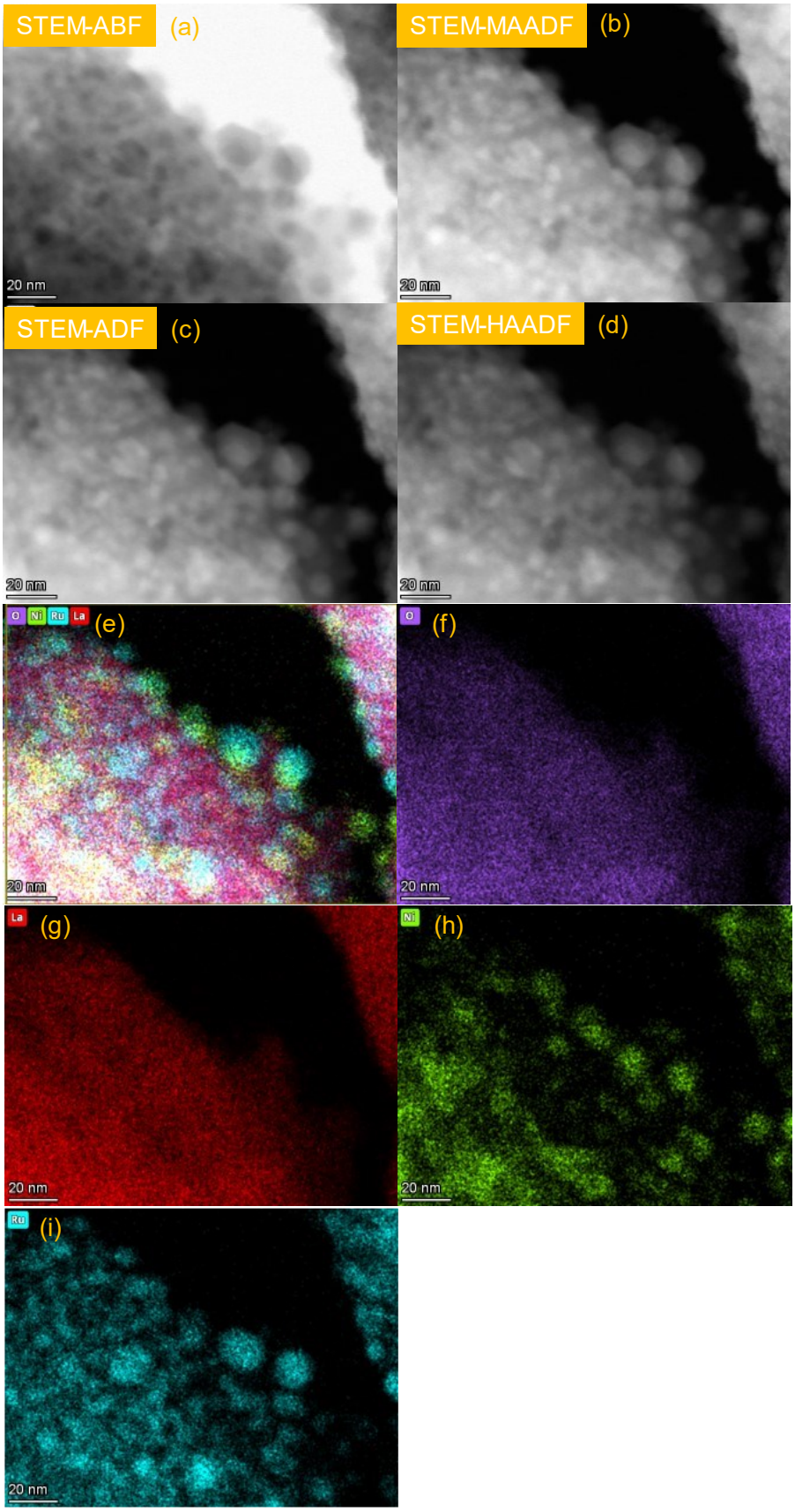


Figure 6.21 (a) STEM-ABF, (b) STEM-MAADF, (c) STEM-ADF, (d) STEM-HAADF images and (e-i) EDX maps of the L1.85NR quenched after reduction at 450°C

However, aside from the effects of elevated temperature and high vacuum, beam interaction inevitably has an impact on the probed particles and grains. Beam damage typically falls into three categories: displacement damage, ionization damage, and electrostatic damage [314]. Displacement damage occurs when energetic beam electrons transfer kinetic energy and momentum to atoms, resulting in direct atomic displacements. Ionization damage or radiolysis is caused by the electronic excitation of atomic electrons, leading to the breakage of chemical bonds and the formation of point defects inside oxides. In electrostatic damage, positive charge and electrons are generated as a result of ionization and excitation of the specimen. The electron field has been reported to cause the ejection of cations and the precipitation of metal phases, forming nanoparticles. Given the stepwise heat treatment and the need for signal accumulation during EDX signal acquisition, the characterized L1.85NR was continuously exposed to electron flux. Hence, there's still remain unclear the contribution of focus electron beam effect in the exsolution observed in Figure 18-21, the dose rate of the electron beam reached maximum around $107 e Å^{-2} s^{-1}$ (at 630kx of magnification). Therefore, in this work, the severe exsolution might be partially contributed to by the beam effect during the *in-situ* probing session [315].

To mitigate the effects of long-term beam damage, another L1.85NR grain was characterized by BF TEM images before and after the temperature-dependent *in-situ* TEM/STEM probing session. As shown in Figure 6.22, the same area was observed before and after the heat treatment in high vacuum. Nanoparticles were observed on the surface of this L1.85NR grain, indicating that, apart from possible beam damage effects, thermal reduction in high vacuum led to the exsolution of nanoparticles. Furthermore, in contrast to the effects of electrostatic damage [315], a rough rather than smooth specimen surface was observed in this L1.85NR grain.

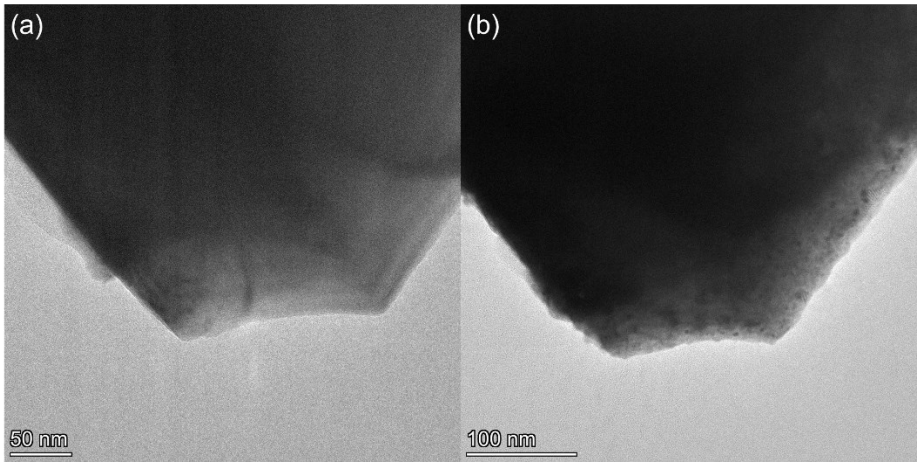


Figure 6.22 BF TEM images of same L1.85NR grain before (a) and after (b) the temperature-dependent *in-situ* TEM/STEM probing session.

6.5 Synchrotron X-ray scattering analysis

To further investigate the mechanism and exsolution behaviour of the A-site deficient double perovskite L1.85NR, a collaboration with Prof. Simone Mascotto from the University of Koblenz and Deutsches Elektronen-Synchrotron (DESY) centre was undertaken, employing synchrotron X-ray scattering techniques. Anomalous small-angle X-ray scattering (ASAXS) was used to characterize the nucleation and particles at both the Ni and Ru X-ray absorption edges in an *in-situ* environment of 5%H_2/N_2 at reduction temperatures of 450°C and 550°C (Appendix.1). Additionally, wide-angle X-ray scattering (WAXS) data were acquired during the *in-situ* session. In this section, the analysis of the WAXS data measured at the Ru edge is discussed.

The *in-situ* characterization was conducted using the sample holder depicted in Figure 6.23. The L1.85NR sample was loaded into a quartz capillary tube and secured with quartz wool to ensure the sample's alignment with the X-ray beam.

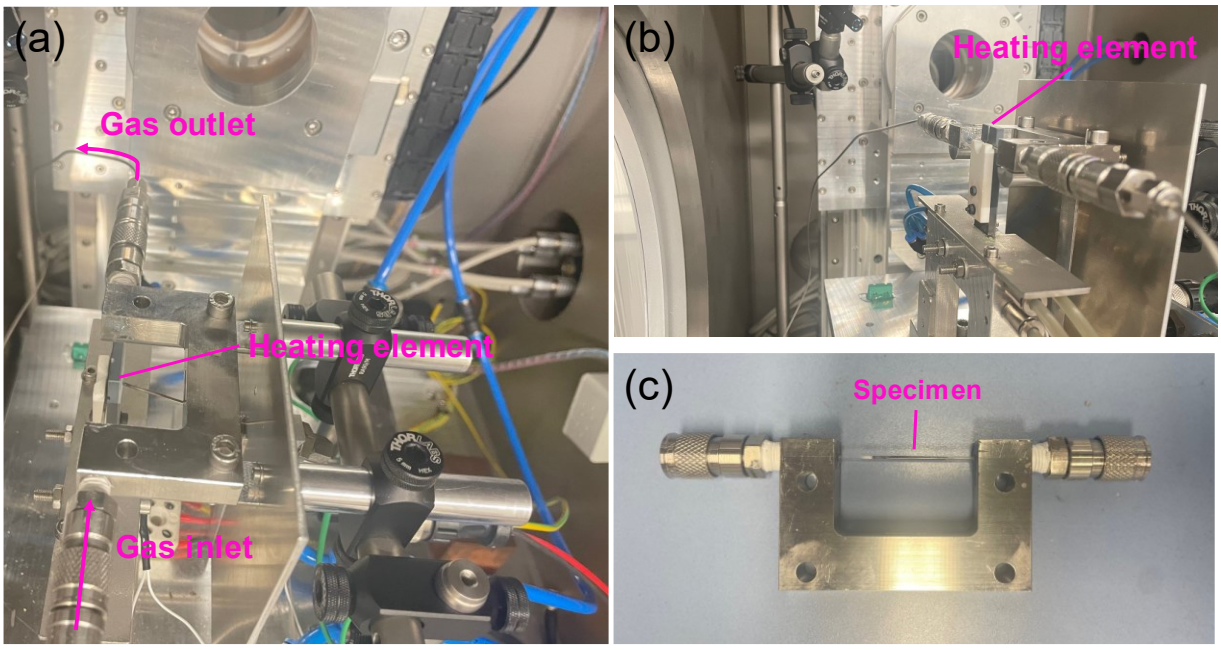


Figure 6.23 photos of the *in-situ* measurement instrument set-up for the ASAXS and WAXS characterization.

Six energies near the absorption edge of Ni and Ru were selected for acquiring the scattering patterns. The X-ray absorption energy of Ru is at 22,1172 keV. For Ru scattering patterns in this work, data were collected at 21,831 keV, 21,981 keV, 22,056 keV, 22,081 keV, 22,106 keV, and 22,121 keV. ASAXS and WAXS data were obtained at these energies, with 1 scan per minute during the reduction at both 450°C and 550°C.

The WAXS data, ranging from 20 to 90 in q (nm^{-1}), were converted into anomalous X-ray diffraction (AXRD) patterns, as shown in Figure 6.24. The AXRD patterns obtained at these six

energies exhibited similar diffraction/scattering peaks and peak shapes. Therefore, for the following analysis, the WAXS data at 21,831 keV were chosen as examples.

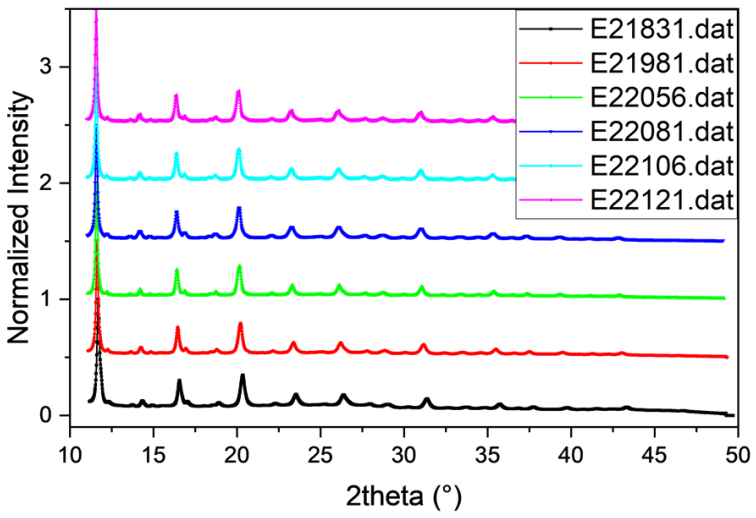


Figure 6.24 WAXS data converted AXRD patterns of L1.85NR measured at room temperature in compressed gas air.

Figure 6.25 presents contour graphs and waterfall plots of the WAXS data measured using a 21,831 keV X-ray beam. The characterization session consisted of three stages: (1) X-ray scattering started at room temperature with an air flow rate of 10 ml/min; (2) the sample L1.85NR was heated to the target temperature and the atmosphere was switched to 5%H_2/N_2 with flow rate of 10 ml/min; (3) after reduction for 3 hours, a re-oxidation treatment was applied to the L1.85NR sample to further investigate the behaviour of exsolved nanoparticles. The response of L1.85NR during these three stages was more pronounced for the reduction at 550°C, as shown in Figure 6.26. With the reduction progressing, additional peaks appeared in the 30-40 q (nm^{-1}) range, as depicted in Figure 6.26(a). Therefore, the WAXS data of these three stages were converted to AXRD for comparison.

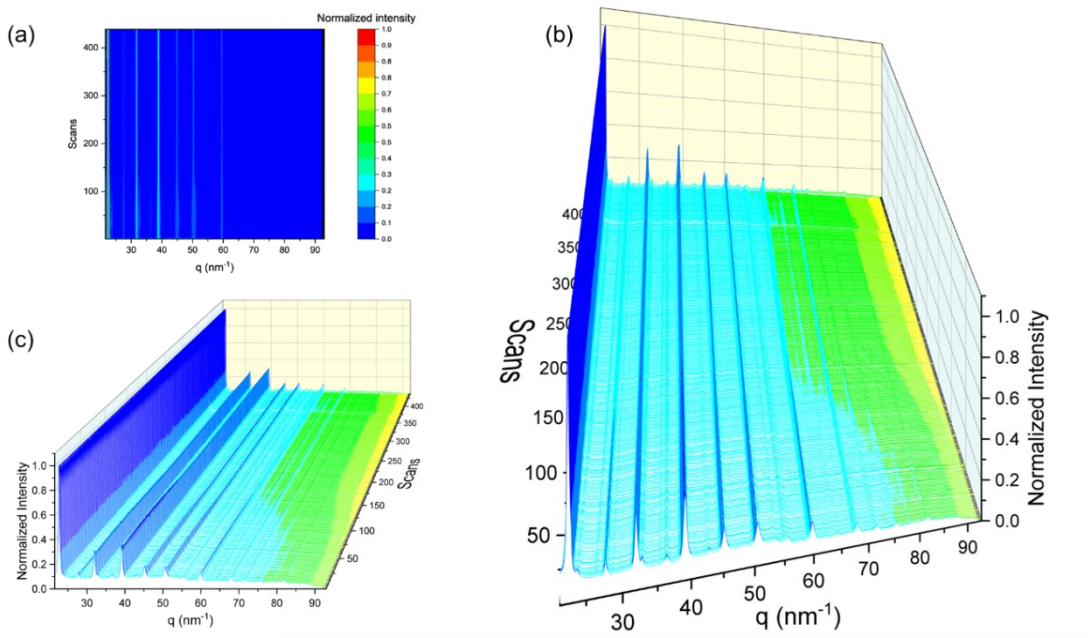


Figure 6.25 contour graph (a) and waterfall plots (b,c) of WAXS data of L1.85NR reduced at 450°C under 5% H_2/N_2. measured with 21,831 keV X-ray beam

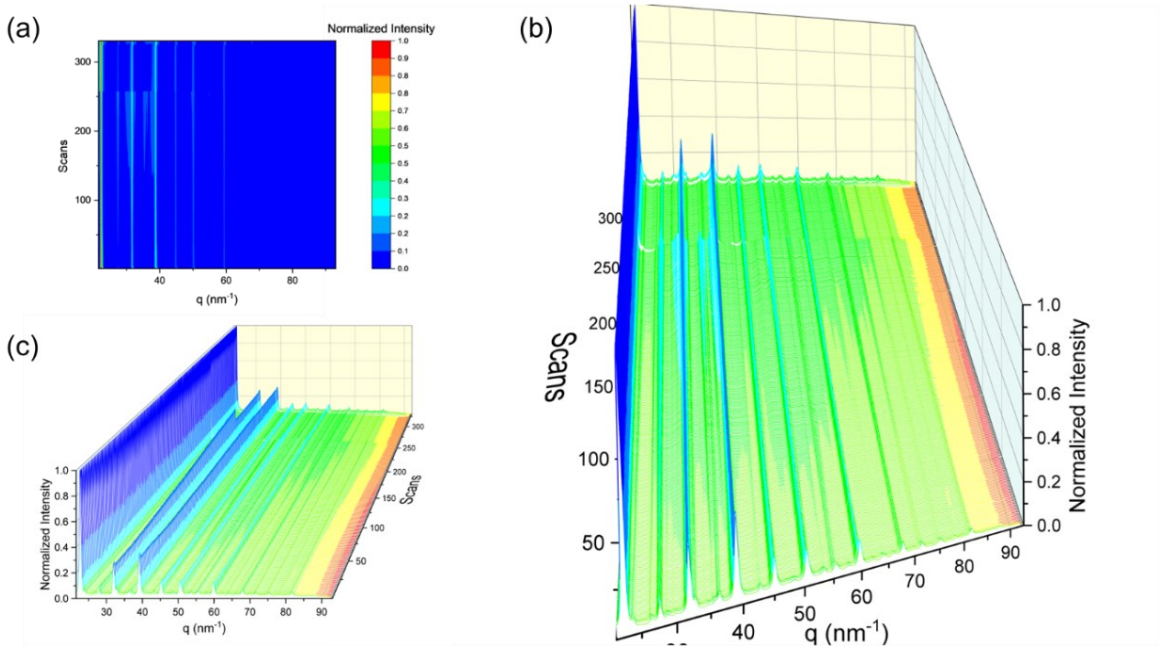


Figure 6.26 contour graph (a) and waterfall plots (b,c) of WAXS data measured with 21.831 keV X-ray beam of L1.85NR underwent the reduction treatment at 550°C.

Figure 6.27 and Figure 6.28 display the converted AXRD patterns of the WAXS scans. In Figure 6.27, the AXRD patterns at the three thermal treatment stages show the maintenance of the double perovskite structure with a subtle feature (marked by a purple arrow in the inserted plots of Figure 6.27) indicating the presence of a Ni-Ru alloy phase for the sample after reduction in 5%H_2/N_2 for 6 hours. It's interesting to find that after reoxidation, the Ni-Ru metallic phase disappears, while no NiO or RuO_2 secondary peak is observed, implying the re-incorporation of the metal phase into the double perovskite structure. Besides, the

converted AXRD plot of pristine L1.85NR measured in air at room temperature shows a higher background compared to the plots of reduced and re-oxidized L1.85NR. This explains the decreasing intensity and less obvious peak evolution during reduction observed in Figure 6.25. However, the 2θ position shifting of the 'black line' L1.85NR pristine measured in air at room temperature compared to the plots of reduced and re-oxidized L1.85NR is attributed to the thermal expansion of the lattice.

The converted AXRD pattern of the L1.85NR sample subjected to reduction at 550°C exhibited a more pronounced exsolution/ decomposition phenomenon in comparison to the L1.85NR sample reduced at 450°C, as demonstrated in Figure 6.28. Notably, the AXRD pattern of the L1.85NR sample, reduced for 4 hours at 550°C in a 5%H_2/N_2 atmosphere, revealed the presence of La_2O_3 peaks, indicative of partial perovskite decomposition during the reduction process. Interestingly, upon exposure of the L1.85NR sample reduced at 550°C to an oxidizing atmosphere (compressed air), a sudden disappearance of diffraction/scattering peaks associated with metallic phases and lanthanum oxides was observed, as depicted in Figure 6.26. This intriguing observation suggests an immediate reoxidation process, leading to the incorporation of exsolved and decomposed cations back into the perovskite lattice. While previous studies have reported to the phenomenon of cation reincorporation upon exsolution [86], the precise mechanisms and pathways involved in this process remain elusive. The current investigation has unveiled the rapid and responsive nature of exsolved nanoparticles and reduced materials to reoxidation conditions, thereby highlighting the need for comprehensive exploration in future research.

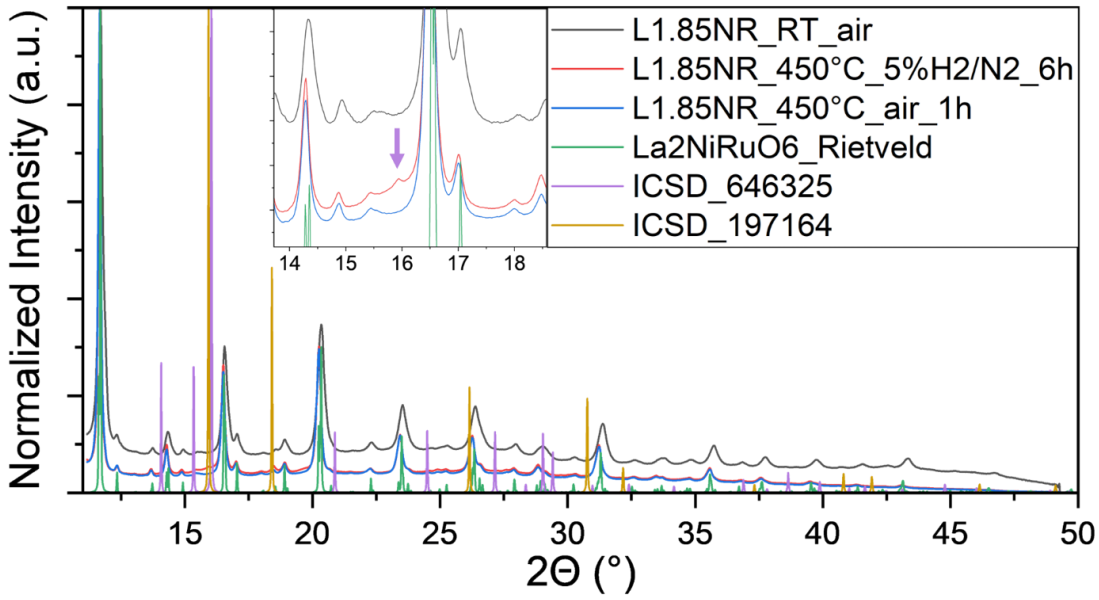


Figure 6.27 WAXS data converted AXRD patterns of *in-situ* observations: L1.85NR pristine in air, L1.85NR reduced at 450°C for 6 hours and L1.85NR re-oxidized for 1 hour.

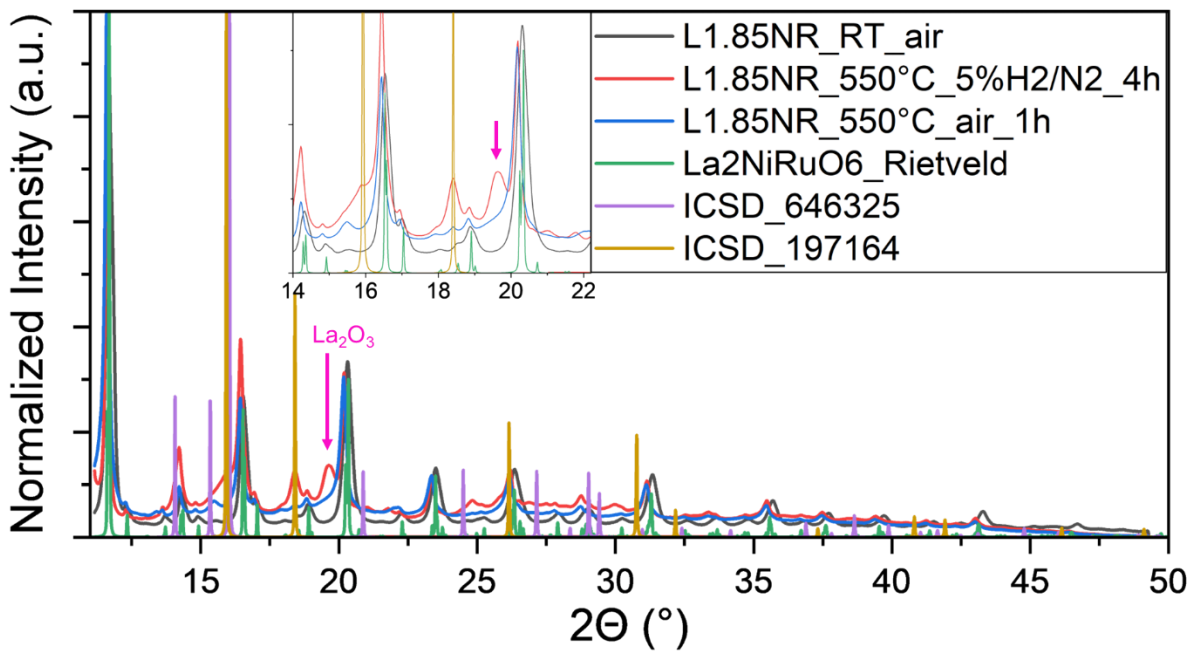


Figure 6.28 WAXS data converted AXRD patterns of *in-situ* observations: L1.85NR pristine in air, L1.85NR reduced at 550°C for 4 hours and L1.85NR re-oxidized for 1 hour.

In this section, the *in-situ* measurement of ASAXS (Appendix 1) and WAXS data L1.85NR were conducted under help from Prof. Simone Mascotto from University of Koblenz, Dr Xiao Sun and Dr. Sylvio Haas from DESY and Miss Princess Inangha University of Hamburg. Author would like to acknowledge their contribution in design and set up of the *in-situ* measurement instrument, help with the data acquiring and the ASAXS data analysis in the collaboration work.

6.6 Summary and future work

In this chapter, TGA was used to monitor the mass loss of L1.85NR during its *in-situ* reduction and exsolution in a 5%H_2/Ar atmosphere. Findings indicated that mass loss commenced between 300°C to 360°C, suggesting exsolution initiation at relatively low temperatures. *In-situ* EIS observations on a symmetric cell revealed rapid exsolution kinetics and significant performance enhancement within 25 minutes of reduction in a wet 5%H_2/Ar environment. Furthermore, evaluation of full cells with L1.85NR and L2NR as fuel electrodes underscored the vital role of A-site deficiency in promoting exsolution, with reduced impedance and increased power output following A-site deficient L1.85NR electrode reduction. However, achieved performance still falls short of state-of-the-art fuel cells. Future research should explore unresolved secondary phases after reduction in pure hydrogen at 600°C and optimize cell fabrication processes for significant improvements.

During *in-situ* examination of L1.85NR exsolution behaviour, TEM and STEM-EDX revealed swift exsolution at 450°C in a high vacuum environment, confirming separate exsolution of Ru and Ni, with large Ni chunks initially forming and later dissolving into smaller nanoparticles.

Beam-induced damage may have contributed to the process, suggesting potential for beam-induced exsolution method exploration.

Collaborative synchrotron X-ray scattering with University of Koblenz and DESY confirmed Ni-Ru alloy phase presence during exsolution, with instantaneous Ni and Ru cation reincorporation into the double perovskite structure upon oxidizing atmosphere exposure. This phenomenon presents a promising avenue for future research into self-regeneration capabilities of Ni-Ru nanoparticles and cation diffusion mechanisms.

Chapter 7 *In-situ* investigation of ruthenium doped lanthanum nickel titanium double perovskite exsolution

7.1 Introduction

Building on the discussion presented earlier, it has been demonstrated that Ni and Ru, each present at a 50% concentration on the B-site of a double perovskite structure, exhibit a remarkable propensity for exsolution. This underscores the distinct advantages of employing a double perovskite structure with ordered B-site cations, particularly in exsolution. As detailed in Chapter 2, most reported investigations into exsolution primarily involved the formation of solid solutions with dopant cations, followed by the exsolution of these dopant cations. Given the substantial exsolution of B-site ordered cations, it becomes increasingly compelling to explore the exsolution of both dopant cations and B-site ordered cations within a single system. Consequently, in this chapter, we have reduced the proportion of Ru cations to 5% as dopant cations in lanthanum nickel titanate double perovskite, wherein Ni and Ti are arranged in ordered positions on the B-site. Titanium was selected for its inherent stability and robust bonding with oxygen, rendering it stable at the B-site position during the exsolution process. Furthermore, titanates have drawn recognition as stable and highly impurity-tolerant materials suitable for use as fuel electrodes in SOCs. Therefore, this chapter focuses on the synthesis of A-site deficient lanthanum nickel titanates and their comprehensive examination, encompassing lattice structure, exsolution behaviour, electrochemical performance as electrodes in symmetric cells, and potential enhancements through topotactic exchange.

The samples and acronyms mentioned in this chapters are: La_2NiTiO_6 (L2NT), $La_2NiTi_{0.9}Ru_{0.1}O_{6\pm\delta}$ (L2NTR), $La_{1.85}NiTi_{0.9}Ru_{0.1}O_{6-y}$ (L1.85NTR).

7.2 Synthesis of lanthanum nickel titanates

As discussed in Chapters 4-6, the investigation of lanthanum nickel ruthenates revealed that A-site deficiencies facilitated the exsolution of metal nanoparticles from the double perovskite parent structure. Consequently, A-site deficiencies were incorporated into the Ru-doped lanthanum nickel titanium double perovskites. In light of prior research, the sol-gel method was employed to synthesize the pristine double perovskite. As outlined in Section 3.2, specific quantities of lanthanum nitrate, nickel nitrate, and ruthenium nitrosyl nitrate were dissolved in a 10 wt% citric acid solution. Subsequently, titanium dioxide powder was added into the solution to form a suspension, ensuring continuous stirring throughout the water evaporation and gelation process. Following decomposition and calcination treatments, the synthesized products were analysed using XRD.

Stoichiometric lanthanum nickel titanate double perovskite, La_2NiTiO_6 and lanthanum nickel titanate double perovskite with 5 at% ruthenium dopants on the B-site, $La_2NiTi_{0.9}Ru_{0.1}O_{6\pm\delta}$,

denoted as L2NT and L2NTR, were synthesised as initial materials prior to the introduction of A-site deficiencies within the structure. Based on the Goldschmidt tolerance factor equation, the tolerance factors for L2NT and L2NTR were both evaluated as 0.96, as depicted in Equations 7-1. In the equation, the ionic radius of B-site cations, r_B, represents the average radius of all B-site cations, which is Ni and Ti cations in L2NT, while Ni, Ti and Ru cations in L2NTR. The values of tolerance factors for L2NT and Ru-doped L2NT complied with the perovskite structure requirement, which stipulated that $0.78 \leq t \leq 1.05$.

$$t_{L2NT/L2NTR} = \frac{r_{La} + r_O}{\sqrt{2}(r_B + r_O)} \qquad 7-1$$

Figure 7.1 presents the XRD patterns, and the Le Bail refinement results, for both L2NT and L2NTR. Both L2NT and Ru-doped L2NTR samples exhibited a monoclinic double perovskite structure with the space group $P2_1/n$. The Le Bail refinement was conducted in accordance with reference ICSD 186433 [316]. Upon the incorporation of 5 at% Ru at the titanium site, the tolerance factor actually decreased by approximately 0.04%, suggesting a slight distortion of the double perovskite structure from the ideal cubic form. The Le Bail refinement results revealed that the lattice parameters a ranged from 5.552(1) to 5.555(2) Å, b from 5.559(1) to 5.564(1) Å, c from 7.847(1) to 7.852(1)Å, and β decreased from 90.05(1)° to 90.02(1)°. Lattice expansion was anticipated since the dopant Ru cations (r_{Ru4+}=0.62) were larger than Ti cations (r_{Ti4+}=0.605). Consequently, it could be inferred that the sol-gel method was suitable for the synthesis of lanthanum nickel titanate-based double perovskite materials.

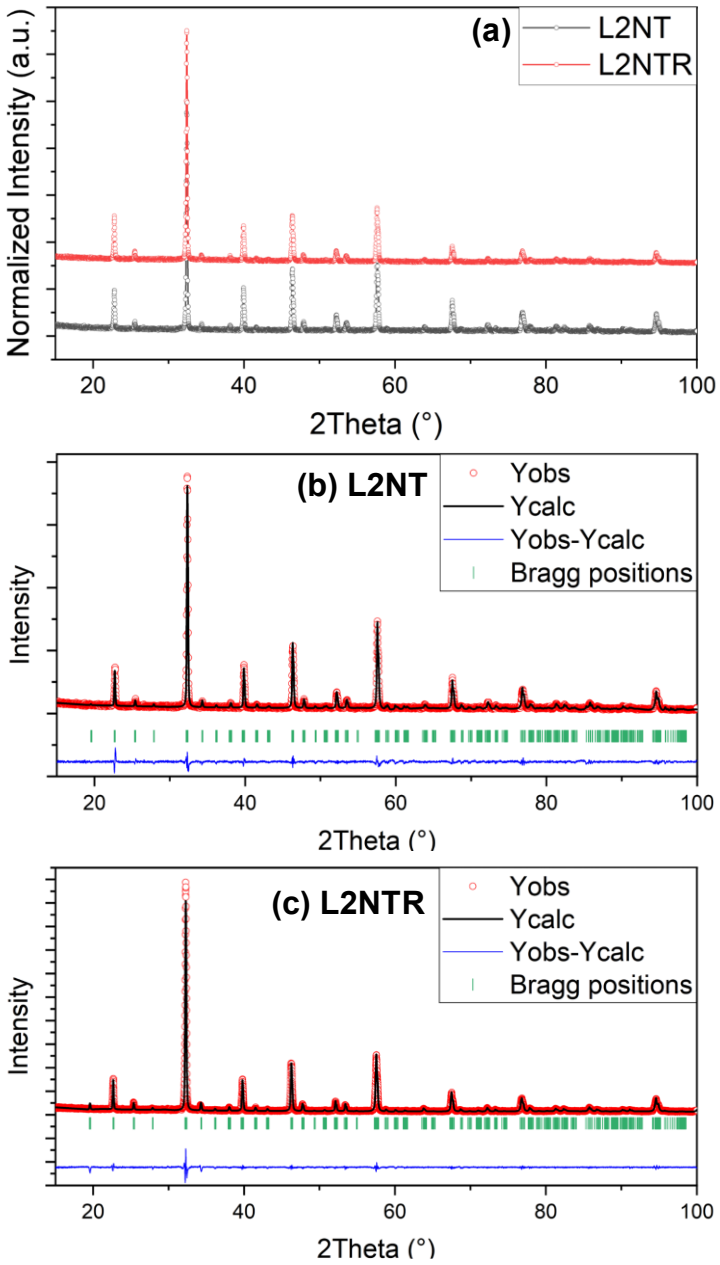


Figure 7.1 (a) XRD patterns of stoichiometric lanthanum nickel titanate L2NT and Ru-doped lanthanum nickel titanate L2NTR; (b) Le Bail refinement profiles of L2NT with R_p = 6.87, R_{wp} = 10.30, R_{exp} = 6.24 and χ^2= 2.71; (c) Le Bail refinement profiles of L2NT with R_p = 7.00, R_{wp} = 11.30, R_{exp} = 6.27 and χ^2= 3.23.

Upon synthesizing stoichiometric lanthanum nickel titanates, 7.5 at% A-site deficiency was introduced into the structure, designated as L1.85NTR. To accurately examine the degree of A-site deficiency and the ordering of L1.85NTR, an XRD diffractometer with a set-up optimized for Rietveld refinement and the Rietveld refinement was employed to investigate the phase and verify the purity of the product, as detailed in Section 3.3.1.1. Figure 7.2 displays the XRD patterns and the Rietveld fitting plots. Within this pattern, subtle features were present that could not be attributed to the Cu K_α diffraction of the double perovskite lattice. The faint peak at 29.05° and the peak shoulder at 31.12°, denoted by the green arrow in Figure 7.2, represented diffraction signals from the Cu K_β line due to the unavoidable insufficient filtering

of the X-ray source, which became evident after extended scanning. Nevertheless, two unresolved features still remained, as highlighted in Figure 7.2 as inserted plots, located at 33.2° and 62.5°. Future exploration is needed to identify the sources of these features. While, since the unresolved features were subtle and the majority of the diffraction suggested a double perovskite structure, indicating a relatively pure product of A-site deficient lanthanum nickel titanate double perovskite, the subsequent study proceeded using sol-gel synthesized products.

In accordance with the stoichiometric sample L2NTR, *P2₁/n* based on reference ICSD186433 [316] , calculations were employed for the evaluation of the A-site deficient double perovskite specimen L1.85NTR. The outcome of the Rietveld refinement is provided in Table 7.1. During the refinement process of the XRD pattern, unresolved regions, as well as Cu K_β diffraction peaks, were excluded. The refined lattice parameters exhibited a decrease in lattice dimensions and an increase in the β angle compared to the Le Bail refined data of the stoichiometric phase L2NTR, as illustrated in Figure 7.1. This suggested that the introduction of A-site vacancies contributed to the contraction of the lattice volume, which was congruent with the findings of the ruthenate sample discussed in Chapters 4.

During the refinement process, constraints were incorporated into the calculations of the XRD profiles. Refined atomic parameters encompassed the position of La cations, cation occupancy, and thermal factors. However, the atomic parameters of oxygen anions were not refined for the accuracy and validity of the refinement. In terms of refining cation parameters, rather than fixing the B-site cations at a singular site, the occupancy of Ti, Ni, and Ru cations was refined on both (0, ½, 0) and (½, 0, 0) positions. The refinement results indicated a preference for nickel cations at the (0, ½, 0) position and titanium cations at the (½, 0, 0) position. Furthermore, ruthenium cations primarily substituted the titanium position as anticipated, due to the similarity in ionic radius and valence states between Ru and Ti cations. By presuming Ru cations to substitute Ti sites, the ordering of B-cations was assessed through the degree of ordering, S[36]:

$$S = 2g_B - 1 = 0.616 \qquad 7-3$$

where g_B represents the correct occupancy of Ni or Ti-Ru cations at either the (0, ½, 0) or (½, 0, 0) positions. It became evident that the A-site deficient Ru-doped lanthanum nickel titanates exhibited a relatively high degree of disordering rather than complete rock-salt ordering. This was particularly apparent when contrasted with the ruthenate samples discussed in Chapter 4. The increased disordering could be attributed not only to the introduction of dopants and A-site vacancies but also to the greater ionic radius differences between Ni and Ti cations [36]. This is because in double perovskite, the factors that influences B-site cation arrangement are charge, size, electronic configuration and A/B ratio[268]. A distinct difference of ionic formal valence and ionic radius is necessary to achieve spontaneous B-site rock-salt ordering[317].

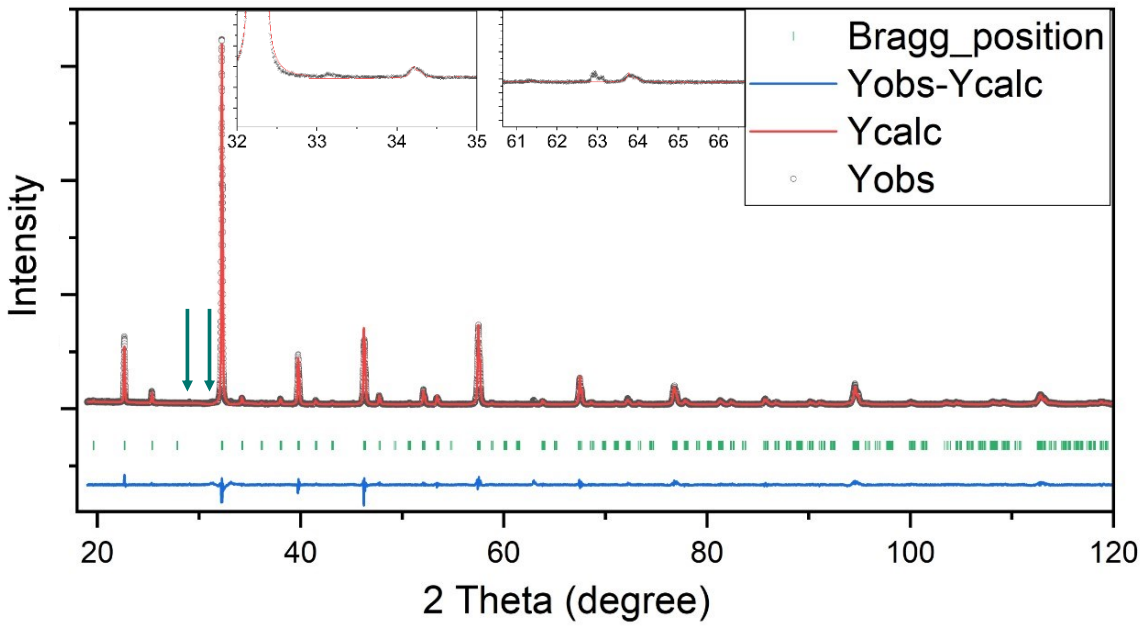


Figure 7.2 XRD pattern and the Rietveld refinement profiles of L1.85NTR. The factors of agreement are R_p = 4.95, R_{wp} = 6.41, R_{exp} = 4.11 and χ^2 = 2.43. Two inset plots are the zoomed pattens of resolved peaks. The green arrows mark the Cu K_β reflections.

Table 7.1 Rietveld refined lattice parameters and atomic parameters of L1.85NTR.

Lattice parameters and atomic parameters					
a (Å)			5.54996(2)		
b (Å)			5.55947(2)		
c (Å)			7.84351(2)		
β (°)			90.0464(3)		
	x	**y**	**z**	**B**	**Occupancy**
La1	0.5007(8)	0.5286(1)	0.249(7)	0.54(0)	1.888(2)
Ti1	0	0.5	0	0.680(3)	0.184(0)
Ru1	0	0.5	0	0.680(3)	0.020(0)
Ni1	0	0.5	0	0.680(3)	0.808(0)
Ni2	0.5	0	0	0.264(3)	0.192(0)
Ti2	0.5	0	0	0.264(3)	0.716(0)
Ru2	0.5	0	0	0.264(3)	0.080(0)
O1	0.214	0.198	-0.023	0.1	0.962
O2	0.279	0.727	-0.044	0.1	0.962
O3	0.423	0.989	0.274	0.1	0.962

The refined La cation occupancy displayed a marginally higher value than the intended figure, indicating a 5.6 at% deficiency. Consequently, ICP was employed to assess the cation concentrations in L2NT, L2NTR, and L1.85NTR. The results are presented in Table 7.2. Stoichiometric samples of L2NT and L2NTR demonstrated a strong concordance between experimental compositions and expected compositions. In the case of the A-site deficient

sample L1.85NTR, ICP results aligned with the Rietveld refinement results, showing lower amount of A-site deficiency than expected. The ICP showed that the A-site deficiency is even lower to approximate 3.5 at% La^{3+} deficiency. The excess nickel and titanium atoms might contribute to the unresolved phases depicted in Figure 7.2 or to the local enrichment of B-site cations, which necessitates further examination in future studies.

Table 7.2 ICP results of stoichiometric sample L2NT and L2NTR and A-site deficient sample L1.85NTR. B-site positions were assumed fully occupied by nickel, titanium and ruthenium cations. Oxygen concentration is calculated based on experimental results of metal cations.

$L_xNT(R)$	Nominal composition	Concentration ratio			Experimental composition
		A/B cations	Ni/Ti-Ru	Ru/Ti	
L2NT	La_2NiTiO_6	1.04(2)	0.98(2)	0.0004(3)	$La_{2.08(5)}Ni_{0.98(2)}Ti_{1.01(8)}O_{6.12}$
L2NTR	$La_2NiTi_{0.9}Ru_{0.1}O_6$	1.03(1)	1.02(1)	0.11(1)	$La_{2.05(2)}Ni_{1.01(2)}Ti_{0.89(4)}Ru_{0.10(1)}O_{6.07}$
L1.85NTR	$La_{1.85}NiTi_{0.9}Ru_{0.1}O_{5.775}$	0.97(1)	0.99(1)	0.11(2)	$La_{1.93(1)}Ni_{0.99(1)}Ti_{0.90(1)}Ru_{0.10(1)}O_{5.885}$

7.2 Exsolution of nickel nanoparticles

The A-site deficient sample, L1.85NTR, underwent reduction treatment in a wet 5% H_2/Ar atmosphere. Analogous to the exsolution analysis of ruthenate samples, reduction under various temperatures was performed to examine the material stability under reducing conditions. The XRD patterns of the L1.85NTR sample reduced at 450°C, 800°C, 900°C, and 1000°C are presented in Figure 7.3. In contrast to the ruthenate samples discussed in Chapters 4-6, the majority of the titanium-based sample retained a double perovskite structure up to 1000°C. However, a subtle peak at the 30° 2θ position signified the presence of a small quantity of La_2O_3 in the sample reduced at temperatures exceeding 800°C. This observation is typically associated with side reactions and exsolution, indicating a slight decomposition of the double perovskite structure [206,318]. Consequently, 800°C was selected as the reduction temperature for the subsequent exsolution investigation of L1.85NTR. A peak at 44.5° was detected in the reduced samples, which was ascribed to the presence of Ni metal as a consequence of the exsolution phenomenon.

To examine the exsolved Ni metal phase and the reduced double perovskite L1.85NTR more closely, Rietveld refinement was applied to the XRD pattern of the L1.85NTR sample reduced at 800°C. The refinement profiles are depicted in Figure 7.4. As outlined in Section 7.2, lattice parameters, La cation positions, cation occupancy, and thermal factors of the double perovskite materials were refined, with constraints on the total occupancy of B-site positions and the total amount of cations. Although the peak intensity was less prominent than in the XRD patterns of L1.85NTR samples reduced at 900°C and 1000°C, the La_2O_3 phase was still included to accurately determine the quantity of lanthanum oxides present in the sample.

Lattice parameters of the Ni metal phase and the lanthanum oxide phase were also refined. The agreement factors suggest that the calculated XRD patterns fit well with the experimental data, as illustrated in Figure 7.4.

The refined lattice parameters and atomic parameters of the double perovskite phase are listed in Table 7.3. The lattice parameters of the double perovskite phase remained similar to those of the as-prepared sample, while the atomic occupancies indicated slightly higher disordering and La-occupancy. This suggests a tendency to re-establish A-site stoichiometry, as reported in references [88,179], as well as B-site disordering accompanying the exclusion of B-site cations. The degree of ordering decreased to 0.54 following reduction, as determined by Equation 7-3. The refined lattice parameter of the Ni metal phase is 3.52395(7) Å, which aligns with the reported reference ICSD 64989 [319], confirming the exsolution of the Ni metal phase. Based on the Rietveld refinement, the exsolution of Ru-doped A-site deficient lanthanum nickel titanate, L1.85NTR, is represented by Equation 7-4:

$$\mathrm{La_{1.888}NiTi(Ru)O_{6-\delta}} \xrightarrow{\text{wet } 5\%\frac{\mathrm{H_2}}{\mathrm{Ar}}} 0.98811\mathrm{La_{1.910}NiTi(Ru)O_{6-y}} + 0.0119\mathrm{Ni} + 0.0006\mathrm{La_2O_3} \quad 7-4$$

Rietveld refinement also provided the calculated weight percentages of the secondary phases. The results indicated that the reduced sample contained 1.58(5) wt% Ni metal and 0.28(2) wt% lanthanum oxides. This finding suggests that under a reducing atmosphere, the majority of the A-site deficient sample undergoes an exsolution process rather than decomposing into metal oxides.

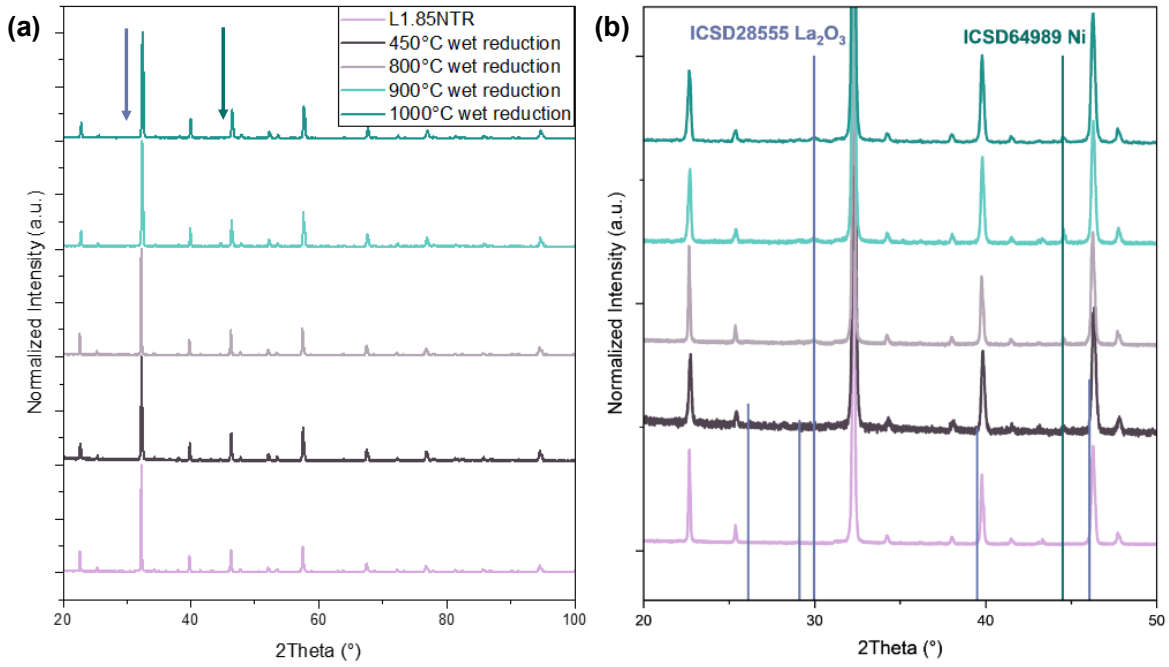


Figure 7.3 (a) XRD patterns of A-site deficient L1.85NTR as prepared and reduced at 450°C, 800°C, 900°C and 1000°C. (b) zoomed-in XRD profiles at 20°-50° range. The droplines indicate the Bragg position of La_2O_3 phase (ICSD28555[289]) and nickel metal phase (ICSD64989[319]).

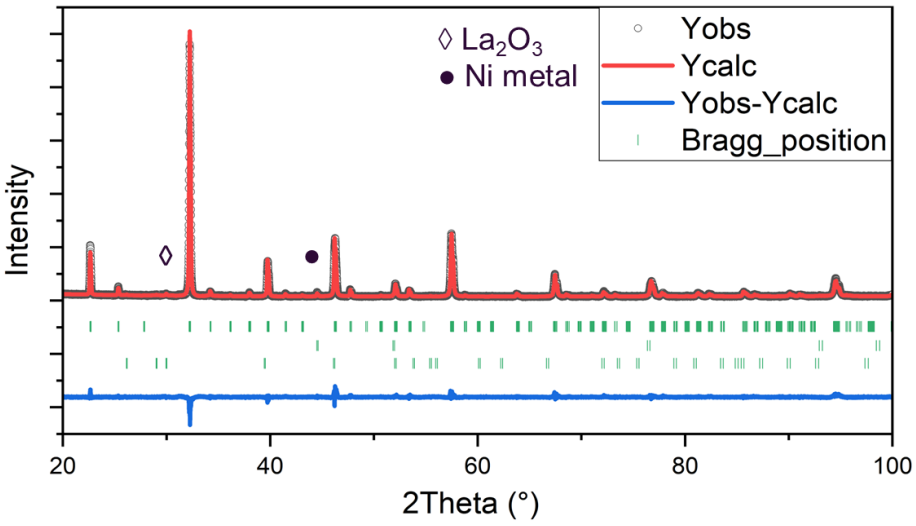


Figure 7.4 XRD pattern and Rietveld refinement profiles of L1.85NR reduced at 800°C. The factors of agreement are R_p = 5.59, R_{wp} = 7.08, R_{exp} = 4.12 and χ^2 = 2.95. Lattice parameters of nickel metal phase were refined based on reference structure ICSD64989 [319]. Lattice parameters of lanthanum oxide phase were refined based on reference structure ICSD28555 [289].

Table 7.3 Rietveld refined lattice parameter and atomic parameters of double perovskite phase in the reduced L1.85NR sample based on reference structure ICSD186433 [316]. The occupancy of the oxygen was fixed as 0.962 according to the nominal composition $La_{1.85}NiTi_{0.9}Ru_{0.1}O_{5.775}$.

Main phase lattice parameters and atomic parameters					
a (Å)			5.55153(3)		
b (Å)			5.55985(2)		
c (Å)			7.84527(4)		
β (°)			90.0545(4)		
	x	**y**	**z**	**B**	**Occupancy**
La1	0.50024(8)	0.52813(1)	0.25025(7)	0.508(1)	0.955(1)
Ti1	0	0.5	0	0.784(3)	0.226(1)
Ru1	0	0.5	0	0.784(3)	0.054(1)
Ni1	0	0.5	0	0.784(3)	0.770(1)
Ni2	0.5	0	0	0.175(5)	0.230(1)
Ti2	0.5	0	0	0.175(5)	0.674(1)
Ru2	0.5	0	0	0.175(5)	0.460(1)
O1	0.214	0.198	-0.023	0.1	0.962
O2	0.279	0.727	-0.044	0.1	0.962
O3	0.423	0.989	0.274	0.1	0.962

Subsequently, the exsolved nickel nanoparticles were examined using microscopy. Figure 7.5 presents the SEM images of the as-prepared L1.85NTR sample and the sample after reduction at 800°C in wet 5%H_2/Ar for 3 hours. In comparison to the as-prepared pristine sample, it is evident that nano-sized particles are homogeneously distributed on the oxide bulk's surface. To further investigate the composition and morphology of the exsolved nanoparticles, TEM and STEM-EDX were employed to analyse the sample reduced in wet 5%H_2/Ar at 800°C for 3 hours, as shown in Figure 7.6. In accordance with the XRD and Rietveld refinement data, the EDX maps reveal the exsolved nanoparticles as a Ni metal phase. In contrast, no significant

of the other three elements is observed, indicating the non-exsolved properties of Ru and Ti under the current conditions. This finding is consistent with reported titanates [88,179], where Ti cations are preferred to remain in the perovskite structure during the exsolution process due to their strong bonds with oxygen anions and low reducibility. Consequently, the stability of the B-site ordered double perovskite structure is enhanced during the reduction and exsolution processes when Ti cations are present at the B-site positions, compared to ruthenate samples reported in Chapter 4-6. The exsolved nanoparticles are approximately 14-15 nm in diameter. From the STEM-HAADF images in Figure 7.6(b), it can be observed that the exsolved nanoparticles are partially merged into the bulk grain, implying a 'socket structure' for the nanoparticles.

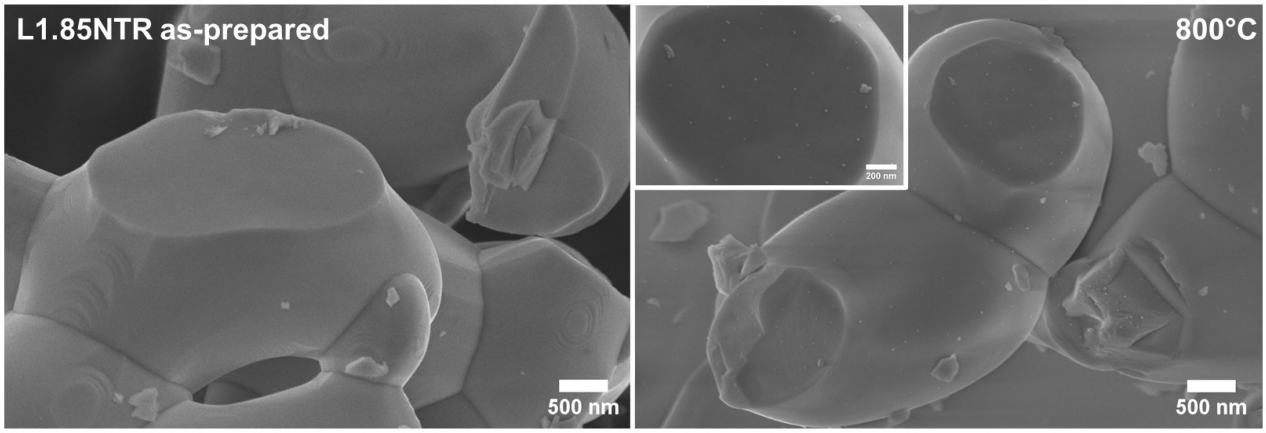


Figure 7.5 SEM images of (a) as prepared and (b) reduced L1.85NTR sample at 800°C for 3hours. The inserted image is the enlarged display of the reduced sample.

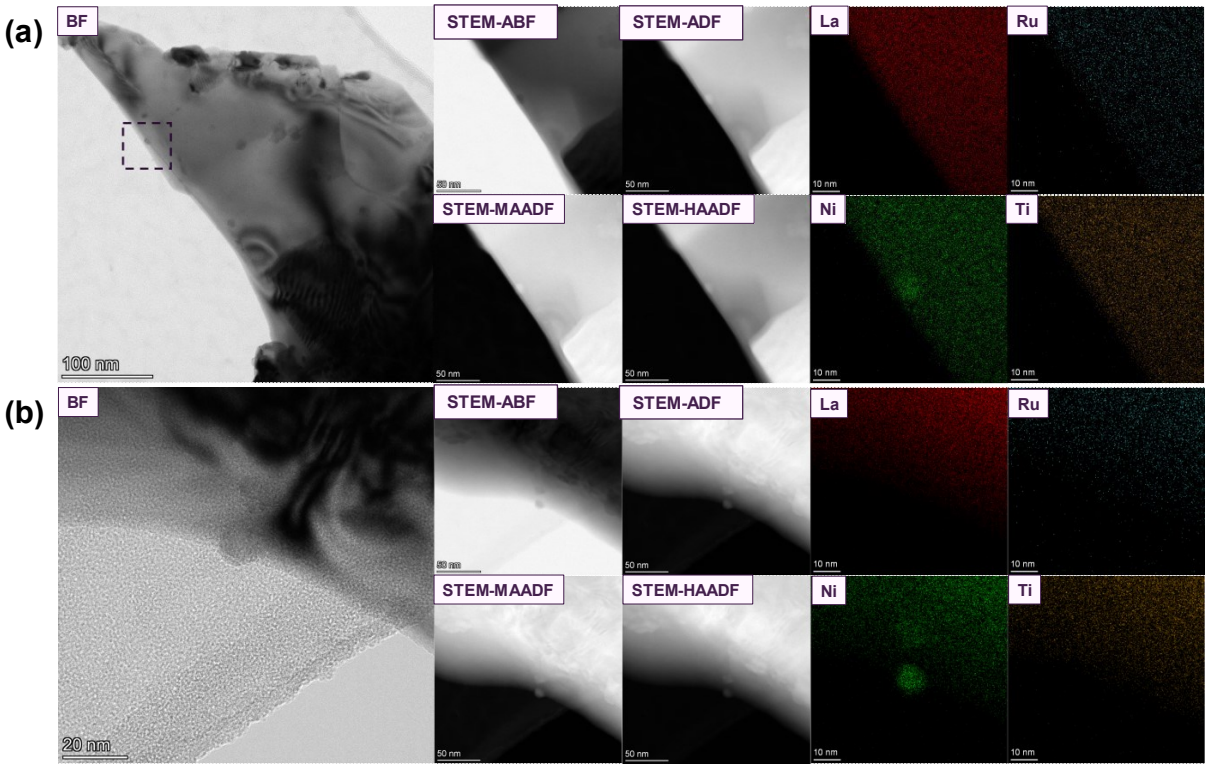


Figure 7.6 TEM bright field (BF) images and STEM annular bright field (ABF), annular dark field (ADF), medium angle annular dark field (MAADF) and high angle annular dark field (HAADF) images of region (a) and (b) of L1.85NTR sample reduced at 800°C in wet 5%H_2/Ar for 3 hours. The corresponding elemental distribution maps of La, Ni, Ru and Ti are listed at the left of the STEM images.

7.3 Temperature-dependent exsolution

7.3.1 Temperature dependent nanoparticles

As discussed in Section 7.2, multiple reduction temperatures were employed for the exsolution of L1.85NTR samples. The XRD pattern of the L1.85NTR sample reduced at 450°C for 3 hours in wet 5%H_2/Ar also displays the diffraction peak of the Ni metal phase at 44.5° (Figure 7.3). Consequently, the morphology of the L1.85NTR sample reduced at 450°C was investigated using SEM and TEM microscopy. As shown in Figure 7.7, the sample reduced at the lower temperature also exhibits homogeneously distributed nanoparticles on the surface of the bulk

grain. The STEM images in Figure 7.7(b) reveal a high population of exsolved nanoparticles. The MAADF images provide a clearer display of the surface morphology, as the inner part of the ADF signal (~35-55mrad) includes more diffraction contrast, compared to HAADF images. This is because the exsolved nickel nanoparticles (Z = 28) are relatively difficult to distinguish within the double perovskite that contains abundant Ti (Z = 22) and Ni cations. The STEM-EDX maps in Figure 7.7(c) confirm that the exsolved nanoparticles are of the Ni metal phase. Additionally, it can be observed that the exsolved nanoparticles are relatively smaller than the exsolved particles at higher temperatures, as seen in Figure 7.6.

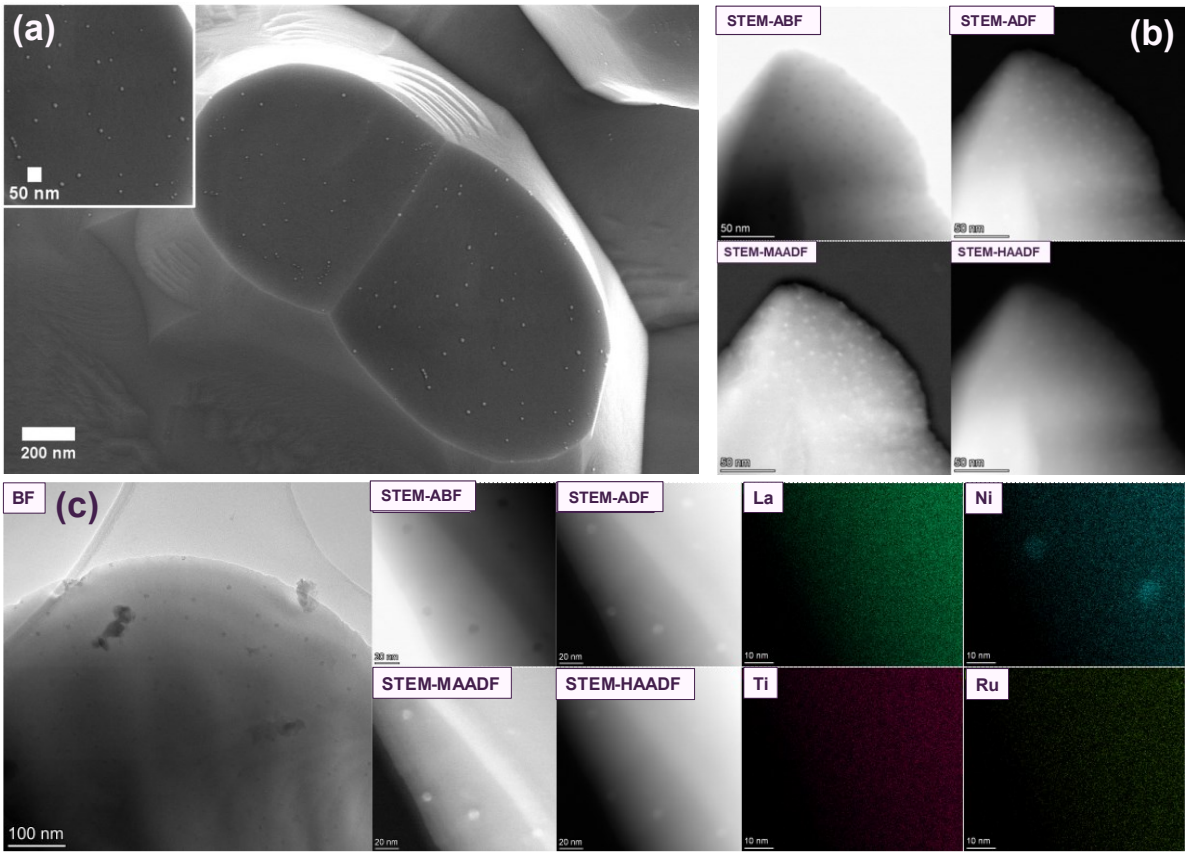


Figure 7.7 (a) SEM images (b) STEM-ABF and ADF images and (c) BF-TEM images, STEM-ABF and ADF images and corresponding EDX maps of the sample L1.85NTR reduced in wet 5%H_2/Ar at 450°C for 3 hours.

To accurately investigate the exsolved particles at different reduction temperatures, SEM images of the L1.85NTR sample reduced at 800°C and 450°C were analysed using ImageJ software [320] for particle analysis. As shown in Figures 7.8 and 7.9, the inserted images display the selected relatively flat areas for analysing particle sizes. Large fragment pieces of grains in Figures 7.8(b) and 7.9(c) were excluded during the analysis. The results of particle size distribution analysis are depicted in Figure 7.10.

As expected, the sample reduced at the higher temperature (800°C) exhibited larger particle sizes. In total, 208 particles from four regions of the sample were analysed, covering an area of 4.9×10^4 nm^2, with 0.6% of the area attributed to the exsolved nanoparticles. The average

size of the exsolved nanoparticles of the L1.85NTR sample reduced at 800°C was approximately 15.8 nm, consistent with Figure 7.6. The majority of the exsolved nanoparticles after reduction in wet 5%H_2/Ar for 3 hours were around 10~20 nm.

In contrast, the sample reduced at 450°C exhibited smaller exsolved nanoparticles compared to the sample reduced at 800°C. In total, 125 particles from four regions covering an area of 0.96×10^4 nm^2 area were analysed, with an average size of approximately 8.7 nm. The size distribution in Figure 7.10(b) shows that 67 of the 125 particles were 5-10 nm, exhibiting a relatively narrower distribution than that of L1.85NTR sample reduced at 800°C. This finding indicates a more uniform morphology of the low temperature exsolved nanoparticles.

Regarding particle population, the counts in Figures 7.8 and 7.9 suggest that low-temperature reduction yields higher particle counts per square nanometre. However, the selected area provides localized information, thus, the actual population difference will need to be investigated in future work.

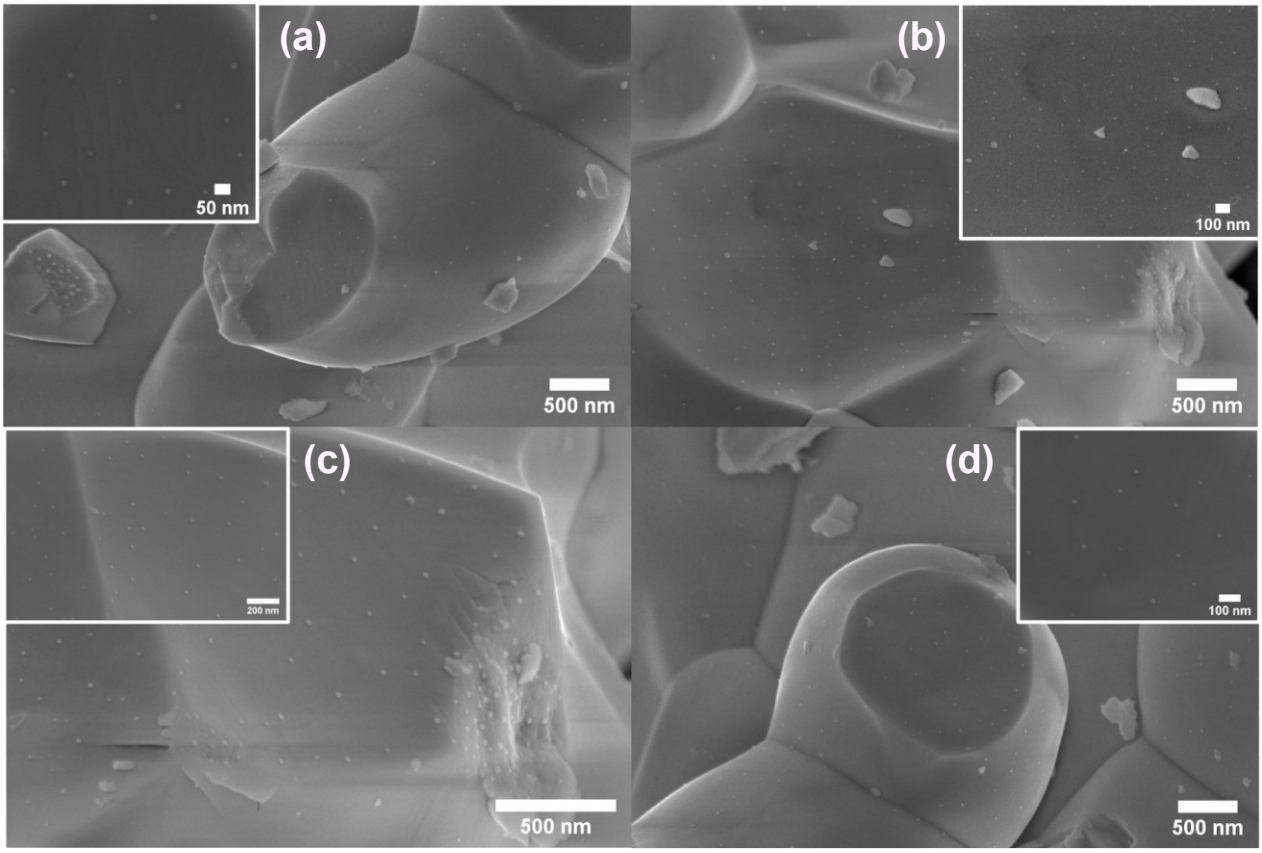


Figure 7.8 SEM images of L1.85NTR sample reduced at 800°C for the particle analysis.

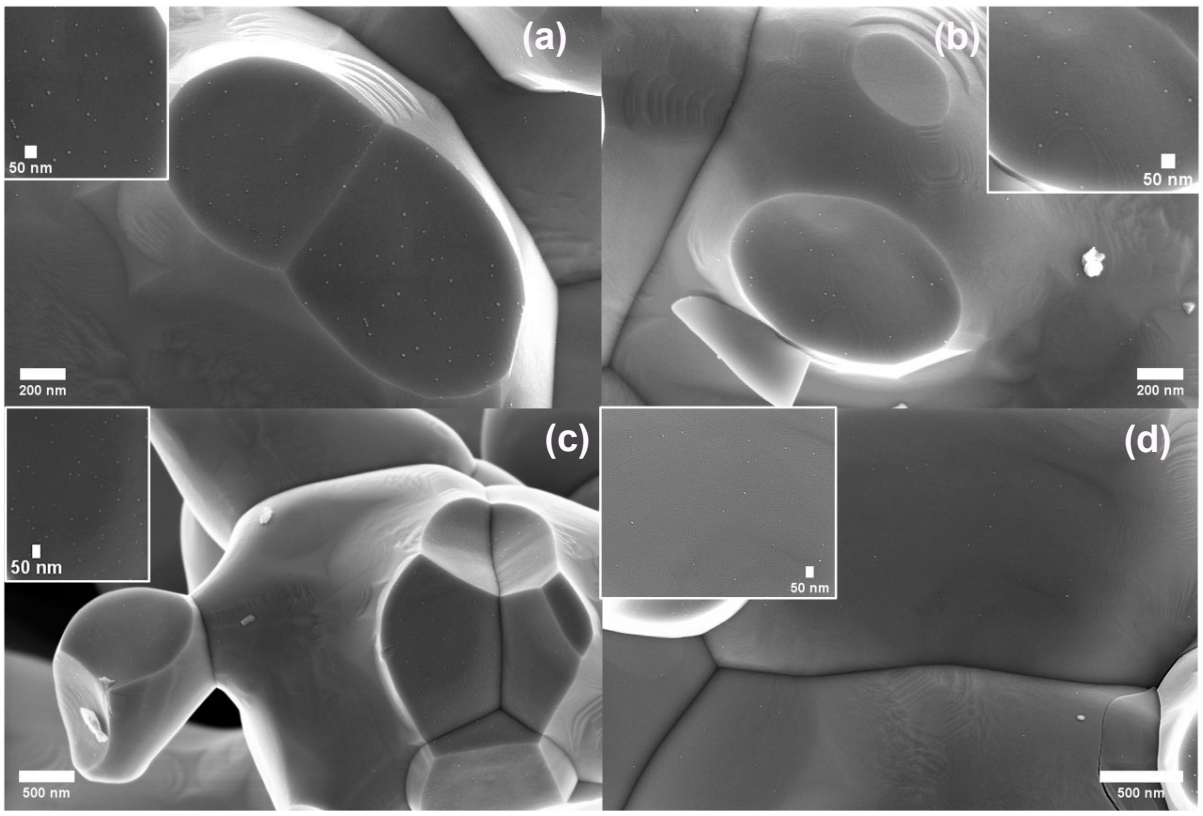


Figure 7.9 SEM images of L1.85NTR sample reduced at 450°C for the particle analysis.

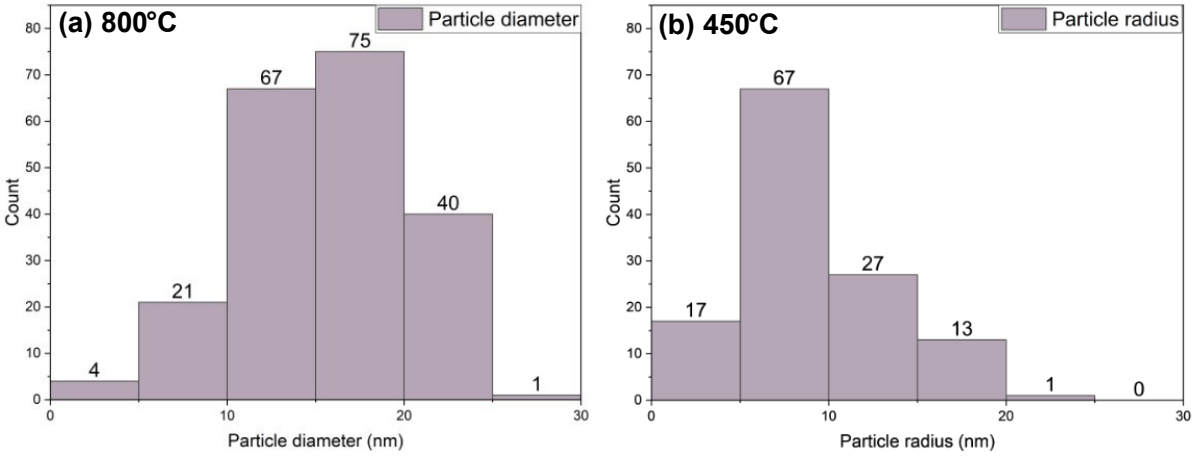


Figure 7.10 Size distribution diagrams of exsolved nanoparticles of L1.85NTR reduced in wet 5%H2/Ar at 800°C(a) and 450°C(b) for 3 hours.

7.3.2 *In-situ observation of the exsolution process*

As discussed in Section 7.3.1, the reduction temperature significantly influences the morphology of exsolved nanoparticles. To further investigate the evolution of exsolution with increasing reduction temperature, *in-situ* characterization techniques including thermogravimetric analysis (TGA) and scanning transmission electron microscopy (STEM) were employed to examine the L1.85NTR sample.

Figure 7.11 displays the TGA and its first derivative (DTG) results for the L1.85NTR sample reduced in a 5% H_2/Ar atmosphere with increasing temperature up to 1000°C and held at

1000°C for 3 hours. The heating rate was 5°C/min, and the gas flow rate was 60 ml/min. Due to the limitations of the testing system, a dry atmosphere was used, resulting in a relatively higher reducing condition compared to a wet atmosphere.

After reduction at 1000°C for 3 hours, the mass loss tended to reach a plateau, indicating a 1.58 wt% mass loss. Prior to reaching 1000°C, two distinct mass loss steps can be clearly observed. The mass loss due to the moisture absorbed on the surface was negligible, given that no distinguishable mass loss observed at temperature range from room temperature to 250°C [321–323]. According to the DTG curve, the first maximum mass loss occurred at approximately 427°C, and the second mass loss occurred over a broader range, centred around 665°C. As the characterization of the L1.85NTR sample reduced at 450°C and 800°C confirmed the exsolution of Ni nanoparticles, both mass loss steps were related to the exsolution process, resulting from the loss of oxygen anions in the perovskite structure [24]. With increasing temperature, the first plateau was achieved at around 500°C with a 0.36 wt% mass loss. Subsequently, when the temperature exceeded 600°C, a continuous mass loss was observed, similar to the reported exsolution of La(Sr)$Cr_{0.85}Ni_{0.15}O_{3-\delta}$ [324] and $La_{0.6}Sr_{0.4}FeO_{3-d}$ [322]. Amaya-Dueñas et al. [324] characterized the Ni exsolution from La(Sr)$Cr_{0.85}Ni_{0.15}O_{3-\delta}$ with TGA in 5%H_2/Ar and calculated the oxygen deficiency, δ. The exsolution and decomposition processes can be assumed as a subsequent reaction after oxygen loss. Consequently, according to the method described, the loss of oxygen can be derived using Equation 7.5:

$$l_O = \frac{MW_{L1.85NTR}}{A_O}\,\Delta m \qquad 7-5$$

Where $M_{L1.85NTR}$ is the molecular weight of L1.85NTR. Δm is the measured mass loss from TG curve. A_O is the atomic mass of oxygen and l_O is the loss of oxygen. Based on the Rietveld refinement results, assuming the molecular formula of L1.85NTR as $La_{1.888}NiTi_{0.9}Ru_{0.1}O_{5.832}$, the l_O of the sample reduced at 800°C is approximately 0.25 mol per mol of L1.85NTR. By dissecting the exsolution process, the main structure was considered as initially reduced to $La_{1.888}NiTi(Ru)O_{5.582}$. Subsequently, the exsolution resulted in Ni metal phase and La_2O_3 phase. As revealed by the Rietveld refinement results, the resulting products were identified as $La_{1.910}NiTi(Ru)O_{6-y}$ along with 1.58(5) wt% Ni metal and 0.28(2) wt% lanthanum oxides. Assuming the oxygen stoichiometry to be $La_{1.910}NiTi(Ru)O_{5.647}$ based on electroneutrality, Equation 7-4 can be extended accordingly, taking into account the molecular weight of $La_{1.910}NiTi(Ru)O_{5.647}$, Ni and La_2O_3:

$$\begin{aligned} &\mathrm{La_{1.888}NiTi(Ru)O_{5.832}} \xrightarrow{5\%\frac{\mathrm{H_2}}{\mathrm{Ar}}} \mathrm{La_{1.888}NiTi(Ru)O_{5.582}} \\ &\xrightarrow{5\%\frac{\mathrm{H_2}}{\mathrm{Ar}}} 0.9881\mathrm{La_{1.910}NiTi(Ru)O_{5.647}} + 0.0119\mathrm{Ni} + 0.0006\mathrm{La_2O_3} \end{aligned} \qquad 7-6$$

However, determining the precise oxygen stoichiometry of the parent phase $La_{1.888}NiTi_{0.9}Ru_{0.1}O_{6-\delta}$ and the product $La_{1.910}NiTi_{0.9}Ru_{0.1}O_{6-y}$ double perovskite experimental remains challenging. TGA with oxygen sensor at the outlet of exhaust gas, combined with quantification of the product phase might be helpful in the future in determine the oxygen stoichiometries.

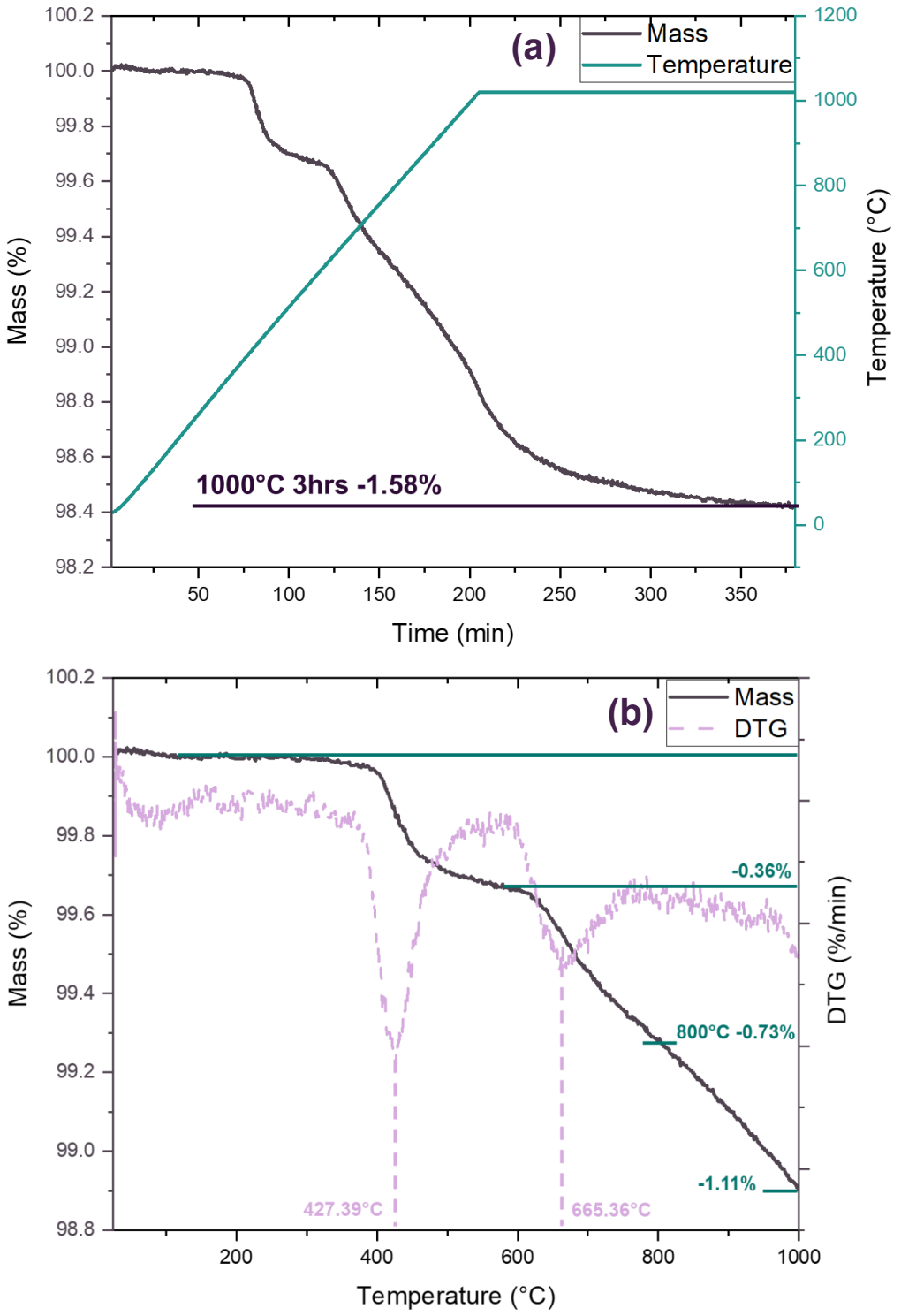


Figure 7.11 (a) TG curves and corresponding temperature profiles as a function of time, encompassing both the heating and dwelling phases; (b) TG and DTG curves as a function of increasing temperature, ranging from room temperature (RT) to 1000°C.

Ex-situ microscopy characterization revealed that exsolution occurred not only in the high-temperature range, but also at relatively lower temperatures. The thermogravimetric analysis indicated two stages of mass loss, implying two different stages of exsolution. Therefore, *in-situ* scanning transmission electron microscopy (STEM) was employed to investigate the

evolution of the sample morphology. The Protochips Fusion Select E-chips and rod were utilized to achieve the high temperature required for the exsolution process. In contrast to the experimental conditions, high vacuum (~10^{-7} torr, equivalent to ~1.33×10^{-5} Pascal) was used as a reducing environment in the TEM equipment. Therefore, the exsolution process may differ in detail from the experimental results that were conducted in 5%H_2/Ar.

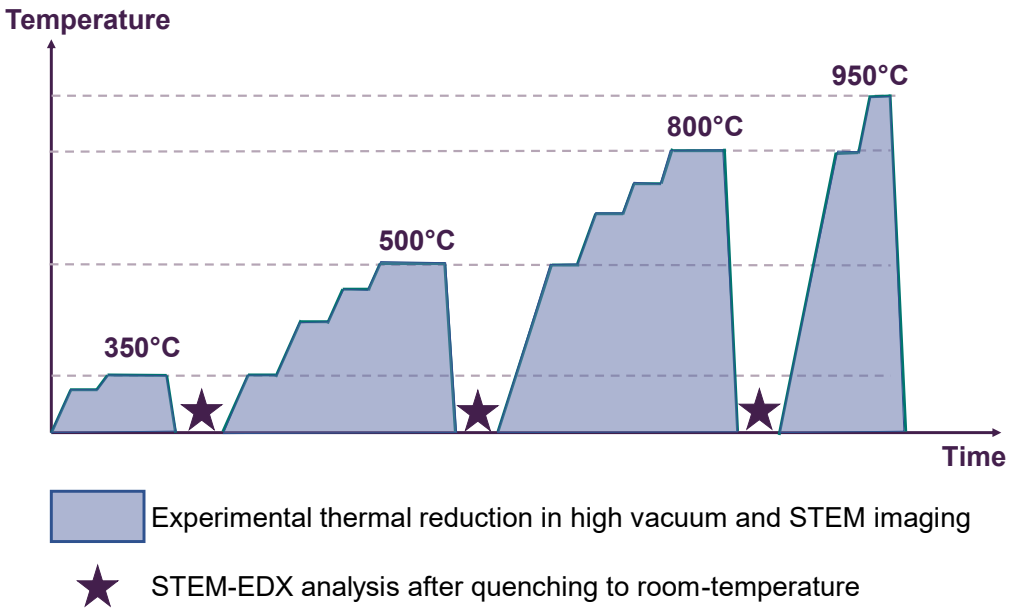


Figure 7.12 Schematic illustration of the thermal cycle applied to the sample.

To examine the evolution of L1.85NTR during the exsolution process, the sample was subjected to a heating procedure by reaching the target temperature incrementally to minimize sample and rod vibrations caused by rapid heating. The thermal cycle applied to the sample is illustrated in Figure 7.12. Furthermore, to analyse the chemical composition of the exsolved nanoparticles during thermal treatment, STEM-EDX analysis was conducted after quenching the sample to room temperature. The heating and quenching rates for the sample were set at 5°C/s.

Figure 7.13 displays the STEM- ADF images of both the initial and heated sample at 350°C, 450°C and 800°C. Three bright dots, marked by arrows, are visible on the surface of the sample grain reduced at 300°C when compared to the initial pristine sample, as shown in Figure 7.13 (a). This observation suggests morphological changes indicative of nanoparticle exsolution. In order to thoroughly investigate the emerging nano-features, the sample was quenched and subsequently analysed using EDX mapping, as depicted in Figure 7.14(e). The corresponding STEM- ABF and STEM-ADF images (Figure 7.13 a-d) reveal spherical clusters present on the surface of the L1.85NTR sample. Figure 7.13(e) demonstrates Ni enrichment, signifying that Ni nanoparticle exsolution had already commenced from reduction at 350°C.

As the reduction temperature increased, the evolution and reconstruction of the exsolved nanoparticles was observed. As demonstrated in Figure 7.13 (c), when the temperature rose to 450°C, two nanoparticles, indicated by green arrows in Figure 7.13 (b), reincorporated/dissolved into the bulk and vanished under microscopic observation. A similar phenomenon was observed when the temperature further increased to 800°C. This suggests the reconstruction of the sample surface morphology and exsolved nanoparticles, coupled with mass transportation within the bulk oxide materials. Cali et al. [185] also observed the movement of nanoclusters until they reached an energetically favoured location, *i.e.* surface defects, and proposed a vapour-liquid-solid (VLS) mechanism for the growth of exsolved Ir nanoparticles from $SrTiO_3$. In this mechanism, if the Ir nanoparticles were smaller than the critical size for particle growth, the Ir particle tended to 'lock' itself in place rather than form a supporting wire. In our case, the reconstruction was possibly due to the exsolution as a dynamic process, continually altering surface morphology until the exsolved nanoclusters/nanoparticles achieved both an energetically favourable state and the critical size for particle growth. Cao et al. [325] calculated the theoretical critical size of Ni nanocrystals to be approximately 1.5 nm. As demonstrated in Figure 7.14, there were two types of nanoparticles present on the surface of the bulk grain reduced at 950°C. One type consisted of small nanoparticles, similar to those in Figure 7.13 (b-d), with sizes of roughly ≤ 3nm, *i.e.*, 12 atomic diameters. The other type, marked by the green circle, had larger particle sizes of approximately 17 nm. The larger particles were considered the result of particle growth, while the smaller particles were still in a metastable state, potentially reincorporating into the bulk or merging with neighbouring large particles.

In line with the discussion in Section 7.3.1, the STEM-EDX analysis of the sample quenched between heating stages revealed a gradual increase in particle size, suggesting the transition of exsolved particles from metastable to stable states. As demonstrated in Figure 7.15, the dot contrasts located at the edge of the bulk grain measure approximately 3 – 3.5 nm after quenching from 350°C. Figure 7.16 presented the STEM images and EDX maps of the exsolved nanoparticles quenched from 500°C, with several particles ranging in size from 3.1 nm to 5.5 nm. It was expected that the smaller particles would reincorporate/dissolve in subsequent processes, while the larger particles will continue to grow through mass transportation and Ostwald ripening [185,326]. Upon heating to 800°C, fully formed spherical socketed nanoparticles were observable, as shown in Figure 7.17. The spherical particle depicted in Figure 7.17 (e) has an approximate diameter of 9 nm. According to the EDX analysis, the nanoparticles or clusters depicted in Figures 7.15, 7.16, and 7.17 all appear to be enriched in the Ni metal phase. This could provide insights into the two-step exsolution process depicted in Figure 7.11 of the TG behaviour of the L1.85NTR during reduction. Below 500°C, the reduction of the oxide bulk resulted in dynamic alterations to the surface

morphology, exsolving smaller nanoclusters which may reincorporate and dissolve into the bulk. Above 500-600°C, the nanoparticles that have achieved the critical size at energy-favoured locations continue to grow, and more cations are expelled from the bulk and reduced into the metal phase, leading to further mass loss.

Apart from particle growth, facets are another important factor that influences the exsolution process as discussed in Chapter 2. This is attributed to variations in thermodynamic nucleation energies and differences in the migration kinetics of cations across different crystal facets [327]. As for the region depicted in Figure 7.13 (d), no prominently larger particles were observed at 800°C. This observation can potentially be attributed to the presence of energy-unfavourable facets or planes, which impeded the migration of nickel cations [185,197,327]. However, the mechanism behind still needs further investigation.

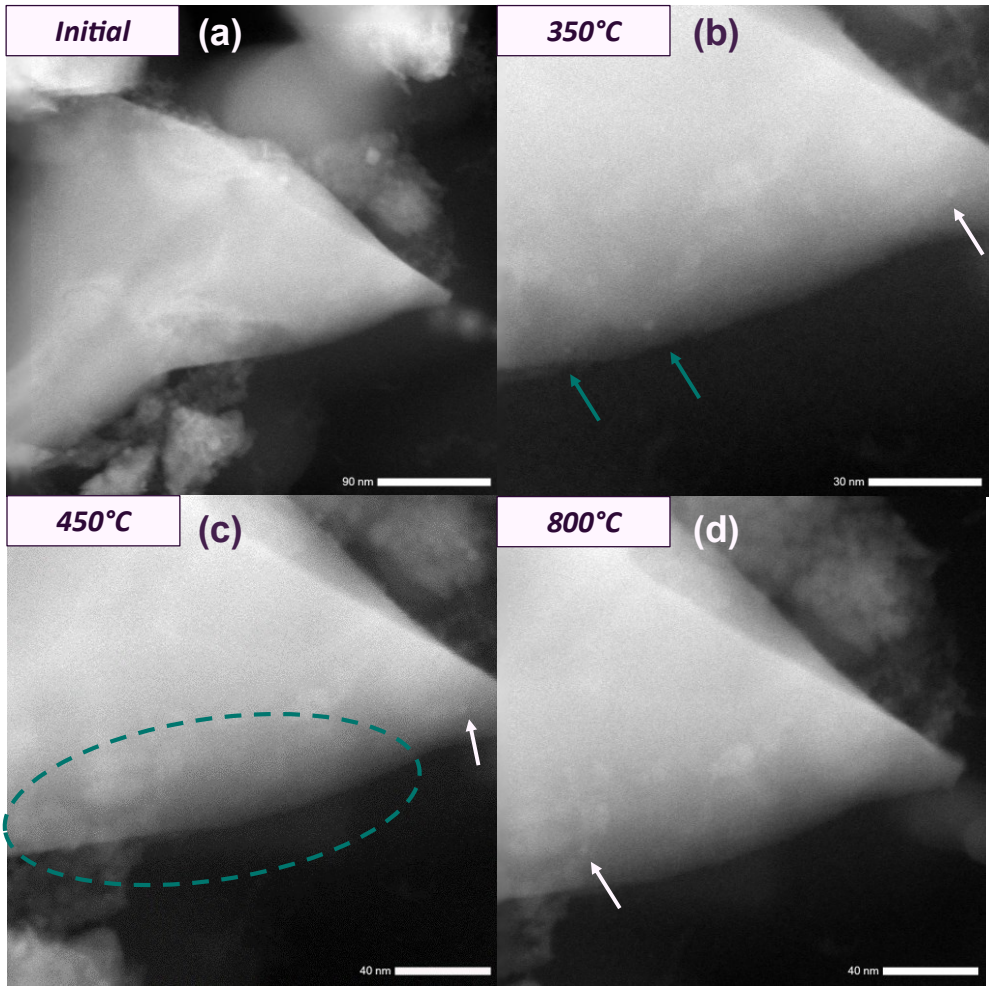


Figure 7.13 *In-situ* STEM-ADF images of (a) initial and reduced L1.85NTR sample at 350°C (b), 450°C (c) and 800°C (d).

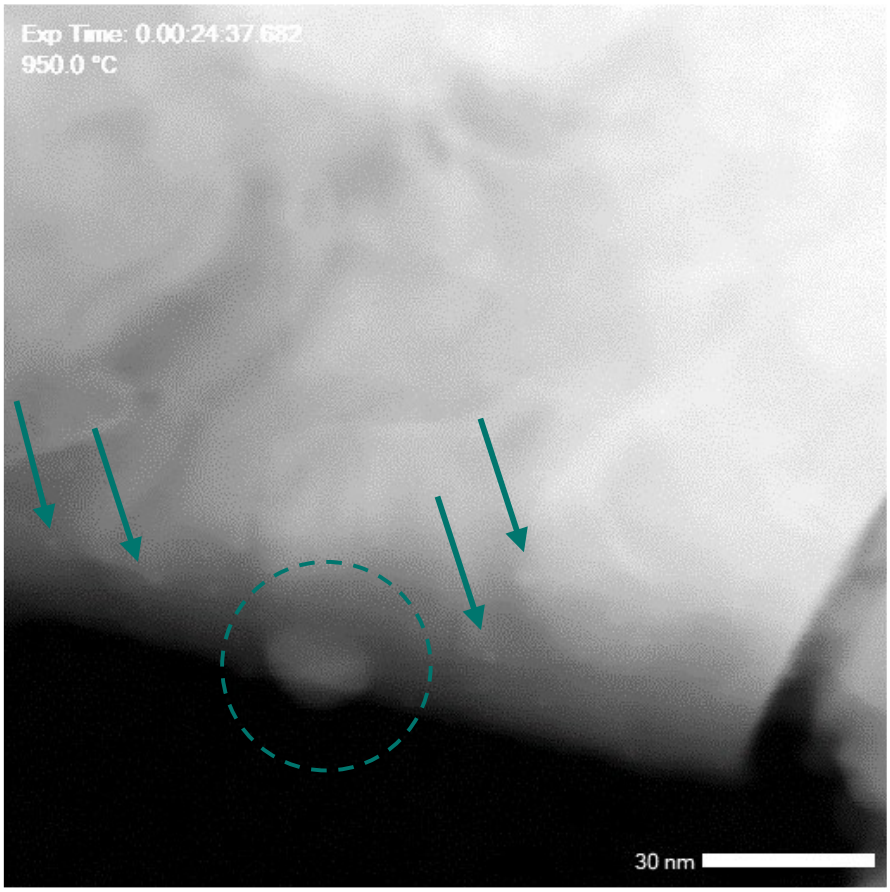


Figure 7.14 *In-situ* STEM-ADF image of the L1.85NTR sample at 950°C in high vacuum.

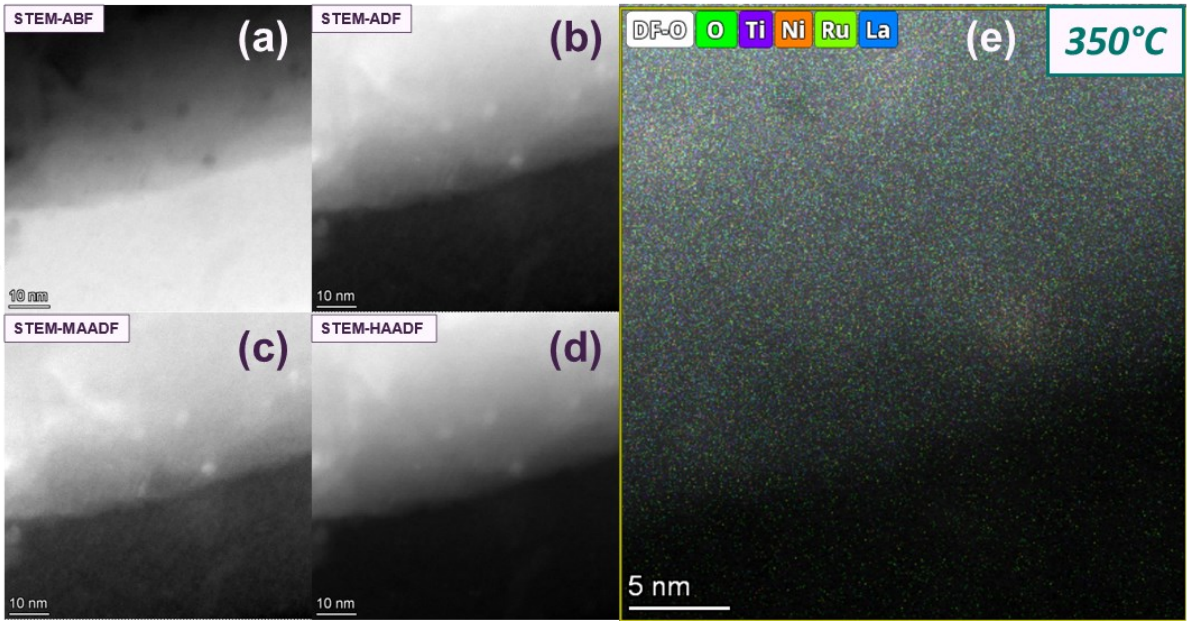


Figure 7.15 (a) STEM-ABF, (b) STEM-ADF, (c) STEM-MAADF, (d) STEM-HAADF images and (e) EDX maps of the quenched L1.85NTR after reduction at 350°C. Same area with the in-situ observation in Figure 7.13.

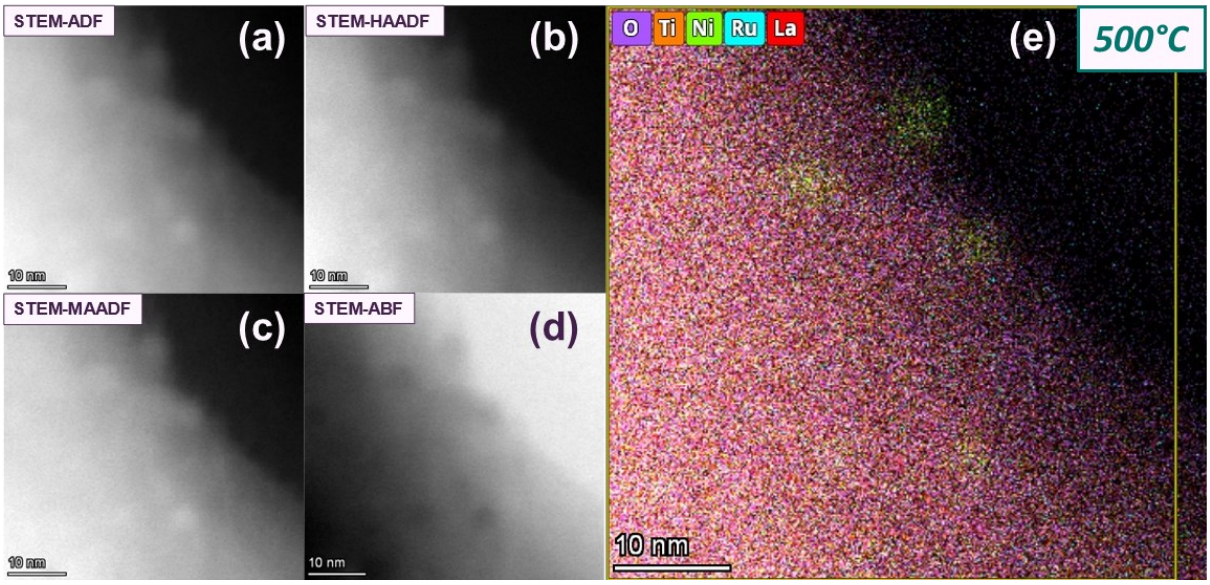


Figure 7.16 (a) STEM-ABF, (b) STEM-ADF, (c) STEM-MAADF, (d) STEM-HAADF images and (e) EDX maps of the quenched L1.85NTR after reduction at 500°C.

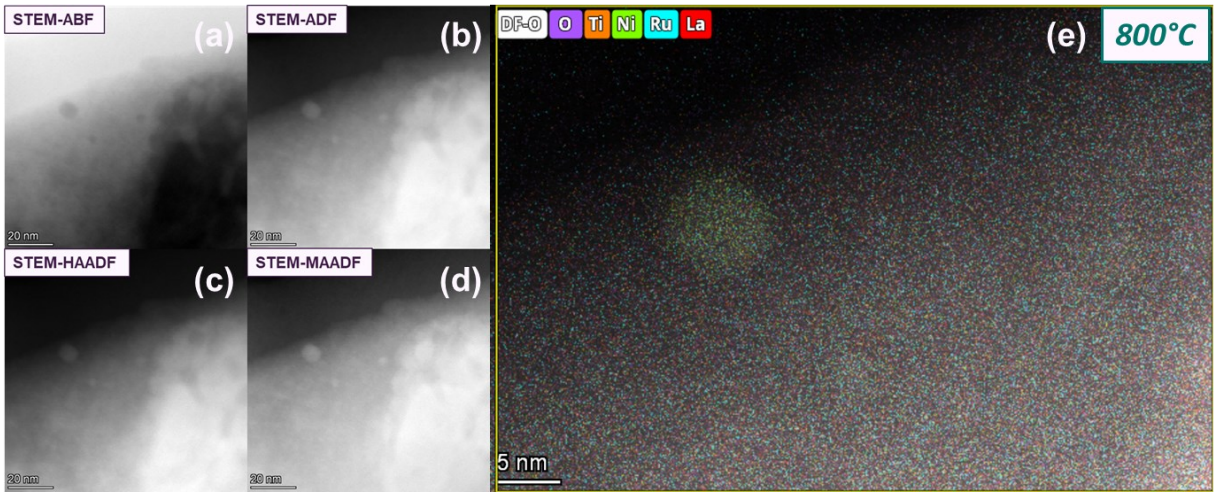


Figure 7.17 (a) STEM-ABF, (b) STEM-ADF, (c) STEM-MAADF, (d) STEM-HAADF images and (e) EDX maps of the quenched L1.85NTR after reduction at 800°C.

7.4 Impedance investigation of lanthanum nickel titanates and exsolution process

The study has revealed that A-site deficient L1.85NTR double perovskite exsolved a Ni metal phase after reduction in a reducing atmosphere at a specific temperature. In this section, the application of A-site deficient L1.85NTR and its exsolution process as a fuel electrode for solid-oxide cells are discussed. EIS was utilized to investigate the electrochemical performance of the Ru-doped A-site deficient lanthanum nickel titanates, along with the evolution of its performance as Ni nanoparticles were exsolved.

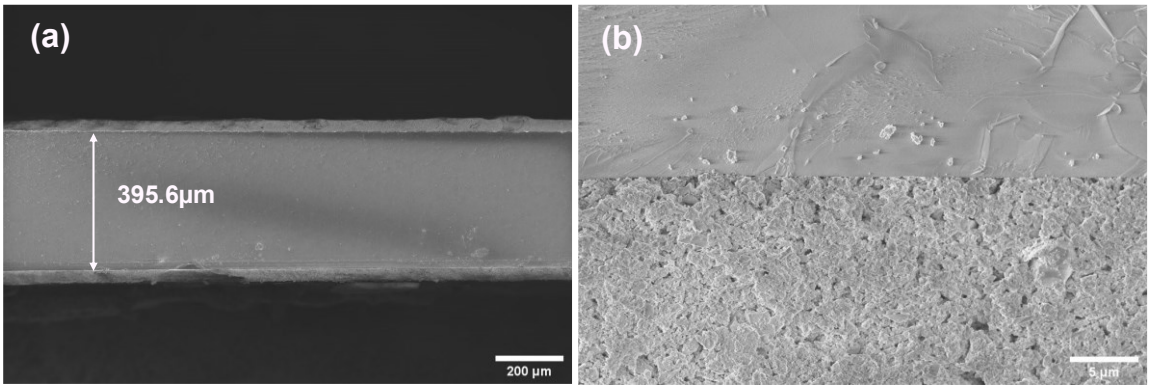


Figure 7.18 SEM images of the microstrucutre of the L1.85NTR/LSGM/L1.85NTR symmetric cell.

Symmetric cells with the as-prepared L1.85NTR double perovskite as electrodes were fabricated as detailed in Section 3.2.4. The thickness of the LSGM electrolyte was approximately 396 μm, as illustrated in Figure 7.18 (a). The printed electrodes had a thickness of roughly 30 μm. Figure 7.18 (b) displays the microstructure of the interface between the electrode and the electrolyte. It can be observed that, after ball-milling, the electrode grain size is relatively smaller compared to the coarsened grain. A certain number of pores, acting as gas channels when measured in a wet 5% H_2/Ar environment, are present in the sintered electrode layer, despite the electrode grains being close-packed, as shown in Figure 7.18 (b). Consequently, the microstructure of the symmetric cell requires further optimization in future work. The symmetric cell was then installed in the impedance testing system, as described in Section 3.3.5, and tested in a wet 5% H_2/Ar atmosphere.

Impedance spectra were measured within a wet 5% H_2/Ar atmosphere using a Solartron 1260A frequency response analyzer (FRA). Frequencies ranged from 15 M*Hz* to 50 m*Hz*, with 20 points measured per decade. As discussed in Section 7.4.2, exsolution was already observed beginning at 350°C. Therefore, to further investigate the temperature-dependence and the timescale of the exsolution process, EIS spectra at 343°C, 437°C, 528°C, and 710°C were measured, utilizing 10 loops of continuous measurements. EIS spectra at 800°C were recorded during the initial 1.5 hours, and the final spectrum was measured after a 4-hour reduction in a wet 5% H_2/Ar atmosphere. Each spectrum required approximately 30 minutes to be scanned from high frequency to low frequency. This method allowed for the tracking of the spectra's evolution as the reduction progressed.

Figure 7.19 displays EIS spectra of L1.85NTR/LSGM/L1.85NTR symmetric cell measured in flowing wet 5%H_2/Ar at different temperatures. The flow rate was 200ml/min. The temperatures annotated in the figure were determined using a thermocouple placed within the sample chamber, as shown in Figure 7.18. Figure 7.19 (a) reveals two complex arcs, which span from the high-frequency to the low-frequency range, presented in the spectra measured at 343°C. The gradual evolution of the ten spectra over five hours suggests a slight decrease in

impedance as the exsolution proceeds, with the spectra appearing to stabilize after 30 minutes of measurement at this temperature.

Figure 7.20 displays the fitting of the final spectrum from Figure 7.19 (a), based on the assumption that after five hours of reduction, the symmetric cell had reached an equilibrium state. The inset graphs illustrate the usage of two R/CPE components to simulate the frequency-dependent impedance response, suggesting that the impedance was primarily contributed by two types of response during the measurement. As indicated in Table 7.4, the ASR of the R1/CPE1 was approximately 1512 Ωcm^2. The capacitance of R1/CPE1 seems to originate from the LSGM electrolyte, a finding that aligns with the reference value, stating that the conductivity of LSGM at this temperature range was between 10^{-5} to 10^{-6} S/cm [328]. The second R2/CPE2 component was ascribed to the electrode-electrolyte interface with an ASR of 5702 Ωcm^2. This was expected as the first arc of the spectra remained constant with time, while the low-frequency arc displayed a slight decrease, implying an improvement in the conductivity at the interface due to the progression of Ni cation exsolution.

When the temperature rose to 437°C, an intriguing phenomenon was noted: as the reduction proceeded, the low-frequency impedance arc showed a slight increase. Similar fitting was conducted with the 10^{th} spectrum of the measurement at 437°C, as presented in Table 7.4. With the calculated capacitance of the R/CPE components, it was revealed that the resistance of interface layer increased over time and as the exsolution proceeded. According to previous *in-situ* TEM investigations, the exsolved Ni nanoparticles were too small to reach the critical size necessary for subsequent growth and might undergo reconstruction within this temperature range. This could potentially explain the observed increase in impedance: the reconstruction of nanoparticles and the incorporation of Ni into the structure, coupled with the loss of smaller nanoparticles, might hinder the desorption of hydrogen and decrease conductivity. However, the mechanism of this synergistic effect of exsolution and nanoparticle reconstruction remains unclear, necessitating further investigation in future work.

Upon further increasing the temperature to above 500°C, the impedance arcs exhibited a more pronounced decrease, as depicted in Figure 7.19 (c-e). Contrary to Figure 7.19 (a), the spectra measured at 528°C and 710°C suggested that exsolution continued for a longer duration. The spectra taken at 528°C seemed to stabilize after 4 hours of reduction, while the spectra obtained at 710°C continued to decrease until 5 hours of reduction.

Due to constraints of the testing system and FRA, only four spectra were measured at 800°C. These spectra demonstrated significant changes in both the shape and size of the impedance arcs. One notable observation is the gradual shift of the impedance arc intersections towards a higher resistance value. This can be attributed to the proximity of the reduction temperature, 800°C, to the melting point of the silver wires and current collector, which is 961°C. This might

result in thermal fatigue, expansion, mismatch, and loss of connection with the sample electrode, even as the total impedance of the symmetric cell decreased. The spectrum measured after 4 hours of reduction at 800°C was fitted as shown in Figure 7.21. The total ASR of the symmetric cell was approximately 13.99 Ωcm^2, in which the resistance of testing rigs and connection was also contributes. The fitting results suggested that the resistance contributed by the LSGM electrolyte bulk and grain boundary was merged into the intercept impedance arc (R_s), and the electrode-electrolyte interface dominated the low-frequency and high frequency arcs response and the resistance decreased to around 5.2 Ωcm^2.

In conjunction with the *in-situ* investigation, it can be concluded that the exsolution process occurs over a broad temperature range, spanning from low to high operational temperatures of the solid-oxide cell. The exsolution of the Ni nanoparticles resulted in a more substantial enhancement in the temperature range above 500°C, where the exsolution and particle growth are more consistent. The impedance spectra at 437°C exhibited an intriguing trend where the impedance gradually increased as the reduction process progressed. This phenomenon warrants further investigation.

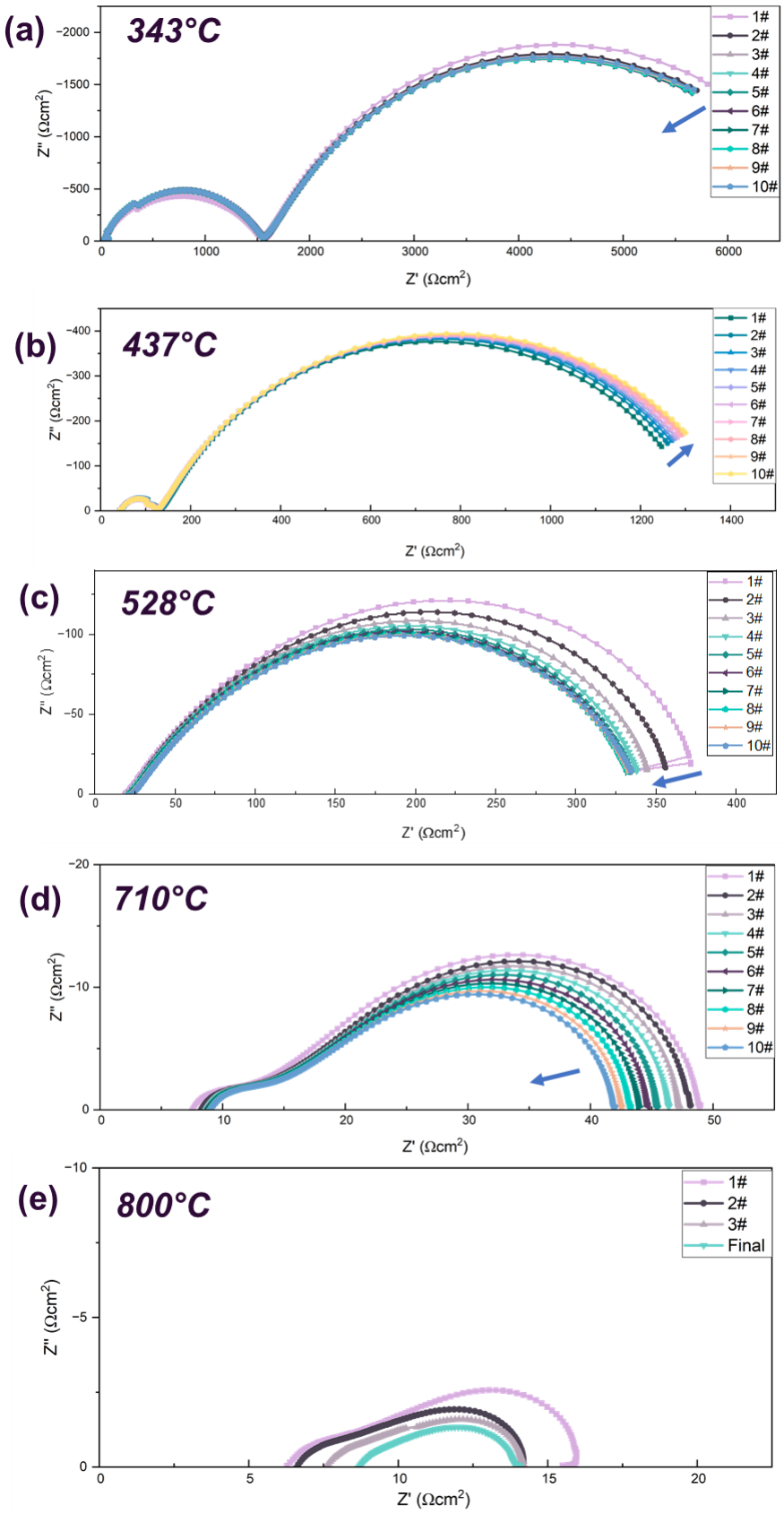


Figure 7.19 EIS spectra of L1.85NTR/LSGM/L1.85NTR symmetric cell measured in flowing wet 5%H_2/Ar at different temperatures. The spectra of each temperature were measured continuous with the reduction progressing. Each spectrum was scanned for 30mins.

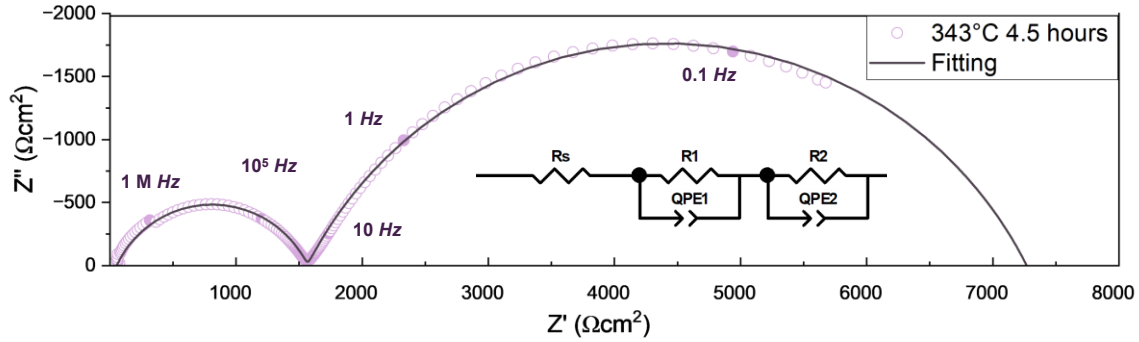


Figure 7.20 EIS spectrum of L1.85NTR/LSGM/L1.85NTR symmetric cell measured after reduction in flowing wet 5%H_2/Ar for 4.5 hours at 343°C, and the fitted plots. The inserted sketches illustrate the equivalent circuits.

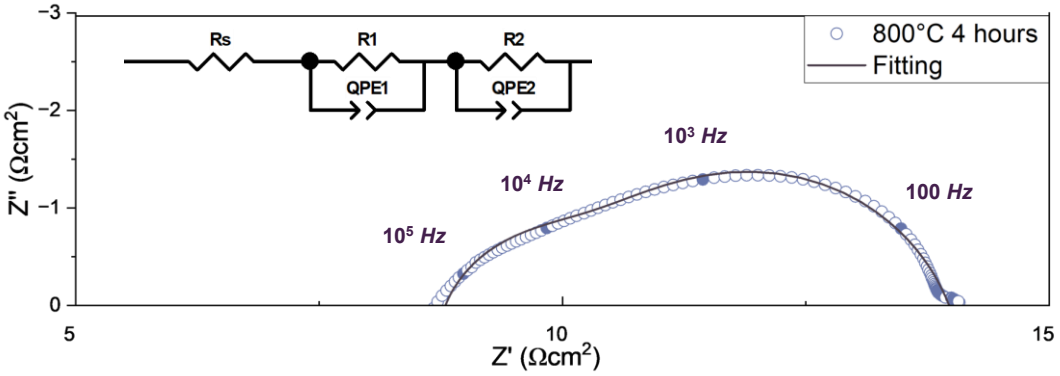


Figure 7.21 EIS spectrum of L1.85NTR/LSGM/L1.85NTR symmetric cell measured after reduction in flowing wet 5%H_2/Ar for 4.5 hours at 800°C, and the fitted plots. The inserted sketches illustrate the equivalent circuits.

Table 7.4 Fitted parameters of the components in the equivalent circuits at 343°C, 437°C and 800°C.

Temperature	Rs(Ωcm²)	R_1(Ωcm²)	QPE_1-Q	QPE_1-n	Capacitance(C_1,F)	R_2(Ωcm²)	QPE_2-Q	QPE_2-n	Capacitance(C_2,F)
343°C	53(5)	1512(6)	$5.3(2)\times10^{-9}$	0.724(3)	1.03×10^{-10}	5702(36)	$4.95(2)\times10^{-5}$	0.705(2)	5.02×10^{-5}
437°C	42.2(8)	88(2)	$8.6(8)\times10^{-7}$	0.87(2)	7.8×10^{-11}	1304(3)	$8.2(3)\times10^{-5}$	0.691(1)	5.4×10^{-5}
800°C	8.79(2)	1.5(2)	$2.9(1)\times10^{-9}$	0.75(3)	7.8×10^{-6}	3.7(2)	$1.34(8)\times10^{-4}$	0.76(1)	1.93×10^{-5}

7.5 Topotactic exchange enhanced Ru-exsolution

As elaborated in Section 7.3, Ni nanoparticles were exsolved from L1.85NTR during reduction within the temperature range of 350°C to 800°C. Contrary to our observations of A-site deficient lanthanum nickel ruthenates, the ruthenium cations displayed no noticeable enrichment as depicted in Figures 7.6 and 7.7. As a result, the advantages linked to the incorporation of the Ru dopant are diminished, due to the low concentration and strong lattice interaction of Ru dopant cations, which need higher reduction temperature or alternatives to provide extra 'driving forces' for Ru exsolution [144]. On the other hand, there's possibility of Ru cations nucleate and remain in the subsurface of the perovskite parent phase, forming endogenous nanoparticles. Therefore, to further explore Ru-exsolution, the L1.85NTR sample, reduced above 800°C in a wet 5%H_2/Ar environment for 3 hours, was examined using STEM-EDX.

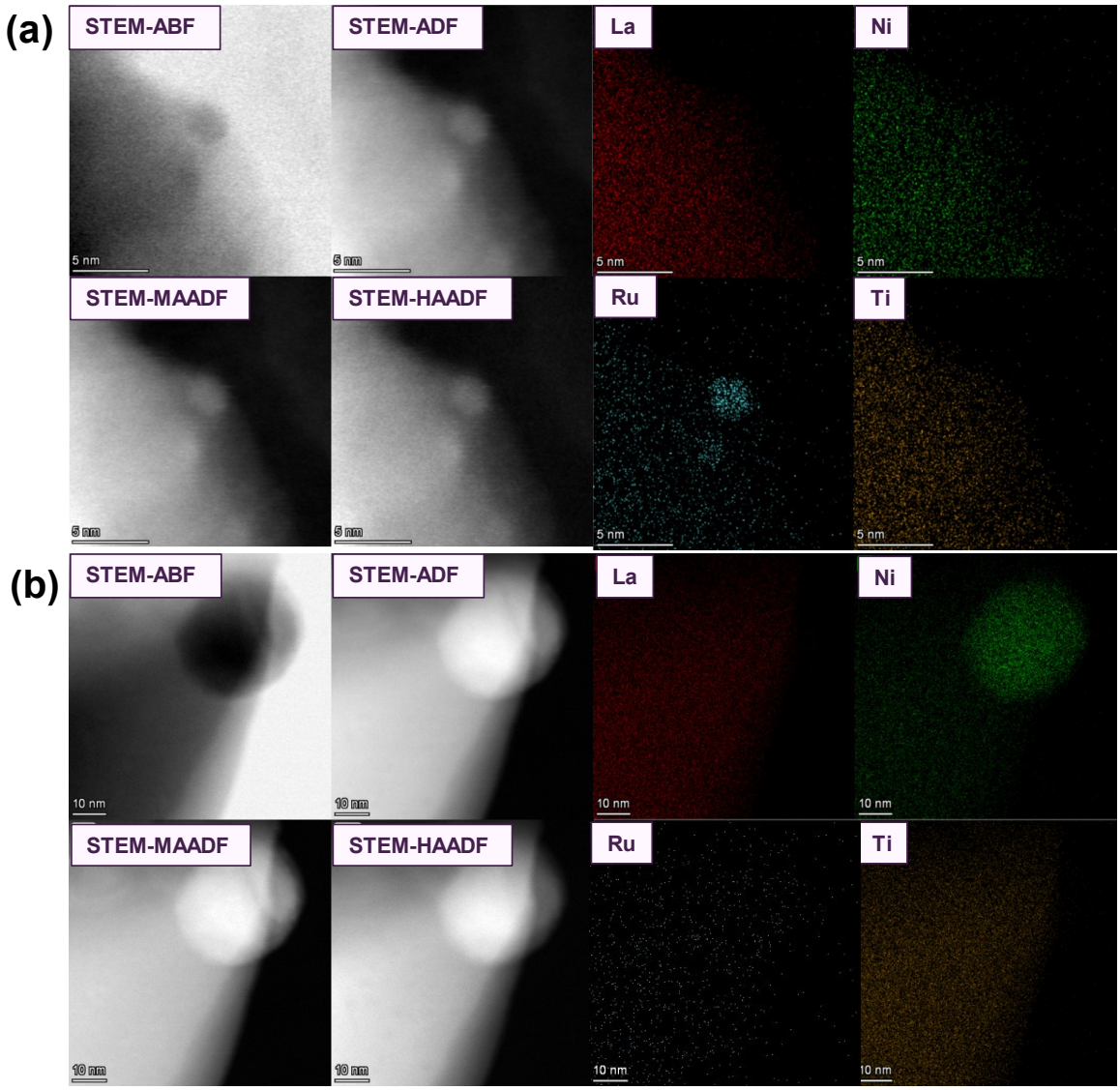


Figure 7.22 STEM images and EDX maps of two distinct regions (a) and (b) of the L1.85NTR sample reduced at 1000°C in a wet 5%H_2/Ar for 3 hours.

Figure 7.22 presented the STEM-EDX analysis of two distinct particles located on the surface of the L1.85NTR sample reduced at 1000°C in a wet 5%H_2/Ar environment for 3 hours. Ru exsolution was observed in Figure 7.22 (a) with particle sizes ranging from approximately 2.5 - 3 nm, while no Ni enrichment is detected in these exsolved nanoparticles. Figure 7.22 (b) demonstrated the exsolution of Ni particles measuring ~35 nm. This suggested that the onset of ruthenium exsolution from the lanthanum nickel titanates necessitates higher reduction temperatures. This occurrence may be attributed to the sluggish migration of transition metal cations in perovskite structure [329], which was Ru cations in the Ru-doped lanthanum nickel titanates in this work, especially in comparison to ruthenates, where the Ru cations are more abundantly distributed within the material.

In recent years, a novel approach to promoting the exsolution reaction was introduced [203] . This approach involves infiltrating exotic cations onto the surface of perovskite and substituting

the B-site cations during the reduction process, typically resulting in bimetallic alloy nanoparticles. This method has been reported to improve instability issues associated with high temperature reduction [206]. In this work, we employed this method to enhance exsolution and maintain stability during high-temperature reduction of L1.85NTR.

Iron was chosen as the guest cations for topotactic exchange due to its relatively high exchangeable energy [206,330]. Following the infiltration method outlined in reference [331] , a 10 wt% $Fe(NO_3)_3 \cdot 9H_2O$ (Sigma-Aldrich) aqueous solution was prepared as the cation swapping exchange precursor. The infiltrated L1.85NTR sample was annealed at 450°C for 4 hours, resulting in the presence of Fe_2O_3 on the surface of the L1.85NTR sample. The total fraction of infiltration was 5.37 wt% Fe_2O_3 on the L1.85NTR sample. The infiltrated sample, noted as Fe-L1.85NTR, was then reduced in wet 5% H_2/Ar at a specific temperature for 3 hours.

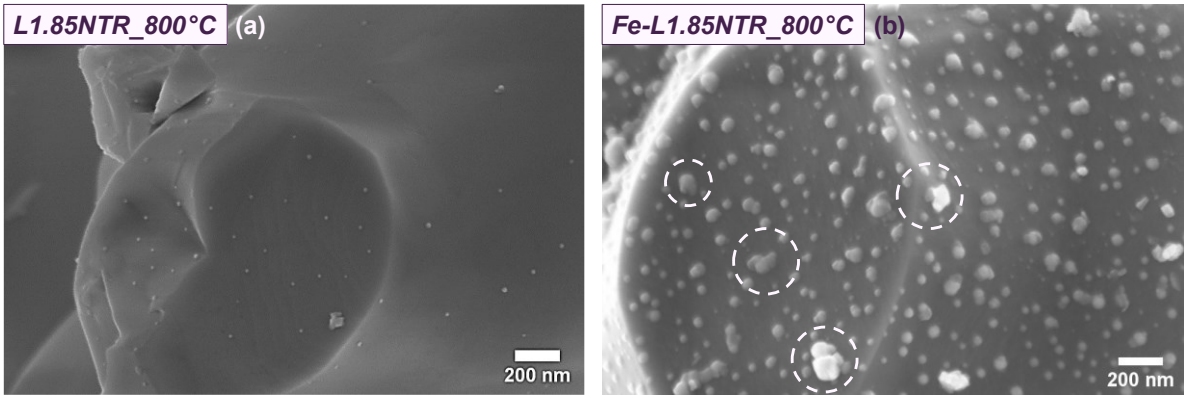


Figure 7.23 SEM images of (a) L1.85NTR sample and (b) Fe_2O_3 infiltrated L1.85NTR sample reduced at 800°C in wet 5% H_2/Ar for 3 hours. The dashed circles mark some of the sintered-like particles present on the surface of L1.85NR which was considered as unexchanged iron oxide.

Figure 7.23 shows the SEM images of the L1.85NTR sample and Fe-L1.85NTR sample reduced at 800°C. A higher number of nanoparticles can be observed on the surface of the bulk grain in the reduced Fe-L1.85NTR sample compared to the reduced L1.85NTR sample. This observation suggests that the topotactic exchange of Fe cations with the B-site cations of L1.85NTR promotes the exsolution reaction as expected. However, there appear to be sintered-like nano grains or particles on the surface, which resemble unexchanged Fe_2O_3 grains rather than exsolved nanoparticles (marked by the dash circles in Figure 7.23).

To investigate the species on the reduced Fe-L1.85NTR sample further, TEM and STEM-EDX were employed, as shown in Figure 7.24 and 7.25. Figure 7.24 displays the TEM bright-field images of the reduced Fe-L1.85NTR. The contrast between the brighter grain and the dark bulk indicates thickness or phase differences. In Figure 7.24(b), dark nanoparticles can be observed on the brighter grain, likely representing the exsolved nanoparticles. Yet, some dark particles/inclusions are also present, as indicated by the arrow in Figure 7.24(a). Figure 7.25 reveals the STEM-EDX analysis results, demonstrating enrichment of both nickel and

ruthenium at a spherical feature. This confirms the exsolution of a Ni-Ru alloy ~23.77 nm in diameter. In addition, Ru atoms also showed enrichment in features approximately 6 – 9 nm in diameter. This suggests that the topotactic exchange method enhanced the exsolution of ruthenium at 800°C as expected. However, it is intriguing that the enrichment of both Ni and Ru atoms appears atop the Fe_2O_3 phase, raising an interesting question about how Ru and Ni migrated into the iron oxide phase. Due to project time constraints, this mechanism has not yet been investigated.

In general, preliminary data offers an alternative approach to the exsolution treatment of Ru-doped A-site deficient lanthanum nickel titanates. By infiltrating a guest Fe source onto the surface of L1.85NTR, the population of exsolved nanoparticles was enhanced after reduction in wet 5%H_2/Ar at 800°C for 3 hours. The STEM-EDX analysis revealed the presence of alloy nanoparticles atop the unexchanged Fe_2O_3. The exsolution of ruthenium cations mitigated the need for high-temperature reduction in L1.85NTR for Ru-exsolution. However, the mechanisms of the exsolution process, including the guest cation swapping with B-site cations, migration of exsolved atoms, nucleation, and particle growth, require further investigation in the future.

This section represents a collaborative project with Dr. Arim Seong. The author would like to acknowledge Dr. Arim Seong for her assistance with the topotactic exchange method and infiltration operation.

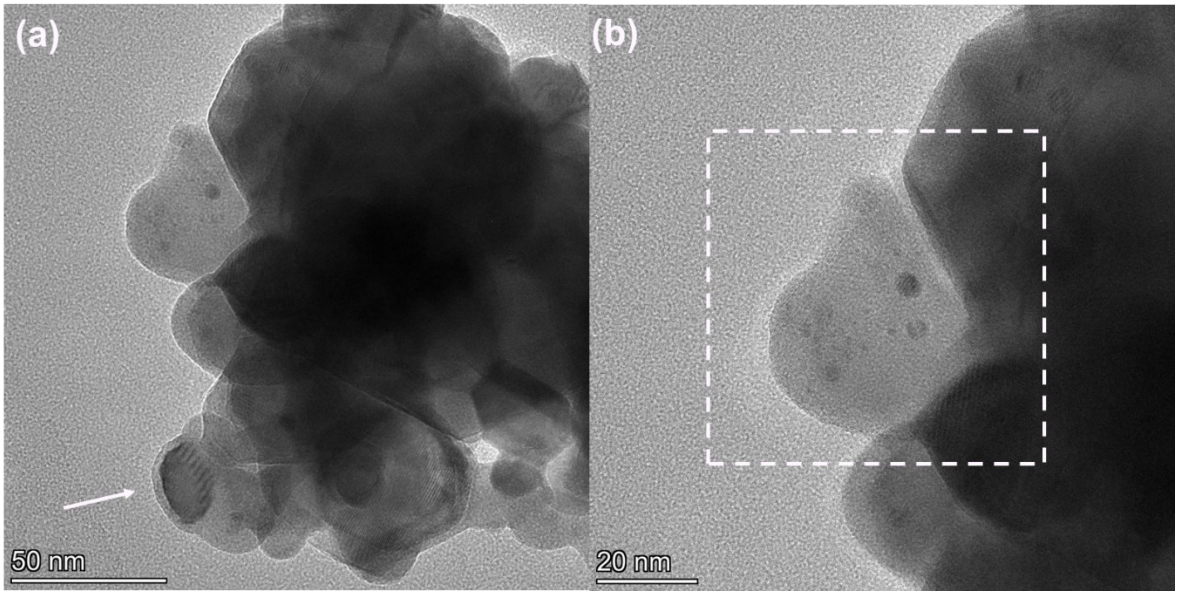


Figure 7.24 TEM images of Fe-L1.85NTR sample reduced in wet 5%H_2/Ar at 800°C for 3 hours.

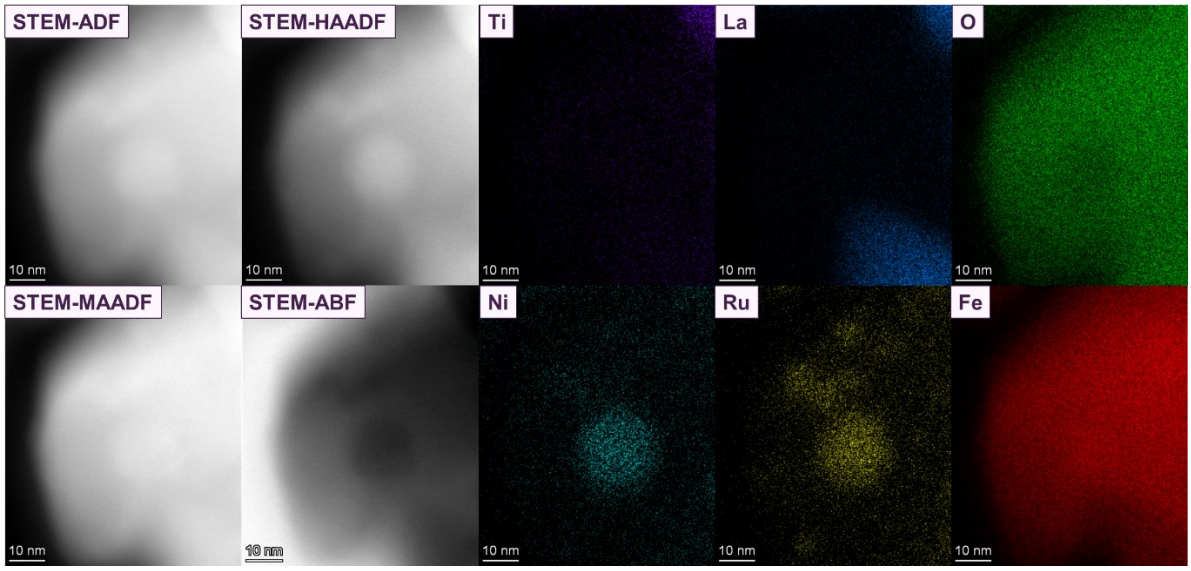


Figure 7.25 STEM images and EDX maps Fe- L1.85NTR sample reduced in wet 5%H_2/Ar at 800°C for 3 hours.

7.6 Summary

This chapter presents the synthesis of Ru-doped A-site deficient double perovskite L1.85NTR via the sol-gel method. Rietveld refinement revealed a monoclinic structure (space group $P2_1/n$) with 0.616 degree of B-site ordering for the product, L1.85NTR. Reduction in wet 5% H_2/Ar at 800°C for three hours led to exsolution of Ni nanoparticles from the bulk double perovskite grain. Surprisingly, exsolution of Ni nanoparticles was also observed at low temperature, 450°C, displaying smaller particle size and narrower size distribution compared to higher temperature exsolution. TG analysis showed two exsolution steps during reduction, occurring at 427°C and 665°C. *In-situ* STEM coupled with EDX analysis revealed grain morphology reconstruction around 450°C and particle growth with increasing temperature. *Ex-situ* STEM-EDX confirmed Ru exsolution in the sample reduced at 1000°C. Topotactic exchange promoted Ru exsolution and maintained double perovskite structure stability, resulting in Ni-Ru alloy exsolution and increased nanoparticle population. EIS measurements on L1.85NTR/LSGM/L1.85NTR symmetric cells showed decreased impedance after reduction in wet 5% H_2/Ar, except at 437°C, where slight impedance increase occurred. After four hours of reduction, impedance decreased to 5.4 Ωcm^2, indicating potential application of employing exsolution method and L1.85NTR as a fuel electrode in solid-oxide cells.

7.7 Future work

Based on the discussions in Sections 7.2-7.4, the exsolution of Ni nanoparticles is evident across a wide temperature range, from 350°C to 800°C. However, intriguing phenomena observed around 450°C warrant further investigation. Both TG and *in-situ* STEM revealed two stages of mass loss and morphology reconstruction, accompanied by an increase in EIS impedance with reduction time, suggesting a unique exsolution behaviour at this low-

temperature range. Future studies employing modelling and simulation could provide valuable insights.

Another noteworthy finding in this project is the simultaneous exsolution of Ni and Ru after reduction at 800°C, facilitated by topotactic exchange. However, STEM-EDX analysis revealed a peculiar distribution of Ni-Ru nanoparticles atop unexchanged iron oxide, indicating the need for further investigation into the migration of Ni and Ru cations. This observation calls for optimization of the experimental parameters involved in topotactic exchange.

Furthermore, EIS impedance measurements indicated an improvement in electrochemical performance with increasing exsolution. While the impedance of the symmetric cell reached approximately 5.4 Ωcm^2, the electrode interface impedance remained approximately 20 times higher than that of commercial electrodes, suggesting the need for further optimization of microstructure and cell fabrication parameters.

Chapter 8 Conclusion and future work

8.1 Conclusion

Driven by the pressing need for the development of highly efficient and long-lasting Solid Oxide Cells (SOCs), extensive efforts have been directed toward enhancing efficiency and mitigating the rapid degradation of fuel electrodes[8]. Due to the convenient *in-operando* growth of catalytic active nanoparticles and enhancement of stability and impurity tolerance, the exsolution phenomenon and method has drawn drastically increased attention since 2013, in the field of electrochemical devices, especially SOCs[81,88,179]. In this thesis, the exsolution phenomenon was investigated in conjunction with double perovskite materials as potential fuel electrodes for SOCs.

Double perovskite materials, particularly those incorporating Ru as B-site cations, have shown promise as candidates for SOC electrode/electrocatalyst applications. This is attributed to the catalytic activity of Ru cations in facilitating the Oxygen Reduction Reaction (ORR), Oxygen Evolution Reaction (OER), Hydrogen Oxidation Reaction (HOR), and Hydrogen Evolution Reaction (HER). In this study, lanthanum nickel ruthenate double perovskites were synthesised and explored their intrinsic properties [50,283]. The synthesis methods were firstly discussed, comparing the solid-state reaction and sol-gel citric-nitrate route. The sol-gel method demonstrated superior product quality and was subsequently employed in these investigations. Characterization of intrinsic properties confirmed that the synthesized stoichiometric double perovskite La_2NiRuO_6 (L2NR) exhibited a monoclinic structure with space group $P2_1/n$ and rock-salt ordering of B-site Ni and Ru cations. Thermal analysis in an air environment confirmed the stability of L2NR up to a temperature of 800°C and its suitability for fast sintering and densification at 1400°C. X-ray Photoelectron Spectroscopy (XPS) investigations validated the valence states of the cations within the double perovskite structure as +2, +3, and +4 for Ni, La, and Ru, respectively. Solubility of A-site deficiencies was also explored, with results indicating values below 10 at% for subsequent exsolution studies.

In the exsolution studies of lanthanum nickel ruthenates, the crucial role of A-site deficiency in promoting nanoparticle exsolution and ensuring structural stability under reducing conditions was highlighted. Comparative analyses of LxNR samples (x = 2, 1.9, and 1.85) after reduction revealed the exsolution of Ni-Ru bimetallic alloy from the A-site deficient sample L1.85NR following low-temperature reduction (450°C) in a wet 5%H_2/Ar atmosphere. This underscores the advantage of utilizing the double perovskite structure in exsolution treatments, where both B-site cations with a 50% concentration may exsolve, forming alloy nanoparticles at lower temperatures while minimizing long-distance diffusion.

In the investigation of L1.85NR exsolution, various reduction conditions were explored. Dry reduction in 5%H2/Ar at 450°C resulted in the exsolution of metal nanoparticles. Thermal analysis provided *in-situ* observations of mass loss during reduction in dry 5%H_2/Ar, indicating an onset of exsolution at lower temperatures than 450°C. The relatively small amount of oxygen loss compared to previous studies[298,299] implied structural stability, with a high abundance of exsolved nanoparticles observed on the surface within 3 hours.

To examine exsolution behaviour with increasing temperatures, *ex-situ* TEM studies on L1.85NR reduced at 350°C, 400°C, and 450°C were conducted. Lower temperatures favoured nucleation, resulting in a more uniform distribution and smaller particle size observed at 350°C. STEM-EDX analysis at 350°C indicated the separation of exsolved Ni and Ru metallic phases. *In-situ* STEM and STEM-EDX investigations in high vacuum revealed a surprising phenomenon: at 300°C, Ni metal chunks and small Ru metal nanoparticles were detected for the first time. Subsequent thermal reduction at higher temperatures led to the gradual disappearance of Ni chunks, forming smaller Ni nanoparticles. After reduction at 450°C in high vacuum, overlapping signals of Ni and Ru appeared in the exsolved nanoparticles observed in the EDX analysis maps.

During isothermal reduction at 450°C in high vacuum, rapid nucleation occurred within 20 seconds to 2 minutes, as observed through in-situ TEM observations. A similar response was noted under wet 5%H_2/Ar conditions in EIS investigations of symmetric cells featuring L1.85NR electrodes. The substantial decrease in low-frequency arcs was attributed to the exsolution of Ni-Ru nanoparticles. Following a 25-minute reduction period, the ASR of the symmetric cell improved by approximately 90% compared to initial measurements in static air. Full cell tests with L1.85NR/LSGM/LSCF single cells demonstrated reduced ASR as reduction and exsolution progressed, compared to the stoichiometric phase L2NR as the fuel electrode. Peak power density increased at both 450°C and 600°C, suggesting the potential of Ni-Ru nanoparticle-decorated L1.85NR for SOC applications.

Additionally, collaboration with DESY synchrotron beamline centre enabled the collection of *in-situ* WAXS data, which revealed a growing signal attributed to the Ni-Ru alloy phase during reduction in 5%H_2/N_2. Similar observations were made for L1.85NR reduced at 550°C, where *in-situ* WAXS data exhibited the presence of Ni-Ru metallic phase post-reduction, along with partial decomposition to lanthanum oxides as expected.

Subsequent investigations focused on the exsolution of Ru-doped lanthanum nickel titanate double perovskite, where Ni cations retained a 50% concentration on the B-site, while Ru content reduced to 5at%, and Ti cations were non-exsolvable. Following wet 5%H_2/Ar reduction, Ni nanoparticles were identified over a broad temperature range (350°C - 1000°C). Thermal analysis of the A-site deficient sample L1.85NTR revealed a two-step mass loss

indicative of oxygen loss. *In-situ* STEM observations revealed particle growth with increasing temperature, with surface reconstruction observed around 400-450°C, leading to the disappearance or re-dissolution of unstable nanoparticles into the bulk. Notably, the exsolution of Ru cations as 5at% dopants was only observed after reduction at 1000°C, indicating the dominant role of diffusion and concentration in Ru exsolution. Attempts to promote Ru exsolution through topotactic exchange resulted in enhanced exsolution of binary alloy nanoparticles. Electrochemical performance assessment through EIS investigations of symmetric cells yielded an ASR of 5.4 Ωcm² after 4-hour reduction in wet 5%H_2/Ar at 800°C, underscoring the potential of L1.85NTR for use as a fuel electrode in SOCs.

In conclusion, this research investigated the exsolution phenomenon and its application in different double perovskite materials, such as lanthanum nickel ruthenates and Ru-doped lanthanum nickel titanates. These materials, especially when A-site deficient and featuring exsolved nanoparticles, show considerable potential for SOC applications, as evidenced by enhanced electrochemical performance. The findings presented in this thesis contribute to the progress of SOCs and lay a groundwork for future exploration and development in this domain.

8.2 Future work

8.2.1 Studies on the A-site deficiency concentrations and its effect of exsolution

In this thesis, A-site deficiency systems has been established to facilitates the exsolution process. In Chapter 5, both L1.85NR and L1.9NR exhibited exsolved nanoparticles under microscopic characterization. However, the relationship between exsolved nanoparticles and A-site deficiency concentrations remains unclear. Considering the reported "trapping" effect of A-site vacancies on exsolved cations [185], it is theoretically expected that higher A-site deficiency concentrations would lead to a greater nucleation. Based on preliminary information about the solubility of A-site deficiency in lanthanum nickel ruthenate double perovskites, a delicate design involving $La_{2-x}NiRuO_{6-\delta}$ ($0 \leq x \leq 0.15$) with varying A-site deficiency content could be undertaken. *In-situ* and *ex-situ* microscopy observations of L(2-x)NR undergoing exsolution would aid in differentiating the effects of A-site deficiency concentrations.

8.2.2 Studies on the facet-dependency of the exsolution

In Section 5.3.1, it became evident that exsolved nanoparticles on dense pellets exhibited differences in population across different grains. Investigating the preferred orientation of exsolved nanoparticles in the monoclinic $P2_1/n$ structured L1.85NR double perovskite is worthwhile. Two viable approaches can be pursued for studying orientation preferences and facet dependency. The first involves applying polycrystalline ceramic Electron Backscatter Diffraction (EBSD) to dense ceramic pellets to characterize facet orientations, in conjunction with SEM characterization of exsolved nanoparticles. The second approach entails using deposition techniques to fabricate double perovskite thin films with specific orientations.

Characterizing these thin films post-reduction would provide insights into the effects of orientation.

8.2.3 Studies on hydrogen partial pressure and its effect on the exsolution

Throughout this thesis, various reducing atmospheres, including wet 5%H_2/Ar with approximately 3% moisture, dry 5%H_2/Ar, pure hydrogen, and high vacuum, were employed for the reduction and exsolution of A-site deficient lanthanum nickel ruthenates and titanates. Therefore, it is valuable to systematically investigate the extent of reducing conditions and their impact on exsolution behaviour. Balancing hydrogen partial pressure can be achieved by adjusting moisture content or mixing pure hydrogen with inert gases (Ar or N_2). TGA under various atmospheres provides a convenient means to observe the initiation of mass loss and exsolution.

8.2.4 Studies on the electron-beam induced exsolution

In Section 6.4.2, an intriguing phenomenon of large Ni metal particles exsolving and subsequently redissolving into the bulk was observed. Intensive exsolution was noted during *in-situ* STEM investigations in a high vacuum environment. However, the potential beam damage effect remains unclear. Employing *in-situ* TEM or STEM imaging would be ideal to observe the beam's effect on the exsolution. Continuous TEM or STEM observation at room temperature or relatively low temperatures (for example, 150°C) for extended periods would provide insights into the beam's effect on the exsolution phenomenon.

8.2.5 Studies on the re-oxidation and reversibility of the exsolved nanoparticles

Preliminary WAXS data indicated the evolution of Ni-Ru alloy signals with ongoing reduction. However, once the reduced L1.85NR sample was exposed to an oxidation atmosphere, the signal from the metallic phase disappeared, suggesting an instantaneous response of exsolved nanoparticles to the high temperature reducing atmosphere. This raises an intriguing question about whether exsolved nanoparticles exhibit reversibility, akin to a "self-generated" catalyst [83,212]. Further work is required, involving *in-situ* real-time characterization techniques, as the instant response of particles may occur within a second—the scanning time for WAXS data. Redox cycles could also be employed in continuous EIS investigations to verify the effect of self-regeneration.

8.2.6 Studies of cations diffusion in topotactic exchange

Topotactic exchange has been demonstrated to facilitate exsolution and the formation of alloy nanoparticles[203,332]. Preliminary data confirmed the formation of Ni-Ru bimetallic nanoparticles in the presence of Fe_2O_3 as an exotic exchange source. However, the exsolution process and the cation diffusion pathways in this method remain unclear. Metallic phases were

characterized on top of the iron oxide phase, underscoring the need to investigate cation diffusion in the topotactic exchange mechanism.

8.2.7 Studies on optimizing symmetric cell and single cell structure

While the assessment of electrochemical performance in Chapter 6 and 7 has revealed promising prospects for A-site deficient lanthanum nickel ruthenates and titanates as SOC electrodes, the ASR of full cells or symmetric cells still exceeds the common target for applications, which typically requires an ASR of 0.45 Ωcm^2 or lower[11]. Therefore, optimization efforts are essential for application purposes. Various approaches, such as adjusting electrolyte thickness, tuning electrode microstructure, and optimizing electrode composition, can be explored to enhance cell electrochemical performance.

References

1 UK Department for Energy Security and Net Zero, *UK energy in brief 2023*, 2023.

2 UK Department for Business Energy & Industrial Strategy, *Digest of UK Energy Statistics Annual data for UK, 2020*, 2021.

3 HM Government, *Clean Growth Strategy*, 2018.

4 M. B. Mogensen, *Curr Opin Electrochem*, 2020, **21**, 265–273.

5 M. A. Laguna-Bercero, *J Power Sources*, 2012, **203**, 4–16.

6 K. Nanaeda, F. Mueller, J. Brouwer and S. Samuelsen, *J Power Sources*, 2010, **195**, 3176–3185.

7 NIST Standard Reference Database, https://janaf.nist.gov/.

8 M. B. Mogensen, *Curr Opin Electrochem*, 2020, **21**, 265–273.

9 C. Sun and U. Stimming, *J Power Sources*, 2007, **171**, 247–260.

10 A. Tesfai and J. T. S. Irvine, in *Comprehensive Renewable Energy*, Elsevier, 2012, pp. 261–276.

11 C. Tsai, PhD Thesis, Imperial College London, 2020.

12 M. Ghatee and J. T. S. Irvine, *Int J Hydrogen Energy*, 2010, **35**, 9427–9433.

13 F. Li, T. Ohkubo, Y. M. Chen, M. Kodzuka, F. Ye, D. R. Ou, T. Mori and K. Hono, *Scr Mater*, 2010, **63**, 332–335.

14 B. Li, S. Liu, X. Liu, G. Hao, H. Wang and W. Su, *Int J Hydrogen Energy*, 2013, **38**, 11392–11397.

15 S. Kim, S. W. Lee, S. Lee, J. H. Kim and T. H. Shin, *Electrochim Acta*, 2023, **463**, 142751.

16 N. Mahato, A. Banerjee, A. Gupta, S. Omar and K. Balani, *Prog Mater Sci*, 2015, **72**, 141–337.

17 S. P. Jiang, *Int J Hydrogen Energy*, 2019, **44**, 7448–7493.

18 C.-C. T. Yang, W.-C. J. Wei and A. Roosen, *Mater Chem Phys*, 2003, **81**, 134–142.

19 A. Hauch, S. H. Jensen, J. B. Bilde-Sorensen and M. Mogensen, *J Electrochem Soc*, 2007, **154**, A619.

20 M. B. Mogensen, *Curr Opin Electrochem*, 2020, **21**, 265–273.

21 T. L. Skafte, B. R. Sudireddy, P. Blennow and C. Graves, *ECS Trans*, 2016, **72**, 201–214.

22 J. T. S. Irvine, D. Neagu, M. C. Verbraeken, C. Chatzichristodoulou, C. Graves and M. B. Mogensen, *Nat Energy*, 2016, **1**, 15014.

23 M. B. Mogensen, A. Hauch, X. Sun, M. Chen, Y. Tao, S. D. Ebbesen, K. V. Hansen and P. V. Hendriksen, *Fuel Cells*, 2017, **17**, 434–441.

24 J. Myung, D. Neagu, D. N. Miller and J. T. S. Irvine, *Nature*, 2016, **537**, 528–531.

25 A. R. Chakhmouradian and P. M. Woodward, *Phys Chem Miner*, 2014, **41**, 387–391.

26 X. Chen, J. Xu, Y. Xu, F. Luo and Y. Du, *Inorg Chem Front*, 2019, **6**, 2226–2238.

27 S. N. Ruddlesden and P. Popper, *Acta Crystallogr*, 1958, **11**, 54–55.

28 W. Zhang, K. Fujii, E. Niwa, M. Hagihala, T. Kamiyama and M. Yashima, *Nat Commun*, 2020, **11**, 1224.

29 G. King and P. M. Woodward, *J Mater Chem*, 2010, **20**, 5785–5796.

30 B. Frit and J. P. Mercurio, *J Alloys Compd*, 1992, **188**, 27–35.

31 V. M. Goldschmidt, *Naturwissenschaften*, 1926, **14**, 477–485.

32 A. Hossain, P. Bandyopadhyay and S. Roy, *J Alloys Compd*, 2018, **740**, 414–427.

33 J.-H. Kim and A. Manthiram, *J Mater Chem A Mater*, 2015, **3**, 24195–24210.

34 A. A. Taskin, A. N. Lavrov and Y. Ando, *Appl Phys Lett*, 2005, **86**, 1–3.

35 S. Sengodan, S. Choi, A. Jun, T. H. Shin, Y. W. Ju, H. Y. Jeong, J. Shin, J. T. S. Irvine and G. Kim, *Nat Mater*, 2015, **14**, 205–209.

36 S. Vasala and M. Karppinen, *Progress in Solid State Chemistry*, 2015, **43**, 1–36.

37 J. Zhou, N. Wang, J. Cui, J. Wang, J. Yang, Z. Zong, Z. Zhang, Q. Chen, X. Zheng and K. Wu, *J Alloys Compd*, 2019, **792**, 1132–1140.

38 C. Hu, J. Xu, Y. Tan and X. Huang, *Trends Chem*, 2023, **5**, 225–239.

39 F. Zhou, L. Zhang, J. Li, Q. Wang, Y. Chen, H. Chen, G. Lu, G. Chen, H. Jin, S. Wang and J. Wang, *Engineering Reports*, , DOI:10.1002/eng2.12437.

40 Y. Yang, Y. Yu, J. Li, Q. Chen, Y. Du, P. Rao, R. Li, C. Jia, Z. Kang, P. Deng, Y. Shen and X. Tian, *Nanomicro Lett*, 2021, **13**, 160.

41 J. Hwang, R. R. Rao, L. Giordano, Y. Katayama, Y. Yu and Y. Shao-Horn, *Perovskites in catalysis and electrocatalysis*, .

42 P. D. Battle and W. J. Macklin, *The Crystal and Magnetic Structures of CazYRuOs and the Electronic Properties of the Series Mz+X3+Ru5+Os (Ad = Ca, Sr, Ba; X = La, Y)*, .

43 K. P. Hong, Y. H. Choi, Y. U. Kwon, D. Y. Jung, J. S. Lee, H. S. Shim and C. H. Lee, *J Solid State Chem*, 2000, **150**, 383–390.

44 R. I. Dass, J. Q. Yan and J. B. Goodenough, *Phys Rev B Condens Matter Mater Phys*, , DOI:10.1103/PhysRevB.69.094416.

45 P. Kayser, J. A. Alonso, A. Muñoz and M. T. Fernández-Díaz, *Acta Mater*, 2017, **126**, 114–123.

46 T. Xia, C. Liu, Y. Lu, W. Jiang, H. Li, Y. Ma, Y. Wu and G. Che, *Appl Surf Sci*, , DOI:10.1016/j.apsusc.2022.154727.

47 C. Sun, J. A. Alonso and J. Bian, *Adv Energy Mater*, 2021, 11.

48 S. Dani, R. Pandit, H. Sharma, A. Arya, R. J. Choudhary, N. Goyal, J. Singh and R. Kumar, *J Mater Chem C Mater*, , DOI:10.1039/d2tc05072b.

49 C. L. Chen, S. M. Rao, K. J. Wang, F. C. Hsu, Y. C. Lee, C. L. Dong, T. S. Chan, J. F. Lee, M. C. Ling, H. L. Liu and M. K. Wu, *New J Phys*, , DOI:10.1088/1367-2630/11/7/073024.

50 M. Retuerto, F. Calle-Vallejo, L. Pascual, G. Lumbeeck, M. T. Fernandez-Diaz, M. Croft, J. Gopalakrishnan, M. A. Peña, J. Hadermann, M. Greenblatt and S. Rojas, *ACS Appl Mater Interfaces*, 2019, **11**, 21454–21464.

51 P. D. Battle and W. J. Macklin, *The Crystal and Magnetic Structures of Sr2YRu06*, 1984, vol. 52.

52 Y. Hinatsu, Y. Izumiyama, Y. Doi, A. Alemi, M. Wakeshima, A. Nakamura and Y. Morii, *J Solid State Chem*, 2004, **177**, 38–44.

53 T. KAWANO, J. TAKAHASHI, T. YAMADA and H. YAMANE, *Journal of the Ceramic Society of Japan*, 2007, **115**, 792–796.

54 R. Kumar, C. V. Tomy, R. Nagarajan, P. L. Paulose and S. K. Malik, *Physica B Condens Matter*, 2009, **404**, 2369–2373.

55 R. Takahashi, R. Okazaki, Y. Yasui, I. Terasaki, T. Sudayama, H. Nakao, Y. Yamasaki, J. Okamoto, Y. Murakami and Y. Kitajima, *J Appl Phys*, , DOI:10.1063/1.4757632.

56 K. Naveen, M. Reehuis, P. Adler, P. Pattison, A. Hoser, T. K. Mandal, U. Arjun, P. K. Mukharjee, R. Nath, C. Felser and A. K. Paul, *Phys Rev B*, , DOI:10.1103/PhysRevB.98.224423.

57 M. Das, P. Dutta, S. Giri and S. Majumdar, *Journal of Physics Condensed Matter*, , DOI:10.1088/1361-648X/ab27f5.

58 M. R. Palacín, J. Bassas, J. Rodríguez-Carvajal and P. Gómez-Romero, *J. Mater. Chem.*, 1993, **3**, 1171–1177.

59 M. Yuste, J. C. Pérez-Flores, J. R. De Paz, M. T. Azcondo, F. García-Alvarado and U. Amador, *Dalton Transactions*, 2011, **40**, 7908–7915.

60 S. Shafeie, J. Grins, S. Ya. Istomin, L. Karvonen, S. A. Chen, T. H. Chen, J. M. Chen, A. Weidenkaff, M. Karppinen, T. Sirtl and G. Svensson, *J Solid State Chem*, 2011, **184**, 177–190.

61 A. Aguadero, J. A. Alonso, M. J. Martínez-Lope and M. T. Fernández-Díaz, *Solid State Sci*, 2011, **13**, 13–18.

62 B. Niu, F. Jin, J. Liu, Y. Zhang, P. Jiang, T. Feng, B. Xu and T. He, *Int J Hydrogen Energy*, 2019, **44**, 20404–20415.

63 B. He, Z. Wang, L. Zhao, X. Pan, X. Wu and C. Xia, *J Power Sources*, 2013, **241**, 627–633.

64 M. K. Rath, A. Kossenko, M. Zinigrad and A. Kalashnikov, *J Power Sources*, 2020, **476**, 228630.

65 E. Rodríguez, M. L. López, J. Campo, M. L. Veiga and C. Pico, *J Mater Chem*, 2002, **12**, 2798–2802.

66 V. Vashook, D. Nitsche, L. Vasylechko, J. Rebello, J. Zosel and U. Guth, *J Alloys Compd*, 2009, **485**, 73–81.

67 K. R. S. P. Meher and K. B. R. Varma, *J Appl Phys*, 2009, **105**, 034113.

68 W. Z. Yang, X. Q. Liu, Y. Q. Lin and X. M. Chen, *J Appl Phys*, , DOI:10.1063/1.4704392.

69 P. Kayser, J. A. Alonso, F. J. Mompeán, M. Retuerto, M. Croft, A. Ignatov and M. T. Fernández-Díaz, *Eur J Inorg Chem*, 2015, **2015**, 5027–5038.

70 N. Das, R. Singh, A. Das, L. C. Gupta and A. K. Ganguli, *J Solid State Chem*, 2017, **253**, 355–359.

71 D. M. Arciniegas Jaimes, J. M. De Paoli, V. Nassif, P. G. Bercoff, G. Tirao, R. E. Carbonio and F. Pomiro, *Inorg Chem*, 2021, **60**, 4935–4944.

72 K. Zheng, M. Albrycht, M. Chen, K. Qi and P. Czaja, *Materials*, 2022, **15**, 8268.

73 X. Yang, W. Sun, M. Ma, C. Xu, R. Ren, J. Qiao, Z. Wang, S. Zhen and K. Sun, *Ind Eng Chem Res*, 2021, **60**, 7826–7834.

74 A. I. Tsiotsias, B. Ehrhardt, B. Rudolph, L. Nodari, S. Kim, W. Jung, N. D. Charisiou, M. A. Goula and S. Mascotto, *ACS Nano*, , DOI:10.1021/acsnano.1c11111.

75 W. Zhang, H. Wang, K. Guan, J. Meng, Z. Wei, X. Liu and J. Meng, *ACS Appl Mater Interfaces*, 2020, **12**, 461–473.

76 D. Neagu, T.-S. Oh, D. N. Miller, H. Ménard, S. M. Bukhari, S. R. Gamble, R. J. Gorte, J. M. Vohs and J. T. S. Irvine, *Nat Commun*, 2015, **6**, 8120.

77 S. Park, Y. Kim, Y. Noh, T. Kim, H. Han, W. Yoon, J. Choi, S. H. Yi, W. J. Lee and W. B. Kim, *J Mater Chem A Mater*, 2020, **8**, 138–148.

78 B. Hua, M. Li, Y. F. Sun, J. H. Li and J. L. Luo, *ChemSusChem*, 2017, **10**, 3333–3341.

79 C. J. Fu, Q. Ma, L. Gao and S. Li, *ChemCatChem*, , DOI:10.1002/cctc.202300389.

80 D. Yoon, Y. Lee, G. Y. Kim, Y. Kang, S. Y. Choi and J. Son, *Adv Funct Mater*, 2021, **31**, 1–9.

81 D. Neagu, J. T. S. Irvine, J. Wang, B. Yildiz, A. K. Opitz, J. Fleig, Y. Wang, J. Liu, L. Shen, F. Ciucci, B. A. Rosen, Y. Xiao, K. Xie, G. Yang, Z. Shao, Y. Zhang, J. Reinke, T. A. Schmauss, S. A. Barnett, R. Maring, V. Kyriakou, U. Mushtaq, M. N. Tsampas, Y. Kim, R. O'Hayre, A. J. Carrillo, T. Ruh, L. Lindenthal, F. Schrenk, C. Rameshan, E. I. Papaioannou, K. Kousi, I. S. Metcalfe, X. Xu and G. Liu, *Journal of Physics: Energy*, 2023, **5**, 031501.

82 R. Shiozaki, A. G. Andersen, T. Hayakawa, S. Hamakawa, K. Suzuki, M. Shimizu and K. Takehira, *Journal of the Chemical Society - Faraday Transactions*, 1997, **93**, 3235–3242.

83 Y. Nishihata, J. Mizuki, T. Akao, H. Tanaka, M. Uenishi, M. Kimura, T. Okamoto and N. Hamada, *Nature*, 2002, **418**, 164–167.

84 B. D. Madsen, W. Kobsiriphat, Y. Wang, L. D. Marks and S. A. Barnett, *J Power Sources*, 2007, **166**, 64–67.

85 W. Kobsiriphat, B. D. Madsen, Y. Wang, M. Shah, L. D. Marks and S. A. Barnett, *J Electrochem Soc*, 2010, **157**, B279.

86 H. Tanaka, M. Uenishi, M. Taniguchi, I. Tan, K. Narita, M. Kimura, K. Kaneko, Y. Nishihata and J. Mizuki, *Catal Today*, 2006, **117**, 321–328.

87 S. Pavlova, L. Kapokova, R. Bunina, G. Alikina, N. Sazonova, T. Krieger, A. Ishchenko, V. Rogov, R. Gulyaev, V. Sadykov and C. Mirodatos, *Catal Sci Technol*, 2012, **2**, 2099.

88 D. Neagu, G. Tsekouras, D. N. Miller, H. Ménard and J. T. S. Irvine, *Nat Chem*, 2013, **5**, 916–923.

89 Y. Sun, J. Li, Y. Zeng, B. S. Amirkhiz, M. Wang, Y. Behnamian and J. Luo, *J Mater Chem A Mater*, 2015, **3**, 11048–11056.

90 J. H. Kim, J. Hong, D. K. Lim, S. Ahn, J. Kim, J. K. Kim, D. H. Oh, S. H. Jeon, S. J. Song and W. C. Jung, *Energy Environ Sci*, 2021, **15**, 1097–1105.

91 C. Duan, R. J. Kee, H. Zhu, C. Karakaya, Y. Chen, S. Ricote, A. Jarry, E. J. Crumlin, D. Hook, R. Braun, N. P. Sullivan and R. O'Hayre, *Nature*, 2018, **557**, 217–222.

92 J. H. Kim, J. K. Kim, H. G. Seo, D. K. Lim, S. J. Jeong, J. Seo, J. Kim and W. C. Jung, *Adv Funct Mater*, , DOI:10.1002/adfm.202001326.

93 Z. Zhan, W. Kobsiriphat, J. R. Wilson, M. Pillai, I. Kim and S. A. Barnett, *Energy and Fuels*, 2009, **23**, 3089–3096.

94 Y. Zhu, W. Zhou, R. Ran, Y. Chen, Z. Shao and M. Liu, *Nano Lett*, 2016, **16**, 512–518.

95 B. Niu, C. Lu, W. Yi, S. Luo, X. Li, X. Zhong, X. Zhao and B. Xu, *Appl Catal B*, 2020, **270**, 118842.

96 Y. Yang, Y. Wang, Z. Yang, Y. Chen and S. Peng, *J Power Sources*, 2020, **478**, 229082.

97 Z. Zhan, W. Kobsiriphat, J. R. Wilson, M. Pillai, I. Kim and S. A. Barnett, *Energy and Fuels*, 2009, **23**, 3089–3096.

98 H. Li, Y. Song, M. Xu, W. Wang, R. Ran, W. Zhou and Z. Shao, *Energy and Fuels*, 2020, **34**, 11449–11457.

99 X. Chen, W. Ni, J. Wang, Q. Zhong, M. Han and T. Zhu, *Electrochim Acta*, 2018, **277**, 226–234.

100 S.-L. Zhang, H. Wang, T. Yang, M. Y. Lu, C.-X. Li, C.-J. Li and S. A. Barnett, *J Mater Chem A Mater*, 2020, **8**, 25867–25879.

101 S. A. Horlick, Y. L. Huang, I. A. Robinson and E. D. Wachsman, *Nano Energy*, 2021, **87**, 106193.

102 W. Kobsiriphat, B. D. Madsen, Y. Wang, L. D. Marks and S. A. Barnett, *Solid State Ion*, 2009, **180**, 257–264.

103 Y. Wang, Z. Wang, C. Jin, C. Li, X. Li, Y. Li, R. Yang and M. Liu, *Electrochim Acta*, 2019, **318**, 120–129.

104 W. Li, Y. Zhu, W. Guo, H. Xu, C. Gong and G. Xue, *Journal of Chemical Sciences*, 2022, **134**, 38.

105 L. Zhang, Y. Yang, Z. Zhou, J. Li, G. Chen, L. Zhou, Y. Qiu and Y. Sun, *Chemical Engineering Journal*, 2023, **452**, 139273.

106 Z. Wang, Z. Hao, F. Shi, K. Zhu, X. Zhu and W. Yang, *Journal of Energy Chemistry*, 2022, **69**, 434–441.

107 H. Guo, Y. Yang, G. Yang, X. Cao, N. Yan, Z. Li, E. Chen, L. Tang, M. Peng, L. Shi, S. Xie, H. Tao, C. Xu, Y. Zhu, X. Fu, Y. Pan, N. Chen, J. Lin, X. Tu, Z. Shao and Y. Sun, *ACS Catal*, 2023, **13**, 5007–5019.

108 X. Xu, G. Liu and A. K. Azad, *Int J Hydrogen Energy*, 2015, **40**, 3672–3678.

109 Y. F. Sun, Y. L. Yang, J. Chen, M. Li, Y. Q. Zhang, J. H. Li, B. Hua and J. L. Luo, *Chemical Communications*, 2018, **54**, 1505–1508.

110 J. Wang, A. Kumar, J. L. Wardini, Z. Zhang, H. Zhou, E. J. Crumlin, J. T. Sadowski, K. B. Woller, W. J. Bowman, J. M. LeBeau and B. Yildiz, *Nano Lett*, 2022, **22**, 5401–5408.

111 J. Yu, L. Zhang, J. Qian, Z. Zhu, S. Ni, G. Liu and X. Xu, *Appl Catal B*, 2019, **256**, 117818.

112 Y. Kim, H. S. Kim, D. Kang, M. Kim and J. W. Lee, *Chemical Engineering Journal*, 2023, **468**, 143662.

113 L. Tan, Z. Jiang, Y. Gao and S. Zhang, *Int J Hydrogen Energy*, 2022, **47**, 20016–20026.

114 S. Lee, J. Song, Y. R. Jo, K. S. Choi, J. Lee, S. Seo, T. L. Kim, H. W. Jang, C. Jeon, B. J. Kim, B. Kim and S. Lee, *ACS Appl Mater Interfaces*, 2019, **11**, 44069–44076.

115 K. S. Roy, C. Subramaniam and L. S. Panchakarla, *ACS Appl Mater Interfaces*, 2021, **13**, 9897–9907.

116 J. Cavazzani, E. Squizzato, E. Brusamarello and A. Glisenti, *Int J Hydrogen Energy*, 2022, **47**, 13921–13932.

117 Y. Yi, J. Chen, M. Xu, G. Yang, R. Ran, W. Zhou, W. Wang and Z. Shao, *Catalysts*, 2023, **13**, 996.

118 R. Li, T. Li, X. Liu, C. Xie, Q. Zhen, S. Bashir and J. L. Liu, *Energy Sci Eng*, 2023, 2293–2301.

119 A. Badakhsh, H. M. Vieri, H. Sohn, S. P. Yoon and S. H. Choi, *Int J Energy Res*, 2023, **2023**, 1–14.

120 H. Kim, A. Jan, D. H. Kwon, H. Il Ji, K. J. Yoon, J. H. Lee, Y. Jun, J. W. Son and S. Yang, *Small*, 2023, **19**, 1–12.

121 F. Kosaka, N. Noda, T. Nakamura and J. Otomo, *J Mater Sci*, 2017, **52**, 2825–2835.

122 X. Xiong, J. Yu, X. Huang, D. Zou, Y. Song, M. Xu, R. Ran, W. Wang, W. Zhou and Z. Shao, *J Mater Sci Technol*, 2022, **125**, 51–58.

123 F. Kosaka, T. Nakamura and J. Otomo, *J Electrochem Soc*, 2017, **164**, F1323–F1330.

124 T. Wei, X. Pan, Y. Jia, J. Wang, C. Zheng and P. Qiu, *ACS Appl Nano Mater*, 2023, **6**, 10599–10608.

125 M. J. Mekkering, J. Biemolt, J. de Graaf, Y. A. Lin, N. P. van Leest, A. Troglia, R. Bliem, B. de Bruin, G. Rothenberg and N. Yan, *Catal Sci Technol*, 2023, **13**, 2255–2260.

126 D. H. Kim, J. R. Youn, J. C. Seo, S. B. Kim, M. J. Kim and K. Lee, *Catal Today*, 2023, **411–412**, 113910.

127 S. Lou, X. Meng, N. Liu and L. Shi, *Chem Eng Sci*, 2023, **274**, 118690.

128 J. G. Lee, *Inorg Chem*, 2023, **62**, 5831–5835.

129 D. He, Y. Gong, J. Ni and C. Ni, *Sep Purif Technol*, 2023, **315**, 123739.

130 P. B. Managutti, H. Yu, O. Hernandez, C. Prestipino, V. Dorcet, H. Wang, T. C. Hansen and M. Bahout, *ACS Appl Mater Interfaces*, 2023, **15**, 23040–23050.

131 Y. Kim, H. S. Kim, D. Kang, M. Kim and J. W. Lee, *Chemical Engineering Journal*, 2023, **468**, 143662.

132 S. Vecino-Mantilla, E. Quintero, C. Fonseca, G. H. Gauthier and P. Gauthier-Maradei, *ChemCatChem*, 2020, **12**, 1453–1466.

133 A. J. Carrillo and J. M. Serra, *Catalysts*, 2021, **11**, 741.

134 S. Joo, K. Kim, O. Kwon, J. Oh, H. J. Kim, L. Zhang, J. Zhou, J. Q. Wang, H. Y. Jeong, J. W. Han and G. Kim, *Angewandte Chemie - International Edition*, 2021, **60**, 15912–15919.

135 Y. Xiao and K. Xie, *Angewandte Chemie - International Edition*, 2022, **61**, 1–8.

136 Y. H. Kim, Y. Kang, S. Jo, H. Jeong, D. Neagu and J. ha Myung, *Chemical Engineering Journal*, 2022, **441**, 136025.

137 X. Yao, Q. Cheng, Y. Attada, S. Ould-Chikh, A. Ramírez, X. Bai, H. O. Mohamed, G. Li, G. Shterk, L. Zheng, J. Gascon, Y. Han, O. M. Bakr and P. Castaño, *Appl Catal B*, , DOI:10.1016/j.apcatb.2023.122479.

138 D. Papargyriou, D. N. Miller and J. T. Sirr Irvine, *J Mater Chem A Mater*, 2019, **7**, 15812–15822.

139 S. H. Lee, Y. J. Kwak, J. W. Park and K. T. Lee, *Journal of the Korean Ceramic Society*, 2023, **60**, 536–546.

140 D. Zubenko, S. Singh and B. A. Rosen, *Appl Catal B*, 2017, **209**, 711–719.

141 S. Joo, C. Lim, O. Kwon, L. Zhang, J. Zhou, J. Q. Wang, H. Y. Jeong, Y. wook Sin, S. Choi and G. Kim, *Materials Reports: Energy*, 2021, **1**, 100021.

142 M. A. Naeem, P. M. Abdala, A. Armutlulu, S. M. Kim, A. Fedorov and C. R. Müller, *ACS Catal*, 2020, **10**, 1923–1937.

143 V. Kyriakou, D. Neagu, E. I. Papaioannou, I. S. Metcalfe, M. C. M. van de Sanden and M. N. Tsampas, *Appl Catal B*, 2019, **258**, 117950.

144 S. A. Ali, M. Safi, L.-P. Merkouri, S. Soodi, A. Iakovidis, M. S. Duyar, D. Neagu, T. R. Reina and K. Kousi, *Front Energy Res*, 2023, **11**, 1–9.

145 X. Yang, W. Sun, M. Ma, C. Xu, R. Ren, J. Qiao, Z. Wang, Z. Li, S. Zhen and K. Sun, *ACS Appl Mater Interfaces*, 2021, **13**, 20060–20069.

146 L. Bai, H. Li, Z. Yan, X. Hao, M. Ke, K. Xie and B. Li, *Adv Mater Interfaces*, 2021, **8**, 1–9.

147 S. Ding, M. Li, W. Pang, B. Hua, N. Duan, Y. Q. Zhang, S. N. Zhang, Z. Jin and J. L. Luo, *Electrochim Acta*, 2020, **335**, 135683.

148 J. Zhu, W. Zhang, Y. Li, W. Yue, G. Geng and B. Yu, *Appl Catal B*, 2020, **268**, 118389.

149 H. Lv, L. Lin, X. Zhang, Y. Song, H. Matsumoto, C. Zeng, N. Ta, W. Liu, D. Gao, G. Wang and X. Bao, *Advanced Materials*, 2020, **32**, 1–9.

150 S. Liu, Q. Liu and J.-L. Luo, *J Mater Chem A Mater*, 2016, **4**, 17521–17528.

151 S. Park, Y. Kim, H. Han, Y. S. Chung, W. Yoon, J. Choi and W. B. Kim, *Appl Catal B*, 2019, **248**, 147–156.

152 P. Steiger, O. Kröcher and D. Ferri, *Appl Catal A Gen*, 2020, **590**, 117328.

153 Y. F. Sun, Y. Q. Zhang, J. Chen, J. H. Li, Y. T. Zhu, Y. M. Zeng, B. S. Amirkhiz, J. Li, B. Hua and J. L. Luo, *Nano Lett*, 2016, **16**, 5303–5309.

154 R. Thalinger, M. Gocyla, M. Heggen, R. Dunin-Borkowski, M. Grünbacher, M. Stöger-Pollach, D. Schmidmair, B. Klötzer and S. Penner, *J Catal*, 2016, **337**, 26–35.

155 X. Yue, A. Pukhova, S. He and N. Zhang, *J Electrochem Soc*, 2021, **168**, 104514.

156 M. Wang, B. Zhang, J. Ding, F. Zhang, R. Tu, M. T. Bernards, Y. He, P. Xie and Y. Shi, *Small*, 2022, **18**, 1–9.

157 Y. Jiang, L. Ye, S. Zhang and C. Xia, *J Mater Chem A Mater*, 2022, **10**, 9380–9383.

158 H. M. Ansari, A. S. Bass, N. Ahmad and V. I. Birss, *J Mater Chem A Mater*, 2022, **10**, 2280–2294.

159 J. Lv, W. Sun, C. Xu, X. Yang, M. Ma, L. Zhang, S. Zhang, J. Qiao, S. Zhen and K. Sun, *Sep Purif Technol*, 2022, **294**, 121127.

160 J. Choi, M. Kim, S. K. Kang, J. Kim, J. Ha, H. H. Shin, T. Park and W. B. Kim, *ACS Sustain Chem Eng*, 2022, **10**, 7595–7602.

161 S. Zhang, Y. Jiang, H. Han, Y. Li and C. Xia, *ACS Appl Mater Interfaces*, 2022, **14**, 28854–28864.

162 S. Zhen, L. Zhang, C. Xu, D. Zhang, Q. Yi, W. Sun and K. Sun, *Front Chem*, 2022, **10**, 1–11.

163 D. Zhang, W. Yang, Z. Wang, C. Ren, Y. Wang, M. Ding and T. Liu, *Sep Purif Technol*, 2023, **304**, 122287.

164 Y. Tian, C. Yang, Y. Wang, M. Xu, Y. Ling, J. Pu, F. Ciucci, J. T. S. Irvine and B. Chi, *J Mater Chem A Mater*, 2022, **10**, 16490–16496.

165 P. Li, P. Yang, F. Liu, W. Xiao, F. Yan, T. Gan, K. Zhao and D. Fu, *Ceram Int*, 2023, **49**, 12980–12989.

166 X. Gao, L. Ye and K. Xie, *J Power Sources*, 2023, **561**, 232740.

167 L. Ye, K. Zhu, Y. Jiang, S. Zhang, R. Peng and C. Xia, *J Mater Chem A Mater*, 2023, **11**, 10646–10658.

168 X. Yang, K. Sun, W. Sun, M. Ma, R. Ren, J. Qiao, Z. Wang, S. Zhen and C. Xu, *J Eur Ceram Soc*, 2023, **43**, 3414–3420.

169 W. Lin, W. Su, Y. Li, T. Chiu, M. Singh, Z. Pan and L. Fan, *Small*, 2023, **2303305**, 1–11.

170 C. Lu, C. Xu, W. Sun, R. Ren, J. Qiao, Z. Wang, K. Sun, G. Pan and Y. Cao, *J Power Sources*, 2023, **574**, 233134.

171 B. Zhang, M. Zhu, M. Gao, J. Chen, X. Xi, J. Shen, R. Feng, N. Semagina, N. Duan, H. Zeng and J. Luo, *Angewandte Chemie International Edition*, 2023, **62**, e202305552.

172 H. Chang, W. Tian, H. Chen, S. D. Li and Z. Shao, *Electrochim Acta*, 2023, **439**, 141699.

173 M. Xu, C. Liu, A. B. Naden, H. Früchtl, M. Bühl and J. T. S. Irvine, *Small*, 2023, **19**, 2204682–2204682.

174 M. Marasi, L. Duranti, I. Luisetto, E. Fabbri, S. Licoccia and E. Di Bartolomeo, *J Power Sources*, 2023, **555**, 232399.

175 L. Liu, M. Wu, X. Zhou, H. Chen, X. Qian, Z. Wang, F. He, Y. Sheng, J. Qian and L. Pan, *ACS Appl Energy Mater*, 2023, **6**, 841–855.

176 L. Zhang, Y. Yang, Z. Zhou, J. Li, G. Chen, L. Zhou, Y. Qiu and Y. Sun, *Chemical Engineering Journal*, 2023, **452**, 139273.

177 H. Lv, L. Lin, X. Zhang, R. Li, Y. Song, H. Matsumoto, N. Ta, C. Zeng, Q. Fu, G. Wang and X. Bao, *Nat Commun*, , DOI:10.1038/s41467-021-26001-8.

178 S. Hou and K. Xie, *Electrochim Acta*, 2019, **301**, 63–68.

179 K. Kousi, C. Tang, I. S. Metcalfe and D. Neagu, *Small*, 2021, **17**, 2006479.

180 D. Stradi, C. Díaz, F. Martín and M. Alcamí, *Theor Chem Acc*, 2011, **128**, 497–503.

181 J. Wang, J. Yang, A. K. Opitz, W. Bowman, R. Bliem, G. Dimitrakopoulos, A. Nenning, I. Waluyo, A. Hunt, J.-J. Gallet and B. Yildiz, *Chemistry of Materials*, 2021, **33**, 5021–5034.

182 Y. Gao, D. Chen, M. Saccoccio, Z. Lu and F. Ciucci, *Nano Energy*, 2016, **27**, 499–508.

183 T. S. Oh, E. K. Rahani, D. Neagu, J. T. S. Irvine, V. B. Shenoy, R. J. Gorte and J. M. Vohs, *Journal of Physical Chemistry Letters*, 2015, **6**, 5106–5110.

184 D. Neagu, V. Kyriakou, I.-L. Roiban, M. Aouine, C. Tang, A. Caravaca, K. Kousi, I. Schreur-Piet, I. S. Metcalfe, P. Vernoux, M. C. M. van de Sanden and M. N. Tsampas, *ACS Nano*, 2019, **13**, 12996–13005.

185 E. Calì, M. P. Thomas, R. Vasudevan, J. Wu, O. Gavalda-Diaz, K. Marquardt, E. Saiz, D. Neagu, R. R. Unocic, S. C. Parker, B. S. Guiton and D. J. Payne, *Nat Commun*, 2023, **14**, 1754.

186 K. Kousi, D. Neagu, L. Bekris, E. I. Papaioannou and I. S. Metcalfe, *Angewandte Chemie International Edition*, 2020, **59**, 2510–2519.

187 K. Kousi, D. Neagu, L. Bekris, E. Calì, G. Kerherve, E. I. Papaioannou, D. J. Payne and I. S. Metcalfe, *J Mater Chem A Mater*, 2020, **8**, 12406–12417.

188 O. Kwon, S. Sengodan, K. Kim, G. G. G. G. Kim, H. Y. Jeong, J. Shin, Y. W. Ju, J. W. Han and G. G. G. G. Kim, *Nat Commun*, 2017, **8**, 1–7.

189 J. H. Kim, J. K. Kim, J. Liu, A. Curcio, J.-S. Jang, I.-D. Kim, F. Ciucci and W. Jung, *ACS Nano*, 2021, **15**, 81–110.

190 S. Sengodan, Y. W. Ju, O. Kwon, A. Jun, H. Y. Jeong, T. Ishihara, J. Shin and G. Kim, *ACS Sustain Chem Eng*, 2017, **5**, 9207–9213.

191 Y. F. Sun, Y. Q. Zhang, J. Chen, J. H. Li, Y. T. Zhu, Y. M. Zeng, B. S. Amirkhiz, J. H. Li, B. Hua and J. L. Luo, *Nano Lett*, 2016, **16**, 5303–5309.

192 H. Kim, C. Lim, O. Kwon, J. Oh, M. T. Curnan, H. Y. Jeong, S. Choi, J. W. Han and G. Kim, *Nat Commun*, 2021, **12**, 6814.

193 J. H. Kim and A. Manthiram, *J Mater Chem A Mater*, 2015, **3**, 24195–24210.

194 H. Han, J. Park, S. Y. Nam, K. J. Kim, G. M. Choi, S. S. P. Parkin, H. M. Jang and J. T. S. Irvine, *Nat Commun*, 2019, **10**, 1–8.

195 K. Kim, B. Koo, Y.-R. Jo, S. Lee, J. K. Kim, B.-J. Kim, W. Jung and J. W. Han, *Energy Environ Sci*, 2020, **13**, 3404–3411.

196 K. J. Kim, H. Han, T. Defferriere, D. Yoon, S. Na, S. J. Kim, A. M. Dayaghi, J. Son, T.-S. Oh, H. M. Jang and G. M. Choi, *J Am Chem Soc*, 2019, **141**, 7509–7517.

197 M. L. Weber, M. Kindelmann, E. Wessel, A. Sarantopoulos, N. H. Menzler, R. Dittmann, R. Waser, O. Guillon, C. Lenser and F. Gunkel, *Journal of Physics: Energy*, 2023, **5**, 014002.

198 D. Neagu, V. Kyriakou, I. L. Roiban, M. Aouine, C. Tang, A. Caravaca, K. Kousi, I. Schreur-Piet, I. S. Metcalfe, P. Vernoux, M. C. M. Van De Sanden and M. N. Tsampas, *ACS Nano*, 2019, **13**, 12996–13005.

199 Y. R. Jo, B. Koo, M. J. Seo, J. K. Kim, S. Lee, K. Kim, J. W. Han, W. C. Jung and B. J. Kim, *J Am Chem Soc*, 2019, **141**, 6690–6697.

200 C. Tang, K. Kousi, D. Neagu, J. Portolés, E. I. Papaioannou and I. S. Metcalfe, *Nanoscale*, 2019, **11**, 16935–16944.

201 H. M. Ansari, A. S. Bass, N. Ahmad and V. I. Birss, *J Mater Chem A Mater*, 2022, **10**, 2280–2294.

202 W. Fan, B. Wang, R. Gao, G. Dimitrakopoulos, J. Wang, X. Xiao, L. Ma, K. Wu, B. Yildiz and J. Li, *J Am Chem Soc*, 2022, **144**, 7657–7666.

203 S. Joo, O. Kwon, K. Kim, S. Kim, H. Kim, J. Shin, H. Y. Jeong, S. Sengodan, J. W. Han and G. Kim, *Nat Commun*, 2019, **10**, 697.

204 S. Joo, O. Kwon, S. Kim, H. Y. Jeong and G. Kim, *J Electrochem Soc*, 2020, **167**, 064518.

205 S. Joo, A. Seong, O. Kwon, K. Kim, J. H. Lee, R. J. Gorte, J. M. Vohs, J. W. Han and G. Kim, *Sci Adv*, 2020, **6**, 1–9.

206 B.-W. Zhang, M.-N. Zhu, M.-R. Gao, X. Xi, N. Duan, Z. Chen, R.-F. Feng, H. Zeng and J.-L. Luo, *Nat Commun*, 2022, **13**, 4618.

207 H. Khalid, A. ul Haq, B. Alessi, J. Wu, C. D. Savaniu, K. Kousi, I. S. Metcalfe, S. C. Parker, J. T. S. Irvine, P. Maguire, E. I. Papaioannou and D. Mariotti, *Adv Energy Mater*, , DOI:10.1002/aenm.202201131.

208 V. Kyriakou, R. K. Sharma, D. Neagu, F. Peeters, O. De Luca, P. Rudolf, A. Pandiyan, W. Yu, S. W. Cha, S. Welzel, M. C. M. van de Sanden and M. N. Tsampas, *Small Methods*, 2021, **5**, 1–7.

209 F. Tao, *Chem Soc Rev*, 2012, **41**, 7977–7979.

210 C. Tang, K. Kousi, D. Neagu and I. S. Metcalfe, *Chemistry – A European Journal*, 2021, **27**, 6666–6675.

211 O. Kwon, K. Kim, S. Joo, H. Y. Jeong, J. Shin, J. W. Han, S. Sengodan and G. Kim, *J Mater Chem A Mater*, 2018, **6**, 15947–15953.

212 H. Lv, L. Lin, X. Zhang, Y. Song, H. Matsumoto, C. Zeng, N. Ta, W. Liu, D. Gao, G. Wang and X. Bao, *Advanced Materials*, 2020, **32**, 1–9.

213 D. D. Athayde, D. F. Souza, A. M. A. Silva, D. Vasconcelos, E. H. M. Nunes, J. C. Diniz da Costa and W. L. Vasconcelos, *Ceram Int*, 2016, **42**, 6555–6571.

214 C. P. Romao, K. J. Miller, C. A. Whitman, M. A. White and B. A. Marinkovic, in *Comprehensive Inorganic Chemistry II (Second Edition): From Elements to Applications*, Elsevier, 2013, vol. 4, pp. 127–151.

215 K. Nassau, H. J. Levinstein and G. M. Loiacono, *Journal of Physics and Chemistry of Solids*, 1965, **26**, 1805–1816.

216 C. Y. Tsai, A. Aguadero and S. J. Skinner, *J Solid State Chem*, 2020, **289**, 121533.

217 A. E. Danks, S. R. Hall and Z. Schnepp, *Mater Horiz*, 2016, **3**, 91–112.

218 K. De Buysser, P. F. Smet, B. Schoofs, E. Bruneel, D. Poelman, S. Hoste and I. Van Driessche, *J Solgel Sci Technol*, 2007, **43**, 347–353.

219 Z. Du, H. Zhao, S. Yi, Q. Xia, Y. Gong, Y. Zhang, X. Cheng, Y. Li, L. Gu and K. Świerczek, *ACS Nano*, 2016, **10**, 8660–8669.

220 N. Hou, T. Yao, P. Li, X. Yao, T. Gan, L. Fan, J. Wang, X. Zhi, Y. Zhao and Y. Li, *ACS Appl Mater Interfaces*, 2019, **11**, 6995–7005.

221 K. Y. Lai and A. Manthiram, *Chemistry of Materials*, 2018, **30**, 2838–2847.

222 C. Arrivé, T. Delahaye, O. Joubert and G. H. Gauthier, *Ceram Int*, 2020, **46**, 5841–5849.

223 J. E. Bauerle, *Solid State Commun*, 1969, **7**, ii.

224 M. A. Yatoo, A. Aguadero and S. J. Skinner, *APL Mater*, 2019, **7**, 0–8.

225 J. M. S. Eng, K. Km and H. Motjotji, *X-ray Characterization of Materials*, Wiley, 1999, vol. 04.

226 S. Vasamsetti, L. Dumpala and V. V. Subbarao, *International Journal of Mechanical Engineering and Technology*, 2018, **9**, 1579–1589.

227 S. Gandavarapu, E. Sabolsky, K. Sabolsky and K. Gerdes, *Int J Appl Ceram Technol*, 2015, **12**, 199–211.

228 T. NGUYEN, K. KOBAYASHI, T. HONDA, Y. IIMURA, K. KATO, A. NEGHISI, K. NOZAKI, F. TAPPERO, K. SASAKI and H. SHIRAHAMA, *Solid State Ion*, 2004, **174**, 163–174.

229 B. Son, M. H. Ryou, J. Choi, T. Lee, H. K. Yu, J. H. Kim and Y. M. Lee, *ACS Appl Mater Interfaces*, 2014, **6**, 526–531.

230 X. Zhang, M. Espinoza, T. Li and M. Andersson, *Int J Hydrogen Energy*, 2021, **46**, 37440–37459.

231 S. Luo, R. Yang, Y. Meng, K. Maliutina, M. Singh, T.-W. Chiu and L. Fan, *Mater Res Bull*, 2023, **168**, 112452.

232 A. Le Bail, *Powder Diffr*, 2005, **20**, 316–326.

233 A. Le Bail, H. Duroy and J. L. Fourquet, *Mater Res Bull*, 1988, **23**, 447–452.

234 H. M. Rietveld, *Acta Crystallogr*, 1967, **22**, 151–152.

235 H. M. Rietveld, *J Appl Crystallogr*, 1969, **2**, 65–71.

236 P. W. H. Bragg and W. L. Bragg, *Proceedings of the Royal Society of London. Series A, Containing Papers of a Mathematical and Physical Character*, 1913, **88**, 428–438.

237 G. Bergerhoff, R. Hundt, R. Sievers and I. D. Brown, *J Chem Inf Comput Sci*, 1983, **23**, 66–69.

238 J. Rodríguez-Carvajal, *Physica B: Physics of Condensed Matter*, 1993, **192**, 55–69.

239 A. Le Bail, H. Duroy and J. L. Fourquet, *Mater Res Bull*, 1988, **23**, 447–452.

240 B. H. Toby, *Powder Diffr*, 2006, **21**, 67–70.

241 D. E. McREE, in *Practical Protein Crystallography*, Elsevier, 1999, pp. 91-cp1.

242 L. B. McCusker, R. B. Von Dreele, D. E. Cox, D. Louër and P. Scardi, *J Appl Crystallogr*, 1999, **32**, 36–50.

243 R. R. Mather, in *Surface Modification of Textiles*, Elsevier, 2009, pp. 296–317.

244 G. Greczynski and L. Hultman, *Prog Mater Sci*, 2020, **107**, 100591.

245 F. A. Stevie and C. L. Donley, *Journal of Vacuum Science & Technology A: Vacuum, Surfaces, and Films*, 2020, **38**, 063204.

246 A. R. West, *Basic solid state chemistry*, 2nd Editio., 1999.

247 T. London and D. Philosophical, *The London, Edinburgh, and Dublin Philosophical Magazine and Journal of Science*, 2009, **8**, 261–274.

248 P. J. Goodhew, J. Humphreys and J. Humphreys, *Electron Microscopy and Analysis*, CRC Press, 2000, vol. 95.

249 M. Auffan, C. Santaella, A. Thiéry, C. Paillès, J. Rose, W. Achouak, A. Thill, A. Masion, M. Wiesner, J.-Y. Bottero, F. Mouchet, P. Landois, F. Bourdiol, I. Fourquaux, P. Puech, E. Flahaut, L. Gauthier, M. J. Rybak-Smith, Y. Song, M. J. Heller, D. Holmes, B. L. J. Webb, T. Sun, T. S. Mayer, J. S. Mayer, C. D. Keating, A. Ghosh, I. V. Pobelov, C. Li, T. Wandlowski, M. G. Helander, Z. Wang, Z.-H. Lu, F. Carpino, L. R. Gibson, D. A. Grismer, P. W. Bohn, N. Pala, M. Karabiyik, A. Porter, E. McGuire, G. Xie, A. Lopez-Bezanilla, S. Roche, E. Cruz-Silva, B. G. Sumpter, V. Meunier, M. J. Laudenslager, W. M. Sigmund, N. A. Hall, C. Kim, G. Wang, R. J. Greenberg, C. Mbanaso, G. Denbeaux, C. Coutris and E. J. Joner, in *Encyclopedia of Nanotechnology*, Springer Netherlands, Dordrecht, 2012, pp. 741–749.

250 Y. Lin, M. Zhou, X. Tai, H. Li, X. Han and J. Yu, *Matter*, 2021, **4**, 2309–2339.

251 L. Cornet, L. Yedra, Héripré, V. Aubin, J. H. Schmitt and M. L. Giorgi, *J Electron Mater*, 2022, **51**, 1568–1582.

252 J. Y. Jung, H. Jin, M. W. Kim, S. Kim, J. G. Kim, P. Kim, Y. E. Sung, S. J. Yoo and N. D. Kim, *Appl Catal B*, 2023, **323**, 122172.

253 TEM Processing Software: AXON Studio, https://www.protochips.com/solutions/tem-data-correlation/processing-software/.

254 X. Hou and B. T. Jones, in *Encyclopedia of Analytical Chemistry*, John Wiley & Sons, Ltd, Chichester, UK, 2000, pp. 655–678.

255 W. Nernst, *Zeitschrift für Elektrotechnik und Elektrochemie*, 1896, **2**, 629–636.

256 M. E. Orazem and B. Tribollet, *Electrochemical Impedance Spectroscopy*, John Wiley & Sons, Inc., Hoboken, NJ, USA, 2008.

257 A. Pinkelstein, *Zeitschrift für Physikalische Chemie*, 1902, **39U**, 91–110.

258 Gamry, Basics of Electrochemical Impedance Spectroscopy, https://www.gamry.com/application-notes/EIS/basics-of-electrochemical-impedance-spectroscopy/.

259 M. Schönleber, D. Klotz and E. Ivers-Tiffée, *Electrochim Acta*, 2014, **131**, 20–27.

260 J. T. S. Irvine, D. C. Sinclair and A. R. West, *Advanced Materials*, 1990, **2**, 132–138.

261 P. A. Seinen, F. P. F. van Berkel, W. A. Groen and D. J. W. Ijdo, *Mater Res Bull*, 1987, **22**, 535–542.

262 P. D. Battle and C. W. Jones, *Mater Res Bull*, 1987, **22**, 1623–1627.

263 J. Z. Liu, N. Miyahara, S. Miwa, M. Takano, A. Hidaka and M. Osaka, *Journal of Nuclear Materials*, 2019, **527**, 151819.

264 C. Y. Tsai, C. M. McGilvery, A. Aguadero and S. J. Skinner, *Int J Hydrogen Energy*, 2019, **44**, 31458–31465.

265 K. Yoshii, H. Abe, M. Mizumaki, H. Tanida and N. Kawamura, *J Alloys Compd*, 2003, **348**, 236–240.

266 M. Gateshki, J. M. Igartua and Y. Brouard, *Mater Res Bull*, 2003, **38**, 1661–1668.

267 K. Yoshii, N. Ikeda, S. Mori, Y. Yoneda, M. Mizumaki, H. Tanida and N. Kawamura, *Transactions of the Materials Research Society of Japan*, 2007, **32**, 51–54.

268 M. ANDERSON, K. GREENWOOD, G. TAYLOR and K. POEPPELMEIER, *Progress in Solid State Chemistry*, 1993, **22**, 197–233.

269 S. M. M. Zamani and K. Behdinan, *Ceram Int*, 2017, **43**, 12239–12248.

270 S. SASAKI, K. FUJINO and Y. TAKÉUCHI, *Proceedings of the Japan Academy, Series B*, 1979, **55**, 43–48.

271 C.-E. Boman, J. Danielsen, A. Haaland, B. Jerslev, C. E. Schäffer, E. Sunde and N. A. Sørensen, *Acta Chem Scand*, 1970, **24**, 116–122.

272 J. Guo, R. Cai, E. Cali, G. E. Wilson, G. Kerherve, S. J. Haigh and S. J. Skinner, *Small*, 2022, **2107020**, 2107020.

273 M. C. Biesinger, B. P. Payne, A. P. Grosvenor, L. W. M. Lau, A. R. Gerson and R. St. C. Smart, *Appl Surf Sci*, 2011, **257**, 2717–2730.

274 M. C. Biesinger, B. P. Payne, L. W. M. Lau, A. Gerson and R. S. C. Smart, *Surface and Interface Analysis*, 2009, **41**, 324–332.

275 A. P. Grosvenor, M. C. Biesinger, R. St. C. Smart and N. S. McIntyre, *Surf Sci*, 2006, **600**, 1771–1779.

276 M. F. Sunding, K. Hadidi, S. Diplas, O. M. Løvvik, T. E. Norby and A. E. Gunnæs, *J Electron Spectros Relat Phenomena*, 2011, **184**, 399–409.

277 J. C. Pérez Flores, C. Ritter, D. Pérez-Coll, G. C. Mather, F. García-Alvarado and U. Amador, *J Mater Chem*, 2011, **21**, 13195–13204.

278 S.-J. Kim, G. Demazeau, J. A. Alonso and J.-H. Choy, *J Mater Chem*, 2001, **11**, 487–492.

279 S. J. Kim, M. J. Martinez-Lope, M. T. Fernandez-Diaz, J. A. Alonso, I. Presniakov and G. Demazeau, *Chemistry of Materials*, 2002, **14**, 4926–4932.

280 Y. Tsujimoto, K. Yamaura and T. Uchikoshi, *Inorg Chem*, 2013, **52**, 10211–10216.

281 P. Vishnoi, J. L. Zuo, T. A. Strom, G. Wu, S. D. Wilson, R. Seshadri and A. K. Cheetham, *Angewandte Chemie International Edition*, 2020, **59**, 8974–8981.

282 M. Retuerto, L. Pascual, F. Calle-Vallejo, P. Ferrer, D. Gianolio, A. G. Pereira, Á. García, J. Torrero, M. T. Fernández-Díaz, P. Bencok, M. A. Peña, J. L. G. Fierro and S. Rojas, *Nat Commun*, 2019, **10**, 2041.

283 T. Xia, C. Liu, Y. Lu, W. Jiang, H. Li, Y. Ma, Y. Wu and G. Che, *Appl Surf Sci*, 2022, **605**, 154727.

284 S. Dani, R. Pandit, H. Sharma, A. Arya, R. J. Choudhary, N. Goyal, J. Singh and R. Kumar, *J Mater Chem C Mater*, 2023, **11**, 4081–4093.

285 M. C. Biesinger, *Appl Surf Sci*, 2022, **597**, 153681.

286 D. J. Morgan, *Surface and Interface Analysis*, 2015, **47**, 1072–1079.

287 M. Lü, X. Deng, J. C. Waerenborgh, X. Wu and J. Meng, *Dalton Transactions*, 2012, **41**, 11507.

288 M. C. Biesinger, L. W. M. Lau, A. R. Gerson and R. S. C. Smart, *Physical Chemistry Chemical Physics*, 2012, **14**, 2434.

289 Hk. Müller-Buschbaum and H. G. V. Schnering, *ZAAC - Journal of Inorganic and General Chemistry*, 1965, **340**, 232–245.

290 I. I. Kornilov and MYASNIKO. KP, *RUSSIAN METALLURGY-METALLY-USSR*, 1964, 95.

291 E. Raub and D. Menzel, *International Journal of Materials Research*, 1961, **52**, 831–833.

292 O. Kwon, S. Joo, S. Choi, S. Sengodan and G. Kim, *Journal of Physics: Energy*, 2020, **2**, 032001.

293 D. Briggs, *Surface and Interface Analysis*, 1981, **3**, v–v.

294 D. R. G. Mitchell and B. Schaffer, *Ultramicroscopy*, 2005, **103**, 319–332.

295 C. A. Schneider, W. S. Rasband and K. W. Eliceiri, *Nat Methods*, 2012, **9**, 671–675.

296 1964, 10011.

297 J. F. Wu, C. Y. Tai, W. K. Yang and L. P. Leu, *Ind Eng Chem Res*, 1991, **30**, 2226–2233.

298 Y. Sun, J. Li, Y. Zeng, B. S. Amirkhiz, M. Wang, Y. Behnamian and J. Luo, *J Mater Chem A Mater*, 2015, **3**, 11048–11056.

299 S. Liu, Q. Liu and J. L. Luo, *ACS Catal*, 2016, **6**, 6219–6228.

300 D. M. Amaya-Dueñas, G. Chen, A. Weidenkaff, N. Sata, F. Han, I. Biswas, R. Costa and K. A. Friedrich, *J Mater Chem A Mater*, 2021, **9**, 5685–5701.

301 D. Chen, S. R. Bishop and H. L. Tuller, *J Electroceram*, 2012, **28**, 62–69.

302 J. B. Goodenough, *Physical Review*, 1955, **100**, 564–573.

303 S. Kogler, A. Nenning, G. M. Rupp, A. K. Opitz and J. Fleig, *J Electrochem Soc*, 2015, **162**, F317–F326.

304 S. Yu, D. Yoon, Y. Lee, H. Yoon, H. Han, N. Kim, C. J. Kim, K. Ihm, T. S. Oh and J. Son, *Nano Lett*, 2020, **20**, 3538–3544.

305 J. Wang, K. Syed, S. Ning, I. Waluyo, A. Hunt, E. J. Crumlin, A. K. Opitz, C. A. Ross, W. J. Bowman and B. Yildiz, *Adv Funct Mater*, , DOI:10.1002/adfm.202108005.

306 H. Wu and F. Li, *Phys Lett A*, 2019, **383**, 210–214.

307 J. Feng, J. Qiao, W. Wang, Z. Wang, W. Sun and K. Sun, *Electrochim Acta*, 2016, **215**, 592–599.

308 D. Luo, W. Xiao, F. Lin, C. Luo and X. Li, *Advanced Powder Technology*, 2016, **27**, 481–485.

309 J. Wang, D. Kalaev, J. Yang, I. Waluyo, A. Hunt, J. T. Sadowski, H. L. Tuller and B. Yildiz, *J Am Chem Soc*, 2023, **145**, 1714–1727.

310 H. X-ray and L. Holland, .

311 A. Skowron, P. Huang and A. Petric, *J Solid State Chem*, 1999, **143**, 202–209.

312 D. Neagu, V. Kyriakou, I.-L. Roiban, M. Aouine, C. Tang, A. Caravaca, K. Kousi, I. Schreur-Piet, I. S. Metcalfe, P. Vernoux, M. C. M. M. van de Sanden and M. N. Tsampas, *ACS Nano*, 2019, **13**, 12996–13005.

313 N. Winckelmans, T. Altantzis, M. Grzelczak, A. Sánchez-Iglesias, L. M. Liz-Marzán and S. Bals, *The Journal of Physical Chemistry C*, 2018, **122**, 13522–13528.

314 J. Ran, O. Dyck, X. Wang, B. Yang, D. B. Geohegan and K. Xiao, *Adv Energy Mater*, 2020, **10**, 1–19.

315 N. Jiang, *Reports on Progress in Physics*, , DOI:10.1088/0034-4885/79/1/016501.

316 W. Z. Yang, X. Q. Liu, Y. Q. Lin and X. M. Chen, *J Appl Phys*, , DOI:10.1063/1.4704392.

317 J. E. Kleibeuker, E. M. Choi, E. D. Jones, T. M. Yu, B. Sala, B. A. Maclaren, D. Kepaptsoglou, D. Hernandez-Maldonado, Q. M. Ramasse, L. Jones, J. Barthel, I. Maclaren and J. L. Macmanus-Driscoll, *NPG Asia Mater*, , DOI:10.1038/AM.2017.113.

318 S. Pavlova, L. Kapokova, R. Bunina, G. Alikina, N. Sazonova, T. Krieger, A. Ishchenko, V. Rogov, R. Gulyaev, V. Sadykov and C. Mirodatos, *Catal Sci Technol*, 2012, **2**, 2099–2108.

319 H. E. Swanson and E. Tatge, *Standard X-ray Diffraction Powder Patterns*, 1966.

320 C. A. Schneider, W. S. Rasband and K. W. Eliceiri, *Nat Methods*, 2012, **9**, 671–675.

321 S. Vyazovkin, in *Characterization of Materials*, John Wiley & Sons, Inc., Hoboken, NJ, USA, 2012, pp. 87–118.

322 T. Götsch, L. Schlicker, M. F. Bekheet, A. Doran, M. Grünbacher, C. Praty, M. Tada, H. Matsui, N. Ishiguro, A. Gurlo, B. Klötzer and S. Penner, *RSC Adv*, 2018, **8**, 3120–3131.

323 Y. F. Sun, Y. Q. Zhang, B. Hua, Y. Behnamian, J. Li, S. H. Cui, J. H. Li and J. L. Luo, *J Power Sources*, 2016, **301**, 237–241.

324 D. M. Amaya-Dueñas, G. Chen, A. Weidenkaff, N. Sata, F. Han, I. Biswas, R. Costa and K. A. Friedrich, *J Mater Chem A Mater*, 2021, **9**, 5685–5701.

325 L. F. Cao, G. Y. Xu, D. Xie, M. X. Guo, L. Luo, Z. Li and M. P. Wang, *Phys Status Solidi B Basic Res*, 2006, **243**, 2745–2755.

326 H. M. Ansari, A. S. Bass, N. Ahmad and V. I. Birss, *J Mater Chem A Mater*, 2022, **10**, 2280–2294.

327 K. J. Kim, H. Han, T. Defferriere, D. Yoon, S. Na, S. J. Kim, A. M. Dayaghi, J. Son, T. S. Oh, H. M. Jang and G. M. Choi, *J Am Chem Soc*, 2019, **141**, 7509–7517.

328 R. Scurtu, G. Nechifor, C. Andronescu, V. Fruth and P. Osiceanu, *La 0.8 Sr 0.2 Ga 0.83 Mg 0.17 O 3-δ PEROVKITES INVESTIGATED BY IMPEDANCE SPECTROSCOPY AND X-RAY PHOTOELECTRON SPECTROSCOPY*, 2014, vol. 76.

329 S. Miyoshi and M. Martin, *Physical Chemistry Chemical Physics*, 2009, **11**, 3063.

330 S. Joo, A. Seong, O. Kwon, K. Kim, J. Hoon Lee, R. J. Gorte, J. M. Vohs, J. Woo Han and G. Kim, *Highly active dry methane reforming catalysts with boosted in situ grown Ni-Fe nanoparticles on perovskite via atomic layer deposition*, 2020.

331 S. Joo, O. Kwon, S. Kim, H. Y. Jeong and G. Kim, *J Electrochem Soc*, 2020, **167**, 064518.

332 S. Joo, O. Kwon, S. Kim, H. Y. Jeong and G. Kim, *J Electrochem Soc*, 2020, **167**, 064518.

Appendix

5.1 ASAXS analysis

As demonstrated in Section 6.5, Anomalous Small-Angle X-ray Scattering (ASAXS) was employed to further investigate the nucleation and particle growth process of the L1.85NR sample in an in-situ environment of 5% H_2/N_2 at reduction temperatures of 450°C and 550°C. In this appendix section, preliminary data and analysis of ASAXS patterns at the Ru edge of the L1.85NR sample reduced at 450°C are included. Author would like to acknowledge the invaluable assistance of Prof. Simone Mascotto from the University of Koblenz, Dr. Xiao Sun and Dr. Sylvio Haas from DESY, and Miss Princess Inangha from the University of Hamburg for their support in data collection and analysis.

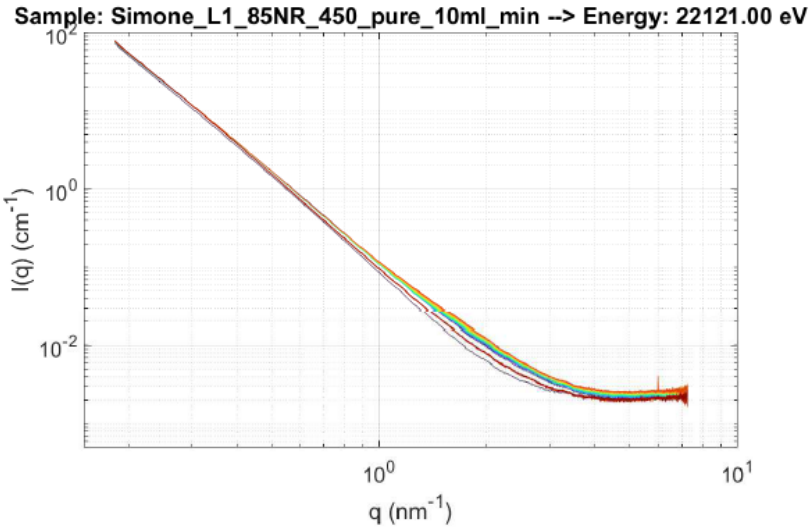


Figure A.26 ASAXS curves of the L1.85NR sample during the reduction in 5%H_2/N_2 at 450°C at 22.121 KeV energy: the intensity of high-q range increased with the reduction progressing.

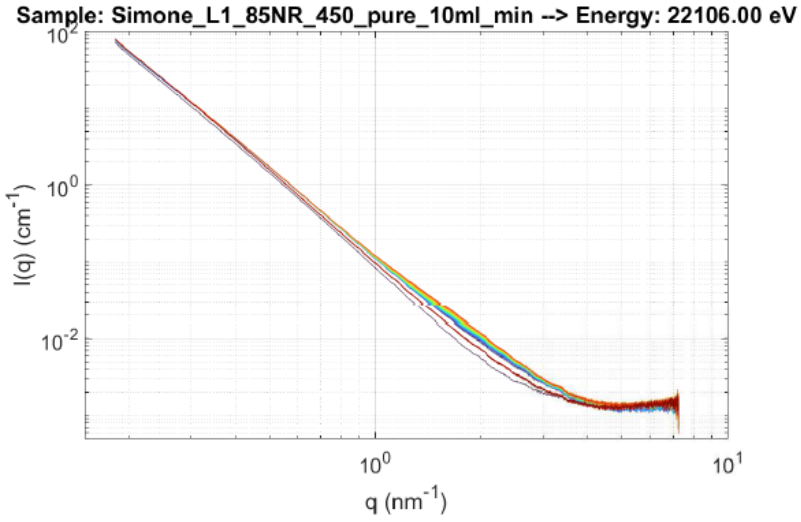


Figure A.27 ASAXS curves of the L1.85NR sample during the reduction in 5%H_2/N_2 at 450°C at 22.106 KeV energy. A similar trend with higher energy that with the reduction progressing, the high-q range showed elevated intensity.

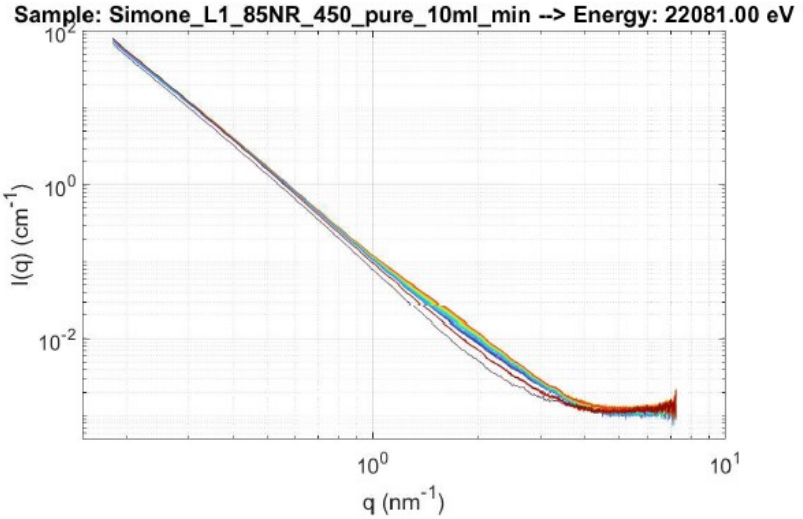


Figure A.28 ASAXS curves of the L1.85NR sample during the reduction in 5%H_2/N_2 at 450°C at 22.106 KeV energy.

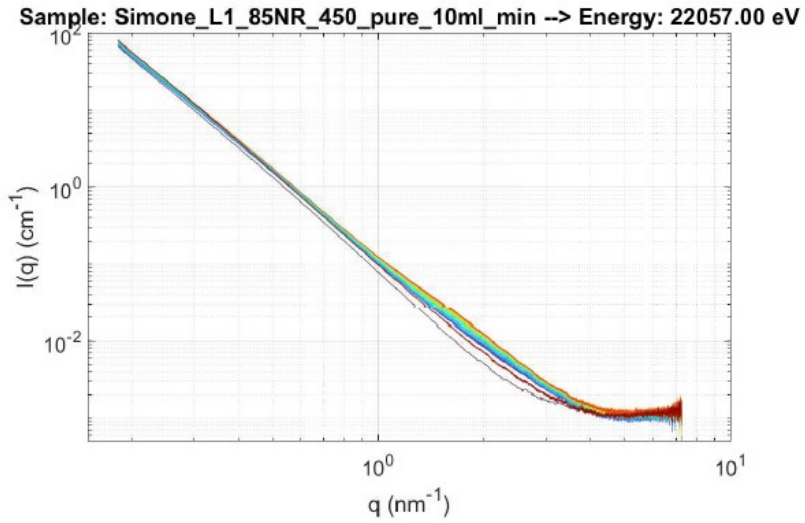


Figure A.29 ASAXS curves of the L1.85NR sample during the reduction in 5%H_2/N_2 at 450°C at 22.057 KeV energy.
A

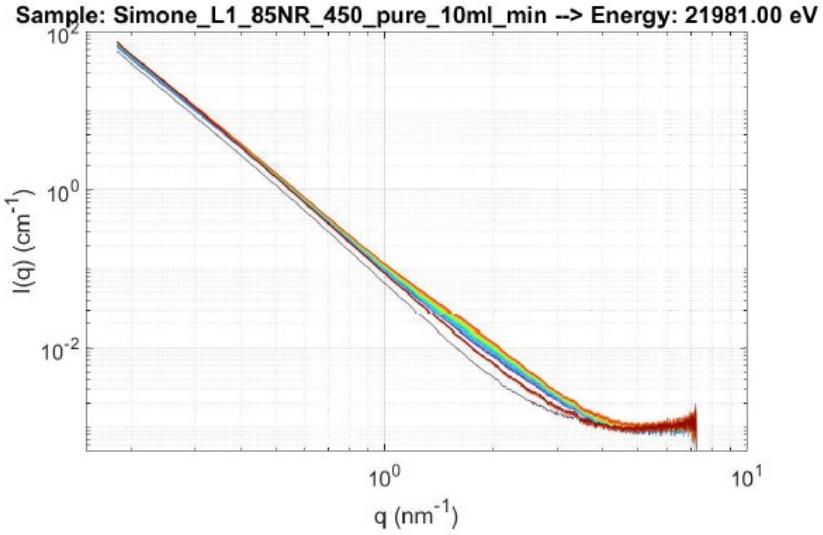


Figure A.30 ASAXS curves of the L1.85NR sample during the reduction in 5%H_2/N_2 at 450°C at 221.981 KeV energy.

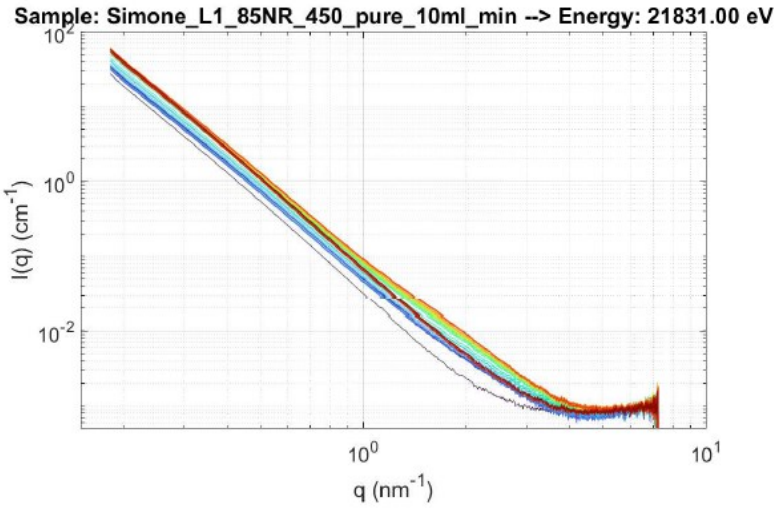


Figure A.31 ASAXS curves of the L1.85NR sample during the reduction in 5%H_2/N_2 at 450°C at 21.831 KeV energy. Similar with the discussion in section 6.5 on WAXS, the initial scanning at the beginning of experiments showed distinguished lower intensity and background which might attributed to the setting of measurement.

The deconvolution and fitting of the ASAXS data were conducted with the assistance of Prof. Simone Mascotto from the University of Koblenz and Dr. Xiao Sun from DESY. Figure 7 displays the fitted particle size distribution of the Ru nanoparticles. Two sets of particle sizes were employed for fitting the integrated curves in Figures 1-6. According to the fitted results, the first type of Ru-containing particles had a size of approximately 1 nm with a narrow size distribution, roughly equivalent to 3-4 atomic diameters. These smaller particles' signals were attributed to the scattering of Ru nuclei at the initial stage of exsolution, either below or on the surface. These nuclei were considered non-stable, as discussed in Chapters 6 and 7, until they agglomerated into larger sizes exceeding the critical size for particle growth.

The second type of exsolved particles had a size of around 5 nm, consistent with the observations under TEM (as discussed in Section 5.5). These particles were considered as an alloy phase present on the surface of the bulk double perovskite. With the reduction progressing, both the small nuclei/cluster and the particles showed enhanced intensity, implying the higher extend of exsolution happened.

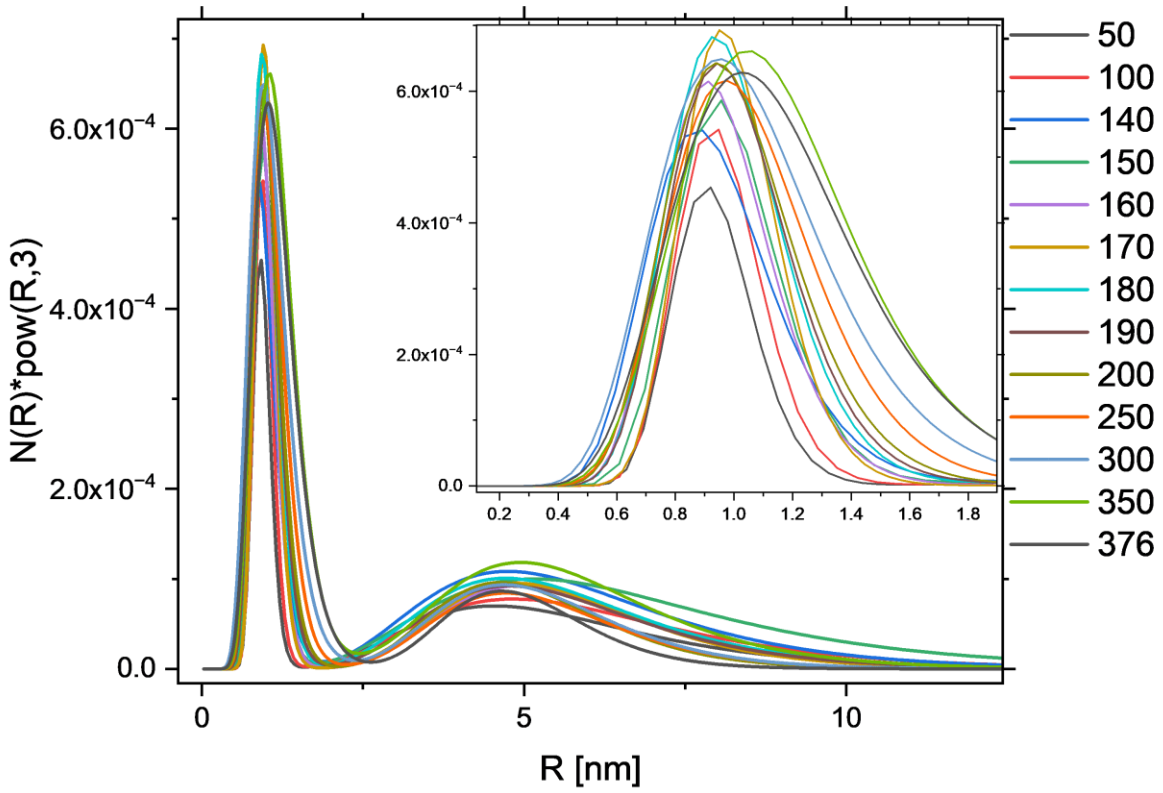


Figure A.32 Respective size distribution of the exsolved nanoparticles contained Ru. The legend of the plots indicates the number of scans collected. The scanning rate was 1 scan/min.

5.2 Copyright

Below are the electronic copies of all permission documents for the figures reused from their original sources:

ELSEVIER LICENSE
TERMS AND CONDITIONS

Jul 25, 2023

This Agreement between Miss. Jia Guo ("You") and Elsevier ("Elsevier") consists of your license details and the terms and conditions provided by Elsevier and Copyright Clearance Center.

License Number	5595890340228
License date	Jul 25, 2023
Licensed Content Publisher	Elsevier
Licensed Content Publication	Nano Energy
Licensed Content Title	From material design to mechanism study: Nanoscale Ni exsolution on a highly active A-site deficient anode material for solid oxide fuel cells
Licensed Content Author	Yang Gao,Dengjie Chen,Mattia Saccoccio,Ziheng Lu,Francesco Ciucci
Licensed Content Date	Sep 1, 2016
Licensed Content Volume	27
Licensed Content Issue	n/a
Licensed Content Pages	10
Start Page	499
End Page	508
Type of Use	reuse in a thesis/dissertation

Portion	figures/tables/illustrations
Number of figures/tables/illustrations	1
Format	both print and electronic
Are you the author of this Elsevier article?	No
Will you be translating?	No
Title	Lanthanum Nickel Oxide-Based Double Perovskites and their Exsolution Phenomena
Institution name	Imperial College London
Expected presentation date	Dec 2023
Portions	figure 6
Requestor Location	Miss. Jia Guo RSM, Imperial College London London, London SW7 2AZ United Kingdom Attn: Imperial College London
Publisher Tax ID	GB 494 6272 12
Total	0.00 GBP

Terms and Conditions

INTRODUCTION

1. The publisher for this copyrighted material is Elsevier. By clicking "accept" in connection with completing this licensing transaction, you agree that the following terms and conditions apply to this transaction (along with the Billing and Payment terms and conditions established by Copyright Clearance Center, Inc. ("CCC"), at the time that you opened your RightsLink account and that are available at any time at https://myaccount.copyright.com).

GENERAL TERMS

2. Elsevier hereby grants you permission to reproduce the aforementioned material subject to the terms and conditions indicated.

3. Acknowledgement: If any part of the material to be used (for example, figures) has appeared in our publication with credit or acknowledgement to another source, permission must also be sought from that source. If such permission is not obtained then that material may not be included in your publication/copies. Suitable acknowledgement to the source must be made, either as a footnote or in a reference list at the end of your publication, as follows:

"Reprinted from Publication title, Vol /edition number, Author(s), Title of article / title of chapter, Pages No., Copyright (Year), with permission from Elsevier [OR APPLICABLE SOCIETY COPYRIGHT OWNER]." Also Lancet special credit - "Reprinted from The Lancet, Vol. number, Author(s), Title of article, Pages No., Copyright (Year), with permission from Elsevier."

4. Reproduction of this material is confined to the purpose and/or media for which permission is hereby given. The material may not be reproduced or used in any other way, including use in combination with an artificial intelligence tool (including to train an algorithm, test, process, analyse, generate output and/or develop any form of artificial intelligence tool), or to create any derivative work and/or service (including resulting from the use of artificial intelligence tools).

5. Altering/Modifying Material: Not Permitted. However figures and illustrations may be altered/adapted minimally to serve your work. Any other abbreviations, additions, deletions and/or any other alterations shall be made only with prior written authorization of Elsevier Ltd. (Please contact Elsevier's permissions helpdesk here). No modifications can be made to any Lancet figures/tables and they must be reproduced in full.

6. If the permission fee for the requested use of our material is waived in this instance, please be advised that your future requests for Elsevier materials may attract a fee.

7. Reservation of Rights: Publisher reserves all rights not specifically granted in the combination of (i) the license details provided by you and accepted in the course of this licensing transaction, (ii) these terms and conditions and (iii) CCC's Billing and Payment terms and conditions.

8. License Contingent Upon Payment: While you may exercise the rights licensed immediately upon issuance of the license at the end of the licensing process for the transaction, provided that you have disclosed complete and accurate details of your proposed use, no license is finally effective unless and until full payment is received from you (either by publisher or by CCC) as provided in CCC's Billing and Payment terms and conditions. If full payment is not received on a timely basis, then any license preliminarily granted shall be deemed automatically revoked and shall be void as if never granted. Further, in the event that you breach any of these terms and conditions or any of CCC's Billing and Payment terms and conditions, the license is automatically revoked and shall be void as if never granted. Use of materials as described in a revoked license, as well as any use of the materials beyond the scope of an unrevoked license, may constitute copyright infringement and publisher reserves the right to take any and all action to protect its copyright in the materials.

9. Warranties: Publisher makes no representations or warranties with respect to the licensed material.

10. Indemnity: You hereby indemnify and agree to hold harmless publisher and CCC, and their respective officers, directors, employees and agents, from and against any and all claims arising out of your use of the licensed material other than as specifically authorized pursuant to this license.

11. No Transfer of License: This license is personal to you and may not be sublicensed, assigned, or transferred by you to any other person without publisher's written permission.

12. No Amendment Except in Writing: This license may not be amended except in a writing signed by both parties (or, in the case of publisher, by CCC on publisher's behalf).

13. Objection to Contrary Terms: Publisher hereby objects to any terms contained in any purchase order, acknowledgment, check endorsement or other writing prepared by you, which terms are inconsistent with these terms and conditions or CCC's Billing and Payment terms and conditions. These terms and conditions, together with CCC's Billing and Payment terms and conditions (which are incorporated herein), comprise the entire agreement between you and publisher (and CCC) concerning this licensing transaction. In the event of any conflict between your obligations established by these terms and conditions and those established by CCC's Billing and Payment terms and conditions, these terms and conditions shall control.

14. Revocation: Elsevier or Copyright Clearance Center may deny the permissions described in this License at their sole discretion, for any reason or no reason, with a full refund payable to you. Notice of such denial will be made using the contact information provided by you. Failure to receive such notice will not alter or invalidate the denial. In no event will Elsevier or Copyright Clearance Center be responsible or liable for any costs, expenses or damage incurred by you as a result of a denial of your permission request, other than a refund of the amount(s) paid by you to Elsevier and/or Copyright Clearance Center for denied permissions.

LIMITED LICENSE

The following terms and conditions apply only to specific license types:

15. **Translation**: This permission is granted for non-exclusive world **English** rights only unless your license was granted for translation rights. If you licensed translation rights you may only translate this content into the languages you requested. A professional translator must perform all translations and reproduce the content word for word preserving the integrity of the article.

16. **Posting licensed content on any Website**: The following terms and conditions apply as follows: Licensing material from an Elsevier journal: All content posted to the web site must maintain the copyright information line on the bottom of each image; A hyper-text must be included to the Homepage of the journal from which you are licensing at http://www.sciencedirect.com/science/journal/xxxxx or the Elsevier homepage for books at http://www.elsevier.com; Central Storage: This license does not include permission for a scanned version of the material to be stored in a central repository such as that provided by Heron/XanEdu.

Licensing material from an Elsevier book: A hyper-text link must be included to the Elsevier homepage at http://www.elsevier.com . All content posted to the web site must maintain the copyright information line on the bottom of each image.

Posting licensed content on Electronic reserve: In addition to the above the following clauses are applicable: The web site must be password-protected and made available only to bona fide students registered on a relevant course. This permission is granted for 1 year only. You may obtain a new license for future website posting.

17. **For journal authors:** the following clauses are applicable in addition to the above:

Preprints:

A preprint is an author's own write-up of research results and analysis, it has not been peer-reviewed, nor has it had any other value added to it by a publisher (such as formatting, copyright, technical enhancement etc.).

Authors can share their preprints anywhere at any time. Preprints should not be added to or enhanced in any way in order to appear more like, or to substitute for, the final versions of articles however authors can update their preprints on arXiv or RePEc with their Accepted Author Manuscript (see below).

If accepted for publication, we encourage authors to link from the preprint to their formal publication via its DOI. Millions of researchers have access to the formal publications on ScienceDirect, and so links will help users to find, access, cite and use the best available version. Please note that Cell Press, The Lancet and some society-owned have different preprint policies. Information on these policies is available on the journal homepage.

Accepted Author Manuscripts: An accepted author manuscript is the manuscript of an article that has been accepted for publication and which typically includes author-incorporated changes suggested during submission, peer review and editor-author communications.

Authors can share their accepted author manuscript:

- immediately
  - via their non-commercial person homepage or blog
  - by updating a preprint in arXiv or RePEc with the accepted manuscript
  - via their research institute or institutional repository for internal institutional uses or as part of an invitation-only research collaboration work-group
  - directly by providing copies to their students or to research collaborators for their personal use
  - for private scholarly sharing as part of an invitation-only work group on commercial sites with which Elsevier has an agreement
- After the embargo period
  - via non-commercial hosting platforms such as their institutional repository
  - via commercial sites with which Elsevier has an agreement

In all cases accepted manuscripts should:

- link to the formal publication via its DOI
- bear a CC-BY-NC-ND license - this is easy to do
- if aggregated with other manuscripts, for example in a repository or other site, be shared in alignment with our hosting policy not be added to or enhanced in any way to appear more like, or to substitute for, the published journal article.

Published journal article (JPA): A published journal article (PJA) is the definitive final record of published research that appears or will appear in the journal and embodies all value-adding publishing activities including peer review co-ordination, copy-editing, formatting, (if relevant) pagination and online enrichment.

Policies for sharing publishing journal articles differ for subscription and gold open access articles:

Subscription Articles: If you are an author, please share a link to your article rather than the full-text. Millions of researchers have access to the formal publications on ScienceDirect, and so links will help your users to find, access, cite, and use the best available version.

Theses and dissertations which contain embedded PJAs as part of the formal submission can be posted publicly by the awarding institution with DOI links back to the formal publications on ScienceDirect.

If you are affiliated with a library that subscribes to ScienceDirect you have additional private sharing rights for others' research accessed under that agreement. This includes use for classroom teaching and internal training at the institution (including use in course packs and courseware programs), and inclusion of the article for grant funding purposes.

Gold Open Access Articles: May be shared according to the author-selected end-user license and should contain a CrossMark logo, the end user license, and a DOI link to the formal publication on ScienceDirect.

Please refer to Elsevier's posting policy for further information.

18. **For book authors** the following clauses are applicable in addition to the above: Authors are permitted to place a brief summary of their work online only. You are not allowed to download and post the published electronic version of your chapter, nor may you scan the printed edition to create an electronic version. **Posting to a repository:** Authors are permitted to post a summary of their chapter only in their institution's repository.

19. **Thesis/Dissertation**: If your license is for use in a thesis/dissertation your thesis may be submitted to your institution in either print or electronic form. Should your thesis be published commercially, please reapply for permission. These requirements include permission for the Library and Archives of Canada to supply single copies, on demand, of the complete thesis and include permission for Proquest/UMI to supply single copies, on demand, of the complete thesis. Should your thesis be published commercially, please reapply for permission. Theses and dissertations which contain embedded PJAs as part of the formal submission can be posted publicly by the awarding institution with DOI links back to the formal publications on ScienceDirect.

Elsevier Open Access Terms and Conditions

You can publish open access with Elsevier in hundreds of open access journals or in nearly 2000 established subscription journals that support open access publishing. Permitted third party re-use of these open access articles is defined by the author's choice of Creative Commons user license. See our open access license policy for more information.

Terms & Conditions applicable to all Open Access articles published with Elsevier:

Any reuse of the article must not represent the author as endorsing the adaptation of the article nor should the article be modified in such a way as to damage the author's honour or reputation. If any changes have been made, such changes must be clearly indicated.

The author(s) must be appropriately credited and we ask that you include the end user license and a DOI link to the formal publication on ScienceDirect.

If any part of the material to be used (for example, figures) has appeared in our publication with credit or acknowledgement to another source it is the responsibility of the user to ensure their reuse complies with the terms and conditions determined by the rights holder.

Additional Terms & Conditions applicable to each Creative Commons user license:

CC BY: The CC-BY license allows users to copy, to create extracts, abstracts and new works from the Article, to alter and revise the Article and to make commercial use of the Article (including reuse and/or resale of the Article by commercial entities), provided the user gives appropriate credit (with a link to the formal publication through the relevant DOI), provides a link to the license, indicates if changes were made and the licensor is not represented as endorsing the use made of the work. The full details of the license are available at http://creativecommons.org/licenses/by/4.0.

CC BY NC SA: The CC BY-NC-SA license allows users to copy, to create extracts, abstracts and new works from the Article, to alter and revise the Article, provided this is not done for commercial purposes, and that the user gives appropriate credit (with a link to the formal publication through the relevant DOI), provides a link to the license, indicates if changes were made and the licensor is not represented as endorsing the use made of the work. Further, any new works must be made available on the same conditions. The full details of the license are available at http://creativecommons.org/licenses/by-nc-sa/4.0.

CC BY NC ND: The CC BY-NC-ND license allows users to copy and distribute the Article, provided this is not done for commercial purposes and further does not permit distribution of the Article if it is changed or edited in any way, and provided the user gives appropriate credit (with a link to the formal publication through the relevant DOI), provides a link to the license, and that the licensor is not represented as endorsing the use made of the work. The full details of the license are available at http://creativecommons.org/licenses/by-nc-nd/4.0. Any commercial reuse of Open Access articles published with a CC BY NC SA or CC BY NC ND license requires permission from Elsevier and will be subject to a fee.

Commercial reuse includes:

- Associating advertising with the full text of the Article
- Charging fees for document delivery or access
- Article aggregation
- Systematic distribution via e-mail lists or share buttons

Posting or linking by commercial companies for use by customers of those companies.

20. **Other Conditions**:

v1.10

Questions? customercare@copyright.com.

ELSEVIER LICENSE
TERMS AND CONDITIONS

Jul 12, 2023

This Agreement between Miss. Jia Guo ("You") and Elsevier ("Elsevier") consists of your license details and the terms and conditions provided by Elsevier and Copyright Clearance Center.

License Number	5586420950814
License date	Jul 12, 2023
Licensed Content Publisher	Elsevier
Licensed Content Publication	Catalysis Today
Licensed Content Title	The intelligent catalyst having the self-regenerative function of Pd, Rh and Pt for automotive emissions control
Licensed Content Author	Hirohisa Tanaka,Mari Uenishi,Masashi Taniguchi,Isao Tan,Keiichi Narita,Mareo Kimura,Kimiyoshi Kaneko,Yasuo Nishihata,Jun'ichiro Mizuki
Licensed Content Date	Sep 30, 2006
Licensed Content Volume	117
Licensed Content Issue	1-3
Licensed Content Pages	8
Start Page	321
End Page	328
Type of Use	reuse in a thesis/dissertation

Portion	figures/tables/illustrations
Number of figures/tables/illustrations	12
Format	both print and electronic
Are you the author of this Elsevier article?	No
Will you be translating?	No
Title	Lanthanum Nickel Oxide-Based Double Perovskites and their Exsolution Phenomena
Institution name	Imperial College London
Expected presentation date	Dec 2023
Portions	Figure 12
Requestor Location	Miss. Jia Guo RSM, Imperial College London London, London SW7 2AZ United Kingdom Attn: Imperial College London
Publisher Tax ID	GB 494 6272 12
Total	0.00 GBP

Terms and Conditions

INTRODUCTION

1. The publisher for this copyrighted material is Elsevier. By clicking "accept" in connection with completing this licensing transaction, you agree that the following terms and conditions apply to this transaction (along with the Billing and Payment terms and conditions established by Copyright Clearance Center, Inc. ("CCC"), at the time that you opened your RightsLink account and that are available at any time at https://myaccount.copyright.com).

GENERAL TERMS

2. Elsevier hereby grants you permission to reproduce the aforementioned material subject to the terms and conditions indicated.

3. Acknowledgement: If any part of the material to be used (for example, figures) has appeared in our publication with credit or acknowledgement to another source, permission must also be sought from that source. If such permission is not obtained then that material may not be included in your publication/copies. Suitable acknowledgement to the source must be made, either as a footnote or in a reference list at the end of your publication, as follows:

"Reprinted from Publication title, Vol /edition number, Author(s), Title of article / title of chapter, Pages No., Copyright (Year), with permission from Elsevier [OR APPLICABLE SOCIETY COPYRIGHT OWNER]." Also Lancet special credit - "Reprinted from The Lancet, Vol. number, Author(s), Title of article, Pages No., Copyright (Year), with permission from Elsevier."

4. Reproduction of this material is confined to the purpose and/or media for which permission is hereby given. The material may not be reproduced or used in any other way, including use in combination with an artificial intelligence tool (including to train an algorithm, test, process, analyse, generate output and/or develop any form of artificial intelligence tool), or to create any derivative work and/or service (including resulting from the use of artificial intelligence tools).

5. Altering/Modifying Material: Not Permitted. However figures and illustrations may be altered/adapted minimally to serve your work. Any other abbreviations, additions, deletions and/or any other alterations shall be made only with prior written authorization of Elsevier Ltd. (Please contact Elsevier's permissions helpdesk here). No modifications can be made to any Lancet figures/tables and they must be reproduced in full.

6. If the permission fee for the requested use of our material is waived in this instance, please be advised that your future requests for Elsevier materials may attract a fee.

7. Reservation of Rights: Publisher reserves all rights not specifically granted in the combination of (i) the license details provided by you and accepted in the course of this licensing transaction, (ii) these terms and conditions and (iii) CCC's Billing and Payment terms and conditions.

8. License Contingent Upon Payment: While you may exercise the rights licensed immediately upon issuance of the license at the end of the licensing process for the transaction, provided that you have disclosed complete and accurate details of your proposed use, no license is finally effective unless and until full payment is received from you (either by publisher or by CCC) as provided in CCC's Billing and Payment terms and conditions. If full payment is not received on a timely basis, then any license preliminarily granted shall be deemed automatically revoked and shall be void as if never granted. Further, in the event that you breach any of these terms and conditions or any of CCC's Billing and Payment terms and conditions, the license is automatically revoked and shall be void as if never granted. Use of materials as described in a revoked license, as well as any use of the materials beyond the scope of an unrevoked license, may constitute copyright infringement and publisher reserves the right to take any and all action to protect its copyright in the materials.

9. Warranties: Publisher makes no representations or warranties with respect to the licensed material.

10. Indemnity: You hereby indemnify and agree to hold harmless publisher and CCC, and their respective officers, directors, employees and agents, from and against any and all claims arising out of your use of the licensed material other than as specifically authorized pursuant to this license.

11. No Transfer of License: This license is personal to you and may not be sublicensed, assigned, or transferred by you to any other person without publisher's written permission.

12. No Amendment Except in Writing: This license may not be amended except in a writing signed by both parties (or, in the case of publisher, by CCC on publisher's behalf).

13. Objection to Contrary Terms: Publisher hereby objects to any terms contained in any purchase order, acknowledgment, check endorsement or other writing prepared by you, which terms are inconsistent with these terms and conditions or CCC's Billing and Payment terms and conditions. These terms and conditions, together with CCC's Billing and Payment terms and conditions (which are incorporated herein), comprise the entire agreement between you and publisher (and CCC) concerning this licensing transaction. In the event of any conflict between your obligations established by these terms and conditions and those established by CCC's Billing and Payment terms and conditions, these terms and conditions shall control.

14. Revocation: Elsevier or Copyright Clearance Center may deny the permissions described in this License at their sole discretion, for any reason or no reason, with a full refund payable to you. Notice of such denial will be made using the contact information provided by you. Failure to receive such notice will not alter or invalidate the denial. In no event will Elsevier or Copyright Clearance Center be responsible or liable for any costs, expenses or damage incurred by you as a result of a denial of your permission request, other than a refund of the amount(s) paid by you to Elsevier and/or Copyright Clearance Center for denied permissions.

LIMITED LICENSE

The following terms and conditions apply only to specific license types:

15. **Translation**: This permission is granted for non-exclusive world **English** rights only unless your license was granted for translation rights. If you licensed translation rights you may only translate this content into the languages you requested. A professional translator must perform all translations and reproduce the content word for word preserving the integrity of the article.

16. **Posting licensed content on any Website**: The following terms and conditions apply as follows: Licensing material from an Elsevier journal: All content posted to the web site must maintain the copyright information line on the bottom of each image; A hyper-text must be included to the Homepage of the journal from which you are licensing at http://www.sciencedirect.com/science/journal/xxxxx or the Elsevier homepage for books at http://www.elsevier.com; Central Storage: This license does not include permission for a scanned version of the material to be stored in a central repository such as that provided by Heron/XanEdu.

Licensing material from an Elsevier book: A hyper-text link must be included to the Elsevier homepage at http://www.elsevier.com . All content posted to the web site must maintain the copyright information line on the bottom of each image.

Posting licensed content on Electronic reserve: In addition to the above the following clauses are applicable: The web site must be password-protected and made available only to bona fide students registered on a relevant course. This permission is granted for 1 year only. You may obtain a new license for future website posting.

17. **For journal authors**: the following clauses are applicable in addition to the above:

Preprints:

A preprint is an author's own write-up of research results and analysis, it has not been peer-reviewed, nor has it had any other value added to it by a publisher (such as formatting, copyright, technical enhancement etc.).

Authors can share their preprints anywhere at any time. Preprints should not be added to or enhanced in any way in order to appear more like, or to substitute for, the final versions of articles however authors can update their preprints on arXiv or RePEc with their Accepted Author Manuscript (see below).

If accepted for publication, we encourage authors to link from the preprint to their formal publication via its DOI. Millions of researchers have access to the formal publications on ScienceDirect, and so links will help users to find, access, cite and use the best available version. Please note that Cell Press, The Lancet and some society-owned have different preprint policies. Information on these policies is available on the journal homepage.

Accepted Author Manuscripts: An accepted author manuscript is the manuscript of an article that has been accepted for publication and which typically includes author-incorporated changes suggested during submission, peer review and editor-author communications.

Authors can share their accepted author manuscript:

- immediately
  - via their non-commercial person homepage or blog
  - by updating a preprint in arXiv or RePEc with the accepted manuscript
  - via their research institute or institutional repository for internal institutional uses or as part of an invitation-only research collaboration work-group
  - directly by providing copies to their students or to research collaborators for their personal use
  - for private scholarly sharing as part of an invitation-only work group on commercial sites with which Elsevier has an agreement
- After the embargo period
  - via non-commercial hosting platforms such as their institutional repository
  - via commercial sites with which Elsevier has an agreement

In all cases accepted manuscripts should:

- link to the formal publication via its DOI
- bear a CC-BY-NC-ND license - this is easy to do
- if aggregated with other manuscripts, for example in a repository or other site, be shared in alignment with our hosting policy not be added to or enhanced in any way to appear more like, or to substitute for, the published journal article.

Published journal article (JPA): A published journal article (PJA) is the definitive final record of published research that appears or will appear in the journal and embodies all value-adding publishing activities including peer review co-ordination, copy-editing, formatting, (if relevant) pagination and online enrichment.

Policies for sharing publishing journal articles differ for subscription and gold open access articles:

Subscription Articles: If you are an author, please share a link to your article rather than the full-text. Millions of researchers have access to the formal publications on ScienceDirect, and so links will help your users to find, access, cite, and use the best available version.

Theses and dissertations which contain embedded PJAs as part of the formal submission can be posted publicly by the awarding institution with DOI links back to the formal publications on ScienceDirect.

If you are affiliated with a library that subscribes to ScienceDirect you have additional private sharing rights for others' research accessed under that agreement. This includes use for classroom teaching and internal training at the institution (including use in course packs and courseware programs), and inclusion of the article for grant funding purposes.

Gold Open Access Articles: May be shared according to the author-selected end-user license and should contain a CrossMark logo, the end user license, and a DOI link to the formal publication on ScienceDirect.

Please refer to Elsevier's posting policy for further information.

18. **For book authors** the following clauses are applicable in addition to the above: Authors are permitted to place a brief summary of their work online only. You are not allowed to download and post the published electronic version of your chapter, nor may you scan the printed edition to create an electronic version. **Posting to a repository:** Authors are permitted to post a summary of their chapter only in their institution's repository.

19. **Thesis/Dissertation**: If your license is for use in a thesis/dissertation your thesis may be submitted to your institution in either print or electronic form. Should your thesis be published commercially, please reapply for permission. These requirements include permission for the Library and Archives of Canada to supply single copies, on demand, of the complete thesis and include permission for Proquest/UMI to supply single copies, on demand, of the complete thesis. Should your thesis be published commercially, please reapply for permission. Theses and dissertations which contain embedded PJAs as part of the formal submission can be posted publicly by the awarding institution with DOI links back to the formal publications on ScienceDirect.

Elsevier Open Access Terms and Conditions

You can publish open access with Elsevier in hundreds of open access journals or in nearly 2000 established subscription journals that support open access publishing. Permitted third party re-use of these open access articles is defined by the author's choice of Creative Commons user license. See our open access license policy for more information.

Terms & Conditions applicable to all Open Access articles published with Elsevier:

Any reuse of the article must not represent the author as endorsing the adaptation of the article nor should the article be modified in such a way as to damage the author's honour or reputation. If any changes have been made, such changes must be clearly indicated.

The author(s) must be appropriately credited and we ask that you include the end user license and a DOI link to the formal publication on ScienceDirect.

If any part of the material to be used (for example, figures) has appeared in our publication with credit or acknowledgement to another source it is the responsibility of the user to ensure their reuse complies with the terms and conditions determined by the rights holder.

Additional Terms & Conditions applicable to each Creative Commons user license:

CC BY: The CC-BY license allows users to copy, to create extracts, abstracts and new works from the Article, to alter and revise the Article and to make commercial use of the Article (including reuse and/or resale of the Article by commercial entities), provided the user gives appropriate credit (with a link to the formal publication through the relevant DOI), provides a link to the license, indicates if changes were made and the licensor is not represented as endorsing the use made of the work. The full details of the license are available at http://creativecommons.org/licenses/by/4.0.

CC BY NC SA: The CC BY-NC-SA license allows users to copy, to create extracts, abstracts and new works from the Article, to alter and revise the Article, provided this is not done for commercial purposes, and that the user gives appropriate credit (with a link to the formal publication through the relevant DOI), provides a link to the license, indicates if changes were made and the licensor is not represented as endorsing the use made of the work. Further, any new works must be made available on the same conditions. The full details of the license are available at http://creativecommons.org/licenses/by-nc-sa/4.0.

CC BY NC ND: The CC BY-NC-ND license allows users to copy and distribute the Article, provided this is not done for commercial purposes and further does not permit distribution of the Article if it is changed or edited in any way, and provided the user gives appropriate credit (with a link to the formal publication through the relevant DOI), provides a link to the license, and that the licensor is not represented as endorsing the use made of the work. The full details of the license are available at http://creativecommons.org/licenses/by-nc-nd/4.0. Any commercial reuse of Open Access articles published with a CC BY NC SA or CC BY NC ND license requires permission from Elsevier and will be subject to a fee.

Commercial reuse includes:

- Associating advertising with the full text of the Article
- Charging fees for document delivery or access
- Article aggregation
- Systematic distribution via e-mail lists or share buttons

Posting or linking by commercial companies for use by customers of those companies.

20. **Other Conditions**:

v1.10

Questions? customercare@copyright.com.

SPRINGER NATURE ORDER DETAILS

Jul 12, 2023

Order Number	501829635
Order date	Jul 12, 2023
Licensed Content Publisher	Springer Nature
Licensed Content Publication	Nature Chemistry
Licensed Content Title	In situ growth of nanoparticles through control of non-stoichiometry
Licensed Content Author	Dragos Neagu et al
Licensed Content Date	Oct 6, 2013
Type of Use	Thesis/Dissertation
Requestor type	non-commercial (non-profit)
Format	print and electronic
Portion	figures/tables/illustrations
Number of figures/tables/illustrations	6
Would you like a high resolution image with your order?	no
Will you be translating?	no
Circulation/distribution	1 - 29
Author of this Springer Nature content	no

Title	Lanthanum Nickel Oxide-Based Double Perovskites and their Exsolution Phenomena
Institution name	Imperial College London
Expected presentation date	Dec 2023
Portions	figure 6
Requestor Location	Miss. Jia Guo RSM, Imperial College London London, London SW7 2AZ United Kingdom Attn: Imperial College London
Total	Not Available

JOHN WILEY AND SONS LICENSE TERMS AND CONDITIONS

Aug 10, 2023

This Agreement between Miss. Jia Guo ("You") and John Wiley and Sons ("John Wiley and Sons") consists of your license details and the terms and conditions provided by John Wiley and Sons and Copyright Clearance Center.

License Number	5605391501438
License date	Aug 10, 2023
Licensed Content Publisher	John Wiley and Sons
Licensed Content Publication	Small Methods
Licensed Content Title	Plasma Driven Exsolution for Nanoscale Functionalization of Perovskite Oxides
Licensed Content Author	Floran Peeters, Oreste De Luca, Petra Rudolf, et al
Licensed Content Date	Oct 22, 2021
Licensed Content Volume	5
Licensed Content Issue	12
Licensed Content Pages	7
Type of use	Dissertation/Thesis
Requestor type	University/Academic
Format	Print and electronic
Portion	Figure/table

Number of figures/tables	2
Will you be translating?	No
Title	Lanthanum Nickel Oxide-Based Double Perovskites and their Exsolution Phenomena
Institution name	Imperial College London
Expected presentation date	Dec 2023
Portions	Figure 1,2
Requestor Location	Miss. Jia Guo RSM, Imperial College London London, London SW7 2AZ United Kingdom Attn: Imperial College London
Publisher Tax ID	EU826007151
Total	0.00 GBP
Terms and Conditions	

TERMS AND CONDITIONS

This copyrighted material is owned by or exclusively licensed to John Wiley & Sons, Inc. or one of its group companies (each a"Wiley Company") or handled on behalf of a society with which a Wiley Company has exclusive publishing rights in relation to a particular work (collectively "WILEY"). By clicking "accept" in connection with completing this licensing transaction, you agree that the following terms and conditions apply to this transaction (along with the billing and payment terms and conditions established by the Copyright Clearance Center Inc., ("CCC's Billing and Payment terms and conditions"), at the time that you opened your RightsLink account (these are available at any time at http://myaccount.copyright.com).

Terms and Conditions

- The materials you have requested permission to reproduce or reuse (the "Wiley Materials") are protected by copyright.
- You are hereby granted a personal, non-exclusive, non-sub licensable (on a stand-alone basis), non-transferable, worldwide, limited license to reproduce the Wiley

Materials for the purpose specified in the licensing process. This license, **and any CONTENT (PDF or image file) purchased as part of your order,** is for a one-time use only and limited to any maximum distribution number specified in the license. The first instance of republication or reuse granted by this license must be completed within two years of the date of the grant of this license (although copies prepared before the end date may be distributed thereafter). The Wiley Materials shall not be used in any other manner or for any other purpose, beyond what is granted in the license. Permission is granted subject to an appropriate acknowledgement given to the author, title of the material/book/journal and the publisher. You shall also duplicate the copyright notice that appears in the Wiley publication in your use of the Wiley Material. Permission is also granted on the understanding that nowhere in the text is a previously published source acknowledged for all or part of this Wiley Material. Any third party content is expressly excluded from this permission.

- With respect to the Wiley Materials, all rights are reserved. Except as expressly granted by the terms of the license, no part of the Wiley Materials may be copied, modified, adapted (except for minor reformatting required by the new Publication), translated, reproduced, transferred or distributed, in any form or by any means, and no derivative works may be made based on the Wiley Materials without the prior permission of the respective copyright owner.**For STM Signatory Publishers clearing permission under the terms of the STM Permissions Guidelines only, the terms of the license are extended to include subsequent editions and for editions in other languages, provided such editions are for the work as a whole in situ and does not involve the separate exploitation of the permitted figures or extracts,** You may not alter, remove or suppress in any manner any copyright, trademark or other notices displayed by the Wiley Materials. You may not license, rent, sell, loan, lease, pledge, offer as security, transfer or assign the Wiley Materials on a stand-alone basis, or any of the rights granted to you hereunder to any other person.

- The Wiley Materials and all of the intellectual property rights therein shall at all times remain the exclusive property of John Wiley & Sons Inc, the Wiley Companies, or their respective licensors, and your interest therein is only that of having possession of and the right to reproduce the Wiley Materials pursuant to Section 2 herein during the continuance of this Agreement. You agree that you own no right, title or interest in or to the Wiley Materials or any of the intellectual property rights therein. You shall have no rights hereunder other than the license as provided for above in Section 2. No right, license or interest to any trademark, trade name, service mark or other branding ("Marks") of WILEY or its licensors is granted hereunder, and you agree that you shall not assert any such right, license or interest with respect thereto

- NEITHER WILEY NOR ITS LICENSORS MAKES ANY WARRANTY OR REPRESENTATION OF ANY KIND TO YOU OR ANY THIRD PARTY, EXPRESS, IMPLIED OR STATUTORY, WITH RESPECT TO THE MATERIALS OR THE ACCURACY OF ANY INFORMATION CONTAINED IN THE MATERIALS, INCLUDING, WITHOUT LIMITATION, ANY IMPLIED WARRANTY OF MERCHANTABILITY, ACCURACY, SATISFACTORY QUALITY, FITNESS FOR A PARTICULAR PURPOSE, USABILITY, INTEGRATION OR NON-INFRINGEMENT AND ALL SUCH WARRANTIES ARE HEREBY EXCLUDED BY WILEY AND ITS LICENSORS AND WAIVED BY YOU.

- WILEY shall have the right to terminate this Agreement immediately upon breach of this Agreement by you.

- You shall indemnify, defend and hold harmless WILEY, its Licensors and their respective directors, officers, agents and employees, from and against any actual or threatened claims, demands, causes of action or proceedings arising from any breach of this Agreement by you.

- IN NO EVENT SHALL WILEY OR ITS LICENSORS BE LIABLE TO YOU OR ANY OTHER PARTY OR ANY OTHER PERSON OR ENTITY FOR ANY SPECIAL, CONSEQUENTIAL, INCIDENTAL, INDIRECT, EXEMPLARY OR PUNITIVE DAMAGES, HOWEVER CAUSED, ARISING OUT OF OR IN CONNECTION WITH THE DOWNLOADING, PROVISIONING, VIEWING OR USE OF THE MATERIALS REGARDLESS OF THE FORM OF ACTION, WHETHER FOR BREACH OF CONTRACT, BREACH OF WARRANTY, TORT, NEGLIGENCE, INFRINGEMENT OR OTHERWISE (INCLUDING, WITHOUT LIMITATION, DAMAGES BASED ON LOSS OF PROFITS, DATA, FILES, USE, BUSINESS OPPORTUNITY OR CLAIMS OF THIRD PARTIES), AND WHETHER OR NOT THE PARTY HAS BEEN ADVISED OF THE POSSIBILITY OF SUCH DAMAGES. THIS LIMITATION SHALL APPLY NOTWITHSTANDING ANY FAILURE OF ESSENTIAL PURPOSE OF ANY LIMITED REMEDY PROVIDED HEREIN.

- Should any provision of this Agreement be held by a court of competent jurisdiction to be illegal, invalid, or unenforceable, that provision shall be deemed amended to achieve as nearly as possible the same economic effect as the original provision, and the legality, validity and enforceability of the remaining provisions of this Agreement shall not be affected or impaired thereby.

- The failure of either party to enforce any term or condition of this Agreement shall not constitute a waiver of either party's right to enforce each and every term and condition of this Agreement. No breach under this agreement shall be deemed waived or excused by either party unless such waiver or consent is in writing signed by the party granting such waiver or consent. The waiver by or consent of a party to a breach of any provision of this Agreement shall not operate or be construed as a waiver of or consent to any other or subsequent breach by such other party.

- This Agreement may not be assigned (including by operation of law or otherwise) by you without WILEY's prior written consent.

- Any fee required for this permission shall be non-refundable after thirty (30) days from receipt by the CCC.

- These terms and conditions together with CCC's Billing and Payment terms and conditions (which are incorporated herein) form the entire agreement between you and WILEY concerning this licensing transaction and (in the absence of fraud) supersedes all prior agreements and representations of the parties, oral or written. This Agreement may not be amended except in writing signed by both parties. This Agreement shall be binding upon and inure to the benefit of the parties' successors, legal representatives, and authorized assigns.

- In the event of any conflict between your obligations established by these terms and conditions and those established by CCC's Billing and Payment terms and conditions, these terms and conditions shall prevail.

- WILEY expressly reserves all rights not specifically granted in the combination of (i) the license details provided by you and accepted in the course of this licensing transaction, (ii) these terms and conditions and (iii) CCC's Billing and Payment terms and conditions.

- This Agreement will be void if the Type of Use, Format, Circulation, or Requestor Type was misrepresented during the licensing process.

- This Agreement shall be governed by and construed in accordance with the laws of the State of New York, USA, without regards to such state's conflict of law rules. Any legal action, suit or proceeding arising out of or relating to these Terms and Conditions

or the breach thereof shall be instituted in a court of competent jurisdiction in New York County in the State of New York in the United States of America and each party hereby consents and submits to the personal jurisdiction of such court, waives any objection to venue in such court and consents to service of process by registered or certified mail, return receipt requested, at the last known address of such party.

WILEY OPEN ACCESS TERMS AND CONDITIONS

Wiley Publishes Open Access Articles in fully Open Access Journals and in Subscription journals offering Online Open. Although most of the fully Open Access journals publish open access articles under the terms of the Creative Commons Attribution (CC BY) License only, the subscription journals and a few of the Open Access Journals offer a choice of Creative Commons Licenses. The license type is clearly identified on the article.

The Creative Commons Attribution License

The Creative Commons Attribution License (CC-BY) allows users to copy, distribute and transmit an article, adapt the article and make commercial use of the article. The CC-BY license permits commercial and non-

Creative Commons Attribution Non-Commercial License

The Creative Commons Attribution Non-Commercial (CC-BY-NC)License permits use, distribution and reproduction in any medium, provided the original work is properly cited and is not used for commercial purposes.(see below)

Creative Commons Attribution-Non-Commercial-NoDerivs License

The Creative Commons Attribution Non-Commercial-NoDerivs License (CC-BY-NC-ND) permits use, distribution and reproduction in any medium, provided the original work is properly cited, is not used for commercial purposes and no modifications or adaptations are made. (see below)

Use by commercial "for-profit" organizations

Use of Wiley Open Access articles for commercial, promotional, or marketing purposes requires further explicit permission from Wiley and will be subject to a fee.

Further details can be found on Wiley Online Library
http://olabout.wiley.com/WileyCDA/Section/id-410895.html

Other Terms and Conditions:

v1.10 Last updated September 2015

Questions? customercare@copyright.com.

SPRINGER NATURE LICENSE
TERMS AND CONDITIONS

Aug 12, 2023

This Agreement between Miss. Jia Guo ("You") and Springer Nature ("Springer Nature") consists of your license details and the terms and conditions provided by Springer Nature and Copyright Clearance Center.

License Number	5606581104654
License date	Aug 12, 2023
Licensed Content Publisher	Springer Nature
Licensed Content Publication	Nature
Licensed Content Title	Switching on electrocatalytic activity in solid oxide cells
Licensed Content Author	Jae-ha Myung et al
Licensed Content Date	Aug 22, 2016
Type of Use	Thesis/Dissertation
Requestor type	non-commercial (non-profit)
Format	print and electronic
Portion	figures/tables/illustrations
Number of figures/tables/illustrations	5
Would you like a high resolution image with your order?	no
Will you be translating?	no

Circulation/distribution	1 - 29
Author of this Springer Nature content	no
Title	Lanthanum Nickel Oxide-Based Double Perovskites and their Exsolution Phenomena
Institution name	Imperial College London
Expected presentation date	Dec 2023
Portions	Figure 1 (b), (c) ,(e), (f) and (h)
Requestor Location	Miss. Jia Guo RSM, Imperial College London London, London SW7 2AZ United Kingdom Attn: Imperial College London
Total	0.00 GBP

Terms and Conditions

Springer Nature Customer Service Centre GmbH Terms and Conditions

The following terms and conditions ("Terms and Conditions") together with the terms specified in your [RightsLink] constitute the License ("License") between you as Licensee and Springer Nature Customer Service Centre GmbH as Licensor. By clicking 'accept' and completing the transaction for your use of the material ("Licensed Material"), you confirm your acceptance of and obligation to be bound by these Terms and Conditions.

1. Grant and Scope of License

1. 1. The Licensor grants you a personal, non-exclusive, non-transferable, non-sublicensable, revocable, world-wide License to reproduce, distribute, communicate to the public, make available, broadcast, electronically transmit or create derivative works using the Licensed Material for the purpose(s) specified in your RightsLink Licence Details only. Licenses are granted for the specific use requested in the order and for no other use, subject to these Terms and Conditions. You acknowledge and agree that the rights granted to you under this License do not include the right to modify, edit, translate, include in collective works, or create derivative works of the Licensed Material in whole or in part unless expressly stated in your RightsLink Licence Details. You may use the Licensed Material only as permitted under this Agreement and will not reproduce, distribute, display, perform, or otherwise use or

exploit any Licensed Material in any way, in whole or in part, except as expressly permitted by this License.

1. 2. You may only use the Licensed Content in the manner and to the extent permitted by these Terms and Conditions, by your RightsLink Licence Details and by any applicable laws.

1. 3. A separate license may be required for any additional use of the Licensed Material, e.g. where a license has been purchased for print use only, separate permission must be obtained for electronic re-use. Similarly, a License is only valid in the language selected and does not apply for editions in other languages unless additional translation rights have been granted separately in the License.

1. 4. Any content within the Licensed Material that is owned by third parties is expressly excluded from the License.

1. 5. Rights for additional reuses such as custom editions, computer/mobile applications, film or TV reuses and/or any other derivative rights requests require additional permission and may be subject to an additional fee. Please apply to journalpermissions@springernature.com or bookpermissions@springernature.com for these rights.

2. Reservation of Rights

Licensor reserves all rights not expressly granted to you under this License. You acknowledge and agree that nothing in this License limits or restricts Licensor's rights in or use of the Licensed Material in any way. Neither this License, nor any act, omission, or statement by Licensor or you, conveys any ownership right to you in any Licensed Material, or to any element or portion thereof. As between Licensor and you, Licensor owns and retains all right, title, and interest in and to the Licensed Material subject to the license granted in Section 1.1. Your permission to use the Licensed Material is expressly conditioned on you not impairing Licensor's or the applicable copyright owner's rights in the Licensed Material in any way.

3. Restrictions on use

3. 1. Minor editing privileges are allowed for adaptations for stylistic purposes or formatting purposes provided such alterations do not alter the original meaning or intention of the Licensed Material and the new figure(s) are still accurate and representative of the Licensed Material. Any other changes including but not limited to, cropping, adapting, and/or omitting material that affect the meaning, intention or moral rights of the author(s) are strictly prohibited.

3. 2. You must not use any Licensed Material as part of any design or trademark.

3. 3. Licensed Material may be used in Open Access Publications (OAP), but any such reuse must include a clear acknowledgment of this permission visible at the same time as the figures/tables/illustration or abstract and which must indicate that the Licensed Material is not part of the governing OA license but has been reproduced with permission. This may be indicated according to any standard referencing system but must include at a minimum 'Book/Journal title, Author, Journal Name (if applicable), Volume (if applicable), Publisher, Year, reproduced with permission from SNCSC'.

4. STM Permission Guidelines

4. 1. An alternative scope of license may apply to signatories of the STM Permissions Guidelines ("STM PG") as amended from time to time and made available at

https://www.stm-assoc.org/intellectual-property/permissions/permissions-guidelines/.

4. 2. For content reuse requests that qualify for permission under the STM PG, and which may be updated from time to time, the STM PG supersede the terms and conditions contained in this License.

4. 3. If a License has been granted under the STM PG, but the STM PG no longer apply at the time of publication, further permission must be sought from the Rightsholder. Contact journalpermissions@springernature.com or bookpermissions@springernature.com for these rights.

5. Duration of License

5. 1. Unless otherwise indicated on your License, a License is valid from the date of purchase ("License Date") until the end of the relevant period in the below table:

Reuse in a medical communications project	Reuse up to distribution or time period indicated in License
Reuse in a dissertation/thesis	Lifetime of thesis
Reuse in a journal/magazine	Lifetime of journal/magazine
Reuse in a book/textbook	Lifetime of edition
Reuse on a website	1 year unless otherwise specified in the License
Reuse in a presentation/slide kit/poster	Lifetime of presentation/slide kit/poster. Note: publication whether electronic or in print of presentation/slide kit/poster may require further permission.
Reuse in conference proceedings	Lifetime of conference proceedings
Reuse in an annual report	Lifetime of annual report
Reuse in training/CME materials	Reuse up to distribution or time period indicated in License
Reuse in newsmedia	Lifetime of newsmedia
Reuse in coursepack/classroom materials	Reuse up to distribution and/or time period indicated in license

6. Acknowledgement

6. 1. The Licensor's permission must be acknowledged next to the Licensed Material in print. In electronic form, this acknowledgement must be visible at the same time as the figures/tables/illustrations or abstract and must be hyperlinked to the journal/book's homepage.

6. 2. Acknowledgement may be provided according to any standard referencing system and at a minimum should include "Author, Article/Book Title, Journal name/Book imprint, volume, page number, year, Springer Nature".

7. Reuse in a dissertation or thesis

7. 1. Where 'reuse in a dissertation/thesis' has been selected, the following terms apply: Print rights of the Version of Record are provided for; electronic rights for use only on institutional repository as defined by the Sherpa guideline (www.sherpa.ac.uk/romeo/) and only up to what is required by the awarding institution.

7. 2. For theses published under an ISBN or ISSN, separate permission is required. Please contact journalpermissions@springernature.com or bookpermissions@springernature.com for these rights.

7. 3. Authors must properly cite the published manuscript in their thesis according to current citation standards and include the following acknowledgement: '*Reproduced with permission from Springer Nature*'.

8. License Fee

You must pay the fee set forth in the License Agreement (the "License Fees"). All amounts payable by you under this License are exclusive of any sales, use, withholding, value added or similar taxes, government fees or levies or other assessments. Collection and/or remittance of such taxes to the relevant tax authority shall be the responsibility of the party who has the legal obligation to do so.

9. Warranty

9. 1. The Licensor warrants that it has, to the best of its knowledge, the rights to license reuse of the Licensed Material. **You are solely responsible for ensuring that the material you wish to license is original to the Licensor and does not carry the copyright of another entity or third party (as credited in the published version).** If the credit line on any part of the Licensed Material indicates that it was reprinted or adapted with permission from another source, then you should seek additional permission from that source to reuse the material.

9. 2. EXCEPT FOR THE EXPRESS WARRANTY STATED HEREIN AND TO THE EXTENT PERMITTED BY APPLICABLE LAW, LICENSOR PROVIDES THE LICENSED MATERIAL "AS IS" AND MAKES NO OTHER REPRESENTATION OR WARRANTY. LICENSOR EXPRESSLY DISCLAIMS ANY LIABILITY FOR ANY CLAIM ARISING FROM OR OUT OF THE CONTENT, INCLUDING BUT NOT LIMITED TO ANY ERRORS, INACCURACIES, OMISSIONS, OR DEFECTS CONTAINED THEREIN, AND ANY IMPLIED OR EXPRESS WARRANTY AS TO MERCHANTABILITY OR FITNESS FOR A PARTICULAR PURPOSE. IN NO EVENT SHALL LICENSOR BE LIABLE TO YOU OR ANY OTHER PARTY OR ANY OTHER PERSON OR FOR ANY SPECIAL, CONSEQUENTIAL, INCIDENTAL, INDIRECT, PUNITIVE, OR EXEMPLARY DAMAGES, HOWEVER CAUSED, ARISING OUT OF OR IN CONNECTION WITH THE DOWNLOADING, VIEWING OR USE OF THE LICENSED MATERIAL REGARDLESS OF THE FORM OF ACTION, WHETHER FOR BREACH OF CONTRACT, BREACH OF WARRANTY, TORT, NEGLIGENCE, INFRINGEMENT OR OTHERWISE (INCLUDING, WITHOUT LIMITATION, DAMAGES BASED ON LOSS OF PROFITS, DATA, FILES, USE, BUSINESS OPPORTUNITY OR CLAIMS OF THIRD PARTIES), AND WHETHER OR NOT THE PARTY HAS BEEN ADVISED OF THE POSSIBILITY OF SUCH DAMAGES. THIS LIMITATION APPLIES NOTWITHSTANDING ANY FAILURE OF ESSENTIAL PURPOSE OF ANY LIMITED REMEDY PROVIDED HEREIN.

10. Termination and Cancellation

10. 1. The License and all rights granted hereunder will continue until the end of the applicable period shown in Clause 5.1 above. Thereafter, this license will be terminated and all rights granted hereunder will cease.

10. 2. Licensor reserves the right to terminate the License in the event that payment is not received in full or if you breach the terms of this License.

11. General

11. 1. The License and the rights and obligations of the parties hereto shall be construed, interpreted and determined in accordance with the laws of the Federal Republic of Germany without reference to the stipulations of the CISG (United Nations Convention on Contracts for the International Sale of Goods) or to Germany's choice-of-law principle.

11. 2. The parties acknowledge and agree that any controversies and disputes arising out of this License shall be decided exclusively by the courts of or having jurisdiction for Heidelberg, Germany, as far as legally permissible.

11. 3. This License is solely for Licensor's and Licensee's benefit. It is not for the benefit of any other person or entity.

Questions? For questions on Copyright Clearance Center accounts or website issues please contact springernaturesupport@copyright.com or +1-855-239-3415 (toll free in the US) or +1-978-646-2777. For questions on Springer Nature licensing please visit https://www.springernature.com/gp/partners/rights-permissions-third-party-distribution

Other Conditions:

Version 1.4 - Dec 2022

Questions? customercare@copyright.com.

RightsLink

Home | Help | Email Support | Jia Guo

In Situ Observation of Nanoparticle Exsolution from Perovskite Oxides: From Atomic Scale Mechanistic Insight to Nanostructure Tailoring

ACS Publications

Author: Dragos Neagu, Vasileios Kyriakou, Ioan-Ludan Roiban, et al

Publication: ACS Nano

Publisher: American Chemical Society

Date: Nov 1, 2019

Copyright © 2019, American Chemical Society

PERMISSION/LICENSE IS GRANTED FOR YOUR ORDER AT NO CHARGE

This type of permission/license, instead of the standard Terms and Conditions, is sent to you because no fee is being charged for your order. Please note the following:

- Permission is granted for your request in both print and electronic formats, and translations.
- If figures and/or tables were requested, they may be adapted or used in part.
- Please print this page for your records and send a copy of it to your publisher/graduate school.
- Appropriate credit for the requested material should be given as follows: "Reprinted (adapted) with permission from {COMPLETE REFERENCE CITATION}. Copyright {YEAR} American Chemical Society." Insert appropriate information in place of the capitalized words.
- One-time permission is granted only for the use specified in your RightsLink request. No additional uses are granted (such as derivative works or other editions). For any uses, please submit a new request.

If credit is given to another source for the material you requested from RightsLink, permission must be obtained from that source.

BACK CLOSE WINDOW

© 2023 Copyright - All Rights Reserved | Copyright Clearance Center, Inc. | Privacy statement | Data Security and Privacy | For California Residents | Terms and ConditionsComments? We would like to hear from you. E-mail us at customercare@copyright.com

JOHN WILEY AND SONS LICENSE
TERMS AND CONDITIONS

Aug 12, 2023

This Agreement between Miss. Jia Guo ("You") and John Wiley and Sons ("John Wiley and Sons") consists of your license details and the terms and conditions provided by John Wiley and Sons and Copyright Clearance Center.

License Number	5606610383903
License date	Aug 12, 2023
Licensed Content Publisher	John Wiley and Sons
Licensed Content Publication	Angewandte Chemie International Edition
Licensed Content Title	Endogenous Nanoparticles Strain Perovskite Host Lattice Providing Oxygen Capacity and Driving Oxygen Exchange and CH4 Conversion to Syngas
Licensed Content Author	Ian S. Metcalfe, Evangelos I. Papaioannou, Leonidas Bekris, et al
Licensed Content Date	Jan 3, 2020
Licensed Content Volume	59
Licensed Content Issue	6
Licensed Content Pages	10
Type of use	Dissertation/Thesis

Requestor type	University/Academic
Format	Print and electronic
Portion	Figure/table
Number of figures/tables	4
Will you be translating?	No
Title	Lanthanum Nickel Oxide-Based Double Perovskites and their Exsolution Phenomena
Institution name	Imperial College London
Expected presentation date	Dec 2023
Portions	Figure 2.a-d
Requestor Location	Miss. Jia Guo RSM, Imperial College London London, London SW7 2AZ United Kingdom Attn: Imperial College London
Publisher Tax ID	EU826007151
Total	0.00 GBP

Terms and Conditions

TERMS AND CONDITIONS

This copyrighted material is owned by or exclusively licensed to John Wiley & Sons, Inc. or one of its group companies (each a"Wiley Company") or handled on behalf of a society with which a Wiley Company has exclusive publishing rights in relation to a particular work (collectively "WILEY"). By clicking "accept" in connection with completing this licensing transaction, you agree that the following terms and conditions apply to this transaction (along with the billing and payment terms and conditions established by the Copyright

Clearance Center Inc., ("CCC's Billing and Payment terms and conditions"), at the time that you opened your RightsLink account (these are available at any time at http://myaccount.copyright.com).

Terms and Conditions

- The materials you have requested permission to reproduce or reuse (the "Wiley Materials") are protected by copyright.
- You are hereby granted a personal, non-exclusive, non-sub licensable (on a stand-alone basis), non-transferable, worldwide, limited license to reproduce the Wiley Materials for the purpose specified in the licensing process. This license, **and any CONTENT (PDF or image file) purchased as part of your order,** is for a one-time use only and limited to any maximum distribution number specified in the license. The first instance of republication or reuse granted by this license must be completed within two years of the date of the grant of this license (although copies prepared before the end date may be distributed thereafter). The Wiley Materials shall not be used in any other manner or for any other purpose, beyond what is granted in the license. Permission is granted subject to an appropriate acknowledgement given to the author, title of the material/book/journal and the publisher. You shall also duplicate the copyright notice that appears in the Wiley publication in your use of the Wiley Material. Permission is also granted on the understanding that nowhere in the text is a previously published source acknowledged for all or part of this Wiley Material. Any third party content is expressly excluded from this permission.
- With respect to the Wiley Materials, all rights are reserved. Except as expressly granted by the terms of the license, no part of the Wiley Materials may be copied, modified, adapted (except for minor reformatting required by the new Publication), translated, reproduced, transferred or distributed, in any form or by any means, and no derivative works may be made based on the Wiley Materials without the prior permission of the respective copyright owner.**For STM Signatory Publishers clearing permission under the terms of the STM Permissions Guidelines only, the terms of the license are extended to include subsequent editions and for editions in other languages, provided such editions are for the work as a whole in situ and does not involve the separate exploitation of the permitted figures or extracts,** You may not alter, remove or suppress in any manner any copyright, trademark or other notices displayed by the Wiley Materials. You may not license, rent, sell, loan, lease, pledge, offer as security, transfer or assign the Wiley Materials on a stand-alone basis, or any of the rights granted to you hereunder to any other person.
- The Wiley Materials and all of the intellectual property rights therein shall at all times remain the exclusive property of John Wiley & Sons Inc, the Wiley Companies, or their respective licensors, and your interest therein is only that of having possession of and the right to reproduce the Wiley Materials pursuant to Section 2 herein during the continuance of this Agreement. You agree that you own no right, title or interest in or to the Wiley Materials or any of the intellectual property rights therein. You shall have no rights hereunder other than the license as provided for above in Section 2. No right, license or interest to any trademark, trade name, service mark or other branding ("Marks") of WILEY or its licensors is granted hereunder, and you agree that you shall not assert any such right, license or interest with respect thereto
- NEITHER WILEY NOR ITS LICENSORS MAKES ANY WARRANTY OR REPRESENTATION OF ANY KIND TO YOU OR ANY THIRD PARTY, EXPRESS, IMPLIED OR STATUTORY, WITH RESPECT TO THE MATERIALS OR THE ACCURACY OF ANY INFORMATION CONTAINED IN THE MATERIALS, INCLUDING, WITHOUT LIMITATION, ANY IMPLIED WARRANTY OF MERCHANTABILITY, ACCURACY, SATISFACTORY QUALITY, FITNESS FOR

A PARTICULAR PURPOSE, USABILITY, INTEGRATION OR NON-INFRINGEMENT AND ALL SUCH WARRANTIES ARE HEREBY EXCLUDED BY WILEY AND ITS LICENSORS AND WAIVED BY YOU.

- WILEY shall have the right to terminate this Agreement immediately upon breach of this Agreement by you.
- You shall indemnify, defend and hold harmless WILEY, its Licensors and their respective directors, officers, agents and employees, from and against any actual or threatened claims, demands, causes of action or proceedings arising from any breach of this Agreement by you.
- IN NO EVENT SHALL WILEY OR ITS LICENSORS BE LIABLE TO YOU OR ANY OTHER PARTY OR ANY OTHER PERSON OR ENTITY FOR ANY SPECIAL, CONSEQUENTIAL, INCIDENTAL, INDIRECT, EXEMPLARY OR PUNITIVE DAMAGES, HOWEVER CAUSED, ARISING OUT OF OR IN CONNECTION WITH THE DOWNLOADING, PROVISIONING, VIEWING OR USE OF THE MATERIALS REGARDLESS OF THE FORM OF ACTION, WHETHER FOR BREACH OF CONTRACT, BREACH OF WARRANTY, TORT, NEGLIGENCE, INFRINGEMENT OR OTHERWISE (INCLUDING, WITHOUT LIMITATION, DAMAGES BASED ON LOSS OF PROFITS, DATA, FILES, USE, BUSINESS OPPORTUNITY OR CLAIMS OF THIRD PARTIES), AND WHETHER OR NOT THE PARTY HAS BEEN ADVISED OF THE POSSIBILITY OF SUCH DAMAGES. THIS LIMITATION SHALL APPLY NOTWITHSTANDING ANY FAILURE OF ESSENTIAL PURPOSE OF ANY LIMITED REMEDY PROVIDED HEREIN.
- Should any provision of this Agreement be held by a court of competent jurisdiction to be illegal, invalid, or unenforceable, that provision shall be deemed amended to achieve as nearly as possible the same economic effect as the original provision, and the legality, validity and enforceability of the remaining provisions of this Agreement shall not be affected or impaired thereby.
- The failure of either party to enforce any term or condition of this Agreement shall not constitute a waiver of either party's right to enforce each and every term and condition of this Agreement. No breach under this agreement shall be deemed waived or excused by either party unless such waiver or consent is in writing signed by the party granting such waiver or consent. The waiver by or consent of a party to a breach of any provision of this Agreement shall not operate or be construed as a waiver of or consent to any other or subsequent breach by such other party.
- This Agreement may not be assigned (including by operation of law or otherwise) by you without WILEY's prior written consent.
- Any fee required for this permission shall be non-refundable after thirty (30) days from receipt by the CCC.
- These terms and conditions together with CCC's Billing and Payment terms and conditions (which are incorporated herein) form the entire agreement between you and WILEY concerning this licensing transaction and (in the absence of fraud) supersedes all prior agreements and representations of the parties, oral or written. This Agreement may not be amended except in writing signed by both parties. This Agreement shall be binding upon and inure to the benefit of the parties' successors, legal representatives, and authorized assigns.
- In the event of any conflict between your obligations established by these terms and conditions and those established by CCC's Billing and Payment terms and conditions,

these terms and conditions shall prevail.

- WILEY expressly reserves all rights not specifically granted in the combination of (i) the license details provided by you and accepted in the course of this licensing transaction, (ii) these terms and conditions and (iii) CCC's Billing and Payment terms and conditions.
- This Agreement will be void if the Type of Use, Format, Circulation, or Requestor Type was misrepresented during the licensing process.
- This Agreement shall be governed by and construed in accordance with the laws of the State of New York, USA, without regards to such state's conflict of law rules. Any legal action, suit or proceeding arising out of or relating to these Terms and Conditions or the breach thereof shall be instituted in a court of competent jurisdiction in New York County in the State of New York in the United States of America and each party hereby consents and submits to the personal jurisdiction of such court, waives any objection to venue in such court and consents to service of process by registered or certified mail, return receipt requested, at the last known address of such party.

WILEY OPEN ACCESS TERMS AND CONDITIONS

Wiley Publishes Open Access Articles in fully Open Access Journals and in Subscription journals offering Online Open. Although most of the fully Open Access journals publish open access articles under the terms of the Creative Commons Attribution (CC BY) License only, the subscription journals and a few of the Open Access Journals offer a choice of Creative Commons Licenses. The license type is clearly identified on the article.

The Creative Commons Attribution License

The Creative Commons Attribution License (CC-BY) allows users to copy, distribute and transmit an article, adapt the article and make commercial use of the article. The CC-BY license permits commercial and non-

Creative Commons Attribution Non-Commercial License

The Creative Commons Attribution Non-Commercial (CC-BY-NC)License permits use, distribution and reproduction in any medium, provided the original work is properly cited and is not used for commercial purposes.(see below)

Creative Commons Attribution-Non-Commercial-NoDerivs License

The Creative Commons Attribution Non-Commercial-NoDerivs License (CC-BY-NC-ND) permits use, distribution and reproduction in any medium, provided the original work is properly cited, is not used for commercial purposes and no modifications or adaptations are made. (see below)

Use by commercial "for-profit" organizations

Use of Wiley Open Access articles for commercial, promotional, or marketing purposes requires further explicit permission from Wiley and will be subject to a fee.

Further details can be found on Wiley Online Library
http://olabout.wiley.com/WileyCDA/Section/id-410895.html

Other Terms and Conditions:

v1.10 Last updated September 2015

Questions? customercare@copyright.com.

CCC Marketplace

Order Confirmation

Thank you, your order has been placed. An email confirmation has been sent to you. Your order license details and printable licenses will be available within 24 hours. Please access Manage Account for final order details.

This is not an invoice. Please go to manage account to access your order history and invoices.

CUSTOMER INFORMATION

Payment by invoice: You can cancel your order until the invoice is generated by contacting customer service.

Billing Address

Miss Jia Guo
RSM, Imperial College London
London, London SW7 2AZ
United Kingdom

+44 7745298851
jia.guo17@imperial.ac.uk

Customer Location

Miss Jia Guo
RSM, Imperial College London
London, London SW7 2AZ
United Kingdom

PO Number (optional)

N/A

Payment options

Invoice

PENDING ORDER CONFIRMATION

Confirmation Number: Pending

Order Date: 14-Aug-2023

1. Journal of materials chemistry. A, Materials for energy and sustainability

0.00 GBP

Article: Self-assembled alloy nanoparticles in a layered double perovskite as a fuel oxidation catalyst for solid oxide fuel cells

Order License ID	Pending	**Publisher**	Royal Society of Chemistry
ISSN	2050-7488		
Type of Use	Republish in a thesis/dissertation	**Portion**	Image/photo/illustration

LICENSED CONTENT

Publication Title	journal of materials chemistry. A, Materials for energy and sustainability	**Rightsholder**	Royal Society of Chemistry
Article Title	Self-assembled alloy nanoparticles in a layered double perovskite as a fuel oxidation catalyst for solid oxide fuel cells	**Publication Type**	Journal
		Start Page	15947
		End Page	15953
		Issue	33
		Volume	6
Author/Editor	Royal Society of Chemistry (Great Britain)		
Date	01/01/2012		
Language	English		
Country	United Kingdom of Great Britain and Northern Ireland		

REQUEST DETAILS

Portion Type	Image/photo/illustration	**Distribution**	U.K. and Commonwealth (excluding Canada)
Number of Images / Photos / Illustrations	1	**Translation**	Original language of publication
Format (select all that apply)	Print, Electronic		
Who Will Republish the Content?	Not-for-profit entity	**Copies for the Disabled?**	No
		Minor Editing Privileges?	Yes
Duration of Use	Current edition and up to 5 years	**Incidental Promotional Use?**	No
		Currency	GBP
Lifetime Unit Quantity	Up to 499		
Rights Requested	Main product and any product related to main product		

NEW WORK DETAILS

Title	Lanthanum Nickel Oxide-Based Double Perovskites and their Exsolution Phenomena	**Institution Name**	Imperial College London
		Expected Presentation Date	2023-10-23
Instructor Name	Jia Guo		

ADDITIONAL DETAILS

Order Reference Number	N/A	**The Requesting Person/Organization to Appear on the License**	Jia Guo

REQUESTED CONTENT DETAILS

Title, Description or Numeric Reference of the Portion(s)	Figure 3	**Title of the Article/Chapter the Portion Is From**	Self-assembled alloy nanoparticles in a layered double perovskite as a fuel oxidation catalyst for solid oxide fuel cells
Editor of Portion(s)	Han, Jeong Woo; Jeong, Hu Young; Joo, Sangwook; Kim, Guntae; Kim, Kyeounghak; Kwon, Ohhun; Sengodan, Sivaprakash; Shin, Jeeyoung	**Author of Portion(s)**	Han, Jeong Woo; Jeong, Hu Young; Joo, Sangwook; Kim, Guntae; Kim, Kyeounghak; Kwon, Ohhun; Sengodan, Sivaprakash; Shin, Jeeyoung
Volume / Edition	6		
Page or Page Range of Portion	15947-15953	**Issue, if Republishing an Article From a Serial**	33
		Publication Date of Portion	2018-01-01

Total Items: 1

Total Due: 0.00 GBP

Accepted: Marketplace Permissions General Terms and Conditions and any applicable Publisher Terms and Conditions

CCC Marketplace

Order Confirmation

Thank you, your order has been placed. An email confirmation has been sent to you. Your order license details and printable licenses will be available within 24 hours. Please access Manage Account for final order details.

This is not an invoice. Please go to manage account to access your order history and invoices.

CUSTOMER INFORMATION

Payment by invoice: You can cancel your order until the invoice is generated by contacting customer service.

Billing Address

Miss Jia Guo
RSM, Imperial College London
London, London SW7 2AZ
United Kingdom

+44 7745298851
jia.guo17@imperial.ac.uk

Customer Location

Miss Jia Guo
RSM, Imperial College London
London, London SW7 2AZ
United Kingdom

PO Number (optional)

N/A

Payment options

Invoice

PENDING ORDER CONFIRMATION

Confirmation Number: Pending

Order Date: 14-Aug-2023

1. CrystEngComm

0.00 GBP

Article: Expanding Possibilities for Solid-Phase Crystallization by Exsolving Tunable Pd-NiO Core-Shell Nanostructures

Order License ID	Pending	**Publisher**	ROYAL SOCIETY OF CHEMISTRY
ISSN	1466-8033		
Type of Use	Republish in a thesis/dissertation	**Portion**	Image/photo/illustration

LICENSED CONTENT

Publication Title	CrystEngComm	**Publication Type**	e-journal
Article Title	Expanding Possibilities for Solid-Phase Crystallization by Exsolving Tunable Pd-NiO Core-Shell Nanostructures	**Start Page**	6372
		End Page	6376
		Issue	41
		Volume	20
Author/Editor	Royal Society of Chemistry (Great Britain)	**URL**	http://www.rsc.org/Publishing/journals/ce/index.asp
Date	01/01/1999		
Language	English		
Country	United Kingdom of Great Britain and Northern Ireland		
Rightsholder	Royal Society of Chemistry		

REQUEST DETAILS

Portion Type	Image/photo/illustration

Number of Images / Photos / Illustrations	1	**Distribution**	U.K. and Commonwealth (excluding Canada)
Format (select all that apply)	Print, Electronic	**Translation**	Original language of publication
Who Will Republish the Content?	Not-for-profit entity	**Copies for the Disabled?**	No
Duration of Use	Current edition and up to 5 years	**Minor Editing Privileges?**	Yes
		Incidental Promotional Use?	No
Lifetime Unit Quantity	Up to 499	**Currency**	GBP
Rights Requested	Main product and any product related to main product		

NEW WORK DETAILS

Title	Lanthanum Nickel Oxide-Based Double Perovskites and their Exsolution Phenomena	**Institution Name**	Imperial college london
		Expected Presentation Date	2023-10-23
Instructor Name	Jia Guo		

ADDITIONAL DETAILS

Order Reference Number	N/A	**The Requesting Person/Organization to Appear on the License**	Jia Guo

REQUESTED CONTENT DETAILS

Title, Description or Numeric Reference of the Portion(s)	Figure 3	**Title of the Article/Chapter the Portion Is From**	Expanding Possibilities for Solid-Phase Crystallization by Exsolving Tunable Pd-NiO Core-Shell Nanostructures
Editor of Portion(s)	Buharon, Mariana; Komarala, Eswaravara Prasadarao; Rosen, Brian Ashley; Singh, Sarika	**Author of Portion(s)**	Buharon, Mariana; Komarala, Eswaravara Prasadarao; Rosen, Brian Ashley; Singh, Sarika
Volume / Edition	20		
Page or Page Range of Portion	6372-6376	**Issue, if Republishing an Article From a Serial**	41
		Publication Date of Portion	2018-01-01

Total Items: 1

Total Due: 0.00 GBP

Accepted: Marketplace Permissions General Terms and Conditions and any applicable Publisher Terms and Conditions

CCC Marketplace

Order Confirmation

Thank you, your order has been placed. An email confirmation has been sent to you. Your order license details and printable licenses will be available within 24 hours. Please access Manage Account for final order details.

This is not an invoice. Please go to manage account to access your order history and invoices.

CUSTOMER INFORMATION

Payment by invoice: You can cancel your order until the invoice is generated by contacting customer service.

Billing Address

Miss Jia Guo
RSM, Imperial College London
London, London SW7 2AZ
United Kingdom

+44 7745298851
jia.guo17@imperial.ac.uk

Customer Location

Miss Jia Guo
RSM, Imperial College London
London, London SW7 2AZ
United Kingdom

PO Number (optional)

N/A

Payment options

Invoice

PENDING ORDER CONFIRMATION

Confirmation Number: Pending

Order Date: 09-Sep-2023

1. Physical chemistry chemical physics — 0.00 GBP

Article: The role of the Auger parameter in XPS studies of nickel metal, halides and oxides.

Order License ID	Pending	Publisher	ROYAL SOCIETY OF CHEMISTRY
ISSN	1463-9084		
Type of Use	Republish in a thesis/dissertation	Portion	Chart/graph/table/figure

LICENSED CONTENT

Publication Title	Physical chemistry chemical physics	Publication Type	e-journal
Article Title	The role of the Auger parameter in XPS studies of nickel metal, halides and oxides.	Start Page	2434
		End Page	2442
		Issue	7
		Volume	14
Author/Editor	Royal Society of Chemistry (Great Britain)	URL	http://firstsearch.oclc.org/journal=1463-9076;screen=info;ECOIP
Date	01/01/1999		
Language	English		
Country	United Kingdom of Great Britain and Northern Ireland		
Rightsholder	Royal Society of Chemistry		

REQUEST DETAILS

Portion Type	Chart/graph/table/figure	Distribution	U.K. and Commonwealth (excluding Canada)
Number of Charts / Graphs / Tables / Figures Requested	3	Translation	Original language of publication
Format (select all that apply)	Print, Electronic	Copies for the Disabled?	No
Who Will Republish the Content?	Not-for-profit entity	Minor Editing Privileges?	No
Duration of Use	Current edition and up to 5 years	Incidental Promotional Use?	No
Lifetime Unit Quantity	Up to 499	Currency	GBP
Rights Requested	Main product and any product related to main product		

NEW WORK DETAILS

Title	Lanthanum Nickel Oxide-Based Double Perovskitesand their Exsolution Phenomena	Institution Name	Imperial College London
		Expected Presentation Date	2023-12-30
Instructor Name	Jia Guo		

ADDITIONAL DETAILS

Order Reference Number	N/A	The Requesting Person/Organization to Appear on the License	Jia Guo

REQUESTED CONTENT DETAILS

Title, Description or Numeric Reference of the Portion(s)	figure 3	Title of the Article/Chapter the Portion Is From	The role of the Auger parameter in XPS studies of nickel metal, halides and oxides.
Editor of Portion(s)	Biesinger, Mark C.; LauCurrent address: Chengdu Green Energy and Green Manufacturing Technology R&D Center, Chengdu, Sichuan, China, 610207., Leo W. M.; Gerson, Andrea R.; Smart, Roger St. C.	Author of Portion(s)	Biesinger, Mark C.; LauCurrent address: Chengdu Green Energy and Green Manufacturing Technology R&D Center, Chengdu, Sichuan, China, 610207., Leo W. M.; Gerson, Andrea R.; Smart, Roger St. C.
Volume / Edition	14		
Page or Page Range of Portion	2434-2442	Issue, if Republishing an Article From a Serial	7
		Publication Date of Portion	2012-02-21

Total Items: 1 **Total Due: 0.00 GBP**

Accepted: Marketplace Permissions General Terms and Conditions and any applicable Publisher Terms and Conditions

CCC Marketplace

Order Confirmation

Thank you, your order has been placed. An email confirmation has been sent to you. Your order license details and printable licenses will be available within 24 hours. Please access Manage Account for final order details.

This is not an invoice. Please go to manage account to access your order history and invoices.

CUSTOMER INFORMATION

Payment by invoice: You can cancel your order until the invoice is generated by contacting customer service.

Billing Address

Miss Jia Guo
RSM, Imperial College London
London, London SW7 2AZ
United Kingdom

+44 7745298851
jia.guo17@imperial.ac.uk

Customer Location

Miss Jia Guo
RSM, Imperial College London
London, London SW7 2AZ
United Kingdom

PO Number (optional)

N/A

Payment options

Invoice

PENDING ORDER CONFIRMATION

Confirmation Number: Pending

Order Date: 23-Sep-2023

1. Physical chemistry chemical physics — 0.00 GBP

Article: The role of the Auger parameter in XPS studies of nickel metal, halides and oxides.

Order License ID	Pending	Publisher	ROYAL SOCIETY OF CHEMISTRY
ISSN	1463-9084		
Type of Use	Republish in a thesis/dissertation	Portion	Image/photo/illustration

LICENSED CONTENT

Publication Title	Physical chemistry chemical physics	Publication Type	e-journal
Article Title	The role of the Auger parameter in XPS studies of nickel metal, halides and oxides.	Start Page	2434
		End Page	2442
		Issue	7
		Volume	14
Author/Editor	Royal Society of Chemistry (Great Britain)	URL	http://firstsearch.oclc.org/journal=1463-9076;screen=info;ECOIP
Date	01/01/1999		
Language	English		
Country	United Kingdom of Great Britain and Northern Ireland		
Rightsholder	Royal Society of Chemistry		

REQUEST DETAILS

Portion Type	Image/photo/illustration	Distribution	U.K. and Commonwealth (excluding Canada)
Number of Images / Photos / Illustrations	1	Translation	Original language of publication
Format (select all that apply)	Print, Electronic	Copies for the Disabled?	No
Who Will Republish the Content?	Not-for-profit entity	Minor Editing Privileges?	No
Duration of Use	Current edition and up to 5 years	Incidental Promotional Use?	No
Lifetime Unit Quantity	Up to 499	Currency	GBP
Rights Requested	Main product		

NEW WORK DETAILS

Title	Lanthanum Nickel Oxide-Based Double Perovskitesand their Exsolution Phenomena	Institution Name	Imperial College London
		Expected Presentation Date	2023-12-31
Instructor Name	Jia Guo		

ADDITIONAL DETAILS

Order Reference Number	N/A	The Requesting Person/Organization to Appear on the License	Jia Guo

REQUESTED CONTENT DETAILS

Title, Description or Numeric Reference of the Portion(s)	Fig 1	Title of the Article/Chapter the Portion Is From	The role of the Auger parameter in XPS studies of nickel metal, halides and oxides.
Editor of Portion(s)	Biesinger, Mark C.; LauCurrent address: Chengdu Green Energy and Green Manufacturing Technology R&D Center, Chengdu, Sichuan, China, 610207., Leo W. M.; Gerson, Andrea R.; Smart, Roger St. C.	Author of Portion(s)	Biesinger, Mark C.; LauCurrent address: Chengdu Green Energy and Green Manufacturing Technology R&D Center, Chengdu, Sichuan, China, 610207., Leo W. M.; Gerson, Andrea R.; Smart, Roger St. C.
Volume / Edition	14		
Page or Page Range of Portion	2434-2442	Issue, if Republishing an Article From a Serial	7
		Publication Date of Portion	2012-02-21

Total Items: 1 **Total Due: 0.00 GBP**

Accepted: Marketplace Permissions General Terms and Conditions and any applicable Publisher Terms and Conditions

ELSEVIER LICENSE
TERMS AND CONDITIONS

Sep 05, 2023

This Agreement between Miss. Jia Guo ("You") and Elsevier ("Elsevier") consists of your license details and the terms and conditions provided by Elsevier and Copyright Clearance Center.

License Number	5622530675786
License date	Sep 05, 2023
Licensed Content Publisher	Elsevier
Licensed Content Publication	Surface Science
Licensed Content Title	New interpretations of XPS spectra of nickel metal and oxides
Licensed Content Author	Andrew P. Grosvenor,Mark C. Biesinger,Roger St.C. Smart,N. Stewart McIntyre
Licensed Content Date	1 May 2006
Licensed Content Volume	600
Licensed Content Issue	9
Licensed Content Pages	9
Start Page	1771
End Page	1779
Type of Use	reuse in a thesis/dissertation
Portion	figures/tables/illustrations

Number of figures/tables/illustrations	1
Format	both print and electronic
Are you the author of this Elsevier article?	No
Will you be translating?	No
Title	Lanthanum Nickel Oxide-Based Double Perovskites and their Exsolution Phenomena
Institution name	Imperial College London
Expected presentation date	Dec 2023
Portions	Figure 7
Requestor Location	Miss. Jia Guo RSM, Imperial College London London, London SW7 2AZ United Kingdom Attn: Imperial College London
Publisher Tax ID	GB 494 6272 12
Total	0.00 GBP

Terms and Conditions

INTRODUCTION

1. The publisher for this copyrighted material is Elsevier. By clicking "accept" in connection with completing this licensing transaction, you agree that the following terms and conditions apply to this transaction (along with the Billing and Payment terms and conditions established by Copyright Clearance Center, Inc. ("CCC"), at the time that you opened your RightsLink account and that are available at any time at https://myaccount.copyright.com).

GENERAL TERMS

2. Elsevier hereby grants you permission to reproduce the aforementioned material subject to the terms and conditions indicated.

3. Acknowledgement: If any part of the material to be used (for example, figures) has appeared in our publication with credit or acknowledgement to another source, permission must also be sought from that source. If such permission is not obtained then that material may not be included in your publication/copies. Suitable acknowledgement to the source must be made, either as a footnote or in a reference list at the end of your publication, as follows:

"Reprinted from Publication title, Vol /edition number, Author(s), Title of article / title of chapter, Pages No., Copyright (Year), with permission from Elsevier [OR APPLICABLE SOCIETY COPYRIGHT OWNER]." Also Lancet special credit - "Reprinted from The Lancet, Vol. number, Author(s), Title of article, Pages No., Copyright (Year), with permission from Elsevier."

4. Reproduction of this material is confined to the purpose and/or media for which permission is hereby given. The material may not be reproduced or used in any other way, including use in combination with an artificial intelligence tool (including to train an algorithm, test, process, analyse, generate output and/or develop any form of artificial intelligence tool), or to create any derivative work and/or service (including resulting from the use of artificial intelligence tools).

5. Altering/Modifying Material: Not Permitted. However figures and illustrations may be altered/adapted minimally to serve your work. Any other abbreviations, additions, deletions and/or any other alterations shall be made only with prior written authorization of Elsevier Ltd. (Please contact Elsevier's permissions helpdesk here). No modifications can be made to any Lancet figures/tables and they must be reproduced in full.

6. If the permission fee for the requested use of our material is waived in this instance, please be advised that your future requests for Elsevier materials may attract a fee.

7. Reservation of Rights: Publisher reserves all rights not specifically granted in the combination of (i) the license details provided by you and accepted in the course of this licensing transaction, (ii) these terms and conditions and (iii) CCC's Billing and Payment terms and conditions.

8. License Contingent Upon Payment: While you may exercise the rights licensed immediately upon issuance of the license at the end of the licensing process for the transaction, provided that you have disclosed complete and accurate details of your proposed use, no license is finally effective unless and until full payment is received from you (either by publisher or by CCC) as provided in CCC's Billing and Payment terms and conditions. If full payment is not received on a timely basis, then any license preliminarily granted shall be deemed automatically revoked and shall be void as if never granted. Further, in the event that you breach any of these terms and conditions or any of CCC's Billing and Payment terms and conditions, the license is automatically revoked and shall be void as if never granted. Use of materials as described in a revoked license, as well as any use of the materials beyond the scope of an unrevoked license, may constitute copyright infringement and publisher reserves the right to take any and all action to protect its copyright in the materials.

9. Warranties: Publisher makes no representations or warranties with respect to the licensed material.

10. Indemnity: You hereby indemnify and agree to hold harmless publisher and CCC, and their respective officers, directors, employees and agents, from and against any and all claims arising out of your use of the licensed material other than as specifically authorized pursuant to this license.

11. No Transfer of License: This license is personal to you and may not be sublicensed, assigned, or transferred by you to any other person without publisher's written permission.

12. No Amendment Except in Writing: This license may not be amended except in a writing signed by both parties (or, in the case of publisher, by CCC on publisher's behalf).

13. Objection to Contrary Terms: Publisher hereby objects to any terms contained in any purchase order, acknowledgment, check endorsement or other writing prepared by you, which terms are inconsistent with these terms and conditions or CCC's Billing and Payment terms and conditions. These terms and conditions, together with CCC's Billing and Payment terms and conditions (which are incorporated herein), comprise the entire agreement between you and publisher (and CCC) concerning this licensing transaction. In the event of any conflict between your obligations established by these terms and conditions and those established by CCC's Billing and Payment terms and conditions, these terms and conditions shall control.

14. Revocation: Elsevier or Copyright Clearance Center may deny the permissions described in this License at their sole discretion, for any reason or no reason, with a full refund payable to you. Notice of such denial will be made using the contact information provided by you. Failure to receive such notice will not alter or invalidate the denial. In no event will Elsevier or Copyright Clearance Center be responsible or liable for any costs, expenses or damage incurred by you as a result of a denial of your permission request, other than a refund of the amount(s) paid by you to Elsevier and/or Copyright Clearance Center for denied permissions.

LIMITED LICENSE

The following terms and conditions apply only to specific license types:

15. **Translation**: This permission is granted for non-exclusive world **English** rights only unless your license was granted for translation rights. If you licensed translation rights you may only translate this content into the languages you requested. A professional translator must perform all translations and reproduce the content word for word preserving the integrity of the article.

16. **Posting licensed content on any Website**: The following terms and conditions apply as follows: Licensing material from an Elsevier journal: All content posted to the web site must maintain the copyright information line on the bottom of each image; A hyper-text must be included to the Homepage of the journal from which you are licensing at http://www.sciencedirect.com/science/journal/xxxxx or the Elsevier homepage for books at http://www.elsevier.com; Central Storage: This license does not include permission for a scanned version of the material to be stored in a central repository such as that provided by Heron/XanEdu.

Licensing material from an Elsevier book: A hyper-text link must be included to the Elsevier homepage at http://www.elsevier.com . All content posted to the web site must maintain the copyright information line on the bottom of each image.

Posting licensed content on Electronic reserve: In addition to the above the following clauses are applicable: The web site must be password-protected and made available only to bona fide students registered on a relevant course. This permission is granted for 1 year only. You may obtain a new license for future website posting.

17. **For journal authors:** the following clauses are applicable in addition to the above:

Preprints:

A preprint is an author's own write-up of research results and analysis, it has not been peer-reviewed, nor has it had any other value added to it by a publisher (such as formatting, copyright, technical enhancement etc.).

Authors can share their preprints anywhere at any time. Preprints should not be added to or enhanced in any way in order to appear more like, or to substitute for, the final versions of articles however authors can update their preprints on arXiv or RePEc with their Accepted Author Manuscript (see below).

If accepted for publication, we encourage authors to link from the preprint to their formal publication via its DOI. Millions of researchers have access to the formal publications on ScienceDirect, and so links will help users to find, access, cite and use the best available version. Please note that Cell Press, The Lancet and some society-owned have different preprint policies. Information on these policies is available on the journal homepage.

Accepted Author Manuscripts: An accepted author manuscript is the manuscript of an article that has been accepted for publication and which typically includes author-incorporated changes suggested during submission, peer review and editor-author communications.

Authors can share their accepted author manuscript:

- immediately
  - via their non-commercial person homepage or blog
  - by updating a preprint in arXiv or RePEc with the accepted manuscript
  - via their research institute or institutional repository for internal institutional uses or as part of an invitation-only research collaboration work-group
  - directly by providing copies to their students or to research collaborators for their personal use
  - for private scholarly sharing as part of an invitation-only work group on commercial sites with which Elsevier has an agreement
- After the embargo period
  - via non-commercial hosting platforms such as their institutional repository
  - via commercial sites with which Elsevier has an agreement

In all cases accepted manuscripts should:

- link to the formal publication via its DOI
- bear a CC-BY-NC-ND license - this is easy to do
- if aggregated with other manuscripts, for example in a repository or other site, be shared in alignment with our hosting policy not be added to or enhanced in any way to appear more like, or to substitute for, the published journal article.

Published journal article (JPA): A published journal article (PJA) is the definitive final record of published research that appears or will appear in the journal and embodies all value-adding publishing activities including peer review co-ordination, copy-editing, formatting, (if relevant) pagination and online enrichment.

Policies for sharing publishing journal articles differ for subscription and gold open access articles:

Subscription Articles: If you are an author, please share a link to your article rather than the full-text. Millions of researchers have access to the formal publications on ScienceDirect, and so links will help your users to find, access, cite, and use the best available version.

Theses and dissertations which contain embedded PJAs as part of the formal submission can be posted publicly by the awarding institution with DOI links back to the formal publications on ScienceDirect.

If you are affiliated with a library that subscribes to ScienceDirect you have additional private sharing rights for others' research accessed under that agreement. This includes use for classroom teaching and internal training at the institution (including use in course packs and courseware programs), and inclusion of the article for grant funding purposes.

work. Further, any new works must be made available on the same conditions. The full details of the license are available at http://creativecommons.org/licenses/by-nc-sa/4.0.

CC BY NC ND: The CC BY-NC-ND license allows users to copy and distribute the Article, provided this is not done for commercial purposes and further does not permit distribution of the Article if it is changed or edited in any way, and provided the user gives appropriate credit (with a link to the formal publication through the relevant DOI), provides a link to the license, and that the licensor is not represented as endorsing the use made of the work. The full details of the license are available at http://creativecommons.org/licenses/by-nc-nd/4.0. Any commercial reuse of Open Access articles published with a CC BY NC SA or CC BY NC ND license requires permission from Elsevier and will be subject to a fee.

Commercial reuse includes:

- Associating advertising with the full text of the Article
- Charging fees for document delivery or access
- Article aggregation
- Systematic distribution via e-mail lists or share buttons

Posting or linking by commercial companies for use by customers of those companies.

20. **Other Conditions**:

v1.10

Questions? customercare@copyright.com.

Gold Open Access Articles: May be shared according to the author-selected end-user license and should contain a CrossMark logo, the end user license, and a DOI link to the formal publication on ScienceDirect.

Please refer to Elsevier's posting policy for further information.

18. **For book authors** the following clauses are applicable in addition to the above: Authors are permitted to place a brief summary of their work online only. You are not allowed to download and post the published electronic version of your chapter, nor may you scan the printed edition to create an electronic version. **Posting to a repository:** Authors are permitted to post a summary of their chapter only in their institution's repository.

19. **Thesis/Dissertation**: If your license is for use in a thesis/dissertation your thesis may be submitted to your institution in either print or electronic form. Should your thesis be published commercially, please reapply for permission. These requirements include permission for the Library and Archives of Canada to supply single copies, on demand, of the complete thesis and include permission for Proquest/UMI to supply single copies, on demand, of the complete thesis. Should your thesis be published commercially, please reapply for permission. Theses and dissertations which contain embedded PJAs as part of the formal submission can be posted publicly by the awarding institution with DOI links back to the formal publications on ScienceDirect.

Elsevier Open Access Terms and Conditions

You can publish open access with Elsevier in hundreds of open access journals or in nearly 2000 established subscription journals that support open access publishing. Permitted third party re-use of these open access articles is defined by the author's choice of Creative Commons user license. See our open access license policy for more information.

Terms & Conditions applicable to all Open Access articles published with Elsevier:

Any reuse of the article must not represent the author as endorsing the adaptation of the article nor should the article be modified in such a way as to damage the author's honour or reputation. If any changes have been made, such changes must be clearly indicated.

The author(s) must be appropriately credited and we ask that you include the end user license and a DOI link to the formal publication on ScienceDirect.

If any part of the material to be used (for example, figures) has appeared in our publication with credit or acknowledgement to another source it is the responsibility of the user to ensure their reuse complies with the terms and conditions determined by the rights holder.

Additional Terms & Conditions applicable to each Creative Commons user license:

CC BY: The CC-BY license allows users to copy, to create extracts, abstracts and new works from the Article, to alter and revise the Article and to make commercial use of the Article (including reuse and/or resale of the Article by commercial entities), provided the user gives appropriate credit (with a link to the formal publication through the relevant DOI), provides a link to the license, indicates if changes were made and the licensor is not represented as endorsing the use made of the work. The full details of the license are available at http://creativecommons.org/licenses/by/4.0.

CC BY NC SA: The CC BY-NC-SA license allows users to copy, to create extracts, abstracts and new works from the Article, to alter and revise the Article, provided this is not done for commercial purposes, and that the user gives appropriate credit (with a link to the formal publication through the relevant DOI), provides a link to the license, indicates if changes were made and the licensor is not represented as endorsing the use made of the

ELSEVIER LICENSE
TERMS AND CONDITIONS

Sep 09, 2023

This Agreement between Miss. Jia Guo ("You") and Elsevier ("Elsevier") consists of your license details and the terms and conditions provided by Elsevier and Copyright Clearance Center.

License Number	5624951230805
License date	Sep 09, 2023
Licensed Content Publisher	Elsevier
Licensed Content Publication	Journal of Electron Spectroscopy and Related Phenomena
Licensed Content Title	XPS characterisation of in situ treated lanthanum oxide and hydroxide using tailored charge referencing and peak fitting procedures
Licensed Content Author	M.F. Sunding,K. Hadidi,S. Diplas,O.M. Løvvik,T.E. Norby,A.E. Gunnæs
Licensed Content Date	Jul 1, 2011
Licensed Content Volume	184
Licensed Content Issue	7
Licensed Content Pages	11
Start Page	399
End Page	409
Type of Use	reuse in a thesis/dissertation

Portion	figures/tables/illustrations
Number of figures/tables/illustrations	1
Format	both print and electronic
Are you the author of this Elsevier article?	No
Will you be translating?	No
Title	Lanthanum Nickel Oxide-Based Double Perovskites and their Exsolution Phenomena
Institution name	Imperial College London
Expected presentation date	Dec 2023
Portions	figure 3
Requestor Location	Miss. Jia Guo RSM, Imperial College London London, London SW7 2AZ United Kingdom Attn: Imperial College London
Publisher Tax ID	GB 494 6272 12
Total	0.00 GBP

Terms and Conditions

INTRODUCTION

1. The publisher for this copyrighted material is Elsevier. By clicking "accept" in connection with completing this licensing transaction, you agree that the following terms and conditions apply to this transaction (along with the Billing and Payment terms and conditions established by Copyright Clearance Center, Inc. ("CCC"), at the time that you opened your RightsLink account and that are available at any time at https://myaccount.copyright.com).

GENERAL TERMS

2. Elsevier hereby grants you permission to reproduce the aforementioned material subject to the terms and conditions indicated.

3. Acknowledgement: If any part of the material to be used (for example, figures) has appeared in our publication with credit or acknowledgement to another source, permission must also be sought from that source. If such permission is not obtained then that material may not be included in your publication/copies. Suitable acknowledgement to the source must be made, either as a footnote or in a reference list at the end of your publication, as follows:

"Reprinted from Publication title, Vol /edition number, Author(s), Title of article / title of chapter, Pages No., Copyright (Year), with permission from Elsevier [OR APPLICABLE SOCIETY COPYRIGHT OWNER]." Also Lancet special credit - "Reprinted from The Lancet, Vol. number, Author(s), Title of article, Pages No., Copyright (Year), with permission from Elsevier."

4. Reproduction of this material is confined to the purpose and/or media for which permission is hereby given. The material may not be reproduced or used in any other way, including use in combination with an artificial intelligence tool (including to train an algorithm, test, process, analyse, generate output and/or develop any form of artificial intelligence tool), or to create any derivative work and/or service (including resulting from the use of artificial intelligence tools).

5. Altering/Modifying Material: Not Permitted. However figures and illustrations may be altered/adapted minimally to serve your work. Any other abbreviations, additions, deletions and/or any other alterations shall be made only with prior written authorization of Elsevier Ltd. (Please contact Elsevier's permissions helpdesk here). No modifications can be made to any Lancet figures/tables and they must be reproduced in full.

6. If the permission fee for the requested use of our material is waived in this instance, please be advised that your future requests for Elsevier materials may attract a fee.

7. Reservation of Rights: Publisher reserves all rights not specifically granted in the combination of (i) the license details provided by you and accepted in the course of this licensing transaction, (ii) these terms and conditions and (iii) CCC's Billing and Payment terms and conditions.

8. License Contingent Upon Payment: While you may exercise the rights licensed immediately upon issuance of the license at the end of the licensing process for the transaction, provided that you have disclosed complete and accurate details of your proposed use, no license is finally effective unless and until full payment is received from you (either by publisher or by CCC) as provided in CCC's Billing and Payment terms and conditions. If full payment is not received on a timely basis, then any license preliminarily granted shall be deemed automatically revoked and shall be void as if never granted. Further, in the event that you breach any of these terms and conditions or any of CCC's Billing and Payment terms and conditions, the license is automatically revoked and shall be void as if never granted. Use of materials as described in a revoked license, as well as any use of the materials beyond the scope of an unrevoked license, may constitute copyright infringement and publisher reserves the right to take any and all action to protect its copyright in the materials.

9. Warranties: Publisher makes no representations or warranties with respect to the licensed material.

10. Indemnity: You hereby indemnify and agree to hold harmless publisher and CCC, and their respective officers, directors, employees and agents, from and against any and all claims arising out of your use of the licensed material other than as specifically authorized pursuant to this license.

11. No Transfer of License: This license is personal to you and may not be sublicensed, assigned, or transferred by you to any other person without publisher's written permission.

12. No Amendment Except in Writing: This license may not be amended except in a writing signed by both parties (or, in the case of publisher, by CCC on publisher's behalf).

13. Objection to Contrary Terms: Publisher hereby objects to any terms contained in any purchase order, acknowledgment, check endorsement or other writing prepared by you, which terms are inconsistent with these terms and conditions or CCC's Billing and Payment terms and conditions. These terms and conditions, together with CCC's Billing and Payment terms and conditions (which are incorporated herein), comprise the entire agreement between you and publisher (and CCC) concerning this licensing transaction. In the event of any conflict between your obligations established by these terms and conditions and those established by CCC's Billing and Payment terms and conditions, these terms and conditions shall control.

14. Revocation: Elsevier or Copyright Clearance Center may deny the permissions described in this License at their sole discretion, for any reason or no reason, with a full refund payable to you. Notice of such denial will be made using the contact information provided by you. Failure to receive such notice will not alter or invalidate the denial. In no event will Elsevier or Copyright Clearance Center be responsible or liable for any costs, expenses or damage incurred by you as a result of a denial of your permission request, other than a refund of the amount(s) paid by you to Elsevier and/or Copyright Clearance Center for denied permissions.

LIMITED LICENSE

The following terms and conditions apply only to specific license types:

15. **Translation**: This permission is granted for non-exclusive world **English** rights only unless your license was granted for translation rights. If you licensed translation rights you may only translate this content into the languages you requested. A professional translator must perform all translations and reproduce the content word for word preserving the integrity of the article.

16. **Posting licensed content on any Website**: The following terms and conditions apply as follows: Licensing material from an Elsevier journal: All content posted to the web site must maintain the copyright information line on the bottom of each image; A hyper-text must be included to the Homepage of the journal from which you are licensing at http://www.sciencedirect.com/science/journal/xxxxx or the Elsevier homepage for books at http://www.elsevier.com; Central Storage: This license does not include permission for a scanned version of the material to be stored in a central repository such as that provided by Heron/XanEdu.

Licensing material from an Elsevier book: A hyper-text link must be included to the Elsevier homepage at http://www.elsevier.com . All content posted to the web site must maintain the copyright information line on the bottom of each image.

Posting licensed content on Electronic reserve: In addition to the above the following clauses are applicable: The web site must be password-protected and made available only to bona fide students registered on a relevant course. This permission is granted for 1 year only. You may obtain a new license for future website posting.

17. **For journal authors:** the following clauses are applicable in addition to the above:

Preprints:

A preprint is an author's own write-up of research results and analysis, it has not been peer-reviewed, nor has it had any other value added to it by a publisher (such as formatting, copyright, technical enhancement etc.).

Authors can share their preprints anywhere at any time. Preprints should not be added to or enhanced in any way in order to appear more like, or to substitute for, the final versions of articles however authors can update their preprints on arXiv or RePEc with their Accepted Author Manuscript (see below).

If accepted for publication, we encourage authors to link from the preprint to their formal publication via its DOI. Millions of researchers have access to the formal publications on ScienceDirect, and so links will help users to find, access, cite and use the best available version. Please note that Cell Press, The Lancet and some society-owned have different preprint policies. Information on these policies is available on the journal homepage.

Accepted Author Manuscripts: An accepted author manuscript is the manuscript of an article that has been accepted for publication and which typically includes author-incorporated changes suggested during submission, peer review and editor-author communications.

Authors can share their accepted author manuscript:

- immediately
  - via their non-commercial person homepage or blog
  - by updating a preprint in arXiv or RePEc with the accepted manuscript
  - via their research institute or institutional repository for internal institutional uses or as part of an invitation-only research collaboration work-group
  - directly by providing copies to their students or to research collaborators for their personal use
  - for private scholarly sharing as part of an invitation-only work group on commercial sites with which Elsevier has an agreement
- After the embargo period
  - via non-commercial hosting platforms such as their institutional repository
  - via commercial sites with which Elsevier has an agreement

In all cases accepted manuscripts should:

- link to the formal publication via its DOI
- bear a CC-BY-NC-ND license - this is easy to do
- if aggregated with other manuscripts, for example in a repository or other site, be shared in alignment with our hosting policy not be added to or enhanced in any way to appear more like, or to substitute for, the published journal article.

Published journal article (JPA): A published journal article (PJA) is the definitive final record of published research that appears or will appear in the journal and embodies all value-adding publishing activities including peer review co-ordination, copy-editing, formatting, (if relevant) pagination and online enrichment.

Policies for sharing publishing journal articles differ for subscription and gold open access articles:

Subscription Articles: If you are an author, please share a link to your article rather than the full-text. Millions of researchers have access to the formal publications on ScienceDirect, and so links will help your users to find, access, cite, and use the best available version.

Theses and dissertations which contain embedded PJAs as part of the formal submission can be posted publicly by the awarding institution with DOI links back to the formal publications on ScienceDirect.

If you are affiliated with a library that subscribes to ScienceDirect you have additional private sharing rights for others' research accessed under that agreement. This includes use for classroom teaching and internal training at the institution (including use in course packs and courseware programs), and inclusion of the article for grant funding purposes.

Gold Open Access Articles: May be shared according to the author-selected end-user license and should contain a CrossMark logo, the end user license, and a DOI link to the formal publication on ScienceDirect.

Please refer to Elsevier's posting policy for further information.

18. **For book authors** the following clauses are applicable in addition to the above: Authors are permitted to place a brief summary of their work online only. You are not allowed to download and post the published electronic version of your chapter, nor may you scan the printed edition to create an electronic version. **Posting to a repository:** Authors are permitted to post a summary of their chapter only in their institution's repository.

19. **Thesis/Dissertation**: If your license is for use in a thesis/dissertation your thesis may be submitted to your institution in either print or electronic form. Should your thesis be published commercially, please reapply for permission. These requirements include permission for the Library and Archives of Canada to supply single copies, on demand, of the complete thesis and include permission for Proquest/UMI to supply single copies, on demand, of the complete thesis. Should your thesis be published commercially, please reapply for permission. Theses and dissertations which contain embedded PJAs as part of the formal submission can be posted publicly by the awarding institution with DOI links back to the formal publications on ScienceDirect.

Elsevier Open Access Terms and Conditions

You can publish open access with Elsevier in hundreds of open access journals or in nearly 2000 established subscription journals that support open access publishing. Permitted third party re-use of these open access articles is defined by the author's choice of Creative Commons user license. See our open access license policy for more information.

Terms & Conditions applicable to all Open Access articles published with Elsevier:

Any reuse of the article must not represent the author as endorsing the adaptation of the article nor should the article be modified in such a way as to damage the author's honour or reputation. If any changes have been made, such changes must be clearly indicated.

The author(s) must be appropriately credited and we ask that you include the end user license and a DOI link to the formal publication on ScienceDirect.

If any part of the material to be used (for example, figures) has appeared in our publication with credit or acknowledgement to another source it is the responsibility of the user to ensure their reuse complies with the terms and conditions determined by the rights holder.

Additional Terms & Conditions applicable to each Creative Commons user license:

CC BY: The CC-BY license allows users to copy, to create extracts, abstracts and new works from the Article, to alter and revise the Article and to make commercial use of the Article (including reuse and/or resale of the Article by commercial entities), provided the user gives appropriate credit (with a link to the formal publication through the relevant DOI), provides a link to the license, indicates if changes were made and the licensor is not represented as endorsing the use made of the work. The full details of the license are available at http://creativecommons.org/licenses/by/4.0.

CC BY NC SA: The CC BY-NC-SA license allows users to copy, to create extracts, abstracts and new works from the Article, to alter and revise the Article, provided this is not done for commercial purposes, and that the user gives appropriate credit (with a link to the formal publication through the relevant DOI), provides a link to the license, indicates if changes were made and the licensor is not represented as endorsing the use made of the work. Further, any new works must be made available on the same conditions. The full details of the license are available at http://creativecommons.org/licenses/by-nc-sa/4.0.

CC BY NC ND: The CC BY-NC-ND license allows users to copy and distribute the Article, provided this is not done for commercial purposes and further does not permit distribution of the Article if it is changed or edited in any way, and provided the user gives appropriate credit (with a link to the formal publication through the relevant DOI), provides a link to the license, and that the licensor is not represented as endorsing the use made of the work. The full details of the license are available at http://creativecommons.org/licenses/by-nc-nd/4.0. Any commercial reuse of Open Access articles published with a CC BY NC SA or CC BY NC ND license requires permission from Elsevier and will be subject to a fee.

Commercial reuse includes:

- Associating advertising with the full text of the Article
- Charging fees for document delivery or access
- Article aggregation
- Systematic distribution via e-mail lists or share buttons

Posting or linking by commercial companies for use by customers of those companies.

20. **Other Conditions**:

v1.10

Questions? customercare@copyright.com.

ELSEVIER LICENSE
TERMS AND CONDITIONS

Oct 14, 2023

This Agreement between Miss. Jia Guo ("You") and Elsevier ("Elsevier") consists of your license details and the terms and conditions provided by Elsevier and Copyright Clearance Center.

License Number	5647711430446
License date	Oct 14, 2023
Licensed Content Publisher	Elsevier
Licensed Content Publication	Ceramics International
Licensed Content Title	Review of perovskite ceramic synthesis and membrane preparation methods
Licensed Content Author	Daniel D. Athayde,Douglas F. Souza,Alysson M.A. Silva,Daniela Vasconcelos,Eduardo H.M. Nunes,João C. Diniz da Costa,Wander L. Vasconcelos
Licensed Content Date	1 May 2016
Licensed Content Volume	42
Licensed Content Issue	6
Licensed Content Pages	17
Start Page	6555
End Page	6571
Type of Use	reuse in a thesis/dissertation

Portion	figures/tables/illustrations
Number of figures/tables/illustrations	1
Format	both print and electronic
Are you the author of this Elsevier article?	No
Will you be translating?	No
Title of new work	Lanthanum Nickel Oxide-Based Double Perovskites and their Exsolution Phenomena
Institution name	Imperial College London
Expected presentation date	Dec 2023
Portions	Figure 3
Requestor Location	Miss. Jia Guo RSM, Imperial College London London, London SW7 2AZ United Kingdom Attn: Imperial College London
Publisher Tax ID	GB 494 6272 12
Total	0.00 GBP

Terms and Conditions

INTRODUCTION

1. The publisher for this copyrighted material is Elsevier. By clicking "accept" in connection with completing this licensing transaction, you agree that the following terms and conditions apply to this transaction (along with the Billing and Payment terms and conditions established by Copyright Clearance Center, Inc. ("CCC"), at the time that you opened your RightsLink account and that are available at any time at https://myaccount.copyright.com).

GENERAL TERMS

2. Elsevier hereby grants you permission to reproduce the aforementioned material subject to the terms and conditions indicated.

3. Acknowledgement: If any part of the material to be used (for example, figures) has appeared in our publication with credit or acknowledgement to another source, permission must also be sought from that source. If such permission is not obtained then that material may not be included in your publication/copies. Suitable acknowledgement to the source must be made, either as a footnote or in a reference list at the end of your publication, as follows:

"Reprinted from Publication title, Vol /edition number, Author(s), Title of article / title of chapter, Pages No., Copyright (Year), with permission from Elsevier [OR APPLICABLE SOCIETY COPYRIGHT OWNER]." Also Lancet special credit - "Reprinted from The Lancet, Vol. number, Author(s), Title of article, Pages No., Copyright (Year), with permission from Elsevier."

4. Reproduction of this material is confined to the purpose and/or media for which permission is hereby given. The material may not be reproduced or used in any other way, including use in combination with an artificial intelligence tool (including to train an algorithm, test, process, analyse, generate output and/or develop any form of artificial intelligence tool), or to create any derivative work and/or service (including resulting from the use of artificial intelligence tools).

5. Altering/Modifying Material: Not Permitted. However figures and illustrations may be altered/adapted minimally to serve your work. Any other abbreviations, additions, deletions and/or any other alterations shall be made only with prior written authorization of Elsevier Ltd. (Please contact Elsevier's permissions helpdesk here). No modifications can be made to any Lancet figures/tables and they must be reproduced in full.

6. If the permission fee for the requested use of our material is waived in this instance, please be advised that your future requests for Elsevier materials may attract a fee.

7. Reservation of Rights: Publisher reserves all rights not specifically granted in the combination of (i) the license details provided by you and accepted in the course of this licensing transaction, (ii) these terms and conditions and (iii) CCC's Billing and Payment terms and conditions.

8. License Contingent Upon Payment: While you may exercise the rights licensed immediately upon issuance of the license at the end of the licensing process for the transaction, provided that you have disclosed complete and accurate details of your proposed use, no license is finally effective unless and until full payment is received from you (either by publisher or by CCC) as provided in CCC's Billing and Payment terms and conditions. If full payment is not received on a timely basis, then any license preliminarily granted shall be deemed automatically revoked and shall be void as if never granted. Further, in the event that you breach any of these terms and conditions or any of CCC's Billing and Payment terms and conditions, the license is automatically revoked and shall be void as if never granted. Use of materials as described in a revoked license, as well as any use of the materials beyond the scope of an unrevoked license, may constitute copyright infringement and publisher reserves the right to take any and all action to protect its copyright in the materials.

9. Warranties: Publisher makes no representations or warranties with respect to the licensed material.

10. Indemnity: You hereby indemnify and agree to hold harmless publisher and CCC, and their respective officers, directors, employees and agents, from and against any and all

claims arising out of your use of the licensed material other than as specifically authorized pursuant to this license.

11. No Transfer of License: This license is personal to you and may not be sublicensed, assigned, or transferred by you to any other person without publisher's written permission.

12. No Amendment Except in Writing: This license may not be amended except in a writing signed by both parties (or, in the case of publisher, by CCC on publisher's behalf).

13. Objection to Contrary Terms: Publisher hereby objects to any terms contained in any purchase order, acknowledgment, check endorsement or other writing prepared by you, which terms are inconsistent with these terms and conditions or CCC's Billing and Payment terms and conditions. These terms and conditions, together with CCC's Billing and Payment terms and conditions (which are incorporated herein), comprise the entire agreement between you and publisher (and CCC) concerning this licensing transaction. In the event of any conflict between your obligations established by these terms and conditions and those established by CCC's Billing and Payment terms and conditions, these terms and conditions shall control.

14. Revocation: Elsevier or Copyright Clearance Center may deny the permissions described in this License at their sole discretion, for any reason or no reason, with a full refund payable to you. Notice of such denial will be made using the contact information provided by you. Failure to receive such notice will not alter or invalidate the denial. In no event will Elsevier or Copyright Clearance Center be responsible or liable for any costs, expenses or damage incurred by you as a result of a denial of your permission request, other than a refund of the amount(s) paid by you to Elsevier and/or Copyright Clearance Center for denied permissions.

LIMITED LICENSE

The following terms and conditions apply only to specific license types:

15. **Translation**: This permission is granted for non-exclusive world **English** rights only unless your license was granted for translation rights. If you licensed translation rights you may only translate this content into the languages you requested. A professional translator must perform all translations and reproduce the content word for word preserving the integrity of the article.

16. **Posting licensed content on any Website**: The following terms and conditions apply as follows: Licensing material from an Elsevier journal: All content posted to the web site must maintain the copyright information line on the bottom of each image; A hyper-text must be included to the Homepage of the journal from which you are licensing at http://www.sciencedirect.com/science/journal/xxxxx or the Elsevier homepage for books at http://www.elsevier.com; Central Storage: This license does not include permission for a scanned version of the material to be stored in a central repository such as that provided by Heron/XanEdu.

Licensing material from an Elsevier book: A hyper-text link must be included to the Elsevier homepage at http://www.elsevier.com . All content posted to the web site must maintain the copyright information line on the bottom of each image.

Posting licensed content on Electronic reserve: In addition to the above the following clauses are applicable: The web site must be password-protected and made available only to bona fide students registered on a relevant course. This permission is granted for 1 year only. You may obtain a new license for future website posting.

17. **For journal authors:** the following clauses are applicable in addition to the above:

Preprints:

A preprint is an author's own write-up of research results and analysis, it has not been peer-reviewed, nor has it had any other value added to it by a publisher (such as formatting, copyright, technical enhancement etc.).

Authors can share their preprints anywhere at any time. Preprints should not be added to or enhanced in any way in order to appear more like, or to substitute for, the final versions of articles however authors can update their preprints on arXiv or RePEc with their Accepted Author Manuscript (see below).

If accepted for publication, we encourage authors to link from the preprint to their formal publication via its DOI. Millions of researchers have access to the formal publications on ScienceDirect, and so links will help users to find, access, cite and use the best available version. Please note that Cell Press, The Lancet and some society-owned have different preprint policies. Information on these policies is available on the journal homepage.

Accepted Author Manuscripts: An accepted author manuscript is the manuscript of an article that has been accepted for publication and which typically includes author-incorporated changes suggested during submission, peer review and editor-author communications.

Authors can share their accepted author manuscript:

- immediately
  - via their non-commercial person homepage or blog
  - by updating a preprint in arXiv or RePEc with the accepted manuscript
  - via their research institute or institutional repository for internal institutional uses or as part of an invitation-only research collaboration work-group
  - directly by providing copies to their students or to research collaborators for their personal use
  - for private scholarly sharing as part of an invitation-only work group on commercial sites with which Elsevier has an agreement
- After the embargo period
  - via non-commercial hosting platforms such as their institutional repository
  - via commercial sites with which Elsevier has an agreement

In all cases accepted manuscripts should:

- link to the formal publication via its DOI
- bear a CC-BY-NC-ND license - this is easy to do
- if aggregated with other manuscripts, for example in a repository or other site, be shared in alignment with our hosting policy not be added to or enhanced in any way to appear more like, or to substitute for, the published journal article.

Published journal article (JPA): A published journal article (PJA) is the definitive final record of published research that appears or will appear in the journal and embodies all value-adding publishing activities including peer review co-ordination, copy-editing, formatting, (if relevant) pagination and online enrichment.

Policies for sharing publishing journal articles differ for subscription and gold open access articles:

Subscription Articles: If you are an author, please share a link to your article rather than the full-text. Millions of researchers have access to the formal publications on ScienceDirect, and so links will help your users to find, access, cite, and use the best available version.

Theses and dissertations which contain embedded PJAs as part of the formal submission can be posted publicly by the awarding institution with DOI links back to the formal publications on ScienceDirect.

If you are affiliated with a library that subscribes to ScienceDirect you have additional private sharing rights for others' research accessed under that agreement. This includes use for classroom teaching and internal training at the institution (including use in course packs and courseware programs), and inclusion of the article for grant funding purposes.

Gold Open Access Articles: May be shared according to the author-selected end-user license and should contain a CrossMark logo, the end user license, and a DOI link to the formal publication on ScienceDirect.

Please refer to Elsevier's posting policy for further information.

18. **For book authors** the following clauses are applicable in addition to the above: Authors are permitted to place a brief summary of their work online only. You are not allowed to download and post the published electronic version of your chapter, nor may you scan the printed edition to create an electronic version. **Posting to a repository:** Authors are permitted to post a summary of their chapter only in their institution's repository.

19. **Thesis/Dissertation**: If your license is for use in a thesis/dissertation your thesis may be submitted to your institution in either print or electronic form. Should your thesis be published commercially, please reapply for permission. These requirements include permission for the Library and Archives of Canada to supply single copies, on demand, of the complete thesis and include permission for Proquest/UMI to supply single copies, on demand, of the complete thesis. Should your thesis be published commercially, please reapply for permission. Theses and dissertations which contain embedded PJAs as part of the formal submission can be posted publicly by the awarding institution with DOI links back to the formal publications on ScienceDirect.

Elsevier Open Access Terms and Conditions

You can publish open access with Elsevier in hundreds of open access journals or in nearly 2000 established subscription journals that support open access publishing. Permitted third party re-use of these open access articles is defined by the author's choice of Creative Commons user license. See our open access license policy for more information.

Terms & Conditions applicable to all Open Access articles published with Elsevier:

Any reuse of the article must not represent the author as endorsing the adaptation of the article nor should the article be modified in such a way as to damage the author's honour or reputation. If any changes have been made, such changes must be clearly indicated.

The author(s) must be appropriately credited and we ask that you include the end user license and a DOI link to the formal publication on ScienceDirect.

If any part of the material to be used (for example, figures) has appeared in our publication with credit or acknowledgement to another source it is the responsibility of the user to ensure their reuse complies with the terms and conditions determined by the rights holder.

Additional Terms & Conditions applicable to each Creative Commons user license:

CC BY: The CC-BY license allows users to copy, to create extracts, abstracts and new works from the Article, to alter and revise the Article and to make commercial use of the Article (including reuse and/or resale of the Article by commercial entities), provided the user gives appropriate credit (with a link to the formal publication through the relevant DOI), provides a link to the license, indicates if changes were made and the licensor is not represented as endorsing the use made of the work. The full details of the license are available at http://creativecommons.org/licenses/by/4.0.

CC BY NC SA: The CC BY-NC-SA license allows users to copy, to create extracts, abstracts and new works from the Article, to alter and revise the Article, provided this is not done for commercial purposes, and that the user gives appropriate credit (with a link to the formal publication through the relevant DOI), provides a link to the license, indicates if changes were made and the licensor is not represented as endorsing the use made of the work. Further, any new works must be made available on the same conditions. The full details of the license are available at http://creativecommons.org/licenses/by-nc-sa/4.0.

CC BY NC ND: The CC BY-NC-ND license allows users to copy and distribute the Article, provided this is not done for commercial purposes and further does not permit distribution of the Article if it is changed or edited in any way, and provided the user gives appropriate credit (with a link to the formal publication through the relevant DOI), provides a link to the license, and that the licensor is not represented as endorsing the use made of the work. The full details of the license are available at http://creativecommons.org/licenses/by-nc-nd/4.0. Any commercial reuse of Open Access articles published with a CC BY NC SA or CC BY NC ND license requires permission from Elsevier and will be subject to a fee.

Commercial reuse includes:

- Associating advertising with the full text of the Article
- Charging fees for document delivery or access
- Article aggregation
- Systematic distribution via e-mail lists or share buttons

Posting or linking by commercial companies for use by customers of those companies.

20. **Other Conditions**:

v1.10

Questions? customercare@copyright.com.

AIP PUBLISHING LICENSE
TERMS AND CONDITIONS

Oct 14, 2023

This Agreement between Miss. Jia Guo ("You") and AIP Publishing ("AIP Publishing") consists of your license details and the terms and conditions provided by AIP Publishing and Copyright Clearance Center.

License Number	5647730325953
License date	Oct 14, 2023
Licensed Content Publisher	American Vacuum Society
Licensed Content Publication	Journal of Vacuum Science & Technology A
Licensed Content Title	Introduction to x-ray photoelectron spectroscopy
Licensed Content Author	Stevie, Fred A.; Donley, Carrie L.
Licensed Content Date	Sep 24, 2020
Licensed Content Volume	38
Licensed Content Issue	6
Type of Use	Thesis/Dissertation
Requestor type	Student
Format	Print and electronic
Portion	Figure/Table
Number of figures/tables	1

Will you be translating?	No
Title of new work	Lanthanum Nickel Oxide-Based Double Perovskites and their Exsolution Phenomena
Institution name	Imperial College London
Expected presentation date	Dec 2023
Portions	Figure 1
Requestor Location	Miss. Jia Guo RSM, Imperial College London London, London SW7 2AZ United Kingdom Attn: Imperial College London
Total	0.00 GBP

Terms and Conditions

American Vacuum Society -- Terms and Conditions: Permissions Uses

American Vacuum Society ("AVS") hereby grants to you the non-exclusive right and license to use and/or distribute the Material according to the use specified in your order, on a one-time basis, for the specified term, with a maximum distribution equal to the number that you have ordered. Any links or other content accompanying the Material are not the subject of this license.

1. You agree to include the following copyright and permission notice with the reproduction of the Material:"Reprinted with permission from [FULL CITATION]. Copyright [PUBLICATION YEAR], American Vacuum Society." For an article, the copyright and permission notice must be printed on the first page of the article or book chapter. For photographs, covers, or tables, the copyright and permission notice may appear with the Material, in a footnote, or in the reference list.
2. If you have licensed reuse of a figure, photograph, cover, or table, it is your responsibility to ensure that the material is original to AVS and does not contain the copyright of another entity, and that the copyright notice of the figure, photograph, cover, or table does not indicate that it was reprinted by AVS, with permission, from another source. Under no circumstances does AVS, purport or intend to grant permission to reuse material to which it does not hold copyright.
3. You may not alter or modify the Material in any manner. You may translate the Material into another language only if you have licensed translation rights. You may not use the Material for promotional purposes. AVS reserves all rights not specifically granted herein.
4. The foregoing license shall not take effect unless and until AVS or its agent, Copyright Clearance Center, receives the Payment in accordance with Copyright

Clearance Center Billing and Payment Terms and Conditions, which are incorporated herein by reference.

5. AVS or the Copyright Clearance Center may, within two business days of granting this license, revoke the license for any reason whatsoever, with a full refund payable to you. Should you violate the terms of this license at any time, AVS, American Vacuum Society, or Copyright Clearance Center may revoke the license with no refund to you. Notice of such revocation will be made using the contact information provided by you. Failure to receive such notice will not nullify the revocation.
6. AVS makes no representations or warranties with respect to the Material. You agree to indemnify and hold harmless AVS, American Vacuum Society, and their officers, directors, employees or agents from and against any and all claims arising out of your use of the Material other than as specifically authorized herein.
7. The permission granted herein is personal to you and is not transferable or assignable without the prior written permission of AVS. This license may not be amended except in a writing signed by the party to be charged.
8. If purchase orders, acknowledgments or check endorsements are issued on any forms containing terms and conditions which are inconsistent with these provisions, such inconsistent terms and conditions shall be of no force and effect. This document, including the CCC Billing and Payment Terms and Conditions, shall be the entire agreement between the parties relating to the subject matter hereof.

This Agreement shall be governed by and construed in accordance with the laws of the State of New York. Both parties hereby submit to the jurisdiction of the courts of New York County for purposes of resolving any disputes that may arise hereunder.

Questions? **customercare@copyright.com**.

ELSEVIER LICENSE
TERMS AND CONDITIONS

Oct 14, 2023

This Agreement between Miss. Jia Guo ("You") and Elsevier ("Elsevier") consists of your license details and the terms and conditions provided by Elsevier and Copyright Clearance Center.

License Number	5647740053109
License date	Oct 14, 2023
Licensed Content Publisher	Elsevier
Licensed Content Publication	Matter
Licensed Content Title	Analytical transmission electron microscopy for emerging advanced materials
Licensed Content Author	Yue Lin,Min Zhou,Xiaolin Tai,Hangfei Li,Xiao Han,Jiaguo Yu
Licensed Content Date	Jul 7, 2021
Licensed Content Volume	4
Licensed Content Issue	7
Licensed Content Pages	31
Start Page	2309
End Page	2339
Type of Use	reuse in a thesis/dissertation
Portion	figures/tables/illustrations

Number of figures/tables/illustrations	1
Format	both print and electronic
Are you the author of this Elsevier article?	No
Will you be translating?	No
Title of new work	Lanthanum Nickel Oxide-Based Double Perovskites and their Exsolution Phenomena
Institution name	Imperial College London
Expected presentation date	Dec 2023
Portions	Figure 2
Requestor Location	Miss. Jia Guo RSM, Imperial College London London, London SW7 2AZ United Kingdom Attn: Imperial College London
Publisher Tax ID	GB 494 6272 12
Total	0.00 GBP

Terms and Conditions

INTRODUCTION

1. The publisher for this copyrighted material is Elsevier. By clicking "accept" in connection with completing this licensing transaction, you agree that the following terms and conditions apply to this transaction (along with the Billing and Payment terms and conditions established by Copyright Clearance Center, Inc. ("CCC"), at the time that you opened your RightsLink account and that are available at any time at https://myaccount.copyright.com).

GENERAL TERMS

2. Elsevier hereby grants you permission to reproduce the aforementioned material subject to the terms and conditions indicated.

3. Acknowledgement: If any part of the material to be used (for example, figures) has appeared in our publication with credit or acknowledgement to another source, permission must also be sought from that source. If such permission is not obtained then that material may not be included in your publication/copies. Suitable acknowledgement to the source must be made, either as a footnote or in a reference list at the end of your publication, as follows:

"Reprinted from Publication title, Vol /edition number, Author(s), Title of article / title of chapter, Pages No., Copyright (Year), with permission from Elsevier [OR APPLICABLE SOCIETY COPYRIGHT OWNER]." Also Lancet special credit - "Reprinted from The Lancet, Vol. number, Author(s), Title of article, Pages No., Copyright (Year), with permission from Elsevier."

4. Reproduction of this material is confined to the purpose and/or media for which permission is hereby given. The material may not be reproduced or used in any other way, including use in combination with an artificial intelligence tool (including to train an algorithm, test, process, analyse, generate output and/or develop any form of artificial intelligence tool), or to create any derivative work and/or service (including resulting from the use of artificial intelligence tools).

5. Altering/Modifying Material: Not Permitted. However figures and illustrations may be altered/adapted minimally to serve your work. Any other abbreviations, additions, deletions and/or any other alterations shall be made only with prior written authorization of Elsevier Ltd. (Please contact Elsevier's permissions helpdesk here). No modifications can be made to any Lancet figures/tables and they must be reproduced in full.

6. If the permission fee for the requested use of our material is waived in this instance, please be advised that your future requests for Elsevier materials may attract a fee.

7. Reservation of Rights: Publisher reserves all rights not specifically granted in the combination of (i) the license details provided by you and accepted in the course of this licensing transaction, (ii) these terms and conditions and (iii) CCC's Billing and Payment terms and conditions.

8. License Contingent Upon Payment: While you may exercise the rights licensed immediately upon issuance of the license at the end of the licensing process for the transaction, provided that you have disclosed complete and accurate details of your proposed use, no license is finally effective unless and until full payment is received from you (either by publisher or by CCC) as provided in CCC's Billing and Payment terms and conditions. If full payment is not received on a timely basis, then any license preliminarily granted shall be deemed automatically revoked and shall be void as if never granted. Further, in the event that you breach any of these terms and conditions or any of CCC's Billing and Payment terms and conditions, the license is automatically revoked and shall be void as if never granted. Use of materials as described in a revoked license, as well as any use of the materials beyond the scope of an unrevoked license, may constitute copyright infringement and publisher reserves the right to take any and all action to protect its copyright in the materials.

9. Warranties: Publisher makes no representations or warranties with respect to the licensed material.

10. Indemnity: You hereby indemnify and agree to hold harmless publisher and CCC, and their respective officers, directors, employees and agents, from and against any and all claims arising out of your use of the licensed material other than as specifically authorized pursuant to this license.

11. No Transfer of License: This license is personal to you and may not be sublicensed, assigned, or transferred by you to any other person without publisher's written permission.

12. No Amendment Except in Writing: This license may not be amended except in a writing signed by both parties (or, in the case of publisher, by CCC on publisher's behalf).

13. Objection to Contrary Terms: Publisher hereby objects to any terms contained in any purchase order, acknowledgment, check endorsement or other writing prepared by you, which terms are inconsistent with these terms and conditions or CCC's Billing and Payment terms and conditions. These terms and conditions, together with CCC's Billing and Payment terms and conditions (which are incorporated herein), comprise the entire agreement between you and publisher (and CCC) concerning this licensing transaction. In the event of any conflict between your obligations established by these terms and conditions and those established by CCC's Billing and Payment terms and conditions, these terms and conditions shall control.

14. Revocation: Elsevier or Copyright Clearance Center may deny the permissions described in this License at their sole discretion, for any reason or no reason, with a full refund payable to you. Notice of such denial will be made using the contact information provided by you. Failure to receive such notice will not alter or invalidate the denial. In no event will Elsevier or Copyright Clearance Center be responsible or liable for any costs, expenses or damage incurred by you as a result of a denial of your permission request, other than a refund of the amount(s) paid by you to Elsevier and/or Copyright Clearance Center for denied permissions.

LIMITED LICENSE

The following terms and conditions apply only to specific license types:

15. **Translation**: This permission is granted for non-exclusive world **English** rights only unless your license was granted for translation rights. If you licensed translation rights you may only translate this content into the languages you requested. A professional translator must perform all translations and reproduce the content word for word preserving the integrity of the article.

16. **Posting licensed content on any Website**: The following terms and conditions apply as follows: Licensing material from an Elsevier journal: All content posted to the web site must maintain the copyright information line on the bottom of each image; A hyper-text must be included to the Homepage of the journal from which you are licensing at http://www.sciencedirect.com/science/journal/xxxxx or the Elsevier homepage for books at http://www.elsevier.com; Central Storage: This license does not include permission for a scanned version of the material to be stored in a central repository such as that provided by Heron/XanEdu.

Licensing material from an Elsevier book: A hyper-text link must be included to the Elsevier homepage at http://www.elsevier.com . All content posted to the web site must maintain the copyright information line on the bottom of each image.

Posting licensed content on Electronic reserve: In addition to the above the following clauses are applicable: The web site must be password-protected and made available only to bona fide students registered on a relevant course. This permission is granted for 1 year only. You may obtain a new license for future website posting.

17. **For journal authors:** the following clauses are applicable in addition to the above:

Preprints:

A preprint is an author's own write-up of research results and analysis, it has not been peer-reviewed, nor has it had any other value added to it by a publisher (such as formatting, copyright, technical enhancement etc.).

Authors can share their preprints anywhere at any time. Preprints should not be added to or enhanced in any way in order to appear more like, or to substitute for, the final versions of articles however authors can update their preprints on arXiv or RePEc with their Accepted Author Manuscript (see below).

If accepted for publication, we encourage authors to link from the preprint to their formal publication via its DOI. Millions of researchers have access to the formal publications on ScienceDirect, and so links will help users to find, access, cite and use the best available version. Please note that Cell Press, The Lancet and some society-owned have different preprint policies. Information on these policies is available on the journal homepage.

Accepted Author Manuscripts: An accepted author manuscript is the manuscript of an article that has been accepted for publication and which typically includes author-incorporated changes suggested during submission, peer review and editor-author communications.

Authors can share their accepted author manuscript:

- immediately
  - via their non-commercial person homepage or blog
  - by updating a preprint in arXiv or RePEc with the accepted manuscript
  - via their research institute or institutional repository for internal institutional uses or as part of an invitation-only research collaboration work-group
  - directly by providing copies to their students or to research collaborators for their personal use
  - for private scholarly sharing as part of an invitation-only work group on commercial sites with which Elsevier has an agreement
- After the embargo period
  - via non-commercial hosting platforms such as their institutional repository
  - via commercial sites with which Elsevier has an agreement

In all cases accepted manuscripts should:

- link to the formal publication via its DOI
- bear a CC-BY-NC-ND license - this is easy to do
- if aggregated with other manuscripts, for example in a repository or other site, be shared in alignment with our hosting policy not be added to or enhanced in any way to appear more like, or to substitute for, the published journal article.

Published journal article (JPA): A published journal article (PJA) is the definitive final record of published research that appears or will appear in the journal and embodies all value-adding publishing activities including peer review co-ordination, copy-editing, formatting, (if relevant) pagination and online enrichment.

Policies for sharing publishing journal articles differ for subscription and gold open access articles:

Subscription Articles: If you are an author, please share a link to your article rather than the full-text. Millions of researchers have access to the formal publications on ScienceDirect, and so links will help your users to find, access, cite, and use the best available version.

Theses and dissertations which contain embedded PJAs as part of the formal submission can be posted publicly by the awarding institution with DOI links back to the formal publications on ScienceDirect.

If you are affiliated with a library that subscribes to ScienceDirect you have additional private sharing rights for others' research accessed under that agreement. This includes use

for classroom teaching and internal training at the institution (including use in course packs and courseware programs), and inclusion of the article for grant funding purposes.

Gold Open Access Articles: May be shared according to the author-selected end-user license and should contain a CrossMark logo, the end user license, and a DOI link to the formal publication on ScienceDirect.

Please refer to Elsevier's posting policy for further information.

18. **For book authors** the following clauses are applicable in addition to the above: Authors are permitted to place a brief summary of their work online only. You are not allowed to download and post the published electronic version of your chapter, nor may you scan the printed edition to create an electronic version. **Posting to a repository:** Authors are permitted to post a summary of their chapter only in their institution's repository.

19. **Thesis/Dissertation**: If your license is for use in a thesis/dissertation your thesis may be submitted to your institution in either print or electronic form. Should your thesis be published commercially, please reapply for permission. These requirements include permission for the Library and Archives of Canada to supply single copies, on demand, of the complete thesis and include permission for Proquest/UMI to supply single copies, on demand, of the complete thesis. Should your thesis be published commercially, please reapply for permission. Theses and dissertations which contain embedded PJAs as part of the formal submission can be posted publicly by the awarding institution with DOI links back to the formal publications on ScienceDirect.

Elsevier Open Access Terms and Conditions

You can publish open access with Elsevier in hundreds of open access journals or in nearly 2000 established subscription journals that support open access publishing. Permitted third party re-use of these open access articles is defined by the author's choice of Creative Commons user license. See our open access license policy for more information.

Terms & Conditions applicable to all Open Access articles published with Elsevier:

Any reuse of the article must not represent the author as endorsing the adaptation of the article nor should the article be modified in such a way as to damage the author's honour or reputation. If any changes have been made, such changes must be clearly indicated.

The author(s) must be appropriately credited and we ask that you include the end user license and a DOI link to the formal publication on ScienceDirect.

If any part of the material to be used (for example, figures) has appeared in our publication with credit or acknowledgement to another source it is the responsibility of the user to ensure their reuse complies with the terms and conditions determined by the rights holder.

Additional Terms & Conditions applicable to each Creative Commons user license:

CC BY: The CC-BY license allows users to copy, to create extracts, abstracts and new works from the Article, to alter and revise the Article and to make commercial use of the Article (including reuse and/or resale of the Article by commercial entities), provided the user gives appropriate credit (with a link to the formal publication through the relevant DOI), provides a link to the license, indicates if changes were made and the licensor is not represented as endorsing the use made of the work. The full details of the license are available at http://creativecommons.org/licenses/by/4.0.

CC BY NC SA: The CC BY-NC-SA license allows users to copy, to create extracts, abstracts and new works from the Article, to alter and revise the Article, provided this is not done for commercial purposes, and that the user gives appropriate credit (with a link to the formal publication through the relevant DOI), provides a link to the license, indicates if changes were made and the licensor is not represented as endorsing the use made of the work. Further, any new works must be made available on the same conditions. The full details of the license are available at http://creativecommons.org/licenses/by-nc-sa/4.0.

CC BY NC ND: The CC BY-NC-ND license allows users to copy and distribute the Article, provided this is not done for commercial purposes and further does not permit distribution of the Article if it is changed or edited in any way, and provided the user gives appropriate credit (with a link to the formal publication through the relevant DOI), provides a link to the license, and that the licensor is not represented as endorsing the use made of the work. The full details of the license are available at http://creativecommons.org/licenses/by-nc-nd/4.0. Any commercial reuse of Open Access articles published with a CC BY NC SA or CC BY NC ND license requires permission from Elsevier and will be subject to a fee.

Commercial reuse includes:

- Associating advertising with the full text of the Article
- Charging fees for document delivery or access
- Article aggregation
- Systematic distribution via e-mail lists or share buttons

Posting or linking by commercial companies for use by customers of those companies.

20. **Other Conditions**:

v1.10

Questions? **customercare@copyright.com**.

JOHN WILEY AND SONS LICENSE
TERMS AND CONDITIONS

Oct 14, 2023

This Agreement between Miss. Jia Guo ("You") and John Wiley and Sons ("John Wiley and Sons") consists of your license details and the terms and conditions provided by John Wiley and Sons and Copyright Clearance Center.

License Number	5647750823788
License date	Oct 14, 2023
Licensed Content Publisher	John Wiley and Sons
Licensed Content Publication	Advanced Materials
Licensed Content Title	Electroceramics: Characterization by Impedance Spectroscopy
Licensed Content Author	Anthony R. West, Derek C. Sinclair, John T. S. Irvine
Licensed Content Date	Sep 15, 2004
Licensed Content Volume	2
Licensed Content Issue	3
Licensed Content Pages	7
Type of use	Dissertation/Thesis
Requestor type	University/Academic
Format	Print and electronic
Portion	Figure/table

Number of figures/tables	1
Will you be translating?	No
Title of new work	Lanthanum Nickel Oxide-Based Double Perovskites and their Exsolution Phenomena
Institution name	Imperial College London
Expected presentation date	Dec 2023
Portions	table 1
Requestor Location	Miss. Jia Guo RSM, Imperial College London London, London SW7 2AZ United Kingdom Attn: Imperial College London
Publisher Tax ID	EU826007151
Total	0.00 GBP

Terms and Conditions

TERMS AND CONDITIONS

This copyrighted material is owned by or exclusively licensed to John Wiley & Sons, Inc. or one of its group companies (each a"Wiley Company") or handled on behalf of a society with which a Wiley Company has exclusive publishing rights in relation to a particular work (collectively "WILEY"). By clicking "accept" in connection with completing this licensing transaction, you agree that the following terms and conditions apply to this transaction (along with the billing and payment terms and conditions established by the Copyright Clearance Center Inc., ("CCC's Billing and Payment terms and conditions"), at the time that you opened your RightsLink account (these are available at any time at http://myaccount.copyright.com).

Terms and Conditions

- The materials you have requested permission to reproduce or reuse (the "Wiley Materials") are protected by copyright.
- You are hereby granted a personal, non-exclusive, non-sub licensable (on a stand-alone basis), non-transferable, worldwide, limited license to reproduce the Wiley

Materials for the purpose specified in the licensing process. This license, **and any CONTENT (PDF or image file) purchased as part of your order,** is for a one-time use only and limited to any maximum distribution number specified in the license. The first instance of republication or reuse granted by this license must be completed within two years of the date of the grant of this license (although copies prepared before the end date may be distributed thereafter). The Wiley Materials shall not be used in any other manner or for any other purpose, beyond what is granted in the license. Permission is granted subject to an appropriate acknowledgement given to the author, title of the material/book/journal and the publisher. You shall also duplicate the copyright notice that appears in the Wiley publication in your use of the Wiley Material. Permission is also granted on the understanding that nowhere in the text is a previously published source acknowledged for all or part of this Wiley Material. Any third party content is expressly excluded from this permission.

- With respect to the Wiley Materials, all rights are reserved. Except as expressly granted by the terms of the license, no part of the Wiley Materials may be copied, modified, adapted (except for minor reformatting required by the new Publication), translated, reproduced, transferred or distributed, in any form or by any means, and no derivative works may be made based on the Wiley Materials without the prior permission of the respective copyright owner.**For STM Signatory Publishers clearing permission under the terms of the STM Permissions Guidelines only, the terms of the license are extended to include subsequent editions and for editions in other languages, provided such editions are for the work as a whole in situ and does not involve the separate exploitation of the permitted figures or extracts,** You may not alter, remove or suppress in any manner any copyright, trademark or other notices displayed by the Wiley Materials. You may not license, rent, sell, loan, lease, pledge, offer as security, transfer or assign the Wiley Materials on a stand-alone basis, or any of the rights granted to you hereunder to any other person.
- The Wiley Materials and all of the intellectual property rights therein shall at all times remain the exclusive property of John Wiley & Sons Inc, the Wiley Companies, or their respective licensors, and your interest therein is only that of having possession of and the right to reproduce the Wiley Materials pursuant to Section 2 herein during the continuance of this Agreement. You agree that you own no right, title or interest in or to the Wiley Materials or any of the intellectual property rights therein. You shall have no rights hereunder other than the license as provided for above in Section 2. No right, license or interest to any trademark, trade name, service mark or other branding ("Marks") of WILEY or its licensors is granted hereunder, and you agree that you shall not assert any such right, license or interest with respect thereto
- NEITHER WILEY NOR ITS LICENSORS MAKES ANY WARRANTY OR REPRESENTATION OF ANY KIND TO YOU OR ANY THIRD PARTY, EXPRESS, IMPLIED OR STATUTORY, WITH RESPECT TO THE MATERIALS OR THE ACCURACY OF ANY INFORMATION CONTAINED IN THE MATERIALS, INCLUDING, WITHOUT LIMITATION, ANY IMPLIED WARRANTY OF MERCHANTABILITY, ACCURACY, SATISFACTORY QUALITY, FITNESS FOR A PARTICULAR PURPOSE, USABILITY, INTEGRATION OR NON-INFRINGEMENT AND ALL SUCH WARRANTIES ARE HEREBY EXCLUDED BY WILEY AND ITS LICENSORS AND WAIVED BY YOU.
- WILEY shall have the right to terminate this Agreement immediately upon breach of this Agreement by you.

- You shall indemnify, defend and hold harmless WILEY, its Licensors and their respective directors, officers, agents and employees, from and against any actual or threatened claims, demands, causes of action or proceedings arising from any breach of this Agreement by you.
- IN NO EVENT SHALL WILEY OR ITS LICENSORS BE LIABLE TO YOU OR ANY OTHER PARTY OR ANY OTHER PERSON OR ENTITY FOR ANY SPECIAL, CONSEQUENTIAL, INCIDENTAL, INDIRECT, EXEMPLARY OR PUNITIVE DAMAGES, HOWEVER CAUSED, ARISING OUT OF OR IN CONNECTION WITH THE DOWNLOADING, PROVISIONING, VIEWING OR USE OF THE MATERIALS REGARDLESS OF THE FORM OF ACTION, WHETHER FOR BREACH OF CONTRACT, BREACH OF WARRANTY, TORT, NEGLIGENCE, INFRINGEMENT OR OTHERWISE (INCLUDING, WITHOUT LIMITATION, DAMAGES BASED ON LOSS OF PROFITS, DATA, FILES, USE, BUSINESS OPPORTUNITY OR CLAIMS OF THIRD PARTIES), AND WHETHER OR NOT THE PARTY HAS BEEN ADVISED OF THE POSSIBILITY OF SUCH DAMAGES. THIS LIMITATION SHALL APPLY NOTWITHSTANDING ANY FAILURE OF ESSENTIAL PURPOSE OF ANY LIMITED REMEDY PROVIDED HEREIN.
- Should any provision of this Agreement be held by a court of competent jurisdiction to be illegal, invalid, or unenforceable, that provision shall be deemed amended to achieve as nearly as possible the same economic effect as the original provision, and the legality, validity and enforceability of the remaining provisions of this Agreement shall not be affected or impaired thereby.
- The failure of either party to enforce any term or condition of this Agreement shall not constitute a waiver of either party's right to enforce each and every term and condition of this Agreement. No breach under this agreement shall be deemed waived or excused by either party unless such waiver or consent is in writing signed by the party granting such waiver or consent. The waiver by or consent of a party to a breach of any provision of this Agreement shall not operate or be construed as a waiver of or consent to any other or subsequent breach by such other party.
- This Agreement may not be assigned (including by operation of law or otherwise) by you without WILEY's prior written consent.
- Any fee required for this permission shall be non-refundable after thirty (30) days from receipt by the CCC.
- These terms and conditions together with CCC's Billing and Payment terms and conditions (which are incorporated herein) form the entire agreement between you and WILEY concerning this licensing transaction and (in the absence of fraud) supersedes all prior agreements and representations of the parties, oral or written. This Agreement may not be amended except in writing signed by both parties. This Agreement shall be binding upon and inure to the benefit of the parties' successors, legal representatives, and authorized assigns.
- In the event of any conflict between your obligations established by these terms and conditions and those established by CCC's Billing and Payment terms and conditions, these terms and conditions shall prevail.
- WILEY expressly reserves all rights not specifically granted in the combination of (i) the license details provided by you and accepted in the course of this licensing transaction, (ii) these terms and conditions and (iii) CCC's Billing and Payment terms and conditions.

- This Agreement will be void if the Type of Use, Format, Circulation, or Requestor Type was misrepresented during the licensing process.

- This Agreement shall be governed by and construed in accordance with the laws of the State of New York, USA, without regards to such state's conflict of law rules. Any legal action, suit or proceeding arising out of or relating to these Terms and Conditions or the breach thereof shall be instituted in a court of competent jurisdiction in New York County in the State of New York in the United States of America and each party hereby consents and submits to the personal jurisdiction of such court, waives any objection to venue in such court and consents to service of process by registered or certified mail, return receipt requested, at the last known address of such party.

WILEY OPEN ACCESS TERMS AND CONDITIONS

Wiley Publishes Open Access Articles in fully Open Access Journals and in Subscription journals offering Online Open. Although most of the fully Open Access journals publish open access articles under the terms of the Creative Commons Attribution (CC BY) License only, the subscription journals and a few of the Open Access Journals offer a choice of Creative Commons Licenses. The license type is clearly identified on the article.

The Creative Commons Attribution License

The Creative Commons Attribution License (CC-BY) allows users to copy, distribute and transmit an article, adapt the article and make commercial use of the article. The CC-BY license permits commercial and non-

Creative Commons Attribution Non-Commercial License

The Creative Commons Attribution Non-Commercial (CC-BY-NC)License permits use, distribution and reproduction in any medium, provided the original work is properly cited and is not used for commercial purposes.(see below)

Creative Commons Attribution-Non-Commercial-NoDerivs License

The Creative Commons Attribution Non-Commercial-NoDerivs License (CC-BY-NC-ND) permits use, distribution and reproduction in any medium, provided the original work is properly cited, is not used for commercial purposes and no modifications or adaptations are made. (see below)

Use by commercial "for-profit" organizations

Use of Wiley Open Access articles for commercial, promotional, or marketing purposes requires further explicit permission from Wiley and will be subject to a fee.

Further details can be found on Wiley Online Library
http://olabout.wiley.com/WileyCDA/Section/id-410895.html

Other Terms and Conditions:

v1.10 Last updated September 2015

Questions? customercare@copyright.com.

ELSEVIER LICENSE
TERMS AND CONDITIONS

Oct 15, 2023

This Agreement between Miss. Jia Guo ("You") and Elsevier ("Elsevier") consists of your license details and the terms and conditions provided by Elsevier and Copyright Clearance Center.

License Number	5650351475792
License date	Oct 15, 2023
Licensed Content Publisher	Elsevier
Licensed Content Publication	Catalysis Today
Licensed Content Title	The intelligent catalyst having the self-regenerative function of Pd, Rh and Pt for automotive emissions control
Licensed Content Author	Hirohisa Tanaka,Mari Uenishi,Masashi Taniguchi,Isao Tan,Keiichi Narita,Mareo Kimura,Kimiyoshi Kaneko,Yasuo Nishihata,Jun'ichiro Mizuki
Licensed Content Date	Sep 30, 2006
Licensed Content Volume	117
Licensed Content Issue	1-3
Licensed Content Pages	8
Start Page	321
End Page	328
Type of Use	reuse in a thesis/dissertation

Portion	figures/tables/illustrations
Number of figures/tables/illustrations	1
Format	both print and electronic
Are you the author of this Elsevier article?	No
Will you be translating?	No
Title of new work	Lanthanum Nickel Oxide-Based Double Perovskites and their Exsolution Phenomena
Institution name	Imperial College London
Expected presentation date	Dec 2023
Portions	Figure12
Requestor Location	Miss. Jia Guo RSM, Imperial College London London, London SW7 2AZ United Kingdom Attn: Imperial College London
Publisher Tax ID	GB 494 6272 12
Total	0.00 GBP

Terms and Conditions

INTRODUCTION

1. The publisher for this copyrighted material is Elsevier. By clicking "accept" in connection with completing this licensing transaction, you agree that the following terms and conditions apply to this transaction (along with the Billing and Payment terms and conditions established by Copyright Clearance Center, Inc. ("CCC"), at the time that you opened your RightsLink account and that are available at any time at https://myaccount.copyright.com).

GENERAL TERMS

2. Elsevier hereby grants you permission to reproduce the aforementioned material subject to the terms and conditions indicated.

3. Acknowledgement: If any part of the material to be used (for example, figures) has appeared in our publication with credit or acknowledgement to another source, permission must also be sought from that source. If such permission is not obtained then that material may not be included in your publication/copies. Suitable acknowledgement to the source must be made, either as a footnote or in a reference list at the end of your publication, as follows:

"Reprinted from Publication title, Vol /edition number, Author(s), Title of article / title of chapter, Pages No., Copyright (Year), with permission from Elsevier [OR APPLICABLE SOCIETY COPYRIGHT OWNER]." Also Lancet special credit - "Reprinted from The Lancet, Vol. number, Author(s), Title of article, Pages No., Copyright (Year), with permission from Elsevier."

4. Reproduction of this material is confined to the purpose and/or media for which permission is hereby given. The material may not be reproduced or used in any other way, including use in combination with an artificial intelligence tool (including to train an algorithm, test, process, analyse, generate output and/or develop any form of artificial intelligence tool), or to create any derivative work and/or service (including resulting from the use of artificial intelligence tools).

5. Altering/Modifying Material: Not Permitted. However figures and illustrations may be altered/adapted minimally to serve your work. Any other abbreviations, additions, deletions and/or any other alterations shall be made only with prior written authorization of Elsevier Ltd. (Please contact Elsevier's permissions helpdesk here). No modifications can be made to any Lancet figures/tables and they must be reproduced in full.

6. If the permission fee for the requested use of our material is waived in this instance, please be advised that your future requests for Elsevier materials may attract a fee.

7. Reservation of Rights: Publisher reserves all rights not specifically granted in the combination of (i) the license details provided by you and accepted in the course of this licensing transaction, (ii) these terms and conditions and (iii) CCC's Billing and Payment terms and conditions.

8. License Contingent Upon Payment: While you may exercise the rights licensed immediately upon issuance of the license at the end of the licensing process for the transaction, provided that you have disclosed complete and accurate details of your proposed use, no license is finally effective unless and until full payment is received from you (either by publisher or by CCC) as provided in CCC's Billing and Payment terms and conditions. If full payment is not received on a timely basis, then any license preliminarily granted shall be deemed automatically revoked and shall be void as if never granted. Further, in the event that you breach any of these terms and conditions or any of CCC's Billing and Payment terms and conditions, the license is automatically revoked and shall be void as if never granted. Use of materials as described in a revoked license, as well as any use of the materials beyond the scope of an unrevoked license, may constitute copyright infringement and publisher reserves the right to take any and all action to protect its copyright in the materials.

9. Warranties: Publisher makes no representations or warranties with respect to the licensed material.

10. Indemnity: You hereby indemnify and agree to hold harmless publisher and CCC, and their respective officers, directors, employees and agents, from and against any and all

claims arising out of your use of the licensed material other than as specifically authorized pursuant to this license.

11. No Transfer of License: This license is personal to you and may not be sublicensed, assigned, or transferred by you to any other person without publisher's written permission.

12. No Amendment Except in Writing: This license may not be amended except in a writing signed by both parties (or, in the case of publisher, by CCC on publisher's behalf).

13. Objection to Contrary Terms: Publisher hereby objects to any terms contained in any purchase order, acknowledgment, check endorsement or other writing prepared by you, which terms are inconsistent with these terms and conditions or CCC's Billing and Payment terms and conditions. These terms and conditions, together with CCC's Billing and Payment terms and conditions (which are incorporated herein), comprise the entire agreement between you and publisher (and CCC) concerning this licensing transaction. In the event of any conflict between your obligations established by these terms and conditions and those established by CCC's Billing and Payment terms and conditions, these terms and conditions shall control.

14. Revocation: Elsevier or Copyright Clearance Center may deny the permissions described in this License at their sole discretion, for any reason or no reason, with a full refund payable to you. Notice of such denial will be made using the contact information provided by you. Failure to receive such notice will not alter or invalidate the denial. In no event will Elsevier or Copyright Clearance Center be responsible or liable for any costs, expenses or damage incurred by you as a result of a denial of your permission request, other than a refund of the amount(s) paid by you to Elsevier and/or Copyright Clearance Center for denied permissions.

LIMITED LICENSE

The following terms and conditions apply only to specific license types:

15. **Translation**: This permission is granted for non-exclusive world **English** rights only unless your license was granted for translation rights. If you licensed translation rights you may only translate this content into the languages you requested. A professional translator must perform all translations and reproduce the content word for word preserving the integrity of the article.

16. **Posting licensed content on any Website**: The following terms and conditions apply as follows: Licensing material from an Elsevier journal: All content posted to the web site must maintain the copyright information line on the bottom of each image; A hyper-text must be included to the Homepage of the journal from which you are licensing at http://www.sciencedirect.com/science/journal/xxxxx or the Elsevier homepage for books at http://www.elsevier.com; Central Storage: This license does not include permission for a scanned version of the material to be stored in a central repository such as that provided by Heron/XanEdu.

Licensing material from an Elsevier book: A hyper-text link must be included to the Elsevier homepage at http://www.elsevier.com . All content posted to the web site must maintain the copyright information line on the bottom of each image.

Posting licensed content on Electronic reserve: In addition to the above the following clauses are applicable: The web site must be password-protected and made available only to bona fide students registered on a relevant course. This permission is granted for 1 year only. You may obtain a new license for future website posting.

17. **For journal authors**: the following clauses are applicable in addition to the above:

Preprints:

A preprint is an author's own write-up of research results and analysis, it has not been peer-reviewed, nor has it had any other value added to it by a publisher (such as formatting, copyright, technical enhancement etc.).

Authors can share their preprints anywhere at any time. Preprints should not be added to or enhanced in any way in order to appear more like, or to substitute for, the final versions of articles however authors can update their preprints on arXiv or RePEc with their Accepted Author Manuscript (see below).

If accepted for publication, we encourage authors to link from the preprint to their formal publication via its DOI. Millions of researchers have access to the formal publications on ScienceDirect, and so links will help users to find, access, cite and use the best available version. Please note that Cell Press, The Lancet and some society-owned have different preprint policies. Information on these policies is available on the journal homepage.

Accepted Author Manuscripts: An accepted author manuscript is the manuscript of an article that has been accepted for publication and which typically includes author-incorporated changes suggested during submission, peer review and editor-author communications.

Authors can share their accepted author manuscript:

- immediately
  - via their non-commercial person homepage or blog
  - by updating a preprint in arXiv or RePEc with the accepted manuscript
  - via their research institute or institutional repository for internal institutional uses or as part of an invitation-only research collaboration work-group
  - directly by providing copies to their students or to research collaborators for their personal use
  - for private scholarly sharing as part of an invitation-only work group on commercial sites with which Elsevier has an agreement
- After the embargo period
  - via non-commercial hosting platforms such as their institutional repository
  - via commercial sites with which Elsevier has an agreement

In all cases accepted manuscripts should:

- link to the formal publication via its DOI
- bear a CC-BY-NC-ND license - this is easy to do
- if aggregated with other manuscripts, for example in a repository or other site, be shared in alignment with our hosting policy not be added to or enhanced in any way to appear more like, or to substitute for, the published journal article.

Published journal article (JPA): A published journal article (PJA) is the definitive final record of published research that appears or will appear in the journal and embodies all value-adding publishing activities including peer review co-ordination, copy-editing, formatting, (if relevant) pagination and online enrichment.

Policies for sharing publishing journal articles differ for subscription and gold open access articles:

Subscription Articles: If you are an author, please share a link to your article rather than the full-text. Millions of researchers have access to the formal publications on ScienceDirect, and so links will help your users to find, access, cite, and use the best available version.

Theses and dissertations which contain embedded PJAs as part of the formal submission can be posted publicly by the awarding institution with DOI links back to the formal publications on ScienceDirect.

If you are affiliated with a library that subscribes to ScienceDirect you have additional private sharing rights for others' research accessed under that agreement. This includes use for classroom teaching and internal training at the institution (including use in course packs and courseware programs), and inclusion of the article for grant funding purposes.

Gold Open Access Articles: May be shared according to the author-selected end-user license and should contain a CrossMark logo, the end user license, and a DOI link to the formal publication on ScienceDirect.

Please refer to Elsevier's posting policy for further information.

18. **For book authors** the following clauses are applicable in addition to the above: Authors are permitted to place a brief summary of their work online only. You are not allowed to download and post the published electronic version of your chapter, nor may you scan the printed edition to create an electronic version. **Posting to a repository:** Authors are permitted to post a summary of their chapter only in their institution's repository.

19. **Thesis/Dissertation**: If your license is for use in a thesis/dissertation your thesis may be submitted to your institution in either print or electronic form. Should your thesis be published commercially, please reapply for permission. These requirements include permission for the Library and Archives of Canada to supply single copies, on demand, of the complete thesis and include permission for Proquest/UMI to supply single copies, on demand, of the complete thesis. Should your thesis be published commercially, please reapply for permission. Theses and dissertations which contain embedded PJAs as part of the formal submission can be posted publicly by the awarding institution with DOI links back to the formal publications on ScienceDirect.

Elsevier Open Access Terms and Conditions

You can publish open access with Elsevier in hundreds of open access journals or in nearly 2000 established subscription journals that support open access publishing. Permitted third party re-use of these open access articles is defined by the author's choice of Creative Commons user license. See our open access license policy for more information.

Terms & Conditions applicable to all Open Access articles published with Elsevier:

Any reuse of the article must not represent the author as endorsing the adaptation of the article nor should the article be modified in such a way as to damage the author's honour or reputation. If any changes have been made, such changes must be clearly indicated.

The author(s) must be appropriately credited and we ask that you include the end user license and a DOI link to the formal publication on ScienceDirect.

If any part of the material to be used (for example, figures) has appeared in our publication with credit or acknowledgement to another source it is the responsibility of the user to ensure their reuse complies with the terms and conditions determined by the rights holder.

Additional Terms & Conditions applicable to each Creative Commons user license:

CC BY: The CC-BY license allows users to copy, to create extracts, abstracts and new works from the Article, to alter and revise the Article and to make commercial use of the Article (including reuse and/or resale of the Article by commercial entities), provided the user gives appropriate credit (with a link to the formal publication through the relevant DOI), provides a link to the license, indicates if changes were made and the licensor is not represented as endorsing the use made of the work. The full details of the license are available at http://creativecommons.org/licenses/by/4.0.

CC BY NC SA: The CC BY-NC-SA license allows users to copy, to create extracts, abstracts and new works from the Article, to alter and revise the Article, provided this is not done for commercial purposes, and that the user gives appropriate credit (with a link to the formal publication through the relevant DOI), provides a link to the license, indicates if changes were made and the licensor is not represented as endorsing the use made of the work. Further, any new works must be made available on the same conditions. The full details of the license are available at http://creativecommons.org/licenses/by-nc-sa/4.0.

CC BY NC ND: The CC BY-NC-ND license allows users to copy and distribute the Article, provided this is not done for commercial purposes and further does not permit distribution of the Article if it is changed or edited in any way, and provided the user gives appropriate credit (with a link to the formal publication through the relevant DOI), provides a link to the license, and that the licensor is not represented as endorsing the use made of the work. The full details of the license are available at http://creativecommons.org/licenses/by-nc-nd/4.0. Any commercial reuse of Open Access articles published with a CC BY NC SA or CC BY NC ND license requires permission from Elsevier and will be subject to a fee.

Commercial reuse includes:

- Associating advertising with the full text of the Article
- Charging fees for document delivery or access
- Article aggregation
- Systematic distribution via e-mail lists or share buttons

Posting or linking by commercial companies for use by customers of those companies.

20. **Other Conditions**:

v1.10

Questions? customercare@copyright.com.